

Sediment Suspension Under Water Waves

by

Nicole Metje

A thesis submitted to the Faculty of Engineering of
The University of Birmingham
for the degree of
DOCTOR OF PHILOSOPHY

**School of Civil Engineering
Faculty of Engineering
The University of Birmingham
August 2001**

UNIVERSITY OF
BIRMINGHAM

University of Birmingham Research Archive

e-theses repository

This unpublished thesis/dissertation is copyright of the author and/or third parties. The intellectual property rights of the author or third parties in respect of this work are as defined by The Copyright Designs and Patents Act 1988 or as modified by any successor legislation.

Any use made of information contained in this thesis/dissertation must be in accordance with that legislation and must be properly acknowledged. Further distribution or reproduction in any format is prohibited without the permission of the copyright holder.

Abstract – Sediment Suspension Under Water Waves

Data collected in a large scale laboratory wave flume by a research team using the autonomous bottom boundary layer rig, (STABLE) was the subject of this study.

The near bed suspension processes were examined relating them to the hydrodynamics. The deployment of a number of sensors allowed the assessment of their individual performance including the analysis of the pump-sampling and acoustic concentration data.

Wavelet analysis was applied to identify the influence of STABLE on the vortex ripples in the vicinity of the rig. It revealed that the modification of the ripple dimensions around STABLE's feet was very localised.

Sediment suspension was found to be strongly correlated to wave groups. The measured concentrations and empirical models based on convective and diffusive entrainment mechanisms were compared. A model based on the jet like ejection of particles between a vortex pair was developed and showed that lifting of sediments up to ten ripple heights above the bed was possible. A second model, capable of simulating the pumping effect, included this entrainment process to simulate the suspension under wave groups taking the suspension history into account.

The behaviour of neutrally buoyant particles in a laboratory wave flume was videoed and revealed jet like ejections and horizontal movement over two or more ripple wavelengths.

Acknowledgements

This research project was jointly funded by The University of Birmingham as part of the PGTA programme and Proudman Oceanographic Laboratory (POL) as part of the MAST3 project 'Inlet Dynamics Initiative: Algarve' (INDIA), contract MAS3-CT97-0106.

Special thanks go to:

Dr Lawrence Coates for his supervision, essential guidance, continuing support and inspiration, especially at difficult times throughout the PhD.

Dr Jon Williams from POL for his encouragement and support. Without him the project would not have been possible. Rafi Selwyn for his continuous help with Matlab and the data at the beginning of the project.

Dr Phil Atkins for his continuous support with Matlab and any other questions regarding data analysis. The design and build of the plastic rippled bed for the laboratory wave flume.

All my friends outside the university, who provided encouragement and several meals at vital times. Tess for checking my English.

My friends in the office (Ana, Ben, Hannah, Jay, Jon, Kate, Mark, Neerja, Nick, Perry) for their patience in answering my numerous questions.

Ein spezielles Dankeschön an Prof. R.B. Rokahr vom Institut für Unterirdisches Bauen der Universität Hannover. Ohne seine Ermutigungen und dem Vertrauen in meine Fähigkeiten würde es diese Dissertation nicht geben. Danke auch an Alfred Stärk, dessen Computer ich in Hannover jeder Zeit benutzen durfte und für seine endlose Hilfe in den letzten drei Jahren.

Zum guten Schluß ein grosses Dankeschön an meine Eltern dafür, daß sie nie den Glauben in mich verloren haben.

Contents	page
List of Tables	i
List of Figures	iv
Acronyms and Abbreviations	xiv
Notation	xv
Chapter 1 - Introduction	1
1.1 Introduction	1
1.2 Background	2
1.3 Study Objectives	3
1.4 Structure of the Thesis	3
Figures	5
Chapter 2 - Literature Review	7
2.1 Wave Parameters and Theories	7
2.1.1 Regular Wave Parameters	7
2.1.2 Linear Wave Theory.....	7
2.1.3 Stokes' Higher Order Wave Theories.....	10
2.1.4 Other Higher Order Wave Theories	12
2.1.5 Sea Waves.....	12
2.2 Wave Groups	14
2.3 Bedforms in Oscillatory Flow	16
2.3.1 Mechanism.....	16
2.3.2 Bedform dimensions	18
2.4 Wave Induced Suspended Sediment Concentration Profiles and Transport	22
2.4.1 Introduction	22
2.4.2 Shear stress in oscillatory flow	22

2.4.3	Threshold for initiation of motion under waves	25
2.4.4	Settling Velocity	27
2.4.5	Suspended Sediment Concentration Profiles.....	28
2.4.5.1	Theoretical Background	28
2.4.5.2	Mean Suspended Sediment Concentration Profiles.....	30
2.4.5.3	Expressions for the Reference Concentration	33
2.4.5.4	Examples of Field Measurements of Suspended Sediment Concentrations.....	34
2.4.6	Sediment Transport Rate	38
2.4.6.1	Introduction	38
2.4.6.2	Sediment Transport	40
2.5	Summary	41
Tables	44
Figures	45
Chapter - 3	Instrumentation and Preliminary Data Analysis	57
3.1	Laboratory Work.....	57
3.1.1	Deltaflume.....	57
3.2	Instrumentation	58
3.2.1	Instrumentation on STABLE.....	58
3.2.2	Delft Hydraulics Instrumentation	62
3.3	Data Collection	63
3.4	Data Calibration	63
3.4.1	Pressure and Velocity Data.....	63
3.4.2	ABS Calibration.....	64
3.4.3	Pump Samples.....	65
3.4.4	Acoustic Sand Ripple Profiler Calibration.....	66
3.5	Preliminary Data Analysis	67
3.5.1	Reflection Analysis.....	67
3.5.2	STABLE Velocity Data	68

3.5.3 Pump Samples.....	69
3.5.3.1 Differences between STABLE and DH pump samples.....	69
3.5.3.2 Conclusions.....	74
3.5.4 Acoustic BackScatter Data (ABS).....	76
3.5.4.1 Bed position and bedform geometry.....	76
3.5.4.2 Burst averaged concentration profiles.....	78
3.6 Summary.....	78
Tables.....	80
Figures.....	85

Chapter – 4 Influence of STABLE on its measuring environment..... 103

4.1 Introduction.....	103
4.2 Available Profile Data.....	104
4.3 Analysing Ripple Profiles using Conventional Techniques.....	104
4.4 Motivation for the use of Wavelet Transforms.....	107
4.5 Analysing Ripple Profiles using Wavelets.....	108
4.5.1 Behaviour of Wavelet Transforms with respect to the Data and the Wavelet Functions.....	108
4.5.2 Analysing the Profiling Data using the Morlet Wavelet.....	110
4.6 Conclusions.....	112
4.7 Acknowledgement.....	113
Tables.....	114
Figures.....	121

Chapter - 5 Suspended Sediment Concentrations..... 135

5.1 Mean concentration profiles.....	135
5.1.1 Presentation of results.....	135
5.1.2 Discussion of results.....	140
5.2 Comparison of averaged measured and predicted c-profiles.....	144

5.2.1	Introduction	144
5.2.2	Diffusion, pure convection and combined diffusion/ convection model proposed by Nielsen for the prediction of mean sediment concentration profiles	144
5.2.3	Rouse type concentration profiles	148
5.2.4	Summary	149
5.3	Ensemble averaged c-profiles over a wave cycle for regular waves	151
5.4	Comparison with pump-sampling data	155
5.4.1	Presentation of results	155
5.4.2	Discussion of results and conclusions	155
5.5	Summary and Conclusions	156
	Tables	159
	Figures	161
Chapter - 6	Intra-wave Suspended Sediment Concentration	186
6.1	Introduction	186
6.2	Averaged concentration profiles for different time scales	186
6.2.1	Ten minute averaged concentration	186
6.2.2	One minute averaged concentration	187
6.2.3	Discussion of the results and conclusions	187
6.3	Influence of wave groups	188
6.3.1	Presentation of the data	190
6.3.1.1	Cycle mean profiles of wave groups	190
6.3.1.2	Instantaneous sediment concentrations for wave groups	191
6.3.2	Discussion of results and conclusions	192
6.4	Comparison with field data (MK Bank data)	194
6.4.1	Description of the field conditions	194
6.4.2	Wave groups in the field data	195
6.4.3	Discussion of results and conclusions	196

6.5 A simple model to predict c-profiles under a wave group	197
6.5.1 Background.....	197
6.5.2 Results of the model	199
6.5.3 Discussion and Conclusions	200
6.6 Conclusions	201
Tables	203
Figures	204
Chapter - 7 Vortex Ejections from a rippled bed	216
7.1 Introduction	216
7.2 Evidence of vortices in the literature.....	217
7.3 Visualising vortices ejected from a rippled bed in a laboratory wave flume.....	219
7.3.1 Laboratory Experiment.....	219
7.4 A simple model to determine the influence of a vortex pair on a single particle of sand.....	222
7.4.1 Simplifications for the modelling of vortex ejection.....	225
7.4.2 Sensitivity Analysis of the Model.....	227
7.5 Summary and Conclusions	231
Tables	233
Figures	236
Chapter – 8 Conclusions and Recommendations for Future Work	256
8.1 Conclusions	256
8.2 Recommendations for Future Work.....	259
References	262
Appendix A	272
A.1 Reflection analysis	274

Appendix B	276
B.1 Wavelets	276
B.2 The Continuous Wavelet Transform	276
B.3 Wavelet Energy Density	279
B.4 Wavelet Thresholding	279
B.5 Significance Tests	280
Appendix C	281
C.1 Sediments	281
C.2 Hydrodynamics	282
C.3 Concentration profiles	282
Figures	285
Publications	287

LIST OF TABLES

	<i>Page</i>
2.1 Classification of bedforms as a function of the dimensionless grain diameter D_* (equation 2.34) and the dimensionless bed shear stress parameter T_* (equation 2.35) after VAN RIJN (1989).	44
3.1 Chronological summary of <i>Deltaflume</i> tests, medium sand bed ($d_{50} = 0.329$ mm). The camera fitted on STABLE did not record useful pictures owing to the fine sand in suspension.	80
3.2 Chronological summary of <i>Deltaflume</i> tests, fine sand bed ($d_{50} = 0.162$ mm).	81
3.3 Summary of instrument positions on the STABLE frame using the x, y and z co-ordinate convention illustrated in figure 3.1.	82
3.4 Summary of the overall dimensions and weight of STABLE.	82
3.5 Values of m_0 for the horizontal velocity at STABLE and Delft Hydraulics for the first and second half of a number of bursts.	83
3.6 Bin numbers referring to the position of the peak backscatter signal for the raw ABS data.	83
3.7 Ripple dimensions determined from the acoustic ripple profiler data and predictions using Nielsen's equation for <i>regular waves</i> for the bursts where STABLE is aligned with the flume. The grey shaded cells indicate regular waves.	84
4.1 Positions of the bins for the profiles of survey DBP-1.	114
4.2 Positions of the bins for the profiles of all other surveys.	114
4.3 Average ripple wavelength λ_r in metres from zero down-crossing analysis of profiles of survey DBP-1 after passing the data through a Butterworth bandpass filter.	114
4.4 Average ripple wave height h_r in metres from zero down-crossing analysis of profiles of survey DBP-1 after passing the data through a Butterworth bandpass filter.	115
4.5 Average ripple wavelength λ_r in metres from zero down-crossing analysis of profiles of survey DBP-2 after passing the data through a Butterworth bandpass filter.	115
4.6 Average ripple wave height h_r in metres from zero down-crossing analysis of profiles of survey DBP-2 after passing the data through a Butterworth bandpass filter.	116

4.7	Average ripple wavelength λ_r in metres from zero down-crossing analysis of profiles of survey DBP-3 after passing the data through a Butterworth bandpass filter.	116
4.8	Average ripple wave height h_r in metres from zero down-crossing analysis of profiles of survey DBP-3 after passing the data through a Butterworth bandpass filter.	117
4.9	Average ripple wavelength λ_r in metres from zero down-crossing analysis of profiles of survey DBP-4 after passing the data through a Butterworth bandpass filter.	117
4.10	Average ripple wave height h_r in metres from zero down-crossing analysis of profiles of survey DBP-4 after passing the data through a Butterworth bandpass filter.	118
4.11	Peak ripple wavelength λ_r in metres determined from a FFT for the profiles of survey DBP-1 after passing the data through a Butterworth bandpass filter.	118
4.12	Peak ripple wavelength λ_r in metres determined from a FFT for the profiles of survey DBP-2 after passing the data through a Butterworth bandpass filter.	119
4.13	Peak ripple wavelength λ_r in metres determined from a FFT for the profiles of survey DBP-1 after passing the data through a Butterworth bandpass filter.	119
4.14	Peak ripple wavelength λ_r in metres determined from a FFT for the profiles of survey DBP-4 after passing the data through a Butterworth bandpass filter.	120
5.1	Gradients (absolute values) within the first 3 cm above the bed and main gradient for the bursts with irregular waves on a semilogarithmic plot. They are compared with the theoretical values given by the empirical equation by Nielsen and the Rouse type profile. The gradient determined by the equation suggested by Nielsen is constant for the whole profile. The wave height increases from burst a07a to a12a.	159
5.2	Concentration 1 cm above the bed for burst averaged c-profiles for bursts with irregular waves. The wave height increases from burst a07a to a12a.	159
5.3	Input and calculated parameters used to determine concentration profiles on the medium sand bed.	160
6.1	Relevant wave parameters of the wave group used for the development of the simple model to predict the sediment concentration profiles throughout a wave group.	203
6.2	Model parameters used to simulate the re-suspension of sediment under a wave group due to a convective mechanism (vortex pair).	203
7.1	Initial parameters of the convective entrainment model.	233
7.2	Change in maximum height of the vortex pair, the sediment particle and the time the particle hits the bed with variation of the ripple height. The numbers in bold indicate the initial parameters chosen for the model.	233

7.3	Change in maximum height of the vortex pair, the sediment particle and the time the particle hits the bed with variation of the orbital velocity. The numbers in bold indicate the initial parameters chosen for the model.	234
7.4	Change in maximum height of the vortex pair, the sediment particle and the time the particle hits the bed with variation of the drag coefficient. The numbers in bold indicate the initial parameters chosen for the model.	234
7.5	Change in maximum height of the vortex pair, the sediment particle and the time the particle hits the bed with variation of the enhanced kinematic viscosity. The numbers in bold indicate the initial parameters chosen for the model.	235
7.6	Change in maximum height of the vortex pair, the sediment particle and the time the particle hits the bed with variation of the sediment diameter. The numbers in bold indicate the initial parameters chosen for the model.	235

LIST OF FIGURES

	Page
1.1 a) The autonomous measuring rig STABLE with the three ECMs, the ADV, the pump-sampling array and the three ABS, being lowered into the <i>Deltaflume</i> . b) detailed view of STABLE with the ECMs, ABS, ARP and pump-sampling array.	5
1.2 The <i>Deltaflume</i> at Delft Hydraulics. a) dimensions of the <i>Deltaflume</i> and the medium sand bed before filling the flume. b) large waves in the <i>Deltaflume</i> .	6
2.1 A regular, two-dimensional wave of height H and wavelength L, in water of depth h.	45
2.2 Wave elevation, with a wavelength of 30.11 m, a period of 5.11 s and a wave height of 1 m, calculated using linear and Stokes' second order wave theories.	45
2.3 Validation of wave theories as a function of water depth (note, d is the water depth here), wave height and period (after LE MEHAUTE, 1969). The red line indicates the range of the experiments in the <i>Deltaflume</i> .	46
2.4 Definition of zero down- and up-crossings. Zero down-crossing has been used throughout the present data analysis.	47
2.5 Schematic of a wave record with definition of A, B, C and D as used for the Tucker method (see figure 2.6).	47
2.6 Relationship between a_{rms} and N_z according to the Tucker Method (Sylvester, 1974).	47
2.7 Sketch of the definitions used to calculate the run length (after GODA, 1985).	48
2.8 Classification of bedforms for unidirectional flow as a function of the dimensionless diameter D_* and a bed shear stress parameter T_* . (VAN RIJN, 1989, figure 6.1.2).	49
2.9 Friction factor for waves as a function of the relative roughness determined by equations given by NIELSEN (1992) and SOULSBY (1997). The red lines indicate the range of relative roughness for the <i>Deltaflume</i> experiments.	50
2.10 Forces on a sediment particle due to steady flow.	50
2.11 Shields's curve showing the threshold of sediment movement and the bed formations developing for different grain sizes and flows. Taken from SHIELDS, 1936.	51
2.12 Shields's diagram with the extension of MILLER ET AL. (1977) for small sediment diameters taken from VAN RIJN (1989), (figure 5.1.1).	52
2.13 Shields's curve including some field and wave flume measurements for wave conditions. The error bars indicate the influence of the wave period and the grain roughness (from VAN RIJN (1989), figure 5.4.1).	53

2.14	Threshold orbital velocity as a function of the characteristic wave period and the median grain diameter. The kinematic viscosity was 0.014 cm ² /s and the sediment density was 2.85 g/cm ³ (after SEYMOUR, 1985).	54
2.15	Threshold orbital velocity as a function of the characteristic wave period and the median grain diameter for sea water with a salinity of 35 ppt (after SOULSBY, 1997).	54
2.16	Settling of particles in still and turbulent water, respectively influencing the settling velocity (from NIELSEN, 1992).	55
2.17	Sediment diffusivities derived through equation 2.61 from measured concentration profiles $c(z)$ under the assumption of pure gradient diffusion. Different sediment sizes give different values for the diffusivity ϵ_s (after NIELSEN, 1992, figure 5.1.2. Data from COLEMAN, 1970). Note, D is the water depth.	55
2.18	Time averaged sediment concentrations \bar{c}_z measured over vortex ripples in an oscillating water tunnel. In all cases the sand size was 0.2 mm. Data from BOSMAN, 1982 and DELFT HYDRAULICS, 1989. (Figure from NIELSEN (1992), figure 5.2.7).	56
2.19	In a short time interval δ_t the amount of sand picked up per unit area is $P \cdot \delta_t$. If the average distance travelled by the moving sediment is l_x , the corresponding sediment transport through one unit width of the plane A is seen to be $l_x \cdot P \cdot \delta_t$ (after NIELSEN, 1992, figure 6.2.1).	56
3.1	Cumulative grain size distribution for medium and fine sands used in the <i>Deltaflume</i> tests.	85
3.2	STABLE: a) front elevation, b) side elevation and c) plan. For dimensions and rig statistics see tables 3.3 and 3.4.	86
3.3	Collection of suspended sediment samples from the <i>Deltaflume</i> using pump-sampling equipment.	87
3.4	Schematic of the acoustic ripple profiler (ARP, courtesy of Paul Bell, POL). The ARP recorded data along a 1.5 m zone from its central position underneath STABLE.	87
3.5	Schematic diagram showing the positions of STABLE, the wave probes and the Delft Hydraulics ECMs in the <i>Deltaflume</i> .	88
3.6	Delft Hydraulics lightweight mechanical ripple profiler device. The little wheel is moved along the bed and records the bed profile.	88
3.7	The 4 STABLE velocities at ECM A (≈ 31 cm above the bed) for a) regular waves ($H = 0.85$ m) and b) irregular waves ($H_s = 0.83$ m).	89
3.8	Suspended sediment concentration profiles measured using pump-sampling apparatus above the medium bed (from cylinder analysis next to the <i>Deltaflume</i>).	90
3.9	Suspended sediment concentration profiles measured using pump-sampling apparatus above the medium bed (from volumetric analysis at POL).	91

3.10	Sonar image of the medium sand bed showing the walls of the <i>Deltaflume</i> and imprints left by STABLE's feet. Image was recorded after burst a23a (regular waves, $H = 0.839$ m) at the end of the tests on the medium sand bed.	92
3.11	Samples of ripple profiles measured by the acoustic ripple profiler for a) burst a11a (regular waves, $H = 1.34$ m) and b) burst a10a (irregular waves, $H_s = 1.07$ m). The position of the pump-sampling array is highlighted.	93
3.12	Phase lag for peak correlation between the first time slice and all consecutive time slices measured by the acoustic ripple profiler for a) burst a08a (regular waves, $H = 0.85$ m) and a09a (irregular waves, $H_s = 0.83$ m) and b) burst a11a (regular waves, $H = 1.34$ m) and a10a (irregular waves, $H_s = 1.07$ m).	94
3.13	Last slice recorded by acoustic ripple profiler for burst a06b (regular waves, $H = 0.55$ m) and the first slice for burst a07a (irregular waves, $H_s = 0.53$ m).	95
3.14	Last slice recorded by acoustic ripple profiler for burst a08a (regular waves, $H = 0.85$ m) and the first slice for burst a09a (irregular waves, $H_s = 0.83$ m).	95
3.15	Sorted wave heights for burst a09a (irregular waves, $H_s = 0.83$ m) compared with the mean wave height for burst a08a ($H = 0.85$ m).	96
3.16	Instantaneous bed shear stress for bursts a08a (regular waves, $H = 0.85$ m) and a09a (irregular waves, $H_s = 0.83$ m) for 100 seconds of the 20 minute bursts. The shear stress for regular waves exceeds the threshold ($\tau_{cr} = 0.2$ N/m ²) for every half wave cycle, while the shear stress for irregular waves is below threshold during some wave cycles.	96
3.17	Horizontal velocity for Delft Hydraulics' ECM at a nominal height of 25 cm for burst a07a (irregular waves, $H_s = 0.53$ m).	97
3.18	Horizontal velocity measured by STABLE and by Delft Hydraulics's for burst a08a (regular waves, $H = 0.85$ m).	97
3.19	Velocity spectra of the horizontal velocity for STABLE ECM A and DH sensor, approximately 30 cm and 25 cm above the bed, respectively. The DH sensor has a smaller measuring volume and picks up more energy in the higher frequency range.	98
3.20	Raw ABS data for burst a09a (irregular waves, $H_s = 0.83$ m) for the 2.0 MHz sensor.	98
3.21	Peak backscatter of raw ABS data for a) burst a09a (irregular waves, $H_s = 0.83$ m) and b) burst a08a (regular waves, $H = 0.85$ m).	99
3.22	Measured and predicted (using Nielsen's definitions for regular and irregular waves) ripple dimensions as a function of the sediment mobility number Ψ for tests on the medium sand bed when STABLE was aligned with the flume. a) ripple wavelength, b) ripple height.	100
3.23	Burst averaged suspended sediment concentration for a) burst a08a (regular waves, $H = 0.850$ m) and b) burst a09a (irregular waves, $H_s = 0.83$ m).	101
3.24	Sorted wave heights for a) burst a08a (regular waves, $H = 0.85$ m) and b) burst a09a (irregular waves, $H_s = 0.83$ m) determined using the zero down-crossing method.	102

4.1	Acoustic sand ripple profiling image (ARP) for burst a08a (regular waves, $H = 0.85$ m). Ripple migration can be observed.	121
4.2	Longitudinal profiles of the medium sand test bed measured by the mechanical Delft Bed profiler (DBP). a) at the beginning of the tests before STABLE was deployed, b) at the end of the tests on the medium sand bed. The deformation of the bed is clearly visible.	122
4.3	Longitudinal profiles of the fine sand test bed measured by the mechanical Delft Bed profiler (DBP). a) at the beginning of the tests before STABLE was deployed, b) at the end of the tests on the fine sand bed. There is evidence of scour behind STABLE's foot.	123
4.4	Variation of ripple a) wave height and b) wavelength for all the profiles from survey DBP-2 (medium sand) using the zero down-crossing method. Bins 2 and 3 (joined lines) contain part of a STABLE foot for a number of profiles.	124
4.5	Variation of ripple a) wave height and b) wavelength for all the profiles from survey DBP-4 (fine sand) using the zero down-crossing method. Bin 3 (joined lines) contains part of a STABLE foot for a number of profiles.	125
4.6	Example of a typical energy density spectrum from a FFT for survey DBP-1.	126
4.7	a) Morlet wavelet, b) Construction of a Morlet wavelet as a sine curve modulated by a Gaussian (from TORRENCE, 1999).	126
4.8	a) Unfiltered profile from survey DBP-1 on the medium bed before STABLE was deployed. b) Scalogram of a wavelet power spectrum. Most of the energy is associated with the overall shape of the bed.	127
4.9	Example of a) the Paul and b) the Mexican Hat Wavelet. The dashed line for the Paul wavelet shows the imaginary part (from TORRENCE, 1999).	127
4.10	a) Filtered profile from survey DBP-1 on the medium bed before STABLE was deployed. b) Scalogram of a wavelet power spectrum using the Morlet wavelet. c) global wavelet power spectrum. d) instantaneous amplitude.	128
4.11	a) Filtered profile from survey DBP-1 on the medium bed before STABLE was deployed. b) Scalogram of a wavelet power spectrum using the Mexican Hat wavelet. c) global wavelet power spectrum.	129
4.12	a) Filtered profile from survey DBP-1 on the medium bed before STABLE was deployed. b) Scalogram of a wavelet power spectrum using the Paul wavelet. c) global wavelet power spectrum.	130
4.13	a) Filtered profile from survey DBP-2 on the medium sand. The imprint of one of STABLE's feet is visible. b) Scalogram of a wavelet power spectrum. c) global wavelet power spectrum. d) Instantaneous amplitude.	131
4.14	a) Filtered profile from survey DBP-3 on the fine sand (before deployment). b) Scalogram of the wavelet power spectrum. c) Global wavelet power spectrum. d) Instantaneous amplitude.	132
4.15	a) Filtered profile from survey DBP-4 on the fine sand (STABLE was approximately 25 m along the bed). b) Scalogram of the wavelet power spectrum. c) Global wavelet power spectrum. d) Instantaneous amplitude.	133
4.16	a) Filtered profile from survey DBP-4 on the fine sand. b) Normalised	134

	scalogram of the wavelet power spectrum. c) Normalised global wavelet power spectrum.	
5.1	Burst averaged suspended sediment concentration profiles for burst a07a (irregular waves, $H_s = 0.53$ m).	161
5.2	Burst averaged suspended sediment concentration profiles for burst a08a (regular waves, $H = 0.85$ m).	161
5.3	Burst averaged suspended sediment concentration profiles for burst a09a (irregular waves, $H_s = 0.83$ m).	162
5.4	Burst averaged suspended sediment concentration profiles for the irregular bursts. The gradient increases with increasing wave height.	162
5.5	Suspended sediment concentration time series and synchronous near bed horizontal velocity for burst a07a (irregular waves, $H_s = 0.53$ m).	163
5.6	Suspended sediment concentration time series and synchronous near bed horizontal velocity for burst a08a (regular waves, $H = 0.85$ m).	163
5.7	Suspended sediment concentration time series and synchronous near bed horizontal velocity for burst a09a (irregular waves, $H_s = 0.83$ m).	164
5.8	Suspended sediment concentration time series and synchronous near bed horizontal velocity for burst a10a (irregular waves, $H_s = 1.07$ m).	164
5.9	Suspended sediment concentration time series and synchronous near bed horizontal velocity for burst a11a (regular waves, $H = 1.34$ m).	165
5.10	Suspended sediment concentration time series and synchronous near bed horizontal velocity for burst a12a (irregular waves, $H_s = 1.26$ m).	165
5.11	Sand ripple profile for burst a11a (regular waves, $H = 1.34$ m), measured by the Acoustic Ripple Profiler (ARP).	166
5.12	Variation of sediment diffusivity with distance from the bed for the two ABS transducers for burst a08a (regular waves, $H = 0.85$ m).	166
5.13	Suspended sediment cross correlation coefficients for the 1.0 MHz ABS transducer for burst a08a (regular waves, $H = 0.85$ m). The reference level is at $z = 5$ cm above the bed.	167
5.14	Suspended sediment cross correlation coefficients for the 1.0 MHz ABS transducer for burst a07a (irregular waves, $H_s = 0.53$ m). The reference level is at $z = 5$ cm above the bed.	167
5.15	Suspended sediment cross correlation coefficients for the 1.0 MHz ABS transducer for burst a10a (irregular waves, $H_s = 1.07$ m). The reference level is at $z = 5$ cm above the bed.	168
5.16	Suspended sediment cross correlation coefficient between the 1.0 MHz and 2.0 MHz ABS transducer for burst a07a (irregular waves, $H_s = 0.53$ m).	168
5.17	Suspended sediment cross correlation coefficient between the 1.0 MHz and 2.0 MHz ABS transducer for burst a08a (regular waves, $H = 0.85$ m).	169
5.18	Snap shot of the sediment concentration time series for the two ABS transducers at $z = 5$ cm above the bed for burst a07a (irregular waves,	169

- $H_s = 0.53$ m).
- 5.19 Snap shot of the sediment concentration time series for the two ABS transducers at $z = 5$ cm above the bed for burst a08a (regular waves, $H = 0.85$ m). 170
- 5.20 Measured and predicted reference concentration using the expression suggested by NIELSEN (1986) and its variations as a function of the modified effective Shields parameter. 170
- 5.21 Measured and predicted c-profiles using the equations proposed by NIELSEN (1992) for pure diffusion (dark blue line), pure convection (green line) and diffusion/convection (red line) for burst a07a (irregular waves, $H_s = 0.53$ m). The mean diameter in suspension was taken to be equal to a d_{16} at the bed for the empirical equations and $n=2$ in the convective equation. 171
- 5.22 Measured and predicted c-profiles using the equations proposed by NIELSEN (1992), for pure diffusion (dark blue line), pure convection (green line) and diffusion/convection (red line) for burst a11a (regular waves, $H = 1.34$ m). The mean diameter in suspension was taken to be equal to a d_{16} at the bed for the empirical equations and $n=2$. 172
- 5.23 Predicted (Nielsen) versus measured sediment concentration values for burst a11a (regular waves, $H = 1.34$ m). 172
- 5.24 Measured and predicted c-profiles using the equations proposed by NIELSEN (1992) for pure convection (green line) and diffusion/convection (red line) for burst a12a (irregular waves, $H_s = 1.26$ m). The mean diameter in suspension was taken to be equal to a d_{16} at the bed for the empirical equations and $n=1.8$. 173
- 5.25 Predicted (Nielsen) versus measured sediment concentration values for burst a12a (irregular waves, $H_s = 1.26$ m). 173
- 5.26 Measured and predicted c-profiles using the equations proposed by NIELSEN (1992) for pure convection (green line) and diffusion/convection (red line) for burst a12a (irregular waves, $H_s = 1.26$ m). The mean diameter in suspension was taken to be equal to a d_{16} at the bed for the empirical equations and $n=1.8$. Only the combined diffusion/convection approach can model the complex shape of the measured c-profile varying from an upward convex for the next 25 cm and then upward concave shape. 174
- 5.27 Measured and predicted c-profiles using the Rouse type profile with expressions for the reference concentration proposed by ZYSERMAN AND FREDSDØE (1994) and VAN RIJN (1989) for burst a08a (regular waves, $H = 0.85$ m). The value of d_{50} at the bed was used to determine the reference concentrations while the mean suspended diameter was equal to a d_{16} at the bed and $\gamma = 1$. 175
- 5.28 Measured and predicted c-profiles using the Rouse type profile with expressions for the reference concentration proposed by ZYSERMAN AND FREDSDØE (1994) and Van Rijn (1989) for burst a12a (irregular waves, $H_s = 1.26$ m). The value of d_{50} at the bed was used to determine the reference concentrations while the mean suspended diameter was equal to a d_{16} at the bed. 176

5.29	Predicted (Rouse type profile) versus measured sediment concentration values for burst a08a (regular waves, $H = 0.85$ m).	177
5.30	Measured and predicted c-profiles using the Rouse type profile with the two expressions (Van Rijn and Zyserman and Fredsøe) for the reference concentration for burst a08a (regular waves, $H = 0.85$ m). The ratio of sediment diffusivity to eddy viscosity was $\gamma = 0.6$.	177
5.31	Measured and predicted c-profiles using the Rouse type profile with the two expressions (Van Rijn and Zyserman and Fredsøe) for the reference concentration for burst a12a (irregular waves, $H_s = 1.26$ m). The ratio of sediment diffusivity to eddy viscosity was $\gamma = 0.3$.	178
5.32	Predicted (Rouse type profile with Van Rijn's reference concentration) versus measured sediment concentration values for burst a08a (regular waves, $H = 0.85$ m) and a12a (irregular waves, $H_s = 1.26$ m).	178
5.33	a) Ensemble averaged sediment concentration for 205 waves for burst a11a (regular waves, $H = 1.34$ m) for the 1.0 MHz ABS transducer. b) Corresponding near bed horizontal velocity.	179
5.34	a) Ensemble averaged sediment concentration for 50 waves (about 4 minutes) of burst a11a (regular waves, $H = 1.34$ m) for the 1.0 MHz ABS transducer. b) Corresponding near bed horizontal velocity.	179
5.35	a) Ensemble averaged sediment concentration for 205 waves of burst a08a (regular waves, $H = 0.85$ m) for the 1.0 MHz ABS transducer. b) Corresponding near bed horizontal velocity.	180
5.36	a) Ensemble averaged sediment concentration for 205 waves of burst a08a (regular waves, $H = 0.85$ m) for the 2.0 MHz ABS transducer. b) Corresponding near bed horizontal velocity.	180
5.37	Position of the ABS and ECM sensors relative to the ripples throughout burst a11a (regular waves, $H = 1.34$ m).	181
5.38	Position of the ABS and ECM sensors relative to the ripples throughout burst a08a (regular waves, $H = 0.85$ m).	181
5.39	Measured suspended sediment concentrations for an asymmetric wave with an asymmetry coefficient of 0.66 (from RIBBERINK AND AL-SALEM, 1995).	182
5.40	Measured suspended sediment concentrations for a sinusoidal wave (from RIBBERINK AND AL-SALEM, 1995).	183
5.41	Phase averaged sediment concentrations $\bar{c} + \tilde{c}$ over a flat bed under regular, symmetric oscillatory flow. One peak occurs each half-period at all levels. Near the bed, it occurs shortly before the peak of the free stream velocity ($\omega \cdot t = \pi/2$). From NIELSEN (1992).	184
5.42	Comparison between pump-sampling and ABS data for six bursts. a) burst a08a (regular waves, $H = 0.85$ m), b) burst a11a (regular waves, $H = 1.34$ m), c) burst a07a (irregular waves, $H_s = 0.53$ m), d) burst a09a (irregular waves, $H_s = 0.83$ m), e) burst a10a (irregular waves, $H_s = 1.07$ m), f) burst a12a (irregular waves, $H_s = 1.26$ m).	185

6.1	Burst averaged and mean c-profiles for the first and the second half of a burst for burst a) a07a (irregular waves, $H_s = 0.53$ m) and b) a11a (regular waves, $H = 1.34$ m).	204
6.2	One minute mean concentration profiles for a) burst a07a (irregular waves, $H_s = 0.53$ m) and b) burst a08a (regular waves, $H = 0.83$ m). There is a good consistency between the different profiles for the regular waves, while the c-profiles for irregular waves show significant variations.	205
6.3	Wave cycle mean concentration profiles for a wave group in burst a07a ($H_s = 0.53$ m) and synchronous near bed horizontal velocity.	206
6.4	Wave cycle mean concentration profiles for a wave group in burst a12a ($H_s = 1.26$ m) and synchronous near bed horizontal velocity.	206
6.5	Wave cycle mean concentration profiles for the wave group shown in figure 6.4 plus the four consecutive waves and synchronous near bed horizontal velocity. The burst mean c-profile is indicated by the thick black line.	207
6.6	Wave cycle mean sediment concentration at $z = 5$ cm above the bed for the waves in the wave groups determined for burst a12a ($H_s = 1.26$ m).	207
6.7	a) Calibrated 1.0 MHz ABS record for irregular waves ($H_s = 0.53$ m, red and dark blue indicate high and low suspended sediment concentration, respectively); b) corresponding near bed horizontal fluid particle velocity exhibiting some large waves (ABS data from Dr P.D. Thorne, POL).	208
6.8	a) Calibrated 1.0 MHz ABS record for irregular waves ($H_s = 1.26$ m, red and dark blue indicate high and low suspended sediment concentration, respectively); b) corresponding near bed horizontal fluid particle velocity exhibiting some large waves (ABS data from Dr P.D. Thorne, POL); c) corresponding bed shear stress. The red line indicates the critical shear stress determined from the significant wave height for the burst.	209
6.9	Suspension height as a function of an effective wave height calculated by equation 6.1.	210
6.10	Suspension height as a function of an effective wave height calculated by equation 6.2.	210
6.11	Location of the field site at Middelkerke Bank, Belgium (courtesy of Jon Williams, POL).	211
6.12	Wave cycle mean concentration profiles for a wave group in burst 38 (Middelkerke Bank, $H_s = 2.88$ m).	212
6.13	Wave cycle mean concentration profiles for a wave group in burst 38 (Middelkerke Bank, $H_s = 2.88$ m).	212
6.14	a) ABS record for MK Bank data ($H_s = 2.88$ m, red and dark blue indicate high and low suspended sediment concentration, respectively); b) corresponding near bed (40 cm above the bed) horizontal fluid particle velocity exhibiting some large waves.	213
6.15	Wave elevation for a wave group from burst a12a (irregular waves $H_s = 1.26$ m). Ten individual waves can be identified. Their wave heights and periods are listed in table 6.1.	214

6.16	Schematic of the steps involved in the sediment entrainment model.	214
6.17	Cycle mean c-profiles for the wave group in figure 6.14 determined by the model. The sediment concentration entrained by the "cloud of sediments" was constant. The solid blue line represents the burst mean concentration profile.	215
6.18	Same as figure 6.15, but the sediment concentration entrained by the "cloud of sediments" was determined from the previous cycle mean concentration value 1 cm above the bed. The solid blue line represents the burst mean concentration profile.	215
7.1	Diagrammatic sequence of vortex pair generation, separation and advection under waves. The phase of the wave is shown by rotation of the vector on the left.	236
7.2	Photograph of vortices on a rippled bed under oscillatory flow from BAGNOLD (1946). The ripple wavelength and height were 10 cm and 1.5 cm, respectively. The amplitude and half period were 20 cm and 3.4 seconds, respectively. Aluminium powder was used for flow visualisation.	236
7.3	Successive positions of point vortices in a sinusoidal flow with $U = 0.75 \cdot \sin(\omega t)$ starting from rest at time $t = 0$ (from LONGUET-HIGGINS, 1981).	237
7.4	a) Calculated flow and b) calculated suspended sediment distribution presented by HANSEN ET AL. (1994), based on a discrete vortex model.	238
7.5	Flow visualisation over a ripple in wave only conditions simulated by a numerical model by FREDSSØE ET AL. (1999). The vortex pairing at a phase of 110° can be clearly identified.	239
7.6	a) Schematic of the laboratory wave flume with the 1 m rippled bed section on the bottom of the flume. b) Schematic detail of the rippled bed with its dimensions.	240
7.7	Plastic rippled bed in the laboratory wave flume. The ripple height is 2 cm and the wavelength is 10 cm.	241
7.8	Plastic particles, with a relative density of 1.05 kg/m^3 , laying on the rippled bed. No waves were generated at this time.	241
7.9	Suspension of plastic particles under wave motion. The wave height, wavelength and water depth were about 8 cm, 75 cm and 45 cm, respectively.	242
7.10	Composed picture of the movement of a single particle under waves. The wave height, wavelength and water depth were about 8 cm, 75 cm and 45 cm, respectively. Two stages of movement can be identified. The first one with horizontal and vertical movement and the second one with predominately vertical movement.	242
7.11	Individual frames of particle motion in the laboratory wave flume recorded by a video camera. The wave height, wavelength and water depth were about 8 cm, 75 cm and 45 cm, respectively.	243
7.12	Particle trajectories extracted from the video taken of the particle movement in the laboratory wave flume recorded for a) 3.8 s, b) 6.12 s, c) 3.56 s, d)	246

	1.4 s and e) 1.7 s.	
7.13	a) Trajectory of a plastic particle extracted from the video taken of the particle movements in the laboratory wave flume and tracked over 7.6 seconds. b) cross hairs indicating the position of the particle in every frame (25ths of a second) and highlighting times of acceleration due to the spacing of the crosses.	249
7.14	Path of a sediment particle trapped in a vortex under waves (from NIELSEN (1992), figure 4.11).	250
7.15	Vortex development in the lee of a ripple. Its strength is assumed to be equal to $\Gamma_0 = U_{\max} \cdot \pi \cdot h_r$.	251
7.16	Vortex pair ejection from a ripple crest. a) Actual direction of propagation of the vortex pair. b) Simplified vortex movement in the vertical direction.	251
7.17	Drag coefficient as a function of the Reynolds Number for a sphere (lecture notes from Prof. D.W. Knight, The University of Birmingham).	251
7.18	Trajectory of the sediment particle and the vortex pair as a function of time.	252
7.19	Velocity of the vortex pair and the sediment particle as a function of time. At the time the vortex pair dissipates into the flow the velocity, its velocity is set to zero.	252
7.20	Effects of changes of the ripple height and thus the spacing between the two vortices on the peak elevation of the particle and the vortex pair and the time it hits the bed.	253
7.21	Effects of changes in the orbital velocity on the height the particle travels into the water column and the time it hits the bed.	253
7.22	Effects of changes of the drag coefficient on the height the particle travels into the water column and the time it hits the bed.	254
7.23	Effects of changes of the enhanced kinematic viscosity on the height the particle travels into the water column and the time it hits the bed.	254
7.24	Dimensionless graph to relate the peak elevation of a sediment particle ($d_{50} = 0.329$ mm), the orbital velocity of the waves, the ripple height of the bed and the modified kinematic viscosity.	255
7.25	Effects of the sediment diameter on the peak elevation of the particle and the time it hits the bed.	255
C.1	Burst averaged suspended sediment concentration for burst a10a (irregular waves, $H_s = 1.07$ m).	285
C.2	Burst averaged suspended sediment concentration for burst a11a (regular waves, $H = 1.34$ m).	285
C.3	Burst averaged suspended sediment concentration for burst a12a (irregular waves, $H_s = 1.26$ m).	286

ACRONYMS AND ABBREVIATIONS

ABS	Acoustic BackScatter
ADV	Acoustic Doppler Velocimeter
ARP	Acoustic Ripple Profiler
CSTAB	Circulation and Sediment Transport around Banks
DBP	Delft Bed Profile
ECM	Electro-current meter
FFT	Fast Fourier Transform
MAST	Marine Science and Technology
POL	Proudman Oceanographic Laboratory
PS	Pumps samples
Re	Reynolds number
SPM	Shore Protection Manual
SSS	Sector Scanning Sonar
STABLE	Sediment Transport and Boundary Layer Equipment
SWL	Still Water Level
WFT	Windowed Fourier Transform
rms	root mean square

NOTATION

A	semi-orbital excursion [m]
$\bar{A}(t)$	mean value of envelope function
\hat{A}_δ	peak orbital excursion [m]
a	height at reference concentration [m]
a_i	incident wave amplitude [m]
a_R	reflected wave amplitude [m]
a_{rms}	root mean square of the wave amplitude [m]
C	wave celerity [m/s]
C_d	drag coefficient
c	instantaneous sediment concentration [g/l]
\bar{c}	temporal mean sediment concentration [g/l]
$c(a)$	reference concentration [g/l]
c_0	reference concentration proposed by Nielsen [g/l]
c_g	group wave celerity [m/s]
D_*	non-dimensional particle diameter
D_{*s}	dimensionless grain size
d	particle diameter [m]
d_{10}	10 percentile sediment diameter [m]
d_{35}	35 percentile sediment diameter [m]
d_{50}	mean particle diameter [m]
d_{50s}	suspended mean particle diameter [m]
d_{84}	84 percentile sediment diameter [m]
d_{90}	90 percentile sediment diameter [m]
$F(z)$	vertical distribution function for concentration profile
f	frequency [hz]
f_w	friction factor under waves
f_{wG}	grain wave friction factor
f_{wR}	ripple wave friction factor
$f_{2.5}$	friction factor (after Swart)
GF	groupiness factor

g	acceleration due to gravity [m/s^2]
H	wave height [m]
\bar{H}	average wave height [m]
H_0	deep water wave height [m]
H_s	significant wave height [m]
$H_{1/10}$	mean wave height of the 10 % highest waves [m]
$H_{1/3}$	mean wave height of the 33 % highest waves [m]
H_n	wave height of the n^{th} wave in a group [m]
\bar{H}_{burst}	mean group wave height [m]
\bar{H}_{group}	burst mean wave height [m]
$H_{i,\text{peak}}$	peak incident wave height [m]
$H_{R,\text{peak}}$	peak reflected wave height [m]
h	water depth [m]
h_r	ripple height [m]
K_r	reflection coefficient
K_t	calibration constant for ABS
k	wave number [m^{-1}]
k_s	Nikuradse roughness
k_{sG}	sand grain roughness [m]
k_{sR}	ripple roughness [m]
L	wavelength [m]
L_0	deep water wavelength [m]
L_c	convective entrainment length scale [m]
L_s	diffusive length scale [m]
ℓ	mixing length [m]
m	particle mass [kg]
m^*	submerged particle mass [kg]
m_0	zeroth moment of area under a spectrum
m_2	second moment of area under a spectrum
N	total number of waves in a group
N_z	number of zero-crossings in a wave record
N_{thres}	number of waves over threshold
n	length of wave record [s]
P	pick up rate [m/s]

p	pressure [bar]
$Q(t)$	instantaneous depth integrated sediment transport rate [m^2/s]
\bar{Q}	time averaged, depth integrated sediment transport rate [m^2/s]
Q_B	bedload transport rate for steady flow [m^2/s]
q_c	convective sediment flux [m/s]
r	bed roughness [m]
$r(\text{delay})$	cross correlation coefficient
s	relative density
T	wave period [s]
\bar{T}	mean wave period [s]
T_p	peak wave period [s]
T_z	zero-crossing period [s]
T_s	transport stage parameter
T_s	transport parameter [-]
t	time [s]
U	flow velocity [m/s]
U_c	peak horizontal velocity under the wave crest [m/s]
U_p	speed of propagation of a vortex [m/s]
U_t	peak horizontal velocity under the wave trough [m/s]
U_w	peak orbital velocity [m/s]
U_{\max}	maximum propagation velocity of vortex [m/s]
u	velocity in the horizontal direction [m/s]
u_s	shear stress velocity [m/s]
u_p	portside horizontal velocity [m/s]
u_s	starboard horizontal velocity [m/s]
V	particle velocity [m/s]
w	velocity in the vertical direction [m/s]
w_0	settling velocity [m/s]
w_c	sediment convection velocity [m/s]
w_p	portside vertical velocity [m/s]
w_s	starboard vertical velocity [m/s]
x	horizontal coordinate [m]
$y(i)$	time history
z	vertical length coordinate [m]

$z(i)$	time history
z_1	boundary length scale [m]
α	Rouse type coefficient
α_w	absorption due to water
α_s	attenuation of the suspension
β	calibration factor for pump samples
Γ	vortex strength
Γ_0	initial vortex strength
γ	ratio of sediment diffusivity to eddy viscosity
Δ_d	dune wave height [m]
ε_s	sediment diffusivity [m^2/s]
ε_s^*	enhanced kinematic viscosity [m^2/s]
ζ	elevation from the ripple crest [m]
η	wave elevation [m]
Θ_r	effective Shields parameter over ripples
$\Theta_{2.5}$	grain roughness Shields parameter
Θ_w	skin Shields parameter under waves
Θ_s	skin Shields parameter
Θ'	non-dimensional shear stress
Θ_{cr}	critical shields parameter
λ_d	dune wavelength [m]
λ_r	ripple wavelength [m]
κ	Von Karman constant
ν	kinematic viscosity of water [m^2/s]
ν_t	eddy viscosity [m^2/s]
ξ	horizontal particle displacement [m]
ρ	density of water [kg/m^3]
ρ_s	density of the sediment particle [kg/m^3]
σ_A	standard deviation of envelope function
σ_s	grain sorting parameter

$\bar{\tau}$	time averaged shear stress [N/m ²]
$\bar{\tau}_{CR}$	mean critical shear stress under waves [N/m ²]
τ'_{max}	maximum shear stress corresponding to the skin friction [N/m ²]
$\hat{\tau}_{WG}$	peak grain related shear stress under waves [N/m ²]
τ_w	instantaneous shear stress [N/m ²]
$\bar{\tau}_w$	unperturbed wall shear stress [N/m ²]
Φ	potential
Φ_i	incident phase shift
Φ_R	reflected phase shift
Ψ	sediment mobility number
ω	angular wave frequency [s ⁻¹]

Chapter 1 Introduction

1.1 Introduction

The prediction of sediment transport has been an important element of research for many years and it plays a key role in many engineering projects. The prediction of the short and long term erosion and deposition rates in the marine environment is of general significance to the coastal engineer. Some applications include the maintenance and development of waterways, prediction of coastline and beach erosion, which can lead to a gradual improvement of coastal defence, accurate mapping of seabed topography and navigational waters, and the sediment movement around offshore structures and pipelines. From an environmental point of view the knowledge of suspended sediment transport may also improve the understanding of pollutant transport.

In a marine environment, sediment transport is induced by waves and currents. Before sediment can be transported, it must be entrained into the flow, which means a critical shear stress at the bed has to be exceeded. Both the waves and the currents influence the shear stress. The presence of currents can change the wave parameters and thus influence the sediment entrainment. The present study concentrates on data collected in experiments performed in wave only conditions.

To measure hydro- and morphodynamics in the field, the autonomous measuring rig STABLE (Sediment Transport And Boundary Layer Equipment, HUMPHREY AND MOORES, 1994), figure 1.1, was developed and deployed in various tests by Proudman Oceanographic Laboratory (POL). Though the measured data did not show any obvious influence of STABLE on its measuring environment, some uncertainties remained. To test STABLE under controlled conditions and to analyse wave-induced sediment transport, experiments were carried out in the *Deltaflume* at Delft Hydraulics, Netherlands in July and August 1997.

The *Deltaflume* is 230 m long, 5 m wide and 7 m deep (see figure 1.2). Regular and irregular waves with different heights in the range of 0.5 to 1.3 m and wave periods in the range of 4

to 6 s were generated. Tests were carried out on two separate test sand beds of medium, $d_{50} = 0.329$ mm, and fine sand, $d_{50} = 0.162$ mm. Each bed was approximately 30 m long, 5 m wide and 0.5 m deep and was placed approximately 105 m from the wave generator in the *Deltaflume*. The data were sampled and logged at approximately 4 Hz in burst mode for about 20 minutes. The hydrodynamics and morphodynamics were measured by sensors provided by Delft Hydraulics and sensors mounted on STABLE. Great care was taken to ensure that the set up of STABLE was similar to the set up in the field in order to simulate the field situation.

The controlled conditions in the flume and the number of sensors provide the opportunity of comparing the relative performance of several sensors. For the forthcoming analysis, one of the most comprehensive data sets involving hydrodynamic and sediment sensors is available. This will allow the examination of the small and medium scale interactions involved in re-suspension and transport of bed sediments. This will result in a clearer understanding of the processes involved. A detailed description of the sensors deployed, their calibration and accuracy and also a preliminary data analysis is given in chapter 3.

1.2 Background

The autonomous boundary layer rig STABLE has been deployed successfully in a number of field experiments by POL (e.g. HANNAY ET AL., 1994, O'CONNOR ET AL., 1994, WILLIAMS ET AL., 1999a). Whilst in all cases useful data pertaining to wave-current sediment interaction have been obtained during these deployments, there has always been uncertainty regarding the nature of and changes in the morphology of the sea bed during a given experiment. Furthermore, it has not been possible to obtain samples *in situ* of sediment in suspension. In some cases this has led to ambiguity in the interpretation of certain experimental results. Whilst instruments similar to STABLE have been deployed by various international research groups (e.g. Tetrapod, Bliss, Stress), they have never been tested rigorously in laboratory conditions and thus the validity of their data remains uncertain. By providing an opportunity to use field-scale laboratory facilities, the EU TMR Programme "Access to large-scale facilities" allowed critical evaluation of the accuracy of instruments on STABLE and the interactions between the deployment frame and the sedimentary processes under scrutiny (WILLIAMS ET AL., 1998).

1.3 Study Objectives

The main objectives of the research are:

- I. To further the understanding of the interaction between near bed hydrodynamics and resulting sediment suspension.
- II. To examine the influence of STABLE on its measuring environment. In particular looking at the effects of STABLE on bed profiles.
- III. To parameterise the relationship between near bed hydrodynamics and the resulting sediment behaviour. This will help in further development of numerical models of wave-induced sediment transport.
- IV. To elucidate the mechanisms affecting the re-suspension of sediments at the scale of the wave period (vortex ejections). The effect of coherent structures on sediment suspension will be investigated in these studies.
- V. To examine the possible 'pumping effect' caused by a sequence of high waves. (*A sequence of high waves causes increased sediment transport compared to a single high wave, as the sediment does not have enough time to settle to the bed before the next wave*).
- VI. To compare a range of field sensors in similar conditions. (*These data provide the opportunity to compare the different sensors under controlled conditions, as the sediment and wave properties are known*).
- VII. To compare measured ripple dimensions with calculated dimensions using existing equations (e.g. Nielsen, Van Rijn).
- VIII. To investigate ripple migration. (*The various sensors, which recorded the bed morphology over time, allow the estimation of ripple migration*).

1.4 Structure of the Thesis

The subsequent chapters of this thesis are structured in the following way:

Chapter 2 – Literature Review: An introduction to the physical processes of relevance to this study. A critical review of the published work on bedforms and wave hydrodynamics, resulting in the suspension of sediment into the water column. It highlights the needs for research, justifies the objectives and pulls together information for discussion in the

subsequent chapters. Some literature is reviewed in later chapters where it coincides with the data analysis carried out.

Chapter 3 – Instrumentation and Preliminary Data Analysis: A summary of the study site, the various sensors deployed in the *Deltaflume* and their calibration. Preliminary data analysis is carried out to identify the quality of the data. The accuracy of the different sensors measuring the same parameters is under scrutiny.

Chapter 4 – Influence of STABLE on its measuring environment: The influence of the measuring rig on the bedforms is analysed using Fourier and Wavelet Transforms. The applicability of wavelets to the present data is investigated.

Chapter 5 – Suspended Sediment Concentrations: Considers the sediment suspension measured by the two acoustic transducers as well as the pump-sampling equipment. A comparison with existing empirical equations is made, highlighting the problem associated with empirical equations. The differences between the diffusion and convection processes for sediment suspension are investigated. A number of parameters included in the equations are investigated and changes are suggested. The emphasis will be on the burst mean sediment concentrations.

Chapter 6 – Intra-wave Suspended Sediment Concentrations: After looking at the burst mean concentrations, this chapter concentrates on the intra wave suspension events with the focus on wave groups. The groupiness factor is identified as an additional parameter to describe concentration profiles. The results from the *Deltaflume* experiments are compared with field data and differences pointed out. A simple model is developed that incorporates the history of sediment suspension under a wave group. A convective entrainment process, involving a vortex pair is used to lift sediment into the water column. The significance of the vortex pair mechanism is discussed in chapter 7.

Chapter 7 – Vortex Ejections from a rippled bed: Vortex ejections as a possible mechanism to suspend sediment into the water column are investigated. A small laboratory flume with an artificial plastic bed is utilised to visualise the existence of vortices in the flow. A model is developed that lifts a particle of sand into the water column under the influence of a vortex pair. A sensitivity analysis for this convective entrainment model is performed.

Chapter 8 – Conclusions and Recommendations: The conclusions for the study are drawn together and recommendations for future research are made.

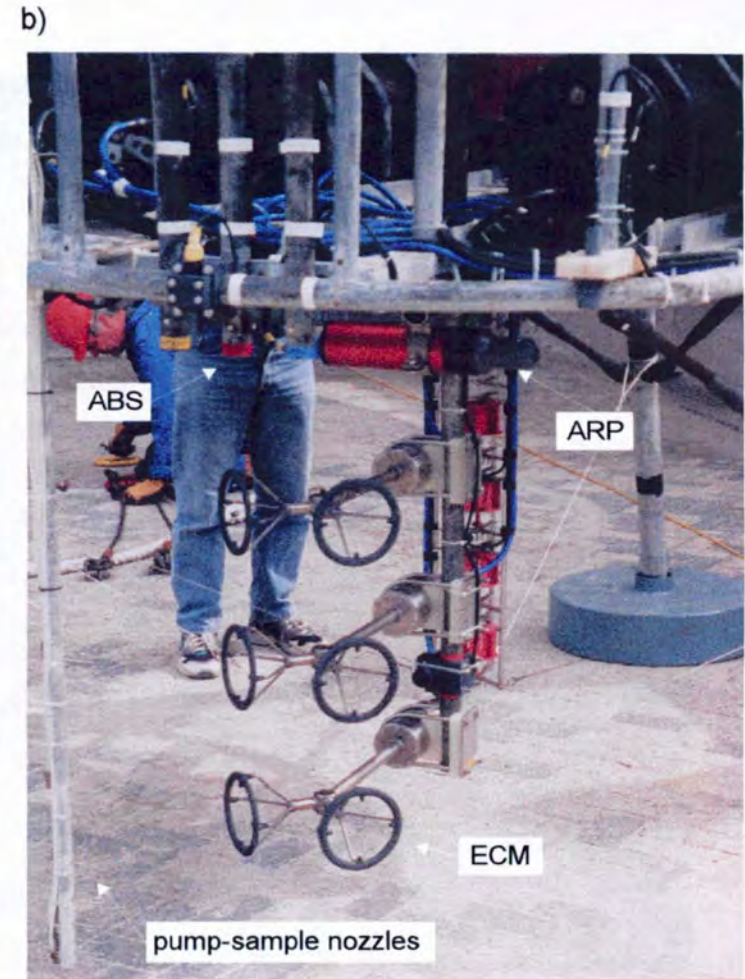
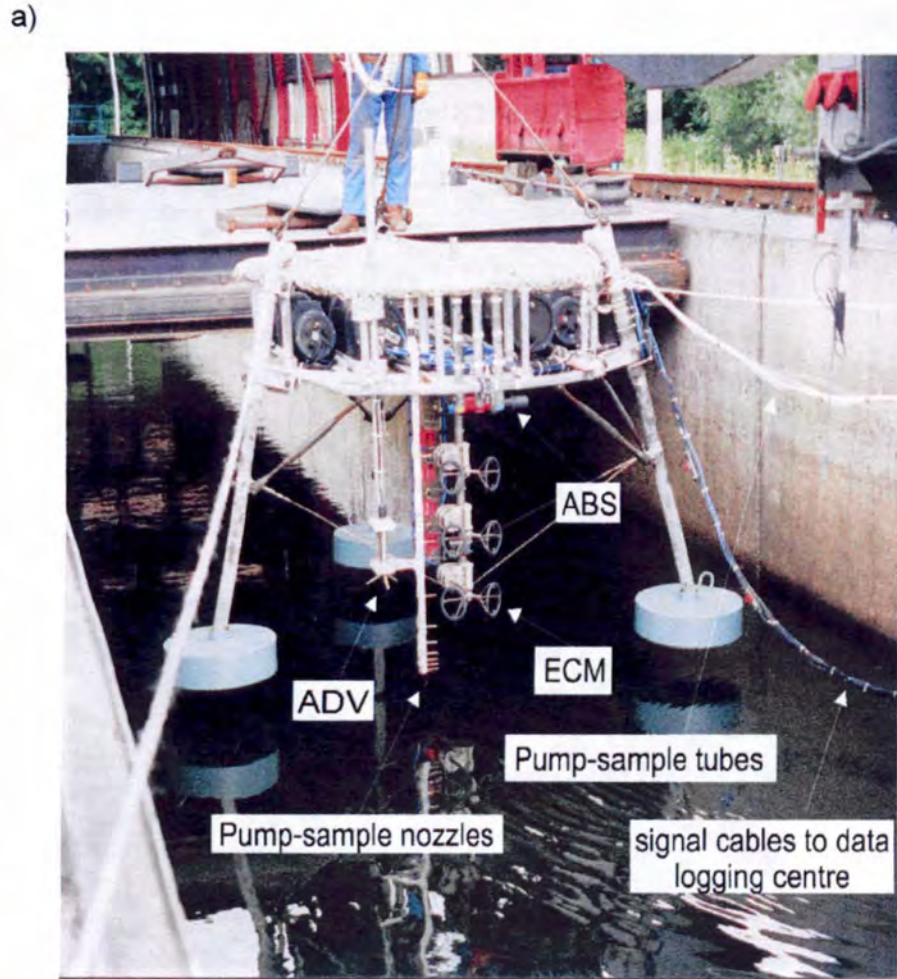
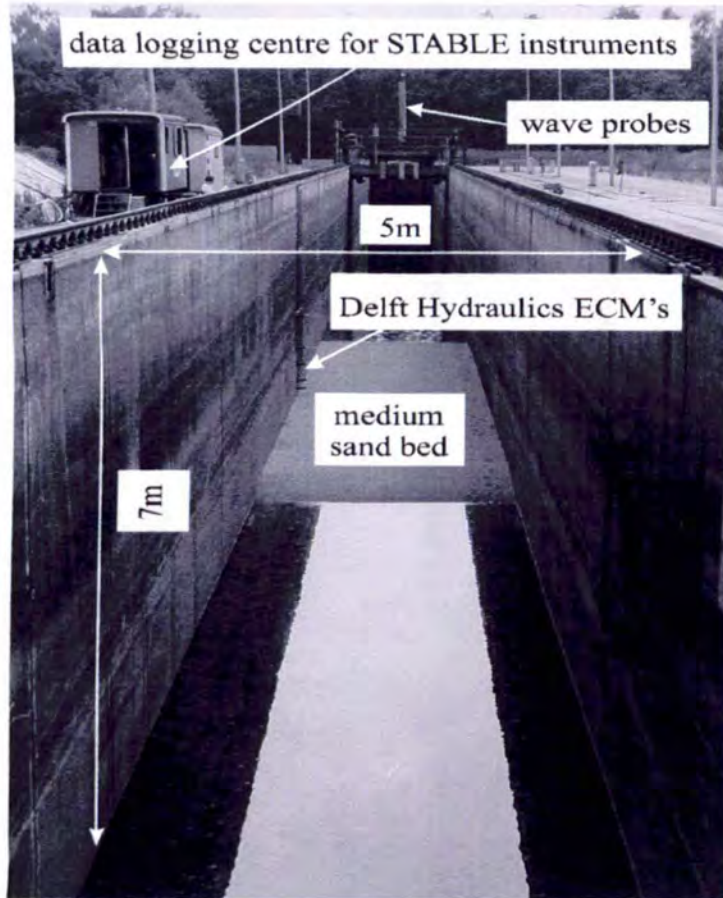


Figure 1.1: a) The autonomous measuring rig STABLE with the three ECMs, the ADV, the pump-sampling array and the three ABS, being lowered into the *Deltaflume*. b) detailed view of STABLE with the ECMs, ABS, ARP and pump-sampling array.

a)



b)

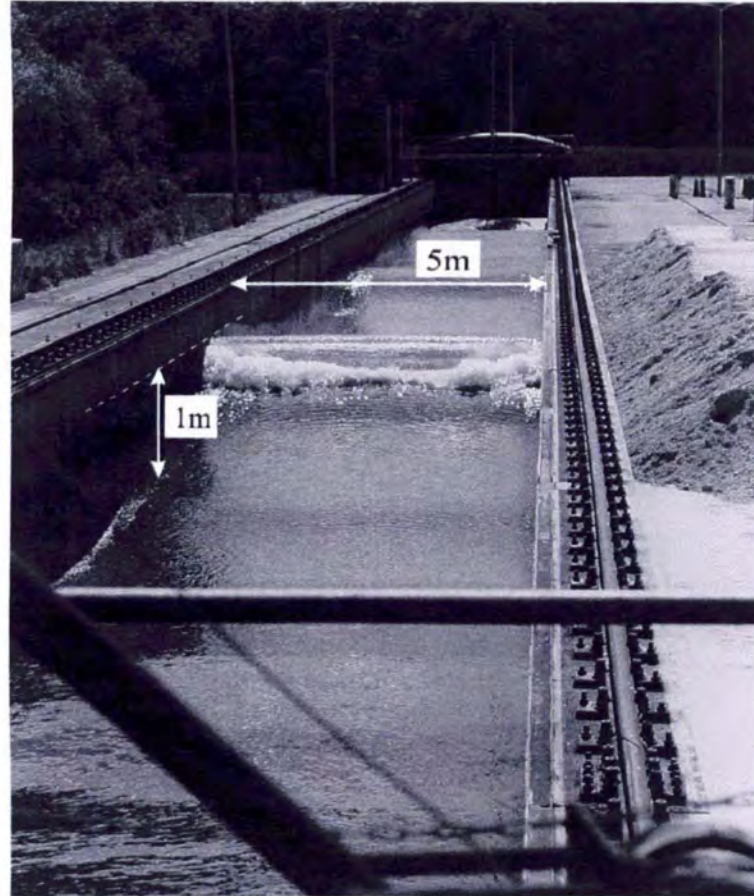


Figure 1.2: The *Deltaflume* at Delft Hydraulics. a) dimensions of the *Deltaflume* and the medium sand bed before filling the flume. b) large waves in the *Deltaflume*.

Chapter 2 Literature Review

2.1 Wave Parameters and Theories

2.1.1 Regular Wave Parameters

The important parameters used to describe waves are their length and height and the water depth over which they are propagating. All other parameters, such as wave-induced water velocities and accelerations, can be theoretically calculated from these quantities. Figure 2.1 shows a regular, two dimensional progressive train of wave period T and frequency $f = 1/T$. The wave height H is the vertical distance between successive troughs and crests. The wavelength L is the horizontal distance between two successive wave crests, or alternatively between two wave troughs.

The definition of the wave angular frequency is

$$\omega = \frac{2 \cdot \pi}{T} \quad (2.1),$$

the wave number is defined as

$$k = \frac{2 \cdot \pi}{L} \quad (2.2)$$

and the wave speed or celerity, C is defined as

$$C = \frac{L}{T} \quad (2.3)$$

2.1.2 Linear Wave Theory

The linear wave theory, attributed to Airy (see SHORE PROTECTION MANUAL (SPM), 1984, DEAN AND DALRYMPLE, 1984), is the first mathematical approximation of periodic progressive waves. It assumes a two-dimensional, inviscid and irrotational fluid flow. The incompressibility of the flow yields the two-dimensional, incompressible continuity equation:

$$\frac{\partial u}{\partial x} + \frac{\partial w}{\partial z} = 0 \quad (2.4)$$

The irrotational flow velocity expression, given in equation 2.5, states that the curl of the velocity vector is zero.

$$\frac{\partial w}{\partial x} - \frac{\partial u}{\partial z} = 0 \quad (2.5)$$

With the assumption of irrotational motion and an incompressible fluid, a velocity potential as presented in equations 2.6 and 2.7, exists.

$$u = -\frac{\partial \Phi}{\partial x} \quad (2.6)$$

$$w = -\frac{\partial \Phi}{\partial z} \quad (2.7)$$

Substituting equations 2.6 and 2.7 into the continuity equation 2.4 yields

$$\frac{\partial^2 \Phi}{\partial x^2} + \frac{\partial^2 \Phi}{\partial z^2} = 0 \quad (2.8)$$

Equation 2.8 is the Laplace equation. Substituting the velocities into the condition for irrotational flow also yields the Laplace equation, except in terms of the stream function.

$$\frac{\partial^2 \Psi}{\partial x^2} + \frac{\partial^2 \Psi}{\partial z^2} = 0 \quad (2.9)$$

The Laplace equation is linear, which allows the use of superposition. To solve the Laplace equation the boundary conditions have to be implemented. Two boundary conditions at the free surface and the bottom can be derived from the kinematic boundary condition. The condition at the surface requires the component of the fluid velocity normal to the surface to be related to the local velocity of the surface. The bottom is usually described as $z = -h$, where the origin is located at the still water level and h represents the water depth. If the bottom is impermeable and horizontal a no flow condition applies, which means that the vertical velocity is zero ($w = 0$) at the bed.

At the free surface the kinematic boundary condition is given by

$$-\frac{\partial \Phi}{\partial z} = \frac{\partial \eta}{\partial t} - \frac{\partial \Phi}{\partial x} \frac{\partial \eta}{\partial x} \quad (2.10)$$

A second boundary condition at the free surface is the dynamic free surface boundary condition. According to DEAN AND DALRYMPLE (1984) a “free” surface such as the air-water interface, cannot support variations in pressure (neglecting surface tension) across the interface and hence must respond in order to maintain the pressure as uniform. Therefore the dynamic boundary condition is required to describe the pressure distribution on this boundary. To evaluate the dynamic free surface boundary condition the generalised Bernoulli equation is applied with the pressure at the wave surface p_η taken as the gauge pressure, i.e. $p_\eta = 0$.

$$-\frac{\partial \Phi}{\partial t} + \frac{1}{2} \left[\left(\frac{\partial \Phi}{\partial x} \right)^2 + \left(\frac{\partial \Phi}{\partial z} \right)^2 \right] + \frac{p_\eta}{\rho} + g \cdot z = 0 \quad \text{on } z = \eta \quad (2.11)$$

The first order wave theory linearises the boundary condition, which means that all higher order terms can be neglected. This assumption is valid for infinitesimally small waves where the wave elevation η is small and therefore the velocities and pressures are small. Thus, any products of these variables are small ($\eta \ll 1$, but $\eta^2 \ll \eta$ or $u \cdot \eta \ll \eta$). The dynamic free surface condition reduces to

$$-\frac{\partial \Phi}{\partial t} + g \cdot \eta = 0 \quad \text{on } z = \eta \quad (2.12)$$

Linearising the kinematic free surface boundary results in

$$w = \frac{\partial \eta}{\partial t} \quad \text{on } z = 0 \quad (2.13)$$

With these boundary conditions the Laplace equation 2.8 can be solved and the velocity potential can be expressed as

$$\Phi = \frac{H \cdot g}{2 \cdot \omega} \cdot \frac{\cosh[k \cdot (h + z)]}{\cosh[k \cdot h]} \cdot \sin(k \cdot x - \omega \cdot t) \quad (2.14)$$

$$\eta = \frac{H}{2} \cdot \cos(k \cdot x - \omega \cdot t) \quad (2.15)$$

- with: k : wave number $k = 2 \cdot \pi / L$
 ω : cycle frequency $\omega = 2 \cdot \pi / T$ [1/s]
 T : wave period [s]
 L : wavelength [m]
 H : wave height [m]
 h : water depth [m]

For a more detailed analysis and background information on linear wave theory see DEAN AND DALRYMPLE (1984) and LAMB (1932).

2.1.3 Stokes' Higher Order Wave Theories

The linear wave theory assumes small amplitude waves, which satisfy the use of linearisation of the kinematic and dynamic free surface boundary conditions. The first order wave theory is used in many applications where the assumption of small amplitude waves is not satisfied any more. Higher order wave theories can explain phenomena such as mass transport which cannot be explained by linear theory. Linear theory applied to a wave predicts the movement of water particles in closed orbits, whereas Stokes' second order wave theory predicts open water particle orbits. Also quantities derived from the velocity potential, such as the velocity and pressure due to waves, are estimated more accurately by higher order wave theories.

The linear wave theory has been extended by Stokes in order to achieve better agreement between theoretical and observed wave behaviour. Stokes' higher order theories are valid for steep waves in deep water. The order of approximation is determined by the highest order term used to predict the wave parameters. The derivation of the second order Stokes' wave theory can be found in DEAN AND DALRYMPLE (1984).

The second order wave profile is described as

$$\eta(x,t) = \frac{H}{2} \cdot \cos\left(\frac{2 \cdot \pi \cdot x}{L} - \frac{2 \cdot \pi \cdot t}{T}\right) + \frac{\pi \cdot H^2}{8 \cdot L} \cdot \frac{\cosh(2 \cdot \pi \cdot h/L)}{\sinh^3(2 \cdot \pi \cdot h/L)} \cdot [2 + \cosh(4 \cdot \pi \cdot h/L)] \cdot \cos\left(\frac{4 \cdot \pi \cdot x}{L} - \frac{4 \cdot \pi \cdot t}{T}\right) \quad (2.16)$$

Figure 2.2 shows one wave period for a wave train derived from linear and Stokes' second order wave theories for a wavelength of 30.1 m, a period of 5.1 s and a wave height of 1 m. These are the same wave parameters as found in some of the wave conditions in the present experiment. The wave profile estimated by Stokes' second order yields a larger value under the crest and a smaller value under the trough compared to linear theory. Also the crest is peakier and the trough is flatter. Linear theory describes a wave that is symmetrical about the SWL (Still Water Level). Stokes' second order theory predicts a wave that is unsymmetrical about the SWL, but still symmetrical about a vertical line through the crest.

The horizontal and vertical velocities are described by

$$u(x,t) = \frac{H \cdot g \cdot T}{2 \cdot L} \cdot \frac{\cosh[2 \cdot \pi \cdot (z+h)/L]}{\cosh(2 \cdot \pi \cdot h/L)} \cdot \cos\left(\frac{2 \cdot \pi \cdot x}{L} - \frac{2 \cdot \pi \cdot t}{T}\right) + \frac{3}{4} \cdot \left(\frac{\pi \cdot H}{L}\right)^2 \cdot C \cdot \frac{\cosh[4 \cdot \pi \cdot (z+h)/L]}{\sinh^4(2 \cdot \pi \cdot h/L)} \cdot \cos\left(\frac{4 \cdot \pi \cdot x}{L} - \frac{4 \cdot \pi \cdot t}{T}\right) \quad (2.17)$$

$$w(x,t) = \frac{H \cdot \pi}{L} \cdot C \cdot \frac{\sinh[2 \cdot \pi \cdot (z+h)/L]}{\sinh(2 \cdot \pi \cdot h/L)} \cdot \sin\left(\frac{2 \cdot \pi \cdot x}{L} - \frac{2 \cdot \pi \cdot t}{T}\right) + \frac{3}{4} \cdot \left(\frac{\pi \cdot H}{L}\right)^2 \cdot C \cdot \frac{\sinh[4 \cdot \pi \cdot (z+h)/L]}{\sinh^4(2 \cdot \pi \cdot h/L)} \cdot \sin\left(\frac{4 \cdot \pi \cdot x}{L} - \frac{4 \cdot \pi \cdot t}{T}\right) \quad (2.18)$$

It can be shown, that for Stokes' second order wave theory the equations for wave celerity and wavelength are the same as obtained for linear theory (SPM, 1984) with

$$C = \frac{g \cdot T}{2 \cdot \pi} \cdot \tanh\left(\frac{2 \cdot \pi \cdot h}{L}\right) \quad (2.19)$$

$$L = \frac{g \cdot T^2}{2 \cdot \pi} \cdot \tanh\left(\frac{2 \cdot \pi \cdot h}{L}\right) \quad (2.20)$$

Of special interest is the horizontal particle displacement ξ

$$\xi(x,t) = -\frac{H \cdot g \cdot T^2}{4 \cdot \pi \cdot L} \cdot \frac{\cosh[2 \cdot \pi \cdot (z+h)/L]}{\cosh(2 \cdot \pi \cdot h/L)} \cdot \sin\left(\frac{2 \cdot \pi \cdot x}{L} - \frac{2 \cdot \pi \cdot t}{T}\right) + \frac{\pi \cdot H^2}{8 \cdot L} \cdot \frac{1}{\sinh^2(2 \cdot \pi \cdot h/L)} \cdot \left\{ 1 - \frac{3}{2} \cdot \frac{\cosh[4 \cdot \pi \cdot (z+h)/L]}{\sinh^2(2 \cdot \pi \cdot h/L)} \right\} \cdot \sin\left(\frac{4 \cdot \pi \cdot x}{L} - \frac{4 \cdot \pi \cdot t}{T}\right) + \left(\frac{\pi \cdot H}{L}\right)^2 \cdot \frac{C \cdot t}{2} \cdot \frac{\cosh[4 \cdot \pi \cdot (z+h)/L]}{\sinh^2(2 \cdot \pi \cdot h/L)} \quad (2.21)$$

The last term in equation 2.21 is not periodic, but depends on time, wave period and water depth. The term predicts a continuously increasing net particle displacement, which leads to a net transport of fluid, in the direction of the wave propagation. If the mass transport leads to an accumulation of mass in any region, the free surface must rise, thus generating a pressure gradient. A current, formed in response to this pressure gradient, will re-establish the distribution of mass. Findings from MITCHIM (1940), MICHE (1944), URSELL (1953), LONGUET-HIGGINS (1953 and 1960) and RUSSELL AND OSORIO (1958) indicated that the vertical distribution of the mass transport velocity is modified so that the net transport of water across a vertical plane is zero.

A progressive gravity wave is physically limited in height by depth and wavelength. The upper limit in deep water is a function of the wavelength, while in shallow water it is a function of both water depth and wavelength. STOKES (1880), predicted that theoretically a wave would remain stable as long as the water velocity at the crest was less than the wave celerity. He found that a wave would break if the crest angle was less than 120°. Later MICHELL (1893), found that in deep water the theoretical limit of wave steepness is

$$\left(\frac{H_0}{L_0}\right)_{\max} = 0.142 \approx \frac{1}{7} \quad (2.22)$$

When deciding which wave theory to use, it is important to keep the additional computational work involved in using non-linear theories in mind. Furthermore, it has to be decided if the improvement due to higher order wave theories can be justified in comparison to other calculations used in the analysis. In view of sediment transport this has to be denied in most cases.

2.1.4 Other Higher Order Wave Theories

Apart from Stokes' second order wave theory, his third and fourth order wave theories are used to describe natural waves. Long, finite-amplitude waves propagating in shallow water can be best described by the cnoidal wave theory. This was originally developed by KORTWEG AND DE VRIES (1895), but first recognised by BOUSSINESQ (1877). Equations for the cnoidal wave theory can be found in the SPM (1984) and DEAN AND DALRYMPLE (1984).

Another wave theory is the stream function wave theory, which in contrast to Stokes' higher orders, can be developed on the computer quite easily according to DEAN AND DALRYMPLE (1984). It allows very accurate calculations of the characteristics of water waves, including heights up to near breaking.

Figure 2.3 indicates the validity range for the different wave theories after LE MEHAUTE (1969). For the present tests $d/(g \cdot T^2)$ is approximately 0.018 and $H/(g \cdot T^2)$ is between 0.002 and 0.005. Note that d is used for the water depth in this diagram. This range is indicated by a red line in figure 2.3. This means that, according to Le Mehaute's diagram, these data are in the range of Stokes' 2nd and 3rd order wave theories.

2.1.5 Sea Waves

In the sea, waves, generated by the wind, are non-stationary and locally variable elevations of the water surface. The different combinations of crests and troughs are called waves,

which can be more or less irregular. The irregularity of a wave is defined by comparing the form of a wave with a sinusoidal regular wave. The wave elevation can be measured as a function of time or a function of locality.

In the sea, waves are classified by their spectrum of amplitudes and directions. Data collected in the sea usually consist of time histories of pressure, velocity and wave surface elevation. The period and wave height of regular waves is easy to determine, while for irregular waves, the wave itself has to be defined. The most commonly used definition of a wave is the zero-crossing method applied to time histories, whereby there is a distinction between zero up- and zero down-crossing (see figure 2.4).

A wave is defined as the event between two successive up- or down-crossings of the SWL. The zero up-crossing method was used to define a wave by TANN (1976). The wave height H is the vertical distance between the highest and lowest points in the wave and the wave period is the time between two zero up- or down-crossings (see figure 2.4). According to the definition the zero up- or down-crossing period is given approximately as

$$T_z = \frac{n}{N_z} \quad (2.23)$$

where n is the length of record in seconds and N_z is the number of up-crossings in the record. This is surprising, as naturally one would estimate the wave period of the record as the average of all the single up- or down-crossing wave periods in the record.

Another simple approach of analysing a time history of water surface elevation is a method named after TUCKER (1963), which is based on analysis by CARTWRIGHT AND LONGUET-HIGGINS (1956) and CARTWRIGHT (1958). Figure 2.5 shows a sketch of a wave record. Having located the SWL, the height of the highest crest (A), the height of the second highest crest (B), the depth of the lowest trough (C) and the depth of the second lowest trough (D) can be recorded. It should be noted that C and D have to be taken as the absolute value (i.e. positive). Also the number of times the wave elevation crosses the SWL in an upward (or alternatively downward) direction during the record (N_z) has to be recorded. With $H_1 = A + C$ and $H_2 = B + D$ the root mean square of the wave amplitude (a_{rms}) can be calculated using figure 2.6. The basis of this graph is the equations in the top right corner of the graph. LONGUET-HIGGINS (1953) found the following relationships between the a_{rms} and characteristic wave heights

$$\bar{H} = 1.77 \cdot \sqrt{2} \cdot a_{rms} \quad (2.24)$$

$$H_{1/3} = 2.83 \cdot \sqrt{2} \cdot a_{rms} \quad (2.25)$$

$$H_{1/10} = 3.60 \cdot \sqrt{2} \cdot a_{\text{rms}} \quad (2.26)$$

In contrast, SYLVESTER (1974) quoted a slightly different relationship

$$H_{1/3} = 2.95 \cdot \sqrt{2} \cdot a_{\text{rms}} \quad (2.27)$$

$$H_{1/10} = 4.00 \cdot \sqrt{2} \cdot a_{\text{rms}} \quad (2.28)$$

These values can be used as a first estimate for wave heights. $H_{1/3}$ is often referred to as the significant wave height.

So far the analysing techniques were limited to the time domain. Using the Fast Fourier Transform (FFT), the time history can be transformed into the frequency domain, where different analysing techniques can be applied. Random sea waves must be interpreted as a linear superposition of an infinite number of sinusoidal progressive waves with different frequencies. The distribution of the energy of these waves versus frequency or wave number is called a wave spectrum. The significant wave height, calculated from the energy spectrum, is defined as

$$H_s = 4 \cdot \sqrt{m_0} \quad (2.29)$$

Similarly the average wave period can be calculated using

$$\bar{T} = \sqrt{\frac{m_0}{m_2}} \quad (2.30)$$

where m_0 is the zeroth moment of area and m_2 is the second moment of area. The peak period T_p can be obtained from a spectral energy density plot and is the period corresponding to the maximum energy density component. Another way of estimating the peak period is as a function of the average period

$$T_p = 1.2 \text{ to } 1.3 \cdot \bar{T} \quad (2.31)$$

However, this relationship is very dependent on the form of the spectrum.

2.2 Wave Groups

Visual observations and wave records show that ocean waves usually appear in sets of groups, each group consisting of about 4 to 8 waves (FREDSØE AND DEIGAARD, 1992). The groupiness is related to the amplitude modulation of the waves. The groups propagate at a velocity of c_g , which is equal to half the wave celerity, C , for deep water waves and tends to the wave celerity for shallow waves. It has been shown that wave groups are important for the re-suspension of sediments leading to a larger suspension compared to individual high waves (e.g. WILLIAMS ET AL., 1996, VINCENT ET AL., 1991).

GODA (1985), defined the run length for wave groups, j , which can be determined by counting the number of consecutive large waves in each run of waves exceeding some threshold wave height (figure 2.7). The problem with Goda's suggestion is the definition of the threshold value of a large wave, which is dependent on the application. This method has the advantage of being simple, but the definition of the threshold is subjective.

LIST (1991), proposed a different definition of the groupiness factor of waves based on the wave envelope. This method starts with a time history of wave elevation, $\eta(t)$, which is then subjected to a high-pass filter to remove infragravity waves. LIST (1991), suggested a high-pass cut off frequency of 0.05 Hz. It then has to be passed through a low-pass filter to remove the incident waves. The groupiness factor, GF, from this envelope function can then be calculated as follows

$$GF = \sqrt{2} \cdot \frac{\sigma_A}{\bar{A}(t)} \quad (2.32)$$

where σ_A and $\bar{A}(t)$ are the standard deviation and the mean value of the envelope function, respectively.

The disadvantages of this method are that the definition of the low-pass cut off frequency is subjective and it is computationally demanding. It also calculates a groupiness factor that is an average over the whole record.

KETABDARI (1999), analysed the groupiness factor GF defined by the SIWEH (Smoothed Instantaneous Wave Energy History) method (see FUNKE AND MANSARD, 1979 for details). He discovered that the SIWEH method determined a groupiness factor of greater than zero for ideal sinusoidal waves, which is in contrast to the expected value of zero. Thus, he concluded that the SIWEH method includes some inaccuracies. Further, he discovered that the SIWEH method cannot distinguish between a sequence of waves with gradual increase in wave height and a wave time series with isolated peak wave heights, but with the identical standard deviation of energy about the mean. Thus, KETABDARI (1999), suggested a new definition of the groupiness factor given by

$$GF = \frac{\sqrt{\frac{1}{N_{\text{thres}}} \cdot \sum_{k=1}^{k=N} j_{1k} \cdot \sum_{i=1}^{i=j} (H_i - H_{1/3})^2}}{H_{1/3}} \quad (2.33)$$

where N_{thres} is the number of waves over the threshold wave height, $H_{1/3}$, N is the number of runs in a record, j_{1k} is the run length and i_j is the total number of waves in each burst. This

definition determines a groupiness factor of zero for ideal, sinusoidal waves. Its advantages over the SIWEH method are the simplicity of the calculation and its reduction in computational demand. Further, KETABDARI (1999) has shown that it is suitable for a range of engineering applications.

Regular and irregular waves were generated in the *Deltaflume* with no specific groupiness factor in mind. Nevertheless, the irregular waves exhibit some groupy behaviour, which will be analysed in terms of sediment re-suspension in chapter 6.

2.3 Bedforms in Oscillatory Flow

2.3.1 Mechanism

The sea bed is very rarely flat. The flow of water over a sea bed of sand often results in a distortion of the bed and the formation of bedforms. The size and form of the bedforms depend on the characteristics of the sand and the flow and is further influenced by the sediment transport. The sequence of bedforms found in oscillatory flow can be classified as (SLEATH, 1984):

ripples – megaripples – dunes/antidunes – sandwaves – sandbanks.

In the case of fine sediment, ripples are formed, while coarse sand will usually form dunes (ENGELUND AND FREDSE, 1982). Smaller bedforms are often superimposed on larger bedforms. The larger bedforms such as sandwaves and sandbanks modify the main flow pattern, such that waves refract, diffract or break. The smaller bedforms such as ripples do not have a direct influence on the flow pattern, but they influence the boundary structure and the turbulence intensity. Thus these features are extremely important for sediment transport. According to NIELSEN (1979), ripples are present, when the non-dimensional shear stress Θ' is between 0.045 and 1.0. With $\Theta' = \frac{\tau'_{\max}}{\rho \cdot (s-1) \cdot g \cdot d}$ and $\tau_{\max} = \frac{1}{2} \cdot \rho \cdot f_w \cdot (A \cdot \omega)^2$ and τ'_{\max} being the part of τ_{\max} corresponding to skin friction. When $\Theta' = 0.045$ the flow is just able to move grains that are close to irregularities of the bed. When $\Theta' = 1.0$ and the ripple steepness is vanishing, the sediment transport is very large.

BAGNOLD (1946), performed basic laboratory experiments relating to sediment transport and the formation of ripples. He used a circular arc filled with sand, which was then oscillated through still water in a narrow tank. He observed two different types of ripples – rolling-grain and vortex ripples. BAGNOLD (1946), noticed that the two types of ripples may be similar in appearance due to the consistency of the angle of repose (about 30° for sand), but they

differ greatly in character. DYER (1986), on the contrary said that wave ripples do not slope at the angle of repose, which was confirmed by NIELSEN (1979), who stated that vortex ripples slope at an angle larger than the angle of repose in still water, as long as the vortex is exerting an upward, stabilising shear stress.

When the velocities are big enough for initiation of motion, the grains first begin to roll to and fro over the surface, but are not lifted up into the flow. In this case the grain movement is confined to times in the wave cycle when the critical velocity for initiation of motion is exceeded (BAGNOLD, 1946).

Initially the rolling grains are distributed randomly, but they become more organised eventually and then accumulate in parallel zones, which form wavy ridges a few grains high. The crests then sway from side to side during successive wave cycle reversals. With growing ridges the troughs are sheltered from water flow and movement is restricted to the crests. When this shelter extends to the next crest, no further grains are collected anywhere and the ridges become stable. If the flow velocity increases, the grains on the flat strips start moving again until a new equilibrium is reached. DYER (1986), however stated that other authors believe that rolling-grain ripples are only an intermediate stage and not permanently stable. According to BAGNOLD (1946), rolling-grain ripples occur on all sands, but the profile varies. With fine grains the surface between two ridges remains flat whereas with large grains this surface becomes nearly a circular arc of large radius.

The essential distinguishing feature of rolling-grain ripples is the entire absence of sediment movement within the trough. The length-height ratio is evidently too big for the formation of vortex ripples. The rolling-grain ripples appear stable for a given orbital amplitude between critical speed for initiation of motion and about double that speed. Within this range, vortex ripples will not form at all, provided there are no irregularities anywhere on the surface higher than 20 grain diameters (BAGNOLD, 1946).

If the speed exceeds twice the critical speed for initiation of motion, the steep lee slopes reach such a height, that the whole regime changes and vortex ripples suddenly appear. SLEATH (1975), found further that vortex formation occurs when the orbital excursion is greater than the ripple wavelength. At larger velocities, the flow is separated from the ripples. The change from rolling-grain to vortex ripples starts at one point, where the crest height exceeds the critical value. If there are some irregularities on the bed surface, the velocity, necessary to form vortex ripples, does not need to exceed the critical speed for initiation of motion on a flat bed.

BAGNOLD (1946), described the mechanism of vortex ripples as follows: During the first half of the wave cycle a vortex develops in the lee of the ripples, which then scoops up sediment from the foot of the ripple crest. At flow reversal the vortex shoots up parallel to the ripple surface towards the crest. DYER (1986), stated that most grains carried by the vortex come to rest at the top of the ripple crest. After the grains have been lifted to the crest, there is a short pause till the vortex on its upward journey parallel with the ripple slope has passed the crest and becomes separated from the ripple altogether. By this time the flow direction has reversed and a jet of water pushes down the outward slope of the ripple between the crest and the departing vortex. At the same time a new vortex develops in the lee of the ripple and the cycle starts again.

Grains with a high fall velocity do not overshoot the crest and no cloud of suspended sediment can be observed. But with very fine sand, a proportion of it gets suspended in the water and carried up with the vortex.

BAGNOLD (1946), noted that in deep water and in short amplitude waves, the ripple pattern is likely to be disturbed by cross ridges in the troughs.

TUNSTALL AND INMAN (1975), have shown that the vertical velocity component induced by the vortices is of the same order as the horizontal orbital wave velocity just outside the boundary layer. The influence of the orbital velocity on the generation of a vortex pair and the subsequent movement of a particle will be investigated in chapter 7. This results in vertical velocities being of the same order as horizontal velocities close to the boundary. Thus, the vortex is the determining mechanism for entrainment and suspension of sediment on a rippled bed. They also noted that the vortex diameter was between 1.0 and 1.4 times the ripple height. DYER (1986), stated that the turbulence induced by the vortices is usually confined to a layer less than about two ripple heights above the bed. A more detailed review of vortex ejection mechanisms mentioned in the literature will be given in chapter 7.

2.3.2 Bedform dimensions

When there is no large vortex formed in the trough during the wave cycle, the velocity of the flow over the crest tends to flatten it by moving the grains towards the trough. With increasing stroke length this effect becomes more and more dominating and the ripple height decreases. Consequently the ripple steepness decreases with increasing orbital velocity as the ripple crest becomes so flattened that no vortex occurs in the lee of it. According to DYER (1986), the maximum steepness, h_r/λ_r is 0.1 to 0.2 whereas SLEATH (1984), quoted a relative steepness of 0.15 to 0.25. The lee vortex is able to erode in the

troughs as strongly as the mean flow will erode from the ripple crest and thus maintain the steepness (NIELSEN, 1979). Also there is a limited growth because the force of gravity is forcing the grains back to the trough. Thus, for any given wave condition there is a limiting steepness.

The type of bedforms can be classified using a particle diameter D_* and a bed shear stress parameter T_* as defined by VAN RIJN (1989):

$$D_* = \left[\frac{(s-1) \cdot g}{v^2} \right]^{1/3} \cdot d_{50} \quad (2.34)$$

$$T_* = \frac{\bar{\tau} - \bar{\tau}_{cr}}{\bar{\tau}_{cr}} \quad (2.35)$$

with $\bar{\tau}_{cr}$ = critical time averaged bed shear stress

The classification of the bedforms for unidirectional flow as a function of D_* and T_* is shown in figure 2.8 and table 2.1. VAN RIJN (1989), stated that ripples are generally generated when the peak orbital velocity (U_w) near the bed is approximately 1.2 times the critical peak velocity of initiation of motion on a flat bed. With a $d_{50} = 0.329$ mm and a $d_{50} = 0.162$ mm for the medium and fine sand, the corresponding values for D_* are 8.32 and 4.10, respectively and values of T_* lie between 0.7 and 6. According to VAN RIJN'S (1989), classification of bedforms, this corresponds to the formation of mini and mega ripples on the sand bed. However, on the medium sand bed the data collected in the present experiment show only evidence for the development of vortex ripples with some large bedforms in the range of 1 to 2 m.

There are a number of equations available in the literature to estimate the ripple height and length depending on the type of ripple and the type of flow. From results of wave flume experiments YALIN (1985), suggested the following relationship for the ripple height and length:

$$h_r = 50 \text{ to } 200 d_{50} \quad (2.36)$$

$$\lambda_r = 500 \text{ to } 1000 d_{50} \quad (2.37)$$

From experiments NIELSEN (1981), found that the mobility parameter Ψ :

$$\Psi = \frac{U_w^2}{(s-1) \cdot g \cdot d_{50}} \quad (2.38)$$

is the best parameter to estimate the wavelength for rolling-grain and vortex ripples. He gave two equations to determine the height and length of the ripples, because natural waves are much less regular than laboratory waves.

- For laboratory data:

$$\frac{h_r}{\hat{A}_\delta} = 0.275 - 0.022 \cdot \Psi^{0.5} \quad \text{for } \Psi \leq 156 \quad (2.39)$$

$$\frac{h_r}{\hat{A}_\delta} = 0 \quad \text{for } \Psi > 156 \quad (2.40)$$

$$\frac{\lambda_r}{\hat{A}_\delta} = 2.2 - 0.345 \cdot \Psi^{0.34} \quad \text{for } 2 < \Psi < 230 \quad (2.41)$$

- For field data and $\Psi \geq 10$:

$$\frac{h_r}{\hat{A}_\delta} = 21 \cdot \Psi^{-1.85} \quad (2.42)$$

$$\frac{\lambda_r}{\hat{A}_\delta} = \exp\left[\frac{693 - 0.37 \cdot \ln^8 \Psi}{1000 + 0.75 \cdot \ln^7 \Psi}\right] \quad (2.43)$$

with:

\hat{A}_δ = peak value of orbital excursion

VAN RIJN (1989), proposed several equations for determining the ripple height and length for irregular waves. He assumed that the ripples disappear when the mobility parameter Ψ exceeds a value of 250 and sheet flow conditions are reached.

$$\frac{h_r}{\hat{A}_\delta} = 0.22 \quad \text{for } \Psi \leq 10 \quad (2.44)$$

$$\frac{h_r}{\hat{A}_\delta} = 2.8 \cdot 10^{-13} (250 - \Psi)^5 \quad \text{for } 10 < \Psi < 250 \quad (2.45)$$

$$\frac{h_r}{\hat{A}_\delta} = 0 \quad \text{for } \Psi \geq 250 \quad (2.46)$$

$$\frac{h_r}{\lambda_r} = 0.18 \quad \text{for } \Psi \leq 10 \quad (2.47)$$

$$\frac{h_r}{\lambda_r} = 2 \cdot 10^{-7} (250 - \Psi)^{2.5} \quad \text{for } 10 < \Psi < 250 \quad (2.48)$$

$$\frac{h_r}{\lambda_r} = 0 \quad \text{for } \Psi \geq 250 \quad (2.49)$$

The equations 2.39 to 2.49 predict the ripple wavelength and height as a function of the mobility number. More recent studies, BOYD ET AL. (1988) and VINCENT AND OSBORNE (1993), have found no clear relationship between the orbital excursion \hat{A}_δ and the ripple wavelength.

The limit of the maximum velocity at which ripples disappear varies in the literature. DINGLER AND INMAN (1976), suggested a value of $\Psi = 240$ which corresponds well with the value of $\Psi = 250$ reported by VAN RIJN (1984). NIELSEN (1979), however pointed out that large scatter can be found in Dingler's data as he ignored the variation of the friction factor. CARSTENS (1966), suggested a value of $\Psi = 169$. SUMER AND BAKIOGLU (1984), used a totally different parameter to establish the existence of ripples. They use the Nikuradse roughness (k_s), determined by Engelund and Hansen's (1967) definition ($k_s=2.5 \cdot d$), the shear velocity u_* and the kinematic viscosity to determine the upper limit of the existence of ripples. Their upper limit was defined by:

$$\frac{k_s \cdot u_*}{\nu} \geq 58.5 \quad \text{or with the definition of } k_s, \quad \frac{d \cdot u_*}{\nu} \geq 23 \quad (\text{and } u_* = \sqrt{\bar{\tau}_w / \rho}), \quad \text{where } \bar{\tau}_w \text{ is}$$

the unperturbed wall shear stress).

Another different parameter is for example used by MANOHAR (1955). This seems to indicate that the determination of an exact limit when the flow transforms into sheet flow and ripples disappear, varies depending on the data used to calculate the limit. However, it is clear that the ripples disappear at high sediment transport rates.

Dunes will form together with ripples in steady flow. Like ripples, dunes have a gentle upstream slope and a steep downstream slope in steady flow conditions. A vortex will form in the lee of the dune crest. Whereas ripples do not influence the free surface, dunes show noticeable effects on the free surface. This effect can usually be observed in a dip in the water surface above the crest and a slight rise in the water level above the trough (SLEATH, 1984). In pure oscillatory flow, in the sea dunes are usually formed by tides or other quasi-steady currents. To determine the height and length of dunes several empirical equations are available. YALIN (1964), suggested a dune length of:

$$\lambda_d = 5 \cdot h \quad (2.50)$$

with: h = mean water depth [m]

whereas HINO (1968) suggested:

$$\lambda_d = 7 \cdot h. \quad (2.51)$$

ALLEN (1963) gave the following expression for the dune height:

$$\Delta_d = 0.08 \cdot \lambda_d \quad (2.52)$$

In the sea, the wavelength of dunes is usually much larger than that of ripples and ripples will form on top of dunes.

Sand-ridges and sandbanks are longitudinal bed features and found in most shelf seas. They are the largest sedimentary feature in marine conditions and can reach up to 10 m in height, 1 km in width and 10 km in length (VAN RIJN, 1989). Sandbanks are formed from medium to coarse sand and are generally stable. However, if the velocity is large enough for initiation of motion, sandwaves and mega-ripples may migrate over the banks.

2.4 Wave induced Suspended Sediment Concentration Profiles and Transport

2.4.1 Introduction

This section discusses the basic concepts of non-cohesive sediment transport under waves. Sediment transport in oscillatory flow is similar to transport in steady flow. It can be divided into transport as bedload, where the sand grains remain more or less continuously in contact with the bed and as suspension, where the particles fall freely relative to the moving fluid (SLEATH, 1984). However, as the wave velocity varies from zero at the zero crossings to a peak under the crest and trough, sediment can be transported as bedload during part of the wave cycle and as suspended load during the rest of the cycle. The emphasis in this section is on sediment suspension. Sediment is entrained into the water column by diffusive and convective processes. For wave conditions significantly exceeding the threshold of motion, the suspended load transport is an important contribution to the total sediment transport rate.

Sediment transport equations usually deal with the bedload or total load material and are based on a steady state approach, where the transport is calculated for each half of the wave cycle.

2.4.2 Shear stress in oscillatory flow

Wave motions over the bed produce an oscillatory boundary layer due to the frictional effects near the bed. Linear wave theory assumes a no slip condition at the bed. The orbital

velocity, U_w , determined by linear theory is then presumed to exist at the outer boundary of the wave boundary layer. It is this boundary layer through which the waves exert a shear stress on the bed. For a smooth bed and relatively small orbital velocities the boundary layer may be laminar, but more often in cases where sediment is in motion it will be turbulent (SOULSBY, 1997). In the absence of a current, the boundary layer is only a few millimetres to centimetres thick, thus justifying the free slip condition.

Within the boundary layer the frictional forces of the waves cause the sediments at the bed to move. At first, it is important to determine the threshold, at which the sediment first starts moving. The frictional force exerted by the flow per unit area of the bed is expressed in the bed shear stress. It is this shear stress, which depends not only on the flow velocity, but also on the roughness of the sea bed, that is important for the entrainment of sediment. The total shear stress acting on the bed is made up of the grain scale and the ripple scale bed roughness. These two scales of shear stress generation are given the symbols τ_{wG} for the sediment grain bed shear stress and τ_{wR} for the ripple bed induced shear stress. The bed shear stress is related to the orbital velocity by:

$$\tau_w = \frac{1}{2} \cdot \rho \cdot f_w \cdot U_w^2 \quad (2.53)$$

where τ_w is the instantaneous bed shear stress, f_w is the wave friction factor and U_w is the orbital velocity at the bed, which is either measured directly or derived indirectly from another measured parameter using wave theory. The wave friction factor is dependent on the type of flow (laminar, smooth turbulent, rough turbulent) and the relative roughness.

The shear stresses in oscillatory flow over small roughness elements and natural ripples are often composed of coherent temporal fluctuations and have a mean of zero (for first order waves). In laminar flow the orbital velocity follows a simple harmonic motion. This then leads to a simple harmonic shear stress, which leads the orbital velocity outside the bottom boundary layer by 45 degrees. According to SLEATH (1984), this is not surprising, because the velocity close to the bed is 45 degrees ahead of that outside the boundary layer. When the ratio of bed roughness to semi-excursion (r/A) increases, the shear stress increasingly deviates from the simple harmonic behaviour. NIELSEN (1992), showed an example of measurements taken by JONSSON AND CARLSEN (1976), with a ratio of $r/A = 0.008$. In this case the phase shift between the orbital velocity and the shear stress was slightly smaller than the 45 degrees determined for smooth, laminar flow. Measurements of instantaneous shear stresses carried out by LOFQUIST (1986), for oscillatory flow over fully developed sand ripples (r/A was in the order of one) showed a completely different behaviour from that of a

simple harmonic. The shear stress variation over fully developed sand ripples is complicated by the rhythmic formation and release of strong vortices. With decreasing wave period, the harmonic component disappears almost completely. The shear stress phase characteristics are complicated, with three coherent peaks, for small wave period, but are roughly sinusoidal for large wave period.

When the flow is rough and turbulent, the friction factor only depends on the relative roughness and the resulting curve has been obtained experimentally (JONSSON, 1966, KAMPHUIS, 1975). These data have been used to obtain empirical relationships. In a review NIELSEN (1992), suggested the following modification to Swart's (1974) expression when analysing measured values of the friction factor:

$$f_w = \exp \left[5.5 \cdot \left(\frac{A}{k_s} \right)^{-0.2} - 6.3 \right] \quad (2.54).$$

Equation 2.54 was developed for rough, turbulent flow.

SOULSBY (1997), suggested an alternative empirical equation derived by fitting the two coefficients in equation 2.55 to 44 measured values.

$$f_w = 0.237 \cdot \left(\frac{A}{k_s} \right)^{-0.52} \quad \text{for all} \left(\frac{A}{k_s} \right) \quad (2.55)$$

The friction factor determined from equations 2.54 and 2.55 as a function of the relative roughness, A/k_s is shown in figure 2.9. For the values of relative roughness less than 610, Soulsby's equation predicts larger values of the friction factor. For a relative roughness of greater than 610, Nielsen's values of the friction factor are greater and diverge from Soulsby's values with increasing relative roughness. For the *Deltaflume* tests, the relative roughness was in the range of 700 to 1800. For this range, the friction factors determined by equations 2.54 and 2.55 are within 30 % of each other.

To calculate the peak shear stress for grain scale turbulence the friction factor is calculated using equation 2.55 with $k_s = 2.5 \cdot d_{50}$. To calculate the peak shear stress for the ripple scale turbulence, the friction factor is calculated with $k_s = 8 \cdot h_r^2 / \lambda_r$, where h_r and λ_r are the ripple height and wavelength, respectively. According to SOULSBY (1997), it is only the skin friction contribution that acts directly on the sediment grains and therefore should be used to calculate the threshold of motion and reference concentration as a first approximation.

When measuring turbulence SLEATH (1987), showed that for his experiments the shear stress calculated from the total acceleration defect was a factor of ten larger than the periodic, turbulent Reynolds stress determined from the turbulent fluctuations of the vertical and horizontal velocities. Thus, as Sleath pointed out, the contribution of the turbulent fluctuation to the shear stress is a lot smaller than the contributions of the periodic velocity component. NIELSEN (1992), highlighted that results obtained by SLEATH (1987), showed a roughly exponential decrease in shear stress amplitude with increasing distance from the bed.

2.4.3 Threshold for initiation of motion under waves

An understanding of the threshold condition for initiation of motion is important to the general problem of sediment transport. Particle movement will occur when the hydraulic forces on a particle are larger than the critical hydraulic forces for initiation of motion. The particle starts moving, when the moment of the disturbing force (a combination of lift and drag force) with respect to the contact point of two sand particles at the surface of the bed is larger than the moment of the stabilising force (figure 2.10). Using the fact that both the drag and the lift force are proportional to \bar{u}_*^2 and to functions of the grain Reynolds number, Shields plotted observed threshold values, Θ_{cr} (critical Shields parameter) against the grain Reynolds number. SHIELDS (1936), performed experiments on a flat bed in a rectangular channel to determine the initiation of motion of sediment in steady currents. He used closely graded material of nearly spherical shape and the flow was fully turbulent. His definition of the critical Shield's parameter (Θ_{cr}) as a function of the grain related Reynolds number, Re_* , is most widely used. SHIELDS (1936), not only determined the threshold for initiation of motion, but also classified a number of bedform regimes as a function of the grain related Reynolds number, Re_* , and the shear stress (figure 2.11). He defined the initiation of motion as the point at which the bed load can be extrapolated to zero.

Strictly speaking the Shields curve only applies to steady flow, however SLEATH (1984) and VAN RIJN (1989), along with other researchers, have shown that it can be applied as a criterion for initiation of motion for oscillatory flow over a plane bed. The threshold of initiation of motion of sand under oscillatory flow depends on the bottom orbital velocity, the wave period, the grain diameter and the density (SOULSBY, 1997). VAN RIJN (1989), stated that for a rippled bed the critical values for initiation of motion are considerably smaller due to the generation of vortices. MILLER ET AL. (1977), replotted the Shields diagram with an extensive range of field data. Figure 2.12 is a Shields curve type diagram from VAN RIJN (1989), showing the extended Shields curve from the measurements of MILLER ET AL.

(1977), and three curves showing the initiation of suspension. The critical number is plotted against a dimensionless particle diameter D_* , defined by equation 2.34.

Figure 2.13 shows a comparison of flume data with the Shields curve taken from VAN RIJN (1989). The error bars indicate the influence of the wave period and the grain roughness taken as $k_s \approx \alpha \cdot d_{90}$, with α being in the range of 1 to 3. The relative large scatter in the data can be mainly attributed to the different definitions of the initiation of motion by the different investigators. This problem was also found by BAGNOLD (1946).

For the *Deltaflume* experiments, the critical shear stress for the initiation of motion based on a steady state approach as described by SOULSBY (1997) for the two sand types ($d_{50} = 0.329$ mm and $d_{50} = 0.162$ mm) is 0.18 N/m² and 0.12 N/m², respectively.

SLEATH (1984), analysed measurements of bedload transport and discovered that there is a well defined critical value of orbital velocity outside the boundary layer, below which no sediment movement occurs. He stated that this is in contrast to steady flow, where it is more difficult to determine an exact value of fluid velocity, at which movement of particles occurs.

Under wave conditions it is often more convenient to determine the threshold orbital velocity, rather than the critical Shields parameter. The threshold velocity of initiation of motion was investigated by SEYMOUR (1985), analysing formulae proposed by HALLERMEIER (1980), based on the relationship in which the horizontal hydrodynamic forces just exceed the frictional resistance of the grains. Figure 2.14 shows the threshold orbital velocity for different wave periods as a function of the median grain diameter (from SEYMOUR, 1985) for a kinematic viscosity of 0.014 cm²/s and a sediment density of 2.85 g/cm³. With a wave period of 5 s and a median grain diameter of 0.329 mm, figure 2.14 yields a threshold velocity just outside the boundary layer of approximately 0.34 m/s. This velocity is exceeded during parts of the wave period for all the tests with different wave heights conducted in the current experiments in the *Deltaflume*. Figure 2.15 shows the critical orbital velocity as a function of the median grain diameter for a number of wave periods suggested by SOULSBY (1997). He deduced the threshold velocity from the threshold of the bed shear stress. Also included in figure 2.15 are results from experimental data by VAN RIJN (1989). Figure 2.15 yields a critical orbital velocity of 0.14 m/s for the median size sand ($d_{50} = 0.329$ mm) used in the *Deltaflume* experiments with a period of 5 s. It has to be kept in mind that the results were obtained in sea water with a salinity of 35 ppt, while fresh water was used in the *Deltaflume* experiments. Though, the two threshold values deviate by more than a factor of two, they indicate that the threshold for initiation of motion was exceeded for part if not most of the wave cycle throughout all the *Deltaflume* tests.

2.4.4 Settling Velocity

The *in situ* particle settling velocity, w_0 , is difficult to measure and, thus empirical relations are often used to express the terminal velocity of a single particle settling through a still fluid. Here, the fluid drag on the particle balances exactly the force of gravity. Hindered settling occurs in large sediment concentrations, because the downward motion of one sediment particle will generate a compensating upward flow elsewhere, which will delay the downward motion of the sediment particles. However, a dense cloud of sediment in a otherwise clear fluid will settle with a larger velocity (NIELSEN, 1992). In turbulent water, the transport of sediment depends on the relative motion of the turbulent fluid and the sediment particles. NIELSEN (1992), pointed out that the settling velocity of a sediment particle in turbulent water can be significantly different from the settling velocity in still water and on average a particle settles slower than it would through still water (figure 2.16). Depending on the surrounding flow field, a particle may be accelerated if the flow is in a downward direction and hindered, if the flow is in an upward direction.

An expression for the terminal velocity of a sphere can be derived using Stokes' law for the drag coefficient, which can be used for grain diameters of less than 100 μm according to GIBBS ET AL. (1971), while SOULSBY (1997), gave a threshold of 62 μm . However, natural grains are non-spherical. Empirical corrections are used to estimate the settling velocity depending on the grain size. GIBBS ET AL. (1971), provided the following empirical equation for w_0

$$w_0 = \frac{-3 \cdot v + \sqrt{9 \cdot v^2 + g \cdot d^2 \cdot (s - 1) \cdot (0.003869 + 0.02480 \cdot d)}}{0.011607 + 0.07440 \cdot d} \quad (2.56),$$

in which all units must be in cgs and w_0 is given in cm/s. They used individual glass spheres, which settled in still water at different temperatures and salinities under the influence of gravity. Soulsby derived an equation for natural sands, based on optimising two coefficients in a combined viscous plus bluff body drag law against data for irregular grains. The equation can be found in SOULSBY (1997), and is given by

$$w_0 = \frac{v}{d} \cdot \left[\left(10.36^2 + 1.049 \cdot D_*^3 \right)^{1/2} - 10.36 \right] \text{ for all } D_* \quad (2.57),$$

where D_* is the dimensionless grain size determined by equation 2.34 and d is a grain diameter in m. Here, all units are in m and w_0 is given in m/s.

SOULSBY (1997), compared the two equations with measurements of settling velocities of natural sands and irregular shaped light-weight grains. He found that 35 % of the predictions

determined by the equation of Gibbs et al. and 66 % of the predictions determined by Soulsby's equation lie within 10% of the measurements. This seems a large scatter. There are no *in situ* measurements of settling velocity available for the *Deltaflume* experiment. Thus, it is only possible to compare the settling velocities given by the two empirical equations with each other. For the sediment sizes used in the *Deltaflume* experiment, equations 2.56 and 2.57 determine settling velocities within 11% of each other.

It is difficult to measure settling velocity of suspended sediment in the field and further, the concept of inertial settling of single grains in an unhindered fashion may not be realistic. An accurate determination of the settling velocity is very important for sediment suspension. Once the sediment is entrained into the water column, it settles back to the bed under its terminal settling velocity. Thus the time the particles stay in suspension is governed by the time it takes the particle to settle back to the bed.

2.4.5 Suspended Sediment Concentration Profiles

2.4.5.1 Theoretical Background

For steady flow situations, it is common to apply a gradient diffusion assumption for the turbulent flux given by

$$w_0 \cdot \bar{c}(z) + \varepsilon_s \cdot \frac{d\bar{c}}{dz} = 0 \quad (2.58)$$

where \bar{c} is the mean sediment concentration at height z , ε_s is the sediment diffusivity and w_0 is the still water settling velocity. Equation 2.58 has been derived from the general three-dimensional, unsteady continuity equation by assuming no horizontal, spatial variability (FREDSØE AND DEIGAARD, 1992) and no temporal variability. Though, there is a significant temporal variability of the sediment concentration under waves, equation 2.58 can be used to estimate burst averaged concentration profiles. NIELSEN (1979), stated that neglecting the horizontal, spatial variability is a very crude approach, because a significant concentration gradient between the sediment clouds and the surrounding fluid exists. However, he concluded that this effect becomes negligible if the mean concentration profile is determined over a ripple length. The gradient diffusion mechanism assumes that it is the turbulence that allows sediment to remain in suspension. Equation 2.58 has also been applied to waves, though SLEATH (1984), mentioned that it is not only a diffusive process on a rippled bed under oscillatory flow that entrains sediment into suspension. According to NIELSEN (1992),

the gradient diffusion can be used to describe the upward sediment flux, as long as the mixing length, ℓ , is small compared to the overall height of the concentration profile.

To obtain values of the sediment diffusivity from measured concentration values, under the assumption of a pure diffusion process, equation 2.58 can be rearranged to give the following expression for the sediment diffusivity:

$$\varepsilon_s = \frac{-w_0 \cdot \bar{c}(z)}{d\bar{c}/dz} \quad (2.59)$$

The sediment diffusivity is related to the eddy viscosity by $\varepsilon_s = \gamma \cdot \nu_t$ (FREDSØE AND DEIGAARD, 1992), where gamma is a constant of proportionality (DYER, 1986). Strictly speaking this is only valid for steady flow situations. NIELSEN (1992), analysed data from COLEMAN (1970), and showed that modelling the sediment distribution as pure gradient diffusion leads to a sediment diffusivity, which differs considerably from the eddy viscosity and is also a function of the relative settling velocity w_0 / \bar{u}_{*c} (figure 2.17, where D is used for the water depth). Further evidence of the inadequate representation of the measurements by gradient diffusion can be found in the data of NIELSEN (1983), and MCFETRIDGE AND NIELSEN (1985), for oscillatory flow over a rippled bed. Thus, NIELSEN (1992), concluded that using a gradient diffusion approach to model sediment concentrations only makes sense if the same value of sediment diffusivity can be used for all particles and if it is closely related to the eddy viscosity. Though, gradient diffusion on its own fails to relate the sediment diffusivity closely to the eddy viscosity, NIELSEN (1992), thought that a combined convective/diffusion approach can provide this relationship. A number of researchers have determined the value of gamma by comparing measured and predicted sediment concentration profiles. This will be discussed in section 2.4.5.2.

The convective process becomes important when the mixing length is of the same order of magnitude as the overall scale of the concentration distribution. An example of a convective process is the entrainment of sediment from rippled sand beds under waves by travelling vortices. NIELSEN (1992), suggested the following expression for a purely convective process keeping in mind that generally sediment suspension is a combination of convection and diffusion:

$$\frac{\partial c}{\partial t} = w_0 \cdot \frac{\partial c}{\partial z} - \frac{\partial q_c}{\partial z} \quad (2.60)$$

where q_c is the convective flux and w_0 is the still water settling velocity. The convective sediment flux can be written in the form

$$q_c(z, t) = P\left(t - \frac{z}{w_c}\right) \cdot F(z) \quad (2.61)$$

where $P(t)$ is the instantaneous pickup rate at the bed, $F(z)$ is the dimensionless convective distribution function and w_c is the sediment convection velocity. A couple of equations based on sediment suspension by a convective process will be presented in section 2.4.5.2.

2.4.5.2 Mean Suspended Sediment Concentration Profiles

A number of semi-empirical and empirical equations for the mean vertical suspended sediment concentration profiles are available in the literature and some are presented here. It has to be emphasised that this is by no means a complete list of the available formulae.

For steady flow conditions, the pure diffusive sediment concentration profiles can be derived from equation 2.58. If the sediment diffusivity, ϵ_s , varies parabolically with height, the Rouse type profile is obtained (e.g. ZYSERMAN AND FREDSE, 1994, SOULSBY, 1997):

$$\bar{c}(z) = c(a) \cdot \left(\frac{z}{a} \cdot \frac{h-a}{h-z}\right)^{-\alpha} \quad (2.62)$$

where $\bar{c}(a)$ is the reference concentration at a height a and h is the water depth. A number of empirical equations for the reference concentration will be presented later in this section. The Rouse parameter α , is the ratio of settling velocity to upward directed fluid velocity given by

$$\alpha = \frac{w_0}{\gamma \cdot \kappa \cdot u_*} \quad (2.63)$$

where u_* is the shear stress velocity and κ is the von Karman constant (≈ 0.4). As mentioned in section 2.4.5.1 γ is a constant of proportionality between the sediment diffusivity and the eddy viscosity. Normally, γ is assumed to be unity, though DYER (1985), reported that values of both greater and less than unity have been obtained. FREDSE AND DEIGAARD (1992), also concluded that γ can deviate from unity, because the centrifugal forces may have larger effects on the sediment particles due to their large density than on the fluid particles. LEES (1981), compared measured and predicted sediment concentration profiles, using a Rouse type profile to evaluate the value of γ . The measurements were taken on the British continental shelf, in the Sizewell Dunwich area of Suffolk, with a mean sediment diameter at the bed of 130 μm . γ was used as a free parameter when fitting the Rouse-profile to the measurements. γ was in the range of one to ten. With increasing grain size, the value of γ increased and decreased with

concentration. The influence of gamma on the current data will be explored in chapter 5. Apart from a deviation of gamma from unity, the value of the von Karman constant might vary from 0.4 in suspended sediments. VINCENT AND GREEN (1990), found that a value of 1.35 for gamma gave good agreements between measured concentrations and GLENN AND GRANT'S (1987), combined-flow model for the first 8 to 10 cm above the bed. GREEN AND BLACK (1999) reported that a gamma value of 0.85 gave a good fit between measured and predicted sediment concentration profiles within the first 10 cm above the bed under waves. In general it has been suggested that values of gamma less than unity represent the inability of grains to follow fully the turbulent motion of the water. In contrast centrifugal forces in eddies might yield gamma values of greater than unity (DYER AND SOULSBY, 1988). In general, it seems that there is a tendency in oscillatory flow for gamma to be less than unity for sheet flow and greater than one for rippled beds.

A modification of the Rouse equation for wave-current flow was suggested by WILLIAMS ET AL. (1996), and is given in the form:

$$\bar{c}(z) = c(a) \cdot \left(\frac{z + \ell \cdot \alpha}{a + \ell \cdot \alpha} \right)^{-\alpha} \quad (2.64)$$

where ℓ is the vertical length scale. NIELSEN (1990), suggested the following expression for the vertical length scale based on laboratory and field data from NIELSEN (1979, 1984, 1986, 1990):

$$\ell = 0.075 \cdot \frac{U_w}{w_0} \cdot h_r \quad \text{for } \frac{U_w}{w_0} < 18 \quad (2.65a)$$

$$\ell = 1.4 \cdot h_r \quad \text{for } \frac{U_w}{w_0} \geq 18 \quad (2.65b)$$

where U_w is the peak orbital velocity amplitude at the bed for waves and h_r is the ripple height. Nielsen used a value of 0.4 for the von Karman constant in his derivation of equations 2.65a and b. WILLIAMS ET AL. (1999a and 1999b), showed that equation 2.64 can simulate measured c-profiles accurately.

Nielsen analysed concentration profiles for different wave conditions over a rippled bed. Figure 2.18 shows four c-profiles with a fixed sediment size for four different wave periods. For the shortest wave period, the profile is upward convex. For the two intermediate periods, the profile is practically linear (on this linear/log plot) over the first 4 ripple heights ($0 < z/\eta < 4$). This lead Nielsen to describe the variation of the concentration near the bed by the simple exponential relationship

$$\bar{c}(z) = c_0 \cdot e^{-z/\ell} \quad (2.66)$$

where c_0 is the reference concentration. Equation 2.66 is obtained if ε_s is assumed to be constant in equation 2.58.

A similar behaviour was observed by NIELSEN (1992), for a fixed wave period but different sand sizes, and thus increasing settling velocity, in the same flow. These changes of profiles are attributed to suspension by a combination of convection and diffusion processes.

Close to the bed, the concentration gradient is large. In this region the entrainment is dominated by sediment diffusion. At larger distances from the bed, the sediment concentration becomes more uniform and thus the concentration gradient is small. In this region the sediment suspension is dominated by convection. The sediment is trapped in vortices and thus gets carried up the water column. The concentration profile for convection can be calculated by

$$\bar{c}(z) = c_0 \cdot F(z) \quad (2.67),$$

where $F(z)$ is the convective distribution function. Additional to the exponential relationship (equation 2.66) proposed by NIELSEN (1992), he also suggested for an upward concave concentration profile the following function

$$F(z) = (1 + z/L_c)^{-n} \quad (2.68)$$

where L_c is the convective length scale. Nielsen chose the vertical scale to be z_1 , which is the equivalent of the laminar Stokes length in an oscillatory boundary layer with constant eddy viscosity. When calibrating equation 2.68 with the data collected by MCFETRIDGE AND NIELSEN (1985), Nielsen found the power n to be equal to 2. As the value of n has been calibrated to give a good fit for a specific data set, it is subject to changes for other data sets. The convective function and Nielsen's empirical equation (2.69) for the c -profile, which takes the diffusion and convection processes into account, were tested on the present data (see chapter 5).

$$\bar{c}(z) = c_0 \cdot e^{-w_0 \cdot z / \varepsilon_s} \cdot \left(\frac{w_0}{\varepsilon_s} \cdot \int_0^z \frac{e^{w_0 \cdot \zeta / \varepsilon_s}}{(1 + \zeta / z_1)^n} d\zeta + 1 \right) \quad (2.69),$$

where w_0 is the settling velocity, ε_s is the sediment diffusivity, ζ is the elevation from the ripple crest and z_1 is the boundary length scale defined as $z_1 = 0.09 \cdot \sqrt{r \cdot A}$.

2.4.5.3 Expressions for the Reference Concentration

A number of different expressions for the reference concentration are available in the literature. NIELSEN (1986), defined his reference concentration, c_0 , at the position of $z = 0$ as

$$c_0 = 0.005 \cdot \rho_s \cdot \Theta_r^3 \quad (2.70)$$

where Θ_r is the modified effective Shields parameter. This relationship between c_0 and Θ_r is based on the analysis of a number of different measurements of the reference concentration in oscillatory flow (see NIELSEN (1986) for details). The modified effective Shields parameter has been defined by NIELSEN (1992), as

$$\Theta_r = \frac{\Theta_{2.5}}{(1 - \pi \cdot h_r / \lambda_r)^2} \quad (2.71),$$

where the grain roughness Shields parameter $\Theta_{2.5}$ was calculated by

$$\Theta_{2.5} = \frac{0.5 \cdot f_{2.5} \cdot U_W^2}{(s - 1) \cdot g \cdot d_{50}} \quad (2.72).$$

The friction factor $f_{2.5}$ is given by Swart's expression (equation 2.54) and $(1 - \pi \cdot h_r / \lambda_r)^2$ is a correction factor for the flow enhancement near the crest of vortex ripples.

WILLIAMS ET AL. (2000), compared two different equations (ZYSERMAN AND FREDSE, 1994 and VAN RIJN, 1989) for the reference concentration under wave only conditions.

In the first case, $c(a)$ values at $z = 2 \cdot d_{50}$ were calculated using the ZYSERMAN AND FREDSE (1994) expression

$$c(a) = \frac{0.331 \cdot (\Theta_s - 0.045)^{1.75}}{1 + 0.72 \cdot (\Theta_s - 0.045)^{1.75}} \quad (2.73)$$

for steady flow conditions. Here the skin Shields parameter, Θ_s , is defined as

$$\Theta_s = \frac{\hat{\tau}_{wG}}{\rho \cdot (s - 1) \cdot g \cdot d_{50}} \quad (2.74).$$

In the second case, $c(a)$ values at $z(a) = 0.5 \cdot h_r$ were calculated using the VAN RIJN (1989) expression

$$c(a) = \frac{0.015 \cdot d_{50} \cdot T_*^{1.5}}{z(a) \cdot D_*^{0.3}} \quad (2.75).$$

In this case, the dimensionless grain size, D_* , was calculated using $d_{50s} = d_{50}$ in equation C.4. In the VAN RIJN formulation, the transport stage parameter, T_* , is defined by equation 2.35.

WILLIAMS ET AL. (1999b), found that the expression by ZYSERMAN AND FREDSE (1994), for the reference concentration agrees well with the reference concentration derived using equation 2.64 for measurements in wave-current flow. However, they stated that the shear stress has to be calculated with a ripple related roughness ($k_s = 8 \cdot h_r / \lambda_r$, with h_r and λ_r the wave height and length, respectively) and not a grain related roughness ($k_s = 2.5 \cdot d$, with d the grain diameter) as proposed by ZYSERMAN AND FREDSE (1994), in their original work. Also WILLIAMS ET AL. (1999b), stated that the expression by Van Rijn (equation 2.75) tends to overpredict the concentrations determined from the measurements by about 50 %.

GREEN AND BLACK (1999), compared two different approaches for predicting time-averaged reference suspended sediment concentration under waves and compared them with field measurements. They analysed the equation by NIELSEN (1992), which relates the reference concentration to the cube of the non-dimensional skin friction, whereas the second model adopts a more complex function of excess skin friction. They found that Nielsen's model predicts the reference concentration accurately, as long as a correction for flow contraction over a rippled bed is applied. Thus, due to its simplicity, Nielsen's model was favoured over the model which uses the excess skin friction.

2.4.5.4 Examples of Field Measurements of Suspended Sediment Concentrations

HANES AND HUNTLEY (1986), reported on measurements taken seaward of the surf zone at Point Sapin, New Brunswick, using a miniature optical backscatter sensor (MOBS) and an electro-magnetic flowmeter. The MOBS had sensing elements at five vertical locations above the sea bed and was sampled at 10 Hz. Waves were dominant during the deployment. Their principal findings were that the suspension of sand was well correlated with the passage of individual waves and also with wave groups, whose influence was progressively dominant at higher elevations above the bed. Further, they discovered that the fluid acceleration may play an important role in sediment suspension and not only the velocity. HAY AND BOWEN (1994b) have also suggested that high concentration eddies might appear at times of maximum fluid acceleration and not just maximum horizontal velocity. However, the findings were not conclusive. Other researchers (e.g. OSBORNE AND VINCENT, 1996, VILLARD ET AL., 2000) concentrated on determining the phase correlation between the horizontal velocity with the sediment suspension. They mentioned that the relative position

of the sensors to the ripple is important for the phase relationship. Time lags between suspension events at different heights, suggested that vertical gradients in sediment flux were more important than horizontal gradients. A group of large waves appeared to suspend sediment higher into the water column than individual waves. This was explained by the suggestion that during wave groups, the turbulence persists and propagates upwards resulting in suspension at great elevations.

GREEN AND VINCENT (1990), presented field measurements obtained seaward of the surf zone on the North Norfolk coast of England on a rippled bed. The modal grain size of the non-cohesive bed sediment was 230 μm . Continuous profiles of suspended sediment concentrations from 48 cm above the bed down to the bed level were obtained every 0.58 s using an 2.8 MHz acoustic backscatter. The horizontal current velocity was measured at 20 cm above the bed by an electromagnetic current meter. They found that the periodic ejection of vortices from a rippled bed can cause a flux of sediment, which may be comparable in magnitude and opposite in sign to the mean suspended sediment flux. Thus, they concluded that transport predictions, based on the time averaged velocity and concentration profiles, lead to a significant error, as the periodic release of clouds of sediment is neglected. Further analysis of these data was presented by VINCENT AND GREEN (1990). Two different types of suspension were identified. The first one associated with wave crests, was probably generated by the local peak shear stress and was restricted to the first 3 to 4 cm above the bed. The second one was characterised by vertically extensive sediment pulses, which were associated with the intermittent shedding of sand laden vortices from rippled crests.

HANES (1991), described field observations of sediment suspension near the seabed under shoaled waves in the nearshore region on a flat bed at Cape Canaveral, Florida. Measurements were taken by a pressure sensor, a two-axis electromagnetic flowmeter and an acoustic concentration meter, which sampled at 4 Hz. He found a significant correlation between near bed concentrations and the cross-shore velocity squared and enhanced sediment suspension, at time scales corresponding to groups of incident waves.

HAY AND BOWEN (1994b), reported on field measurements carried out at Stanhope Lane Beach, Prince Edward Island in 1989 using the Remote Acoustic Sediment Transport (RASTRAN) system. RASTRAN was deployed on the seaward flank of the second bar, about 200 m offshore in a mean water depth of 2.2 m. Measurements were taken by four acoustic sounders, a flowmeter and three optical backscatter sounders. They discovered fluctuations in the acoustic backscatter data assumed to be suspended sediment trapped in

eddies. The concentration in the eddies exceeded the mean sediment concentrations by a factor of 10 or more and occurred in the signal at time scales much shorter than the wave period. The vertical coherence scale of these eddies was found to be 30 cm, which is many times greater than the logarithmic wave boundary layer thickness, but may be comparable to the overall wave boundary layer thickness, depending upon which measure of this thickness is chosen. The size of the eddies was too large to be the separate vortices shed by individual ripples observed in laboratory measurements (HAY AND BOWEN, 1994a). The eddies were present even with no vortex ripples. They concluded vortex shedding from megaripples, enhanced interaction with the bottom during the passage of the largest wave in a group or coherent structures in combined flow turbulence as possible explanations. Further analyses of measurements by the RASTRAN system were made by HAY AND BOWEN (1994a). They observed group generated suspension events. The development sequence, during a suspension event, was characterised by near-bottom stirring during the first 2 to 3 waves, followed by more rapid growth of the suspension cloud. This pumping effect continued after the passage of the largest waves in the group and in some cases well after the entire group had passed. Then rapid dissipation of the sediment cloud occurred at time scales much faster than the settling time scale. This was explained by the fact that compact clouds of sediment formed with a high settling velocity. However, the same measurements are obtained when a cloud of sediments gets advected backwards and forwards through the sensor and are thus only picked up for a short time interval in the measurements.

VINCENT ET AL. (1991), described measurements taken at Queensland Beach, Nova Scotia, by a suite of sensors consisting of electromagnetic current meters, optical backscatter probes, acoustic concentration meters and pressure sensors. No direct measurements of bedforms were available. They also noted the influence of wave groups on suspension events. They explained the effect of a wave group by changes in ripple geometry, due to different size waves generating equilibrium ripples with different steepness. A time lag would be expected in the response of the bed to the waves and thus, a large wave would have a bed which was over steep and which would eject sand laden vortices effectively. When a large wave passes over the sand bed, the bed does not react immediately to the passing of this individual wave by forming new equilibrium ripples. Considering the time it takes for equilibrium ripples to develop, it seems unlikely that they change at all during the passage of a wave group. VINCENT ET AL. (1991), concluded that a knowledge of the bed geometry during suspension events is very important for the prediction of suspended sediment concentrations.

Further experiments to determine the variability of suspended concentrations, transport and eddy diffusivity under waves were performed by VINCENT AND DOWNING (1994) on the seaward bar beyond the break point at Stanhope Lane beach, Prince Edward Island, Canada. Sediment concentrations were obtained using a 3 MHz acoustic backscatter transducer. Bedforms were observed by divers and some information was obtained through multiple bed echoes from the ABS. They commented that it is necessary to average burst measurements over a time scale that is long compared to both groupiness and bedform mobility, to obtain a consistent concentration profile. Their data showed a significant decrease of suspended sediment concentrations within the first 5 cm of the bed with increasing wave height. It will be later shown (chapter 5) that this cannot be seen in the data from the *Deltaflume* experiment. At high levels above the bed they observed an increase in suspended sediment concentrations, which they attributed to enhanced vortex ejection.

Analysis of large scale laboratory tests carried out in the multidirectional wave basin at the NRC Hydraulics laboratory were presented by OSBORNE AND VINCENT (1996). An underwater video camera recorded sequences of vortex generation in the lee of ripple crests and their subsequent ejection and dissipation in the flow above the bed. The vortices appeared to form predominantly under the crests of larger waves. Furthermore, they determined that bedforms did not respond instantaneously to the passage of individual large waves or wave groups, as far as their wavelength was concerned. This coincides with the findings by VINCENT ET AL. (1991).

VILLARD ET AL. (1999a), looked at the influence of wave groups, particularly the effects of antecedent waves, on the patterns of re-suspension at an intra-group time scale. Their measurements were made over a 10 m test section near the mid-point of the 95 m long (2.5 m high and 2 m wide) wave research flume at the National Hydraulics Laboratory in Ottawa, Canada. The sand bed (0.15 m thick) consisted of sand with a mean diameter of 250 μm . Their observations lead them to conclude that the suspended sediment concentration pattern in the upper water column depends largely on antecedent conditions, while events near the bed are more strongly controlled by instantaneous conditions. Further analyses of these data were presented by VILLARD ET AL. (1999b). An additional conclusion was that the peak suspended sediment concentration, under the wave groups close to the bed, did not occur at times of peak skin Shields values, but lagged behind. Their observations also suggested that the settling velocity must be smaller than the mean velocity estimated from empirical equations (VAN RIJN, 1989), which they attributed to the migration of coherent vortices and the fact that the vortices remain coherent over several wave cycles. More analysis of these data was discussed by VILLARD ET AL. (2000).

The role of wave groups in the re-suspension of sediments was analysed by WILLIAMS ET AL. (2001). They presented data collected at the northern end of Middelkerke Bank in the Flemish Banks in wave/current conditions. The measured median grain diameter was 450 μm . The bedforms consisted of sandwaves with a wavelength and height of 200 m and 3 m, respectively and some mega-ripples with wavelength and height of 15 m and 1 m, respectively. They also found a strong correlation between sediment suspension and wave groups in the co-spectra of velocity squared and suspended sediment concentration.

2.4.6 Sediment Transport Rate

2.4.6.1 Introduction

SLEATH (1984), analysed various experiments performed in oscillatory flow and concluded that the net transport strongly depends on the type of transport and bedforms present. He summarised the results as follows:

- For dominantly bedload transport over a rippled bed, the net sediment transport rate is in the direction of the largest peak velocity.
- For dominantly suspended transport over a rippled bed, the net sediment transport rate is in the opposite direction of the largest peak velocity.

VAN RIJN (1989), refined this definition, in view of the existence of cross-shore sediment transport, by distinguishing the following transport mechanisms:

- The asymmetry around the still water level of wave motion yield larger onshore peak velocities under a crest than offshore velocities under a trough. This results in a net sediment transport in the offshore direction on a rippled bed and a net onshore directed transport in case of a plane bed.
- The generation of net mean onshore directed velocities in the near bed region, which may result in a net onshore sediment transport.
- The generation of forced long waves due to a mean water surface decrease under large amplitude wave groups (Shi, 1983), resulting in secondary offshore directed orbital velocities under the trough and a net offshore directed transport, because the sediment concentrations are largest under large amplitude waves.

On a rippled bed vortices form in the lee of ripples during each half of the wave cycle. These vortices pick up sediment from the trough of the ripples. At flow reversal the vortex is lifted

passed the ripple crest and transported in the new flow direction. As the vortex created during the onshore half of the wave cycle is larger than the one created during the offshore half of the wave cycle, it leads to a net transport in the offshore direction on a rippled bed (i.e. the opposite direction of the largest peak velocity).

Wave motion over a movable bed of fine sand can generate sediment suspension with relative large concentrations in the near bed region. The variation of the instantaneous sediment concentrations in space and time is relevant for the cross-shore sediment transport.

Once the instantaneous sediment concentration has been determined, the sediment transport rate per unit width can be given in the form

$$Q(t) = \int_{z=0}^h c(z,t) \cdot u(z,t) dz \quad (2.76)$$

In most cases the time averaged transport rate is of interest and it can be calculated as:

$$\bar{Q} = \frac{1}{T} \cdot \int_t^{t+T} \int_{z=0}^h c(z,t) \cdot u(z,t) dz dt \quad (2.77),$$

where T is the wave period. Here it is assumed that the grains in suspension advect with the same velocity as the ambient flow and this is generally the case (NIELSEN, 1992).

The problem with equation 2.76 is generally the different vertical resolution of concentration and velocity measurements. In recent years acoustic backscatter transducers allowed concentration measurements with a vertical resolution of approximately 1 cm up to about 1 m into the water column. Flowmeters are point samplers and only provide velocity estimates at fixed heights above the bed. Thus, when determining the product of instantaneous velocity and sediment concentration, only values at a few points in the water column are available. The numerical integration of a few points to determine the net transport rate can lead to wrong estimates of the actual sediment transport rate over the total water depth. Furthermore, the lowest velocity measurement in wave only conditions tends to be outside the wave boundary layer and therefore, the transport due to bedload would be omitted when applying equation 2.76. However, OSBORNE AND VINCENT (1996), showed evidence which suggests that suspended load transport may be the dominant mode under combined waves and currents, due to the induced flow separation and turbulence from the bedforms. In wave only conditions, VAN RIJN (1989), stated that the majority of the suspended sediment transport is confined to the first three to five ripple heights above the

bed and hence, wave related sediment transport formulae in analogy with the bedload transport formulae applied in steady currents can be used.

A simple particle trajectory model has been proposed by NIELSEN (1992), for the bedload transport, where some particles are picked up from the bed and then dumped again after a jump length of ℓ (see figure 2.19). For this model a pickup function has to be known and a jump length has to be estimated. The jump length has to be estimated from the complex trajectories of the individual particles.

2.4.6.2 Sediment Transport

VAN RIJN (1989), summarised a number of different empirical equations to estimate the sediment transport rate in analogy with steady flow approaches. Where ripples are present the transport rate is determined for half a period, while on a flat bed some formulae (e.g. MADSEN AND GRANT, 1976) calculate the instantaneous transport rate and then integrate over the complete wave cycle to give a net transport rate.

NIELSEN (1992), proposed a simple particle trajectory model for the bedload transport using Van Rijn's pickup function combined with the Meyer-Peter formula for steady bed load:

$$Q_B = 8 \cdot (\Theta' - \Theta_{cr})^{1.5} \cdot d \cdot \sqrt{(s-1) \cdot g \cdot d} \quad (2.78),$$

where Θ' and Θ_{cr} are the effective and critical Shields parameter, respectively.

SOULSBY (1997), proposed the following equation for the sediment transport rate under half the period:

$$Q_B = 5.1 \cdot \left[g \cdot (s-1) \cdot d^3 \right]^{1/2} \cdot (\Theta_w - \Theta_{cr})^{3/2} \quad (2.79),$$

where Θ_w is the skin Shields parameter under waves. For completely regular, sinusoidal wave, equation 2.79 would predict a zero net-sediment transport under one wave. SOULSBY (1997) compared equation 2.79 with other equations proposed by MADSEN AND GRANT (1976) and SLEATH (1978), and determined that there was a factor of 10 variation in the predicted bedload transport rate between those three equations.

RIBBERINK AND AL-SALEM (1994), reported on sediment transport in oscillatory boundary layers in cases of rippled beds and sheet flow, focusing on the application of quasi-steady transport equations. A number of intra-wave, quasi-steady transport formulae were verified. In the quasi-steady models, it is assumed that the instantaneous transport adjusts itself immediately to the variable conditions within the wave cycle. From experiments in a wave tunnel with quartz sand of mean diameter of 0.21 mm, they found that an increase in the

root mean square orbital velocity (U_{rms}) lead to an increased suspended load with no influence of the wave period on a plane bed. However, on a rippled bed, the suspended load decreased with an increase in U_{rms} and wave period. RIBBERINK AND AL-SALEM (1994), concluded that a quasi-steady approach can be successful, if the grains only reach elevations above the bed such that they settle to the bed within fractions of the wave period. For the net transport rates, the quasi-steady models investigated by RIBBERINK AND AL-SALEM (1994), lead to overpredictions caused by an increase of an offshore directed suspended transport rate due to vortex shedding. Further experiments by RIBBERINK AND AL-SALEM (1995), concentrating on sheet flow on a plane bed have generally revealed a three layer system of time dependent sediment concentrations. The sheet flow layer was separated into two layers, the lower part was considered to be a deposition and pick-up layer, while the upper sheet flow layer contained large sediment concentrations in horizontal oscillatory motion. Again an overprediction in the quasi-steady sediment transport formulae was determined, attributing it to the turbulence damping due to stratification effects.

Depth integrated sand transport was investigated by GRASMEIJER ET AL. (1999). They analysed laboratory and field measurements of sediment concentrations and velocities. From wave tunnel measurements the bedload was predicted accurately using a simple bedload formula proposed by RIBBERINK (1998). The most important components in determining the description and the magnitude of the net suspended transport rate, determined from measurements in the *Deltaflume* and in the field, were the time and the high frequency suspended transport component. The low frequency component was of little significance to the net transport rate. In field conditions the bedload transport rate was found to be of the same order as the suspended transport rate.

2.5 Summary

The literature review addressed the main areas involved in analysing sediment suspension under waves and outlined wave theories, bed shear stresses, generation of bedforms and sediment suspension processes.

The main findings are as follows:

- As the waves are the main driving mechanism for the re-suspension of sediment, a good understanding of wave theories is important. There are different wave theories, which are suitable for particular wave characteristics and water depths. Therefore, establishing the limits of validity for the individual wave theories is very important. Linear wave theory is often used in wave conditions, even when the requirements of linear wave theory have

been violated. However, the uncertainties involved in accurately predicting suspended sediment concentrations often outweigh the improvement gained by using higher order wave theories. Thus, the author suggests that the application of linear wave theory is sufficient for the present data.

- Waves in the field are irregular and random. Wave records have shown that real waves form groups and these groups suspend more sediment than individual waves. The significance of wave groups on the sediment re-suspension has been mentioned by a number of researchers (e.g. HANES AND HUNTLEY, 1986, GREEN AND VINCENT, 1990, WILLIAMS ET AL., 2001).
- The type of bedform present under oscillatory flow strongly depends on the grain size and the type of waves. NIELSEN (1979), proposed empirical equations to estimate the ripple dimensions for regular and irregular waves. The type of bedform has a direct effect on the re-suspension mechanisms. For vortex ripples under oscillatory flow, vortices form in the lee of the ripples which then carry the sediment into the water column.
- Evidence of two different types of sediment re-suspension under waves was discussed. The diffusive process is related to length scales much smaller than the overall length scale of the sediment suspension, while for the convective process, it is of the same order. The convective suspension of sediment is driven by larger flow structures, such as vortices, which develop in the lee of ripples.

It can be concluded from the existing literature, that wave hydrodynamics and the associated sediment transport are complex and that there are great areas of uncertainties caused largely by the difficulties of solving the governing equations in general and the many factors which influence the suspension and transport of sediments. The literature review highlighted the limited knowledge of the basic processes involved in the re-suspension of sediments on an intra-wave time scale, especially under the influence of wave groups. Therefore, the objectives of this thesis are to address some of the following knowledge gaps:

- Analysis of sensor performance under controlled conditions.
- Many field experiments presented in the literature review utilised large deployment frames lowered on the sea bed to measure hydro- and morphodynamics. No evidence of a rigorous analysis of the effects of the deployment frames on the surrounding areas was found in the literature. The controlled conditions in the *Deltaflume* allow an extensive

analysis of bedform data with the view of determining the influence of STABLE on the measuring environment. Thus, the validity of the collected data can be assessed.

- Though the importance of wave groups on the re-suspension of sediments has been recognised by many researchers, no model is available to simulate the change in the concentration profiles during the passage of a wave group. With the extensive measurements of instantaneous orbital velocities and sediment concentrations, an attempt will be made to develop a simple model that predicts the changes in concentration profiles under the passage of a wave group.
- The development of vortices in the lee of ripples has been observed by many researchers. Suggestions have been made that vortex pairing occurs and that this mechanism is responsible for entraining sediment further into the water column. The idea of vortex pairing will be investigated.

Further reviews of the literature will be presented in some sections within the chapters, where they are related to the data analysis carried out. Wavelet analysis as an analysing tool for time histories will be investigated in chapter 4.

TABLES

Bed form classification		$1 \leq D_* \leq 10$	$D_* \geq 10$
		$(50 \mu\text{m} \leq d_{50} \leq 450 \mu\text{m})$	$(d_{50} \geq 450 \mu\text{m})$
Lower flow regime	$0 \leq T_* \leq 3$	Mini ripples	dunes
	$3 \leq T_* \leq 15$	Mega ripples and dunes	
Transitional flow regime	$15 \leq T_* \leq 25$	Washed out dunes and plane bed	
Upper flow regime	$T_* \geq 25$	Plane bed and anti-dunes	

Table 2.1: Classification of bedforms as a function of the dimensionless grain diameter D_* (equation 2.34) and the dimensionless bed shear stress parameter T_* (equation 2.35) after VAN RIJN (1989).

FIGURES

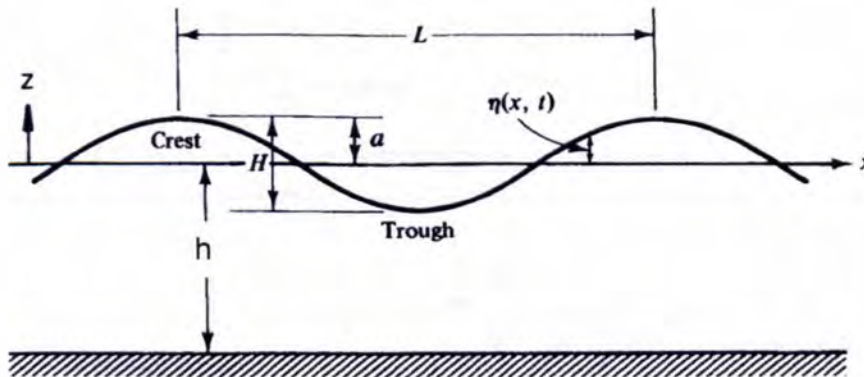


Figure 2.1: A regular, two-dimensional wave of height H and wavelength L , in water of depth h .

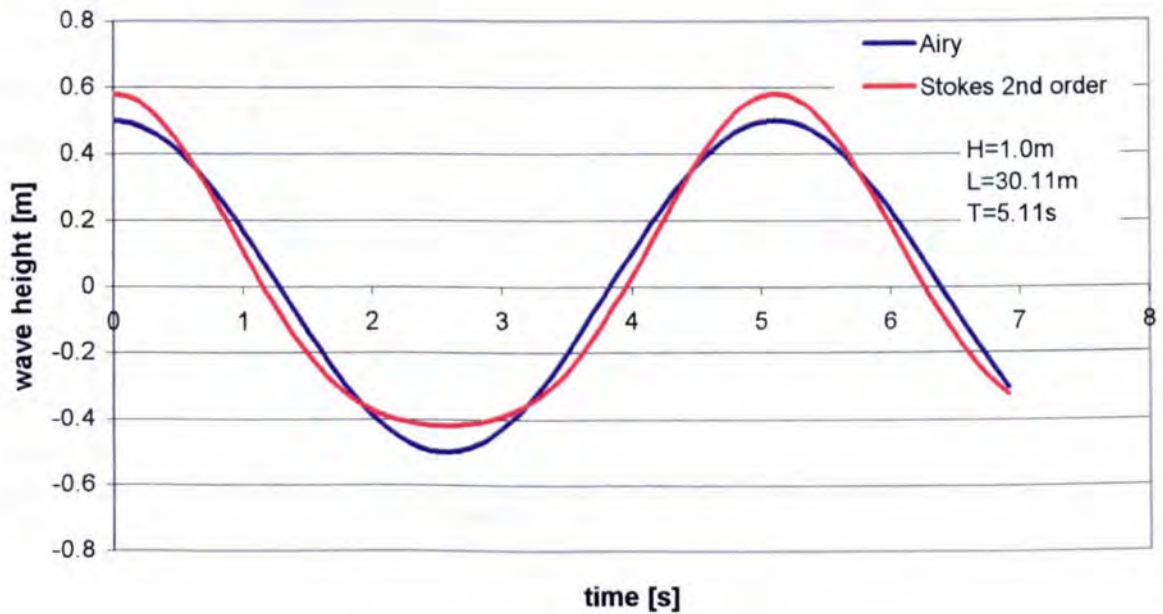


Figure 2.2: Wave elevation, with a wavelength of 30.11 m, a period of 5.11 s and a wave height of 1 m, calculated using linear and Stokes' second order wave theories.

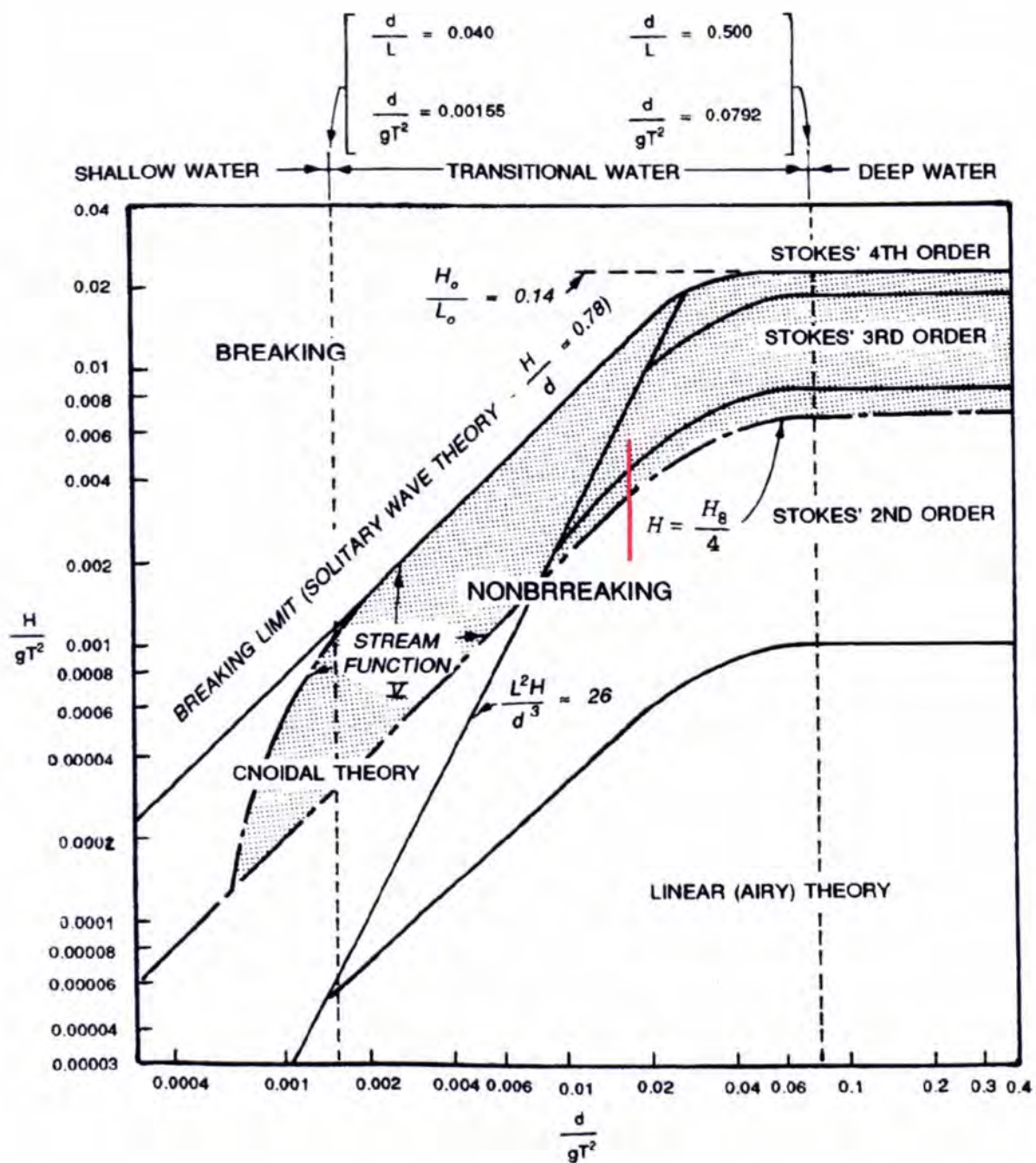


Figure 2.3: Validation of wave theories as a function of water depth (note, d is the water depth here), wave height and period (after LE MEHAUTE, 1969). The red line indicates the range of the experiments in the *Deltaflume*.

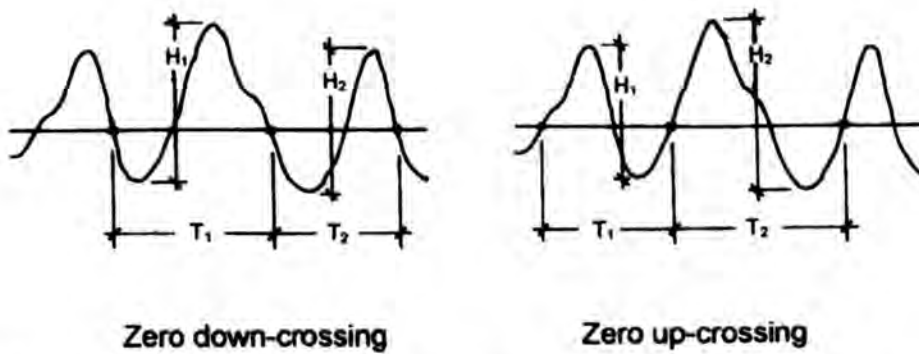


Figure 2.4: Definition of zero down- and up-crossings. Zero down-crossing has been used throughout the present data analysis.

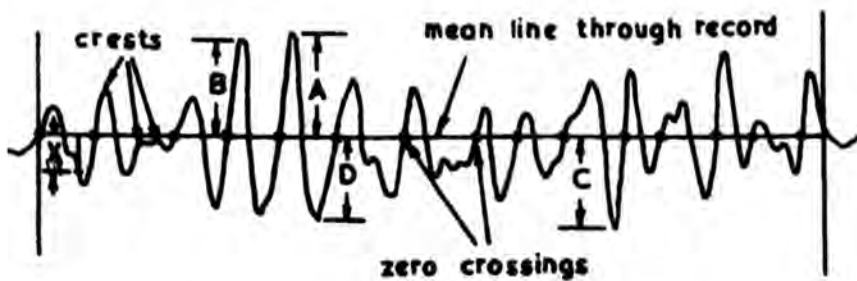


Figure 2.5: Schematic of a wave record with definition of A, B, C and D as used for the Tucker method (see figure 2.6), from Tucker (1963).

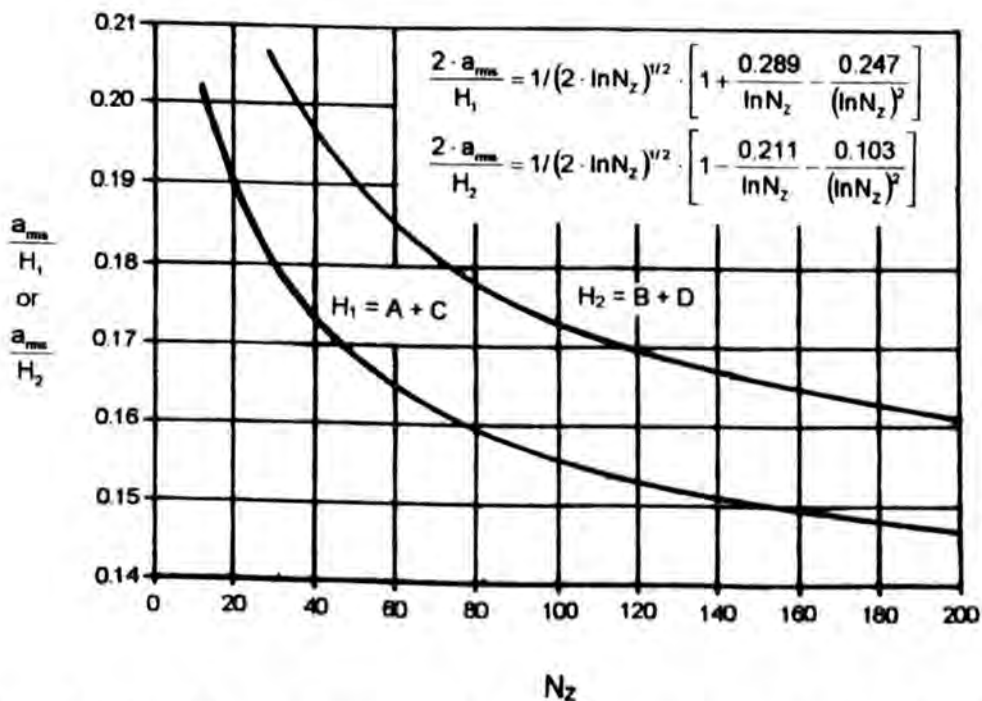


Figure 2.6: Relationship between a_{rms} and N_z according to the Tucker Method (SYLVESTER, 1974), from Tucker (1963).

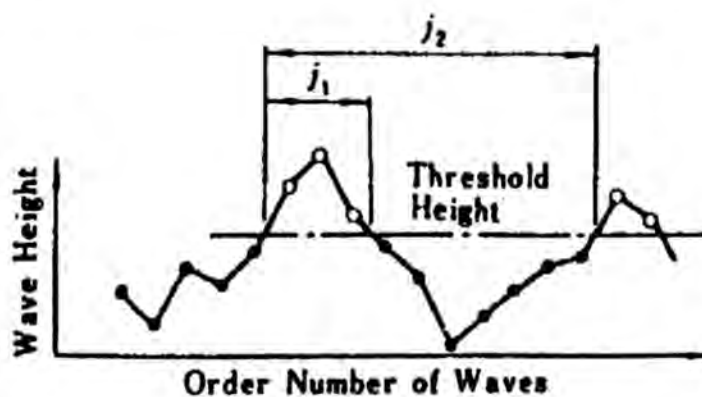


Figure 2.7: Sketch of the definitions used to calculate the run length (after GODA, 1985).

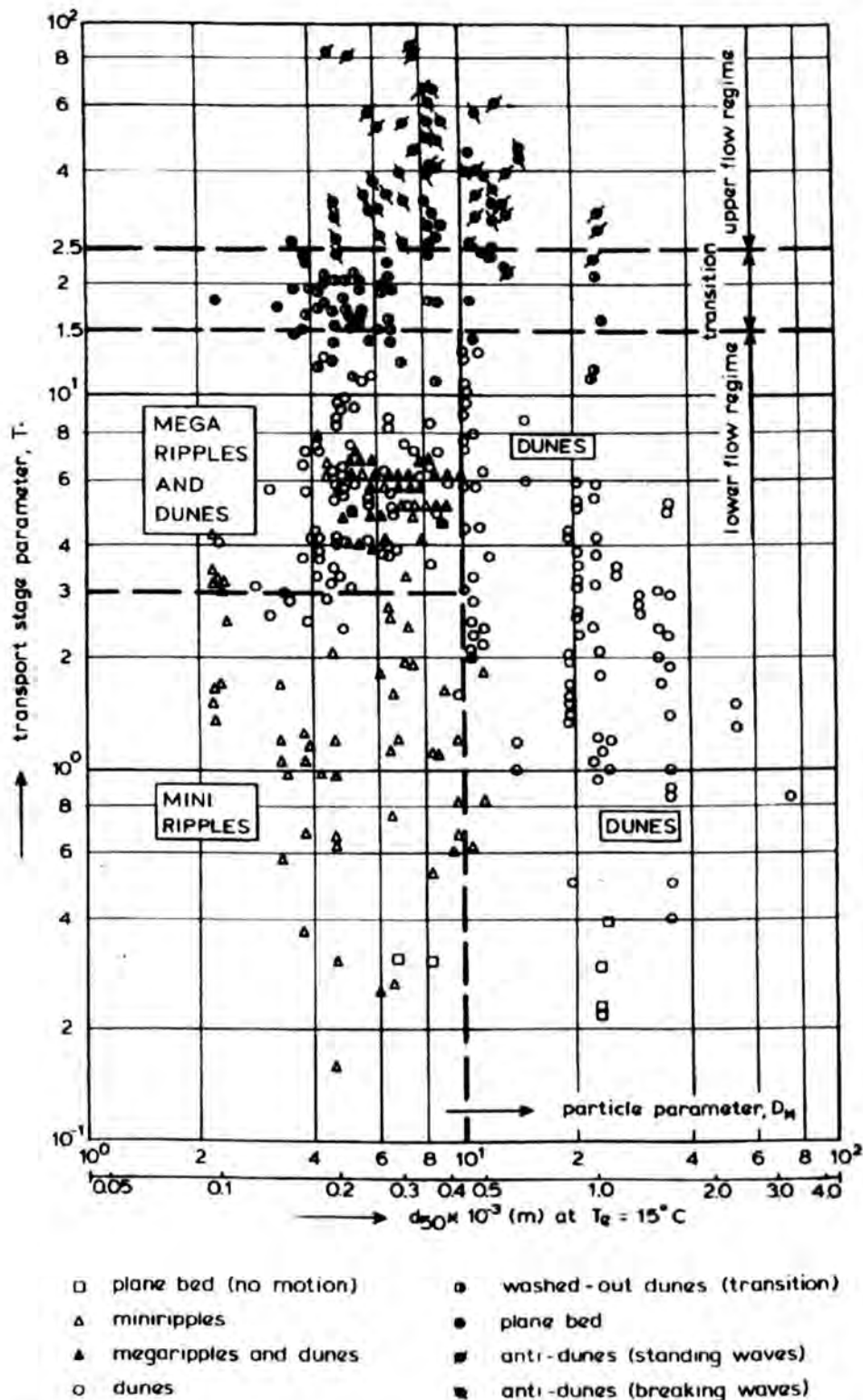


Figure 2.8: Classification of bedforms for unidirectional flow as a function of the dimensionless diameter D and a bed shear stress parameter T . (VAN RIJN, 1989, figure 6.1.2).

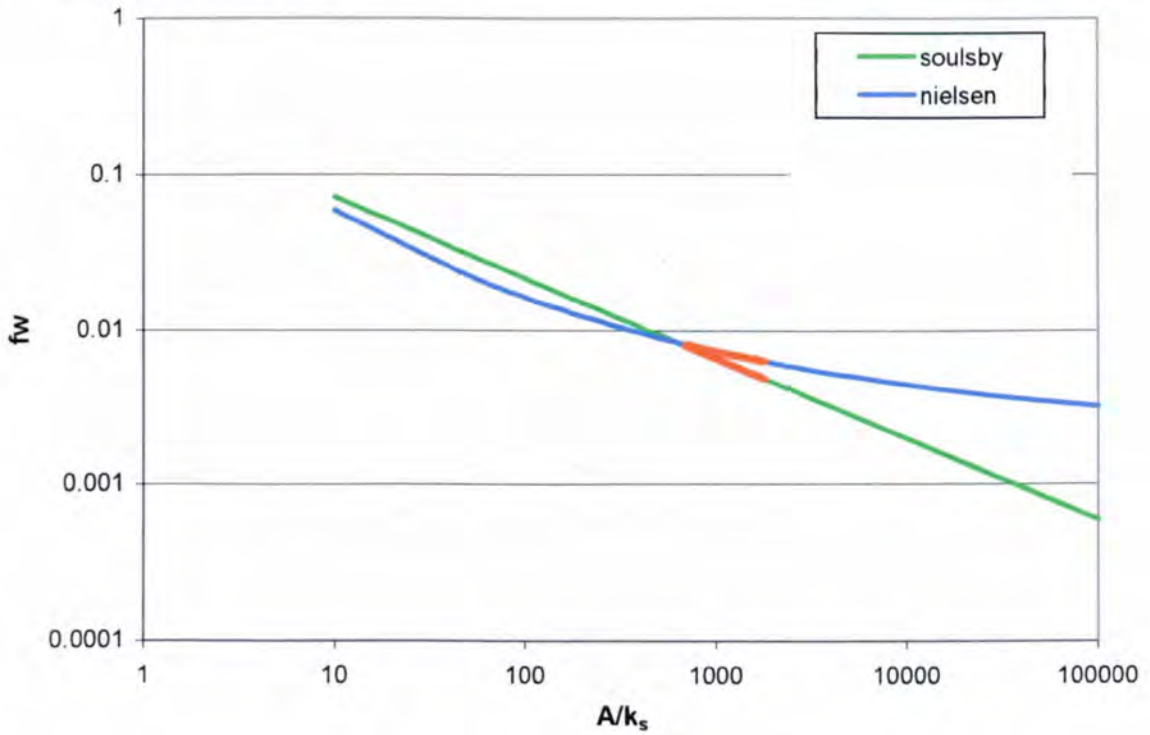


Figure 2.9: Friction factor for waves as a function of the relative roughness determined by equations given by NIELSEN (1992) and SOULSBY (1997). The red lines indicate the range of relative roughness for the *Deltaflume* experiments.

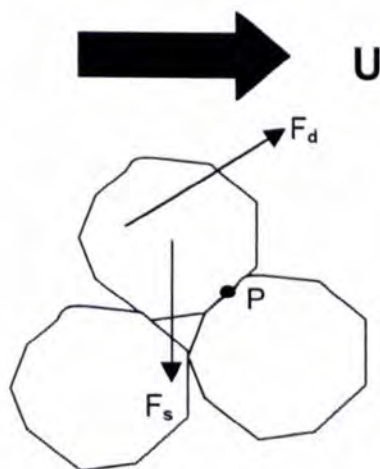


Figure 2.10: Forces on a sediment particle due to steady flow.

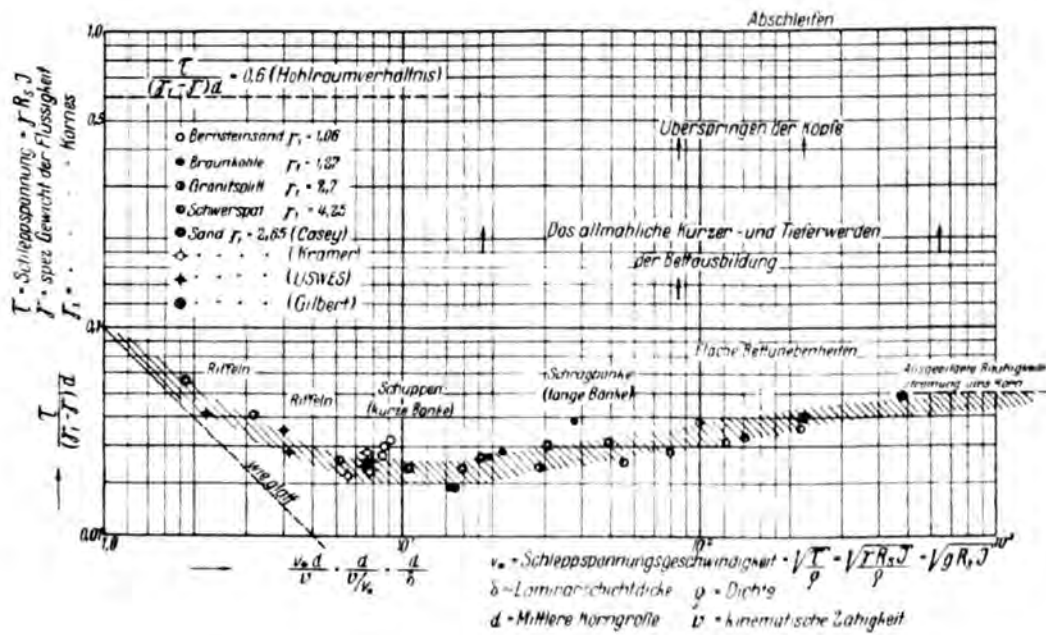


Figure 2.11: Shields’s curve showing the threshold of sediment movement and the bed formations developing for different grain sizes and flows. Taken from SHIELDS (1936).



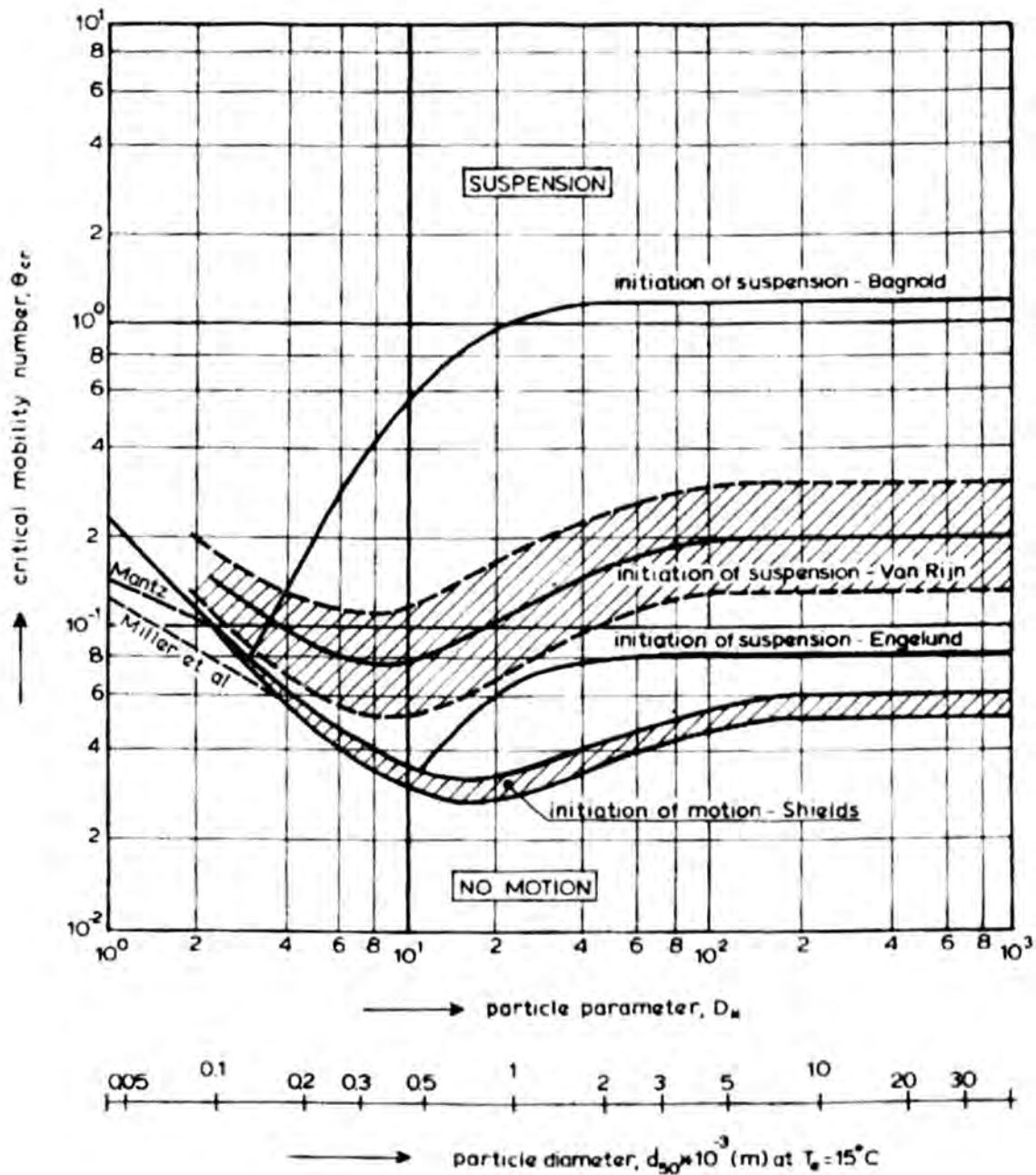


Figure 2.12: Shields's diagram with the extension of MILLER ET AL. (1977) for small sediment diameters taken from VAN RIJN (1989), (figure 5.1.1). Note, θ_{cr} is the critical Shields stress.

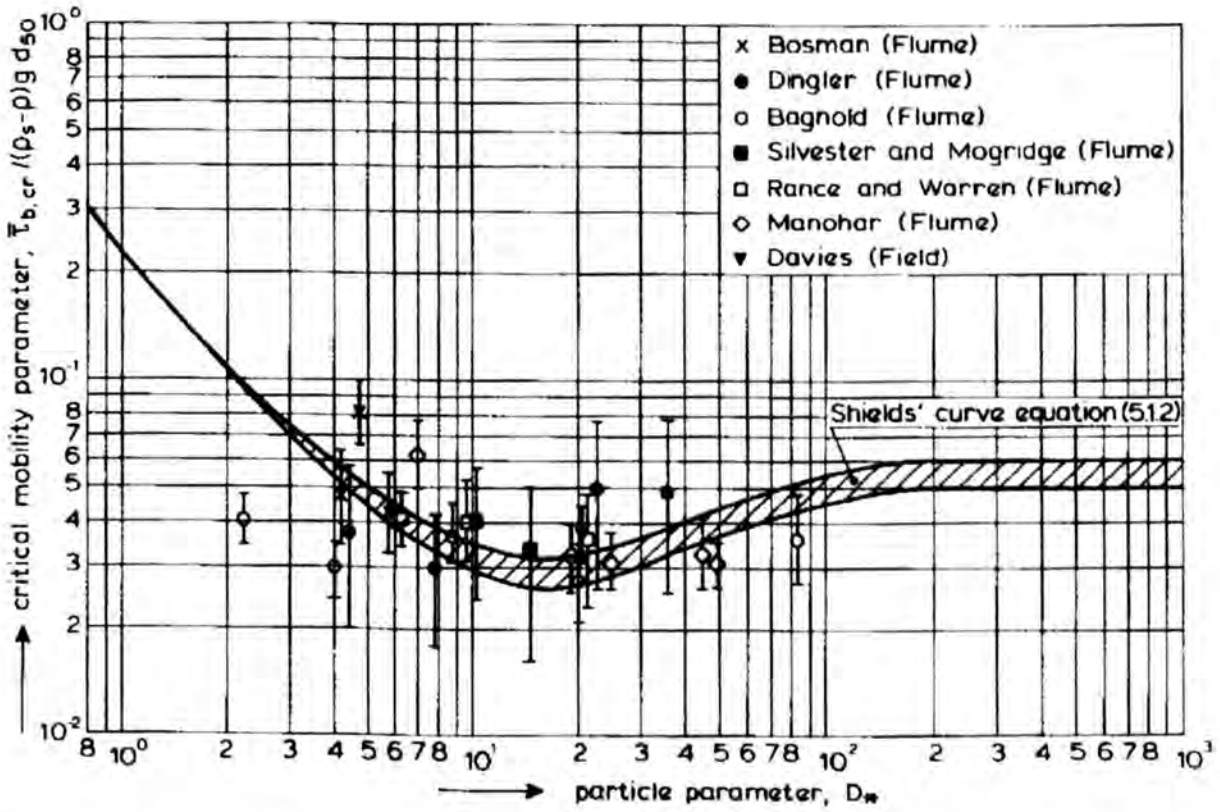


Figure 2.13: Shields's curve including some field and wave flume measurements for wave conditions. The error bars indicate the influence of the wave period and the grain roughness (from VAN RIJN (1989), figure 5.4.1).

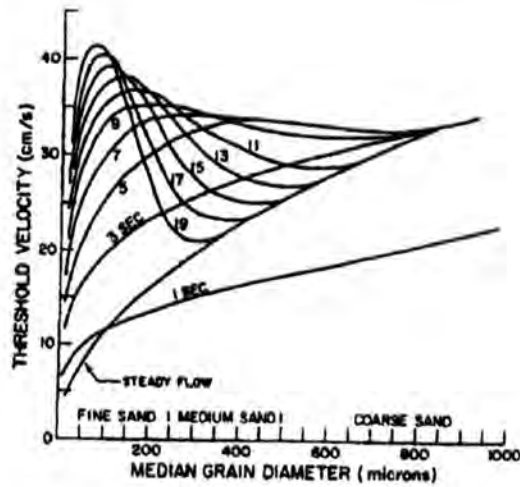


Figure 2.14: Threshold orbital velocity as a function of the characteristic wave period and the median grain diameter. The kinematic viscosity was $0.014 \text{ cm}^2/\text{s}$ and the sediment density was 2.85 g/cm^3 (after SEYMOUR, 1985).

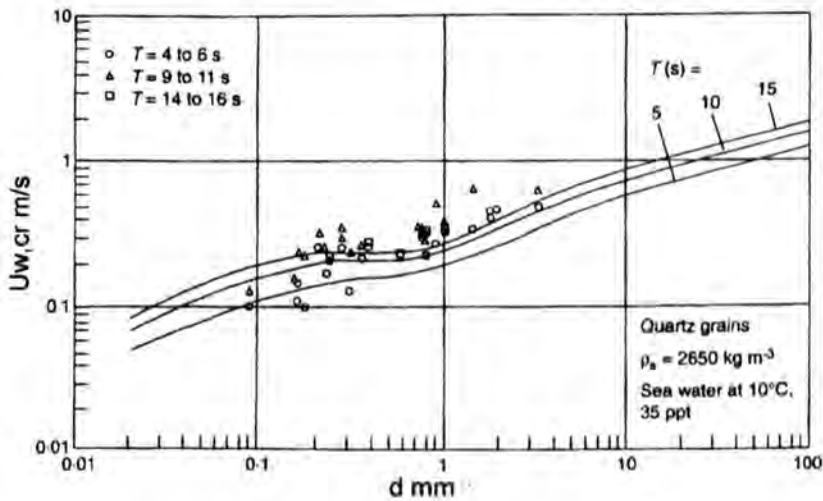


Figure 2.15: Threshold orbital velocity as a function of the characteristic wave period and the median grain diameter for sea water with a salinity of 35 ppt (after SOULSBY, 1997).

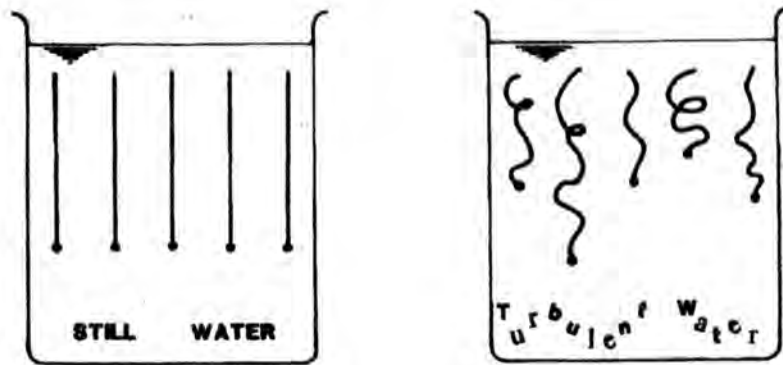


Figure 2.16: Settling of particles in still and turbulent water, respectively influencing the settling velocity (from NIELSEN, 1992).

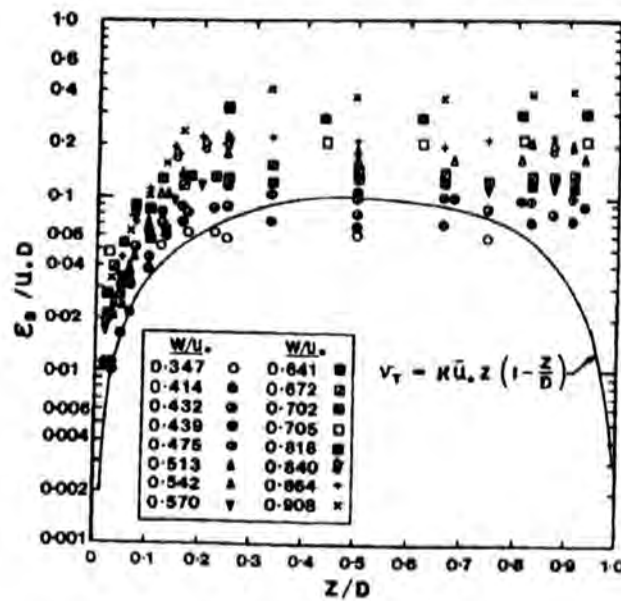


Figure 2.17: Sediment diffusivities derived through equation 2.61 from measured concentration profiles $\bar{c}(z)$ under the assumption of pure gradient diffusion. Different sediment sizes give different values for the diffusivity ε_s (after NIELSEN, 1992, figure 5.1.2. Data from COLEMAN, 1970). Note, D is the water depth.

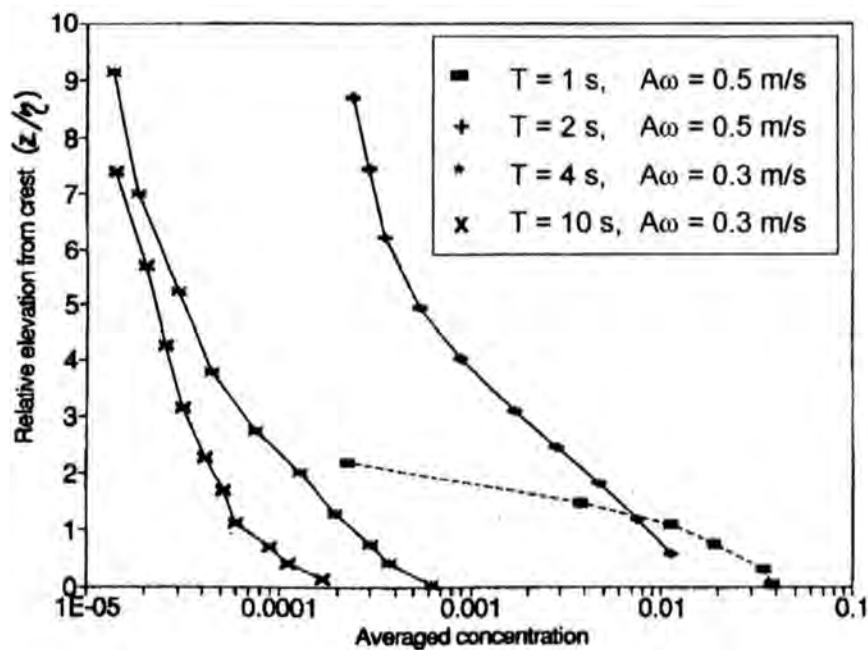


Figure 2.18: Time averaged sediment concentrations \bar{c}_z measured over vortex ripples in an oscillating water tunnel. In all cases the sand size was 0.2 mm. Data from BOSMAN, 1982 and DELFT HYDRAULICS, 1989. (Figure from NIELSEN (1992), figure 5.2.7).

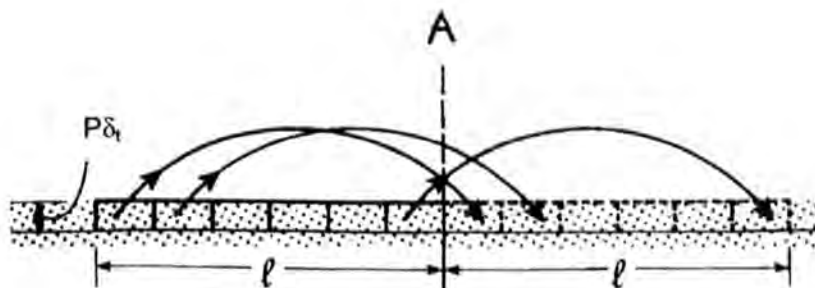


Figure 2.19: In a short time interval δ_t the amount of sand picked up per unit area is $P\delta_t$. If the average distance travelled by the moving sediment is l_x , the corresponding sediment transport through one unit width of the plane A is seen to be $l_x \cdot P\delta_t$. (after NIELSEN, 1992, figure 6.2.1).

Chapter 3 Instrumentation and Preliminary Data Analysis

3.1 Laboratory Work

From the 2nd of July to the 6th of August 1997, STABLE (Sediment Transport And Boundary Layer Equipment), HUMPHERY (1987), HUMPHERY AND MOORES (1994), and other instruments were deployed by Proudman Oceanographic Laboratory (POL) in the *Deltaflume*. The research team was led by J.J. Williams from POL and included P.S. Bell, P.J. Hardcastle, J.D. Humphery, S.P. Moores and P.D. Thorne from POL, K. Trouw from the University of Leuven, Belgium, L.E. Coates from the University of Birmingham, UK and A.G. Davies from the University College of North Wales, UK. A chronological summary of all tests performed in the *Deltaflume* is given in tables 3.1 and 3.2. The controlled conditions allowed the testing of the performance of a number of sensors and the investigation of the influence of STABLE on its measuring environment.

3.1.1 Deltaflume

Located in the De Voorst Laboratory of the Delft Hydraulics Laboratory, and operational since 1980, the *Deltaflume* is a large-scale facility allowing full-scale simulation of waves in controlled laboratory conditions. The *Deltaflume* is 230 m long, 5 m wide and 7 m deep (figures 1.2a and b). Monochromatic and random waves, with heights of up to 2 m, can be generated according to a required time history. A device prevents re-reflection of waves from the wave board and minimises resonant waves. A sand bed approximately 30 m long, 5 m wide and 0.5 m deep was placed approximately 105 m from the wave generator in the *Deltaflume*. Both ends of the test bed were feathered to reduce erosion and drainage was laid beneath the sediment bed to allow the free passage of water during the filling of the *Deltaflume*. Two separate test series were conducted with beds consisting of medium ($d_{50} = 0.329$ mm) and fine sand ($d_{50} = 0.162$ mm), respectively. A grain size distribution for the two different sands is shown in figure 3.1.

The facility was equipped with a range of hydraulic instrumentation and sensors to measure bed morphology. The devices used in the present experiments are described in sections

3.2.1 and 3.2.2.

3.2 Instrumentation

The hydrodynamics and morphodynamics were measured by sensors provided by Delft Hydraulics and sensors mounted on STABLE. Great care was taken to ensure that the set up of STABLE was similar to the set up in the field, in order to simulate field conditions. Thus, STABLE was fully equipped with the same sensors used in the field (figure 1.1).

3.2.1 Instrumentation on STABLE

STABLE is an autonomous instrument platform, which is used to measure near bed hydrodynamics and sediment transport in wave-current flow. In the present experiment STABLE was deployed in wave only conditions. STABLE was lowered onto the sand bed by a crane and only 'crude' adjustments could be made in aligning STABLE with the flume. The rig was designed to withstand hydrodynamic forces generated by the waves. The structure and instruments were further designed to present a minimum obstruction to the flow. The galvanised steel tripod had lead ballast feet and supported the circular instrument platform at approximately 1.4 m above the sand bed.

During the experiments, STABLE was equipped with the following instruments:

- a) An eight bit gimballed digiquartz compass with a resolution of $\pm 1^\circ$ mounted in the centre of the rig to measure the orientation of STABLE relative to the flume
- b) A bead thermistor to measure the water temperature
- c) Orthogonal inclinometers to measure vertical rolls and pitches
- d) A mean and a burst pressure transducer with integral pressure housing to measure the water depth at wave frequencies
- e) Six Valeport Series 800 electromagnetic toroidal open head current meters (ECMs) to measure flow turbulence and wave velocities
- f) Three ABS (Acoustic BackScatter) systems (1.0 MHz, 2.0 MHz and 4.0 MHz) to measure the suspended sediment concentration in the lower 1.2 m of the water column in 1 cm intervals from the bed
- g) A SonTec Acoustic Doppler Velocimeter (ADV), Ocean Probe operating at 5 MHz to measure flow turbulence
- h) A vertical array of ten pump sampling nozzles to measure burst average sediment concentrations

- i) An acoustic ripple profiler to measure the bed geometry

Further instruments deployed were coherent Doppler sensors to measure horizontal and vertical wave induced fluid motion and a sector scanning sonar to provide an image of the bed.

The arrangement of the sensors is shown in figure 3.2. Table 3.3 summarises the instrument positions on the STABLE frame using the x, y and z co-ordinate convention illustrated in figure 3.2. Table 3.4 lists the overall dimensions and weight of STABLE. The relative heights of the instruments mounted on STABLE were determined by placing STABLE at the side of the flume on a concrete surface and measuring the heights of the sensors relative to the ground. The values quoted in the vertical direction in table 3.3 do not account for any rig settlement. Subsequently, a more detailed analysis was carried out and is described in section 3.5.4.1.

The ECMs mounted on STABLE had a diameter of 10 cm, a resolution of ± 0.2 cm/s and a sampling frequency of 8 Hz. They were mounted in three pairs, set at 90° to each other at 30.2 cm, 60.6 cm and 91.0 cm above the bed pre-deployment. The horizontal separation distance between the centre of the measuring volume of each ECM in a pair was 20 cm. The choice of the head size of the ECMs was a compromise, as small sized heads are too vulnerable to the surrounding noise and large sized heads may be unable to resolve smallest scale eddies and interfere with the flow. The sensors used had the desirable properties of a low noise level and a fast response time.

Additionally flow turbulence was measured at $z \approx 30$ cm using an Acoustic Doppler Velocimeter, ADV, operating at 5 MHz and sampling at 25 Hz. The ADV had an accuracy of about ± 0.1 cm/s.

The mean pressure transducer was mounted 170.2 cm above the bed pre-deployment. The sampling frequency was 8 Hz.

The three independent ABS systems (see THORNE ET AL., 1993, THORNE AND HARDCASTLE, 1997) ABS1 (1.0 MHz), ABS2 (2.0 MHz) and ABS3 (4.0 MHz), were mounted approximately 124.0 cm above the bed pre-deployment and about 15 cm in front of the ECMs, to measure non-intrusively vertical suspended sediment concentration profiles. The separation between the ABS sensors was about 11.4 cm in a line normal to the ECM axis (see figure 3.2). The ABS instruments were sampled at a frequency of 4 Hz with an accuracy of approximately 10 %. Tests were performed prior to the work in the *Deltaflume* to establish that the six acoustic instruments mounted on STABLE did not interfere with each other (WILLIAMS ET AL.,

1998). The systems operated in two modes, transmit and receive. In transmit mode the acoustic transceivers transmitted short, high frequency acoustic pulses (1.0, 2.0 and 4.0 MHz) down to the bed. The signals involved consisted of a pencil beam with an initial diameter at the transducer head of the order of 1 cm. Portions of the signals were backscattered to the ABS systems when they met obstacles such as suspended sediments. Additionally some return echoes from the ECM heads were present in the raw ABS signals, especially in the 1.0 MHz sensor. The return echoes received by the instrument depend strongly on sediment characteristics such as grain size, shape and density, which may vary with location and height. The ABS system mode, receiver utilised time-gating in order to receive each backscattered signal over 128 measurement bins. The determined profiles were averaged over 32 records to provide measurements at 0.25 s intervals for each ABS sensor. The ensembled averaging of the data was necessary to smooth out configuration noise which arises from variations in the backscatter signal due to random phase distributions of the echoes, which is due to varying locations of the particles in each measurement volume. The ABS data were logged in bursts, which were synchronous with the wave data.

Besides the ABS sensors a vertical array of pump sampling nozzles was fixed to STABLE in order to measure sediment concentrations. The University of Utrecht loaned the sampling equipment to the research team. The pump sample nozzles were orientated at 90° to the ECM heads (see figure 1.1) pre-deployment. According to BOSMAN ET AL. (1987), the nozzles direction should be normal to the orbital motion. Hence, when STABLE was rotated, special consideration had to be given to the measurements. The nozzle diameter was 4 mm. Each nozzle in the array was connected to a plastic pipe through which a water/sediment mixture was drawn to the surface by means of a peristaltic pump. The resulting water/sand mixture from each sampling position was collected in 10 litre buckets (figure 3.3). Once full, sediment was allowed to settle to the bottom of the buckets and excess water was then poured away. However, occasionally the nozzles were blocked and then the buckets were not filled completely. In those cases the volume of water was noted separately and taken into account in further calculations. The remaining water/sand mixture was then poured carefully into a calibration tube and the volume of sand present was measured. A pre-determined calibration was then applied to convert the volume of sediment into a concentration value with units g/l. All samples were sealed in plastic bags for subsequent grain size and settling velocity analysis and for accurate measurement of the suspended sediment concentration. At POL the water/sand mixture was dried and the dried weight was

determined. With the given volume of water in the buckets, these values were then converted into concentration values with units g/l.

Bedforms beneath STABLE were measured using an acoustic ripple profiler and a sector scanning sonar device. The acoustic ripple profiler (ARP), schematically shown in figure 3.4, took measurements approximately every 30 seconds with an accuracy of ± 2 mm to produce time series of ripple profiles over the full range of wave conditions. The sector scanning sonar sampled at an interval of approximately 60 seconds with an accuracy of ± 2 mm. With the standard ABS systems used to determine sediment suspension, the bed echo was usually evident within the profiles (BELL ET AL., 1998). The ARP extends the concept of the ABS. The sand ripple profiler used a mechanically scanned pencil beam of sound to provide a high-resolution profile of the bed along a two to three metre line. Radial profiles of backscatter signal strength were digitised and recorded as a transducer rotates on a stepper motor assembly. These data were post processed to identify the position of the bed (BELL AND THORNE, 1997, BELL ET AL., 1998). The following detailed system description has been given by BELL ET AL. (1998): The ARP was made to order by Marine Electronics of Guemsey. It consists of a 2 MHz ceramic disc transducer with a beam width of approximately 1° . This transducer was mounted on a stepper motor controlled rotating head with 400 angular positions covering the full 360° . The transducer assembly was enclosed within an oil filled, pressure balanced plastic 'boot', that was acoustically transparent, protecting all mechanical systems from the ambient environment, the latter being particularly important for an instrument designed to operate under conditions of high suspended sediment concentration. The transmitted pulses and stepper motor operation were controlled by an on board microprocessor, allowing all functions to be software selectable. The envelope of the acoustic backscatter signal was captured using an on-board 8 bit analogue to digital converter, and was then transferred to the serial port for logging. The unit was controlled from a PC which set up the profiler with the desired parameters, then collected and stored the captured backscatter profiles for each head position as they were returned via the serial link. The maximum sampling rate was 370 kHz corresponding to a bin length of 2 mm. Such a system enables a 3 m line of the bed to be profiled in approximately 30 seconds. After post processing the position of the bed was given in ASCII files, which were used for further analysis.

Information determined by the acoustic ripple profiler can be used to understand sediment suspension processes, as the interaction between the flow dynamics and the bedforms leads to the entrainment of sediments. The acoustic ripple profiler allows the prediction of the type of bedform present and in the case of rippled beds, the estimation of ripple heights

and wavelength. Thus, the bed roughness, which is an important parameter for the re-suspension of sediment, can be estimated. To date, the input of bedform parameters has been problematical, because of the difficulty of obtaining such measurements (BELL ET AL., 1998). The advantage of an acoustic ripple profiler to direct measurements such as photographic methods is that it does not rely on the water to be sufficiently clear to allow photographs to be taken.

Previous tests by BELL AND THORNE (1997), using the acoustic ripple profiler, have shown that profiles of the bed can be accurately measured over at least a 1 m length centred directly below the sonar, and reasonable indications of the sea bed topography obtainable over a length of up to 2 m. Beyond this, the low grazing angle between the acoustic beam and the bed preclude its use to reasonable sand ripple heights (BELL AND THORNE, 1997). It has been shown that the ARP underestimates the heights of extremities of the sand ripples slightly.

The sector scanning sonar used a mechanically scanned fan-shaped acoustic beam to build an image of the bed over a radius of approximately 5 m. This complemented the measurements taken by the acoustic ripple profiler concerning the orientation and regularity, but not the height, of sand ripples.

3.2.2 Delft Hydraulics Instrumentation

Five Delft Hydraulics ECMs with a 50 mm diameter were fitted to the side of the flume at $y = 120.9$ cm (measured from the wave generator) at distances z above the bed of 25 cm, 50 cm, 100 cm, 150 cm and 250 cm (see figure 3.5). The sampling rate was 25 Hz.

Two wave measurement probes at $y = 117.9$ m and 120.9 m respectively were installed. These resistive devices were mechanically driven up and down to maintain contact with the water surface. The vertical displacement of each probe monitored waves across a broad range of frequencies. Data from each probe were logged at 25 Hz with an accuracy of ± 1 cm.

The bed morphology was measured using a mechanical ripple-profiling device provided by Delft Hydraulics. This was used in still water following cessation of wave action. It consisted of a lightweight wheel mounted on the end of a heavy vertical support (figure 3.6). When driven forwards, the pressure applied to the wheel was held constant by moving the vertical support up and down in response to changes in bed elevation thereby permitting the measurement of bed morphology. The horizontal position of the instrument was referenced

to accurate datum marks installed by Delft Hydraulics. The vertical position of the instrument was calibrated from a zero datum on the beach of the *Deltaflume*. The ripple profiler measured several profiles parallel to the wall of the flume, each of them 0.5 m apart for the profiles for survey DBP-1 (03/07/97) and 0.25 m apart for profiles for surveys DBP-2 (16/07/97), DBP-3 (28/07/1997) and DBP-4 (06/08/1997) and beginning 1 m away from the side of the flume. The profiler recorded a bed elevation every 0.01 m along the bed. When moving the lightweight wheel along the ripples the tops of the crests were flattened slightly as measurements were taken. This had to be considered when analysing and interpreting the ripple profiling data.

Samples of suspended sediment were obtained at 10 heights above the sand bed using pump-sampling equipment on loan from the University of Utrecht. The pump samplers were placed at $y = 121.5$ m. Their accuracy was about ± 20 %. The determination of the sediment concentration was identical to the one for the pump-sampling array on STABLE.

3.3 Data Collection

Instrument calibration and the preliminary analysis of the hydrodynamic data were performed at POL.

The instrument data loggers recorded data as code in various forms. In total, six separate data logging systems were needed to handle the diverse and extensive data. To facilitate data logging flexibility, the rapid assessment of data quality, and to allow preliminary analysis of data from instruments on STABLE, data were logged using PCs located alongside the *Deltaflume* (WILLIAMS ET AL., 1998). This differs from the normal operational mode of STABLE where all data from sensors are recorded by the autonomous logging systems. Once examined, data were backed-up onto CD ROM for subsequent data analysis. In this form the data were available for this thesis. According to WILLIAMS ET AL. (1998), the British Oceanographic Data Centre will produce the final data products approximately 24 months after the end of the project.

3.4 Data Calibration

3.4.1 Pressure and Velocity Data

Calibration was applied to the pressure and velocity signals. This converted the pressure in units of bars, and the velocity in units of cm/s. The atmospheric pressure during the tests at the *Deltaflume* was taken to be approximately 1000 mbar. A calibration test was performed

on the ECM systems in a steady flow smooth bed flume at the University of Liverpool about six months before the *Deltaflume* tests started. The tested velocities at the time were 0, 5, 10, 20, 30, 40, 50, 60, 80, 100, 125, 150, 175 and 200 cm/s (personal communication with Jon Williams).

3.4.2 ABS Calibration

One of the first researchers using acoustic measuring techniques to determine the sediment concentration was JANSEN (1978). He used an ultrasound to determine the sediment transport in the laboratory and the field. Jansen described the function of an ultrasound sensor as follows: Due to the pressure of the sand particles part of the sound is scattered from the beam towards the receiver. The resulting acoustic pressure p_s is converted by the receiving transducer into an electric voltage V_s , proportional to p_s . The square of the voltage is proportional to the scattered acoustic intensity I_s , which is proportional to the concentration c . Factors such as transmission losses due to adsorption of sound in water and extinction due to sand particles along the total length of the sound path can affect the measuring signal. Thus, Jansen implied that an absolute calibration was necessary especially as the scattering cross-section depends, in principle, on the properties of the sand particle. His results using a 4.4 MHz ultrasound in the Wadden Sea, off the Burgzand shoal showed good agreements with results determined by conventional measuring techniques. Jansen was not able to determine sediment concentrations with a high vertical resolution.

In the past decade advances have been made in using acoustic backscatter techniques to describe suspended particulate matter (SHENG AND HAY, 1988, THORNE AND CAMPBELL, 1992). This method has been validated by a series of laboratory and field studies (e.g. HAY AND SHENG, 1992, THORNE ET AL., 1993, HAY AND BOWEN, 1994b, THORNE ET AL., 1996). These studies suggested that acoustic backscatter systems are a viable means of obtaining high resolution *in situ* measurements of suspended sediment concentration and particle sizes.

The root mean square value of the acoustic backscatter, P , can be related to the suspended sediment particle size, $a_s(r)$, and concentration profiles, $c(r)$ as follows (THORNE ET AL., 1996):

$$a(r) = F^{-1} \left(\frac{f_i(r)}{f_j(r)} \right) \quad (3.1)$$

$$\frac{f_i(r)}{f_j(r)} = \frac{(P_i(r)/K_{ij}) \cdot e^{2 \cdot r \cdot (\alpha_i - \alpha_j)}}{(P_j(r)/K_{ij})} \quad (3.2)$$

$$c(r) = \left\{ \frac{r \cdot P_i(r)}{(f_i(r)/\sqrt{a(r) \cdot r_s}) \cdot K_{ij}} \right\}^2 \cdot e^{4 \cdot \alpha_i \cdot r} \quad (3.3)$$

$$\alpha_i = \alpha_{wi} + \alpha_{si} \quad (3.4)$$

$$\alpha_{si} = \frac{1}{r} \int_0^r \xi_i(r) \cdot c(r) dr \quad (3.5)$$

where f is the form function, which describes the scattering properties of the sediments. a is obtained by the inverse transform of the ratios of f . r is the range, α_w is the absorption due to water, α_s is the attenuation of the suspension, ξ describes the attenuation property of the sediments in suspension and K_i is a calibration constant for the ABS system. $i \neq j$ where $i, j = 1, 2, 3$ refer to the three frequencies. Equation 3.3 is an implicit equation of the form $c = f(P, c)$. This must be solved iteratively and requires some calibration of the ABS sensors to find the calibration constant K_i . However, the equation can be re-arranged into an explicit solution (see LEE AND HANES, 1995) of the form $c = f(P)$. The explicit solution requires a reference concentration c_0 at some range r_0 . For the *Deltaflume* experiment data from the pump samples were used as a reference concentration. However, as the pump sample concentrations represented a mean concentration, only the mean concentration profiles for the ABS could be determined using the explicit approach. Using the explicit solution further research at POL determined the calibration constant K_i , which was then used in the implicit equation to find instantaneous concentrations. An iterative inversion algorithm was adopted to solve the implicit equations.

Dr P. Thorne at POL has calibrated temporal mean and instantaneous vertical suspended sediment profiles over the entire deployment of STABLE in the *Deltaflume* at the three frequencies (1.0 MHz, 2.0 MHz and 4.0 MHz). Data from the 4.0 MHz sensor were causing problems in the calibration and instantaneous concentrations for this sensor were not available for this study.

3.4.3 Pump Samples

Pump-sampling devices were used by BOSMAN ET AL. (1987), in laboratory tests. Their experiments yielded a calibration coefficient which was applied for the *Deltaflume* pump samples. BOSMAN ET AL. (1987), performed sediment concentration measurements by

transverse suction under steady flow and waves in a flume. As a result they determined that the suction direction should be normal to the ambient water motion and the intake velocity greater than three times the ambient flow velocity. The tests resulted in the determination of a trapping efficiency of a \varnothing 3 mm suction nozzle as a function of the relative orientation of the nozzle and the velocity ratio of intake over ambient flow velocity. Assuming normal suction, BOSMAN ET AL. (1987), also provided values for the trapping efficiency depending on the grain size d_{50} . This eventually resulted in the definition of a calibration factor, β for different sediment sizes under transverse suction conditions. BOSMAN ET AL. (1987), suggested equation 3.6 for the calculation of the calibration factor:

$$\beta = 1 + \frac{1}{3} \cdot \arctan(d_{50} / d_r) \quad (3.6)$$

with $d_r = 0.090\text{mm}$ and \arctan to be evaluated in radians. Equation 3.6 estimates the transverse suction calibration factor within 3%.

For the present experiment d_{50} was $329 \mu\text{m}$ for the medium and $162 \mu\text{m}$ for the fine sand. Thus, the calibration factor for the medium sand was $\beta = 1.43$ and for the fine sand was $\beta = 1.35$. These two calibration factors were then applied to the dried weight sediment concentrations to give the actual sediment concentrations in units of g/l.

There was no calibration performed on the sediment concentration determined using the measuring cylinders next to the wave flume for the present tests. Graphs were provided to convert the height of sediment in the cylinder into a volume with units of g/l. These graphs took the different grain sizes and their effect on compaction into account. Furthermore, the cylinders were tapped to allow for settling. Problems consisting of the difference in settling velocities and compacting of the sand in the cylinder and thus the determination of the sediment concentration using this method were noted.

3.4.4 Acoustic Sand Ripple Profiler Calibration

The acoustic sand ripple profiler (ARP) was calibrated at POL before the present deployment using a known surface which was scanned. The requirement of the surface was to be of a type likely to be encountered in the field, but under controlled conditions. The tests were performed in a large test tank at POL (see BELL AND THORNE, 1997). A 1.5 by 0.5 metre plaster cast was taken of an area of sand ripples exposed at low tide on a local beach near POL. A series of two-dimensional profiles of the sand ripple cast were scanned by the sonar. These measurements were then compared with measurements taken manually of the plaster cast. Small inaccuracies between the sonar and the manual measurements at

regions further away from the sonar position could be observed. This is due to the reduced grazing angle of the acoustic beam. Nevertheless, the tests demonstrated that profiles of the sea bed can be measured over at least 1 m length centred directly below the sonar and reasonable indications of the sea bed topography are obtainable over a length of up to 2 m. No further calibration of the sand ripple profiler for the present tests was necessary.

3.5 Preliminary Data Analysis

3.5.1 Reflection Analysis

Waves are reflected by beaches, breakwaters, shoreline and offshore structures. The interaction between incident and reflected waves changes the wave field and thus the forces acting on beaches and structures. It can lead to increased wave heights, which can result in the intensification of beach erosion or the amount of scour around a structure.

In many laboratory studies it is necessary to distinguish between incident and reflected waves, so that the model response can be related to the incident wave parameter. In a wave flume, waves are reflected by the structure of the model, the sides of the flume and the sloping beach back to the wave paddle. Then they are re-reflected from the wave paddle towards the structure or the beach where they are reflected again. A multi-reflection system of waves is formed in the wave flume. The wave paddle in the *Deltaflume* was equipped with a wave absorber to absorb reflected waves, thus reducing re-reflection.

Delft Hydraulics provided two wave followers separated by 3 m to measure the wave height in the flume. The spacing was a compromise between the requirements for distinctly different signals whilst resolving sufficiently high frequency components in the signal. For a 3 m spacing, components corresponding to wavelengths down to 6 m could be resolved before the first singularity in the Goda and Suzuki method. The 5 s waves in the flume corresponded to approximately 30 m waves so the 2nd and 3rd harmonics could be resolved. Given the typical maximum wave steepness of 0.05, the amplitude of the 2nd harmonic was 1 % of the fundamental and the 3rd harmonic was even smaller. Further, the separation of 3 m was within the limits ($\Delta l < 0.45 \cdot L = 13.5$ m and $\Delta l < 0.05 \cdot L = 1.5$ m) suggested by GODA AND SUZUKI (1976), in order to avoid singularities in equations A.12 and A.13. These yielded time series of wave elevation, which allowed the analysis of a reflection coefficient using the method of Goda and Suzuki, as described by KETABDARI (1999). A detailed summary of the reflection analysis and the equations involved is presented in appendix A.

One burst (regular waves $H = 0.85$ m) was used to determine the reflection coefficient using this analysis. The first 1024 points of data were used in a Fast Fourier Transform (FFT). For the peak period the reflection coefficient was calculated using equation 3.7:

$$K_R = \frac{H_{R,peak}}{H_{i,peak}} = \frac{2 \cdot a_{R,peak}}{2 \cdot a_{i,peak}} = \frac{a_{R,peak}}{a_{i,peak}} \quad (3.7)$$

The reflection coefficient K_R was equal to approximately 9.5% for the peak period. This was consistent with the analysis performed by Delft Hydraulics who determined a reflection coefficient of 9.3 %. Analysis of other data sets carried out by Delft Hydraulics gave reflection coefficients in the range of 2 to 15 % for the medium and 4 to 25 % for the fine sand. Although the values for the reflection coefficients especially for the fine sand appeared to be quite large, it was decided to use just one wave probe for the determination of the nominal wave height for each burst. The extra work involved in applying a reflection analysis to the wave elevation data, especially for the irregular waves, was thought to be unjustified compared with the uncertainties involved in predicting sediment suspensions. The difference between using just one wave probe to determine nominal wave heights for each burst and the one from the wave elevation signal calculated from reflection analysis was thought to be small. In general, this study mainly concentrates on measurements taken on the medium sand bed, where the reflection coefficients estimated by Delft Hydraulics were in the range of 2 to 15 %. In most cases values measured by the sensors mounted on STABLE were used in the analysis and hence the wave probe measurements were not taken into account. Also there were uncertainties in other measurements (e.g. ripple dimensions) so that a greater accuracy in the wave height calculation was thought to be unnecessary. Also, in any case, the calculation of reflection coefficient will be affected by the presence of STABLE, so the 15 % may be an over-estimate (Lawrence Coates, personal communication).

3.5.2 STABLE Velocity Data

Zero-drift and offsets associated with the ECM sensors require correction when resolving the velocities. Furthermore, it is necessary to zero-mean the time series for subsequent analyses of turbulence.

Each ECM pair recorded two vertical (w_p' and w_s') and two horizontal (u_p' and u_s') velocities, where the indices p and s indicate portside and starboard ECM heads, respectively. Vertical rotation was necessary in order to correctly align each w_p' and w_s' as vertical and each u_p' and u_s' as horizontal velocities. This was achieved by applying the following rotation transformation:

$$w_p = w_p' \cdot \cos\theta - u_p' \cdot \sin\theta \quad w_s = w_s' \cdot \cos\theta - u_s' \cdot \sin\theta \quad (3.8)$$

$$u_p = w_p' \cdot \sin\theta - u_p' \cdot \cos\theta \quad u_s = w_s' \cdot \sin\theta - u_s' \cdot \cos\theta \quad (3.9)$$

where θ is the angle of tilt for each ECM sensor.

For each pair of ECM heads (A, B and C), the two horizontal velocities were converted into a transverse v' and a longitudinal u' (with respect to the flume) velocity, assuming that STABLE was aligned perfectly with the flume at 0° , 45° and 90° . As the ECM heads were at 90° to each other, a horizontal rotation of 45° was applied. Thus the transforms were:

$$u' = u_s \cdot \cos 45^\circ + u_p \cdot \sin 45^\circ \quad (3.10)$$

$$v' = u_s \cdot \sin 45^\circ - u_p \cdot \cos 45^\circ \quad (3.11)$$

The difficulties of aligning STABLE accurately within the flume using the crane, resulted in misalignment of STABLE relative to the wave direction. Corrections were made by assuming a zero mean velocity across the flume (see figures 3.7a and b). The calculated rotation angles for the three ECM heights of STABLE are presented in tables 3.1 and 3.2. The ECM heads were fixed manually in pairs onto STABLE. Thus, it was possible to determine slightly different rotation angles for each ECM pair.

This analysis gave 4 velocities for each ECM pair (UA, VA, WAP, WAS, UB, VB, WBP, WBS, UC, VC, WCP, WCS), where U and V are the horizontal longitudinal and transverse velocities, respectively and WS and WP are the starboard and portside vertical velocities, respectively. The two vertical velocities (portside and starboard) were not averaged, as this would increase the measuring volume and thus increase the minimum size of eddies that can be resolved. On the contrary, the horizontal velocities had to be averaged for the two ECM heads to provide the horizontal velocities in the two directions in the flume (transverse and longitudinal). An example of the four velocities for regular waves and irregular waves for ECMA is shown in figure 3.7a and 3.7b, respectively.

3.5.3 Pump Samples

3.5.3.1 Differences between STABLE and DH pump samples

Pump sample values of suspended sediment concentrations are shown in figure 3.8 for a range of regular and irregular wave conditions on the medium sand test bed. Each graph, labelled (a) to (f), shows suspended sediment concentration profiles (hereafter referred to as c-profiles) obtained using pump-sampling arrays on STABLE and at the side wall of the *Deltaflume*. Suspended sediment concentration values were derived during the tests in the

Deltaflume using the calibration tube method next to the flume (see section 3.4.3). For regular waves, figures 3.8(a), 3.8(c), 3.8(e) show close agreement between c-profiles measured from STABLE and from the side wall of the flume. Whilst any comparisons between c-profiles measured from STABLE and from the side wall of the *Deltaflume* in irregular wave conditions show reasonable agreement, there is clearly a larger divergence between the results shown in figures 3.8(b), 3.8(d) and 3.8(f). Any influence of STABLE on sediment re-suspension processes and on concentration profiles will be present irrespective of the type of wave conditions. It is therefore necessary to consider a number of possible explanations for the above observed difference in c-profiles between the two sites.

(a) Suspended sediment concentration values were determined using two different methods. The two resulting c-profiles were compared. The suspended sediment concentration values in figure 3.8 were determined using the calibration tube method. After determining the concentration values, all samples were sealed in plastic bags for subsequent volumetric analysis at POL. The laboratory analysis is more accurate (Jon Williams, personal communication) and used hereafter when referring to pump sample measurements. Figure 3.9 shows the c-profiles for some regular and irregular waves (as shown in figure 3.8) using concentration values determined in the laboratory. The c-profiles in figure 3.9 follow the same basic trend as those in figure 3.8 with respect to the agreement of c-profiles at the two sites for regular and irregular wave conditions. It has to be emphasised that the concentrations are not the same, because they were determined using two different methods. In general, the suspended sediment concentration values are smaller for the volumetric methods than those determined using the calibration tube at the side of the flume. This is due to void spaces between particles in the tubes and the omission of fines in the laboratory analysis, which has a small, but not insignificant effect. In any case, the different ways of determining the concentration values did not lead to the discrepancies between the two sites.

(b) Ripple dimensions for regular and irregular waves and the position of the pump-sampling array, with respect to a ripple crest or trough, might have differed for the two sites and wave conditions. At the position of STABLE, the acoustic ripple profiler measured instantaneous (approximately two bed profiles per minute) bed profiles for a three metre slice along the bed underneath STABLE. As shown by the sector scanning sonar (SSS) image (figure 3.10), it is reasonable to assume that the ripples were long crested and two dimensional and thus the measured bedforms and dimensions can be transferred to the position of the pump-sampling array, which has an offset of approximately 607 mm relative to the acoustic ripple profiler. Throughout the *Deltaflume* tests the waves were

running for about an hour for each burst before measuring commenced, in order to ensure equilibrium conditions. For regular waves the acoustic ripple profiler shows that the ripples moved considerably during the 20 minute burst (figure 3.11a and 3.12a and b). By contrast for irregular wave conditions the ripples hardly moved during the burst (figure 3.11b and 3.12a and b). This implies that for irregular waves the position of the pump-sampling array, relative to a crest or trough, was stable during a burst, whereas for regular waves, the relative measuring position changed throughout the burst. Evidence has shown that for irregular waves the pump-sampling array was mainly above a ripple crest. The position of the pump-sampling nozzles for two bursts is marked in figure 3.11. There is no information of the bedforms near the side wall of the flume. However, the differences in bedform development described above may account for some of the disagreement between the c-profiles assuming that vortices develop in the lee of ripples and then move up the ripple crest. Thus, the position of the pump-sampling nozzles relative to the ripple crest could influence the amount of sediment sampled. It is also interesting that irregular waves with the same (significant) wave height as regular waves did not disturb the bed to the same extent as regular waves. Figure 3.13 shows the last sample of the acoustic ripple profiler data for burst a06b (regular waves, $H = 0.55$ m) and the first sample for burst a07a (irregular waves, $H_s = 0.53$ m). These two bursts were recorded consecutively. The figure shows that the ripples hardly changed between the two bursts and so the ripples present during burst a07a were relics of the ripples formed during burst a06b. The same effect can also be observed for burst a08a (regular waves, $H = 0.85$ m) and a09a (irregular waves, $H_s = 0.83$ m) even though not as clearly (figure 3.14). Considering that the bed was exposed to the irregular waves for about 1 hour before measuring commenced, this is surprising at first. However, the number of waves in an irregular burst, that exceed the mean wave height of a regular burst with the same m_0 , is approximately 11 % (figure 3.15). Thus, even though the overall wave energy between the regular and irregular burst is the same, the irregular waves do not disturb the bed to the same extent, as most individual waves are too small. This is confirmed in figure 3.16, which shows the instantaneous bed shear stress, τ , for the two bursts compared with the critical shear stress for initiation of motion ($\tau_{cr} = 0.2$ N/m²). The instantaneous shear stress for regular waves exceeds the threshold value for most of the forward and back ward stroke of the wave cycle. In contrast, there are a number of times when the instantaneous shear stress for irregular waves does not pass the critical shear stress for any part of the wave cycle. Furthermore, the shear stress for regular waves exceeds the threshold by a relatively constant value for the forward and backward stroke respectively, while the shear stress for irregular waves is

below the value for regular waves, though above threshold, and only occasionally rises above the value for regular waves.

- (c) The pump-sampling measurements took an average of 10 minutes to complete. As there was only one pump-sampling unit next to the flume to collect the sand/water mixture and to determine the sediment concentration values using the calibration tube, the connection to the pump sampling arrays had to be switched between STABLE and the nozzles at the side wall of the *Deltaflume*. Different lengths of pipe connecting the nozzles and the buckets could have affected measurements. The longer the pipe, the longer it takes to collect the same amount of sand/water mixture. However, according to Koen Trouw (personal communication), who performed the pump-sampling measurements, there was not much difference in the lengths of plastic pipe for the two measuring sites and hence this cannot be an explanation for the observed measurements.
- (d) Since the pump-sampling equipment was swapped over from the STABLE nozzles to the nozzles at the side of the *Deltaflume* and vice versa, there is no guarantee that the measurements were taken under exactly the same hydrodynamic and morphodynamic conditions. The bed was exposed to waves for approximately 1 hour before measuring commenced. This was thought to be long enough for equilibrium ripples to develop. However, as mentioned above, the ripples under regular waves evolved during the burst and thus, there were different conditions for the first and the second half of the burst. Additionally, not only the bedforms changed during one burst, but also the hydrodynamic conditions. For irregular waves there was a repeat period of the spectrum of 1 hour. This means that during the first 10 minutes of a burst, the significant wave height was not necessarily the same as for the second half of the burst. This might explain some of the differences in c-profiles for the two sites under irregular waves. Taking the horizontal velocity closest to the bed (for STABLE ECM A, about 30 cm above the bed and the 25 cm ECM for DH) as a representative for the hydrodynamic conditions under scrutiny, the area under the spectrum (m_0) was determined for the two halves of the burst. The results are presented in table 3.5. It has to be emphasised that the ECM heads for STABLE and DH were of different size and thus no comparison between the two sites is attempted here. The only interest lies in the comparison of m_0 for each sensor, for the first and second half of the burst, respectively.

For regular waves the wave height and hence the velocity for the first half of the burst should not differ considerably from the values measured for the second half of the burst. This is confirmed by the m_0 values for the horizontal velocity measured by the STABLE

ECM at a nominal height of 30 cm. Table 3.5 clearly shows a greater variation in m_0 for irregular waves. The values for the Delft Hydraulics velocity show a similar trend, but not as clearly. Figure 3.17 shows an example of horizontal velocity for the Delft Hydraulics ECM at a nominal height of 25 cm above the bed. It confirms that there is a difference in horizontal velocity strength between the first and second half of the burst. The different significant wave heights for the two halves of the burst were used to determine the effect on the reference sediment concentration evaluated using equation 2.70. The largest variation in energy for the two halves of the bursts is observed for burst a10a, which results in a difference in the reference concentration of 46 %. On average the different significant wave heights resulted in a variation of the reference concentration of 14 %. This indicates the importance of the order of the pump-sampling and the effect on the measured sediment concentrations.

As mentioned above, the differences in hydrodynamics and morphodynamics during the first and the second half of the burst might contribute to some differences in the c -profiles measured by the pump-sampling devices. It has to be acknowledged though, that the best effort was put in to ensure the same conditions throughout a burst. As mentioned the ripples evolve and migrate during a burst for regular waves and hardly change during a burst for irregular waves. For irregular waves, it is impossible to ensure exactly the same m_0 value for any number of sub-sections in a burst. As there was no record in the logbook of the order (STABLE first, side wall second or vice versa) in which the pump sample measurements were taken, it is not possible to evaluate the significance of the difference in hydrodynamics between the first and the second half of a burst for irregular waves.

- (e) The definition of an accurate datum for both pump-sampling arrays (STABLE and DH) is very difficult. The height of the STABLE nozzles was measured with respect to a concrete surface when STABLE was standing at the side of the flume. Thus the distances measured were not relative to the ripples. The pump-sampling array at the side of the flume was not permanently fixed to the wall and thus the relative distances to the bed were also not very accurate. The pump-sampling nozzles were fixed to a metal rod, which was lowered into the flume such that it touched the bed. Hence there was some uncertainty in the exact position of the nozzles relative to the bed as it was not possible to view the bed from the water surface.

The ARP samples give an indication of the position of the STABLE pump-sampling array relative to a ripple crest or trough. The same information on the bedforms, at the position

of the pump-sampling array at the side of the flume is not available. An accurate datum for the nozzles at STABLE and at the side of the flume, cannot be determined. This could lead to some shifts in the c-profiles and explain some of the disagreement encountered. However, it is hoped that the ARP will yield some more information on the relative position of the pump-sampling nozzles on STABLE, though some uncertainty will always remain.

- (f) Assuming continuity in the flume, the velocity at STABLE must be slightly larger than that measured at the side of the flume as STABLE is obstructing the flume and hence reducing the area. This could be another explanation why the suspended sediment concentration values were larger at STABLE than at the side of the *Deltaflume*. However, it would not explain why this only seems to be the case for irregular wave conditions. When analysing the velocity data it turned out that the horizontal velocities for regular waves measured by the Delft Hydraulics sensors were larger (see figure 3.18). For irregular waves this is not so clear. Thus, it cannot explain the higher suspended sediment concentration values for irregular waves.

3.5.3.2 Conclusions

In order to explain the differences between the c-profiles measured by the pump-sampling array on STABLE and the one at the side of the flume, a number of possible explanations have been investigated. Some possible causes could not be proven conclusively, due to lack of data. But it should be emphasised that the present data set is very unique. A large number of sensors were deployed, which made surplus measurements possible. This enabled the comparison of the c-profiles measured by the two pump-sampling arrays and the velocities at the two sites revealing differences that might otherwise not have been observed. These differences suggest the likely level of repeatability of the measurements. Thus, though there is and always will be the need for more data, the present study provides large amounts of data, which will lead to advances in this field.

It may be stated that several of the above issues cannot have caused the observed difference between the data for regular and irregular waves. The method of determining the sediment concentrations from the collected sand/water mixture, the difference in pipe length between the two pump-sampling arrays and the collecting apparatus, and the slightly increased velocity at STABLE due to the obstruction of the flume, have been considered and it has been shown that they are not possible explanations.

Other issues are less conclusive. The difference in wave energy between the first and second half of burst for irregular waves, the difference in bed geometry at the two sites and the uncertainty about the datum of the pump-sampling nozzles (especially the ones at the side of the flume as they were lifted out of the flume between bursts) may have caused the observed differences, but with the knowledge available at present this cannot be proven.

Thus, of the possible causes, the most likely is the difference in wave energy between the first and second half of the burst for irregular waves. This influenced the measured pump-sampling values for the two locations as the pump-sampling equipment had to be swapped between the sampling array on STABLE and the one at the side of the flume half way through the burst. The difference in energy resulted in an average variation in the reference concentration, determined by an empirical equation, of about 14 %. However, as there was no record of the order of measurements, a conclusive proof is unlikely to be obtained. This shows the importance of logging every detail of experimental work, however trivial it might seem at the time.

It was mentioned above that there is a clear difference in wave energy between the first and second half of the burst for irregular waves (table 3.5). Table 3.5 also shows that the m_0 values for the DH sensor are larger than those for the STABLE ECMs and at the same time the difference between the first and second half of the burst is larger. This may be explained by the fact that the DH sensors were smaller and therefore pick up more turbulence, which results in larger m_0 values. This is confirmed in figure 3.19, which shows energy density spectra for the horizontal velocities measured by STABLE ECM A and the DH sensor at approximately 30 cm and 25 cm above the bed, respectively for burst A08a (regular waves, $H = 0.85$ m). Due to the smaller measuring volume the DH sensor picks up more energy in the higher frequency range. The peaks at high frequencies are due to higher harmonics, which developed in the flume. No explanation was found for why these harmonics were only picked up by the ECM sensors mounted on STABLE. The ECMs on STABLE were positioned close to the front of STABLE and therefore any effects due to blockage from the frame seemed unlikely to be picked up by the ECMs. The Delft Hydraulics ECMs and STABLE itself were both placed far away from the beginning of the test sand bed, such that effects on the waves propagating over the test bed should be noticed by both set of sensors.

Though, great care was taken to measure the pump samples on site and store the samples for further measurements in the laboratory at POL, measurements were open to error. In order to reduce the amount of water passed through the filter paper, excess water was poured away. This might have resulted in the loss of very fine sediments such as silt.

Furthermore, the filter papers were not stored in desiccators prior to use and the dry weight of the filter papers were not determined for each filter paper, but estimated as an average value. Once the samples were filtered, the filter papers were not dried in controlled conditions. The combination of these measuring procedures might be cause of error of up to 20 % and thus explain some of the discrepancies described above.

3.5.4 Acoustic BackScatter Data (ABS)

3.5.4.1 Bed position and bedform geometry

Rig settlement into the sand bed changed the distance of the sensors relative to the bed and thus corrections were required. Tests at HR Wallingford on a prototype STABLE foot in a steady flow flume with a mobile sand bed were used as a rough guide to the settlement in the flume. These experiments suggested that the foot settled approximately 10 cm into the sand bed during the first 12 hours after deployment, and no further subsequently.

For the present study, the rig settlement can be determined more accurately (± 1 cm) by using the near bed ABS time series to locate the origin of the bed during each burst. The uncalibrated signal was used for this analysis. The raw acoustic backscatter data were measured in terms of backscatter intensity, which can be calibrated into sediment concentration values with units of g/l. As the sediment concentration was very high at the bed, there was a strong reflection (echo) of the acoustic signal by the bed. In the raw data the increased signal intensity at the bed was clearly visible (figure 3.20). The position of the bed was determined from the peak acoustic return of the three acoustic sensors (VILLARD ET AL., 1999a, VINCENT ET AL., 1991). Figure 3.21 illustrates the time variation of bed position measured by the three ABS transducers during two bursts. For both bursts the bed position series has been smoothed with a 64 point (approximately 16 seconds) moving average filter. As the ABS recorded the backscatter intensity in 1cm intervals (bins) the averaged bin number was rounded up to the nearest integer. Figure 3.21b shows a drastic change in bed elevation for the 2.0 and 4.0 MHz sensor during burst a08a (regular waves, $H = 0.85$ m). As the ripple heights were of the order of 5 cm, the passing of a sand ripple underneath the sensors is a possible explanation for the drastic change in bed elevation. The changes in bed elevation for burst a09a (irregular waves, $H_s = 0.83$ m) in figure 3.21a are in general about 2 cm. However 4 spikes, where the peak backscatter position changes by up to 14 cm for a short period of time (approximately 50 seconds), are evident. These spikes are associated with short periods of energetic near bed suspension and subsequent settling of

the suspended material. The positions of the peak backscatter, and thus the bed, are listed in table 3.6 for the bursts on the medium sand bed.

Bedforms were measured using a mechanical ripple profiler provided by Delft Hydraulics and two acoustic sensors mounted on STABLE. As the mechanical ripple profiler was only used at the beginning and the end of the tests on the medium and the fine sand bed respectively, it does not give any information about ripple dimensions during individual bursts. The advantage of the mechanical ripple profiler was that it measured the ripple dimensions along the whole length of the bed and a number of times across the bed. This allowed the visualisation of the repetitiveness of the ripples over the whole bed and gave an indication of the two-dimensionality of the ripples. On the medium sand bed the ripple wavelength was λ_r , $O(30)$ cm and the ripple height was h_r , $O(4)$ cm. The acoustic ripple profiler recorded the bedforms along a 3 m slice of the bed underneath STABLE during all bursts. These data were used to determine representative ripple dimensions for each burst. For the bursts where STABLE was deployed at an angle no sensible values for ripple dimensions could be determined, as the acoustic beam hit the ripples at an angle. For all the other bursts, where STABLE was in line with the flume, the ripple dimensions were extracted from the acoustic profiling data. The ripple heights, determined by a zero down-crossing analysis and corresponding wavelengths, are presented in table 3.7. Also ripple dimensions predicted using Nielsen's formulae given by equations 2.39 to 2.43 for laboratory conditions (regular waves) and for field conditions (irregular waves) were determined. Table 3.7 shows the results for laboratory conditions (equations 2.39 and 2.41). It turned out that the agreement between the calculated and measured ripple dimensions is reasonably good. This is confirmed in figure 3.22, which presents the predicted and measured ripple dimensions as a function of the sediment mobility number Ψ . The values determined from the acoustic ripple profiler are shown with a 10 % error bar, as the presented value is an average and does not take the minimum or maximum wavelength into account. No distinction between regular and irregular wave conditions was made. It is clear that the equation for laboratory conditions (regular waves) represents the measured values more accurately than the one for irregular waves. As shown before, the bedforms present under irregular waves were relics of the bedforms generated by the previous burst under irregular waves and thus can be better predicted by the equations for regular waves.

The sector-scanning sonar was only deployed twice during the tests. Figure 3.10 shows an image obtained by the sector-scanner. This image was obtained in still water after STABLE had been lifted out of the flume. The side walls of the *Deltaflume* and well developed, long crested ripples are shown clearly. Also imprints left in the sand by STABLE's feet are visible.

The image can be used for a first impression of the bedforms and the two-dimensionality of the ripples. It cannot be used to determine burst averaged ripple dimensions.

3.5.4.2 Burst averaged concentration profiles

Instantaneous suspended sediment concentrations were available for bursts a07a (irregular waves, $H_s = 0.53$ m), a08a (regular waves, $H = 0.85$ m), a09a (irregular waves, $H_s = 0.83$ m), a10a (irregular waves, $H_s = 1.07$ m), a11a (regular waves, $H = 1.34$ m) and a12a (irregular waves, $H_s = 1.26$ m). For each of the bursts concentrations measured by the 1.0 and 2.0 MHz ABS transducers were accessible except for bursts a10a and a12a where the calibration of the 2.0 MHz sensor proved difficult (personal communication with Peter Watkins at POL). Figures 3.23a and b show examples of burst averaged concentration profiles for bursts a08a and a09a. The agreement between the sediment concentration measured by the two sensors is very good. However, at low heights (up to 20 cm above the bed) the concentration measured by the 2.0 MHz sensor is slightly lower than the one measured by the 1.0 MHz sensor. There is a clear difference in the maximum concentration at the bed (approximately 5.2 and 1.8 g/l, respectively). Furthermore, the sediment concentration decreases faster for the irregular waves (figure 3.23b) and is down to about 0.2 g/l at 20 cm above the bed, whereas this value is reached at about 30 cm above the bed for the regular waves (figure 3.23a). Even though the irregular waves generated some very high waves (see figure 3.24b), they did not lift as much sediment as the regular waves, whose wave heights vary by less than ± 15 % from the mean value (figure 3.24a). This is the same effect as seen for the ripple formation. During irregular waves the ripples did not migrate and it was shown that the ripples present under irregular waves were relics from those ripples present during the previous burst with regular waves. A more detailed analysis of the burst mean c-profiles will be presented in chapter 5.

3.6 Summary

This chapter concentrated on the preliminary data analysis including the initial data manipulation and the comparison of different sensors. Also, a quality control on these data was performed. A number of sensors were deployed at a 'control' site away from STABLE at the side of the *Deltaflume* in order to determine the influence of STABLE on its measuring environment. The pump-sampling data from the sampling nozzles at the side of the flume and on STABLE were compared. For some bursts, particular for irregular waves, there was a noticeable difference between the data recorded by the nozzles mounted on STABLE and those at the side of the flume. A number of possible explanations were investigated without

finding a conclusive proof for the differences. Analysing the acoustic ripple profiler it turned out that irregular waves should not follow regular waves with respect to the formation of ripples on the bed. Irregular waves with the same significant wave height as regular waves were not able to form new equilibrium ripples, resulting in present bedform dimensions which were not associated with the hydrodynamics of the specific burst. Chapter 4 will concentrate on the influence of STABLE on its measuring environment.

Further chapters will focus on the detailed data analysis, especially sediment entrainment from the bed. Chapter 5 will look at the burst mean concentration profiles measured by the ABS transducers, while chapter 6 will focus on the intra-wave entrainment processes. Vortex ejections from a rippled bed will be investigated in chapter 7.

TABLES

Date	Experiment	Theoretical θ	θ	d (m)	H (m)	T (sec)	Hs (m)	Tp (sec)	γ
	Medium sand bed completed								
02/07/97	A01a			4.50	0.569	4.96			
02/07/97	A01b			4.50	0.568	5.00			
03/07/97	A02a			4.50	0.797	4.97			
03/07/97	Ripple profiling (DBP-1)								
04/07/97	A03a			4.50			0.747	4.94	3.3
04/07/97	A03b			4.50			0.834	4.78	3.3
04/07/97	A03c			4.50			0.831	5.08	3.3
04/07/97	Assembly of STABLE completed; Wave probe calibration checks; STABLE deployed								
07/07/97	A04a	0	17	4.50	1.041	5.01			
07/07/97	A04b	0	17	4.50	1.101	5.00			
08/07/97	A05a	0	16	4.50	1.103	5.00			
08/07/97	A05b	0	17	4.50	1.111	5.00			
08/07/97	A06a	0		4.50					
08/07/97	A06b	0	17	4.50	0.550	5.00			
09/07/97	A001 (zero run)								
09/07/97	A07a	0	17	4.46			0.532	4.98	3.3
09/07/97	A08a	0	17	4.50	0.850	4.99			
09/07/97	A09a	0	16	4.50			0.826	4.92	3.3
10/07/97	A002 (zero run)								
10/07/97	A10a	0	17	4.50			1.066	5.1	3.3
10/07/97	A11a	0	16	4.50	1.344	5.00			
10/07/97	A12a	0	16	4.50			1.258	5.1	3.3
11/07/97	A003 (zero run)								
11/07/97	STABLE recovered: camera fitted, STABLE turned								
11/07/97	A13a	0		4.50	1.083	5.00			
11/07/97	A14a	45	35	4.50	1.075	5.00			
11/07/97	A15a	45	34	4.50	1.051	4.95			
11/07/97	STABLE turned								
14/07/97	A004 (zero run)								
14/07/97	A16a	90	74	4.50	1.088	4.99			
14/07/97	A17a	90	75	4.50			1.128	4.95	3.3
14/07/97	A18a	90	73	4.50	1.178	5.00			
14/07/97	STABLE turned								
15/07/97	A005 (zero run)								
15/07/97	A19a	0	13	4.50	1.096	5.00			
15/07/97	A20a	0	13	4.50	1.037	4.00			
15/07/97	A21a	0	13	4.50	0.643	5.99			
15/07/97	A22a	0	13	4.50	1.303	4.97			
16/07/97	A23a	0	14	4.50	0.832	5.00			
16/07/97	STABLE recovered								
16/07/97	Ripple profiling (DBP-2)								

Table 3.1: Chronological summary of *Deltaflume* tests, medium sand bed ($d_{50} = 0.329$ mm). The camera fitted on STABLE did not record useful picture owing to the fine sand in suspension.

Date	Experiment	theoretical θ	θ	d (m)	H (m)	T (sec)	Hs (m)	Tp (sec)	γ
23/07/97	Fine sand bed completed								
24/07/97	F01a			4.50	0.815	5.00			
24/07/97	Ripple profiling								
25/07/97	Ripple profiling								
28/07/97	Ripple profiling, DBP-3								
29/07/97	F001 (zero run)								
29/07/97	STABLE deployed								
29/07/97	F02a	0	15	4.50	0.323	4.64			
29/07/97	F02b	0	15	4.50	0.344	4.83			
29/07/97	F02c	0	15	4.50	0.360	4.99			
30/07/97	F002 (zero run)								
30/07/97	F03a	0	15	4.50	0.513	5.00			
30/07/97	F04a	0	15	4.50			0.546	4.963	3.3
30/07/97	F05a	0	15	4.50	0.848	5.00			
31/07/97	F003 (zero run)								
31/07/97	F07a	0	15	4.50			0.815	4.743	3.3
31/07/97	F08a	0	15	4.50	1.104	5.00			
31/07/97	F09a	0	15	4.50	0.723	4.93			
01/08/97	F004 (zero run)								
01/08/97	F10a	0	15	4.50			1.110	5.255	3.3
01/08/97	STABLE turned								
01/08/97	F005 (zero run)								
01/08/97	F11a	45	57	4.50	0.824	5.96			
04/08/97	F006 (zero run)								
04/08/97	F12a	45		4.50			1.473	4.515	
04/08/97	F13a	45	58	4.50			1.473	4.476	
04/08/97	F14a	45	57	4.50	0.821	4.00			
04/08/97	F15a	45	57	4.50	0.927	5.00			
05/08/97	F007 (zero run)								
05/08/97	F16a	45	58	4.50			1.138	5.225	
05/08/97	F17a	45	58	4.50	0.802	5.00			
05/08/97	STABLE recovered								
05/08/97	Ripple profiling, DBP-4								
06/08/97	STABLE dismantled								

Table 3.2: Chronological summary of *Deltaflume* tests, fine sand bed ($d_{50} = 0.162\text{mm}$).

Sensor	x (mm)	y (mm)	z (mm)
ECM 'A' port	123	372	302
ECM 'A' starboard	-117	372	302
ECM 'B' port	123	372	606
ECM 'B' starboard	-117	372	606
ECM 'C' port	123	372	910
ECM 'C' starboard	-117	372	910
SonTec ADV	-564	149	505
Rotor 1	0	1396	396
Rotor 2	0	1396	576
Rotor 3	0	1396	756
Rotor 4	0	1396	936
Horizontal coherent Doppler	50	894	425
Vertical coherent Doppler	0	-17	1295
Correlation transducer 'A' (front)	607	60	1355
Correlation transducer 'B' (back)	607	238	1355
4MHz acoustic backscatter	-114	145	1240
2MHz acoustic backscatter	0	145	1237
1MHz acoustic backscatter	114	145	1247
Acoustic ripple profiler	334	551	1216
Mean pressure transducer	-970	1340	1702
Burst pressure transducer	-560	1465	1725
PS1	-273	138	53
PS2	-273	138	73
PS3	-273	138	102
PS4	-273	138	131
PS5	-273	138	180
PS6	-273	138	255
PS7	-273	138	400
PS8	-273	138	653
PS9	-273	138	1050
PS10	-273	138	1553

Table 3.3: Summary of instrument positions on the STABLE frame using the x, y and z co-ordinate convention illustrated in figure 3.1.

Overall rig length	3305mm
Diameter of instrument platform	2160mm
Height to top of instrument platform	1845mm
Overall width across front feet	3370mm
Diameter of each foot	610mm
Depth of each foot	160mm
Weight of each foot	500kg
Overall rig weight	2200kg

Table 3.4: Summary of the overall dimensions and weight of STABLE.

Burst	Regular	Irregular	STABLE			DELFT HYDRAULICS		
			1st half	2nd half	Diff [%]	1st half	2nd half	Diff [%]
A05a			0.1566	0.1569	0.2	0.2202	0.2298	4.2
A05b			0.1576	0.1600	1.3	0.2173	0.2300	5.5
A07a			0.0189	0.0176	6.9	0.0167	0.0312	46.5
A08a			0.1097	0.1101	0.4	0.1258	0.1146	8.9
A09a			0.0432	0.0422	2.3	0.0494	0.0463	6.3
A10a			0.0816	0.0634	22.3	0.0708	0.0636	10.2
A11a			0.2278	0.2300	1.0	0.2466	0.2780	11.3
A12a			0.0970	0.1049	7.5	0.1042	0.0979	6.0

Table 3.5: Values of m_0 for the horizontal velocity at STABLE and Delft Hydraulics for the first and second half of a number of bursts.

Burst	Regular	Irregular	1 MHz Sensor	2 MHz Sensor	4 MHz Sensor
A07a			123	121	122
A08a			123	123 (1st 500 s of burst)	123 (1st 500 s of burst)
A09a			120	120	124
A10a			120	121	118
A11a			117	117	100
A12a			118	117	112

Table 3.6: Bin numbers referring to the position of the peak backscatter signal for the raw ABS data.

Burst	H	H _s	Mobility number Ψ	Wavelength λ_r	Wave height h _r	Wavelength λ_r Nielsen	Wave height h _r Nielsen
A04b	1.101		69.37	0.423	0.054	0.359	0.045
A05a	1.103		69.63	0.411	0.055	0.359	0.044
A05b	1.111		70.64	0.471	0.063	0.358	0.044
A06b	0.550		17.31	0.286	0.034	0.312	0.044
A07a		0.532	16.2	0.357	0.037	0.31	0.044
A08a	0.850		41.35	0.319	0.041	0.37	0.050
A09a		0.826	38.0	0.353	0.047	0.36	0.049
A10a		1.066	66.63	0.493	0.057	0.37	0.046
A11a	1.344		103.4	0.540	0.066	0.31	0.03
A12a		1.258	92.79	0.495	0.058	0.34	0.036
A19a	1.096		68.74	0.431	0.058	0.360	0.045
A20a	1.037		42.45	0.315	0.037	0.293	0.040
A21a	0.643		28.52	0.304	0.040	0.418	0.059
A22a	1.303		97.16	0.323	0.043	0.324	0.033
A23a	0.839		40.28	0.413	0.055	0.365	0.050

Table 3.7: Ripple dimensions determined from the acoustic ripple profiler data and predictions using Nielsen's equation for *regular waves* for the bursts where STABLE is aligned with the flume. The grey shaded cells indicate regular waves.

FIGURES

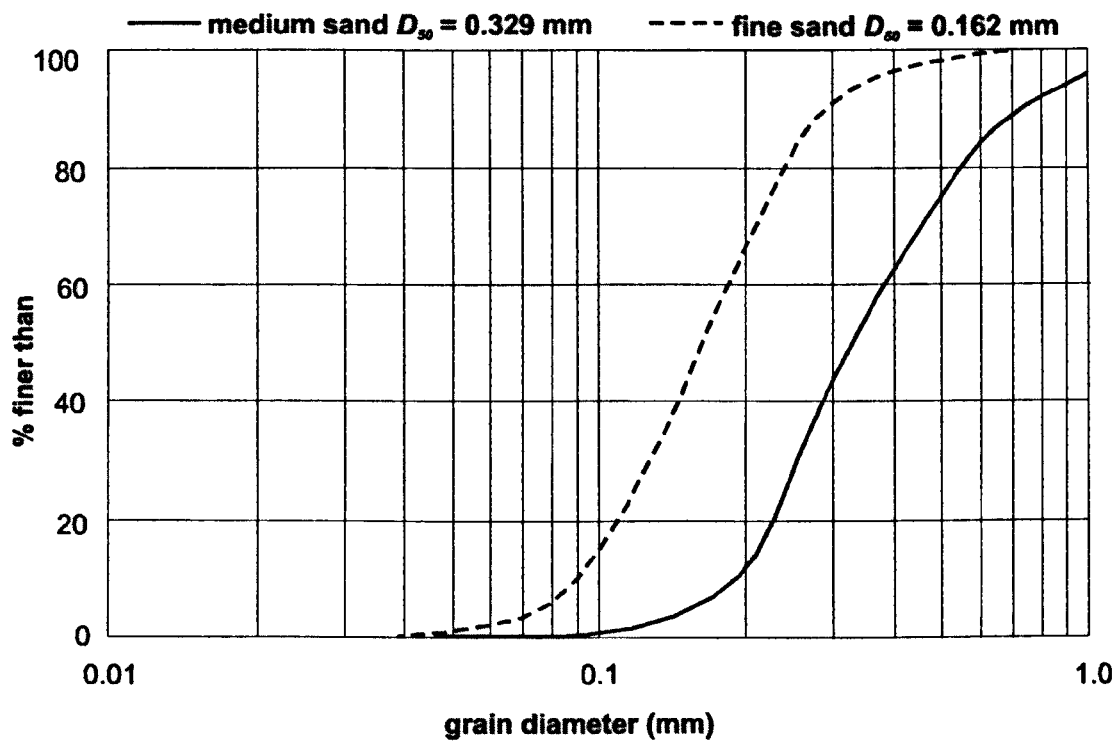
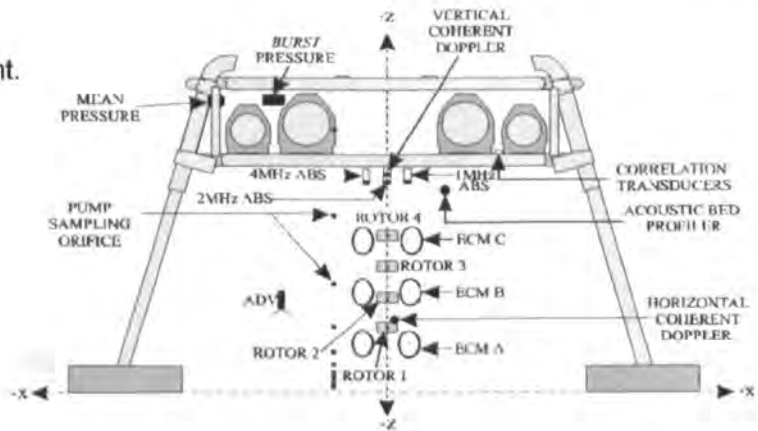
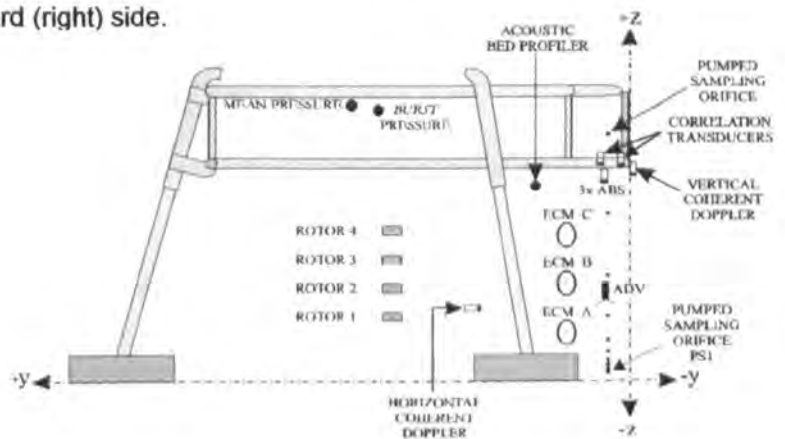


Figure 3.1: Cumulative grain size distribution for medium and fine sands used in the *Deltaflume* tests.

a) STABLE frame – view onto front.



b) STABLE frame – view on starboard (right) side.



c) STABLE frame – plan view.

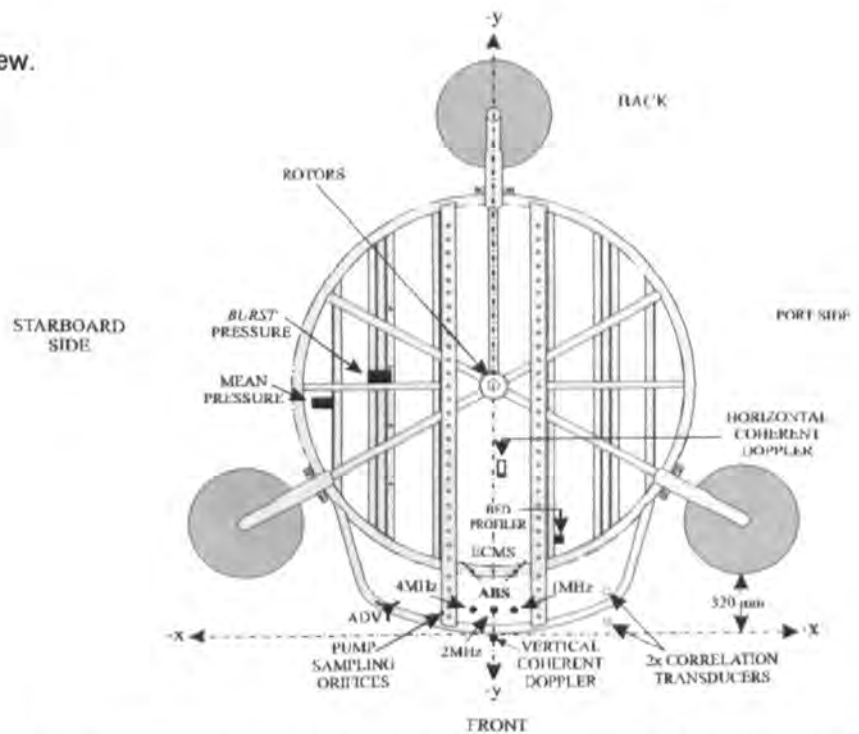


Figure 3.2: STABLE: a) front elevation, b) side elevation and c) plan. For dimensions and rig statistics see tables 3.3 and 3.4.

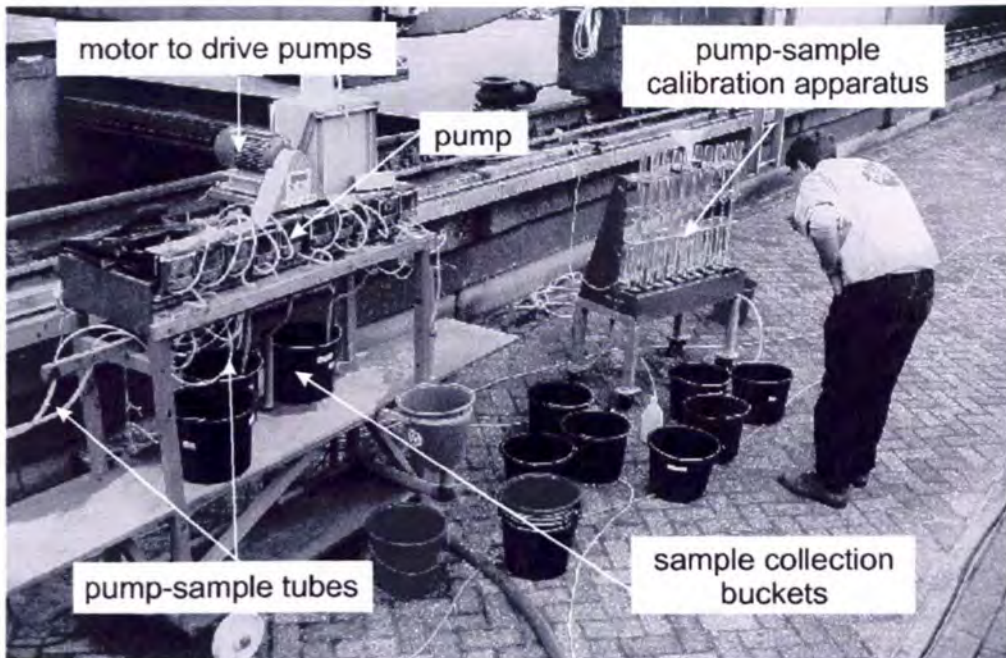


Figure 3.3: Collection of suspended sediment samples from the *Deltaflume* using pump-sampling equipment.

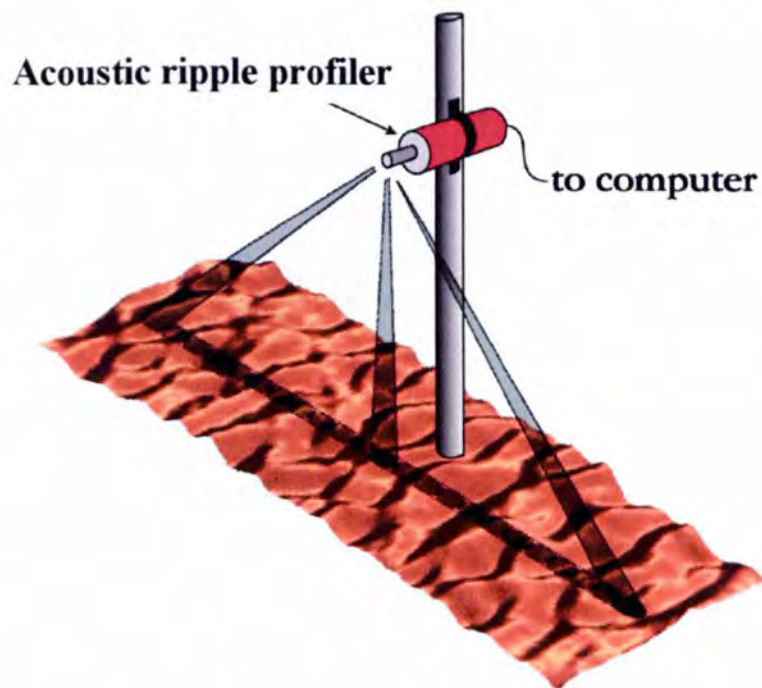


Figure 3.4: Schematic of the acoustic ripple profiler (ARP, courtesy of Paul Bell, POL). The ARP recorded data along a 1.5 m zone from its central position underneath STABLE.

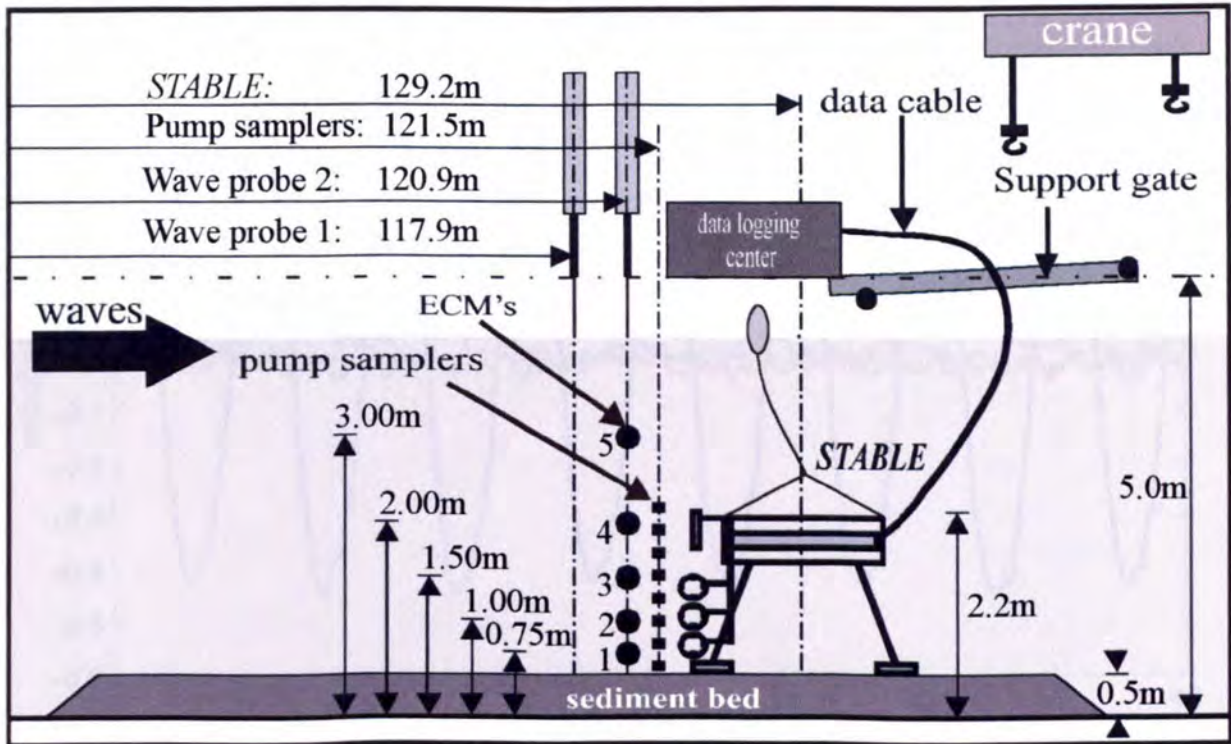


Figure 3.5: Schematic diagram showing the positions of STABLE, the wave probes and the Delft Hydraulics ECMs in the *Deltaflume*.

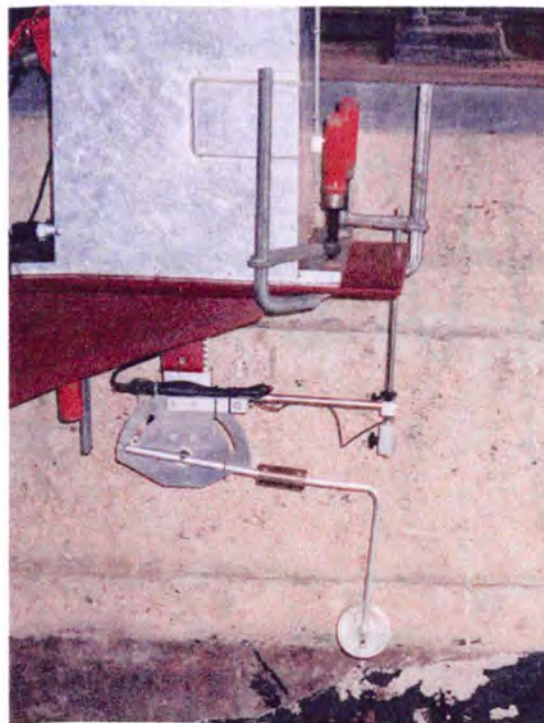


Figure 3.6: Delft Hydraulics lightweight mechanical ripple profiler device. The little wheel is moved along the bed and records the bed profile.

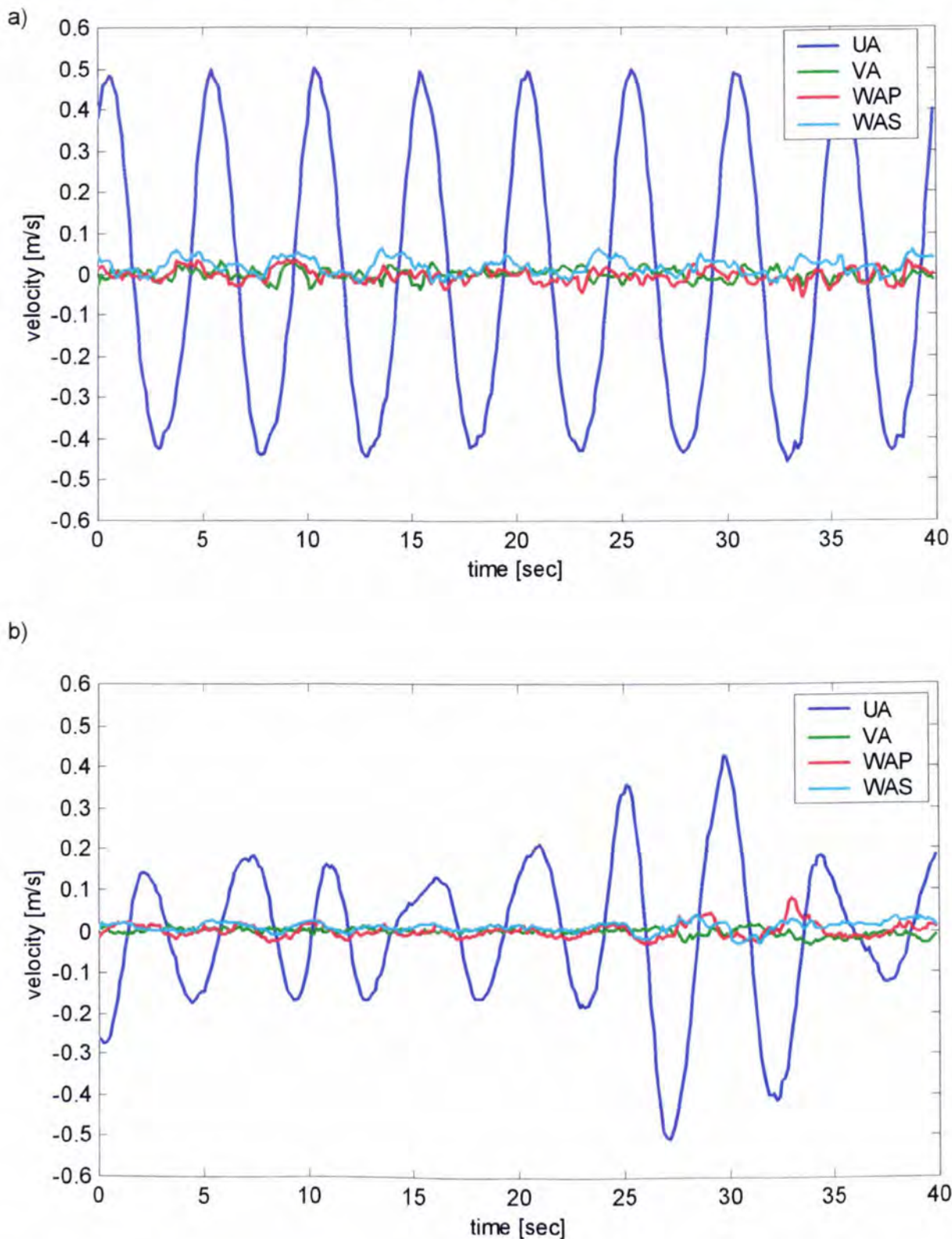


Figure 3.7: The 4 STABLE velocities at ECM A (≈ 31 cm above the bed) for a) regular waves ($H = 0.85$ m) and b) irregular waves ($H_s = 0.83$ m).

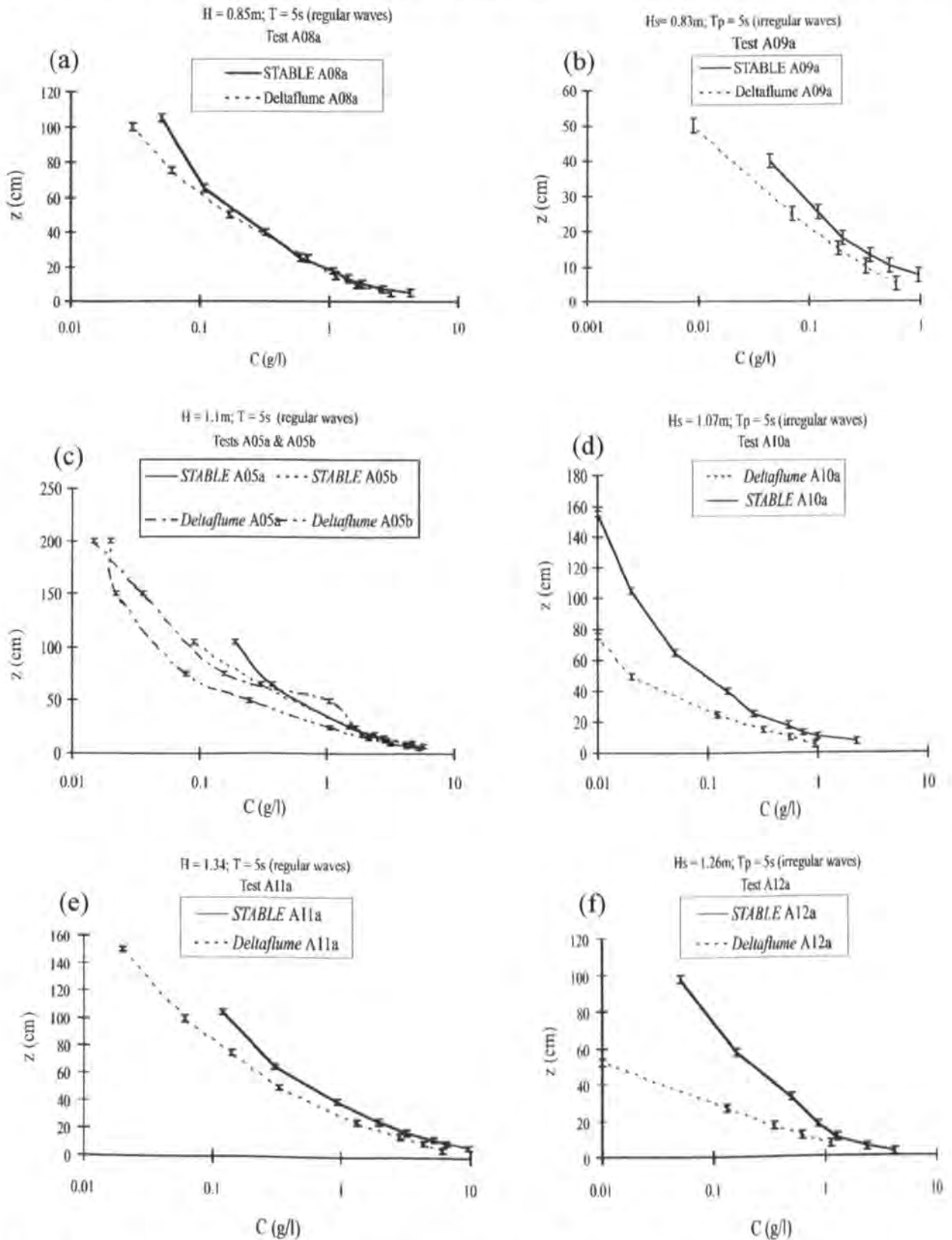


Figure 3.8: Suspended sediment concentration profiles measured using pump-sampling apparatus above the medium bed (from cylinder analysis next to the *Deltaflume*).

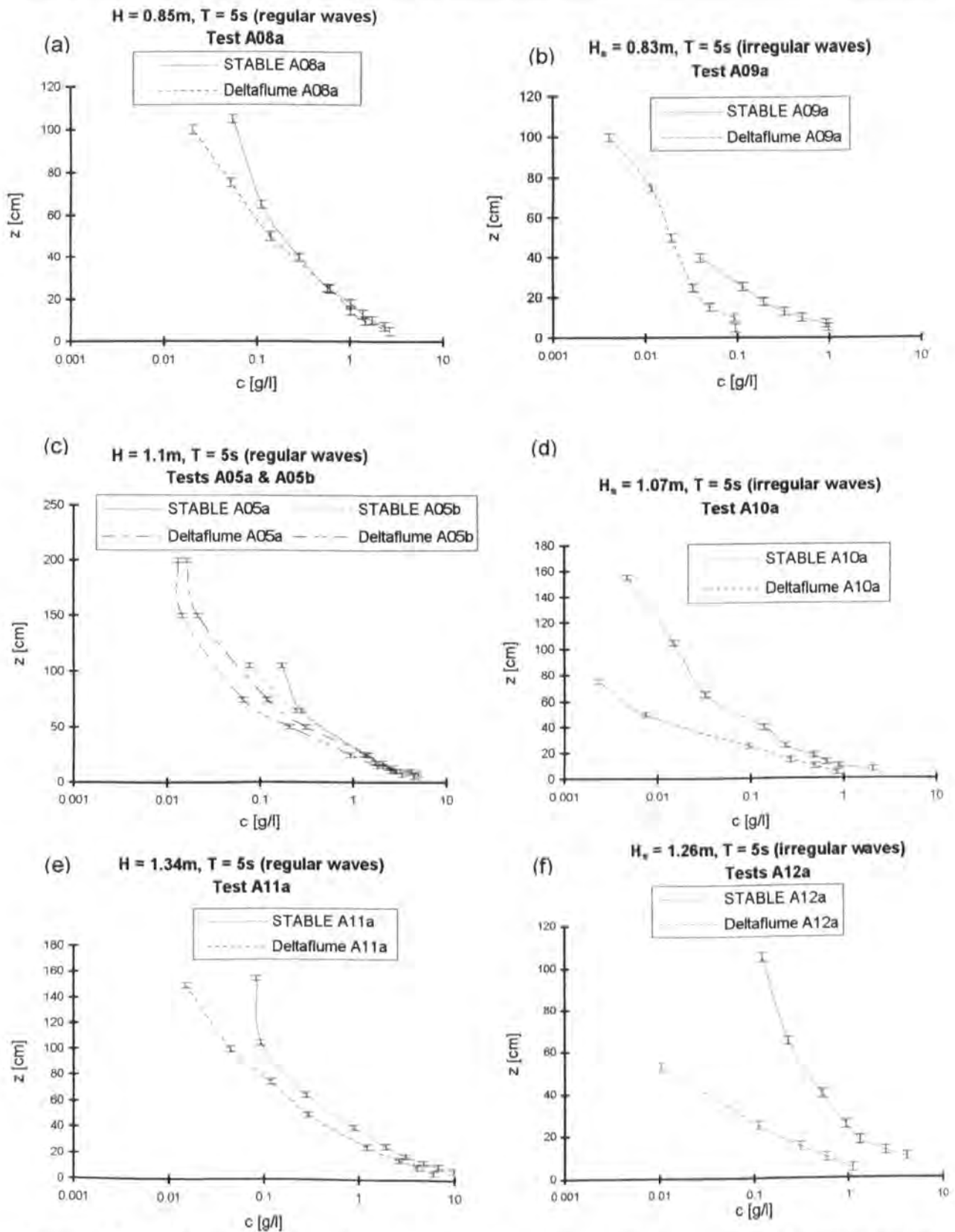


Figure 3.9: Suspended sediment concentration profiles measured using pump-sampling apparatus above the medium bed (from volumetric analysis at POL).

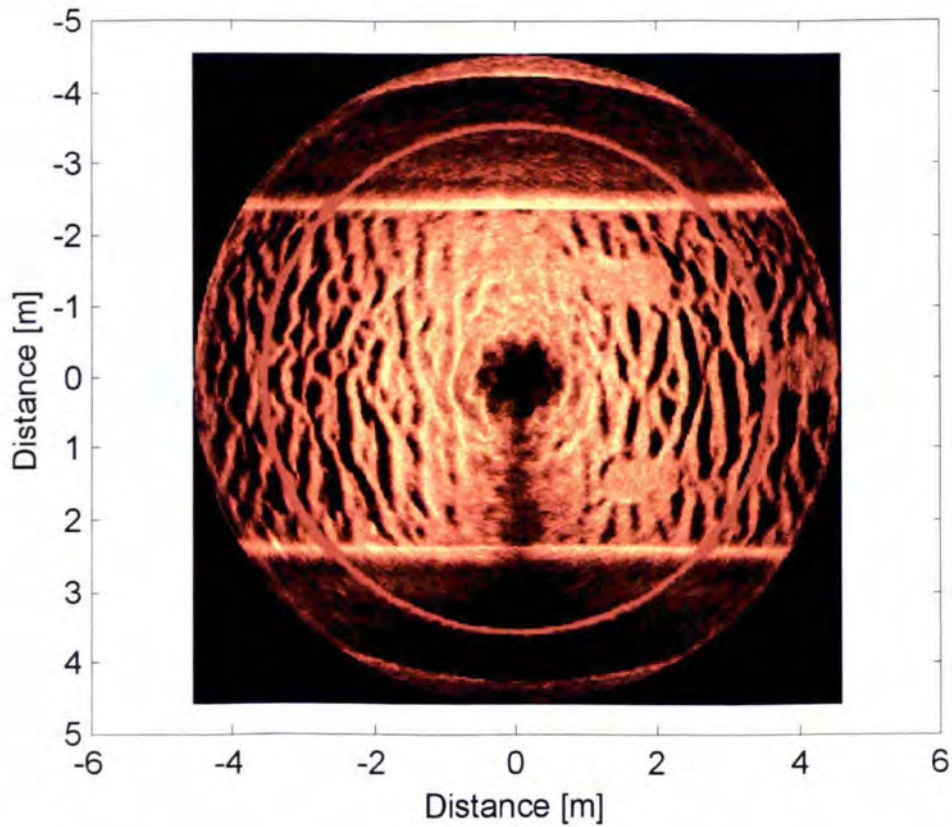


Figure 3.10: Sonar image of the medium sand bed showing the walls of the *Deltaflume* and imprints left by STABLE's feet. Image was recorded after burst a23a (regular waves, $H = 0.839$ m) at the end of the tests on the medium sand bed.

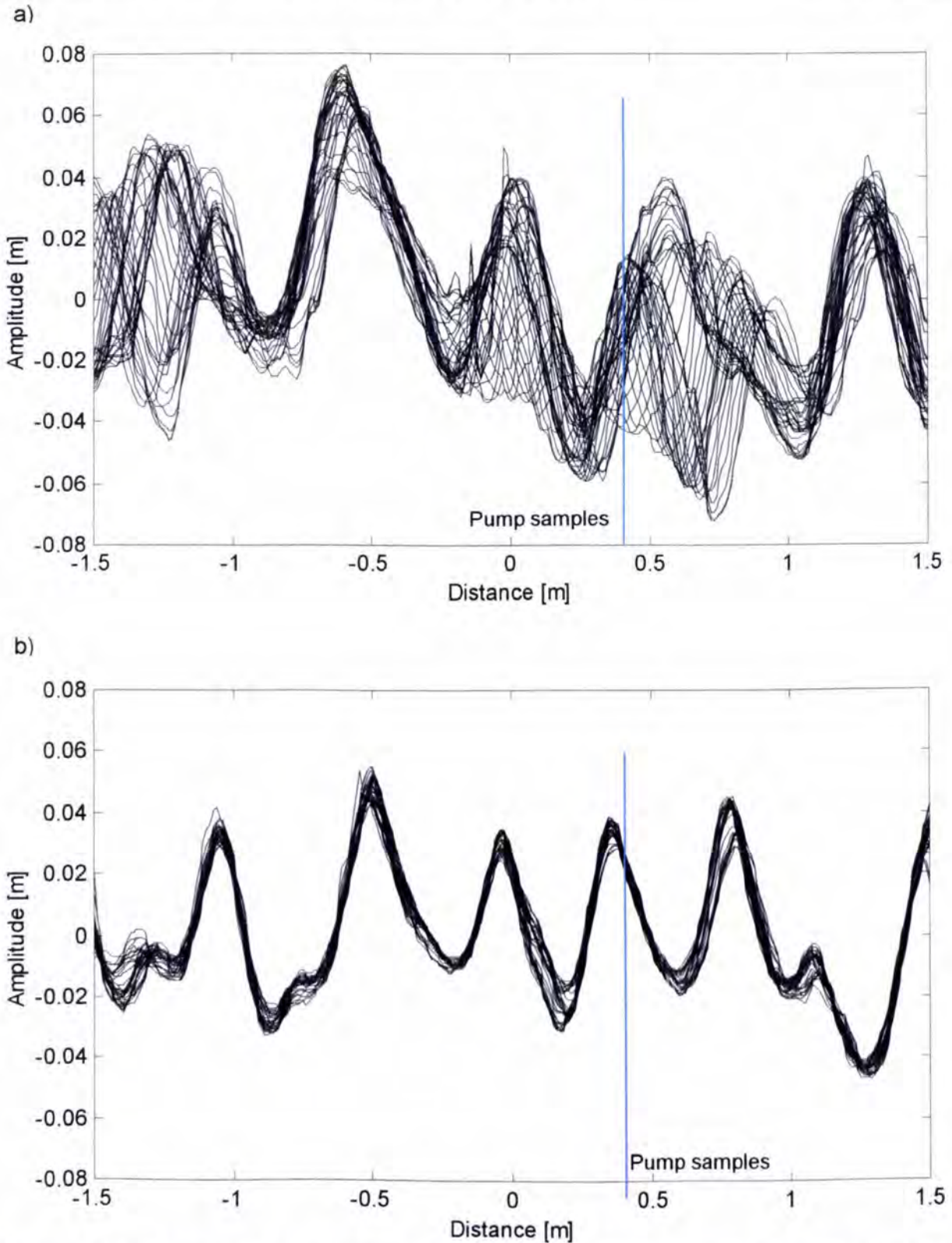


Figure 3.11: Samples of ripple profiles measured by the acoustic ripple profiler for a) burst a11a (regular waves, $H = 1.34$ m) and b) burst a10a (irregular waves, $H_s = 1.07$ m). The position of the pump-sampling array is highlighted.

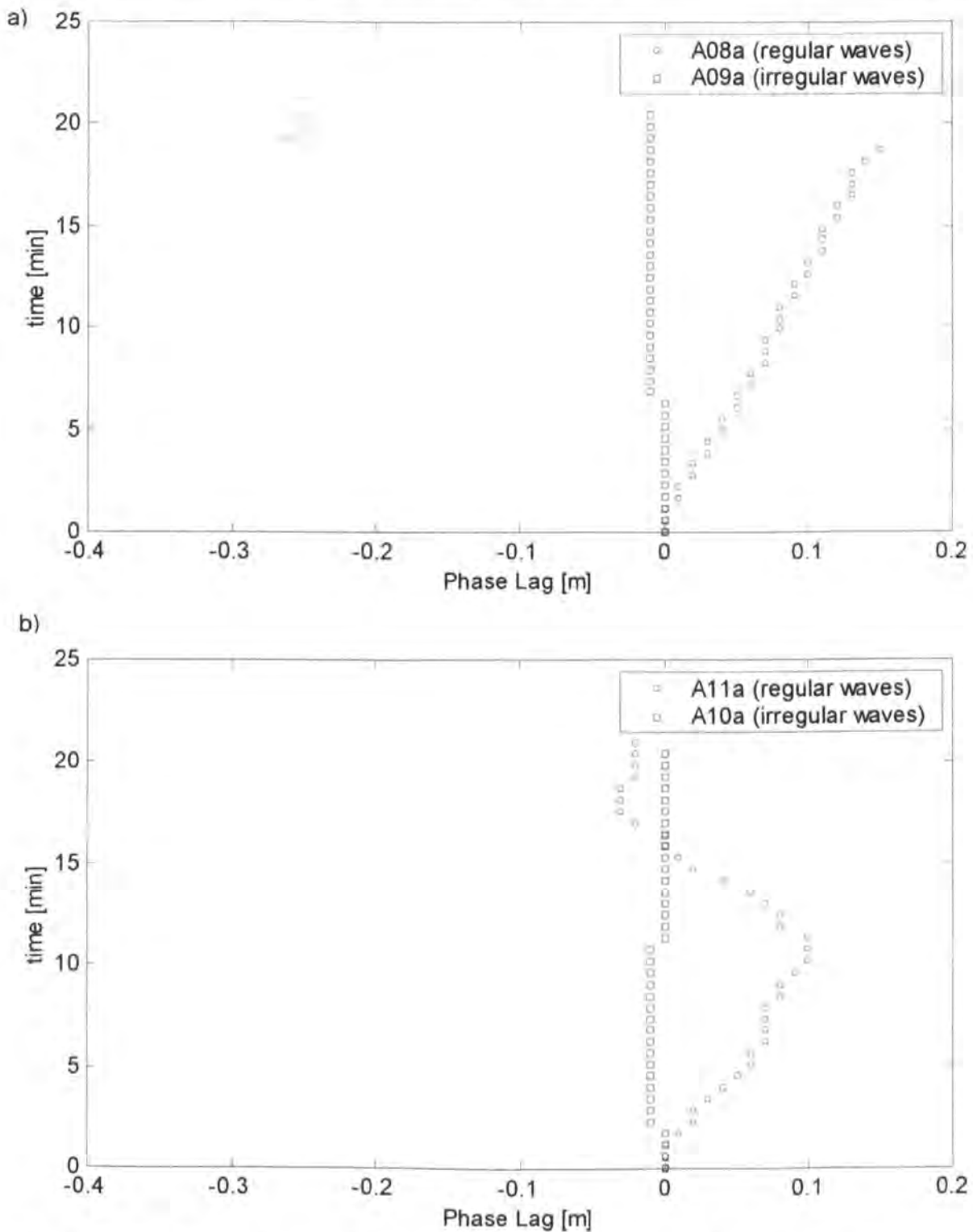


Figure 3.12: Phase lag for peak correlation between the first time slice and all consecutive time slices measured by the acoustic ripple profiler for a) burst a08a (regular waves, $H = 0.85$ m) and a09a (irregular waves, $H_s = 0.83$ m) and b) burst a11a (regular waves, $H = 1.34$ m) and a10a (irregular waves, $H_s = 1.07$ m).

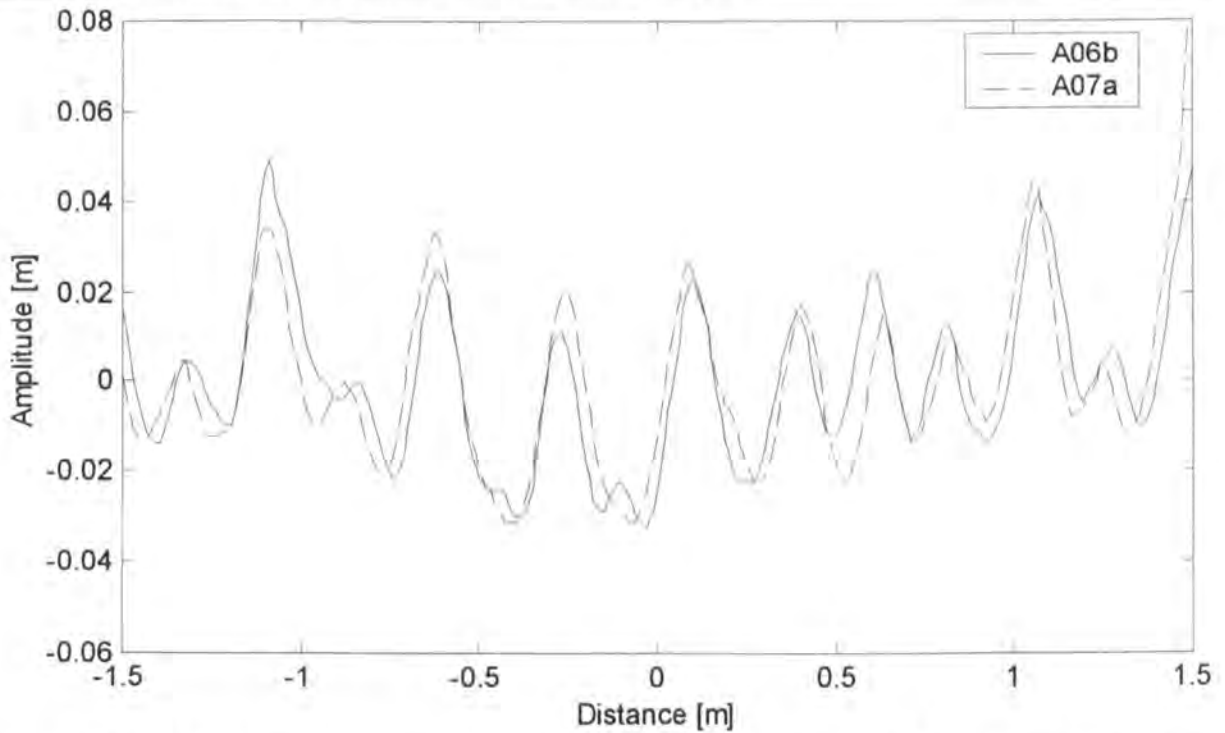


Figure 3.13: Last slice recorded by acoustic ripple profiler for burst a06b (regular waves, $H = 0.55$ m) and the first slice for burst a07a (irregular waves, $H_s = 0.53$ m).

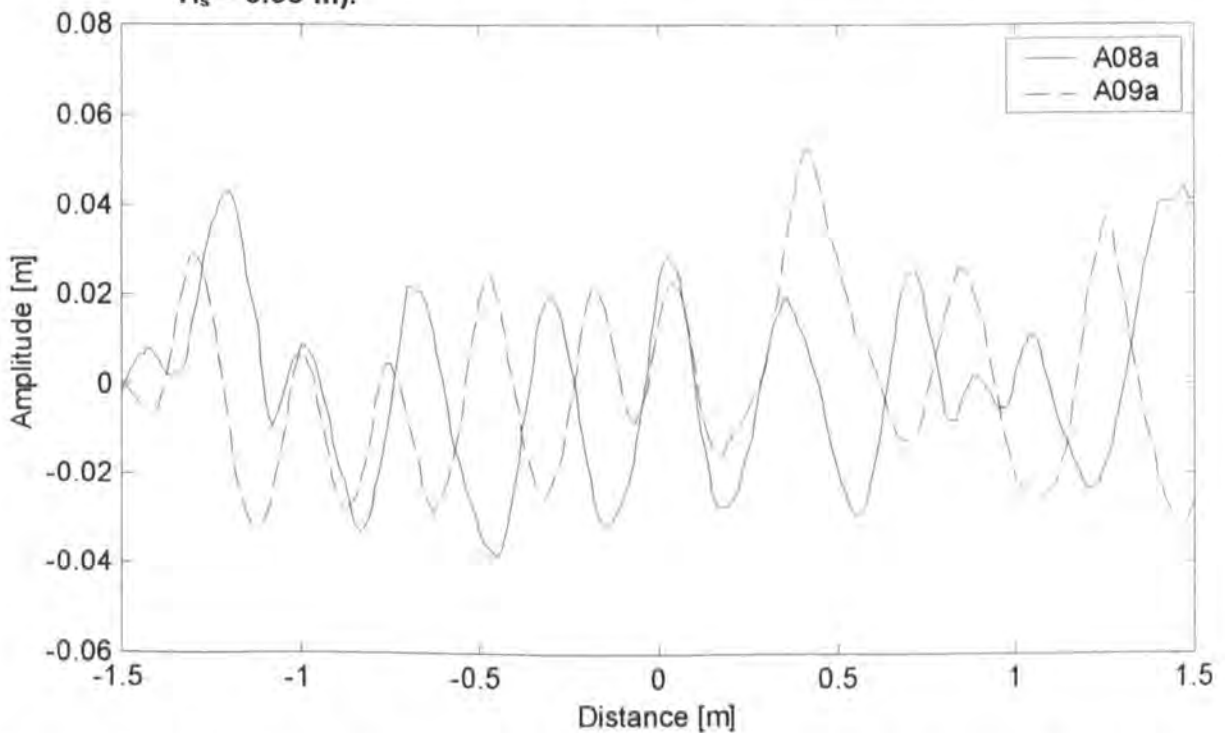


Figure 3.14: Last slice recorded by acoustic ripple profiler for burst a08a (regular waves, $H = 0.85$ m) and the first slice for burst a09a (irregular waves, $H_s = 0.83$ m).

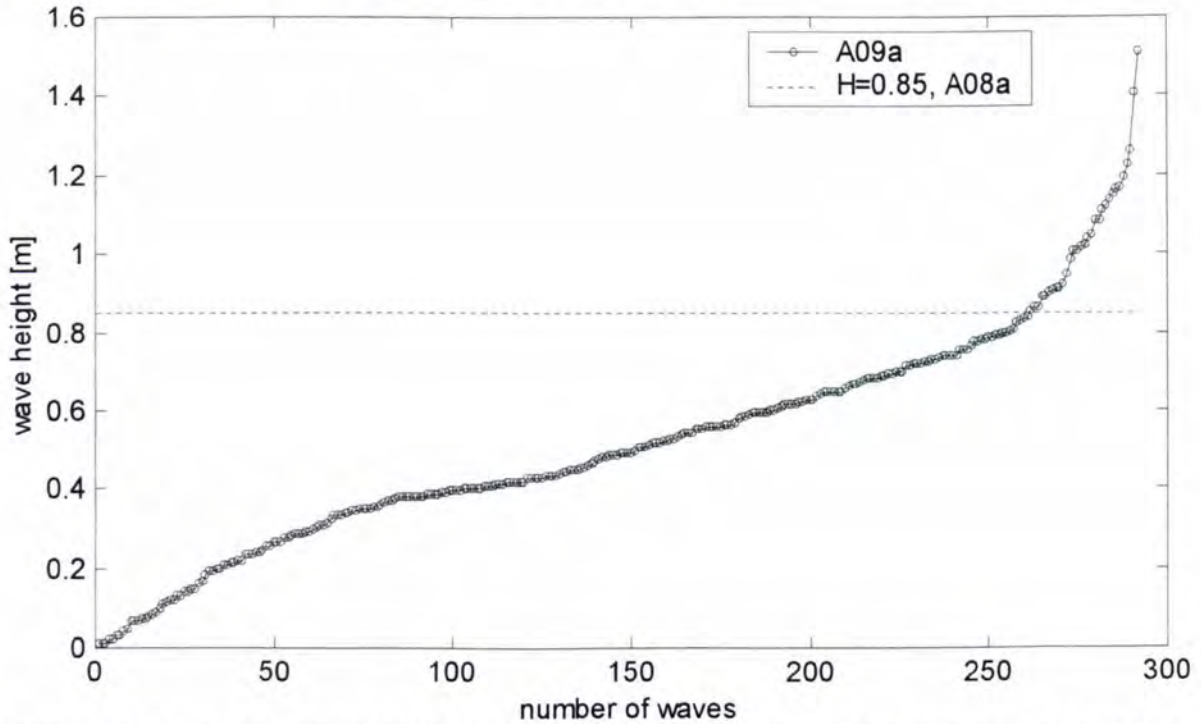


Figure 3.15: Sorted wave heights for burst a09a (irregular waves, $H_s = 0.83$ m) compared with the mean wave height for burst a08a ($H = 0.85$ m).

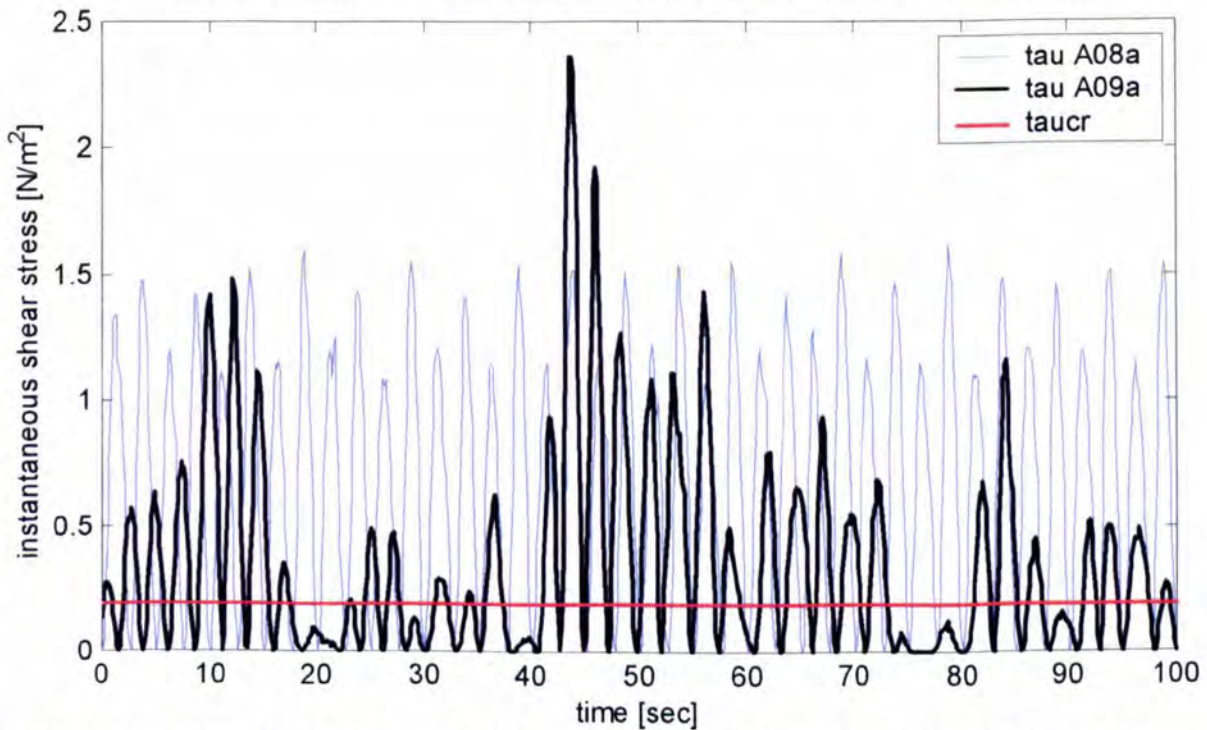


Figure 3.16: Instantaneous bed shear stress for bursts a08a (regular waves, $H = 0.85$ m) and a09a (irregular waves, $H_s = 0.83$ m) for 100 seconds of the 20 minute bursts. The shear stress for regular waves exceeds the threshold ($\tau_{cr} = 0.2$ N/m²) for every half wave cycle, while the shear stress for irregular waves is below threshold during some wave cycles.

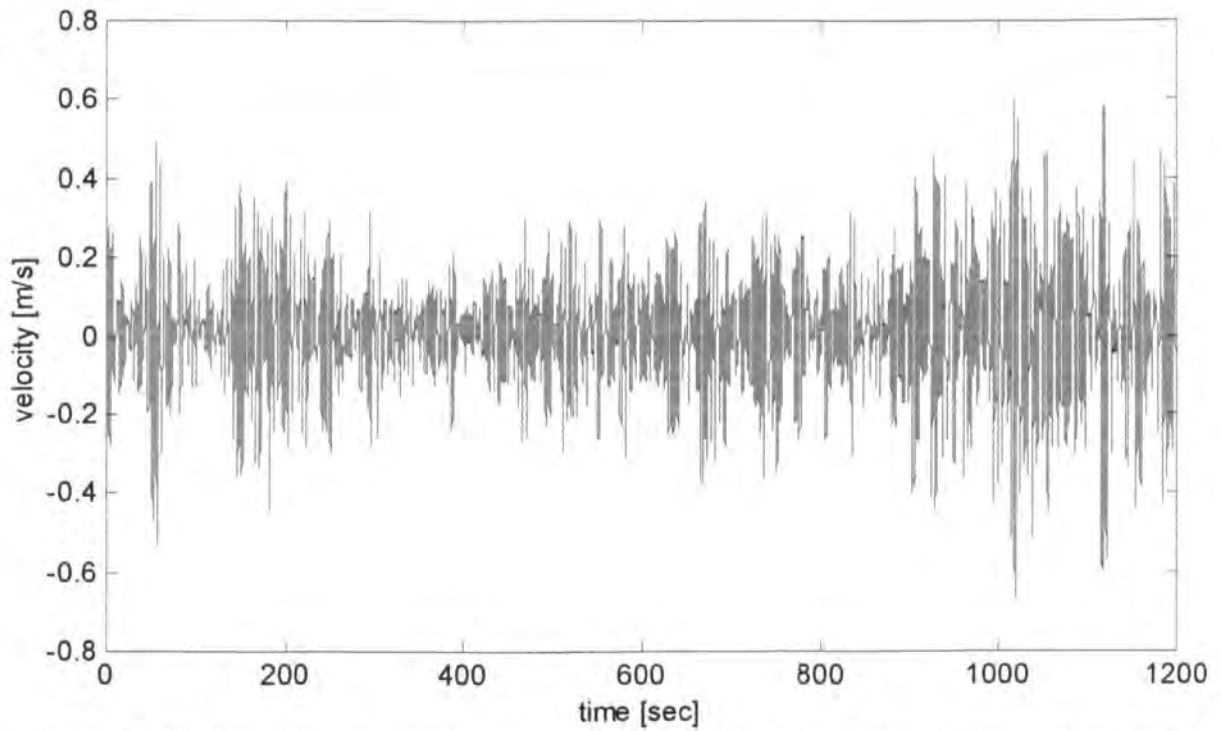


Figure 3.17: Horizontal velocity for Delft Hydraulics's ECM at a nominal height of 25 cm for burst a07a (irregular waves, $H_s = 0.53$ m).

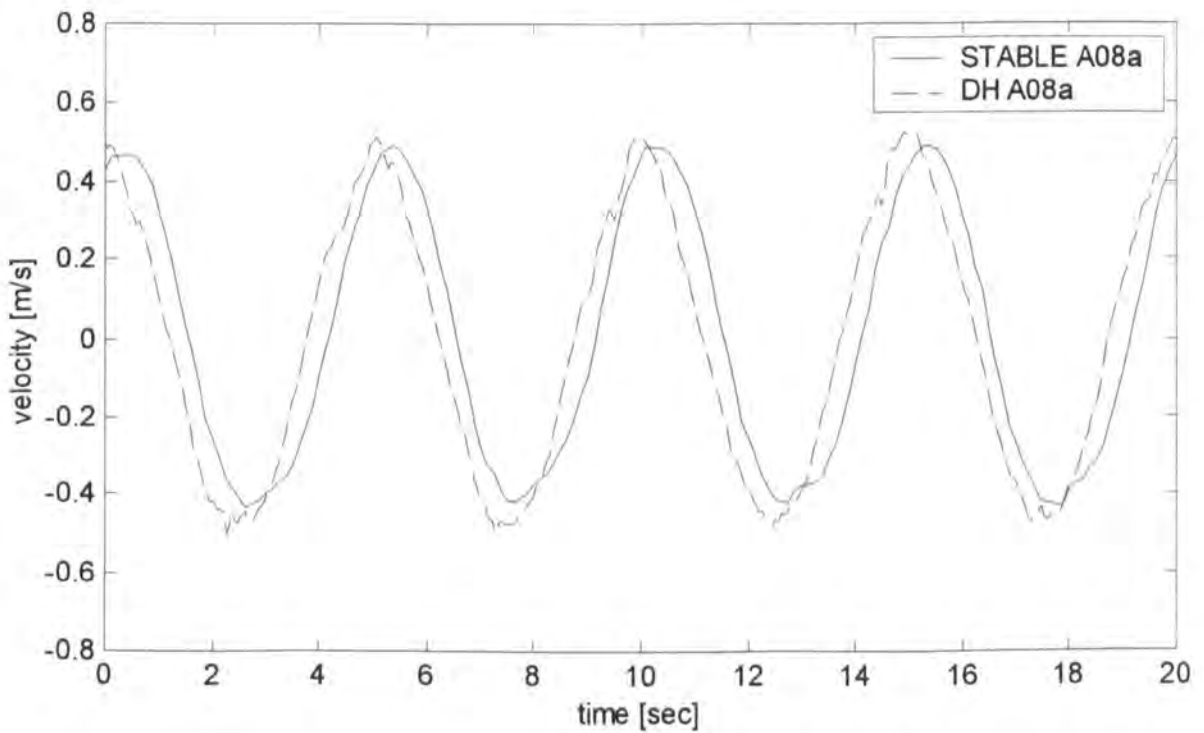


Figure 3.18: Horizontal velocity measured by STABLE and by Delft Hydraulics for burst a08a (regular waves, $H = 0.85$ m).

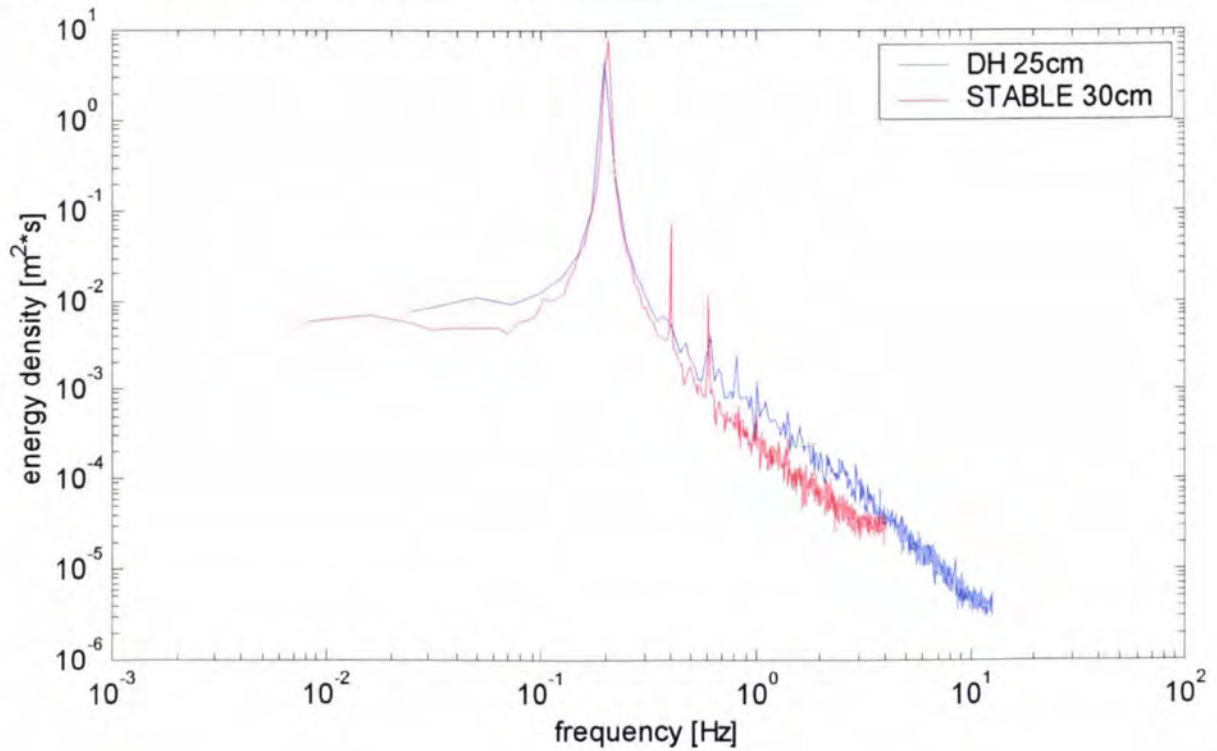


Figure 3.19: Velocity spectra of the horizontal velocity for STABLE ECMA and DH sensor, approximately 30 cm and 25 cm above the bed, respectively. The DH sensor has a smaller measuring volume and picks up more energy in the higher frequency range.

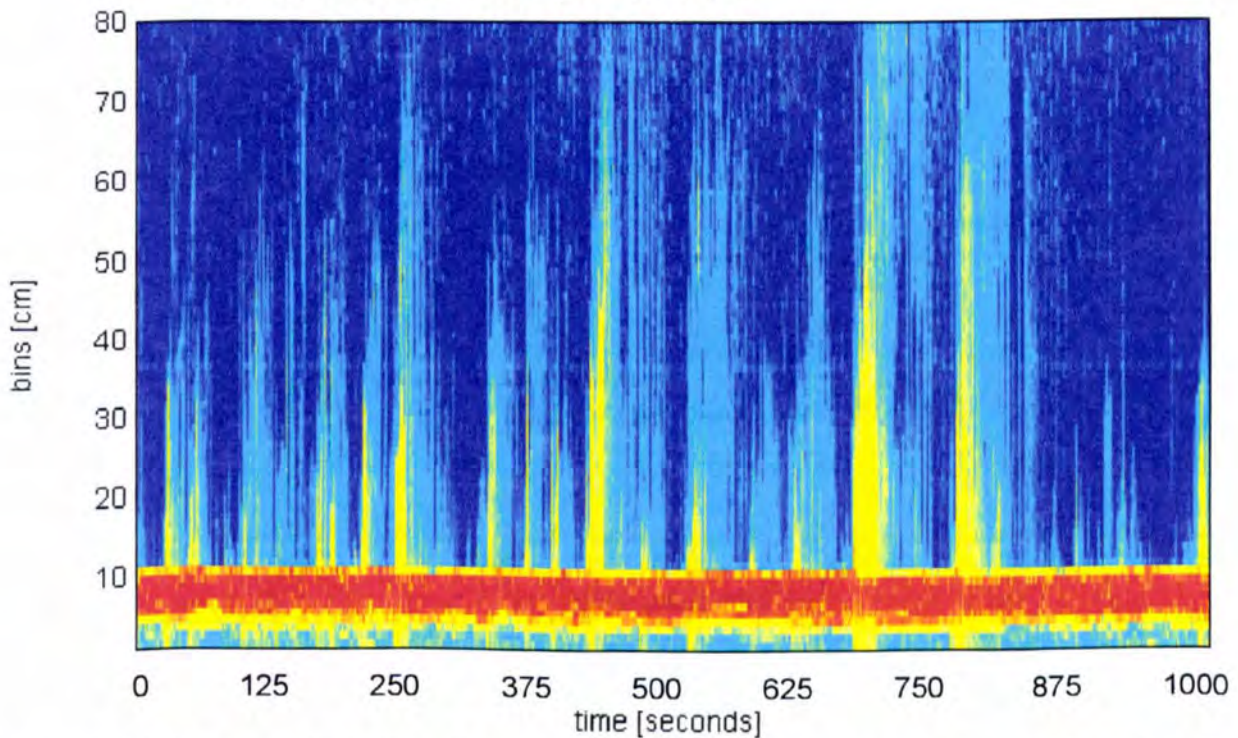


Figure 3.20: Raw ABS data for burst a09a (irregular waves, $H_s = 0.83$ m) for the 2.0 MHz sensor.

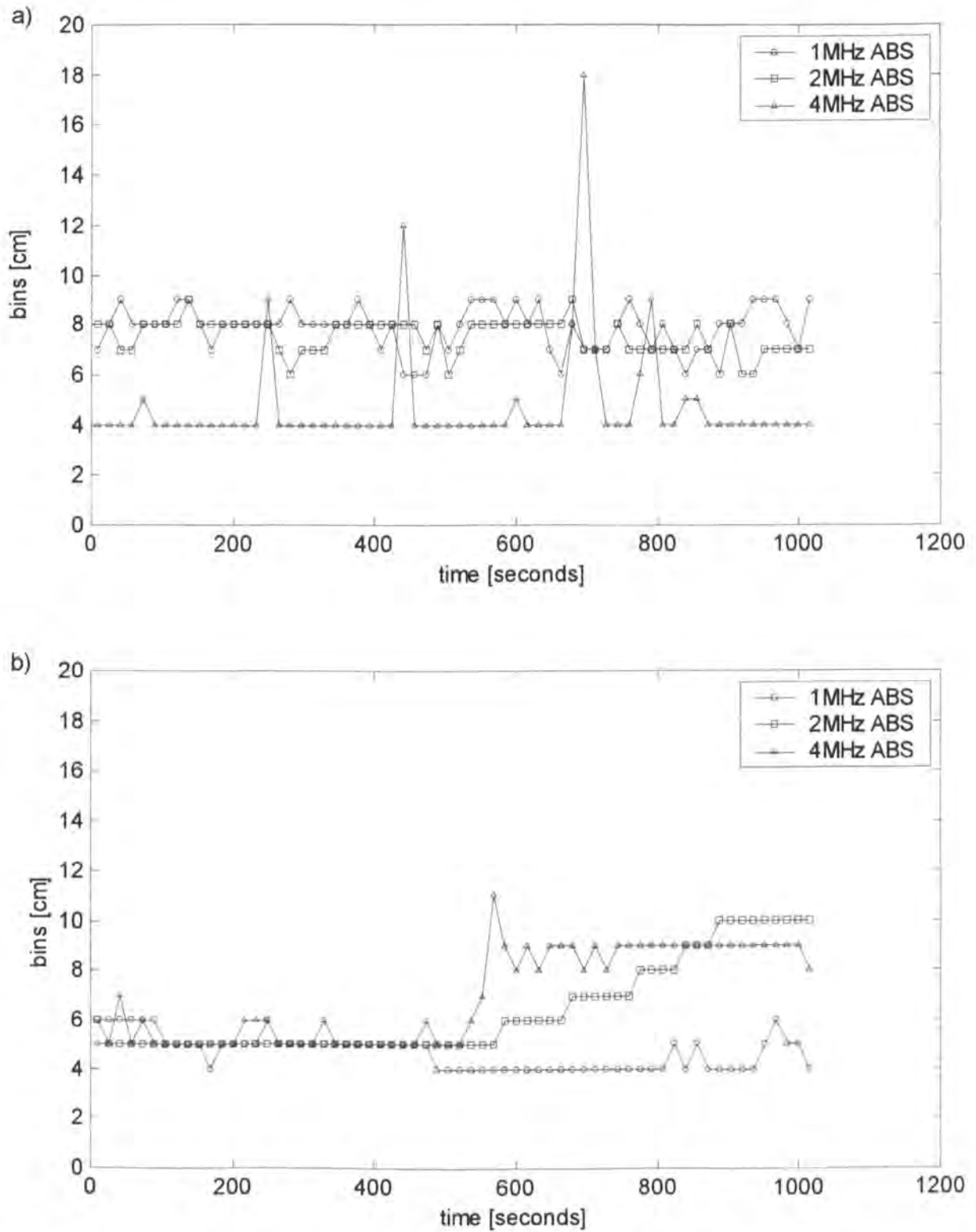


Figure 3.21: Peak backscatter of raw ABS data for a) burst a09a (irregular waves, $H_s = 0.83$ m) and b) burst a08a (regular waves, $H = 0.85$ m).

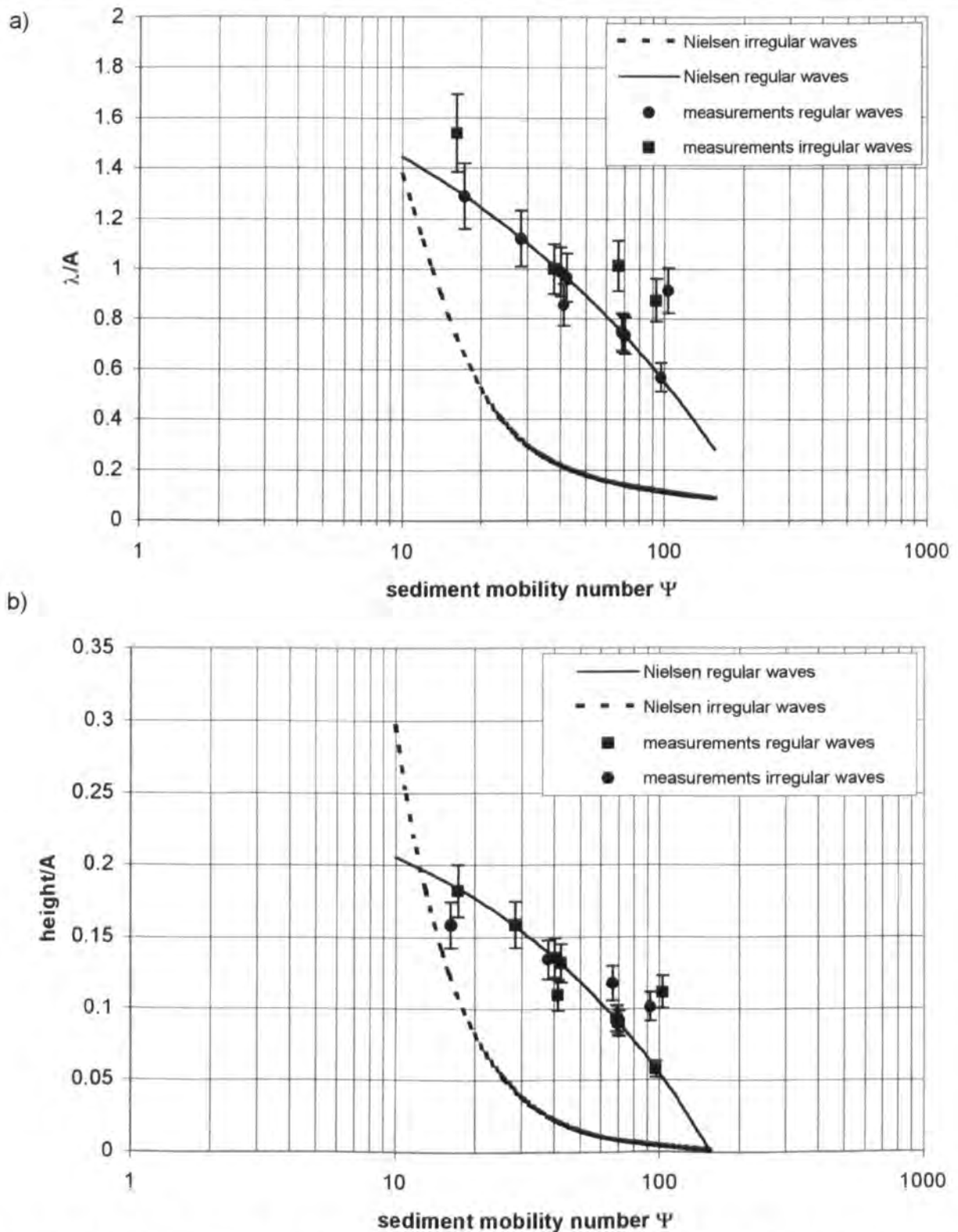


Figure 3.22: Measured and predicted (using Nielsen's definitions for regular and irregular waves) ripple dimensions as a function of the sediment mobility number Ψ for tests on the medium sand bed when STABLE was aligned with the flume. a) ripple wavelength, b) ripple height.

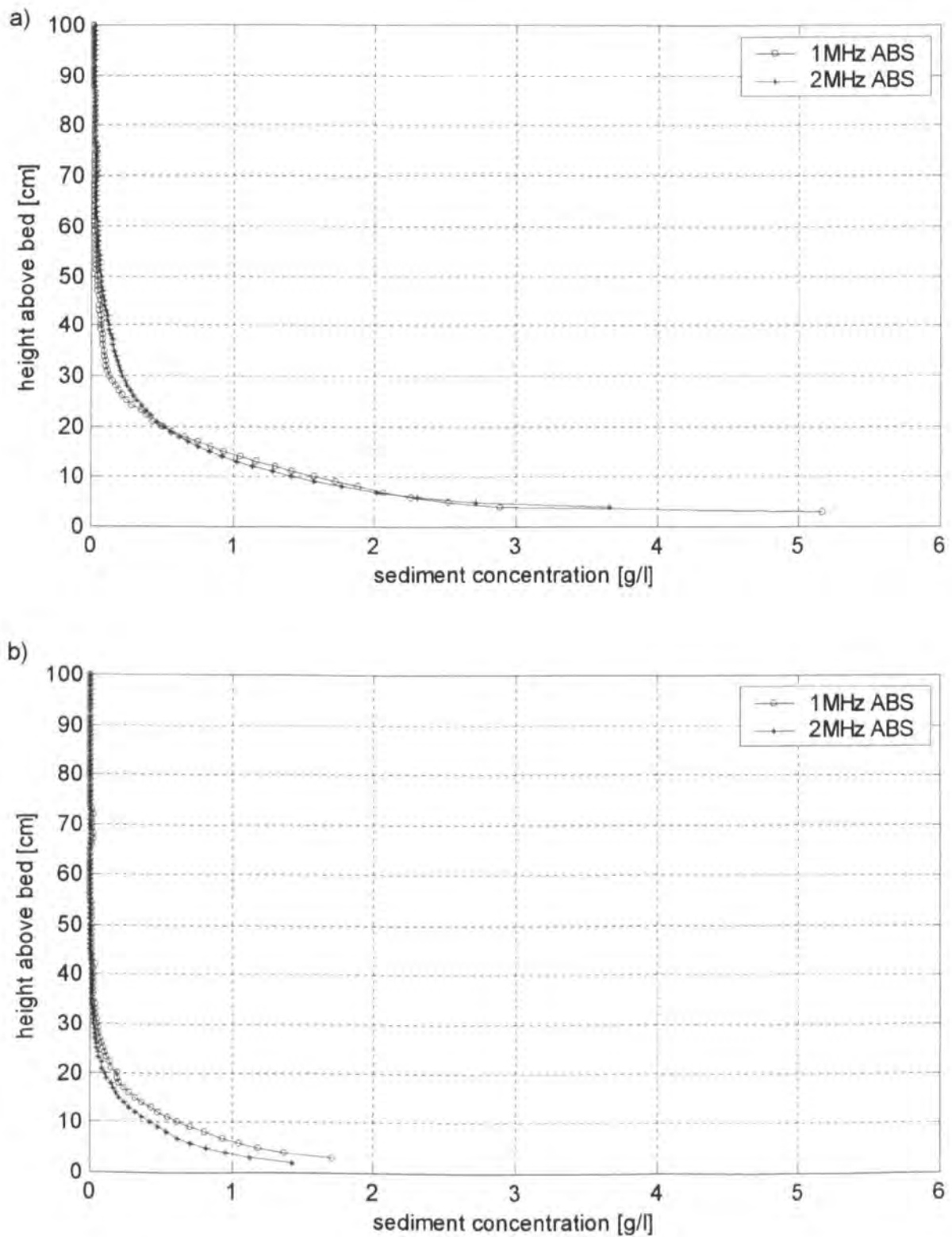


Figure 3.23: Burst averaged suspended sediment concentration for a) burst a08a (regular waves, $H = 0.850$ m) and b) burst a09a (irregular waves, $H_s = 0.83$ m).

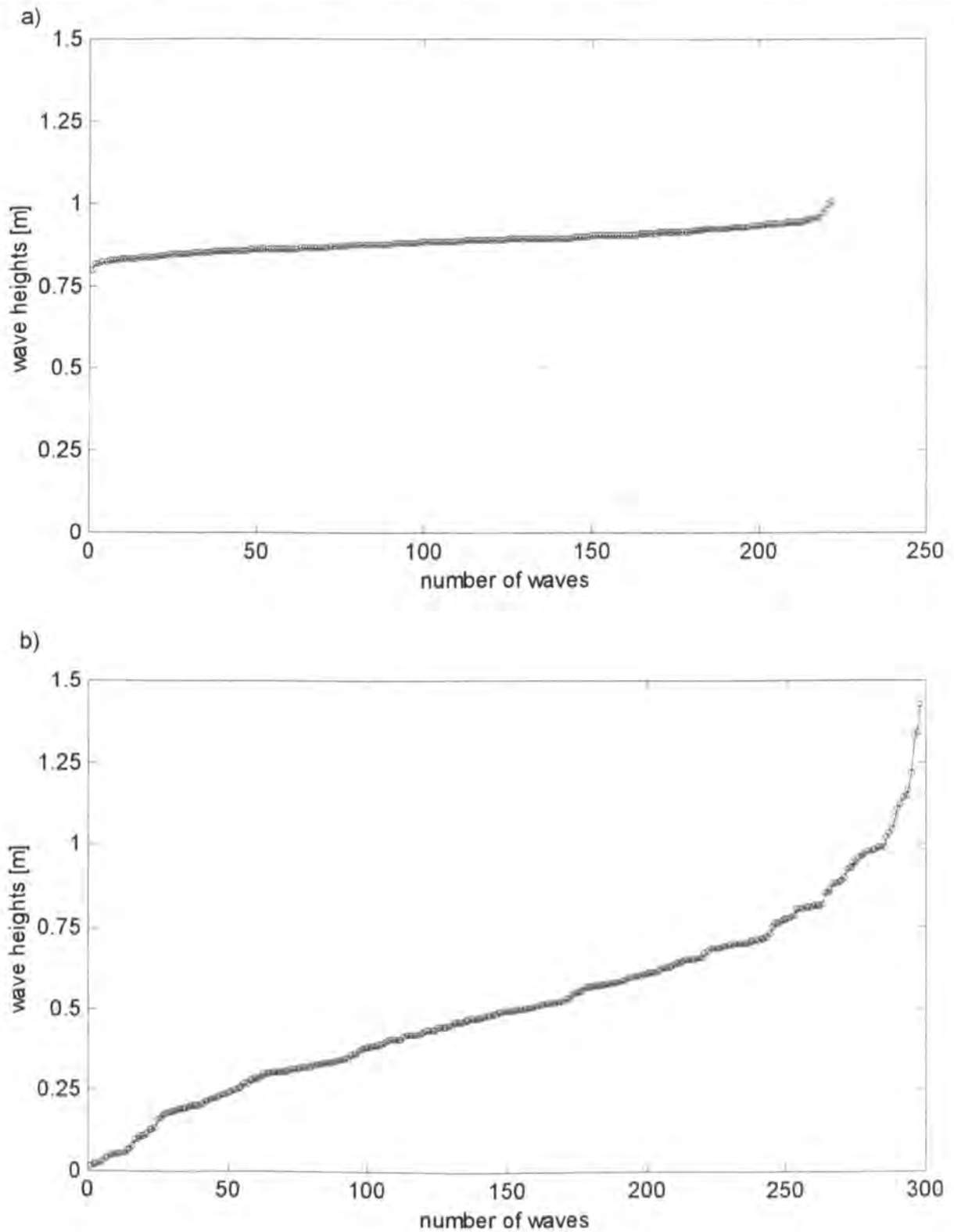


Figure 3.24: Sorted wave heights for a) burst a08a (regular waves, $H = 0.85$ m) and b) burst a09a (irregular waves, $H_s = 0.83$ m) determined using the zero down-crossing method.

Chapter 4 Influence of STABLE on its measuring environment

4.1 Introduction

The overall weight of STABLE is about 2.2 t of which the feet, with a diameter of approximately 610 mm, weigh approximately 1.5 t. The diameter of the legs was about 73 mm. As STABLE was obstructing the flow an increase in velocity was likely to occur. Additionally, extra turbulence might have been generated by the legs and the upper frame. Thus it was reasonable to assume that STABLE influenced the measuring environment and especially the bedforms formed in the vicinity of the rig. However, little was known about the extent of the influence and the effect on any measurements taken.

Additional turbulence generated by STABLE was difficult to detect, as the measuring volume of the sensors on STABLE was either too large or the sensors itself were too far from STABLE's legs to pick up any turbulence shed off the legs. A possible blockage effect due to STABLE leading to a higher water level at STABLE was investigated. Assuming the platform of STABLE to be solid, the ratio of obstructed area to cross-sectional area of the flume was about 6.6 %. As the platform of STABLE is not solid, but allows flow to pass through, this represents the worst case situation. Hence, it was concluded that the blockage effect of STABLE was insignificant.

A comparison of the horizontal velocities measured by STABLE and linear wave theory was performed by THORNE AT AL. (2001) as part of the research team. Beneath STABLE the flow velocity was 9 ± 3 % less than that predicted using linear theory. Although this could be due in part to the presence of STABLE, the shortcomings of linear wave theory to predict the measured waves accurately could also explain the difference. The pump samples were measured by a sampling array mounted on STABLE and one at the side of the flume. A comparison between the different c-profiles was made in chapter 3 and the possible influence of STABLE on the concentrations was discussed.

From the point of sediment suspension the dimensions and shapes of the bedforms are very important in terms of vortex generation. Thus, to assess the influence of STABLE on the measuring environment, this chapter concentrates on the ripple measurements. Data available on the bedforms underneath STABLE were analysed with respect to a possible influence of STABLE. It was considered that the differences in bedform characteristics beneath STABLE and at locations away from the frame would indicate unambiguously any effect of the frame on general sediment dynamics. Results of this analysis are presented in this chapter.

4.2 Available Profile Data

Vortex ripples were measured during wave tests from STABLE using the Acoustic Ripple Profiler (ARP) and the Sector Scanning Sonar (SSS). Figures 4.1 and 3.9 show examples of measurements by the two sensors. In addition, Delft Hydraulics provided a mechanical bed profiler which allowed the measurement of longitudinal ripple profiles along the whole bed parallel to the sides of the flume. In total four different sets of profiles (DBP) were recorded – two on the medium sand bed and two on the fine sand bed. The following definitions for the four sets of profiles were chosen: a) DBP-1, profiles with a spanwise spacing of 0.5 m measured after wave action ($H = 0.745$ m, $T = 5$ s), but before the deployment of STABLE on the medium sand bed; b) DBP-2, profiles with a spanwise spacing of 0.25 m measured after 26 tests with STABLE in the flume on the medium sand bed; c) DBP-3, profiles with a spanwise spacing of 0.25 m measured after wave action ($H = 0.815$ m, $T = 5$ s), but before deployment on STABLE on the fine sand bed and d) DBP-4, profiles with a spanwise spacing of 0.25 m measured after 17 tests with STABLE in the flume on the fine sand bed. These profiles were analysed in view of identifying any possible influence on the ripple geometry due to the frame.

4.3 Analysing Ripple Profiles using Conventional Techniques

Two different types of bed profile data were available - the acoustic data, which were recorded during each burst when STABLE was deployed and the four data sets from the mechanical ripple profiler. The advantages of the acoustic data were that they were recorded during each burst. However, the sensors were only deployed for bursts where STABLE was in the flume. Furthermore, the acoustic ripple profiler could only record along a zone of 1.5 m either side of its central position. Data from the acoustic imager were only recorded successfully once on the medium (figure 3.10) and once on the fine sand bed. Also it only recorded data in a radius of about 3 m of its central position. Even though the sand ripple profiler provided data for every burst it was not found very useful in establishing the

influence of STABLE on the bed geometry. Hence, the four sets of data recorded by the mechanical profiler were used to analyse the influence of STABLE, as the profiles were measured along the whole length of the bed.

The profiles were divided into bins in order to create 'control' regions away from the frame, which could be compared with the bins containing STABLE. The length of the bins was determined by the distance of STABLE's feet (as one bin was supposed to contain STABLE) and the usable data available (about 30 m sampled at 0.01 m intervals). In addition the chosen size of the bins was dependent on the type of analysis to be carried out. For the Fast Fourier Transform (FFT) used, the preferred number of samples in the record had to be an integer power of 2. At the same time the length of record should not be too small in order to reduce the significance of leakage effects from the end of the record. It was decided to choose bins containing 512 (2^9) points which, at a data interval of 0.01 m, resulted in a bin length of 5.12 m. However, due to lack of data the last bin for the first set of profiles (DBP-1) was only 2.56 m long. The chosen bin size allowed the division of the first set of profiles (DBP-1) into 6 bins while all other profiles were divided into 7 bins. The positions of the bins relative to the wave generator are listed in tables 4.1 and 4.2. Unfortunately, due to the difficulties of accurately positioning STABLE in 5 m of water using a crane, the position of STABLE was slightly different from the specified position, which resulted in the feet of STABLE being situated in bins 2 and 3.

Figures 4.2a (DBP-1) and b (DBP-2) and 4.3a (DBP-3) and b (DBP-4) provide a visual impression of some examples of the four different sets of profiles. Turning the attention to figure 4.2a, there is some evidence to suggest that apart from vortex ripples some larger bedforms were present. Furthermore, some variations in vortex ripple dimensions can be observed. In figure 4.2b the imprint left by one of STABLE's feet is clearly visible. However, there does not appear to be any obvious difference in vortex ripples measured at and adjacent to the STABLE deployment site from those measured at other locations on the bed. Figures 4.3a and b show bed profiles recorded on the fine sand. There is a greater variation in ripple dimensions compared to figures 4.2a and b. In contrast to the medium sand bed, there is evidence of scour on the fine sand bed. This effect appears to be very localised. Furthermore, as the profiles were recorded after STABLE had been lifted out of the flume, the visible scour might be due to the disturbance generated by lifting STABLE out of the flume, though this is not considered likely. It is very interesting to observe that the fine sand bed was not damaged to the same extent as the medium sand bed, even though it was exposed to some high waves (see chapter 3). To quantify the visual impressions, the bins for DBP-1, DBP-2, DBP-3 and DBP-4 profiles were analysed.

The sloping ends of the 0.5 m bed and the presence of long wavelength features meant that the raw data required modification before a reliable zero down-crossing analysis could be performed. After various crude attempts at mean-zeroing the data, using regression techniques, the data were conditioned using a Butterworth bandpass filter. The low 'frequency' cut-off was chosen to remove the gross bed variations at a wavelength of about 40 m. The ripple profiler used a small wheel which slightly damaged the crests of ripples but in a way that did not invalidate the wavelength characteristics. It will have led to a slight reduction in measured ripple height. The wheel was not able to respond to structures shorter than a wavelength of 50 mm, so an upper 'frequency' cut-off of 0.08 m was chosen to remove any measurement noise which could not have any physical basis.

After filtering the data, using the bandpass filter, the zero down-crossing wavelength and ripple height for each zero-mean profile and bin were calculated. Results of these analyses are presented in tables 4.3 to 4.10. The numbers in bold are those bins containing the imprint of one foot. Turning attention first to survey DBP-2, vortex ripples of height h_r $O(4)$ cm and wavelength λ_r $O(30)$ cm over the entire surface of the bed were present. Of primary importance to the present investigation is the evidence showing that λ_r values for bins 2 and 3 (containing STABLE) for survey DBP-2 are similar to the values for the other bins and lie within the normal scatter of the data. This is also shown in figure 4.4, which shows the zero down-crossing ripple wavelength and height for all profiles and bins for survey DBP-2. Results for bins 2 and 3 are highlighted by joining up the points. Thus, on the basis of this evidence it may be concluded that the presence of the STABLE frame has no detectable effect on the processes of vortex ripple formation on the medium sand at the position of the sensors.

The profiles from survey DBP-4 show vortex ripples of height, h_r $O(2)$ cm and wavelength λ_r $O(25)$ cm. The variation of ripple wavelength and height with distance along the bed is shown in figure 4.5, which shows the wavelength λ_r for all the bins and profiles from survey DBP-4. There does not seem to be any evidence that λ_r values for bin 3 (containing STABLE) are any different from the values for the other bins. They lie within the overall scatter of the data, though at the top end of the general observations.

After analysing the profiles in the time domain, analyses were carried out in the frequency domain using the Fast Fourier Transform. Figure 4.6 shows a typical amplitude spectrum for one bin for survey DBP-2. The representative wavelength was identified by finding the maximum amplitude and the corresponding spatial 'frequency'. This was then converted into

a ripple wavelength. The results of this analysis are summarised in tables 4.11 to 4.14. Again there is little evidence that STABLE influenced the ripple dimensions.

However, there was some concern that small variations in ripple geometry would not be detected by the FFT analysis since it assumes periodicity. The zero down-crossing analysis might be expected to detect the variations in wavelength, but small changes in ripple geometry could affect the location of individual down-crossings and the technique only uses a few data points around each crossing.

In an attempt to use a technique, which fundamentally recognises the non-periodic nature of ripples, the method of Wavelet transforms was explored. The next section gives a brief summary of the advantages of wavelets. More background information can be found in appendix B.

4.4 Motivation for the use of Wavelet Transforms

Some of the shortcomings of the Fourier Transform for the present data have been mentioned in the previous section. For signals in which time information is not important and the frequency content is of primary interest, Fourier analysis is effective. Thus, Fourier analysis is useful for analysing signals, that repeat regularly over time, and stationary signals that do not change much over time. However, the spectral analysis of non stationary signals cannot describe the local transient features, due to averaging over the duration of the signal. One possibility would be to use a windowed Fourier Transform (WFT), using a certain window size and moving it in the time domain, computing the FFT at each time using only the data within the window. The WFT allows frequency components to be found with a degree of temporal resolution. However, choosing the right window size is always a trade off between a smaller window, which gives a better temporal resolution and a bigger window, which results in a better frequency resolution. Also the FFT relies on the assumption that the signal can be decomposed into sinusoidal components. Sine waves might not be a good representation of the data under investigation.

Wavelet analysis tries to overcome these problems by decomposing a time series into time/frequency space simultaneously. Wavelet analysis can be thought of as a windowing technique with variable windows that yield precise low frequency information using long time intervals and precise high frequency information using shorter intervals. An essential difference between wavelet and Fourier analysis is that wavelet functions are localised in time, whereas the trigonometric functions used in a Fourier Transform are of infinite length in time.

The behaviour of individual ripples is unlikely to be affected by all the ripples in the record. Instead each ripple will be influenced most by its neighbours. The wavelet transform uses a localised basis and attempts to correlate the bed profiles with a wavelet basis representing a 'standard' ripple shape. Thus, choosing the right wavelet basis for these data is very important. A number of different wavelets were investigated (see section 4.5.1). Figure 4.7 shows the Morlet wavelet as an example of a wavelet function. The Morlet wavelet is constructed by overlaying a Gaussian on a sine curve. The parent wavelet is then decomposed into a series of wavelets of finite length consisting of scaled (squeezed or stretched) and translated versions of the parent wavelet. This process is similar to Fourier analysis, where the parent wavelet is analogous to the sine wave, and the basic functions in Fourier decomposition are sine waves of various amplitude, phase and frequency variations of the parent sine wave (GURLEY AND KAREEM, 1999). The localisation of a wavelet is important, because then the behaviour of the signal at infinity does not play any role. This means that the wavelet transform can be performed locally on the signal. This is in contrast to the Fourier transform with its infinite sinusoidal function (e.g. TORRENCE, 1998, ADDISON, 1999).

The scaled and translated wavelets are correlated with the signal and the correlation coefficient can be plotted as a scalogram showing the wavelet spectrum. Averaging the wavelet spectrum over time or in this case length scale yields the global wavelet spectrum, which can be compared to an energy density spectrum. The next section shows the investigation of different wavelet shapes and the analysis of bed profiles using wavelets.

4.5 Analysing Ripple Profiles using Wavelets

4.5.1 Behaviour of Wavelet Transforms with respect to the Data and the Wavelet Functions

In order to establish the behaviour of wavelet transforms survey DBP-1 was investigated as a reference, because these profiles were recorded before the deployment of STABLE. First, a Morlet wavelet was chosen as the wavelet function and the wavelet transform was performed on an unfiltered profile (figure 4.8a shows an unfiltered profile and 4.8b shows a wavelet power spectrum or scalogram). The red colour in the scalogram indicates high wavelet energy and the blue colour indicates low wavelet energy. The regions enclosed by the black contours are significantly above the background level (CHRISTOPHER TORRENCE, personal communication). The black line indicates the cone of influence (c.o.i.), which is the region of the wavelet spectrum outside of which edge effects become important (TORRENCE

AND COMPO, 1998). When the translation of the wavelet is close to the beginning or the end of the signal the time series is padded with zeros. This introduces discontinuities at the endpoints and as one goes to larger scales decreases the amplitude near the edges as more zeros enter the analysis. Therefore, the cone of influence is bigger at larger scales.

The highest energy is associated with the overall shape of the bed and the scale of the vortex ripples is indicated. In order to identify any ripple characteristics over the entire length of the bed, figure 4.8 was not suitable. This shows that a 'blind' application of wavelet transforms does not yield the desired result of showing ripple dimensions and thus, the influence of STABLE on the bed geometry. Thereafter the filtered profiles were used in the analysis.

After identifying the need of filtering the data before subjecting it to wavelet transforms, the effects of different wavelets were investigated. Again survey DBP-1 was used as it did represent the sand bed without any influence of STABLE. After filtering the data, the same profile was subjected to three different wavelet shapes – the Morlet wavelet (as described in section 4.4), the PAUL wavelet and the Mexican Hat (or Derivative Of a Gaussian, DOG) wavelet. The Paul and Mexican Hat wavelet are shown in figure 4.9. The filtered profiles from survey DBP-1 were analysed using all three wavelets respectively. The results are presented in figures 4.10a-d, 4.11a-c and 4.12a-c. In contrast to the scalogram generated by the Morlet wavelet (4.10b), the scalograms determined with the Mexican Hat (4.11b, note the different scale on the ordinate) and Paul (4.12b) wavelet show more scatter in the energy distribution (red colour – high energy, blue colour – low energy). The black contour lines, which enclose significant areas (see above) are spread over a larger scale and more individual contour areas can be distinct. The spread over a larger scale is also noticeable in the global wavelet energy spectra (4.11c and 4.12c), which show a broader spike over the ripple wavelength. However, the position of the peak and thus the dominant wavelength in the signal occurs in the same position in the global wavelet spectra for the three wavelets. As mentioned in section 4.4 the wavelet transform is a correlation of the original signal with scaled versions of the wavelet. The Morlet wavelet has a peak in the centre and 2 relevant ones either side. This means that not only each individual ripple, but up to two either side are considered in the correlation. In practice it is valid to assume that each ripple is influenced by its neighbouring ripples. In contrast to that, the Mexican Hat and Paul wavelets only have one large spike in the centre and thus do not take neighbouring ripples into account in the transform. Mainly representing only one ripple the Mexican Hat and Paul wavelet pick up small changes in wavelength when translated along the bed and thus smear the total energy over a broader band of scales or wavelengths. Though this is a desired

feature of the wavelet transform performed, it makes the interpretation of the scalograms more difficult. Also it does not take into account effects of neighbouring ripples that can be observed in nature. Thus, it was decided to use the Morlet wavelet for further analyses.

4.5.2 Analysing the Profile Data using the Morlet Wavelet

After concentrating on the behaviour of wavelet transforms and their requirements for the signal to be analysed, emphasis is now on identifying the influence of STABLE on its measuring environment. First a typical profile from survey DBP-1 is investigated further (figures 4.10a-d) in order to identify the 'natural' variations of ripple wavelength and characteristics of the ripples over the length of the bed. Figure 4.10a shows a typical filtered profile for survey DBP-1, 4.10b the wavelet power spectrum for this profile, 4.10c the global wavelet power spectrum and 4.10d the instantaneous amplitude of the data. Figure 4.10b shows the ripple wavelength along the bed. When comparing the wavelet power spectrum with the filtered profile it is possible to visually identify patterns in both plots. The wavelet transform detects larger wave forms of $O(1)$ to $O(2)$ m. However the dominant wave length is $O(40)$ cm. In general the wavelet power spectrum shows some scatter in the ripple wavelength along the bed.

The global wavelet spectrum in figure 4.10c is produced by averaging the wavelet spectrum over the whole bed. It gives a summary of what length scales are most interesting. The dashed line is a significance test for the global wavelet power. According to TORRENCE (personal communication) anything that is above the dashed line is unlikely to be caused by random noise and is therefore significant. Hence, over the whole distance the presented profile yields a dominant ripple wavelength of $O(40)$ cm.

Figure 4.10d shows the instantaneous amplitude derived from the magnitude of the complex output of a Hilbert Transform applied to the raw data. This gives some indication of the variation of ripple height h_r along the bed. The average ripple height is $O(3)$ cm, however figure 4.10d shows a variation in amplitude along the bed between $O(1)$ cm and $O(4)$ cm.

Figures 4.13a-d are the same as figures 4.10a-d, but this time show a profile for survey DBP-2. The imprint left by one of STABLE's feet is clearly visible in figure 4.13a at a distance of 25 m. The bed profile was about 65 m long due to the erosion of the original bed of about 50 m. The wavelet power spectrum (figure 4.13b) shows ripple wavelengths of $O(1)$ m to $O(0.125)$ m, with the dominant ripple wavelength of $O(40)$ cm. Around the position of the foot the ripple wavelength increases to about $O(1)$ m. This coincides with the observation in the profile (figure 4.13a) and the diameter of the foot of 0.61m. However,

close to the imprint, values of $O(40)$ cm for the ripple wavelength are present again. Figure 4.13d shows the instantaneous amplitude for this profile. The imprint of the foot is again visible, but there does not seem to be any influence of the foot on the surrounding area. The average ripple height is $O(2)$ cm. This is slightly less (by 1 cm) than the values previously determined using zero down-crossings.

For the fine sand, figures 4.14a-d show an example of a wavelet analysis for a profile for survey DBP-3. This profile was recorded at the beginning of the tests on the fine sand before STABLE was deployed. Compared to the profiles recorded on the medium sand, the variation in ripple height and length over the whole bed is greater (figure 4.14a). This is reflected in the wavelet power spectrum (figure 4.14b), which illustrates a broad band of high energy at scales in the region of 0.0625 m to 2 m. This is also shown in figure 4.14c. The global wavelet spectrum shows a broader spike for this profile than figure 4.13c. The dominant wavelength over the whole bed suggested by the global wavelet spectrum is $O(80)$ cm. This is in contrast to the values determined by the zero down-crossing of $O(25)$ cm. Care has to be taken when interpreting the scalogram and global spectrum. When looking closely at the filtered profile (figure 4.14a), some larger ripples can be detected which contribute to the higher energy at larger scales. The scalogram indicates some significant energy at a scale of about 0.125 m, which is attributable to the smaller vortex ripples. Figure 4.14d shows the instantaneous amplitude, which also illustrates larger variations in ripple height compared to the medium sand.

A wavelet analysis performed on a profile for survey DBP-4 is presented in figures 4.15a-d. The chosen profiles did contain evidence of scour as seen in figure 4.3b. However, the process of filtering the profile smoothed it and resulted in the evidence of scour being hardly noticeable at a distance of about 28 m along the bed. The scalogram indicates a broad band of wavelength scale associated with high energy. In the global wavelet spectrum (figure 4.15c) two peaks can be identified. The smaller one at about 0.18 m corresponds to the vortex ripples, while the bigger one at around 0.5 m corresponds to larger bedforms resulting in higher energy. Assuming a limit steepness for the ripples exists, smaller ripples are associated with smaller ripple wavelengths. Thus, if the wavelet spectrum is normalised by the scale (or ripple wavelength) it should result in a clearer spike at the smaller ripple wavelength. Figure 4.15d shows the instantaneous amplitude. A large variation of up to a factor of 5 can be identified.

The normalised wavelet spectrum (figure 4.16b) is more 'noisy', with smaller scales containing high energy. Due to the normalising procedure the smaller scales are

emphasised. This is confirmed in figure 4.16c, which now shows two clear spikes, one associated with the vortex ripples wavelength and the second associated with larger bedforms.

4.6 Conclusions

Deploying STABLE under controlled conditions provided the opportunity to analyse different sensors and to evaluate the influence of STABLE on its measuring environment. The four bed profiles were quite unique, as they gave the opportunity to determine the bed profiles at a distance away from STABLE, where its influence was thought to be negligible. Though, STABLE had been deployed successfully in other tests, there has never been any data available that could determine the influence of STABLE on its environment.

The evidence presented here suggested that STABLE did not influence the measuring environment by enhancing the turbulence or any blockage effects. The emphasise of this chapter was then directed towards identifying the influence of the frame on the ripple geometry. The results presented in this chapter suggest that the feet or frame of STABLE do not influence the development of vortex ripples on a sand bed. The imprint of one of STABLE's feet was clearly visible in the filtered profile on the medium sand. The bin analysis indicated that the ripple wavelength close to the imprint was not different to the wavelength for bins, which did not contain STABLE. However, some uncertainty remained due to the limitations of the bin-based analysis.

The wavelet transform was used to overcome the problems of bin-based analysis by resolving the profiles in spectral and temporal space. The wavelet power spectrum was found very useful in identifying the variations of ripple wavelength along the bed in one graph. The scalogram provided a good first visual impression. Features in the signal could be identified in the wavelet power spectrum. However, when interpreting scalograms or global wavelet spectra care had to be taken in identifying bed features leading to high energy in the spectrum. Also care has to be taken when choosing the parent wavelet for the analysis as the wavelet transform can only pick up features in the signal that correspond to the chosen scaled and translated wavelet. Thus, one has to have an idea about the features in the signal that are of interest. It was also shown that a 'blind' application of wavelets does not yield the desired result. The analysed signal had to be conditioned first before it was exposed to a wavelet transform in order to give sensible results.

The approach of a FFT was dismissed as the bin size was very small. By identifying the frequency associated with the largest energy, the FFT failed to pick up smaller bed features

(vortex ripples) when larger bedforms were present.

As large deployment frames are deployed in the field the present findings are very interesting and important as they show, in the case of STABLE, that it exerts little influence on the bedforms beneath or in the vicinity of the frame. This is very encouraging for future deployments of STABLE.

4.7 Acknowledgement

Thanks to Christopher Torrence, who has helped to overcome the first steps in using wavelet transforms. He has provided encouraging help throughout the study. The program used to create the graphs is a modification of the program downloaded from Torrence's webpage (see <http://paos.colorado.edu/research/wavelets/>).

TABLES

bins	Bin 6	Bin 5	Bin 4	Bin 3	Bin 2	Bin 1
Distance from wave generator [m]	106.17- 111.28	111.29- 116.40	116.41- 121.52	121.53- 126.64	126.65- 131.76	131.77- 134.32

Table 4.1: Positions of the bins for the profiles of survey DBP-1.

bins	Bin 7	Bin 6	Bin 5	Bin 4	Bin 3	Bin 2	Bin 1
Distance from wave generator [m]	101.06- 106.16	106.17- 111.28	111.29- 116.40	116.41- 121.52	121.53- 126.64	126.65- 131.76	131.77- 136.88

Table 4.2: Positions of the bins for the profiles of all other surveys.

Bin	a011	a013	a015	a017	a019	a021	a023
1	0.3286	0.3214	0.2611	0.4000	0.3417	0.2888	0.3229
2	0.2474	0.2871	0.2761	0.2390	0.2761	0.2794	0.2290
3	0.2731	0.2765	0.3062	0.2788	0.2706	0.3060	0.2925
4	0.2859	0.2700	0.2906	0.2788	0.3300	0.2806	0.2589
5	0.2788	0.2894	0.2969	0.2733	0.2759	0.2700	0.2281
6	0.3850	0.3160	0.3407	0.3280	0.3257	0.3127	0.2661
Ave.	0.2998	0.2934	0.2953	0.2997	0.3033	0.2896	0.2663

Table 4.3: Average ripple wavelength λ_r in metres from zero down-crossing analysis of profiles of survey DBP-1 after passing the data through a Butterworth bandpass filter.

Bin	a011	a013	a015	a017	a019	a021	a023
1	0.0469	0.0579	0.0437	0.0596	0.0524	0.0470	0.0536
2	0.0285	0.0421	0.0439	0.0396	0.0460	0.0435	0.0354
3	0.0434	0.0408	0.0486	0.0425	0.0412	0.0474	0.0467
4	0.0386	0.0434	0.0416	0.0437	0.0463	0.0397	0.0389
5	0.0343	0.0508	0.0403	0.0458	0.0402	0.0370	0.0335
6	0.0626	0.0492	0.0554	0.0529	0.0497	0.0470	0.0415
Ave.	0.0424	0.0474	0.0456	0.0474	0.0460	0.0436	0.0416

Table 4.4: Average ripple wave height h_r in metres from zero down-crossing analysis of profiles of survey DBP-1 after passing the data through a Butterworth bandpass filter.

Bin	b011	b012	b013	b014	b015	b016	b017	b018	b019	b020	b021	b022	b023
1	0.299	0.299	0.317	0.363	0.357	0.376	0.365	0.373	0.401	0.342	0.362	0.350	0.344
2	0.190	0.303	0.242	0.316	0.396	0.361	0.393	0.375	0.349	0.322	0.288	0.281	0.279
3	0.341	0.291	0.258	0.339	0.338	0.293	0.310	0.334	0.303	0.299	0.291	0.351	0.324
4	0.279	0.265	0.254	0.278	0.281	0.297	0.272	0.291	0.264	0.325	0.281	0.268	0.336
5	0.260	0.250	0.295	0.274	0.257	0.241	0.226	0.287	0.222	0.260	0.291	0.231	0.275
6	0.384	0.398	0.422	0.368	0.328	0.313	0.350	0.361	0.331	0.310	0.356	0.375	0.373
7	0.407	0.375	0.377	0.371	0.419	0.407	0.360	0.324	0.368	0.327	0.314	0.363	0.425
Ave.	0.309	0.312	0.309	0.330	0.339	0.327	0.325	0.335	0.320	0.312	0.312	0.317	0.337

Table 4.5: Average ripple wavelength λ_r in metres from zero down-crossing analysis of profiles of survey DBP-2 after passing the data through a Butterworth bandpass filter.

Bin	b011	b012	b013	b014	b015	b016	b017	b018	b019	b020	b021	b022	b023
1	0.034	0.031	0.031	0.036	0.041	0.039	0.039	0.040	0.042	0.039	0.038	0.036	0.030
2	0.018	0.028	0.026	0.033	0.038	0.030	0.034	0.038	0.036	0.032	0.030	0.029	0.023
3	0.028	0.024	0.028	0.037	0.035	0.028	0.032	0.034	0.033	0.033	0.028	0.028	0.025
4	0.027	0.027	0.025	0.030	0.026	0.030	0.028	0.029	0.026	0.031	0.030	0.028	0.032
5	0.025	0.026	0.030	0.030	0.028	0.025	0.026	0.030	0.024	0.025	0.029	0.023	0.025
6	0.037	0.042	0.046	0.042	0.034	0.034	0.036	0.038	0.035	0.033	0.036	0.040	0.034
7	0.044	0.042	0.041	0.039	0.045	0.046	0.041	0.035	0.040	0.036	0.036	0.038	0.040
Ave.	0.030	0.031	0.032	0.035	0.035	0.033	0.034	0.035	0.034	0.033	0.032	0.032	0.030

Table 4.6: Average ripple wave height h_r in metres from zero down-crossing analysis of profiles of survey DBP-2 after passing the data through a Butterworth bandpass filter.

Bin	c011	c012	c013	c014	c015	c016	c017	c018	c019	c020	c021	c022	c023
1	0.232	0.315	0.311	0.356	0.255	0.332	0.249	0.375	0.273	0.382	0.294	0.251	0.312
2	0.214	0.217	0.188	0.202	0.202	0.186	0.188	0.227	0.208	0.210	0.212	0.194	0.169
3	0.350	0.298	0.263	0.319	0.376	0.263	0.278	0.278	0.296	0.359	0.308	0.250	0.277
4	0.259	0.302	0.272	0.285	0.304	0.323	0.223	0.285	0.338	0.332	0.311	0.265	0.196
5	0.218	0.198	0.246	0.205	0.198	0.184	0.197	0.210	0.248	0.176	0.262	0.176	0.198
6	0.341	0.262	0.291	0.308	0.324	0.250	0.303	0.292	0.275	0.296	0.319	0.380	0.382
7	0.216	0.294	0.233	0.234	0.202	0.209	0.235	0.207	0.195	0.231	0.273	0.269	0.207
Ave.	0.261	0.270	0.258	0.273	0.266	0.250	0.239	0.268	0.262	0.284	0.283	0.255	0.249

Table 4.7: Average ripple wavelength λ_r in metres from zero down-crossing analysis of profiles of survey DBP-3 after passing the data through a Butterworth bandpass filter.

BIn	c011	c012	c013	c014	c015	c016	c017	c018	c019	c020	c021	c022	c023
1	0.020	0.020	0.019	0.027	0.017	0.023	0.021	0.024	0.021	0.027	0.025	0.017	0.021
2	0.017	0.016	0.014	0.017	0.016	0.013	0.015	0.018	0.015	0.015	0.015	0.015	0.013
3	0.023	0.021	0.025	0.025	0.027	0.014	0.016	0.023	0.024	0.021	0.019	0.017	0.016
4	0.021	0.018	0.018	0.020	0.020	0.018	0.013	0.020	0.017	0.017	0.019	0.015	0.013
5	0.016	0.015	0.018	0.016	0.023	0.012	0.014	0.013	0.015	0.013	0.015	0.013	0.012
6	0.023	0.021	0.025	0.026	0.026	0.017	0.025	0.025	0.025	0.027	0.027	0.030	0.025
7	0.019	0.023	0.018	0.018	0.017	0.021	0.018	0.017	0.016	0.018	0.020	0.024	0.017
Ave.	0.020	0.019	0.020	0.021	0.021	0.017	0.017	0.020	0.019	0.020	0.020	0.019	0.017

Table 4.8: Average ripple wave height h_r in metres from zero down-crossing analysis of profiles of survey DBP-3 after passing the data through a Butterworth bandpass filter.

BIn	d011	d012	d013	d014	d015	d016	d017	d018	d019	d020	d021	d022	d023
1	0.313	0.334	0.267	0.332	0.267	0.327	0.333	0.260	0.274	0.340	0.341	0.261	0.291
2	0.254	0.202	0.176	0.231	0.178	0.192	0.217	0.194	0.200	0.224	0.223	0.244	0.217
3	0.463	0.339	0.267	0.292	0.294	0.332	0.309	0.363	0.264	0.274	0.326	0.309	0.392
4	0.254	0.272	0.362	0.290	0.396	0.283	0.251	0.360	0.241	0.301	0.263	0.217	0.219
5	0.222	0.223	0.206	0.211	0.204	0.184	0.246	0.216	0.230	0.216	0.227	0.222	0.187
6	0.339	0.214	0.288	0.309	0.237	0.312	0.281	0.317	0.318	0.271	0.319	0.350	0.331
7	0.234	0.240	0.199	0.220	0.224	0.201	0.255	0.258	0.243	0.254	0.289	0.220	0.259
Ave.	0.297	0.261	0.252	0.269	0.257	0.262	0.270	0.281	0.253	0.269	0.284	0.260	0.271

Table 4.9: Average ripple wavelength λ_r in metres from zero down-crossing analysis of profiles of survey DBP-4 after passing the data through a Butterworth bandpass filter.

Bin	d011	d012	d013	d014	d015	d16	d017	d018	d019	d020	d021	d022	d023
1	0.019	0.023	0.018	0.021	0.019	0.030	0.027	0.020	0.023	0.024	0.024	0.013	0.015
2	0.015	0.014	0.012	0.017	0.016	0.022	0.027	0.021	0.016	0.014	0.015	0.013	0.011
3	0.033	0.026	0.019	0.014	0.019	0.024	0.030	0.027	0.020	0.018	0.021	0.022	0.027
4	0.014	0.014	0.020	0.019	0.021	0.014	0.017	0.021	0.014	0.013	0.017	0.017	0.012
5	0.017	0.016	0.014	0.015	0.014	0.014	0.020	0.015	0.016	0.013	0.017	0.017	0.014
6	0.028	0.021	0.019	0.025	0.023	0.026	0.023	0.028	0.021	0.025	0.023	0.027	0.023
7	0.020	0.021	0.016	0.021	0.020	0.019	0.020	0.022	0.020	0.020	0.022	0.019	0.019
Ave.	0.021	0.019	0.017	0.019	0.019	0.021	0.023	0.022	0.019	0.015	0.020	0.018	0.017

Table 4.10: Average ripple wave height h_r in metres from zero down-crossing analysis of profiles of survey DBP-4 after passing the data through a Butterworth bandpass filter.

Bin	a011	a013	a015	a017	a019	a021	a023
1	0.3657	0.3657	0.3657	0.3200	0.4267	0.2844	0.3657
2	0.3200	0.3413	0.3657	0.2560	0.2695	0.3200	0.3938
3	0.3012	0.3413	0.3200	0.3012	0.5120	0.2560	0.3938
4	0.4267	0.3012	0.4655	0.3938	0.3657	0.3413	0.3657
5	0.3413	0.3012	0.3938	0.3412	0.3200	0.3657	0.4267
6	0.4267	0.4267	0.4267	0.4267	0.4655	0.3938	0.5120
Ave.	0.3636	0.3462	0.3900	0.3398	0.3932	0.3269	0.4096

Table 4.11: Peak ripple wavelength λ_r in metres determined from a FFT for the profiles of survey DBP-1 after passing the data through a Butterworth bandpass filter.

Bin	b011	b012	b013	b014	b015	b016	b017	b018	b019	b020	b021	b022	b023
1	0.320	0.512	0.341	0.466	0.466	0.427	0.427	0.367	0.427	0.367	0.512	0.512	0.512
2	0.301	0.362	0.284	0.341	0.427	0.394	0.394	0.394	0.301	0.394	0.341	0.466	0.256
3	0.427	0.341	0.466	0.366	0.366	0.427	0.320	0.427	0.427	0.341	0.427	0.341	0.284
4	0.394	0.320	0.640	0.320	0.341	0.341	0.512	0.341	0.394	0.466	0.301	0.427	0.394
5	0.394	0.341	0.394	0.341	0.301	0.320	0.341	0.466	0.394	0.366	0.366	0.512	0.341
6	0.466	0.427	0.427	0.427	0.427	0.427	0.466	0.466	0.394	0.427	0.569	0.427	0.466
7	0.394	0.394	0.427	0.426	0.426	0.466	0.427	0.512	0.341	0.366	0.320	0.512	0.512
Ave.	0.385	0.386	0.426	0.389	0.399	0.400	0.412	0.424	0.383	0.389	0.405	0.457	0.395

Table 4.12: Peak ripple wavelength λ_r in metres determined from a FFT for the profiles of survey DBP-2 after passing the data through a Butterworth bandpass filter.

Bin	c011	c012	c013	c014	c015	c016	c017	c018	c019	c020	c021	c022	c023
1	0.569	0.731	0.731	0.427	0.731	0.512	0.569	0.640	0.366	0.569	0.640	0.466	0.512
2	0.640	0.512	0.512	0.365	0.426	0.465	0.640	0.731	0.427	0.427	0.167	0.569	0.427
3	0.512	0.569	0.569	0.512	0.569	0.731	0.512	0.731	0.569	0.640	0.640	0.512	0.427
4	0.640	0.853	0.569	0.731	0.731	0.640	0.394	0.640	0.731	0.569	0.512	0.394	0.569
5	0.394	0.466	0.466	0.569	0.731	0.569	0.301	0.569	0.512	0.366	0.512	0.569	0.466
6	0.427	0.394	0.466	0.512	0.731	0.512	0.512	0.640	0.569	0.640	0.569	0.731	0.640
7	0.466	0.640	0.394	0.244	0.427	0.731	0.466	0.731	0.731	0.640	0.569	0.394	0.64
Ave.	0.521	0.595	0.529	0.480	0.621	0.595	0.485	0.669	0.558	0.550	0.520	0.519	0.526

Table 4.13: Peak ripple wavelength λ_r in metres determined from a FFT for the profiles of survey DBP-3 after passing the data through a Butterworth bandpass filter.

Bin	d011	d012	d013	d014	d015	d16	d017	d018	d019	d020	d021	d022	d023
1	0.512	0.466	0.640	0.512	0.341	0.427	0.466	0.853	0.731	0.853	0.853	0.427	0.640
2	0.569	0.467	0.466	0.427	0.320	0.366	0.394	0.569	0.569	0.640	0.366	0.427	0.569
3	0.512	0.512	0.466	0.853	0.466	0.731	0.466	0.731	0.569	0.569	0.569	0.466	0.853
4	1.024	0.731	0.466	0.640	0.569	0.512	0.466	0.512	0.731	0.466	0.569	0.394	0.427
5	0.731	0.569	0.512	0.569	0.512	0.466	0.512	0.640	0.512	0.512	0.341	0.466	0.427
6	0.731	0.512	0.512	0.569	0.569	0.569	0.569	0.427	0.569	0.731	0.853	0.512	0.569
7	0.197	0.569	0.512	0.640	0.512	0.640	0.640	0.731	0.512	0.640	0.569	0.569	0.731
Ave.	0.691	0.541	0.510	0.601	0.469	0.530	0.502	0.638	0.599	0.630	0.589	0.466	0.602

Table 4.14: Peak ripple wavelength λ_r in metres determined from a FFT for the profiles of survey DBP-4 after passing the data through a Butterworth bandpass filter.

FIGURES

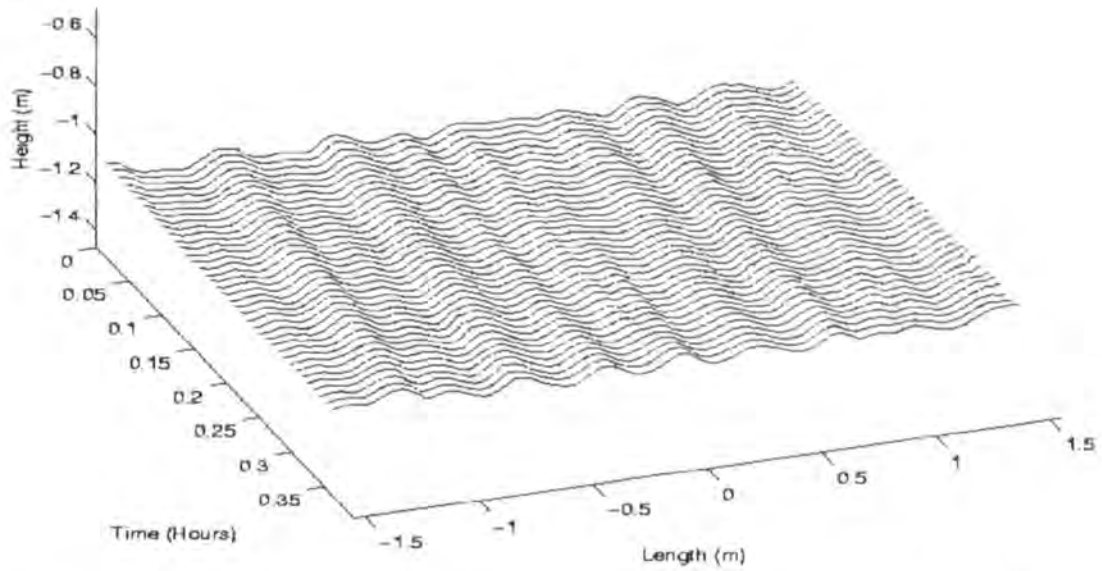


Figure 4.1: Acoustic sand ripple profiling image (ARP) for burst a08a (regular waves, $H = 0.85$ m). Ripple migration can be observed.

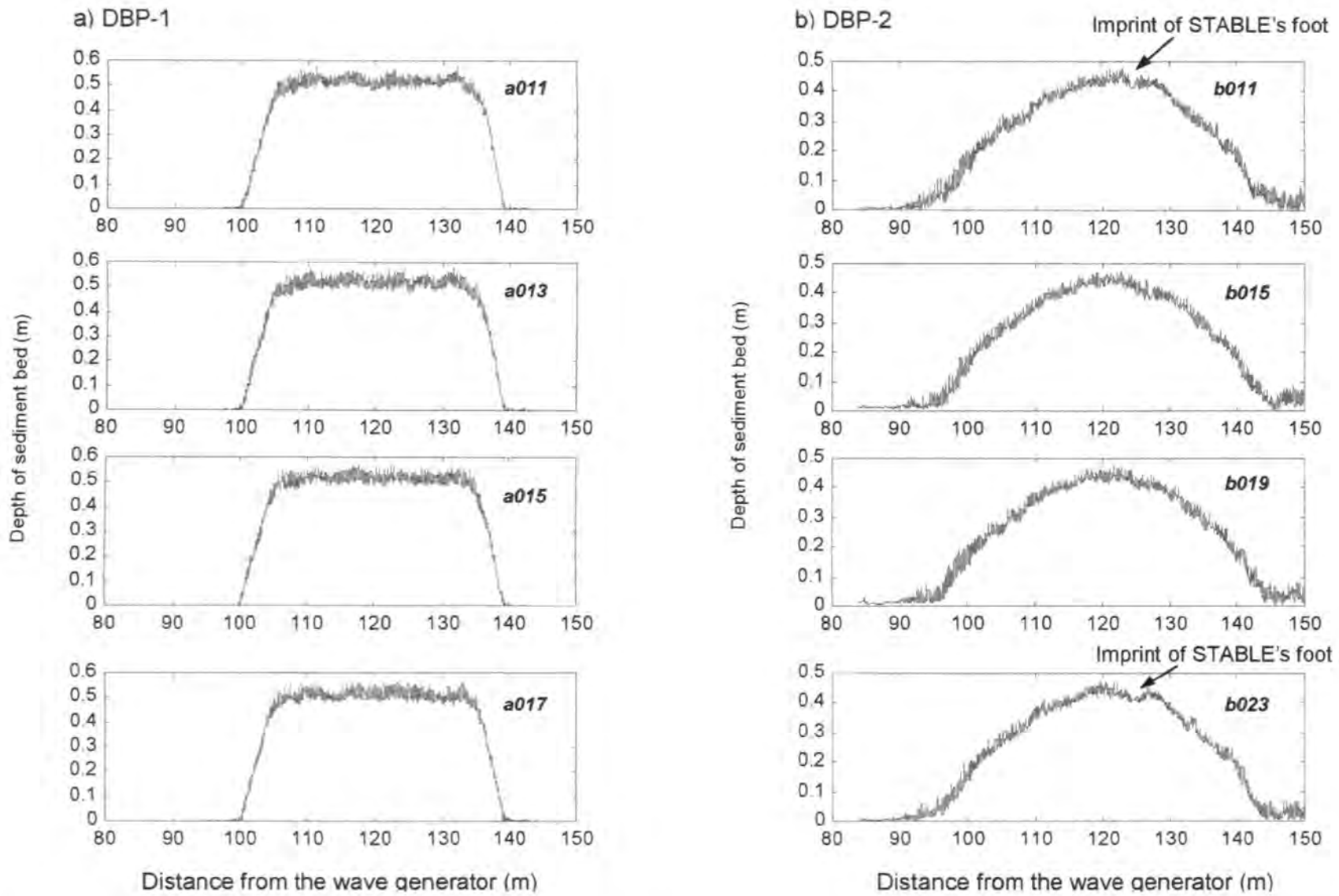


Figure 4.2: Longitudinal profiles of the medium sand test bed measured by the mechanical Delft Bed profiler (DBP). a) at the beginning of the tests before STABLE was deployed, b) at the end of the tests on the medium sand bed. The deformation of the bed is clearly visible.

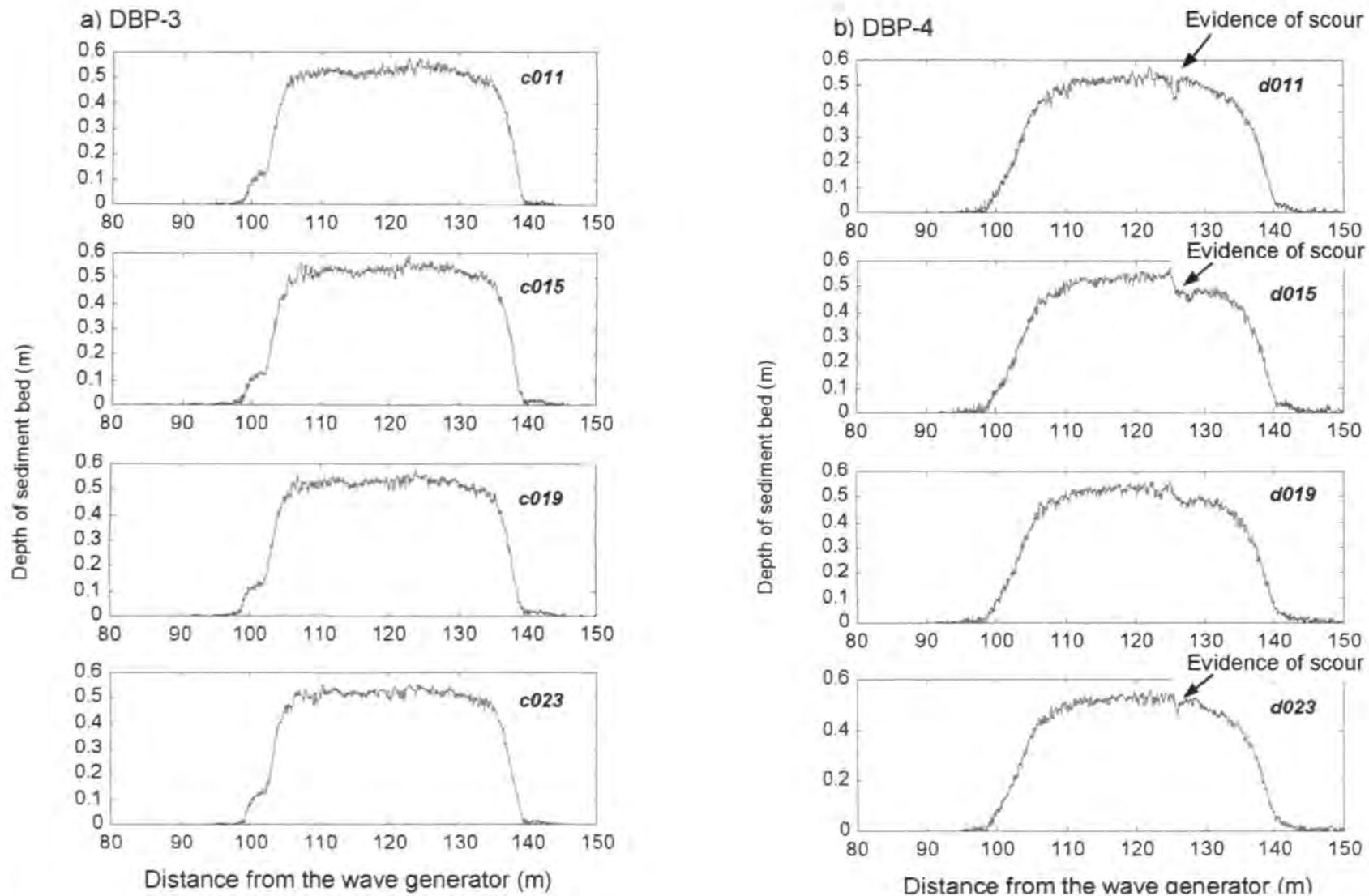


Figure 4.3: Longitudinal profiles of the fine sand test bed measured by the mechanical Delft Bed profiler (DBP). a) at the beginning of the tests before STABLE was deployed, b) at the end of the tests on the fine sand bed. There is evidence of scour behind STABLE's foot.

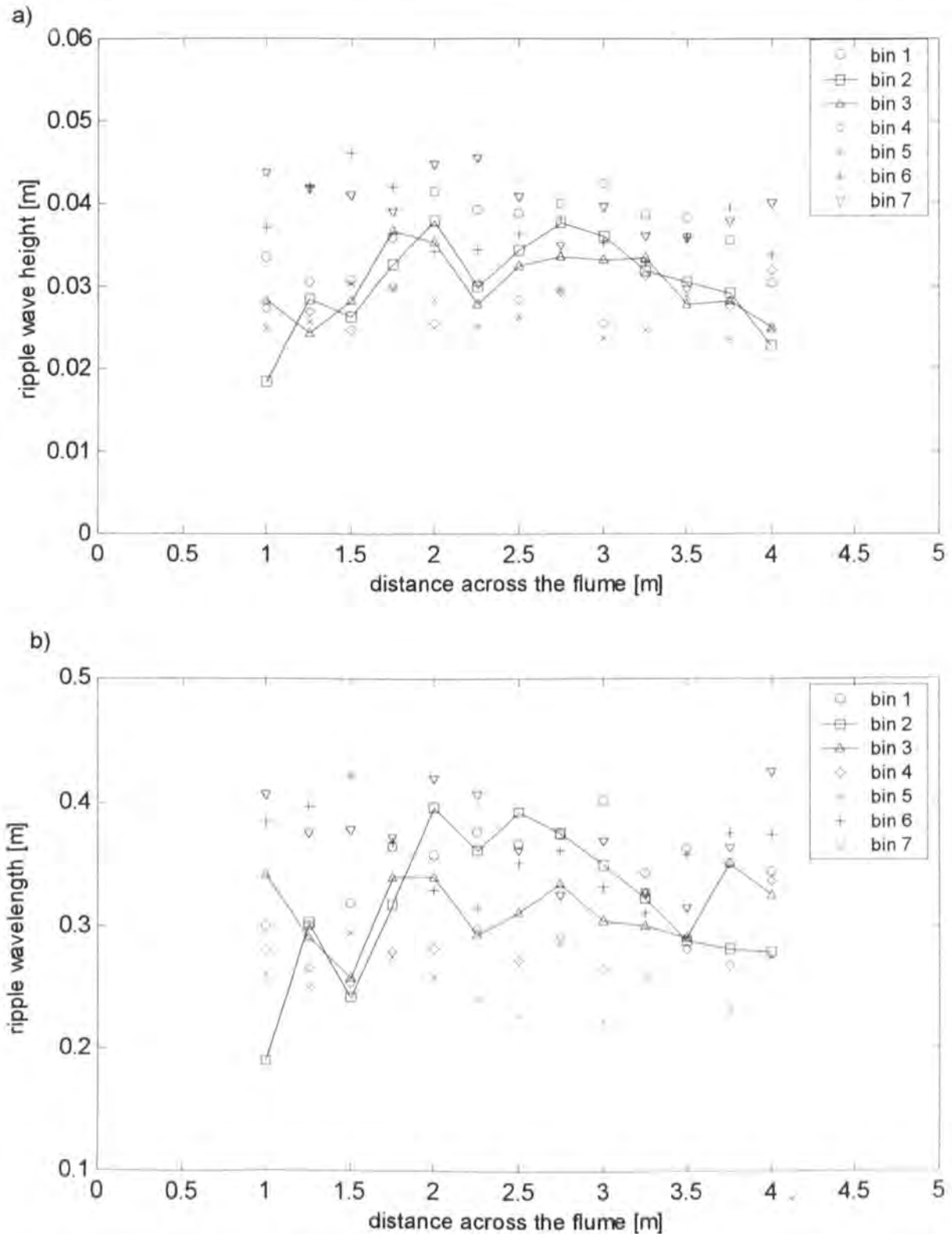


Figure 4.4: Variation of ripple a) wave height and b) wavelength for all the profiles from survey DBP-2 (medium sand) using the zero down-crossing method. Bins 2 and 3 (joined lines) contain part of a STABLE foot for a number of profiles.

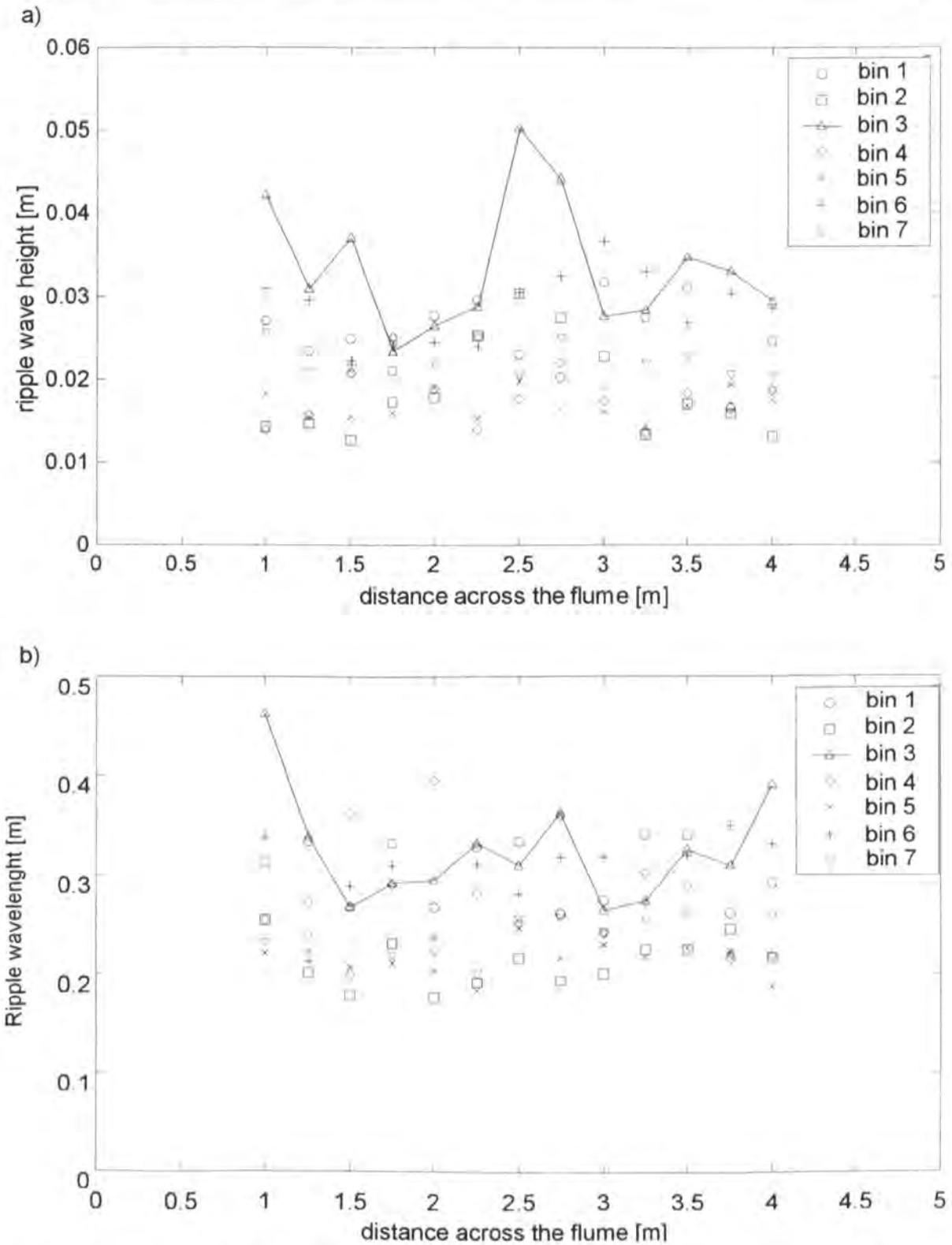


Figure 4.5: Variation of ripple a) wave height and b) wavelength for all the profiles from survey DBP-4 (fine sand) using the zero down-crossing method. Bin 3 (joined lines) contains part of a STABLE foot for a number of profiles.

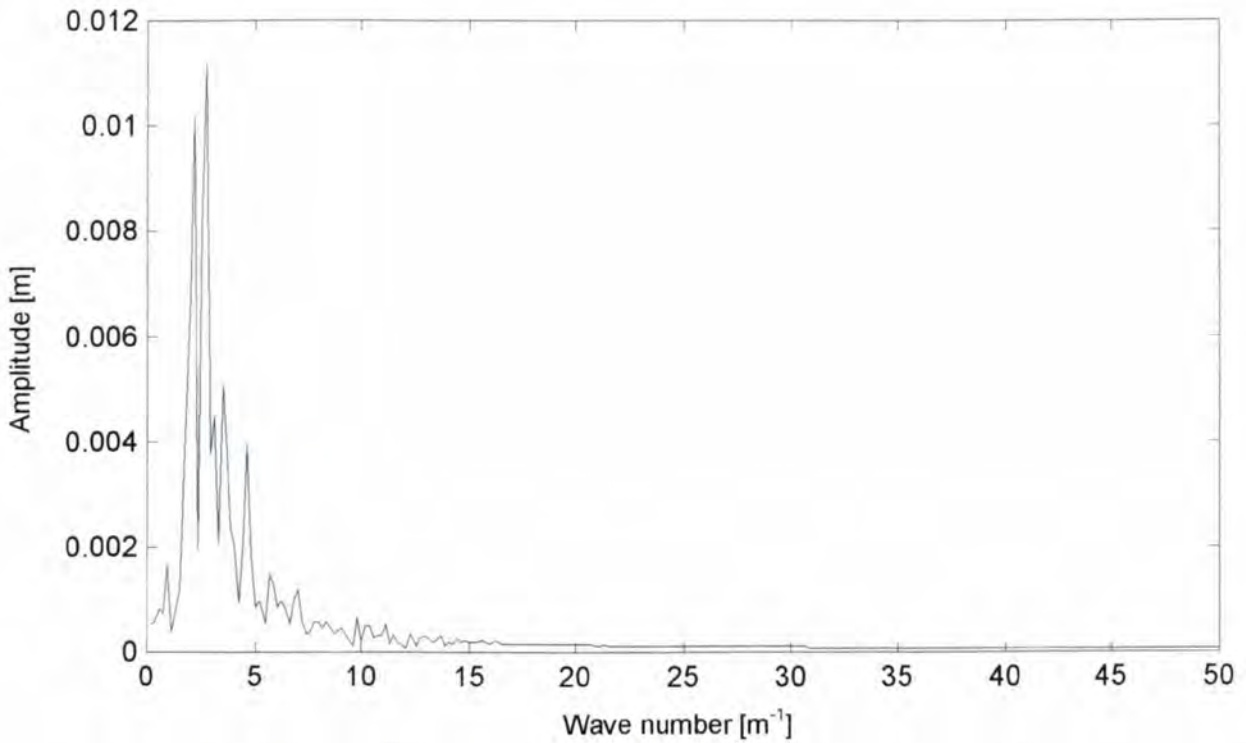


Figure 4.6: Example of a typical energy density spectrum from a FFT for survey DBP-2.

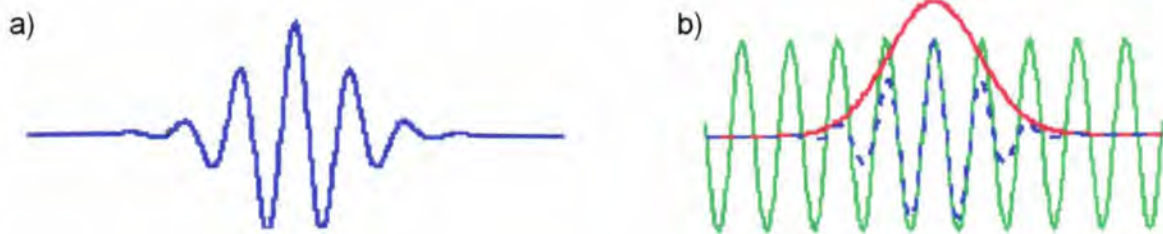


Figure 4.7: a) Morlet wavelet, b) Construction of a Morlet wavelet as a sine curve modulated by a Gaussian (from TORRENCE, 1999).

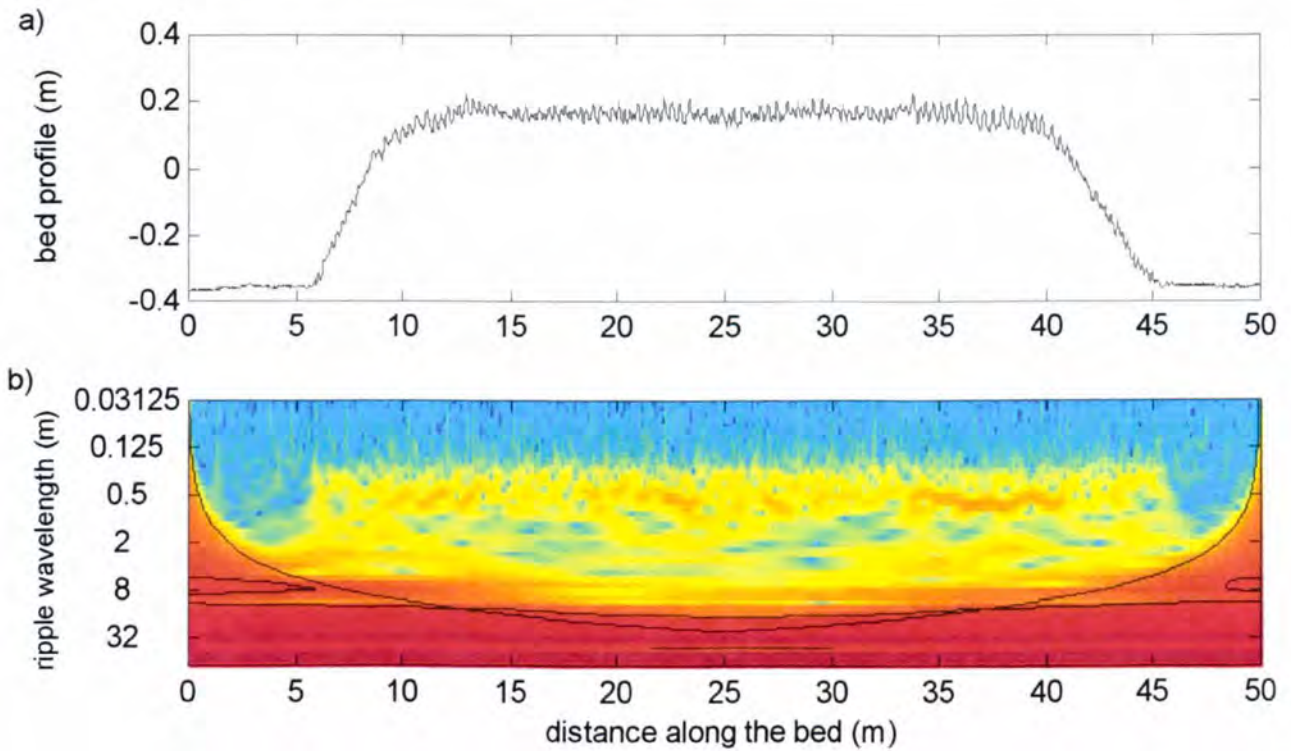


Figure 4.8: a) Unfiltered profile from survey DBP-1 on the medium bed before STABLE was deployed. b) Scalogram of a wavelet power spectrum. Most of the energy is associated with the overall shape of the bed.

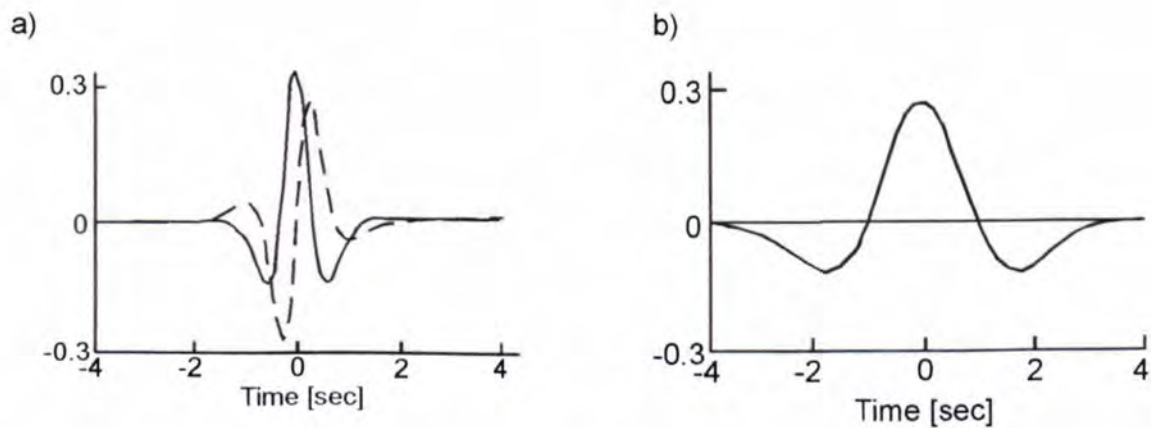


Figure 4.9: Example of a) the Paul and b) the Mexican Hat Wavelet. The dashed line for the Paul wavelet shows the imaginary part (from TORRENCE, 1999).

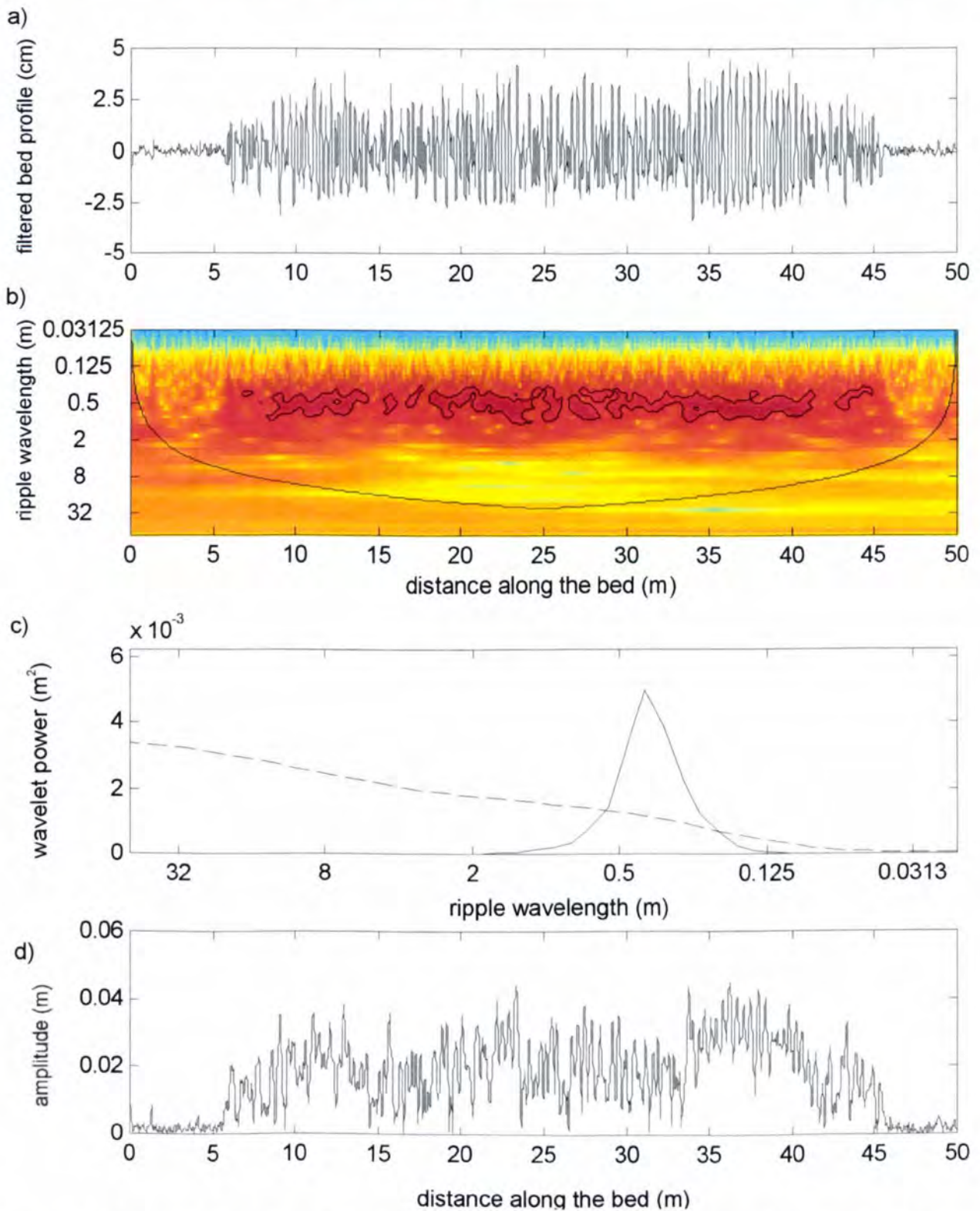


Figure 4.10: a) Filtered profile from survey DBP-1 on the medium bed before STABLE was deployed. b) Scalogram of a wavelet power spectrum using the Morlet wavelet. c) global wavelet power spectrum. d) instantaneous amplitude.

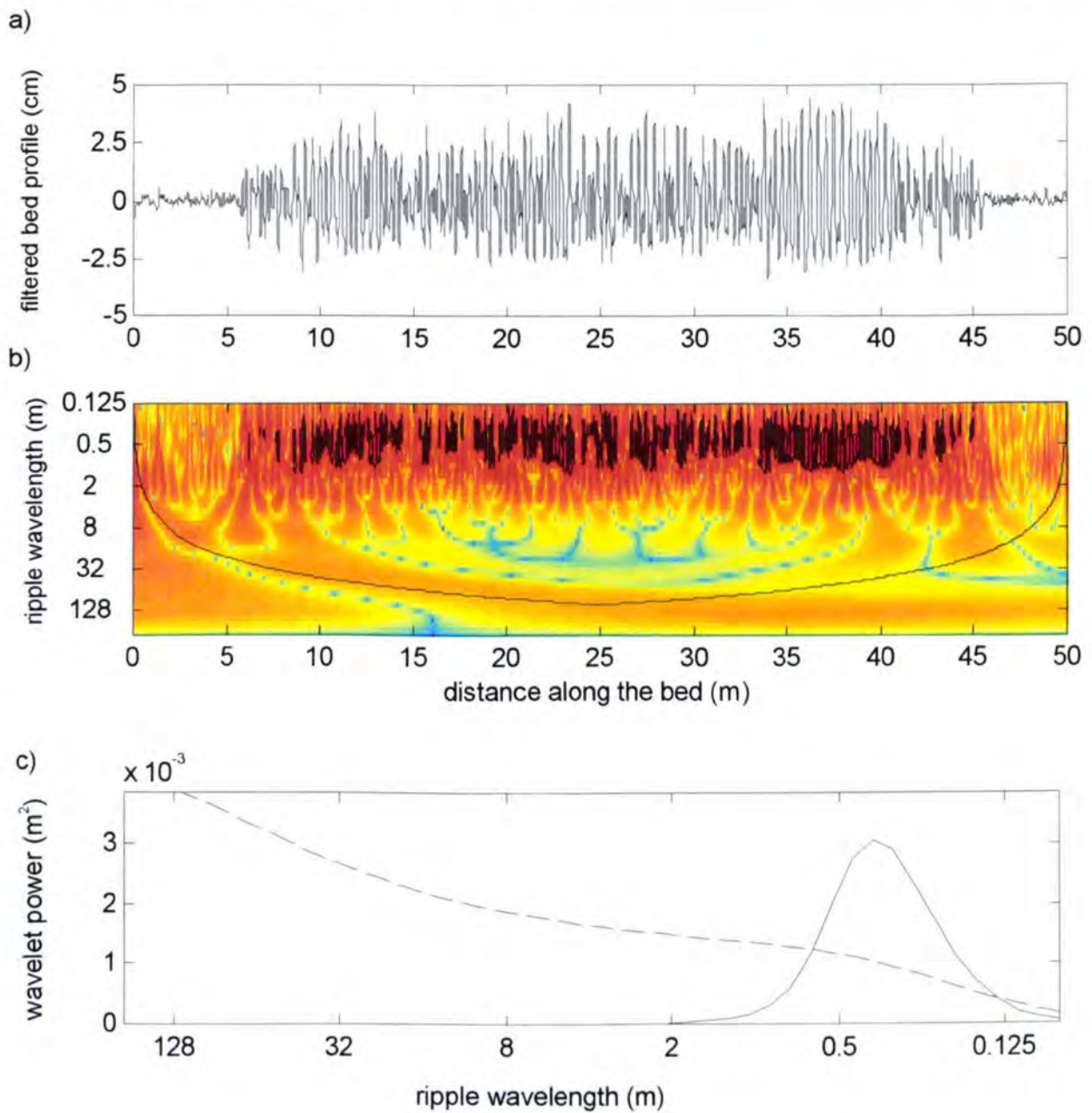


Figure 4.11: a) Filtered profile from survey DBP-1 on the medium bed before STABLE was deployed. b) Scalogram of a wavelet power spectrum using the Mexican Hat wavelet. c) global wavelet power spectrum.

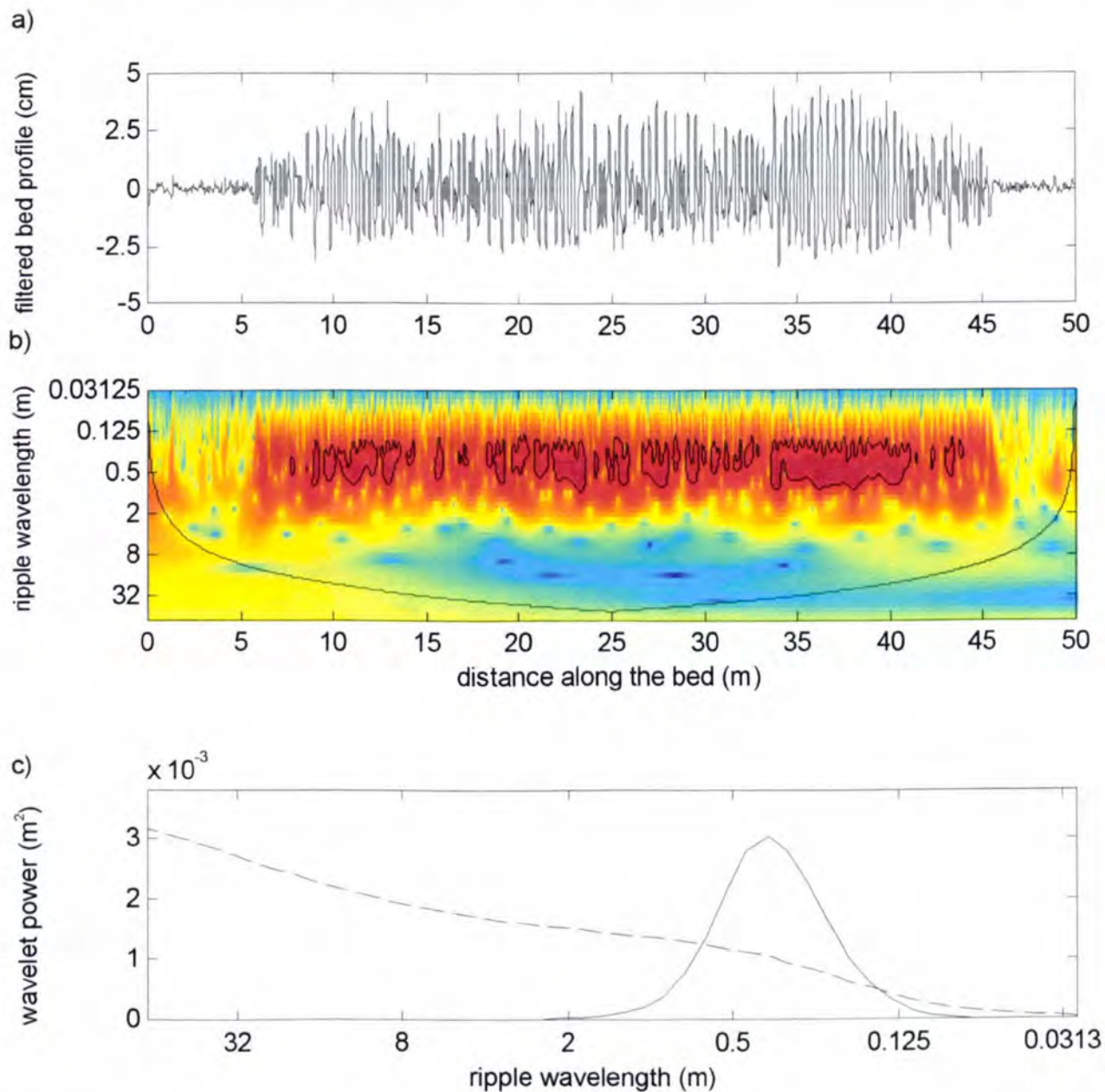


Figure 4.12: a) Filtered profile from survey DBP-1 on the medium bed before STABLE was deployed. b) Scalogram of a wavelet power spectrum using the Paul wavelet. c) global wavelet power spectrum.

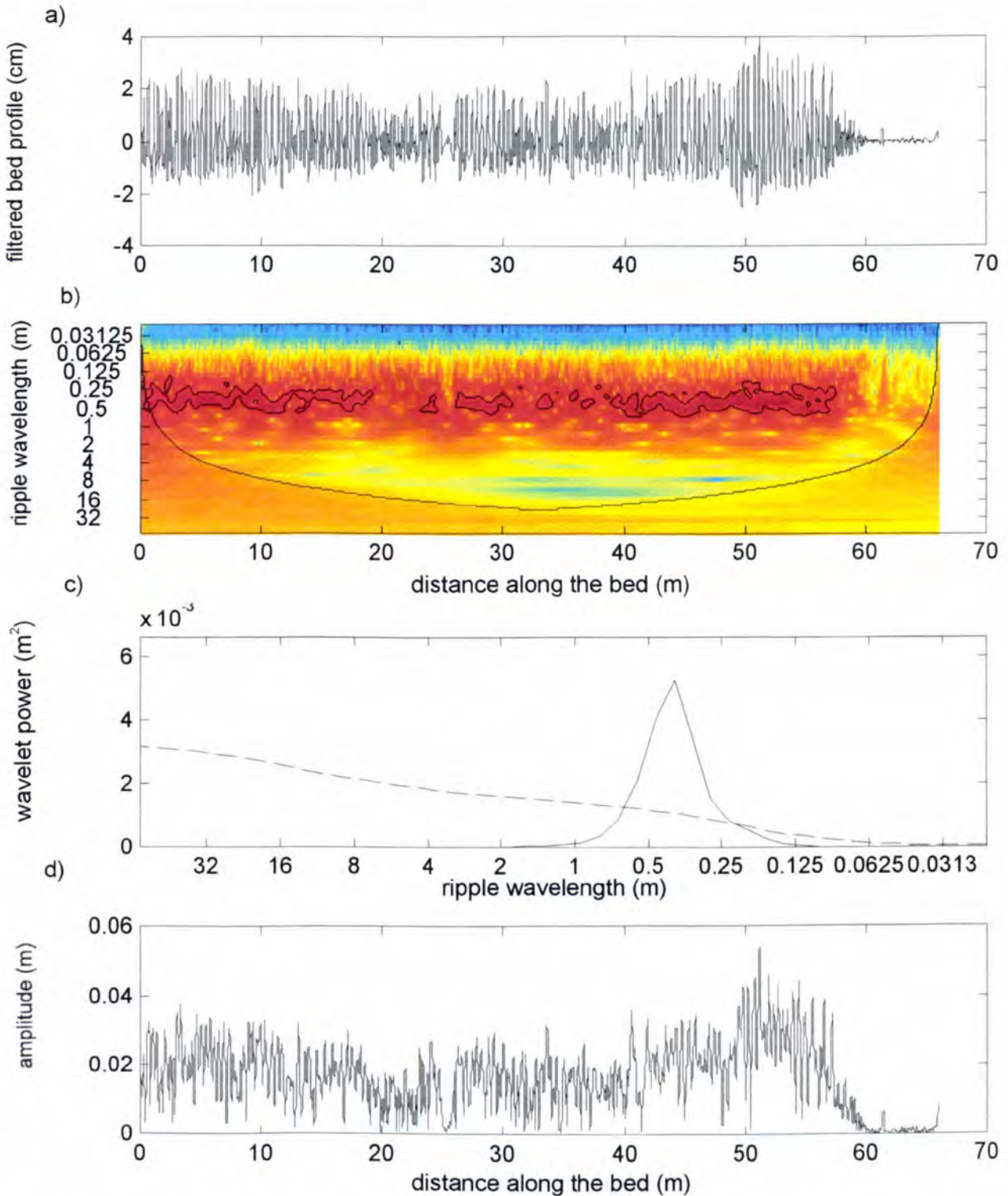


Figure 4.13: a) Filtered profile from survey DBP-2 on the medium sand. The imprint of one of STABLE's feet is visible. b) Scalogram of a wavelet power spectrum. c) global wavelet power spectrum. d) Instantaneous amplitude.

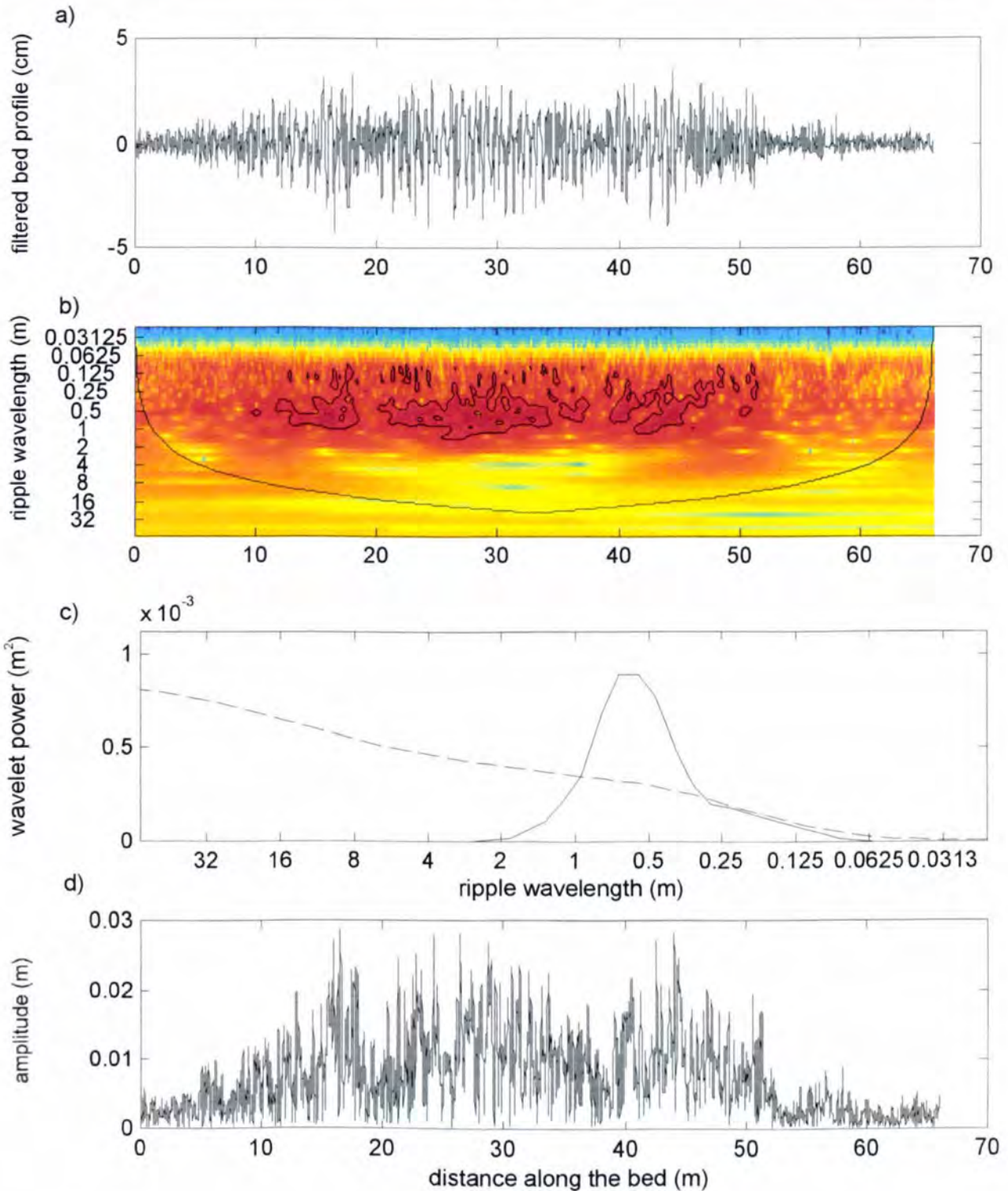


Figure 4.14: a) Filtered profile from survey DBP-3 on the fine sand (before deployment). b) Scalogram of the wavelet power spectrum. c) Global wavelet power spectrum. d) Instantaneous amplitude.

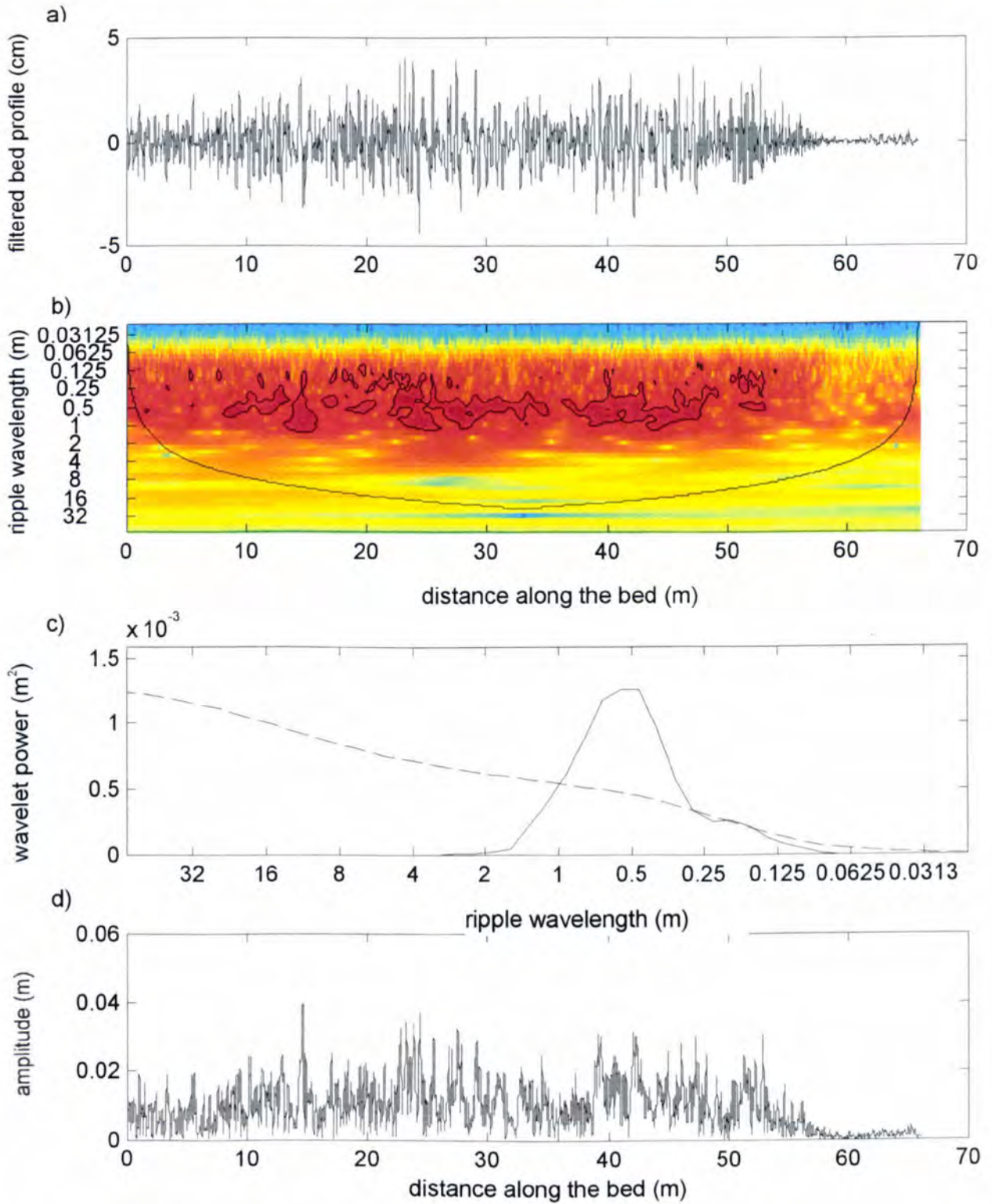


Figure 4.15: a) Filtered profile from survey DBP-4 on the fine sand (STABLE was approximately 25 m along the bed). b) Scalogram of the wavelet power spectrum. c) Global wavelet power spectrum. d) Instantaneous amplitude.

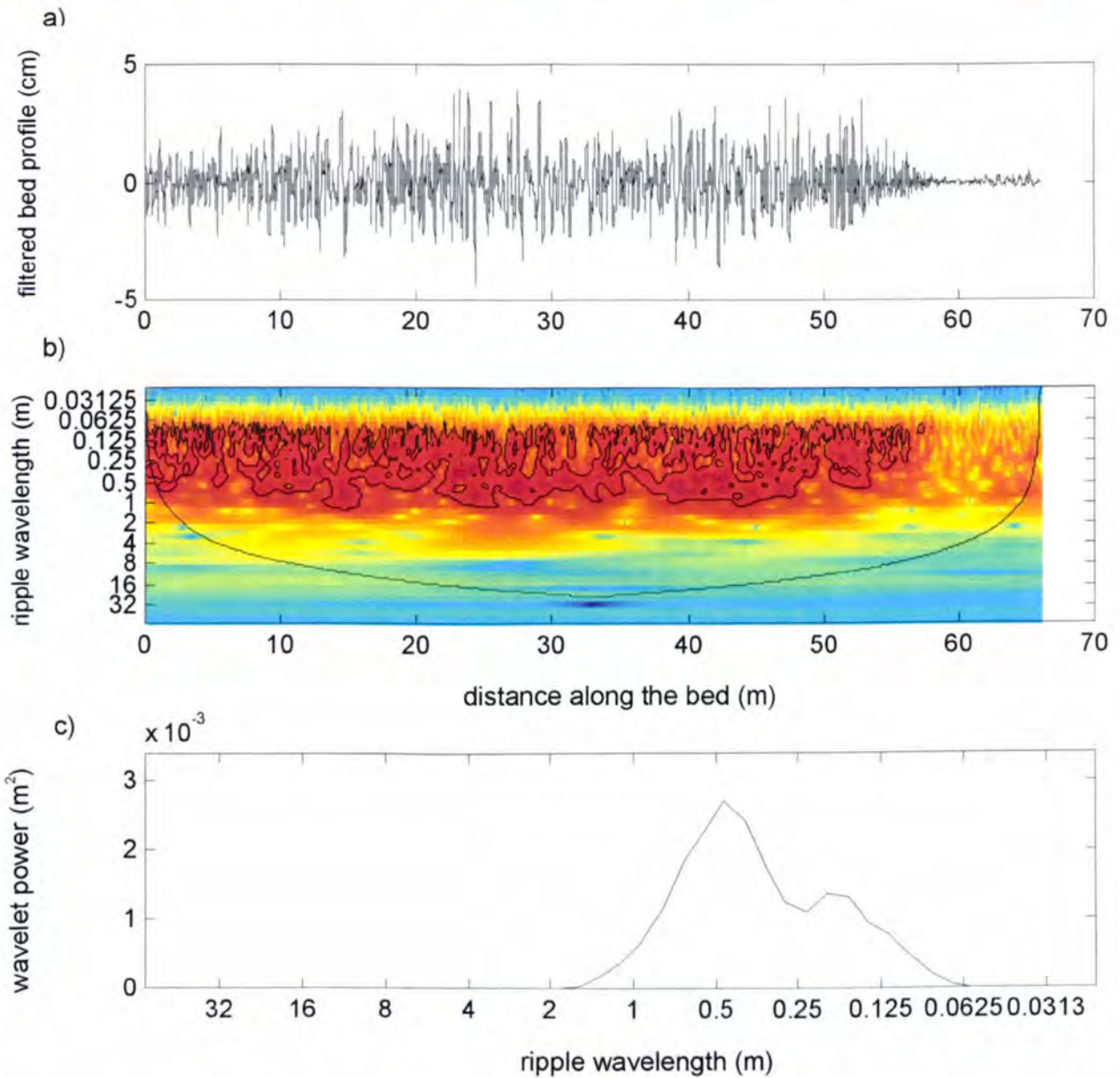


Figure 4.16: a) Filtered profile from survey DBP-4 on the fine sand. b) Normalised scalogram of the wavelet power spectrum. c) Normalised global wavelet power spectrum.

Chapter 5 Suspended Sediment Concentrations

5.1 Mean concentration profiles

This chapter concentrates on the analysis of the burst mean concentration profiles. The differences between the irregular and regular waves are pointed out and some empirical equations are investigated. A comparison of modelled and measured concentration profiles will be made.

5.1.1 Presentation of results

Vertical suspended sediment concentration profiles, temporally averaged over 18 minutes, were determined for two bursts with regular waves (a08a and a11a) and four bursts with irregular waves (a07a, a09a, a10a, a12a). Calibrated data of the 1.0 MHz sensor were available for all bursts and additionally of the 2.0 MHz sensor for bursts a07a, a08a, a09a and a11a. All mean profiles were relatively smooth, apart from the occasional spikes attributed to the reflection of the acoustic signal of the ECM heads at $z \approx 30$ cm, $z \approx 60$ cm and $z \approx 90$ cm above the bed. The spikes were more predominant in the 1.0 MHz data, because it was more sensitive (Jon Williams, personal communication). It is surprising that the strength of reflected signal is not the same for different bursts as the relative position of the sensors did not change. With no more information regarding the calibration of the ABS transducers, no explanation can be given at this point.

Figures 5.1 to 5.3 show vertical mean profiles of the suspended sediment concentrations for bursts a07a, a08a, a09a, respectively, in 1 cm intervals and up to 100 cm above the bed, plotted on a semilogarithmic scale. In the vertical direction, the datum has been chosen to be the bottom of STABLE's feet, as this is the only consistent datum throughout the bursts. The position of the bed was determined from the raw ABS data (see chapter 3.5.4.1). The first concentration measurement was taken to be 1 cm above the bed. This has to be kept in mind, when referring to height above the bed. Furthermore, as mentioned in chapter 3, ripples migrated considerably during bursts of regular waves (between 10 and 40 cm during

the burst resulting in a migration rate of 0.01 cm/s to 0.05 cm/s). Thus, the effect of time averaging the data is to also horizontally spatially average the data in the direction of ripple migration. The graphs for the other three bursts (a10a, a11a, a12a) are shown in appendix C figures C.1 to C.3.

Figure 5.1 displays a comparison between the mean vertical profiles measured independently by the 1.0 MHz and 2.0 MHz ABS sensors for burst a07a (irregular waves, $H_s = 0.53$ m). There is a good agreement between the data measured by the 1.0 MHz and 2.0 MHz ABS sensor up to a height of approximately 40 cm above the bed. Then the two profiles diverge, exhibiting a difference of about a factor of 4 at 100 cm above the bed. This is very surprising, as at the higher levels, the background concentration should be predominant. Hence, there should be no significant difference in concentrations measured by the two sensors, even though the two sensors were spatially separated by about 11 cm laterally. One possible explanation for the difference in concentration at higher levels above the bed could be the way in which the ABS data were calibrated. The burst averaged sediment concentrations, determined from the pump-sampling were used to calibrate the ABS data. However, only one pump sample value at one height was used for the calibration of the ABS measurements. For burst a07a, six values, with the highest one at 25.5 cm above the bed, were available and thus, an error in calibration might have accumulated with height, as there was no reference value available above 25.5 cm. As the calibration was performed by POL, this can only be a speculation. Though the discrepancy in the absolute concentration between the two profiles exists, the gradient of the two profiles is comparable. Also the main interest in the profiles lies within the first 40 cm, where it is likely that suspension events will occur and the concentrations above this level are low.

Figures 5.2 and 5.3 show the suspended sediment concentration profiles for burst a08a (regular waves, $H = 0.85$ m) and a09a (irregular waves, $H_s = 0.83$ m), respectively. Due to the similar wave heights these two bursts can be compared. There is little difference between the corresponding concentration profiles recorded by the 1.0 MHz and 2.0 MHz for both bursts. The concentration is approximately constant above about 70 cm above the bed exposing the background concentration. Though the wave heights are comparable, it is worth noting that the concentrations at the bed differ considerably with values of about 5.2 g/l and 1.8 g/l for the regular and irregular waves, respectively. The reason for this can be seen in figures 5.6 and 5.7, which show the time histories at a number of heights for these two bursts. Though individual events were larger for the irregular waves, over the whole burst there was a more consistent sediment suspension under regular waves leading to larger concentration values in the burst mean profiles. Also worth noting is that for the

irregular waves (figure 5.3), the concentration magnitude decreases more rapidly with elevation than under regular waves (figure 5.2). NIELSEN (1992), reported the same findings and attributed them to the difference in ripple dimensions for regular and irregular waves, respectively. Though there is a difference in ripple size for regular and irregular waves in the present experiments, the ripples present under irregular waves were often relics of the ripples formed in the previous burst with regular waves (see chapter 3.5.3). Thus, the ripples that exist under irregular waves are not formed by the hydrodynamics of the irregular waves and are very similar to the ripples under regular waves. Figure 3.22 showed that the ripple dimensions measured in the current experiment agreed quite well with Nielsen's empirical equation of the ripple dimensions for regular waves. This would contradict Nielsen's argument for the cause of the different decay of sediment concentration with heights for regular and irregular waves, respectively. The different gradients might be explained by the different type of sediment suspension of regular and irregular waves. The suspension under irregular waves is dominated by suspension events under wave groups. These sediment suspension events are then carried up the water column. However, during a considerable part of the burst hardly any sediment is entrained from the bed. This could lead to a larger concentration decay with height in the water column. In contrast, there is a continuous sediment entrainment under regular waves, which is then carried up the water column. Due to the consistency of the sediment suspension, the concentration decay with height might be smaller than the one for irregular waves.

In general the consistency between the 1.0 MHz and 2.0 MHz data is very good. Figure 5.4 shows the sediment concentration profiles for the four bursts with irregular waves for the first 60 cm in the water column. Though, the absolute concentration differs between the c-profiles, there are two common features consistent for all the c-profiles. Within the first two to three centimetres above the bed, the concentration drops more rapidly than for the rest of the c-profiles, resulting in a large negative gradient. This is especially highlighted in bursts a10a and a12a with wave heights of 1.06 m and 1.26 m, respectively. Further above the bed, the c-profiles are linear with an increasing gradient with increasing wave height (left to right on the graph), with the exception of burst a09a. Table 5.1 summarises the gradients and table 5.2 lists the sediment concentrations for the two ABS transducers at 1 cm above the bed. For the measured profiles, two gradients – one for the first 3 cm, and the main gradient – were determined. For the main gradient a straight line was assumed between the concentration value at 4 cm and 50 cm above the bed. Also, presented in table 5.1 are the gradients derived from the theoretical approach using Nielsen's exponential equation ($c = c_0 \cdot e^{-z/\ell}$) for the sediment concentration profiles. The gradient on a logc-z plot is

given by $(-1/\ell \cdot 1/\ln 10)$, which transforms to $(-\ell \cdot \ln 10)$ on a z-logc plot, where ℓ is the mixing length in m. This means that the gradient is constant for the whole profile. In contrast, the Rouse-type profile (see section 5.2) has a varying gradient over the profile. The gradients for the two sections of the profile as predicted by the Rouse-type approach are also given in table 5.1. The measured gradient within the first 3 cm above the bed has a relatively constant value of about -0.10 and -0.12 for the 1.0 MHz and 2.0 MHz ABS transducers, respectively. The values determined by Nielsen's expression increase from -0.05 to -0.19 from burst a07a to a12a. The Rouse-type profile also shows an increase in the gradient from -0.06 to -0.20 in this region of the profile. Though, this increase in gradient steepness is not observed in the measured c-profiles, the values are of the same order. KACZMAREK (1999), suggested a three layer model for sheet flow conditions dividing the bedload layer in a contact load and a bedload layer. The contact load layer is dominated by grain-grain interaction like particle collision and drag effects, and turbulence. According to KACZMAREK (1999), this leads to a sudden reduction in concentration over the width of the contact layer of a few centimetres. Though, this model was developed for sheet flow conditions, a similar phenomenon might exist in the ripple regime and thus, explain the large reduction in concentration over the first 2 to 3 centimetres above the bed.

The main gradient determined from the measured c-profiles is in the range of -0.2 to -0.32. The gradient for burst a09a is influenced by the larger concentration values as a result of the reflection of the acoustic signal of the ECM heads (see figure 5.4). Nevertheless, the Rouse-type profile also predicts a lower value for this burst. This cannot be explained at present. The constant gradients calculated from Nielsen's expression for the c-profiles clearly underestimate the true gradient in this region, while the gradients from the Rouse-type expression are of the right order. It will be shown later that the exponential equation proposed by Nielsen only predicts the measured profiles accurately within approximately the first three centimetres above the bed. The analysis of the gradients seems to indicate that the Rouse-type profile leads to a reasonably good representation of the measured c-profiles.

Figures 5.5 to 5.10 (note the change in scale in figure 5.10) detail the complete recorded time histories of the suspended time series at $z = 2, 5, 10, 20$ cm above the bed for all the available bursts. The heights refer to the distance above the ripple crest, irrespectively of the relative position of the sensors to the ripples. Also, included at the bottom of each graph is the synchronous time series of the instantaneous near bed, horizontal orbital velocity from the lowest ECM pair ($z \approx 30$ cm) on STABLE. There is a clear difference between the time histories for the regular and the irregular waves. For the regular waves there are continuous suspension events over the whole length of the record. In contrast to this, the suspended

sediment concentration time series for the irregular waves are composed of a slowly varying, low concentration of very fine material, as well as discrete and sporadic re-suspension events with a “spike” like appearance. With increasing wave height the suspended sediment concentration values increase. It should be pointed out that there is a large spike at about $t \approx 700$ seconds in figure 5.7 (burst a09a). As this spike is considerably larger than all the other re-suspension events occurring in this burst, and furthermore, it is larger than the concentration values for bursts a10a and a12a with larger wave heights, it is assumed that this spike is not real, but can be attributed to short term electrical interference. Some arc welding was performed near the *Deltaflume* during the time of the experiments (Jon Williams, personal communication). However, there is no record of the time this welding was performed and thus, it can only be suggested as a possible explanation for the spike in the data. The low concentration values between $t = 300$ and 700 seconds for burst a11a (figure 5.9) is very interesting. The reason for the low concentration was thought to be the position of the ABS transducers relative to a ripple crest. Figure 5.11 shows the ripple profile recorded by the acoustic ripple profiler (ARP) for burst a11a. The ABS sensors were positioned at approximately 0.4 m. At the beginning of the burst the ABS sensor was close to the ripple crest. This ripple disappears half way during the burst, while another ripple migrates to the position of the ABS. This can also be seen in figure 5.37, though not as clearly. Assuming vortex development in the lee of ripples, which is then lifted into the water column at the ripple crest, the relative position of the ABS transducers to the ripple crest determines the sediment concentrations measured.

The sediment diffusivity can be determined from the measured concentration profiles using equation 2.59. Figure 5.12 shows an example of the variation of sediment diffusivity with height for burst a08a. It can be seen that the sediment diffusivity is not constant, but increases with height over a range of more than one decade. The sediment diffusivity was in the range of 10^{-3} to 10^{-2} for the six different bursts. The increase in suspended sediment diffusivity with height was also described by NIELSEN (1992). Substituting the equation for the concentration decay with height assuming pure diffusion proposed by NIELSEN (1992) in equation 2.59, the sediment diffusivity equals $\varepsilon_s = w_0 \cdot \ell$ with w_0 being the settling velocity and ℓ the length scale. The sediment diffusivity is constant if the settling velocity is constant. Thus, it seems more reasonable to assume a varying settling velocity with height. Further, a variation of the length scale with height has to be investigated in future research.

5.1.2 Discussion of results

As described in section 5.1.1, the suspended sediment time series were composed of a background concentration and superimposed on top of this were the high concentrations and spiky events. Further up the water column (e.g. above approximately 80 cm above the bed) the concentrations were relatively uniform, which is consistent with the advection of a wash load with negligible particle settling velocity.

In order to determine the consistency of the data with distance from the bed, a cross correlation analysis for the suspended sediment concentration time series at different levels above the bed was performed. The analysis has been used by OSBORNE AND GREENWOOD (1993), who discussed the cross correlation technique in further detail and used it to ascertain the time lags involved in vertical movements of suspended sediments. The cross correlation is a standard method of estimating the degree to which two series are correlated. Given two series $x(i)$ and $y(i)$ with N number of points, the cross correlation coefficient r is defined as

$$r(\text{delay}) = \frac{\sum_i [(x(i) - \bar{x}(i)) \cdot (y(i - \text{delay}) - \bar{y}(i))]}{\sqrt{\sum_i (x(i) - \bar{x}(i))^2} \cdot \sqrt{\sum_i (y(i - \text{delay}) - \bar{y}(i))^2}} \quad (5.1)$$

where $\bar{x}(i)$ and $\bar{y}(i)$ are the means of the corresponding time series (BOURKE, 1996). Equation 5.1 can be calculated for a number of delays ranging from $-N$ to N with the smallest interval equal to the reciprocal of the sampling frequency. The denominator in equation 5.1 serves to normalise the correlation coefficient such that $-1 \leq r(\text{delay}) \leq 1$. The delays were chosen to be in the range of ± 15 seconds, which is equivalent to 60 data points on the assumption that this is the likely range for any significant changes in correlation. Furthermore it is a multiple of the wave period.

In order to discuss the form of the cross correlation function, figures 5.13 to 5.15 detail the correlation coefficient function for the suspended sediment concentration signals using burst a08a (regular waves), a07a and a10a (irregular waves). As a reference signal the time series at $z = 5$ cm was used and this was cross-correlated with time series at $z = 10$ cm, $z = 15$ cm, $z = 20$ cm, $z = 25$ cm, $z = 30$ cm, $z = 35$ cm, $z = 40$ cm, $z = 45$ cm and $z = 50$ cm. All three plots show a maximum correlation at zero lag. The value at maximum correlation is the smallest for regular waves. Though the suspension events occur regularly over the entire record for regular waves, the individual events are considerably smaller (see figures 5.6 and 5.7) than for irregular waves. This leads to a smaller amount of sediment being

entrained high into the water column and results in an immediate drop in the correlation coefficient at zero lag with height.

For the regular waves (figure 5.13), the cross correlation plots are symmetrical and peaks in correlation can be found at lags which are a multiple of the wave period (approximately 5 seconds). This suggests that the acoustic signal is strongly influenced by the periodic velocity signal. There is a strong correlation up to a height of 30 cm above the bed. Further above the bed the highest correlation occurs about - 0.25 seconds earlier than the peaks related to time series closer to the bed. This indicates that the sediment takes some time to be suspended to this height in the water column and hence spikes occur later in the time series.

For irregular waves (figures 5.14 and 5.15) the cross correlation plots also show a series of spikes at a lag of - 5 and - 10 seconds, which can be attributed to the peak period of the waves. In contrast to the regular waves the cross correlation plots do not exhibit a symmetry about zero lag. There is a larger correlation for negative lag than for positive lag. Keeping in mind that negative lag means that the time series is shifted backwards relative to the reference signal, this is not surprising. It takes some time for the particles to suspend into the water column and thus the individual events occur later in time at greater distances above the bed. For burst a07a (figure 5.14) maximum correlation can be found at zero lag only up to 10 cm above the bed. At $z = 15$ cm the maximum correlation occurs at about - 1.5 seconds. This suggests that the sediments are only slowly suspended into the water column. At levels higher than $z = 45$ cm, there is no significance in the cross correlation, showing that the events are not vertically coherent past this height. The phase for maximum correlation is meaningless at this height, as the spiky near bed signal is of a completely different form to the background concentration records higher above the bed.

In contrast, figure 5.15 shows a maximum correlation at zero lag up to about $z = 20$ cm above the bed. For the next 10 cm maximum correlation diverges from zero lag until at $z = 40$ cm it switches to about - 5 seconds. The slow divergence from a maximum correlation at zero lag is due to the time it takes for the sediment to reach higher levels above the bed. Due to the larger waves the distribution of sediment within the first 20 cm above the bed happens immediately after the particles are entrained from the bed. The switch to - 5 seconds for maximum correlation indicates a different mechanism. Five seconds is approximately the peak period of the waves. If a wave entrains the sediment into the water column and the sediment does not settle to the bed before the next wave approaches, the next wave entrains the sediment even further into the water column leading

to a spike in the concentration time history at a later time (one wave period) at these distances above the bed. In a cross correlation analysis, this would result in the peak correlation occurring one wave period earlier. The signals higher above the bed have to be shifted backwards against the time history at 5 cm above the bed to produce a high correlation. Thus, the switch from almost zero lag to - 5 seconds in figure 5.15 could be an indication for the pumping effect experienced by the sediment due to irregular waves. It is however, surprising that this pumping effect, which can be observed under wave groups (see chapter 6), can be detected in the correlation analysis for the time series of the whole burst.

In order to determine the horizontal coherence of the suspended sediments, a cross correlation analysis of the concentration time series measured by the two ABS sensors was performed. The two ABS sensors were spatially separated by approximately 11 cm laterally. Figures 5.16 and 5.17 show a cross correlation plot for bursts a07a (irregular waves) and a08a (regular waves), respectively. The time series at various heights were correlated with each other. The two graphs are of completely different shape. For the irregular waves the maximum correlation at zero lag is about 0.65 and exists for the correlation of the two time series at $z = 5$ cm above the bed. In contrast, the maximum value is only 0.45 for the regular waves and occurs at zero lag at $z = 50$ cm above the bed. The different degree of correlation can also be seen in figures 5.18 and 5.19, which show two time series at $z = 5$ cm above the bed for the two ABS sensors for the two bursts. While there is a good agreement between the time at which individual suspension events occur under irregular waves, there is less correlation between the sediment suspension for regular waves.

Turning the attention first to figure 5.16, it has to be pointed out that for the first 15 cm above the bed the correlation coefficient drops immediately with increasing lag from a maximum value at zero lag. One explanation for this might be the size of the sediment cloud at the various heights. The sediment is entrained and trapped in a small cloud, which then dissipates while being carried upwards. Close to the bed, individual suspension events do not always pass through both ABS sensors. At greater distances, the sediment clouds are large enough to occur over a longer period of time and to pass both sensors. Thus, the correlation coefficient at heights between 20 and 30 cm does not drop off to the same extent as closer to the bed. At heights larger than 35 cm above the bed, the phase for maximum correlation is again meaningless, because of the form of the background concentration. It is also noticeable that the maximum correlation only occurs at zero lag at $z = 5$ cm above the bed. At greater distances from the bed the maximum correlation can be found at some phase lag.

Figure 5.17 has a periodic trend in the correlation coefficient. This reflects the concentration time series for regular waves. The sediment suspension under regular waves is driven by the periodic velocity rather than by individual large waves or wave groups. It is surprising to note that the maximum correlation does not occur closest to the bed, but at $z = 50$ cm above the bed. At this level the presence of a constant wash load leads to larger correlation values. One of the reasons why the maximum horizontal correlation between the two ABS transducers for regular waves does not occur at the bed might be the migration of ripples under regular waves leading to different sediment entrainment for the two ABS sensors and thus the horizontal correlation is small. Further, for regular waves the periodic stretching and squeezing of the background concentration due to the non-zero $u \cdot \partial u / \partial x$ term will give a high correlation at 50 cm above the bed. The normalisation means that a strong correlation can occur in the presence of very low concentrations. If this were true, then a normalised spectrum at 50 cm above the bed should show a more dominant peak at 5 or 2.5 s than one at 20 cm. Also the absence of long crested ripples over the bed might add to the different suspension of sediment under the two ABS transducers. The sediment is then entrained over a ripple crest or a trough, respectively. If the ripples are not long crested (which has been assumed so far), then the vortices, shed from a ripple crest, are at a different position relative to the two ABS sensors. This results in the vortices, which were generated during a wave at one instance in time, passing through the sensors at different heights and times in the signal. This might explain, why the maximum horizontal correlation does not occur at the lowest level above the bed for regular waves. For irregular waves this is not that important as the ripples developed under irregular waves are relics of ripples formed under the previous burst of regular waves. Thus, the ripple dimensions are not related to the hydrodynamics. Also the irregular ABS signal for irregular waves is dominated by individual large re-suspension events resulting in high values of correlation between the two ABS signals.

The evidence presented in this section suggests that the ABS system received “snap shots” of clouds of suspended sediment, which were advected across the sensor region by the flow. The measured sediment concentrations were analysed with respect to their vertically and horizontally coherent structures. In oscillatory flow, a vertical phase lag would be anticipated for a sediment re-suspension event ejected into the flow on flow reversal. A different behaviour was observed for the regular and irregular waves. The sediment suspension under regular waves is driven by the periodicity of the waves, while for irregular waves their groupiness characteristics are more important than the peak period of the waves.

It is intuitive to expect that the intense near bed wave conditions would suspend the sediment with a high upward characteristic velocity and the 0.25 seconds temporal resolution may hide these subtle changes.

5.2 Comparison of averaged measured and predicted c-profiles

5.2.1 Introduction

From an engineering point of view it is important to predict suspended sediment concentration profiles accurately using simple empirical equations. To investigate the applicability of empirical equations to the present wave only data, different equations were used to predict mean suspended concentration profiles, which were then compared with measurements. The wave height and period and the ripple dimensions were determined from measurements and used as input parameters for the models. The remaining parameters needed for the empirical equations were calculated using the equations listed in appendix C. The relevant results of the various empirical equations and the input parameters are given in table 5.3.

5.2.2 Diffusion, pure convection and combined diffusion/convection model proposed by Nielsen for the prediction of mean sediment concentration profiles

As mentioned in chapter 2, Nielsen proposed three different equations based on purely diffusive, convective and combined convective and diffusive entrainment processes. The physical significance of the diffusive and convective processes in oscillatory flow was discussed in chapter 2. Nielsen's equations are all based on the form

$$\bar{c}(z) = c_0 \cdot F(z) \quad (2.67)$$

where c_0 is the reference concentration and $F(z)$ is the vertical distribution function, which depends on the type of entrainment process. NIELSEN (1986), proposed the reference concentration to be a function of the modified effective Shields parameter and given by

$$c_0 = 0.005 \cdot \rho_s \cdot \Theta_r^3 \quad (2.70)$$

To analyse the validity of equation 2.70 for the present data, the concentration at the bed and the modified Shields parameter were obtained from the measurements. The concentration at the bed was based on the 1.0 MHz ABS transducer and defined as the mean concentration at 2 cm above the bed. The lowest concentration value at 1 cm above

the bed was discarded, because it was thought to be possibly influenced by the high bedload concentration. This was in contrast to NIELSEN'S (1986), definition of the reference concentration, which was found by determining the best fit exponential profile to these data and extrapolating it to $z = 0$ cm. The reference concentration as a function of the modified effective Shields parameter is shown in figure 5.20. The blue circles represent the values of reference concentration and modified Shields parameter for the six bursts and the blue line is the regression line through the points. This yields the following equation for the reference concentration

$$c_0 = 0.0012 \cdot \rho_s \cdot \Theta_r^{1.3} \quad (5.2)$$

Forcing a cubic relationship (as proposed by Nielsen) between the modified effective Shields parameter and the reference concentration, the multiplication factor changed to 0.001 (black line). This is shown in figure 5.20 by the black line. An analysis performed by THORNE ET AL. (2001) for the complete set of *Deltaflume* data resulted in

$$c_0 = (0.0025 \pm 0.004) \cdot \rho_s \cdot \Theta_r^{2.9 \pm 0.2} \quad (5.3)$$

for the reference concentration (solid red line in figure 5.20). Here, the reference concentration was obtained by fitting a regression line to the measured sediment concentrations in the range of 2 cm to 8 cm above the ripple crest and extrapolating this line downwards to the crest level. The reduction of the multiplication factor for c_0 was associated with the possibility that the concentration measurements were not taken precisely above a ripple crest. However, it was thought that this factor was unlikely to account for the discrepancy of a factor of 2. Further explanation was given (THORNE ET AL., 2001) by the fact that the mean diameter in suspension was approximately equal to 0.211 mm. Only 16 % of the grains comprising the bed material were smaller or equal to 0.211 mm. Assuming that only 16 % of the bed material were capable of being suspended, this might have put an effective upper bound on the multiplication factor, which possibly did not exist for most of the data considered by NIELSEN (1986).

The investigation into the relationship between the reference concentration and the Shields parameter has shown that the number of available data points and the definition of the reference concentration determined from measurements is of vital importance. The analysis of the *Deltaflume* data suggested that the multiplication factor for the present data differs from the one proposed by NIELSEN (1986). However, due to the limited amount of data available for the present analysis it was thought that no reliable change to equation 2.70 could be proposed. Thus, it is assumed that equation 2.70 gives a better estimate of the

reference concentration. The mean diameter of 0.329 mm and the wave period of about 5 s for the present experiments lie within the range of experiments ($0.08 \leq d_{50} \leq 0.55$ mm and $1.0 \leq T \leq 9.1$ s) included in the study performed by NIELSEN (1986). Thus, equation 2.70 will be applied to estimate the reference concentration for the three different equations proposed by Nielsen. Later in section 5.2.3, two different empirical equations will also be investigated and their performance analysed in combination with a Rouse type distribution profile.

As mentioned in chapter 2, the equations for the suspended sediment concentration profiles proposed by NIELSEN (1992) differentiate between two types of entrainment processes: convection and diffusion. The diffusion process is caused by a concentration gradient, which is more dominant close to the bed. The convective process depends on large scale structures such as vortices, to suspend sediment further into the water column. Therefore, a better fit between predictions and measurements at higher levels above the bed using the convective or combined diffusive/convective approach is expected. The exponent in equations 2.68 and 2.69 was chosen to be equal to two, which is the same value as originally determined by NIELSEN (1992). Further, the mean diameter in suspension was chosen to be equal to a d_{16} at the bed. This assumption was based on sieve analyses from the pump samples. Figures 5.21 and 5.22 show examples of measured and predicted c-profiles for burst a07a (irregular waves, $H_s = 0.53$ m) and for burst a11a (regular waves, $H = 1.34$ m), respectively. Figure 5.21 exhibits a poor fit between measured and predicted c-profiles using any of the equations proposed by Nielsen. All three predicted c-profiles underestimate the measured concentrations. The exponential profile diverges from the measurements most rapidly and fails to produce the right shape for the c-profile. The c-profiles, determined using the empirical equations for convective and combined diffusive/convective entrainment, reproduce the correct shape of the c-profile, though they are about a factor of 300 smaller away from the bed. Turning the attention now to figure 5.22, the c-profiles based on convective entrainment yield a good agreement between measurements and predictions. Up to 10 cm and 20 cm above the bed (pure convection and combined diffusion/convection, respectively) the predicted concentrations are larger than the measured values. At greater distances from the bed they slightly underpredict the measurements. The good fit between the measurements and the predictions can also be seen in figure 5.23, which shows predicted versus measured concentrations. The solid black line is the 45° line representing a perfect fit. The two dashed lines represent $2 \cdot c_{\text{measured}}$ and $1/2 \cdot c_{\text{measured}}$, respectively. Most of the data can be seen to fall within this error band, indicating an agreement between predictions and measurements generally to within a factor of two, over nearly a two decade variation in the concentration. This suggests that there is

some merit in representing the convective entrainment process in the calculation for estimating sediment concentration profiles.

At the beginning of this analysis it was mentioned that the d_{50} value in the calculation was taken to equal the d_{16} value at the bed. An analysis using the d_{50} value at the bed in the equations yielded less agreement between measured and predicted concentrations. Thus, it was concluded that a suspended diameter should be used in the equations proposed by NIELSEN (1992).

After determining that the convective entrainment processes have to be included in the calculation to predict suspended sediment concentration profiles, equations 2.68 and 2.69 were investigated closer. So far, the exponent n in the two equations was taken to equal two, which is the value suggested by NIELSEN (1992), based on a specific set of data. Taking n as a free parameter, the best fit between predictions and measurements was determined. The parameter n was found to be in the range of 1.65 to 2.1. Figure 5.24 shows an example of measured and predicted sediment concentration profiles for burst a12a (irregular waves, $H_s = 1.26$ m), with a value of 1.8 for n . Close to the bed both the pure convective and the combined diffusive/convective approach overpredict the concentration within the first 10 cm and 20 cm, respectively. They then underpredict the measured concentration values up to a height of 50 cm above the bed, before there is a good fit between prediction and estimate up to 1 m above the bed. It should be pointed out, at this stage, that the pure convective approach yielded a better agreement between measurements and predictions close to the bed than the combined diffusive/convective approach. This was slightly surprising, because it is thought that it is the near bed region that is dominated by diffusive entrainment. The fit between measurements and predictions is also highlighted in figure 5.25, which shows the predicted versus the measured sediment concentrations. Over a variation in sediment concentration of over two decades the agreement is generally within at least a factor of two, except for the large concentration values occurring close to the bed.

At first sight, there does not seem to be much difference between the purely convective and the combined diffusive/convective approach apart from close to the bed. A plot of the concentration profiles on a log-log scale gives some more insight (figure 5.26), highlighting the differences in curvature. The measured c -profile is linear over the first 10 cm, then upward convex for the next 25 cm and then upward concave. This complex shape is only modelled by the combined diffusive/convective approach, though the concentration values differ from the measured ones.

5.2.3 Rouse type concentration profiles

Section 5.2.2 has shown the importance of including the convective entrainment process in the empirical equations. This section concentrates on the description of the vertical sediment distribution using the Rouse type distribution with two different expressions for the reference concentration (equations 2.73 and 2.75) proposed by ZYSERMAN AND FREDSE (1994), and VAN RIJN (1989), respectively. Estimating suspended sediment concentrations using the Rouse type distribution has been shown to be successful by WILLIAMS ET AL. (1996 and 1999b), amongst others.

In the empirical equations, the particle diameter at the bed was taken to be equal to the mean diameter ($d_{50} = 0.329$ mm), which affects the reference concentration and the threshold for suspension. Again, the value of d_{16} at the bed was used as the mean diameter in suspension. Initially the value of γ in equation 2.63, which is the ratio of sediment diffusivity to eddy viscosity, is taken to be equal to one as suggested by WILLIAMS ET AL. (2000). The parameter γ can be modified to reflect mechanisms such as grain-grain interaction, hindered settling due to turbulence and the non-linearity of the drag force. The influence of γ will be shown later.

In general, it turned out that the predicted c-profiles systematically overestimated the measured concentration values at almost all heights and bursts. The reference concentration determined using Van Rijn's approach (equation 2.75), generally gave a closer fit with the measured value at the bed. In contrast, the values determined with equation 2.73 suggested by ZYSERMAN AND FREDSE (1994), overestimates the measured concentration at the bed. Figures 5.27 and 5.28 show examples of predicted and measured c-profiles for burst a08a (regular waves, $H = 0.85$ m) and a12a (irregular waves, $H_s = 1.26$ m), respectively. Turning the attention first to figure 5.27, the Rouse type profile together with the reference concentration proposed by VAN RIJN (1989), yields a good fit between measured and predicted c-profiles, especially within the first 20 cm above the bed. This is confirmed in figure 5.29, which shows predicted versus measured (2.0 MHz ABS) concentration values over the whole vertical range. The predicted values are within a factor of two of the measurements over almost a decade variation in concentration.

Figure 5.28 shows a poor fit between the predicted and the measured c-profiles for both expressions of the reference concentration. It should be pointed out though that the equation proposed by VAN RIJN (1989), for the reference concentration, produces a good agreement with the measured value. With increasing distance from the bed, the c-profile diverges from the measurements. Due to the large wave height ($H_s = 1.26$ m) the mean diameter in

suspension might be larger than the chosen value of d_{16} at the bed. This might explain why the predicted concentration values are larger further away from the bed.

Taking the parameter γ as a free parameter and tuning it to the measured c-profiles, it turned out that a value closer to 0.5 produced a better agreement between measured and predicted profiles together with the reference concentration proposed by VAN RIJN (1989), for most of the bursts. An improvement in the square error between measurements and predictions obtained by changing the value of γ from 1.0 to 0.5 of at least 20 % for all the bursts except burst a07a was determined. For the two bursts presented in figures 5.27 and 5.28, the closest fit was achieved with values of gamma of 0.6 and 0.3, respectively. For burst a08a (figure 5.30) and a12a (figure 5.31), there is very good agreement within the first 0.5 m above the bed before it diverges from the measurements. This is confirmed in figure 5.32, which shows predicted versus measured concentrations. The predicted values are within at least a factor of two for concentration values larger than 0.01 g/l. For high concentrations (i.e. close to the bed) they are scattered around the perfect fit (45 degree) line. The reader is reminded that a value of $\gamma = 0.5$ implies that the sediment diffusivity is half the eddy viscosity, i.e. only half the turbulence generated by the waves is utilised to suspend sediment.

5.2.4 Summary

The performance of empirical equations predicting suspended sediment concentration profiles was under scrutiny in this section. Apart from the uncertainties with the equations to predict concentration values and the suggested variations in the equations, remaining uncertainties such as the input parameters and the bed roughness were analysed. Some uncertainties existed with the ripple dimensions, which might have been slightly different at the position of the ABS transducers than those measured by the Acoustic Ripple Profiler (ARP) mounted on STABLE. Further, the value of the sand grain roughness is quoted in the literature to vary from $1.25 \cdot d_{35}$ to $5.1 \cdot d_{84}$, SLEATH (1984). For the present experiment this is a difference of about a factor of ten for the sand grain roughness. Attempts have been made to vary the sand grain roughness within this range and additionally, a sensitivity analysis with respect to the input parameters (H or H_s , T or T_p , h_r , λ_r) determined from the measurements was performed. No consistent trend of improvement between the measured and the predicted concentration profiles was found.

Further, the uncertainties associated with the reference concentration still remain. Three different empirical equations to calculate the reference concentration were analysed. A

possible change to equation 2.70 proposed by NIELSEN (1986), was discussed. However, the suggested change was based on the analysis of a limited amount of data, and thus there was not enough confidence in the resulting relationship to propose a change to Nielsen's equation for the reference concentration.

An analysis of the performance of the empirical equations proposed by NIELSEN (1992), with respect to the *Deltaflume* data was performed by THORNE ET AL. (2001). They investigated the different length scales for the diffusive (L_d) and the convective entrainment (L_c). A relationship between the two different scales was suggested and the implications on the equations discussed. For more detailed information the reader is referred to the paper by THORNE ET AL. (2001).

Using the suspended diameter, the empirical equations and the expressions for the shape functions based on a convective or combined diffusive/convective entrainment, proposed by NIELSEN (1992), performed well at distances more than 40 cm above the bed (except for burst a07a) with a modified exponent. Best agreement between measurements and prediction was found for a value of n of less than two. The exponential shape function, based on a purely diffusive entrainment, performed poorly over the whole vertical range and diverged quickly from any measured concentration values. The bed was rippled for all six bursts under scrutiny. LEE AND HANES (1996), investigated the performance of a pure diffusion, a pure convection and a combined diffusion/convection model for different wave conditions in the field. Their conclusions were that the vertical distribution of suspended sediment was well described by the diffusion model for high wave conditions with no ripples, while the convective model worked better under low wave conditions with a rippled bed. Further, the predictions were improved by the use of multiple velocity classes depending on the sediment diameter classes under high wave conditions, while there was no improvement under low wave conditions. On a flat bed the sediment entrainment is dominated by turbulent diffusion, whereas on a rippled bed the convective entrainment by vortices formed in the lee of ripples is more important.

The Rouse type profile, though based on a diffusive approach, together with an expression by VAN RIJN (1989), for the reference concentration yielded a very good agreement (within a factor of two) between measured and predicted c -profiles. The fit was improved by changing the ratio of sediment diffusivity to eddy viscosity (γ) from unity. A value of around 0.5 gave a good agreement between measured and predicted concentration values. This seems in contrast to the generally accepted value of $\gamma > 1$ for oscillatory flow over rippled beds.

Further, it was found that the reference concentration determined by the equation proposed

by VAN RIJN (1989), yielded a much closer agreement with the measurements than the expression proposed by ZYSERMAN AND FREDSSØE (1994). This is opposite to the findings by WILLIAMS ET AL. (1999b).

Overall it has to be emphasised again that the ripple dimensions present under irregular waves were relics of the ripples formed under the previous burst of regular waves. The bed was not flattened in between bursts. This led to larger ripple dimensions than those that would naturally form under irregular waves with a specific significant wave height.

No further attempt was made to improve on the agreement between measured and predicted suspended sediment concentrations. This section highlighted some of the difficulties associated with empirical equations. Especially for irregular waves, the burst averaged c-profile does not take into account intra-burst suspension events. A more detailed study of intra-burst suspension will be presented in chapter 6.

5.3 Ensemble averaged c-profiles over a wave cycle for regular waves

For two bursts with regular waves calibrated ABS data were available. Figure 5.33 and 5.35 show ensemble sediment concentrations from the 1.0 MHz ABS sensor for one wave cycle up to a height of 20 cm above the bed for bursts a11a ($H = 1.34$ m) and a08a ($H = 0.85$ m), respectively. Also shown at the bottom of each graph is the ensemble horizontal velocity measured by the lowest ECM heads mounted on STABLE. There were a total of 205 waves in the two bursts. Each wave consisted of 21 individual data points. In order to analyse the significance of the data, different number of waves were averaged to produce ensemble average plots. Turning the attention first to figure 5.33, the maximum concentration occurs clearly at the points of flow reversal and after the passing of the crest. The same response was found for the 2.0 MHz ABS transducer (not shown here). A rapid drop (within one data step) in concentration at the trough ($\sim 90^\circ$) is noticeable. This is very surprising as it also only occurs for a very short time ($\sim 35^\circ$) in the cycle. Ensemble averaging different numbers of waves, the drop in concentration occurs in each subsection of the burst and also for both ABS transducers. It is more noticeable in the 2.0 MHz transducer, even though this one is less sensitive. Thus it is concluded, that the drop in concentration at the trough must be real and cannot be attributed to random noise in the signal. For the first 50 waves (figure 5.34) - about 4 minutes of the burst- (and the same applies for the first 100 waves in the burst), there is hardly any re-suspension of sediment at the time of the zero up-crossing for the 2.0 MHz ABS transducer. This is in contrast to the ensemble average plots for the 1.0 MHz

ABS sensor. The difference in the ensemble averaged concentrations for the two ABS transducers is not surprising. The cross correlation of the suspended sediment time histories of the two ABS sensors has shown that there is hardly any correlation between the sediment concentrations measured by the two sensors for heights of less than about 20 cm above the bed.

The analysis of ensemble averaging various numbers of waves showed some inconsistency. First, it has to be considered whether the near bed horizontal velocities shown in figures 5.33 to 5.36 do really represent the near bed velocities at the position of the ABS transducers. The ECM heads are separated from the ABS sensors by about 23 cm along the flume. With a wavelength of approximately 30 m, it is assumed that the longitudinal separation of 23 cm is not significant with respect to phase shifts in the velocity signal. Secondly, the position of the ABS transducers relative to the ripples has to be considered. As mentioned in chapter 3, the ripples migrated under regular waves. For clarification, the bedforms recorded by the Acoustic Ripple Profiler and the position of the ECM heads and the ABS sensors are shown in figures 5.37 and 5.38 for bursts a11a and a08a, respectively. For approximately the first 10 minutes of burst a11a, the ABS sensors were located above a ripple crest. Then, a ripple trough moved through until the ABS transducers were half way up the ripple slope. As the re-suspension events are driven by vortices, which form in the lee of ripples, the position of the ABS transducers relative to a ripple crest or trough is of importance. Furthermore, it has to be kept in mind that the acoustic sensors recorded “snap shots” of sediment clouds that were advected past the sensors. Thus, the measured suspended sediment concentration cannot necessarily be explained by the local hydrodynamics and bedforms at the position of the ABS transducers.

Figures 5.35 and 5.36 show the ensemble average for burst a08a for the 1.0 and 2.0 MHz ABS sensors, respectively. In contrast to burst a11a, figures 5.35 and 5.36 do not show consistency between the data recorded by the 1.0 and 2.0 MHz ABS transducers. Again this can be explained by the lack of correlation between the 1.0 MHz and 2.0 MHz ABS transducers up to a height of 20 cm as mentioned previously. Figure 5.35 exhibits a more or less continuous sediment suspension over the entire wave cycle. At the time of the zero up-crossing, the sediment is entrained to a height of about 20 cm above the bed. This is fairly consistent for the various subsets of ensemble averaged concentrations. However, the ensemble average for the last 50 waves does not follow this pattern, as the sediment only reaches up to about 10 cm above the bed and actually settles after the zero up-crossing. In figure 5.36 the sediment re-suspension peaks at flow reversal and after the passing of the wave crest, where the horizontal velocity is at a maximum. The re-suspension is small at the

zero up-crossing of the wave cycle. This is consistent for all the ensemble averages analysed for this ABS sensor and bursts. Again, the relative position of the acoustic sensors relative to the ripples can explain at least some if not all of the inconsistencies between the ensemble averages of the whole burst and the last 50 waves. At the beginning of burst a08a the ABS transducers are positioned approximately around a ripple trough, while for the last 8 minutes they are positioned close to a ripple crest. The ripple migration rate was 0.04 cm/s for this burst, which is equivalent to about one ripple wavelength during the 20 minute burst. OSBORNE AND VINCENT (1996), stated that the phase relationship between the sediment concentration and the orbital velocity depends strongly on the position of the ABS transducers relative to the bedforms. NIELSEN (1988), noted that most of the sediment transport under waves over vortex ripples occurs above the ripple crest, and that the entrainment happens virtually instantaneously as single events at the time of free stream velocity reversal. At flow reversal the lee vortices with their clouds of sand move upwards into the main flow.

RIBBERINK AND AL-SALEM (1995), presented ensemble averages of measurements of flow and sediment dynamics in a large oscillating tunnel. They analysed the phase relation between the near bed sediment suspension and the orbital velocity of an asymmetric wave and a sinusoidal wave. The degree of asymmetry given by $U_c/(U_t + U_c)$, where the indices c and t denote the crest and trough velocities, respectively, was 0.66. Figures 5.39 and 5.40 show the ensemble average sediment concentration for a number of heights above the bed for the asymmetric wave and the sinusoidal wave, respectively. In figure 5.39 the maximum concentration at $z = 0.5$ cm almost coincides with the maximum crest velocity outside the boundary layer. At higher elevations the concentration peaks reduce in magnitude and show an increasing phase lag. This phase lag was attributed to the travelling time of the grains needed for vertical re-suspension and settling during the wave cycle. Just before flow reversal of the free stream velocity additional concentration peaks occur in the lowest centimetre. These peaks gradually transform into the dominating main concentration peak at higher elevations ($z > 1.5$ cm) in phase with the peak trough velocity. It has been argued that these type of events near the moments of flow reversal are the result of shear instabilities in the wave boundary layer. For the sinusoidal condition (figure 5.40) the concentrations are almost symmetrical about the zero crossing and in phase with each other. There is a small phase lag with respect to the peaks in the free stream velocity. HAY AND BOWEN (1994b), also looked at the ensemble averages of flow and sediment dynamics taken in the field. The waves were slightly asymmetric. In contrast to RIBBERINK AND AL-SALEM (1995) they reported two distinct peaks in phase with the crest and trough velocities,

respectively. The peaks were well separated up to 20 cm above the bed. Under the crest, the concentration peaks were in phase in the first 5 to 15 cm above the bed, while there was a progressive increase in the delay of the returning peak with distance from the bed.

The degree of asymmetry of bursts a11a and a08a were 0.55 and 0.53, respectively, which is close to a pure sinusoidal wave with a value of 0.5. The peaks just before flow reversal after the passing of the crest, as reported by RIBBERINK AND AL-SALEM (1995), can be seen in figures 5.33 and 5.34. However, they are larger than the peaks under the crest, which is in contrast to the findings by RIBBERINK AND AL-SALEM (1995). Further, the lack of re-suspension under the trough can also be observed, though it is only visible for about 0.5 seconds (wave period was approximately 5 s).

NIELSEN (1992), showed that there is a peak in concentration during each half of the wave period, which occurs shortly before the crest and trough velocities, respectively at $z = 1$ mm above the bed. With increasing distance from the bed the peak reduces and is in phase with the peaks of the free stream velocities. Figure 5.41 indicates a peak in concentration just before the passing of the velocity under the crest, which is consistent with the present data. However, no phase shift with increasing distance from the bed can be observed in the present data as seen in figure 5.41.

At this point it has to be emphasised that the results reported by RIBBERINK AND AL-SALEM (1995), and NIELSEN (1992), focused on the first 2 cm above the bed. For the present data, there were only two measuring intervals up to 2 cm above the bed, so that changes in ensemble sediment concentration below 1 cm above the bed cannot be compared and no conclusions can be drawn. Thus, it is not surprising that the present data do not expose the same phase relationships between the sediment concentrations and the free stream velocity as shown by the other researchers.

VILLARD ET AL. (2000), produced ensemble averages of a repetitive wave group and observed holes in the suspended sediment concentrations, where the concentration was significantly lower than at other times in the wave group. HAY AND BOWEN (1994a), suggested that these are the result of coherent antecedent suspension passing through the transducer beam. From the evidence given by VILLARD ET AL. (2000) it is difficult to confirm Hay and Bowen's explanation. The passing of a coherent structure through the ABS transducer seems more likely to be detected as a spike in the concentration measurement than a hole. As the holes were observed at a zero up-crossing, they might be due to the stretching of the velocity due to the acceleration of the particles ($\partial u / \partial x$) described by LIGHTHILL (1979).

From the ensemble averages presented here, it has to be concluded that migration of the ripples during the burst influenced the sediment re-suspension, such that there was no clear phase relationship between the sediment suspension and the free stream velocity. Furthermore, the ripple migration resulted in a lack of consistency between the ensemble averages of different number of waves.

5.4 Comparison with pump-sampling data

5.4.1 Presentation of results

As discussed in chapter 3, there was a difference between the pump-sampling data measured by the sampling nozzles on STABLE and those recorded away by DH at the side of the flume for regular waves. Various possibilities for this phenomenon were discussed. For the comparison of the ABS data with the pump-sampling data, only samples taken at STABLE were taken into account.

Figure 5.42 shows the concentration data for regular waves (5.42a and 5.42b) and for irregular waves (5.42c-f). The individual plots either range up to approximately 100 cm (range of the ABS data) above the bed for bursts where there were no pump-sampling measurements above this height or up to the height of the last pump sample measurement. In general there is a reasonably good fit between the pump-sampling and the ABS data, especially at low heights above the bed. However, it is worth noting that there is an increased discrepancy between the pump-sampling and the ABS data with increased distance from the bed for burst a08a (regular waves, $H = 0.85$ m, figure 5.42a). There is a good agreement within the first 20 cm above the bed, but at a distance of about 100 cm above the bed the sediment concentration determined by the pump samples is about a factor of 50 larger than the one derived from the ABS data. This behaviour is unusual compared to the other bursts in figure 5.42. For burst a07a and a09a (figures 5.42c and d), pump samples were only recorded up to a height of 25 cm and 40 cm, respectively. Thus, no evaluation of the agreement between pump-sampling and ABS data can be made beyond this point.

5.4.2 Discussion of results and conclusions

It was not surprising that there was a reasonably good agreement between the pump-sampling and the ABS data, because the sediment concentration determined from the volumetric analysis of the pump samples was used to calibrate the ABS data. The

calibration of the ABS data was performed by Dr P. Thorne from POL. Thus, it is very difficult for the author to comment on the discrepancies between the pump-sampling and ABS measurements, which could be due to experimental differences between the two measuring devices or the calibration itself.

The efficiency of the pump-sampling nozzles depends on the intake velocity, the grain size, orientation of the nozzle to the flow and the nozzle diameter itself (BOSMAN ET AL., 1987). The preferred orientation of the nozzles under waves is at right angles to the orbital flow. Though, the nozzles were mounted on STABLE to be pointing at right angle to the flow, the misalignment of STABLE with the flume (see chapter 3) meant that the nozzle orientation was no longer at right angles to the flow (by about 16°). However, NELSON AND BENEDICT (1950), reported that up to a 20° misalignment of intake and ambient flow the influence of the trapping coefficient, which in turn influences the sediment concentration, is negligible. Problems associated with the measurement of the pump-sampling concentration was highlighted in chapter 3 and could contribute to the differences between the pump samples and the acoustic concentration measurements.

The ABS signal is influenced by the grain size, the concentration itself, the frequency of the transducer signal and the distance from the transducer. The calibration approach for the acoustic backscatter data was based on a pump sample concentration measurement at one height above the bed as a reference concentration. Thus, the differences between the ABS measurements and the pump samples are in part due to the calibration of the voltage transfer function for the system, and also to the present limited knowledge of the variability of the backscattering and attenuation characteristics of different sediments. VINCENT ET AL. (1994) mentioned that the uncertainties in the concentrations associated with ABS measurements were $\pm 15\%$.

5.5 Summary and Conclusions

The suspended sediment concentration time histories and mean suspended sediment profiles were investigated in this chapter. The main findings can be summarised as follows:

- Sediment suspension under irregular waves was found to be dominated by individual suspension events occurring under large waves and wave groups. These suspension events were in general larger than the continuous suspension under regular waves. The mean sediment concentration close to the bed for the whole burst was larger under regular than irregular waves, due to the continuous suspension throughout the burst.

- The time histories showed good vertical coherence up to about 20 cm above the bed. With increasing height a phase lag was determined, due to the time delay for sediment to be entrained further into the water column. For irregular waves, the dependency of the suspension events on the wave period was observed. The horizontal coherence between the 1.0 MHz and 2.0 MHz ABS transducer was less apparent with high correlation at $z = 5$ cm and $z = 15$ cm above the bed for the irregular and regular waves, respectively. As the ABS sensors recorded “snap shots” of sediment suspension clouds passing through the acoustic beam, it was not surprising to find less horizontal coherence. Only if the advected clouds were large enough, would they have been picked up by the sensors.
- The performance of empirical equations to predict suspended sediment concentration profiles and expressions for the reference concentration was analysed, Nielsen’s expression for the shape function, based on convective or combined diffusive/convective entrainment and the Rouse type function were found to yield good agreement (within a factor of two or better) between measurements and predictions. The expressions proposed by NIELSEN (1992), performed better further away from the bed, where the convective entrainment was dominant, while the Rouse type profile gave a better fit within the first 50 cm above the bed. Close to the bed the diffusive entrainment process is more important, which is the reason for the good performance of the Rouse profile in this region. The ratio of sediment diffusivity to eddy viscosity (γ) used in the Rouse profile was closer to 0.5 in order to yield a better agreement between measured and predicted concentration values.

The need for using a suspended grain diameter was discussed. The equation proposed by VAN RIJN (1989) for the suspended diameter (equations C1 and C2) were within approximately 25 % of the measured values determined from the pump samples.

The expression suggested by VAN RIJN (1989), for the reference concentration performed well and gave the closest fit to measurements, while the other two expressions (NIELSEN, 1986 and ZYSERMAN AND FREDSE, 1994) lead to overpredictions for all bursts except burst a07a.

- The analysis of the ensemble averaged c-profiles for the regular waves highlighted the problems associated with ripple migration and the limited amount of data. Under oscillatory flow over a rippled bed, vortex ejection occurs in the lee of the ripples. Due to ripple migration the relative position of the ABS sensors to a ripple crest varied throughout a burst, resulting in a poor consistency of the ensemble averages for different number of waves. Further, the limited amount of data prevented a definite conclusion of

the phase relationship between cycle averaged sediment concentrations and near bed orbital velocities.

- Based on the limited knowledge of the calibration of the acoustic backscatter data (performed by Dr P. Thorne at POL) the agreement between mean c-profiles determined from the ABS and the pump samples was good. Some discrepancies between the two profiles occurred further away from the bed.

TABLES

BURST	Wave height [m]	Gradient within the first 3 cm from the bed		Main gradient		Theoretical gradient for the first 3 cm above the bed		Main gradient from theory
		1 MHz	2 MHz	1 MHz	2 MHz	Rouse type profile	Nielsen	Rouse type profile
A07a	0.53	0.0931	0.1245	0.2838	0.2501	0.0596	0.051	0.4123
A09a	0.83	0.1141	0.1163	0.1963	0.1972	0.1093	0.097	0.2361
A10a	1.07	0.1006		0.2844		0.1675	0.152	0.3231
A12a	1.26	0.0900		0.3169		0.2033	0.187	0.3780

Table 5.1: Gradients (absolute values) within the first 3 cm above the bed and main gradient for the bursts with irregular waves on a semilogarithmic plot. They are compared with the theoretical values given by the empirical equation by Nielsen and the Rouse type profile. The gradient determined by the equation suggested by Nielsen is constant for the whole profile. The wave height increases from burst a07a to a12a.

BURST	Wave height [m]	Concentration at the bed [g/l]	
		1MHz	2MHz
A07a	0.53	0.96	0.54
A09a	0.83	1.26	1.40
A10a	1.07	2.99	
A12a	1.26	8.45	

Table 5.2: Concentration 1 cm above the bed for burst averaged c-profiles for bursts with irregular waves. The wave height increases from burst a07a to a12a.

parameter	units	regular waves		irregular waves				description
		A08a	A11a	A07a	A09a	A10a	A12a	
<i>Test</i>								
<i>H</i>	<i>m</i>	0.85	1.344					wave height
<i>H_s</i>	<i>m</i>			0.532	0.826	1.066	1.258	significant wave height
<i>T</i>	<i>s</i>	5.0	5.0					wave period
<i>T_p</i>	<i>s</i>			5.0	4.9	5.1	5.1	peak wave period (JONSWAP)
<i>T_z</i>	<i>s</i>			3.5	4.1	3.8	4.1	zero-crossing period (JONSWAP)
<i>ω</i>	<i>s⁻¹</i>	1.26	1.26	1.26	1.28	1.23	1.23	angular wave frequency
<i>U_w</i>	<i>m/s</i>	0.47	0.74	0.29	0.45	0.60	0.70	peak orbital velocity
<i>A</i>	<i>m</i>	0.374	0.591	0.234	0.35	0.484	0.572	semi-orbital excursion
<i>σ_s</i>	*	1.70	1.70	1.70	1.70	1.70	1.70	grain sorting parameter
<i>T_s</i>	*	2.41	5.72	0.706	2.24	3.81	5.14	transport parameter
<i>τ_t</i>	<i>N/m²</i>	0.197	0.197	0.197	0.197	0.197	0.197	threshold bed shear stress
<i>D_s</i>	*	6.41	6.61	6.31	6.40	6.50	6.58	dimensionless grain size
<i>w_s</i>	<i>m/s</i>	0.027	0.027	0.027	0.027	0.027	0.027	settling velocity
<i>h_r</i>	<i>m</i>	0.041	0.066	0.037	0.047	0.057	0.058	measured ripple height
<i>λ_r</i>	<i>m</i>	0.32	0.54	0.36	0.35	0.49	0.50	measured ripple wavelength
<i>k_{sG} · 10⁻⁴</i>	<i>m</i>	3.29	3.29	3.29	3.29	3.29	3.29	sand grain roughness
<i>A/ksG</i>		1136.8	1797.4	711.5	1068.6	1471.9	1737.0	relative roughness
<i>k_{sR}</i>	<i>m</i>	0.042	0.064	0.030	0.051	0.053	0.054	ripple roughness
<i>f_{wG}</i>	*	0.0061	0.0048	0.0078	0.0063	0.0053	0.0049	grain wave friction factor
<i>f_{wR}</i>	*	0.076	0.075	0.082	0.086	0.075	0.069	ripple wave friction factor
<i>U_{wG}</i>	<i>m/s</i>	0.026	0.037	0.018	0.025	0.031	0.035	peak wave shear velocity (grain)
<i>U_{wR}</i>	<i>m/s</i>	0.096	0.144	0.060	0.094	0.116	0.131	peak wave shear velocity (ripple)
<i>2U_{wG}² / Aω²</i>		0.0023	0.0028	0.0018	0.0022	0.0026	0.0028	wave friction factor
<i>L</i>	<i>m</i>	0.038	0.0924	0.022	0.042	0.066	0.081	mixing length
<i>θ_s</i>	*	0.126	0.2487	0.0631	0.120	0.178	0.2273	grain Shields number
<i>Beta</i>	<i>m</i>	1.0	1.0	1.0	1.0	1.0	1.0	multiplier for grain roughness
<i>gamma</i>	<i>m</i>	1	1	1	1	1	1	multiplier for van Rijn ripple roughness
<i>ψ_w</i>	*	41.35	103.4	16.2	38.0	66.63	92.79	sediment mobility number
<i>C₀</i>	<i>g/l</i>	4.96	43.03	0.222	4.99	11.46	26.56	(Nielsen)
<i>C(a) z&R</i>	<i>g/l</i>	10.76	51.94	0.784	9.36	25.15	43.07	(Zyserman & Fredsoe)
<i>C(a) VR</i>	<i>g/l</i>	3.31	8.14	0.670	2.55	4.92	7.87	(van Rijn)
<i>α</i>		2.55	1.82	3.61	2.62	2.15	1.9	Exponent in Rouse type profile for $z_s = v$
<i>h_{r,pred,reg}</i>	<i>m</i>	0.050	0.030	0.044	0.049	0.046	0.036	Ripple height Nielsen reg. waves
<i>λ_{r,pred,reg}</i>	<i>m</i>	0.37	0.31	0.31	0.36	0.37	0.34	Ripple wavelength Nielsen reg. waves

Table 5.3: Input and calculated parameters used to determine concentration profiles on the medium sand bed.

FIGURES

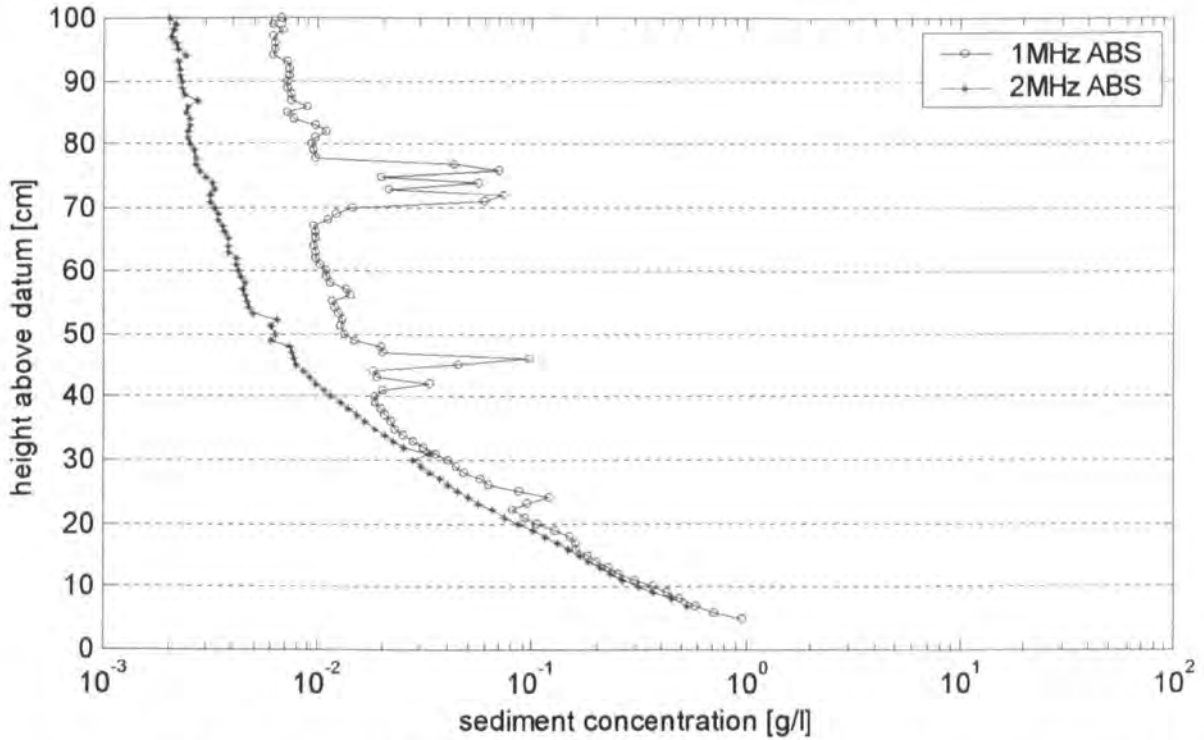


Figure 5.1: Burst averaged suspended sediment concentration profiles for burst a07a (irregular waves, $H_s = 0.53$ m).

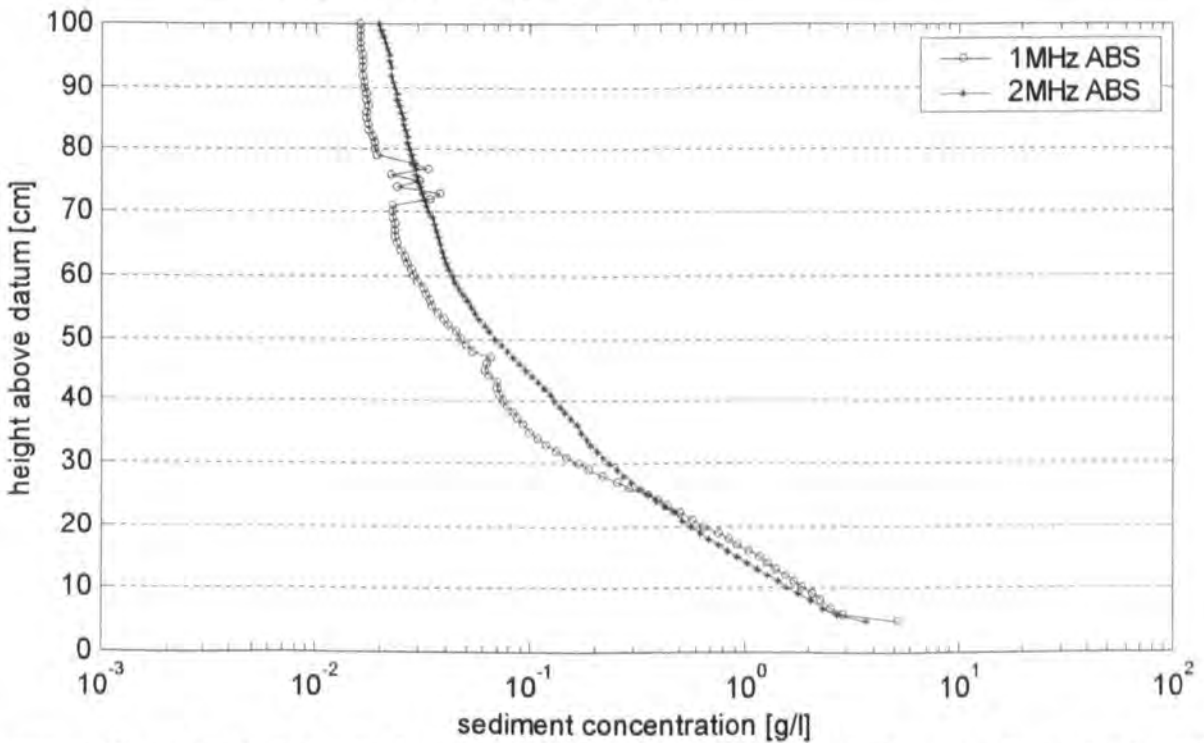


Figure 5.2: Burst averaged suspended sediment concentration profiles for burst a08a (regular waves, $H = 0.85$ m).

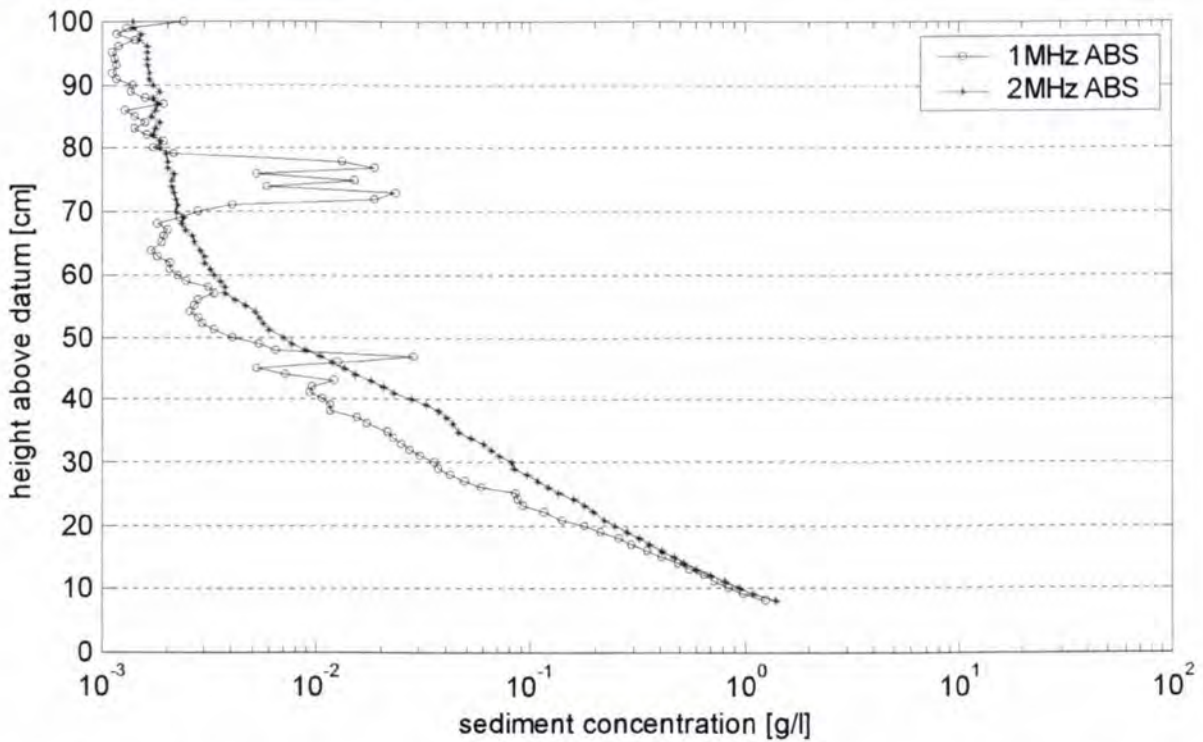


Figure 5.3: Burst averaged suspended sediment concentration profiles for burst a09a (irregular waves, $H_s = 0.83$ m).

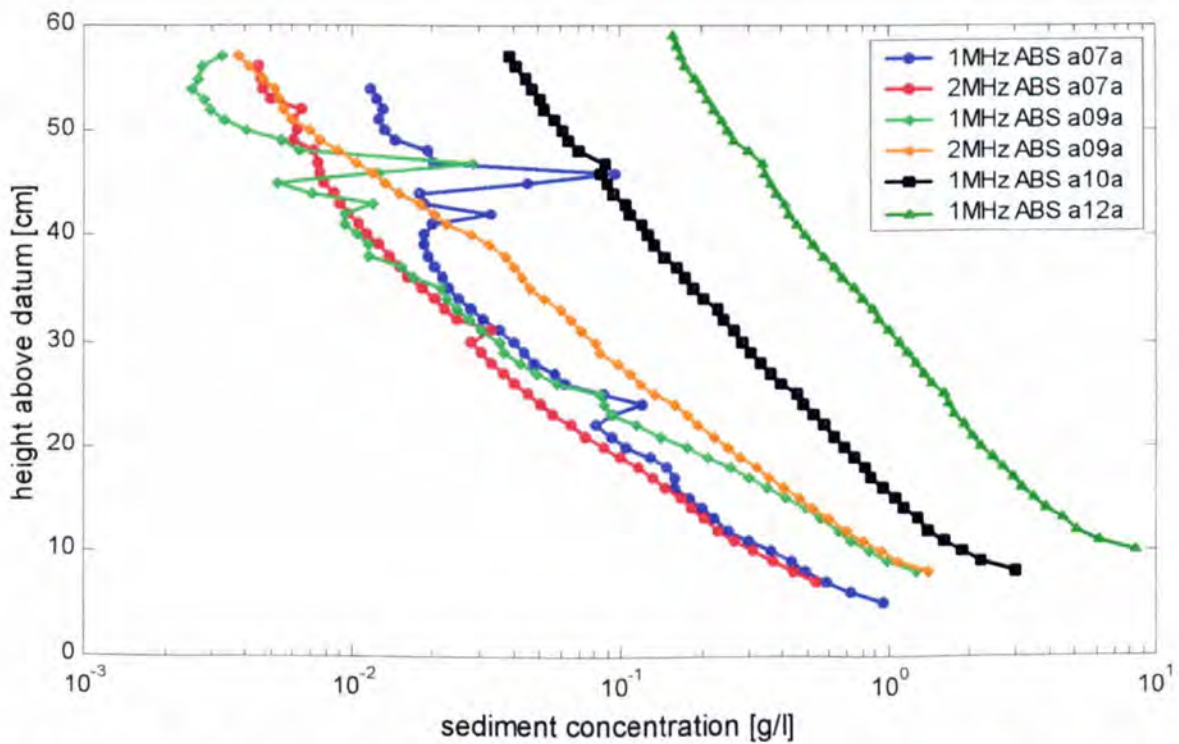


Figure 5.4: Burst averaged suspended sediment concentration profiles for the irregular bursts. The gradient increases with increasing wave height.

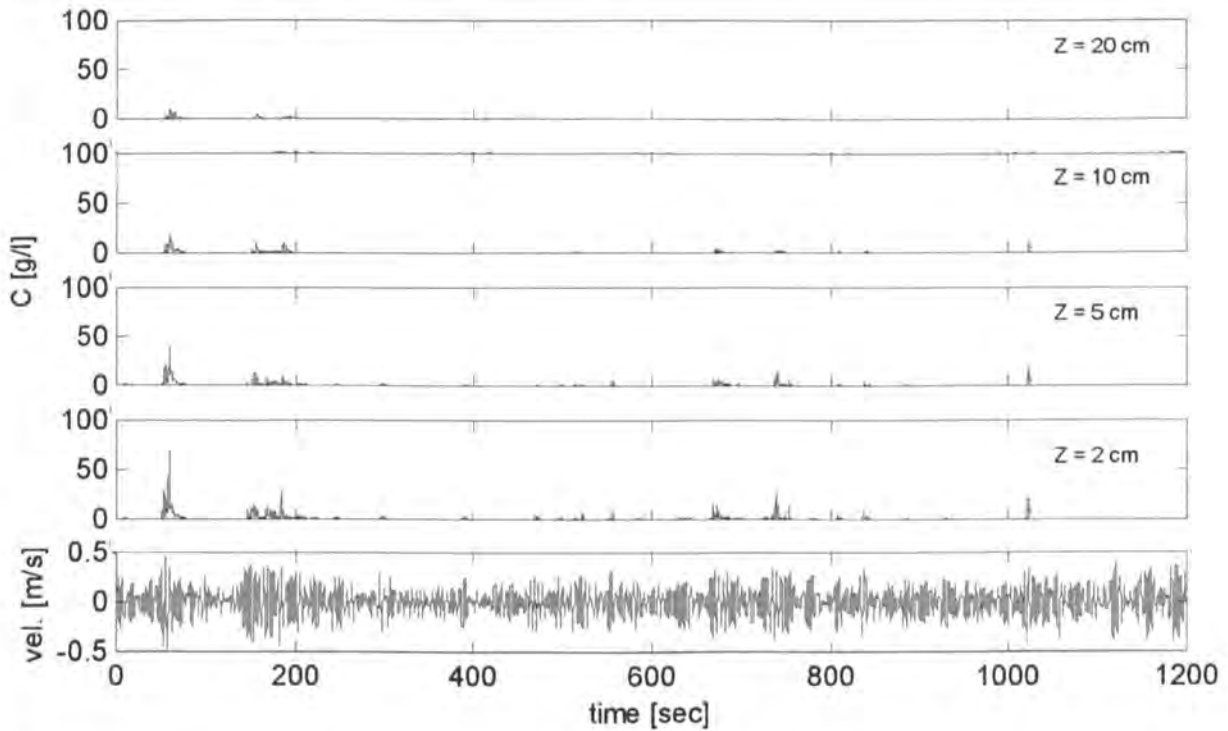


Figure 5.5: Suspended sediment concentration time series and synchronous near bed horizontal velocity for burst a07a (irregular waves, $H_s = 0.53$ m).

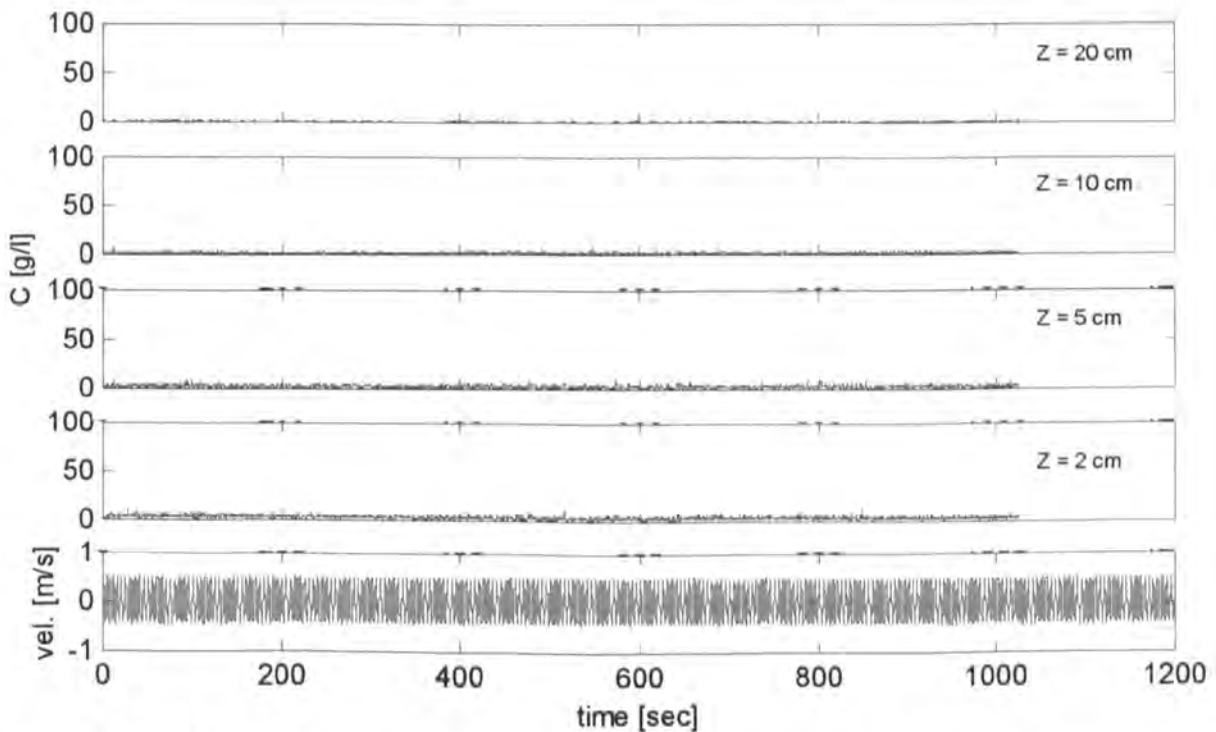


Figure 5.6: Suspended sediment concentration time series and synchronous near bed horizontal velocity for burst a08a (regular waves, $H = 0.85$ m).

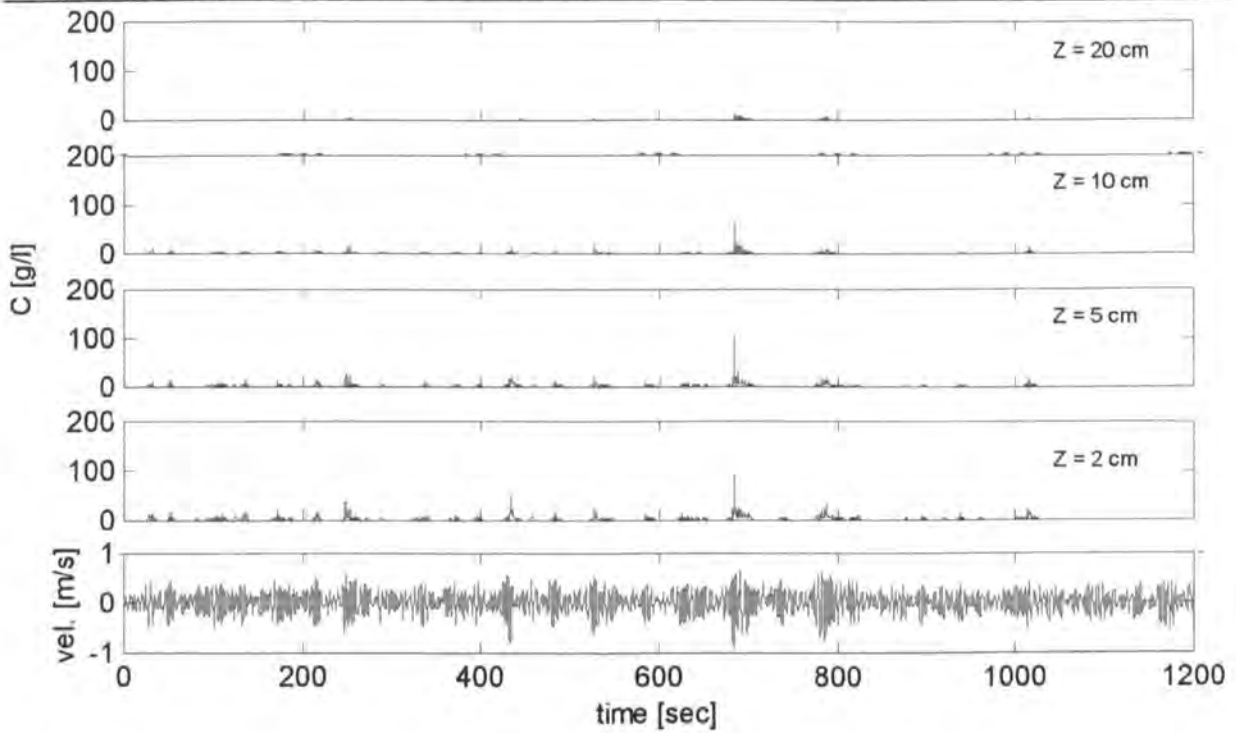


Figure 5.7: Suspended sediment concentration time series and synchronous near bed horizontal velocity for burst a09a (irregular waves, $H_s = 0.83$ m).

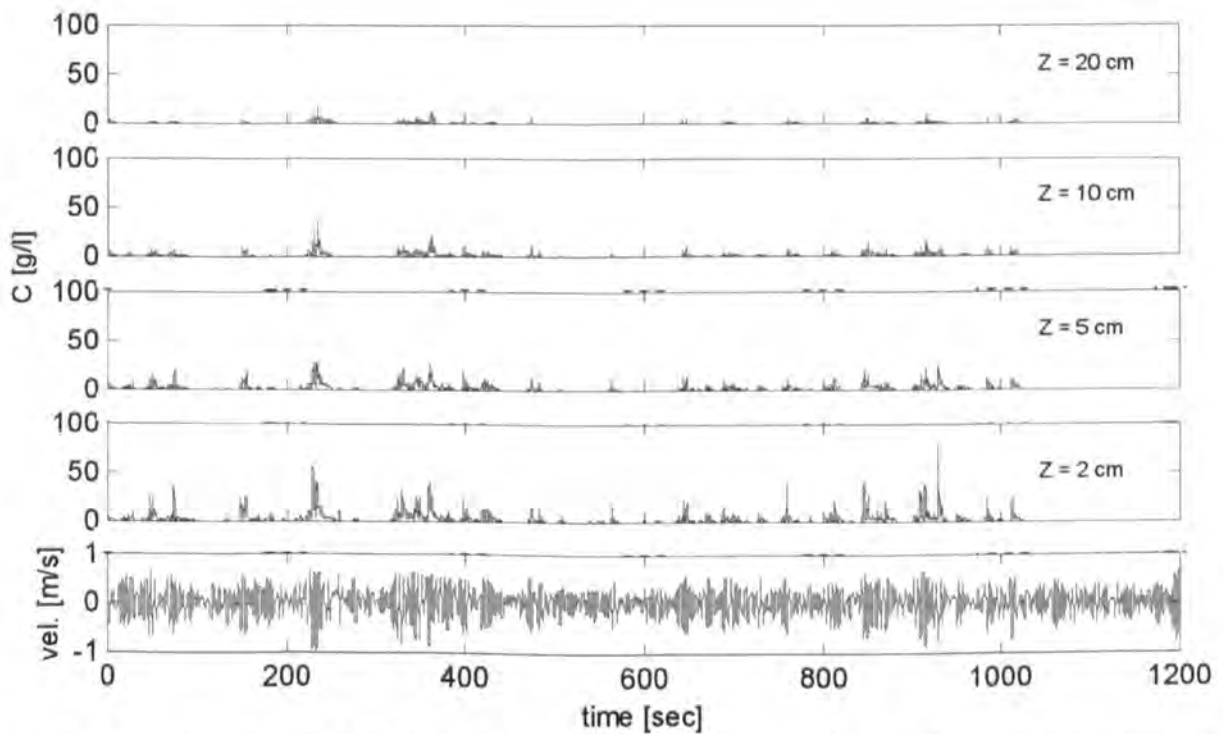


Figure 5.8: Suspended sediment concentration time series and synchronous near bed horizontal velocity for burst a10a (irregular waves, $H_s = 1.07$ m).

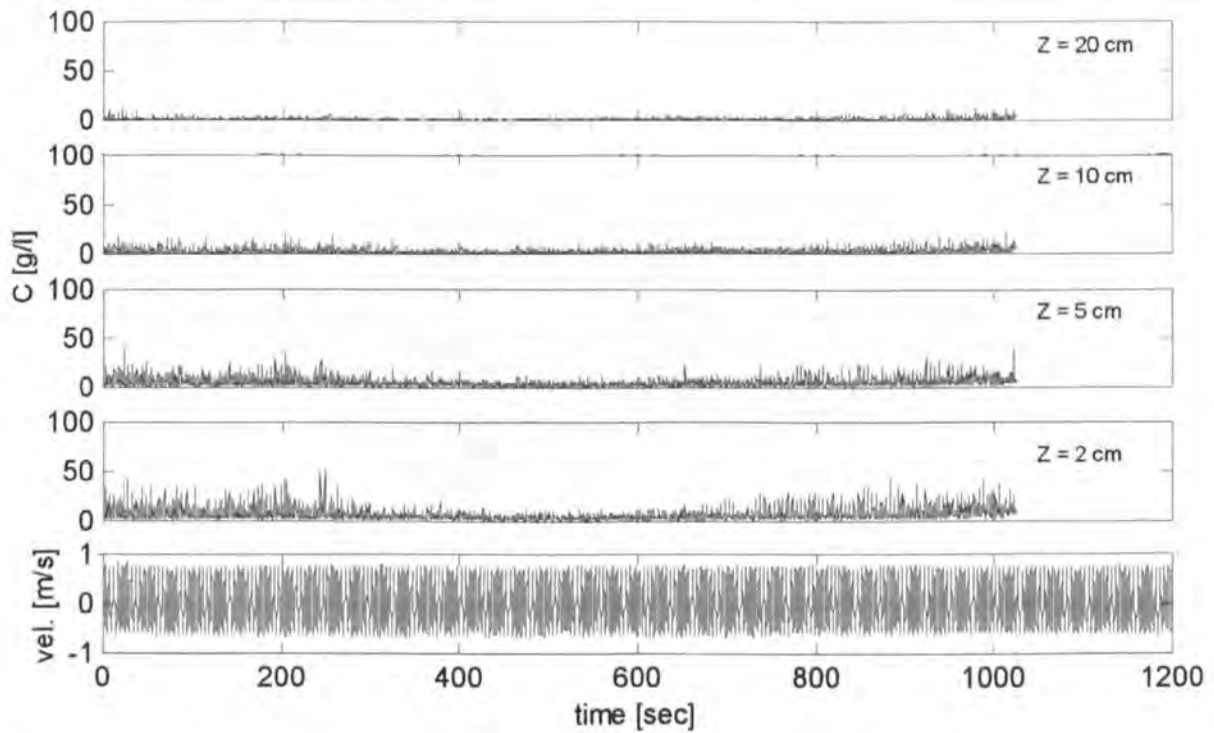


Figure 5.9: Suspended sediment concentration time series and synchronous near bed horizontal velocity for burst a11a (regular waves, $H = 1.34$ m).

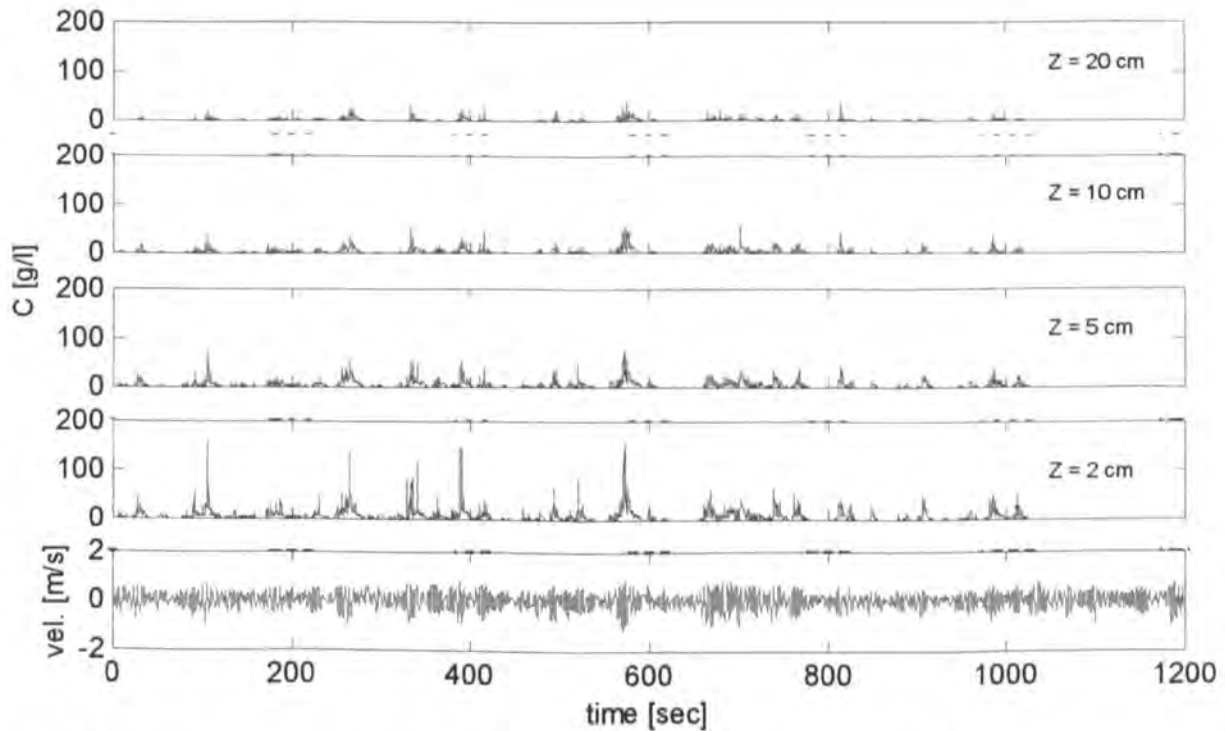


Figure 5.10: Suspended sediment concentration time series and synchronous near bed horizontal velocity for burst a12a (irregular waves, $H_s = 1.26$ m).

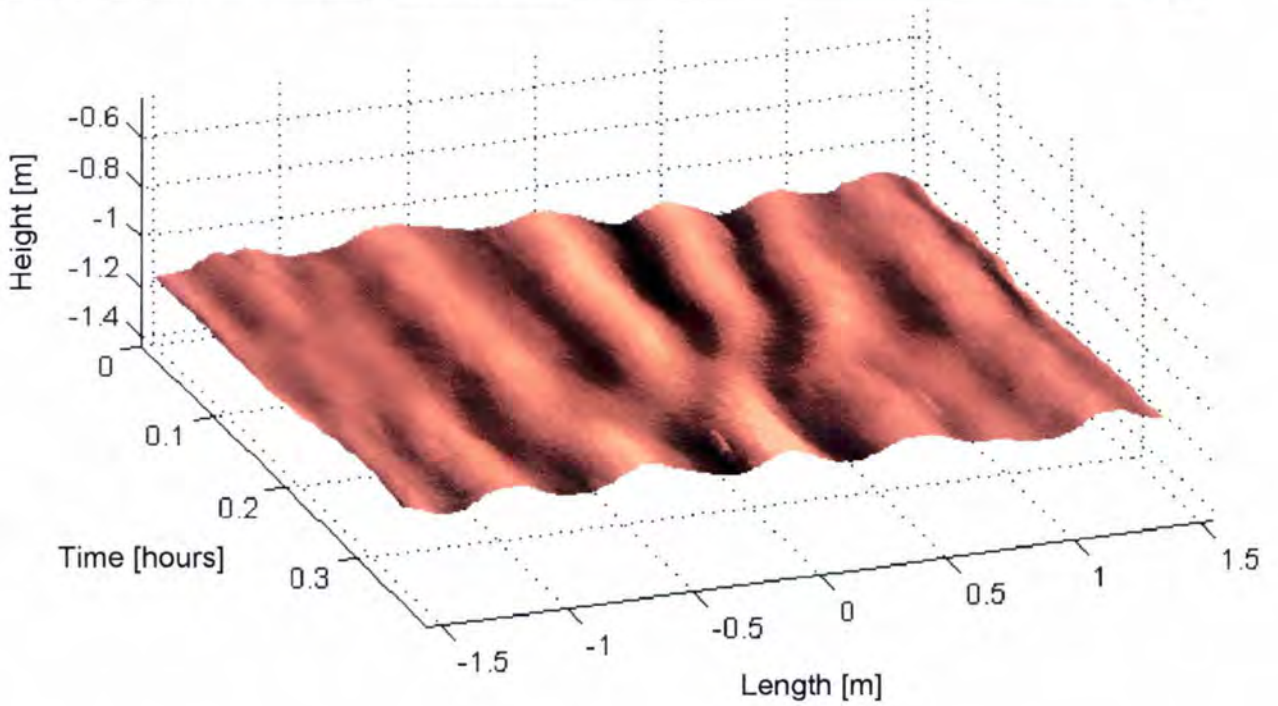


Figure 5.11: Sand ripple profile for burst a11a (regular waves, $H = 1.34$ m), measured by the Acoustic Ripple Profiler (ARP).

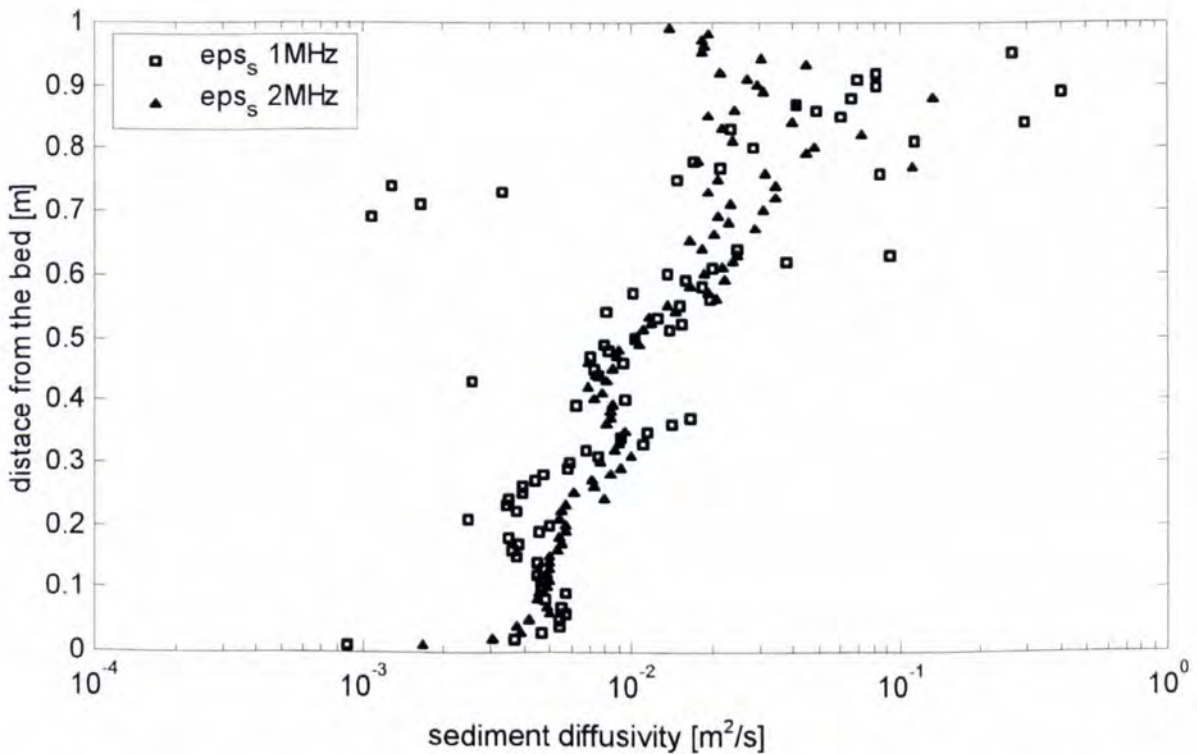


Figure 5.12: Variation of sediment diffusivity with distance from the bed for the two ABS transducers for burst a08a (regular waves, $H = 0.85$ m).

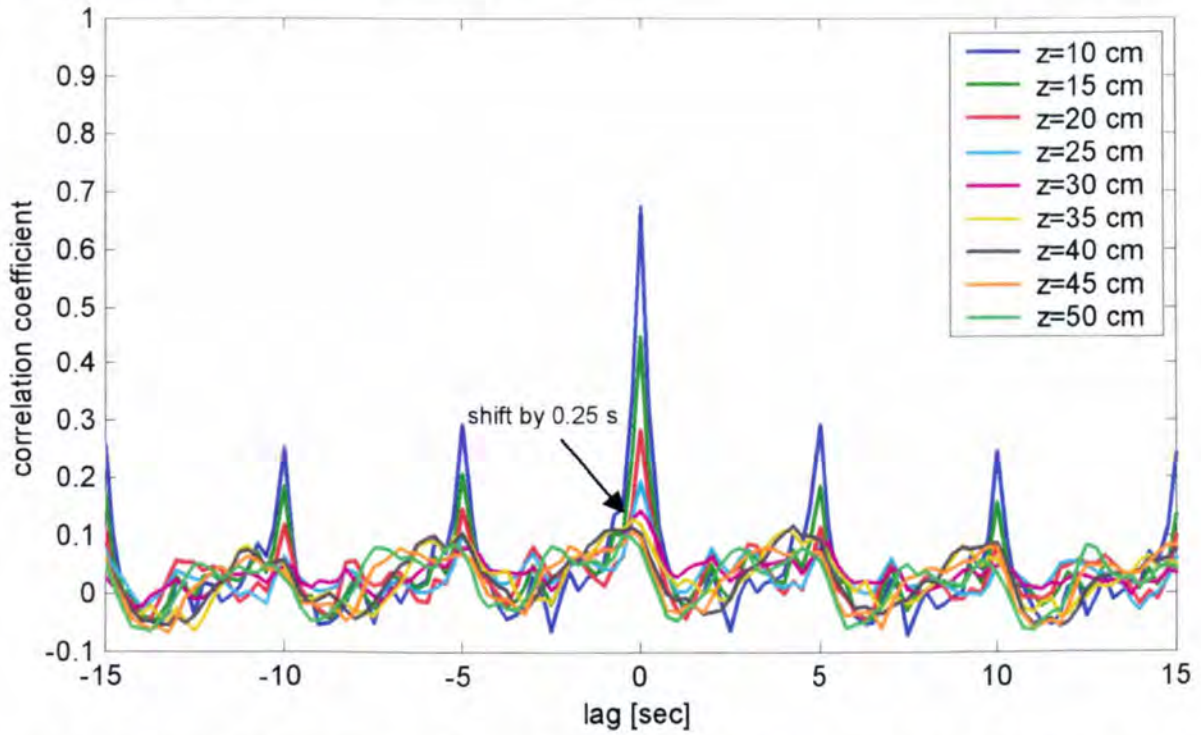


Figure 5.13: Suspended sediment cross correlation coefficients for the 1.0 MHz ABS transducer for burst a08a (regular waves, $H = 0.85$ m). The reference level is at $z = 5$ cm above the bed.

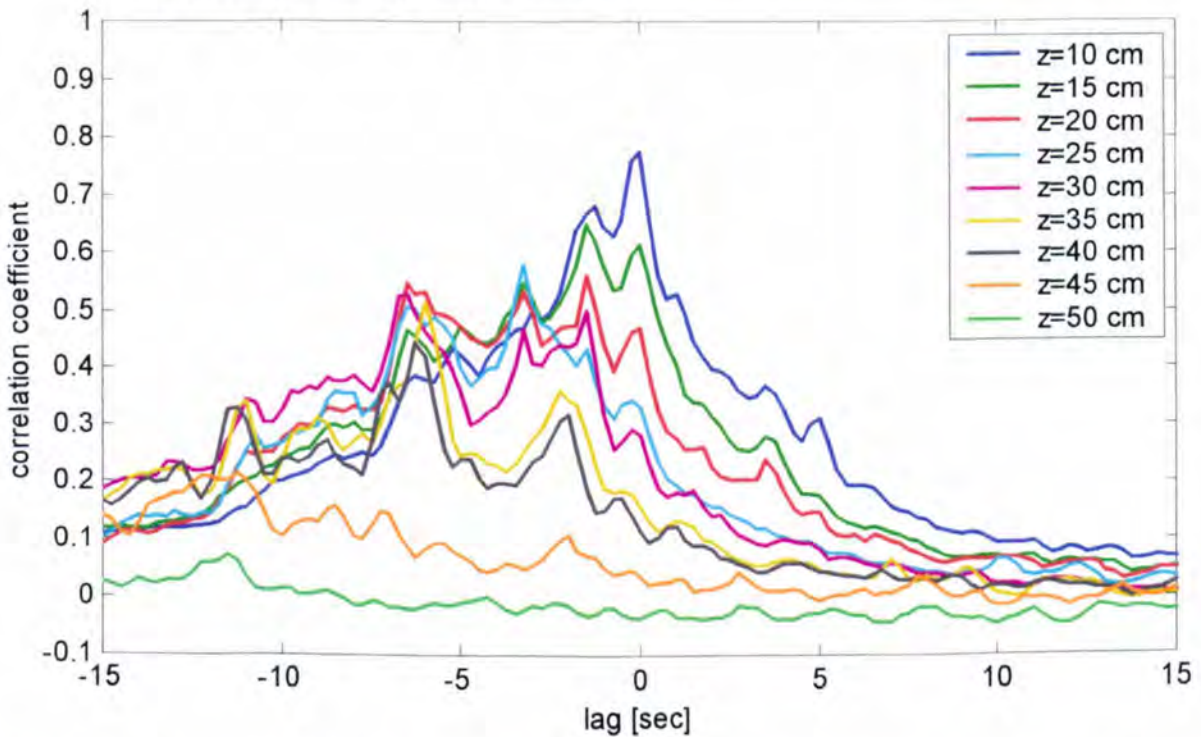


Figure 5.14: Suspended sediment cross correlation coefficients for the 1.0 MHz ABS transducer for burst a07a (irregular waves, $H_s = 0.53$ m). The reference level is at $z = 5$ cm above the bed.

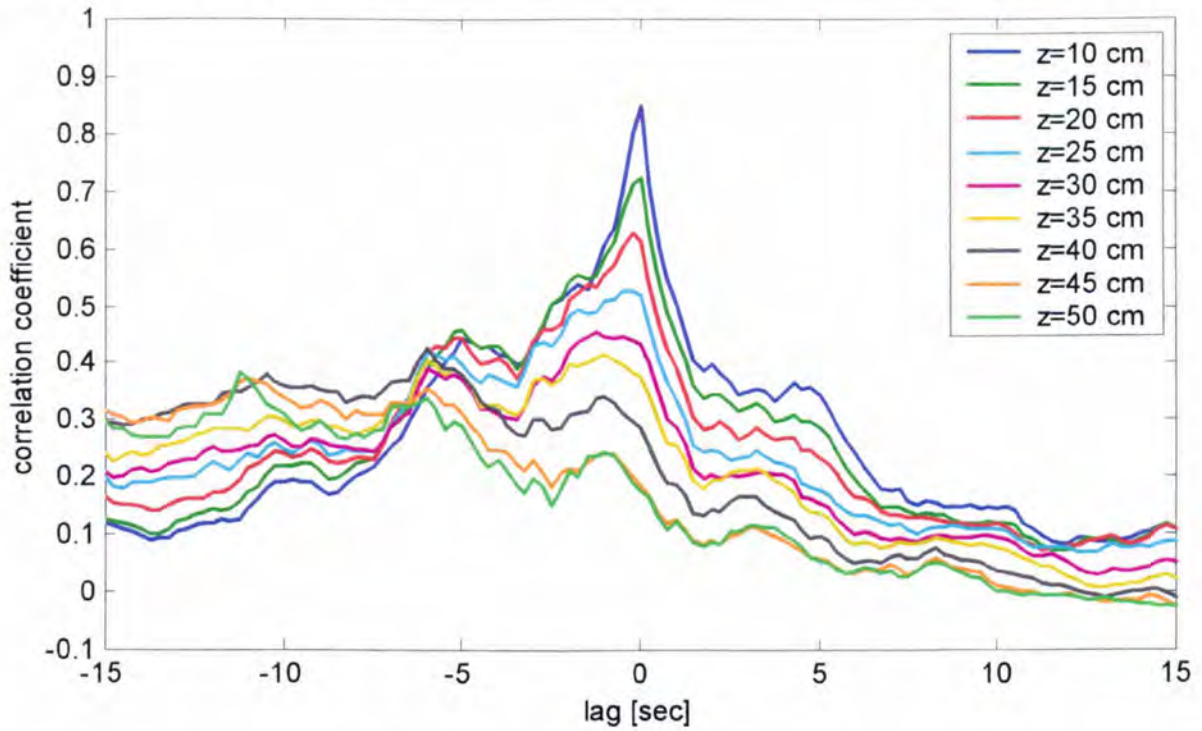


Figure 5.15: Suspended sediment cross correlation coefficients for the 1.0 MHz ABS transducer for burst a10a (irregular waves, $H_s = 1.07$ m). The reference level is at $z = 5$ cm above the bed.

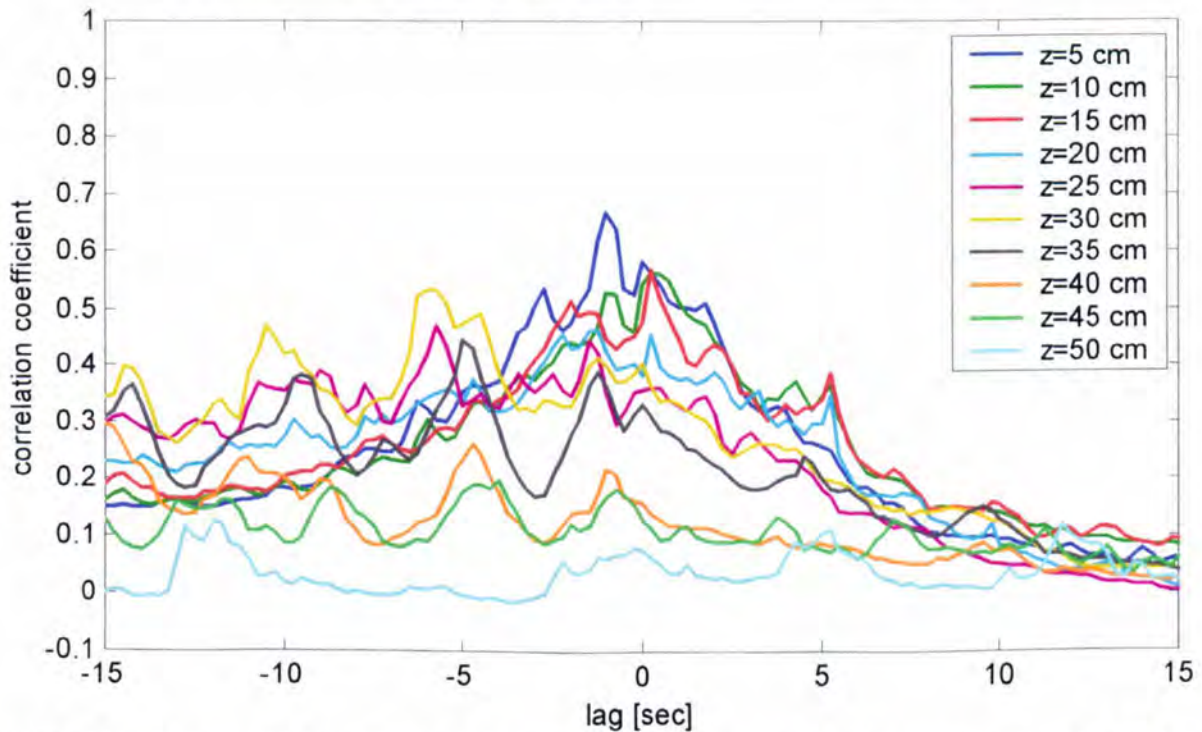


Figure 5.16: Suspended sediment cross correlation coefficient between the 1.0 MHz and 2.0 MHz ABS transducer for burst a07a (irregular waves, $H_s = 0.53$ m).

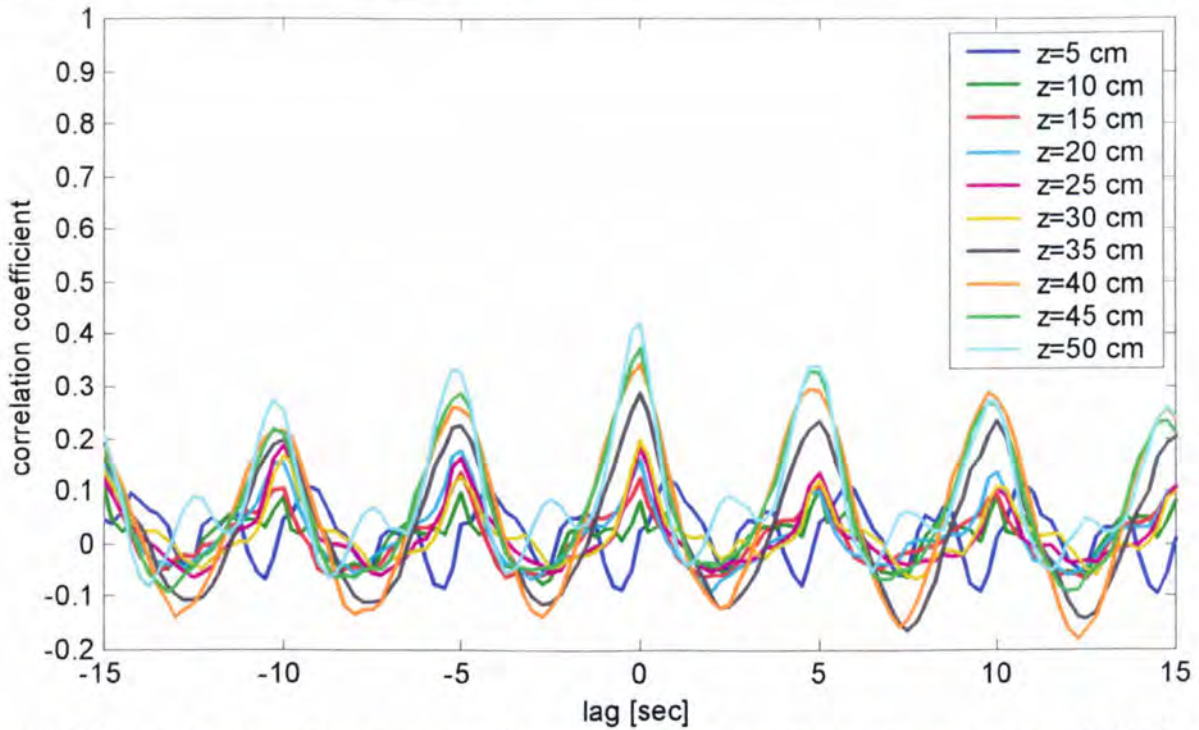


Figure 5.17: Suspended sediment cross correlation coefficient between the 1.0 MHz and 2.0 MHz ABS transducer for burst a08a (regular waves, $H = 0.85$ m).

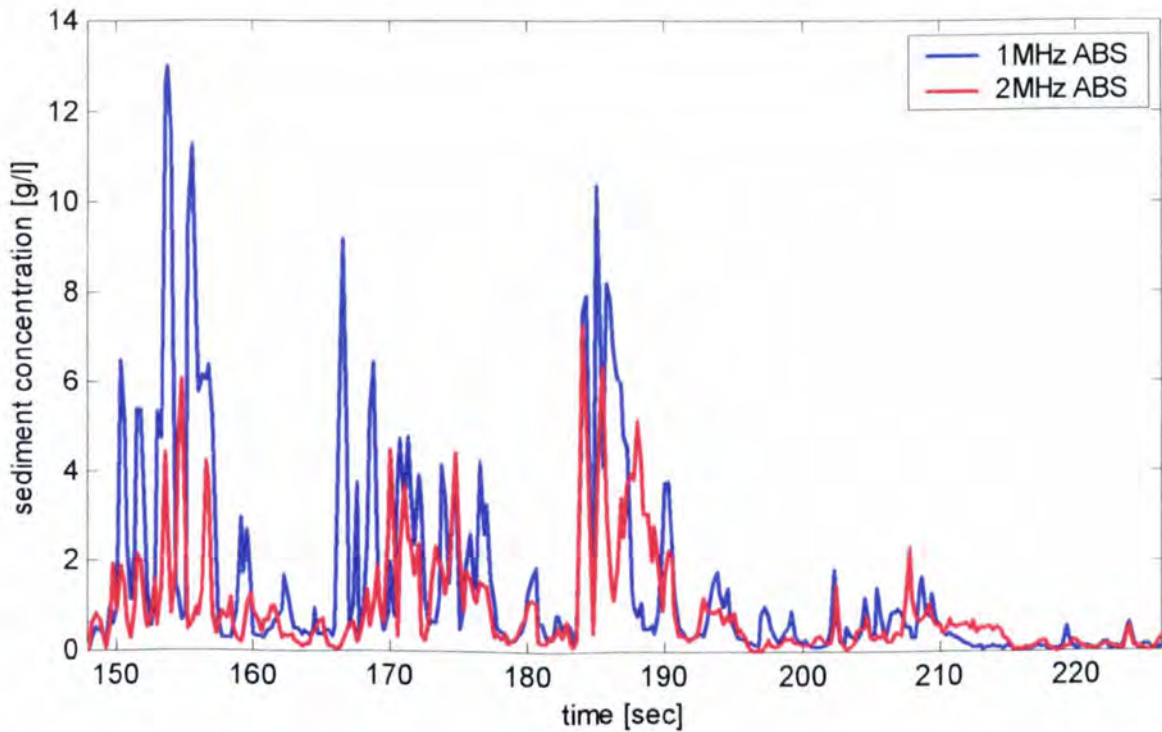


Figure 5.18: Snap shot of the sediment concentration time series for the two ABS transducers at $z = 5$ cm above the bed for burst a07a (irregular waves, $H_s = 0.53$ m).

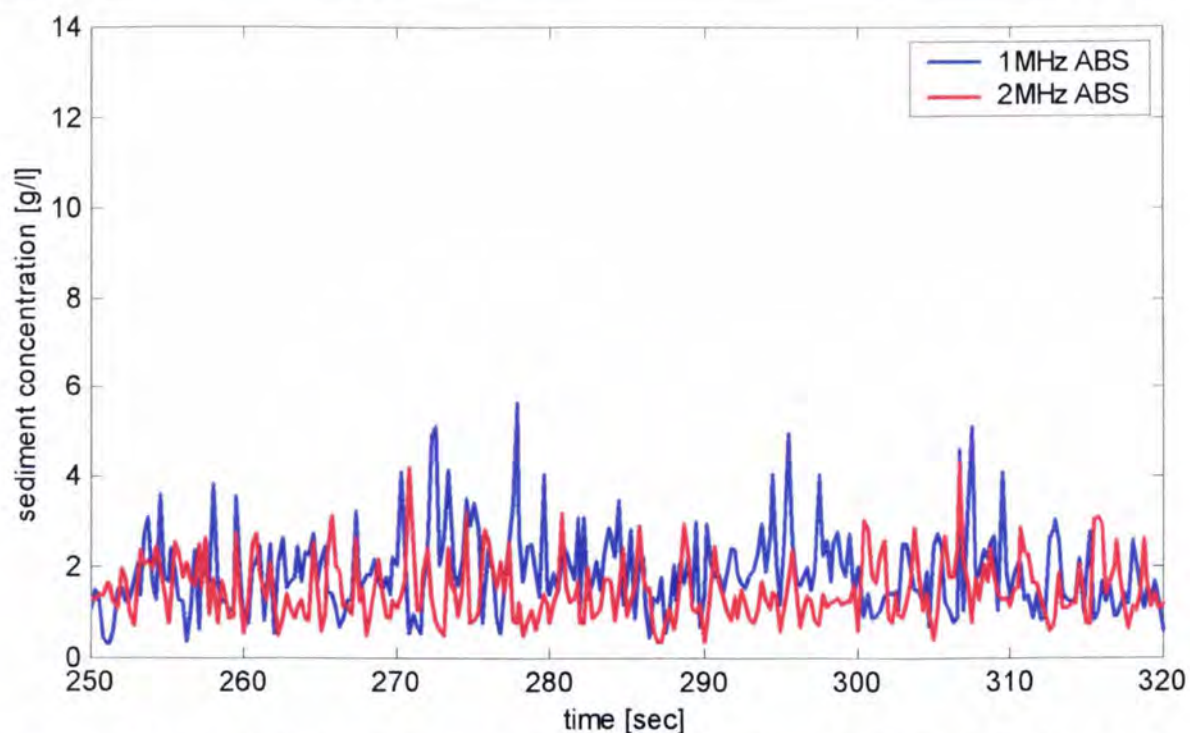


Figure 5.19: Snap shot of the sediment concentration time series for the two ABS transducers at $z = 5$ cm above the bed for burst a08a (regular waves, $H = 0.85$ m).

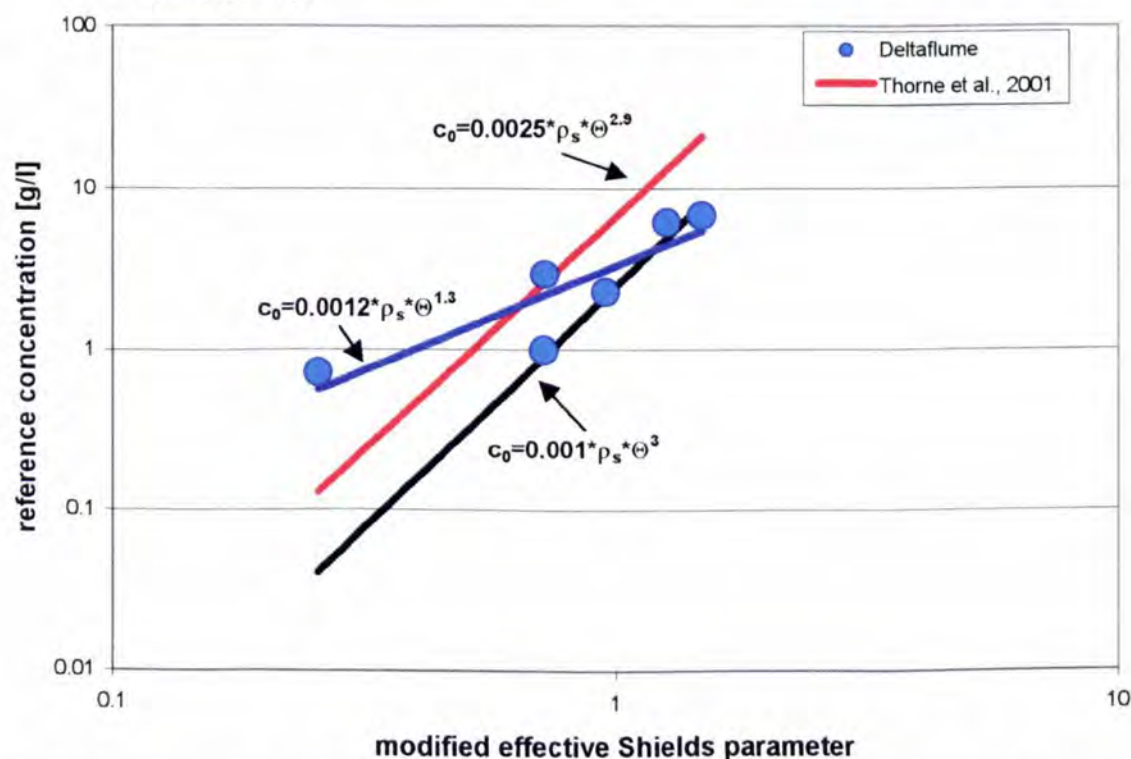


Figure 5.20: Measured and predicted reference concentration using the expression suggested by NIELSEN (1986) and its variations as a function of the modified effective Shields parameter.

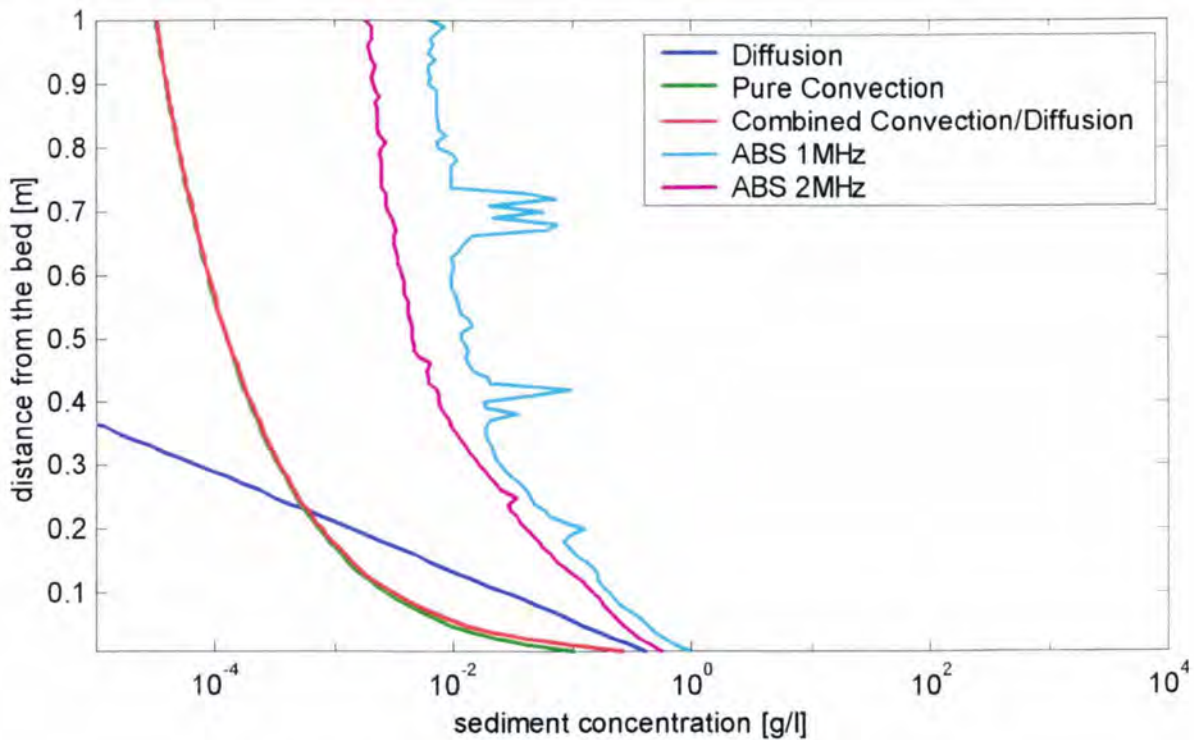


Figure 5.21: Measured and predicted c -profiles using the equations proposed by NIELSEN (1992) for pure diffusion (dark blue line), pure convection (green line) and diffusion/convection (red line) for burst a07a (irregular waves, $H_s = 0.53$ m). The mean diameter in suspension was taken to be equal to a d_{16} at the bed for the empirical equations and $n=2$ in the convective equation.

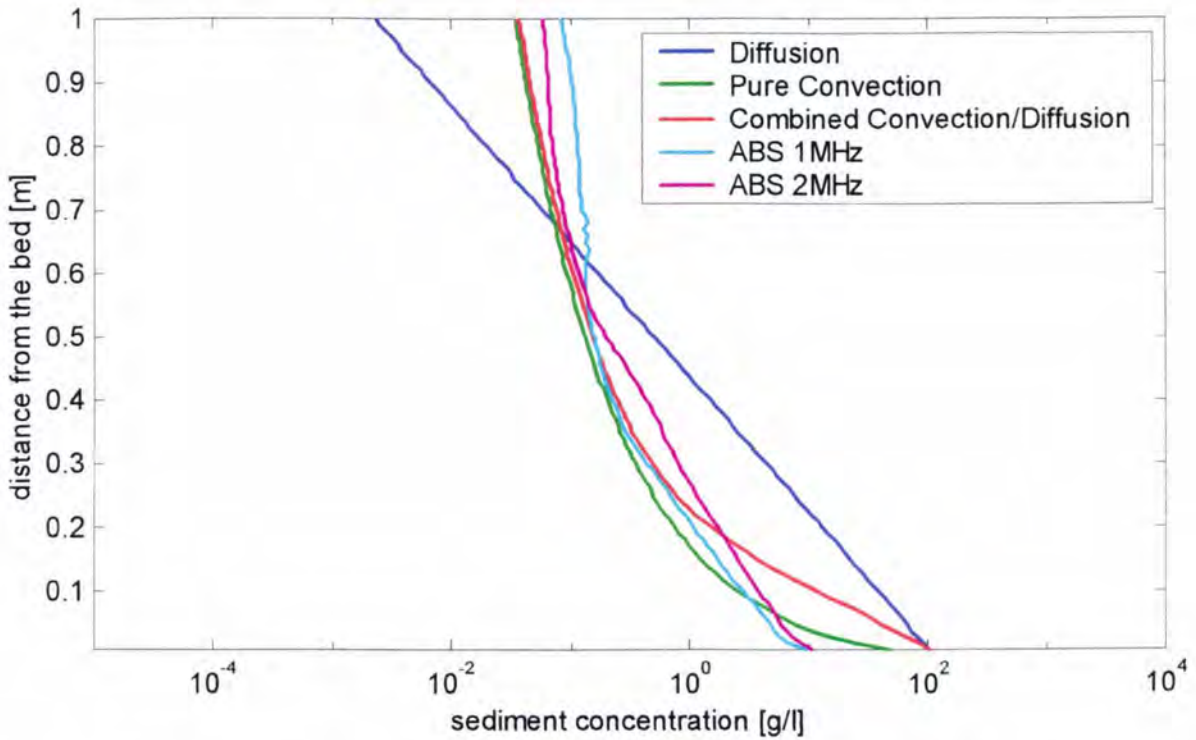


Figure 5.22: Measured and predicted c-profiles using the equations proposed by NIELSEN (1992), for pure diffusion (dark blue line), pure convection (green line) and diffusion/convection (red line) for burst a11a (regular waves, $H = 1.34$ m). The mean diameter in suspension was taken to be equal to a d_{16} at the bed for the empirical equations and $n=2$.

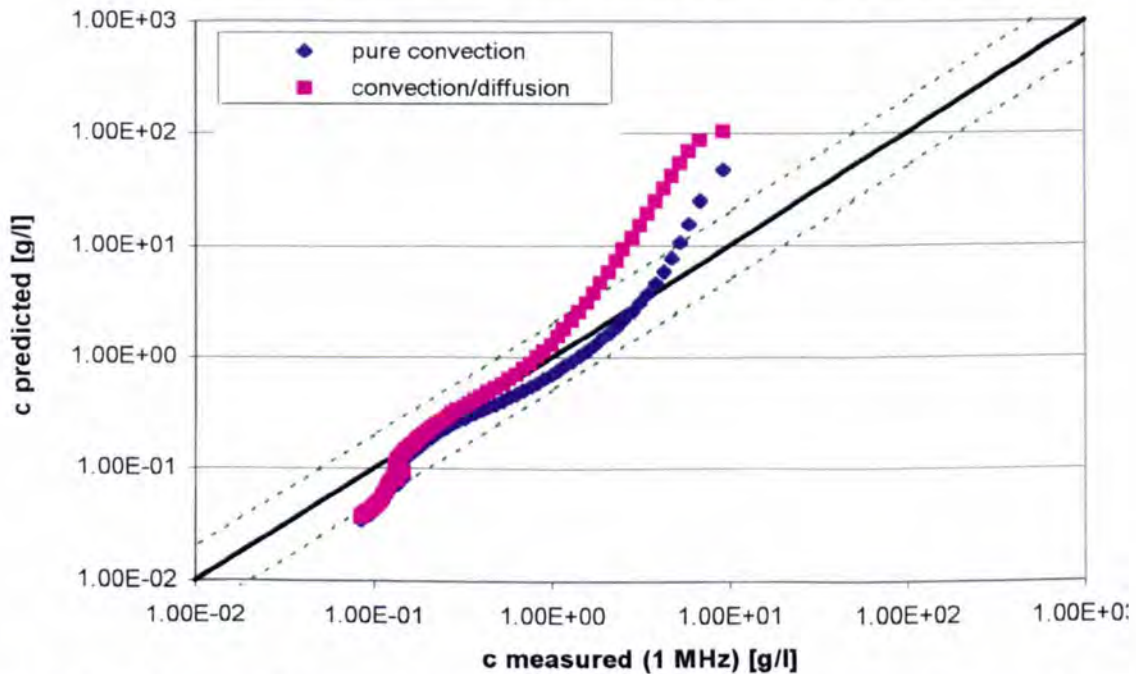


Figure 5.23: Predicted (Nielsen) versus measured sediment concentration values for burst a11a (regular waves, $H = 1.34$ m).

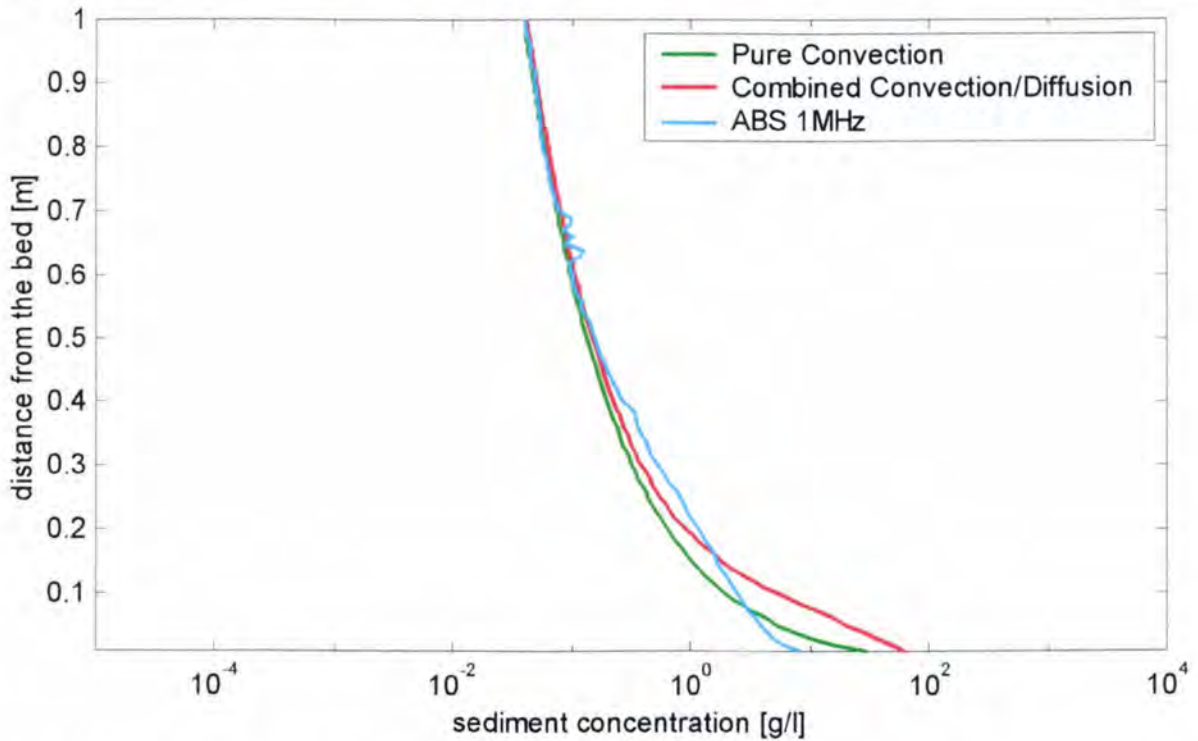


Figure 5.24: Measured and predicted c-profiles using the equations proposed by NIELSEN (1992) for pure convection (green line) and diffusion/convection (red line) for burst a12a (irregular waves, $H_s = 1.26$ m). The mean diameter in suspension was taken to be equal to a d_{16} at the bed for the empirical equations and $n=1.8$.

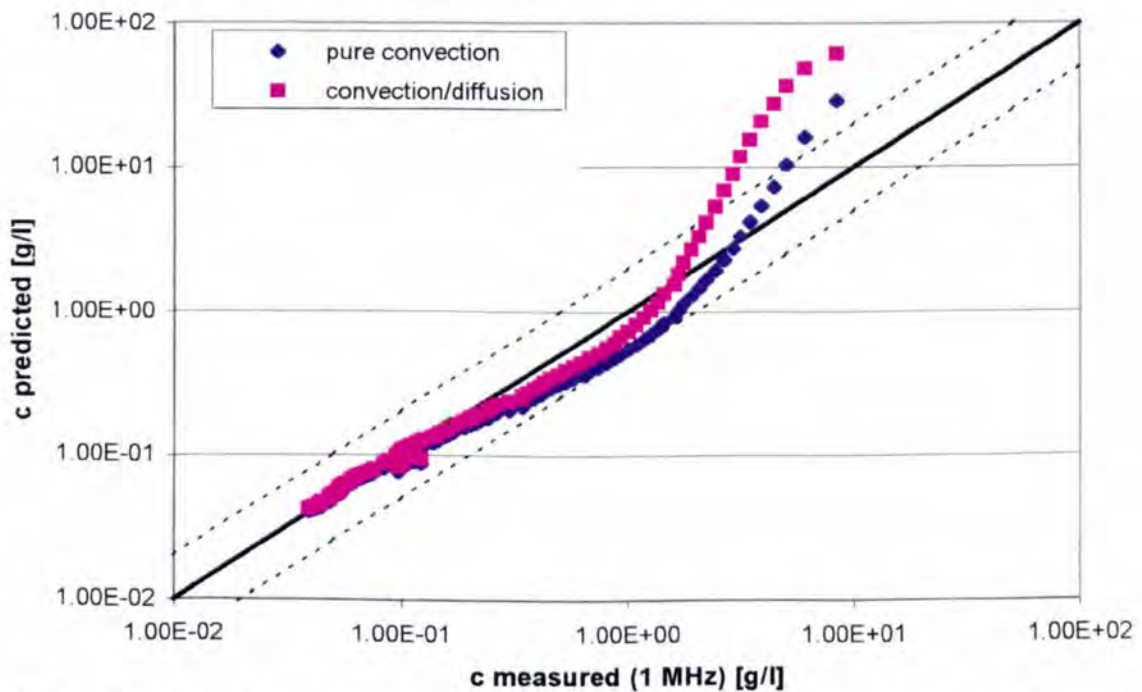


Figure 5.25: Predicted (Nielsen) versus measured sediment concentration values for burst a12a (irregular waves, $H_s = 1.26$ m).

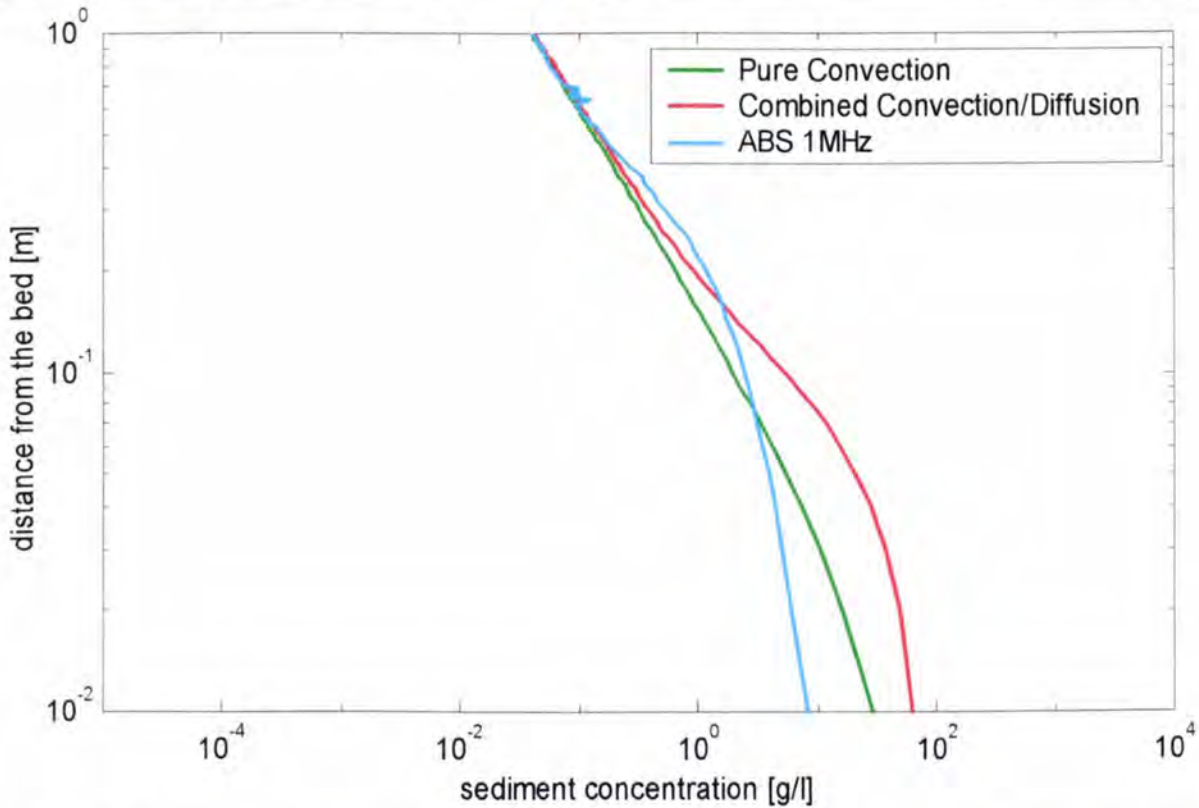


Figure 5.26: Measured and predicted c-profiles using the equations proposed by NIELSEN (1992) for pure convection (green line) and diffusion/convection (red line) for burst a12a (irregular waves, $H_s = 1.26$ m). The mean diameter in suspension was taken to be equal to a d_{16} at the bed for the empirical equations and $n=1.8$. Only the combined diffusion/convection approach can model the complex shape of the measured c-profile varying from an upward convex for the next 25 cm and then upward concave shape.

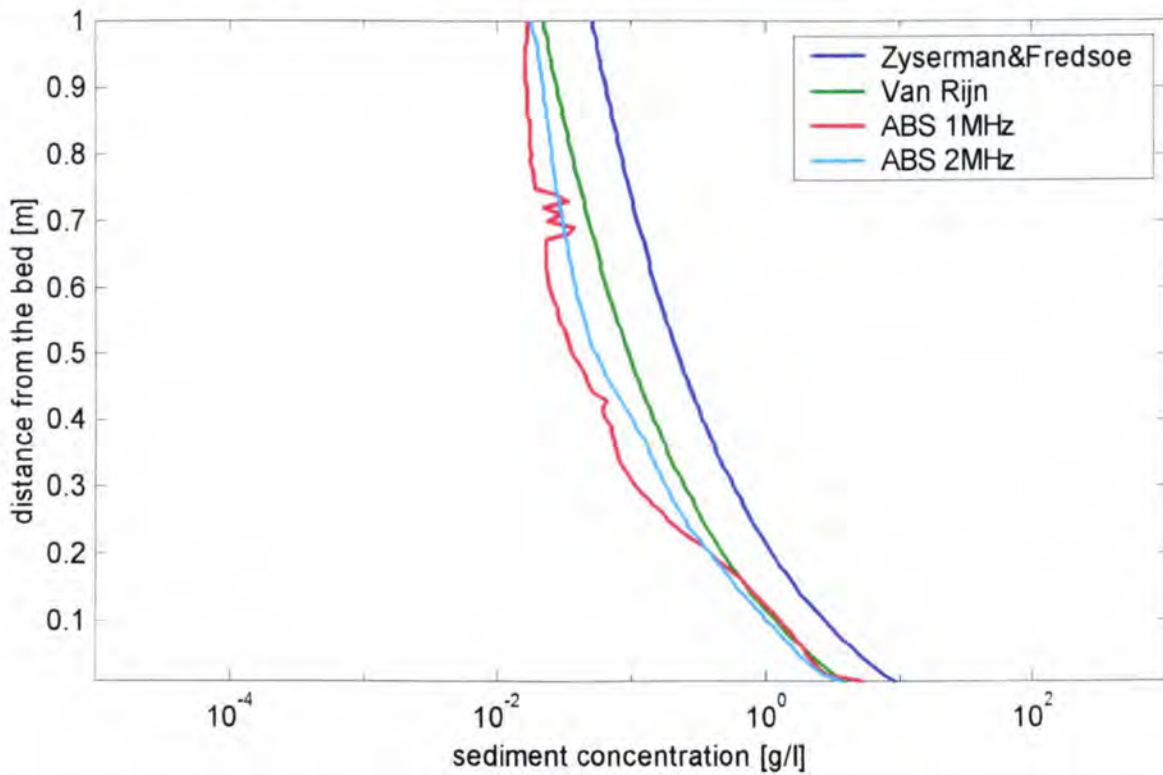


Figure 5.27: Measured and predicted c-profiles using the Rouse type profile with expressions for the reference concentration proposed by ZYSERMAN AND FREDSDØE (1994) and VAN RIJN (1989) for burst a08a (regular waves, $H = 0.85$ m). The value of d_{50} at the bed was used to determine the reference concentrations while the mean suspended diameter was equal to a d_{16} at the bed and $\gamma = 1$.

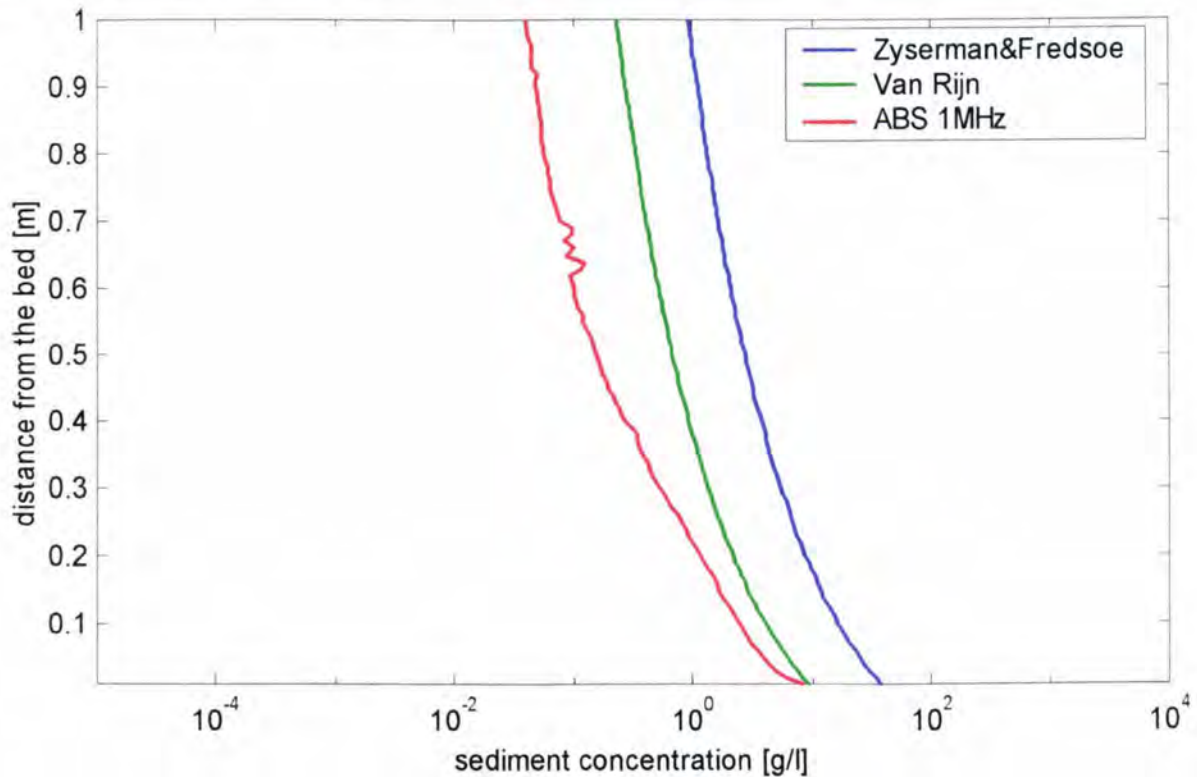


Figure 5.28: Measured and predicted c -profiles using the Rouse type profile with expressions for the reference concentration proposed by ZYSERMAN AND FREDSE (1994) and VAN RIJN (1989) for burst a12a (irregular waves, $H_s = 1.26$ m). The value of d_{50} at the bed was used to determine the reference concentrations while the mean suspended diameter was equal to a d_{16} at the bed.

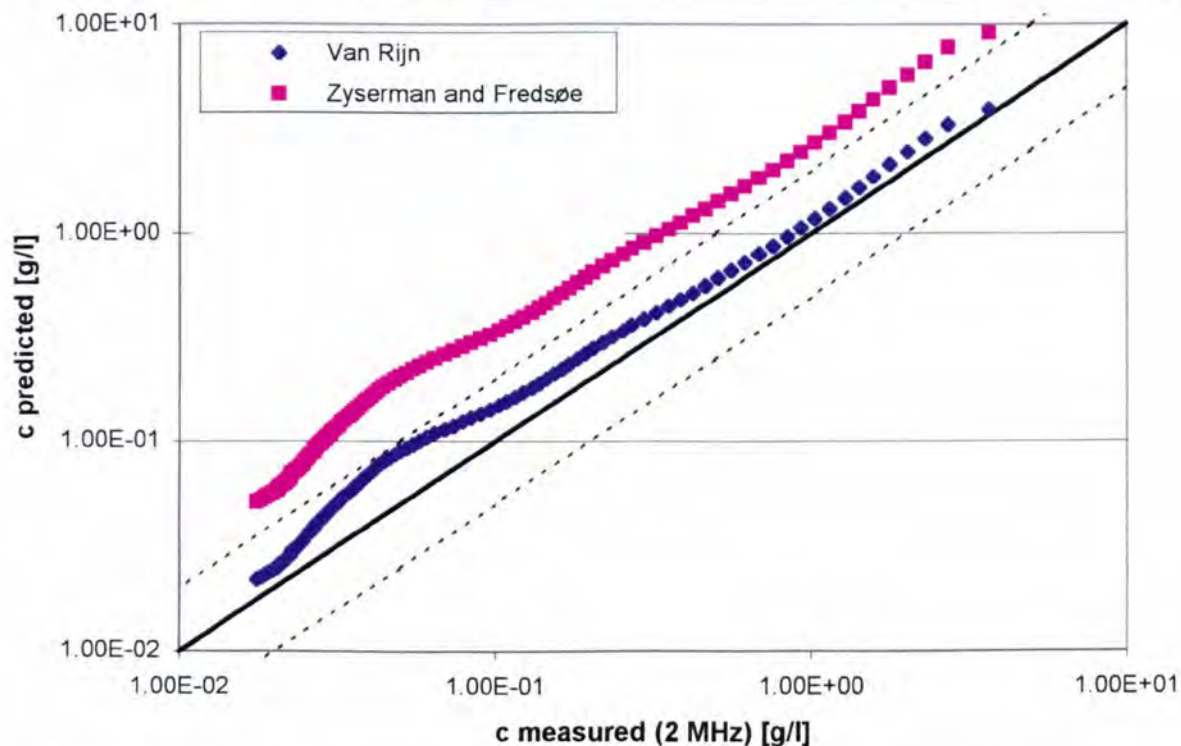


Figure 5.29: Predicted (Rouse type profile) versus measured sediment concentration values for burst a08a (regular waves, $H = 0.85$ m).

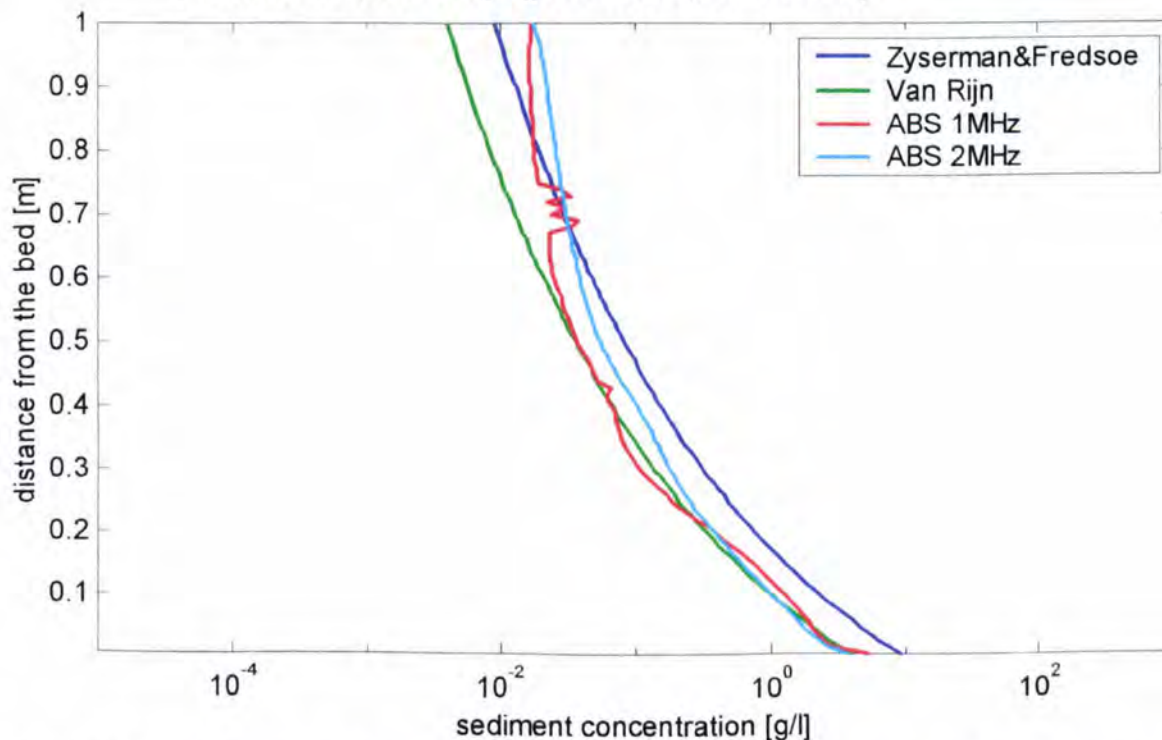


Figure 5.30: Measured and predicted c -profiles using the Rouse type profile with the two expressions (Van Rijn and Zyserman and Fredsøe) for the reference concentration for burst a08a (regular waves, $H = 0.85$ m). The ratio of sediment diffusivity to eddy viscosity was $\gamma = 0.6$.

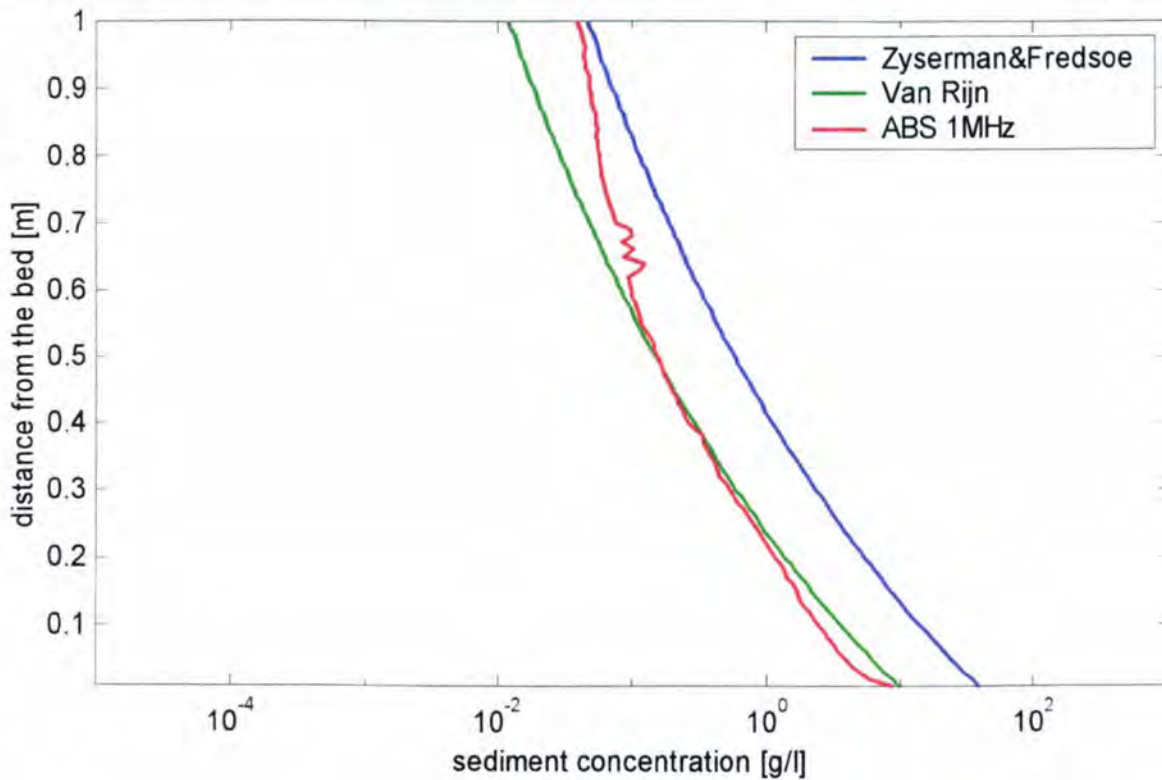


Figure 5.31: Measured and predicted c-profiles using the Rouse type profile with the two expressions (Van Rijn and Zyserman and Fredsøe) for the reference concentration for burst a12a (irregular waves, $H_s = 1.26$ m). The ratio of sediment diffusivity to eddy viscosity was $\gamma = 0.3$.

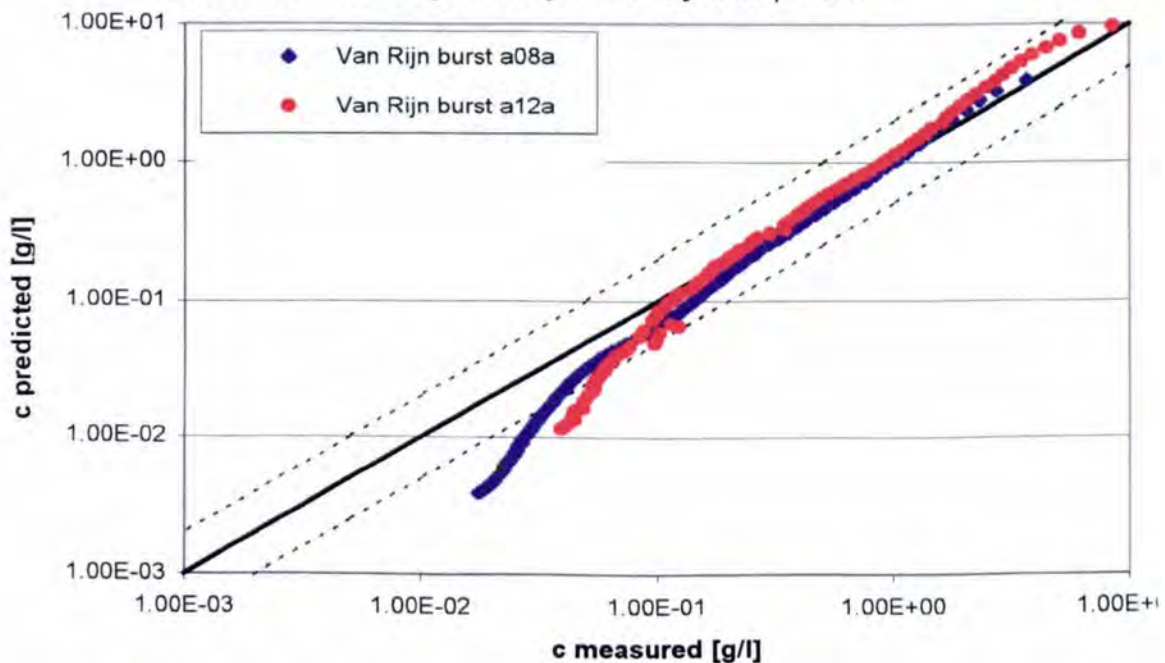


Figure 5.32: Predicted (Rouse type profile with Van Rijn's reference concentration) versus measured sediment concentration values for burst a08a (regular waves, $H = 0.85$ m) and a12a (irregular waves, $H_s = 1.26$ m).

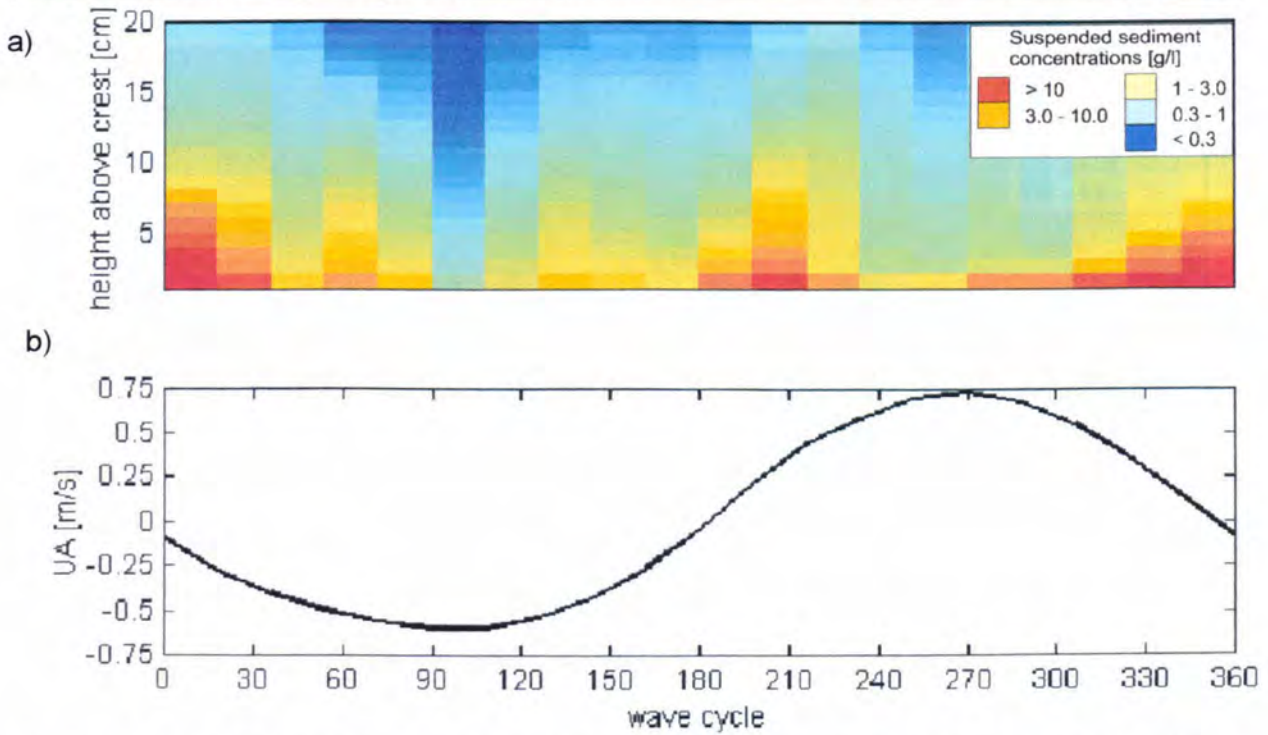


Figure 5.33: a) Ensemble averaged sediment concentration for 205 waves for burst a11a (regular waves, $H = 1.34$ m) for the 1.0 MHz ABS transducer. b) Corresponding near bed horizontal velocity.

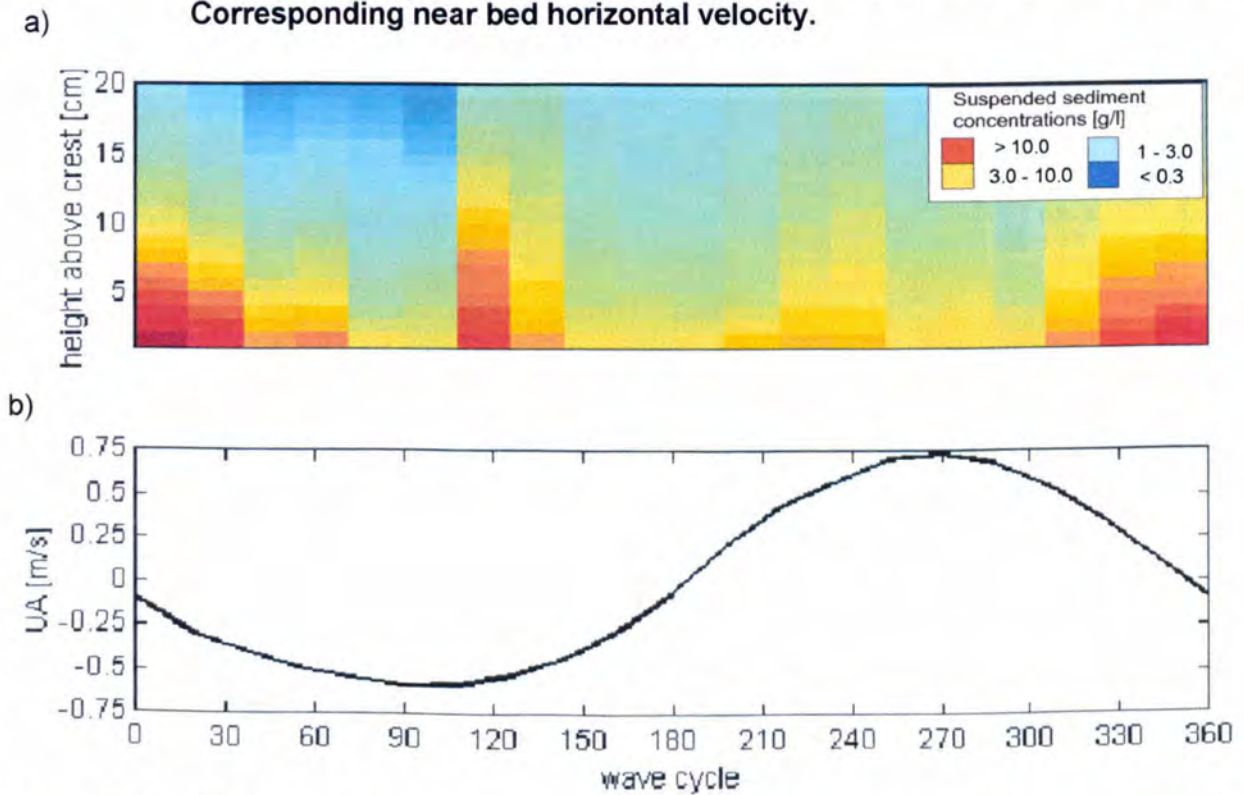


Figure 5.34: a) Ensemble averaged sediment concentration for 50 waves (about 4 minutes) of burst a11a (regular waves, $H = 1.34$ m) for the 1.0 MHz ABS transducer. b) Corresponding near bed horizontal velocity.

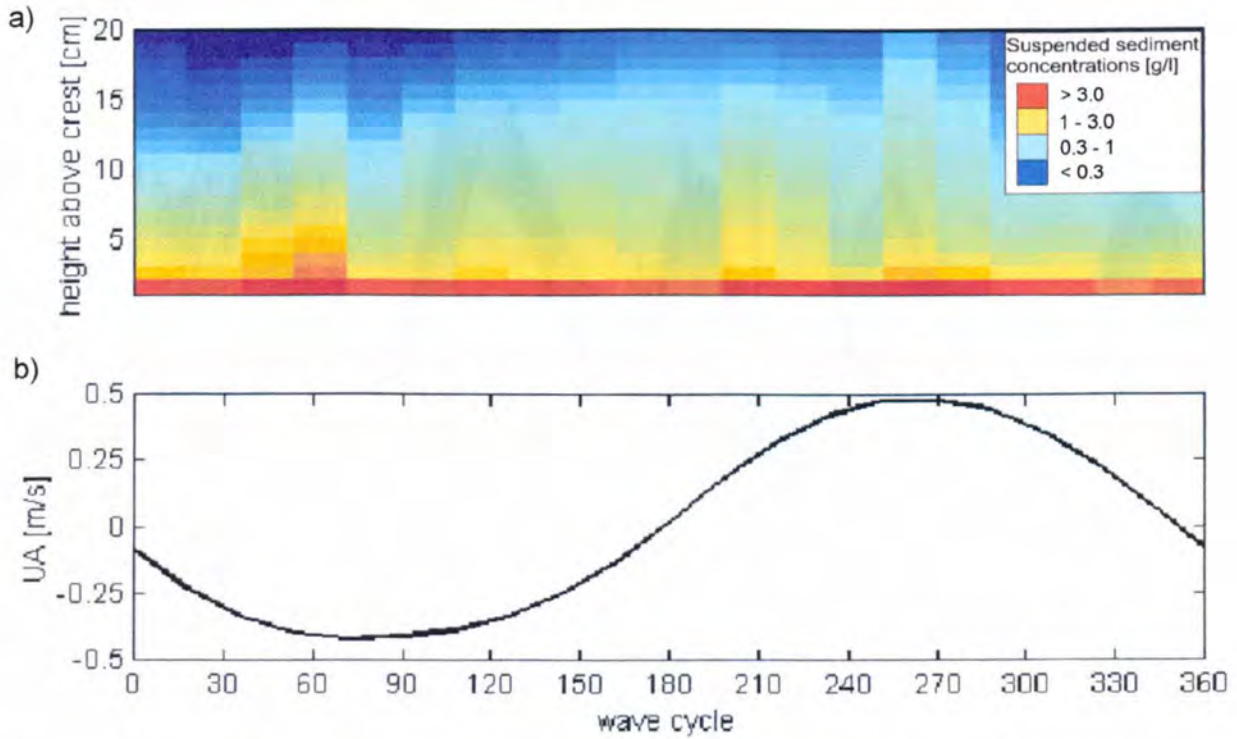


Figure 5.35: a) Ensemble averaged sediment concentration for 205 waves of burst a08a (regular waves, $H = 0.85$ m) for the 1.0 MHz ABS transducer. b) Corresponding near bed horizontal velocity.

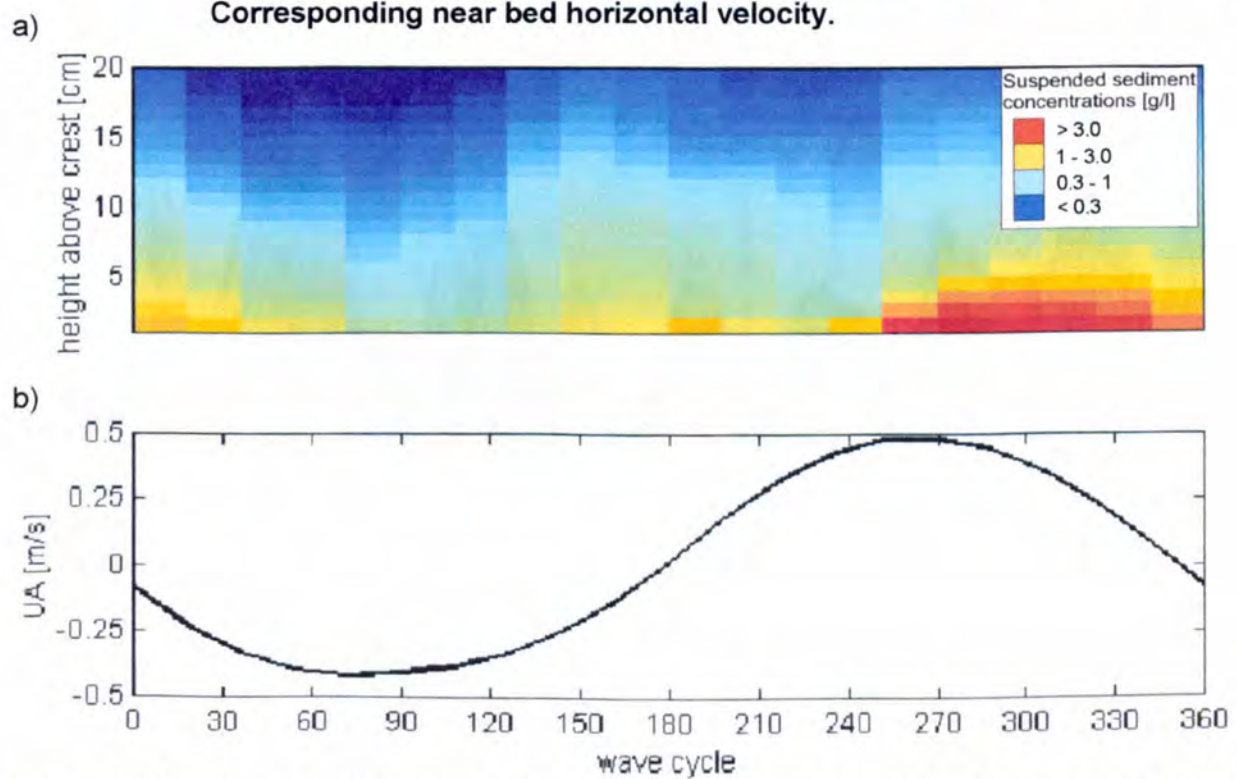


Figure 5.36: a) Ensemble averaged sediment concentration for 205 waves of burst a08a (regular waves, $H = 0.85$ m) for the 2.0 MHz ABS transducer. b) Corresponding near bed horizontal velocity.

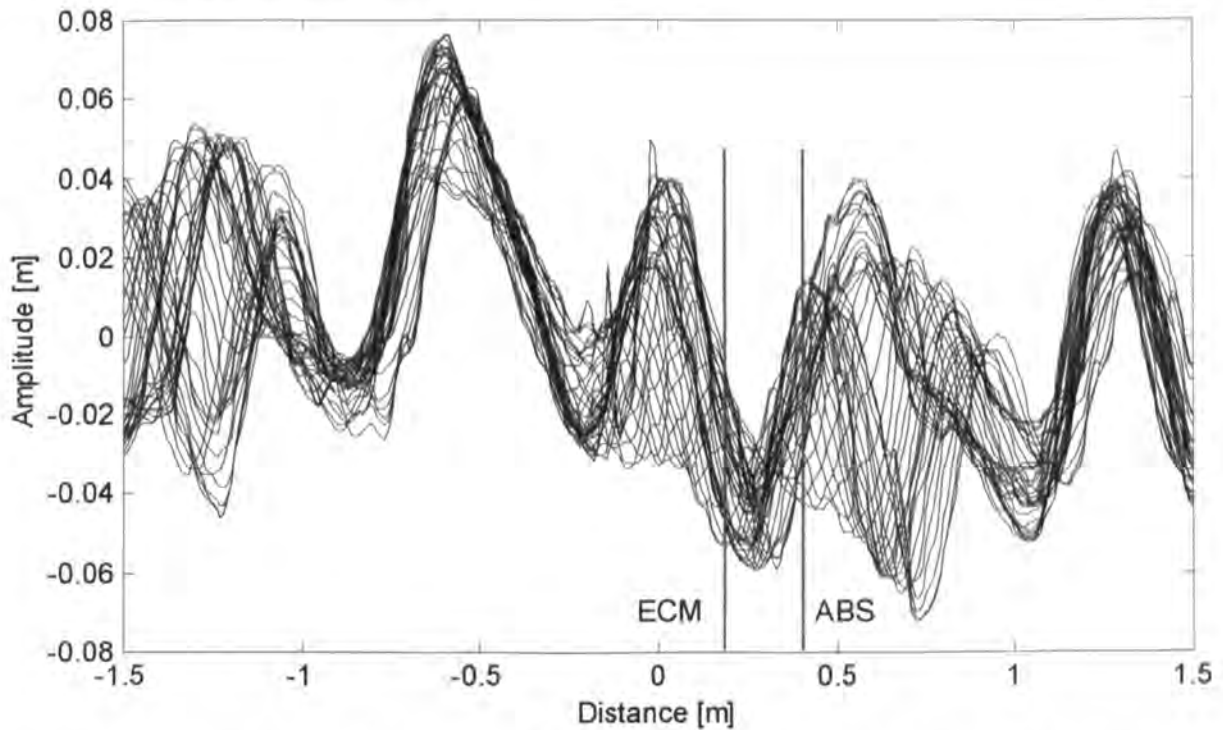


Figure 5.37: Position of the ABS and ECM sensors relative to the ripples throughout burst a11a (regular waves, $H = 1.34$ m).

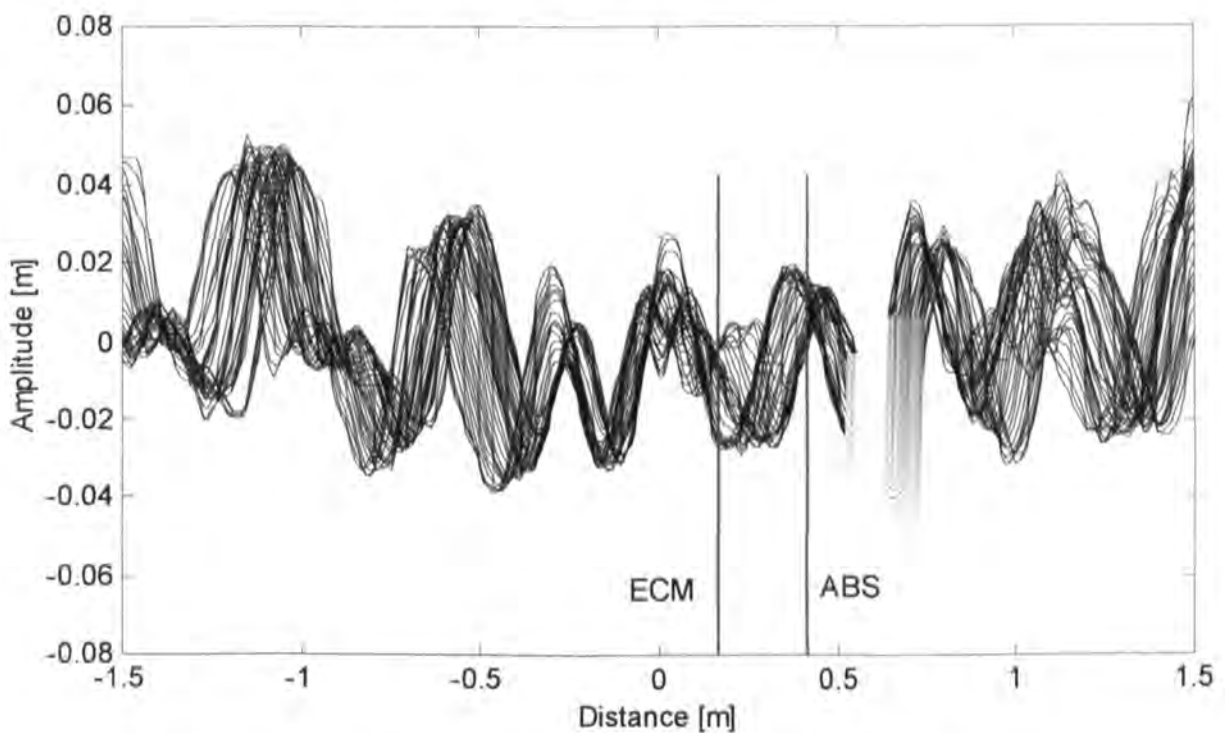


Figure 5.38: Position of the ABS and ECM sensors relative to the ripples throughout burst a08a (regular waves, $H = 0.85$ m).

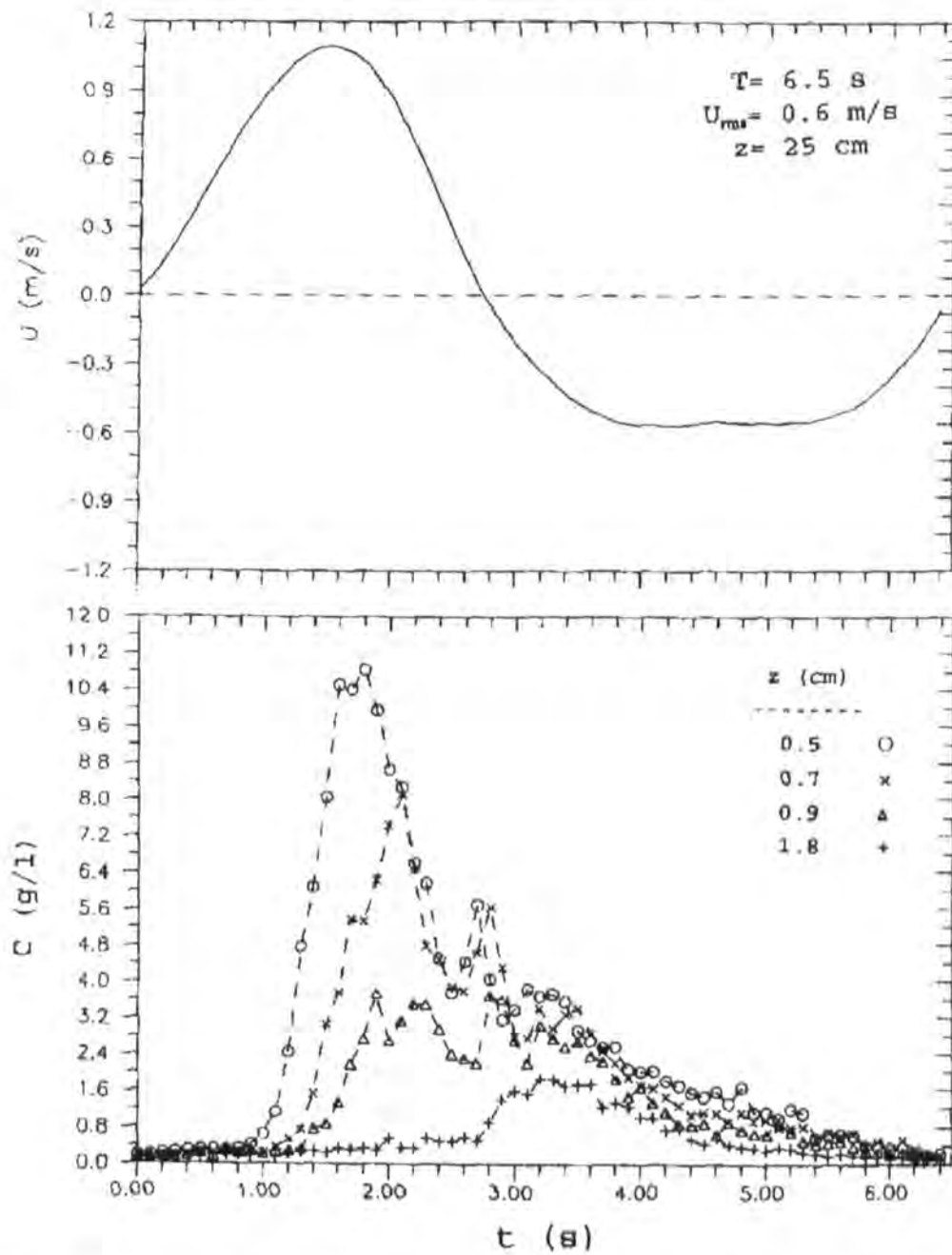


Figure 5.39: Measured suspended sediment concentrations for an asymmetric wave with an asymmetry coefficient of 0.66 (from RIBBERINK AND AL-SALEM, 1995).

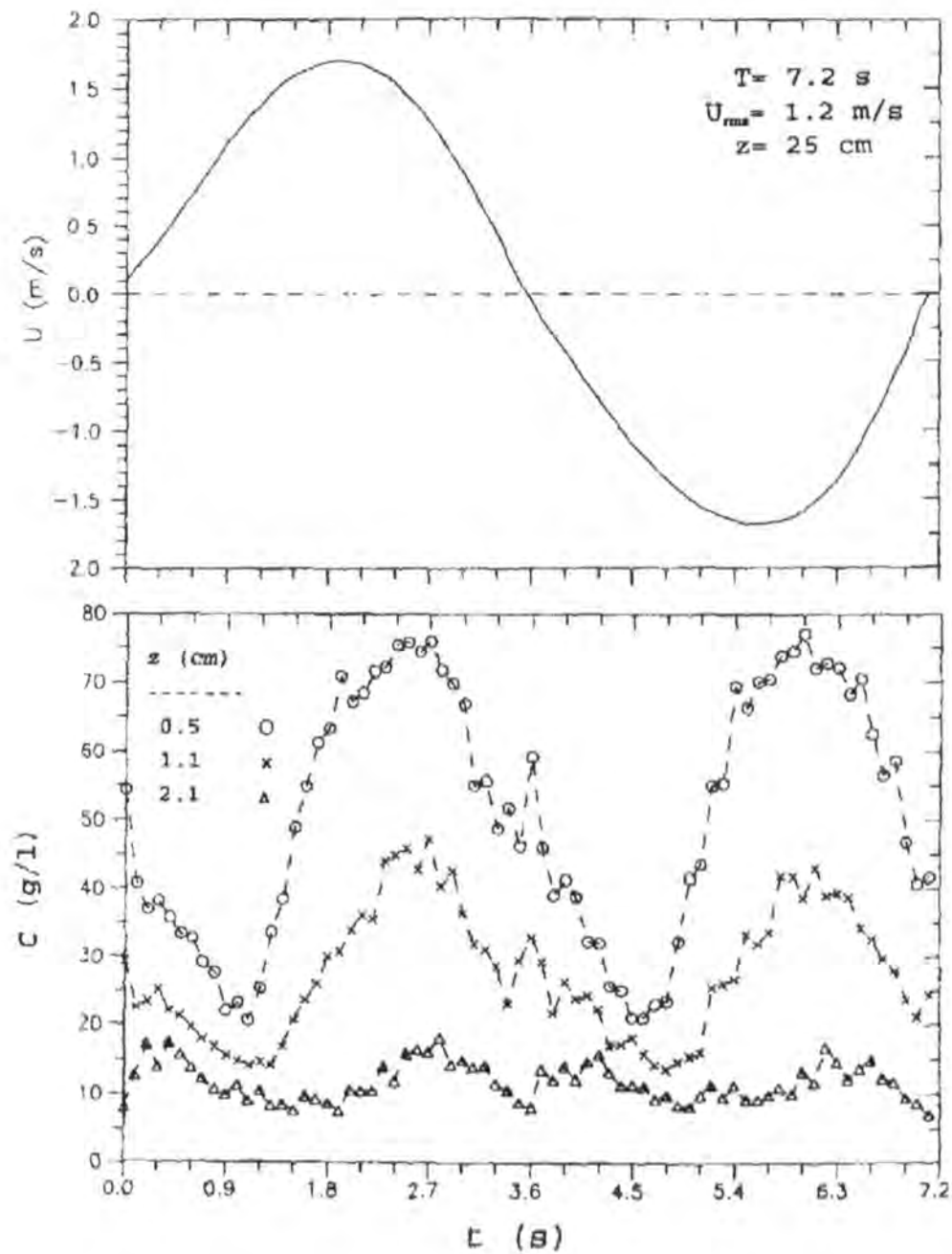


Figure 5.40: Measured suspended sediment concentrations for a sinusoidal wave (from RIBBERINK AND AL-SALEM, 1995).

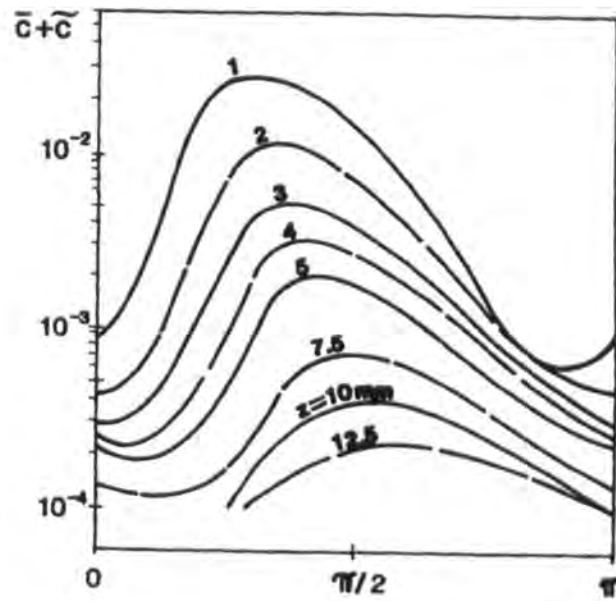


Figure 5.41: Phase averaged sediment concentrations $\bar{c} + \tilde{c}$ over a flat bed under regular, symmetric oscillatory flow. One peak occurs each half-period at all levels. Near the bed, it occurs shortly before the peak of the free stream velocity ($\omega \cdot t = \pi/2$). From NIELSEN (1992).

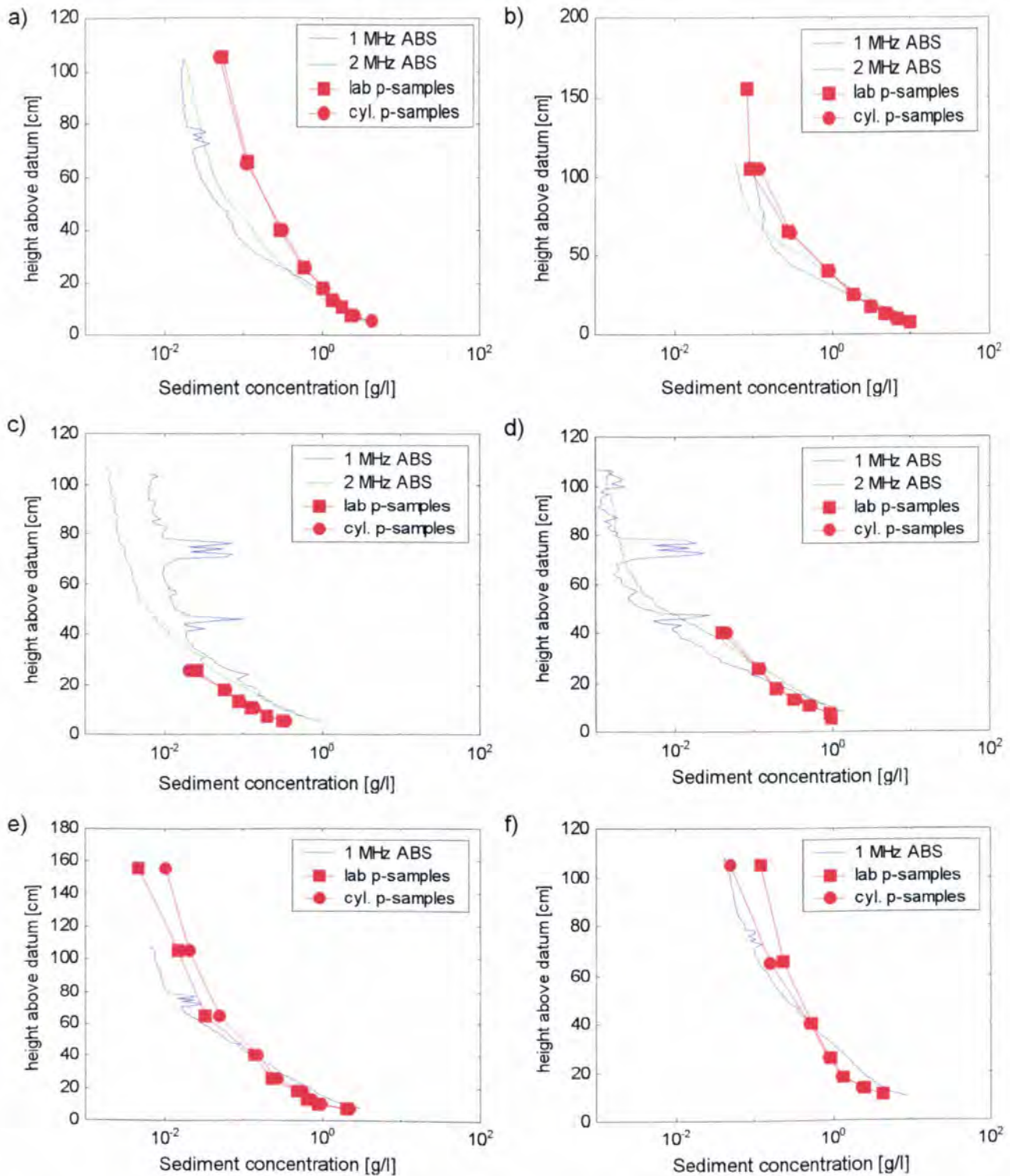


Figure 5.42: Comparison between pump-sampling and ABS data for six bursts. a) burst a08a (regular waves, $H = 0.85$ m), b) burst a11a (regular waves, $H = 1.34$ m), c) burst a07a (irregular waves, $H_s = 0.53$ m), d) burst a09a (irregular waves, $H_s = 0.83$ m), e) burst a10a (irregular waves, $H_s = 1.07$ m), f) burst a12a (irregular waves, $H_s = 1.26$ m).

Chapter 6 Intra-wave Suspended Sediment Concentration

6.1 Introduction

The burst average analysis, discussed in chapter 5, provided some useful results with respect to large scale modelling where simplified equations are used. However, re-suspension of sediment occurs on smaller time scales, which are not resolved in the burst averaged analysis. Examination of the time histories of the ABS data revealed that the re-suspension of sediment under irregular waves is dominated by suspension events under groups of large waves. In this chapter the intra-wave suspension mechanisms are analysed with a view to elucidate the entrainment processes under wave groups.

6.2 Averaged concentration profiles for different time scales

In chapter 5 burst averaged data of about 17 minutes were analysed. The time interval of 17 minutes was chosen arbitrarily as a trade off between the conflicting requirements of on-board computer memory and the necessity to record sufficient wave cycles for analysis. In order to evaluate the consistency of the data, the averaged concentrations for different time scales were analysed.

6.2.1 Ten minute averaged concentration

It has already been shown in chapter 3 that the hydrodynamics vary more during a burst of irregular waves compared to a burst of regular waves. Thus, the effect of the variation in the hydrodynamics on the ABS data was determined by looking at two halves of the ABS data, which was equivalent to about 102 waves per half.

Figures 6.1a and b show the c-profiles for burst a07a (irregular waves, $H_s = 0.53$ m) and burst a11a (regular waves, $H = 1.34$ m), respectively. Presented are the burst averages and the averages for the first and second half of the burst. Turning the attention first to figure 6.1a, there is a clear difference between the consistency of the 1.0 MHz and the 2.0 MHz

data. While there is a reasonable agreement between the different time averaged c-profiles within the first 10 cm above the bed for the 2.0 MHz data, there is a discrepancy in the c-profiles within the first 30 cm for the 1.0 MHz data. In contrast at heights greater than 40 cm above datum, there is a good consistency in the c-profiles for the 1.0 MHz ABS data. It is worth noting that the concentration values for the first half of the burst are larger than those for the second half of the burst for both ABS sensors. This is in agreement with the analysis of the hydrodynamics (table 3.5), which showed that the energy of the first half of burst a07a was larger than the second half of the burst.

Focusing now on figure 6.1b, there is a good consistency in the data, especially for the 2.0 MHz ABS data. There is some variation in the sediment concentration within the first 50 cm for the 1.0 MHz ABS data.

6.2.2 One minute averaged concentration

With a wave period of approximately 5 seconds, about 12 waves were averaged to produce a one minute averaged concentration profile. Figure 6.2 shows the averaged profiles for a) burst a07a (irregular waves, $H_s = 0.53$ m) and b) burst a08a (regular waves, $H = 0.85$ m) recorded by the 1.0 MHz and the 2.0 MHz ABS sensor, respectively. Within the burst there is a difference between the profiles measured by the 1.0 MHz and 2.0 MHz sensors respectively, however there is no pattern in the data for other bursts to suggest that one of the sensors always measured larger or smaller sediment concentration values. There is a clear difference between the spread in concentration profiles of the regular and irregular waves. Close to the bed the averaged sediment concentration for burst a07a varies by up to a factor of 50, while further away from the bed (> 50 cm) it only varies by a factor of about 3. In contrast, the sediment concentration for burst a08a does not differ by more than, approximately, a factor of 3.

6.2.3 Discussion of the results and conclusions

The consistency of the concentration profiles for the regular waves was very good. This supported the analyses of the hydrodynamic data where little variation was found in the velocity or wave elevation data for a burst. The variation in the concentration profiles for irregular waves seemed quite large at first sight. However, taking the different hydrodynamic conditions during a burst for the irregular waves into account, this was not surprising. As mentioned in section 5.1.1, the sediment concentrations at the bed were dominated by event like structures and were more consistent for the mean c-profiles of different time scales for

the 1.0 MHz data. As any suspension events, triggered by groups of large waves, were likely to be apparent in the vicinity of the bed, it was not surprising that there was a greater variation in the c-profiles close to the bed. Further away from the bed, individual suspension events were less important and thus, the variation of the c-profiles at different time scales was less. At this level an almost constant wash load of fine material was observed during most of the burst. This seemed to contradict the observations made for the 2.0 MHz ABS sensor for burst a07a (figure 6.1a), because there was a significant difference in the mean c-profiles for different time scales. The discrepancy at high z values for the 2.0 MHz sensor suggests that there may be a small amount of drift in the calibration. The agreement between the subtle variations in concentration over the range of 60 to 100 cm is quite remarkable. However, the agreement in figure 6.1b suggests that in fact the calibration is steady. The consistent blips in the profiles in 6.1a are probably caused by fixed parts of STABLE, which provide a very weak return signal showing up at these low concentrations. It will be shown later that individual groups of large waves cause a significant sediment suspension at higher levels above the bed.

The one minute averaged c-profiles exhibited considerable scatter, especially within the first 40 cm above datum, indicating the influence of groups of large waves in a burst of irregular waves. There was no consistent increase in concentration values in the one minute averaged c-profiles with increasing elapse of time in the burst.

The influence of wave groups has been shown, especially in the analysis of the one minute averaged c-profiles. The question as to which time scale to use for determining an averaged concentration profile remains. For an overview of sediment distribution with height the burst averaged profiles give a good indication of the sediment entrainment due to irregular waves. This does not replace intra-wave analysis, where the effects of individual, large waves or wave groups are considered. In order to smooth out the effects of individual waves in an averaged profile the maximum length of data should be taken into account for irregular waves, while this is not as important for regular waves. However, for simplicity of analysis and comparison of the results between regular and irregular waves the same length of data (whole burst) was chosen in this study.

6.3 Influence of wave groups

WILLIAMS ET AL. (2001) have shown that under groups of more than five waves, average suspended sediment concentration values, \bar{c} , are approximately 3 times larger than values measured beneath a single wave of comparable height. Further analysis also demonstrated

that the *in situ* grain settling velocity also increases under groups of waves. The reason for this might be the formation of sediment clouds, which then settle as a unit with a larger settling velocity than individual grains.

Calibrated ABS data for four bursts with irregular waves ranging from about 0.5 m to 1.3 m were available. As only the 1.0 MHz sensor was calibrated for all four bursts, the main attention was focused on this sensor keeping in mind that it is more affected by system noise. Furthermore, it was in line with the ECM heads and thus the reflection of the acoustic signal of the ECM heads is more predominant in these data.

The groupiness of the waves was assessed using the definition given in KETABDARI (1999), who defines the groupiness factor as

$$GF = \frac{\sqrt{\frac{1}{N_{thres}} \cdot \sum_{k=1}^{k=N} j_{1k} \cdot \sum_{i=1}^{i=j} (H_i - H_{1/3})^2}}{H_{1/3}} \quad (2.33)$$

where N_{thres} is the number of waves over the threshold wave height, $H_{1/3}$, N is the number of runs in a record, j_1 is the run length and i_j is the total number of waves in each burst. For the bursts analysed here the groupiness factor ranged from 0.4 to 0.49. According to KETABDARI (1999), these were not very groupy waves. This can be explained by the fact that the irregular waves were generated with only some degree of groupiness and not specifically groupy waves. Though, this analysis showed that these waves were not very groupy, groups of large waves and the corresponding wave cycle mean concentration profiles were identified. It was thought that the groupiness factor might be used as an additional parameter for the prediction of sediment suspension under irregular waves. However, due to the lack of bursts with significantly different groupiness factors, this will be the subject of further studies.

A wave group was identified by determining the wave height between two consecutive zero down-crossings and comparing this wave height with the mean wave height of the whole burst. This is the same criterion as used by OSBORNE ET AL. (1994) in their work on suspended sediment sand concentrations in the nearshore. A wave was added to a group if its wave height was larger than the average wave height of the whole burst. The end of a group was reached when the next wave height was below the threshold. Any groups with less than three waves were discarded. Using the significant wave height as a threshold was investigated, but it turned out that this way not enough groups were identified in the bursts.

6.3.1 Presentation of the data

6.3.1.1 Cycle mean profiles of wave groups

Figure 6.3 shows the wave cycle average concentration profiles for a wave group for burst a07a ($H_s = 0.53$ m). Also included at the bottom of this graph is the synchronous time series of the horizontal (along the flume) velocity from the lowest ECM sensors (approximately 30 cm above the bed) on STABLE. There is a systematic increase in the sediment concentration within the first 30 cm above the bed for the first three waves. The cycle mean c-profile for the fourth wave in this group does not follow this pattern. The sediment concentration at the bed is lower than during the previous waves, but at the same time it is larger between 20 and 40 cm above the bed. Above 50 cm above the bed, the concentration profile is almost constant and no influence of individual waves in the group can be detected. Suspension events occurring under individual waves do not reach this height, but a wash load of fine particles is present instead.

Figure 6.4 shows another wave group containing seven waves (burst a12a, $H_s = 1.26$ m). Further, the synchronous horizontal velocity is shown at the bottom of the graph. For the first three waves the sediment concentration at the bed and up to about 70 cm into the water column increases. At heights larger than 70 cm the sediment does not experience the effects of the waves making the background concentration apparent. The fourth wave in this group is the largest with a maximum horizontal velocity of over 1 m/s. This immediately results in a bed concentration about three times larger than the one for the previous wave. However, above approximately 30 cm the sediment concentration is smaller than for the previous cycle mean profile. The next three waves are smaller than the fourth wave in the group. The concentration within the first 40 cm above the bed reduces significantly, while the concentration hardly changes above this level with the passing of the three waves. At the end of the group the concentration profile is similar to one found in cohesive sediments with a small vertical gradient. Figure 6.5 shows the same wave group and additionally the next four waves, whose wave heights are below the threshold criterion and thus they were not included in the original group of high waves. They are shown here to assess the time sediment stays in suspension after the passing of a wave group of large waves and the time it takes for the c-profiles to reduce. Also shown here is the burst mean c-profile (thick black line) to give some idea of the relative magnitude of the sediment concentrations. During the passing of waves 8 and 9 the sediment concentration between 80 and 100 cm in the water column hardly changes and lies above the values of the mean c-profile. At the same time the near bed concentration reduces below the value of the mean c-profile. The cycle mean

c-profile for wave 9 is very interesting. The sediment concentration at approximately 70 cm above the bed is of the same order as the concentration at about 15 cm above the bed. In between these two heights the concentration reduces to the lowest value at about 30 cm above the bed before it increases again. The values of the cycle averaged c-profile for wave 10 are larger up to about 60 cm above the bed, than those of wave 9, and there above they are smaller than the c-profile for wave 9. For the last cycle averaged c-profile (wave 11) the concentration at the bed reduces by about a factor of four compared to wave 10. Also, the concentration above approximately 60 cm above the bed is almost constant.

Figures 6.2 to 6.5 were only examples of the complicated suspension processes occurring under groups of large waves. The near bed concentration values increased with the passing of successive waves in the group until the largest wave in the group is reached. If the waves are large enough to entrain significant amounts of sediment into the water column, the smaller waves in the wave group are capable of entraining the sediment further into the water column while the near bed concentration reduces. Thus, resulting in sediment concentrations away from the bed of the same order as the near bed values at the beginning of the group.

This general observation is confirmed in figure 6.6, which shows the cycle mean sediment concentrations at $z = 5$ cm above the bed for the different waves in a wave group for burst a12a. It suggests that the sediment concentration peaks under the third or fourth wave in a group of waves consisting of more than three waves. This phenomenon was observed for all bursts.

6.3.1.2 Instantaneous sediment concentrations for wave groups

Figure 6.7 (burst a07a, $H_s = 0.53$ m) shows the horizontal orbital velocity at $z \approx 30$ cm above the bed for a wave group with the corresponding instantaneous sediment concentration up to a height of 30 cm above the bed. The sediment is entrained and carried up the water column over some time, but settles almost immediately with an approximately vertical gradient. This behaviour can be observed under all wave groups for the four bursts with waves of different heights. The sand is entrained between the time of largest horizontal acceleration (zero-crossing) and largest horizontal velocity. Figure 6.8 also shows the horizontal orbital velocity, the instantaneous sediment concentrations and additionally the corresponding shear stress, determined using equation 2.53, for burst a12a ($H_s = 1.26$ m). The reaction of the sediment due to the waves is different compared to burst a07a. The sediment entrainment, resulting in the highest concentration, occurs with a delay of half a

wave cycle compared to the passing of a wave trough or crest. This can be clearly seen at $t \approx 102$ seconds, where the highest shear stress of about 5 N/m^2 occurs. The high entrainment of sediment at this time only lasts about 0.25 seconds. The largest sediment concentration exists under the following crest, where the shear stress is only about 2.5 N/m^2 .

6.3.2 Discussion of results and conclusions

The significance of a group of large waves on sediment entrainment into the water column has been clearly demonstrated. If the waves are too small (burst a07a, figure 6.3), a sequence of waves with wave heights exceeding the burst mean wave height does not entrain sediment more than approximately 8 ripple heights above the bed with increasing near bed concentrations. Further away from the bed the concentration is almost unaffected by the passing of a wave group indicating a constant wash load at this level. However, if the waves are large enough to entrain the sediments up to 1 m above the bed (burst a12a, figures 6.4 and 6.5), waves, whose wave heights are below the mean wave height of the burst, can keep it in suspension. Figure 6.5 showed that the sediment concentration did not change significantly in the region of 80 to 100 cm above the bed during waves 6 to 9. This seems to suggest that a constant wash load exists. Alternatively sediment suspended above the ABS sensor might settle during a wave period and then be picked up by the transducer during the next wave. The small change in the wave cycle mean concentrations at this level does not allow the determination of a settling velocity, because the resolution of the wave cycle mean concentrations is not high enough to deduce settling velocities.

The so called pumping effect apparent under wave groups was clearly observed in the present data. However, only waves large enough can lift sediment more than 10 ripple heights into the water column. An attempt was made to parameterise the relationship between the near bed hydrodynamics and the resulting sediment behaviour concentrating on the enhanced suspension under wave groups. The analysis focused on the wave groups found in burst a12a ($H_s = 1.26 \text{ m}$). For each wave in each group, the height z , at which the cycle mean concentration drops below 1 g/l and the corresponding wave height were determined. This is thought to give an indirect indication of the likely volume of sediment in suspension and thus the sediment transport rate. The investigation showed clearly that it is not only the wave height of an individual wave, but more importantly the antecedent wave conditions and the position of the wave in the group that influence the suspension of sediments. The significance of the position of the wave in the group was already shown in figure 6.6. A parameterisation combining the hydrodynamic data into an effective wave height was investigated. The factor $(1+n/N)$ takes the position of the wave in a wave group

into account keeping in mind that the suspension increased during the passing of the group. The group wave height is used to identify the average height of the waves in the group. The burst mean wave height represents the overall wave energy of the burst. A combination of these is thought to be a better representative of the wave energy of irregular waves leading to sediment suspension than the significant wave height. Figures 6.9 and 6.10 show the height z as a function of the effective wave height determined using equations 6.1 and 6.2, respectively. In equation 6.2, the mean of the antecedent wave heights is used rather than the wave height of the n^{th} wave in the group, assuming that the antecedent conditions are more dominant than the individual wave height and that therefore, the suspension occurs with a time lag.

$$H_{\text{eff}}(n) = H_n \cdot \left(1 + \frac{n}{N}\right) \cdot \frac{\bar{H}_{\text{group}}}{\bar{H}_{\text{burst}}} \quad (6.1)$$

$$H_{\text{eff}}(n) = \frac{1}{n-1} \cdot \sum_{i=1}^{n-1} H_i \cdot \left(1 + \frac{n}{N}\right) \cdot \frac{\bar{H}_{\text{group}}}{\bar{H}_{\text{burst}}} \quad (6.2)$$

- where
- H_n = wave height of the n^{th} wave in a group [m]
 - H_i = wave height of the i^{th} wave in a group [m]
 - \bar{H}_{group} = group mean wave height [m]
 - \bar{H}_{burst} = burst mean wave height [m]
 - n = position of wave in the group
 - N = total number of waves in the group

Both figures exhibit the same trend suggesting that there is an increase in the suspension height, z , with increasing effective wave height. It is mentioned here that a plot of z versus the individual wave heights, H_n , showed a lot of scatter and produced a R^2 value for linear regression of 0.15. Figure 6.10 shows slightly less scatter and thus indicates that the antecedent waves are more important than the individual wave. For a linear regression the R^2 values are 0.36 and 0.34, respectively. On this basis there does not seem to be a significant difference between the two figures. Further, the wave period of each wave is of importance in order to assess the ratio of available time to settling velocity of the particles. This then determines whether the particles settle back to the bed before the next wave approaches. The above parameterisations for the effective wave height might prove to be too complicated for field measurements. A parameterisation based on the groupiness factor for each burst seems more applicable. Due to the lack of concentration data and the fact that there was no significant variation in the groupiness ($0.4 \leq GF \leq 0.49$) it was not possible to propose a parameterisation based on the groupiness factor for the present data.

The phase relation between the near bed horizontal, orbital velocity and the sediment suspension was investigated for a wave group. The entrainment of sediment was phase linked to peaks in the velocity signal and a rapid settling of sediments was observed in the ABS data. This rapid settling could be explained by the fact that a cloud of sediment was formed which settled as a unit at a large settling velocity. Alternatively, it could also be consistent with sediment clouds convecting passed the sensor, suggesting that sediment is indeed entrained in discrete packets.

6.4 Comparison with field data (MK Bank data)

6.4.1 Description of the field conditions

In February 1993 STABLE and other instruments were deployed by POL using the NERC research vessel Challenger (WILLIAMS, 1993). The study site was located at the Northwestern end of the Middelkerke Bank, off Oostende, Belgium, 51°20.6'N, 02°46.3'E (figure 6.11). STABLE recorded turbulence, wave and suspended sediment processes in the bottom metre of the flow. The work was conducted as part of the MAST 2 CSTAB programme (Circulation and Sediment Transport Around Banks, CSTAB Handbook, 1996) to investigate the flow structure around an offshore sand bank (MACDONALD AND O'CONNOR, 1996).

The Middelkerke Bank is located in a field of parallel sandbanks or tidal ridges, known as the Flemish Banks. The banks are separated by swales that dip to the North East. The field study was located near the North Western end of the bank, near the swale known as the Negenvaam, which is 2 to 3 km wide and 12 to 20 m deep. The separation distance between the Middelkerke Bank and the next two parallel banks (Oostende Bank to the South East and Kwinte Bank to the North West) is approximately 4 km either side.

The data were obtained in a water depth of 21 m and the mean tidal current reached up to 0.8 m/s during the deployment. The records from a Waverider buoy located 4 km from the STABLE deployment site indicated significant surface wave heights of up to 2.9 m during the deployment period.

For a more detailed description of the deployment site and the data obtained see ROSE (1997). For the present analysis data for one burst (Burst 38) were available. This burst was recorded at the height of a storm with a wave period of about 8 s and a significant wave height of 2.88 m. The mean sediment diameter at the bed was $d_{50} = 0.44$ mm and the ripple wavelength and height were $\lambda_r = 0.56$ m and $h_r = 0.08$ m determined from the ABS

measurements (ROSE, 1997), respectively. The ripple dimensions are comparable with the ones determined for burst a12a in the present study.

6.4.2 Wave groups in the field data

The irregular waves generated in the *Deltaflume* were based on JONSWAP spectra determined under field conditions. However, some uncertainties remained about the influence of the controlled conditions found in the laboratory tests. It is very important to ascertain that the mechanisms observed in the flume were not specific to the flume set-up and that they can also be found in field data.

Figures 6.12 and 6.13 show examples of wave cycle mean concentration profiles for two different wave groups. The criterion for identifying a wave group was the same as used for the *Deltaflume* data. Also shown is the burst mean c-profile indicated by the thick, black line. Turning the attention first to figure 6.12, the near bed concentration at the beginning of the wave group is of the same order as the burst mean concentration. With the passing of the wave group the near bed sediment concentration increases. The concentrations within the first 30 cm are largest under wave 6. Above this level the sediment concentrations do not change significantly over the sequence of the six waves. Waves 7 and 8 suspend more sediment in the region above 30 cm, but at the same time the near bed concentration reduces. The cycle mean profile for the first wave in the wave group in figure 6.13 is below the burst average c-profile. The second and third wave suspend the sediment up to 30 cm above the bed with concentration values greater than the burst mean concentrations. During the fourth wave the sediment is then lifted further into the water column and at the same time the near bed concentration reduces. However, the wave group has no effect on the sediment concentration values at distances greater than 50 cm above the bed.

An example of instantaneous sediment concentration up to 30 cm above the bed and the corresponding horizontal orbital velocity in the direction of the waves are shown in figure 6.14. The circled areas indicate two individual suspension events occurring between the peak trough and the peak crest velocities. For the event highlighted at about 45 s, the first suspension peak is found just after the peak trough velocity, while the second suspension event peaks at the time of the zero up-crossing. In contrast during the second event, indicated at about 53 s, the first suspension event occurs between the peak trough velocity and the zero up-crossing, while the second larger event starts peaking just after the zero up-crossing.

6.4.3 Discussion of results and conclusions

Though, the data of burst 38 were recorded during the height of a storm event the near bed velocities were smaller compared with burst a12a from the *Deltaflume* experiments due to the larger water depth in the field. At the same time the mean sediment diameter at the bed was larger (440 μm) than the one of the medium sand test bed (329 μm) used in the *Deltaflume* tests. This in combination with the smaller orbital motion resulted in less sediment being entrained into the water column compared with burst a12a. Some features relating to the enhanced sediment suspension under wave groups as found in the laboratory data were observed. Sediment was entrained further into the water column up to approximately 7 times the ripple height under the wave groups hence, indicating some wave pumping. However, the orbital motion was not large enough to lift a significant amount of sediment passed 40 cm above the bed. This is in contrast to burst a12a (figure 6.5), but in line with burst a07a (figure 6.3) with smaller orbital motion.

Figure 6.14 highlighted two time periods where two suspension events occurred between the peak trough and peak crest velocity. Two different suspension mechanisms seem to be the cause for the sediment entrainment. The wave exerted shear stress on the bed is large under the wave crest and trough, respectively using a steady state approach. The force exerted by the waves then lifts up sediment into the water column. After a zero crossing coherent structures separate from the ripple crests and can carry sediment into the water column. This is one possible explanation for the different phase relation between sediment entrainment events and the orbital velocity. Further, it has to be kept in mind that the ABS transducers take 'snap shots' of sediments advecting passed the sensor. Thus, any sediment could have been entrained from the bed away from the sensor and it then passed through the acoustic beam. This means that it is difficult to relate instantaneous concentration and velocity measurements if the position of the ABS transducer relative to a ripple crest or trough is unknown. Although, there was no direct information available regarding the ripple dimensions at the Middelkerke Bank for the present study, it is suggested that the ripples were less regular than for the *Deltaflume* experiment, because of a less uniform grading of the bed material. This might have led to different suspension events around the sensor, which were than advected passed the ABS. Also, the same event might be advected during the forward and the backward stroke of the wave and in effect, recorded twice by the ABS transducer.

The analysis of field data was used to evaluate the significance of wave group suspension events observed in the laboratory data. Due to the smaller orbital motion, smaller amounts

of sediments were entrained into the water column compared with some *Deltaflume* tests (e.g. burst a12a). Nevertheless, the significance of the pumping effect under wave groups was observed leading to larger sediment concentrations compared with the mean concentrations further away from the bed. Thus, it was concluded that the features observed in the *Deltaflume* data were not modified by the laboratory boundary conditions. Therefore, any conclusions drawn from the laboratory data were regarded to not be affected by the experimental set up.

6.5 A simple model to predict c-profiles under a wave group

The analysis of the intra-wave sediment concentration profiles revealed that wave groups entrain significant amounts of sediment into the water column. The existing empirical equations analysed in chapter 5 were based on a quasi steady approach assuming that the waves can be characterised by a wave height and period. The equations assumed that sediment was entrained from the bed into sediment free water by the hydrodynamic forces. No entrainment history was taken into account, but each wave cycle was assumed to produce a new equilibrium for the suspending of sediment. A simple model was developed to take the convective entrainment of sediment during the passing of a wave group into account. The model was based on the fact that sediment is still in suspension before the next wave approaches and entrains further sediment.

6.5.1 Background

A simple model was developed that utilises the measured wave height, wave period and near bed horizontal, orbital velocity. A wave group from burst a12a ($H_s = 1.26$ m) was used to advance the present model. To identify the wave group, the same criterion as described in section 6.3 was applied. The wave elevation for this group is shown in figure 6.15. The group consists of ten waves of which the last two are below the threshold criterion. Their wave height, period and mean velocity, $1/2 \cdot (U_c + U_t)$, are presented in table 6.1.

Sediment at the bed is subject to entrainment, while sediment in the water column is subject to two processes – settling and entrainment. The simple model treats these two processes separately.

For each wave cycle a cloud of sediments is entrained from the near bed region into the water column. If this sediment does not settle back to the bed during a wave cycle, it is then subject to re-suspension due to the hydrodynamic forces of the next wave. The forces necessary to lift the sediment that was already suspended into the water column are less

than the forces necessary to entrain the sediment from the bed.

For simplicity, the burst mean concentration profile was used to represent the sediment concentration in the water column before the start of the wave group. The sediment concentration was provided in 1 cm intervals. It was then assumed that the sediment at the various heights settled with a settling velocity associated to the d_{16} value at the bed, thus reducing the concentration values at the different heights. As mentioned before, the analysis of the pump samples had shown that the sediment in suspension had a mean diameter equivalent to a d_{16} value at the bed. The concentrations, associated with the sediments that settled below bed level ($z = 0$), were accumulated and referred to as the bed concentration. At the beginning of the simulation, the concentration at 1 cm above the bed from the burst mean concentration was taken to be equal to the bed concentration. Due to the fact that some particles and the associated concentration values, hit the bed during a time step, some bins were empty at the top of the concentration profile. They were then replaced by a constant background concentration in order to keep the total number of bins and concentration values constant. This was necessary as no further concentration measurements were taken above 1 m above the bed. At the same time as applying a settling mechanism to the sediments already in suspension, it was presumed that a cloud of sediments was entrained from the near bed region under the influence of a vortex pair. It is suggested that a vortex pair is one mechanism that convects particles up the water column. The ejection of a sand particle due to the forces of a vortex pair has been modelled separately and is described extensively in chapter 7. For the purpose of this model, the wave height, period and horizontal, orbital velocity of each wave in the wave group were used to determine an entrainment velocity of the sediments for each wave from modelling the movement of a sand particle due to the influence of a vortex pair. The entrainment velocity was based on the maximum entrainment height and the time elapsed to reach this maximum height.

The entrainment velocity and the time information was then used to convect a "cloud of sediments" up the water column. Once, the maximum height was reached, the "cloud of sediments" was then subject to settling. The "cloud of sediments" was modelled by distributing a percentage of the sediment concentration from the previous cycle mean concentration at 1 cm above the bed over a number of bins, the first one being 1 cm above the bed. In this study, four bins were chosen, spreading the "cloud of sediments" over a range of four centimetres. Further, the "cloud of sediments" was composed of two particle fractions consisting of the d_{16} and d_{84} particle sizes found in the bed. The initial "cloud of sediments" spread out during the entrainment and settling mainly due to the different settling

velocities of the two fractions. For the present wave group, the entrainment velocities for the two fractions were within 6 % in the model thus, having little effect on the entrainment of the “cloud of sediments”.

During each time step, the vertical position of the “cloud of sediments” for the two fractions was calculated. The concentration profile was then determined by adding concentration values associated with the “cloud of sediments” for the two fractions and the concentration profile from the previous time step, which was subject to settling. In this way, a number of c-profiles were determined for each wave in the wave group and then averaged to produce a cycle mean profile, which could then be compared with the c-profiles in figures 6.3 to 6.5. Thus, the concentration profile present at the beginning of the next wave in the group was equivalent to the last one in the previous burst wave cycle. Only the first wave in the group was started with the burst mean c-profile. The different steps of the model are shown schematically in figure 6.16.

6.5.2 Results of the model

A number of parameters can be modified in the model. The fraction of the wave period during which the particles were entrained into the water column and the maximum height the particles reached was governed by the output parameters simulated by the model based on the convection of a particle due to the influence of a vortex pair. The influence of the individual parameters will be explained in detail in chapter 7. Table 6.2 lists the relevant input parameters used for the present study. The simple entrainment model was influenced by the initial c-profile at the beginning of the wave group, and the concentration quantities in the “cloud of sediments”.

Figures 6.17 and 6.18 show the cycle mean c-profiles for the present wave group. The bed concentrations are not shown here. For figure 6.17 the total sediment concentration trapped in the “cloud of sediments” was constant for the two fractions throughout the wave group. For figure 6.18, the sediment concentration was equal to 50 % of the sediment concentration from the previous cycle mean concentration at 1 cm above the bed. This concentration was then split into the two particle fractions.

Turning the attention first to figure 6.17, the different c-profiles are very noisy. This is a direct result of the “cloud of sediments” stepping through certain positions in the water column and missing others due to the entrainment or settling velocities. The solid blue line represents the burst mean c-profile at the beginning of the group. For the first four waves, the concentration above 30 cm above the bed increases and a significant amount of sediment is

present up to 90 cm above the bed. It then settles over the rest of the waves in the wave group. Turning the attention now to figure 6.18 it is less noisy. The reason for this is the smaller amount of sediment that was trapped in the “cloud of sediments”, especially towards the end of the wave group. The second wave in the group entrains a significant amount of sediment up to approximately 50 cm above the bed. The next three waves entrain this sediment further into the water column while the concentration within the first 50 cm reduces. The c-profiles for the last four waves in the group are almost identical and the concentrations are less than in the previous c-profiles. This is mainly due to the period of the seventh wave (8th c-profile) in the group of 11.25 seconds, which allows most of the particles to settle out. Additionally, the concentration trapped in the “cloud of sediments” was small at this stage as it was directly linked to the concentration at 1 cm above the bed of the previous cycle mean c-profile.

6.5.3 Discussion and Conclusion

The results produced by the simple convective model were very encouraging. Figures 6.17 and 6.18 demonstrated clearly that a significant amount of sediment can be entrained further away into the water column and at the same time the sediment concentration in the near bed region reduces. The maximum entrainment height is governed by the input parameters into the vortex pair model (see chapter 7). The reduction of near bed sediment concentration while suspending sediment into the water column is embedded in the present model. The results presented here are in line with the concentration measurements during the passing of wave groups presented in sections 6.3 and 6.4. Thus, this simple convective entrainment model can take the pumping effect observed under a wave group into account.

One of the main weaknesses of the model was the fact that no interaction between settling and entrainment of sediment was accounted for. Further, it was only the “cloud of sediments” that entrained sediments into the water column. No interaction between the particles already in suspension and the particles trapped in the cloud was considered. Also, the entrainment was a purely convective process. To include diffusion in the model a digital filter designed to have the properties corresponding to estimated diffusion coefficients could smooth out the “cloud of sediments”. At this stage, a modification of the parameters that influence the entrainment due to the vortex pair was not considered. A sensitivity analysis of these parameters will be presented in chapter 7.

Overall, the simple entrainment model performed well and was capable of simulating the pumping effect observed under wave groups by including the suspension history of

successive waves. The empirical models used in chapter 5 were not capable of this. They were based on a quasi steady approach entraining sediment into a sediment free environment.

6.6 Conclusions

At the beginning of this chapter the consistency of these concentration data with respect to different time scales were analysed. It turned out that the irregular waves were dominated by individual suspension events triggered by the passing of wave groups. This influenced the time averaged c-profiles at the different time scales. Thus, it was concluded that for the determination of a representative burst mean c-profile the longest available time scale should be considered (about 17 minutes for the present experiments) for irregular waves.

This chapter has also highlighted the importance of intra-wave sediment suspension studies under irregular waves. A group of waves was able to entrain sediment up to about 1 m above the bed (approximately 18 times the ripple height) of the same order as the near bed concentration for a single wave. The importance of the antecedent wave conditions was discussed and an attempt at a parameterisation was made. The suspension height increased with the increase of the effective wave height for two different expressions of the effective wave height.

The analysis of the phase relationship between suspension events and the near bed horizontal, orbital velocity proved inconclusive. There was no consistent link between the passing of a wave crest or trough and the suspension events. This might not be surprising as the measured sediment concentrations represent “snap shots” of the particles in the water column. Thus, the sediment passing through the acoustic beam of the sensor might have been entrained from the bed further away from the sensor and hence, only advected passed the ABS sensor. At other times, the ABS transducer might have measured sediment particles that were entrained underneath the sensor.

The field data were exhibiting two consecutive spikes of which one was thought likely to be advected passed the sensor. Though, there was no information available regarding the bedform geometry for the Middelkerke Bank experiment, it was suggested that the ripples were less two-dimensional and more irregular. This in turn might have led to different suspension events being advected through the ABS beam and thus recorded as two consecutive spikes in the data. The ripples in the *Deltaflume* were more regular and hence, this mechanism was less common, though there was some evidence.

The models investigated in chapter 5 were not capable of including a history of sediment suspensions throughout a wave group. A simple model was developed based on the assumption that the sediments in suspension are susceptible to an entrainment and settling process. The entrainment process was based on a purely convective mechanism due to the movement of a vortex pair. The results of the model were very encouraging as they indicated the lift of sediment up the water column while, at the same time, the near bed concentration reduced under the passing of a wave group. It is suggested that the ideas of the simple model will be expanded in future work and a diffusive entrainment process included in the model.

TABLES

Position of wave in group	Wave height [m]	Wave period [s]	Mean velocity [m/s]
1	0.6778	6.75	0.5066
2	1.2878	5.00	0.6482
3	1.7626	5.00	0.9378
4	1.3423	5.75	0.8096
5	0.8947	4.75	0.5499
6	0.9354	5.00	0.5336
7	0.6915	11.25	0.5362
8	0.8406	4.25	0.2957
9	0.2440	3.75	0.2343
10	0.4067	4.50	0.1844

Table 6.1: Relevant wave parameters of the wave group used for the development of the simple model to predict the sediment concentration profiles throughout a wave group.

	model parameters
ripple height [m]	0.058
drag coefficient [-]	1.0
enhanced kinematic viscosity [m ² /s]	5*10 ⁻⁴

Table 6.2: Model parameters used to simulate the re-suspension of sediment under a wave group due to a convective mechanism (vortex pair).

FIGURES

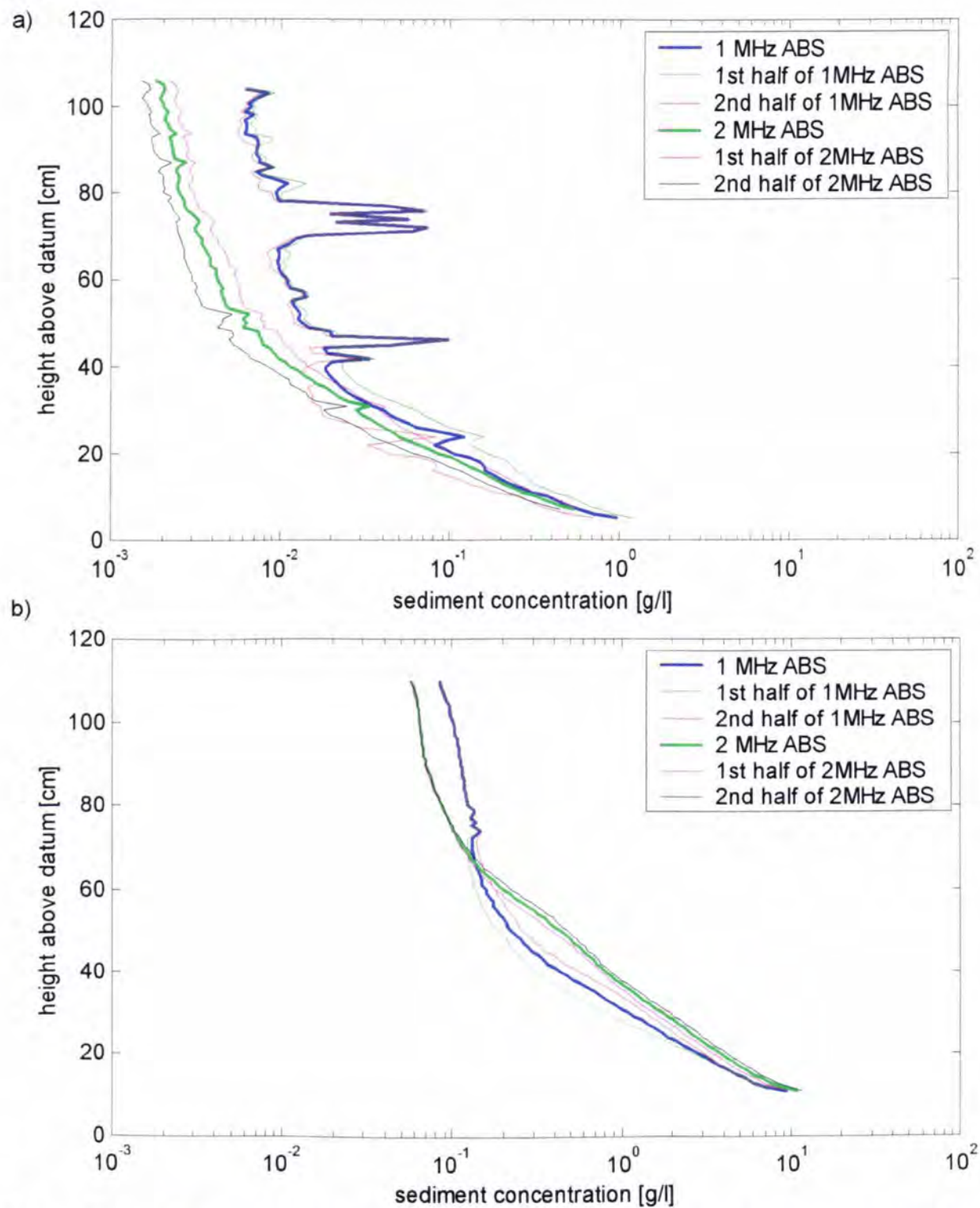


Figure 6.1: Burst averaged and mean c-profiles for the first and the second half of a burst for burst a) a07a (irregular waves, $H_s = 0.53$ m) and b) a11a (regular waves, $H = 1.34$ m).

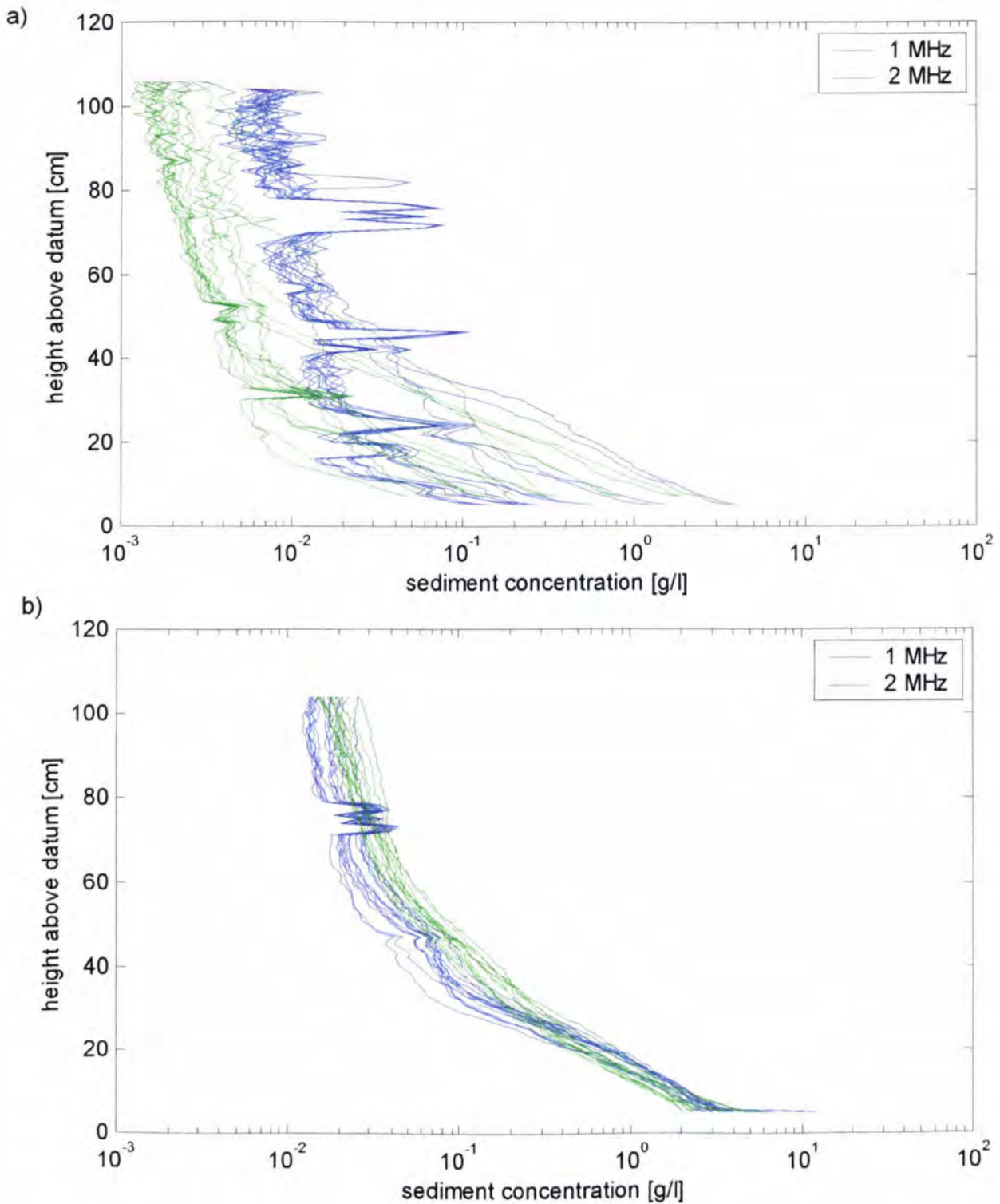


Figure 6.2: One minute mean concentration profiles for a) burst a07a (irregular waves, $H_s = 0.53$ m) and b) burst a08a (regular waves, $H = 0.83$ m). There is a good consistency between the different profiles for the regular waves, while the c-profiles for irregular waves show significant variations.

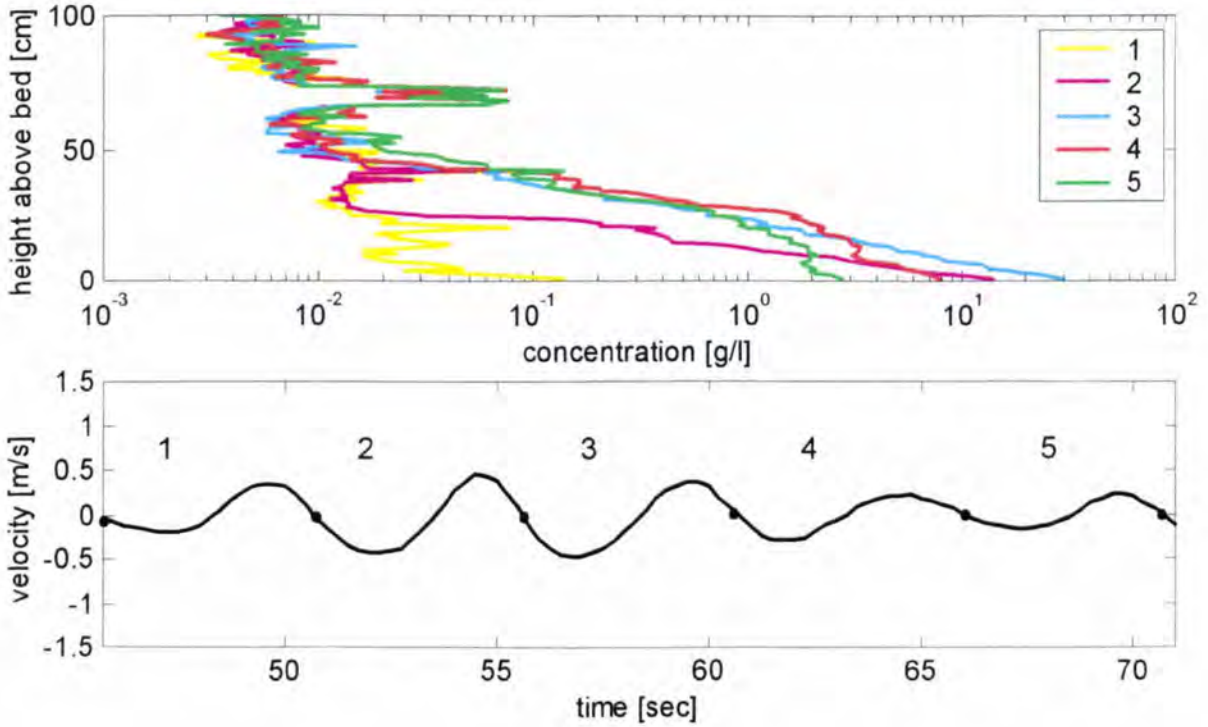


Figure 6.3: Wave cycle mean concentration profiles for a wave group in burst a07a ($H_s = 0.53$ m) and synchronous near bed horizontal velocity.

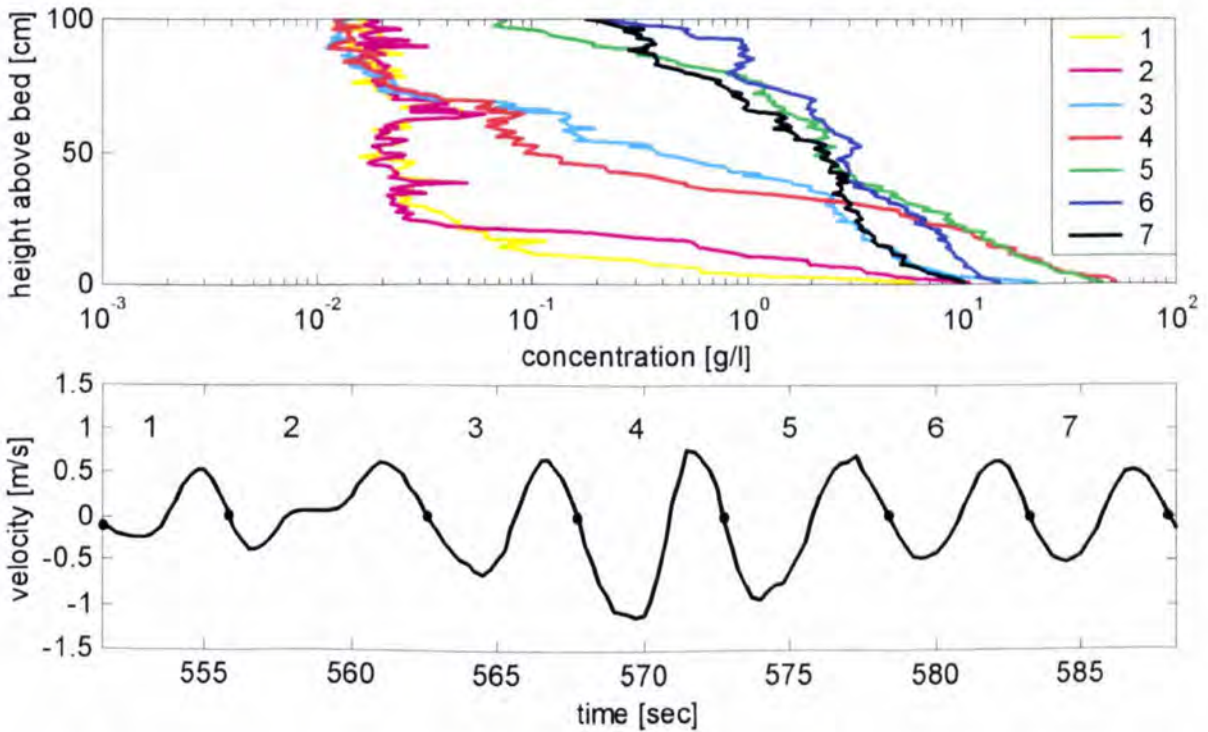


Figure 6.4: Wave cycle mean concentration profiles for a wave group in burst a12a ($H_s = 1.26$ m) and synchronous near bed horizontal velocity.

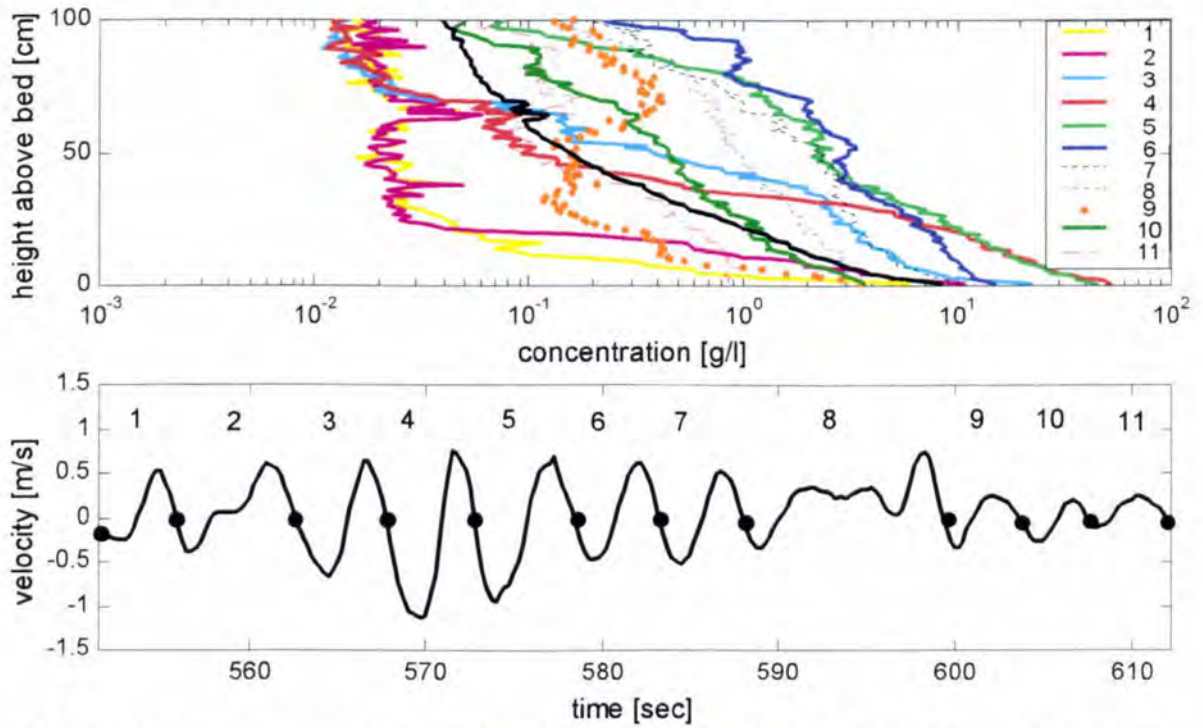


Figure 6.5: Wave cycle mean concentration profiles for the wave group shown in figure 6.4 plus the four consecutive waves and synchronous near bed horizontal velocity. The burst mean c-profile is indicated by the thick black line.

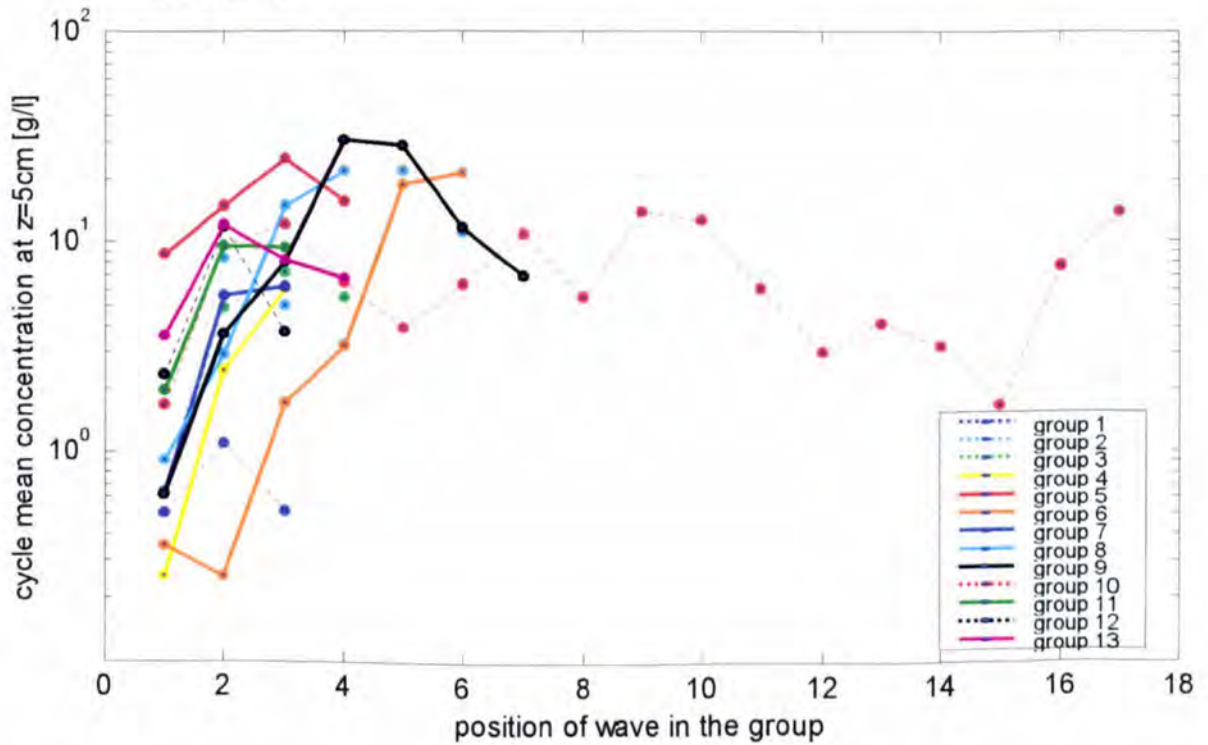


Figure 6.6: Wave cycle mean sediment concentration at $z = 5$ cm above the bed for the waves in the wave groups determined for burst a12a ($H_s = 1.26$ m).

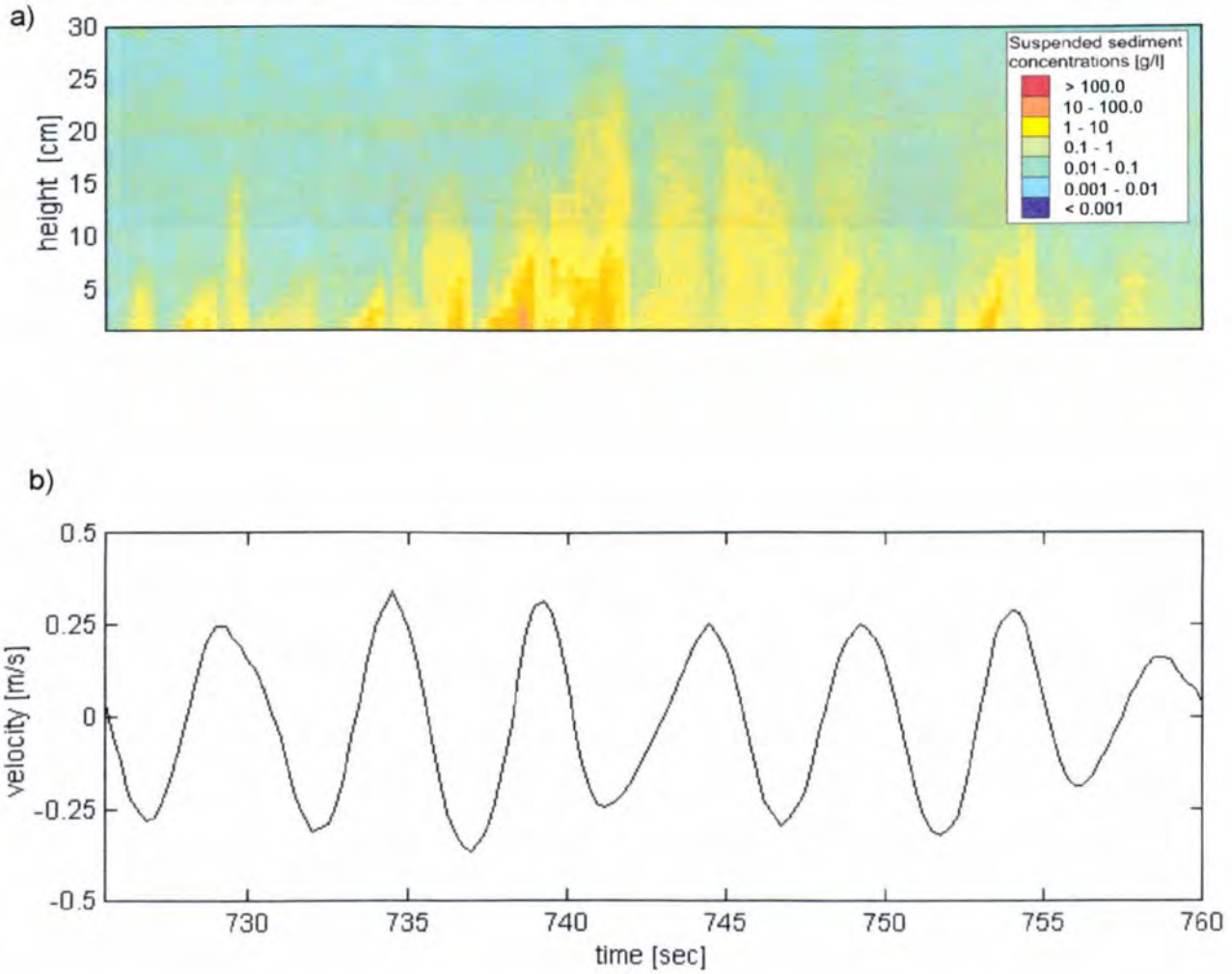


Figure 6.7: a) Calibrated 1.0 MHz ABS record for burst a07a (irregular waves, $H_s = 0.53$ m, red and dark blue indicate high and low suspended sediment concentration, respectively); b) corresponding near-bed horizontal fluid particle velocity exhibiting some large waves (ABS data from Dr P.D. Thorne, POL).

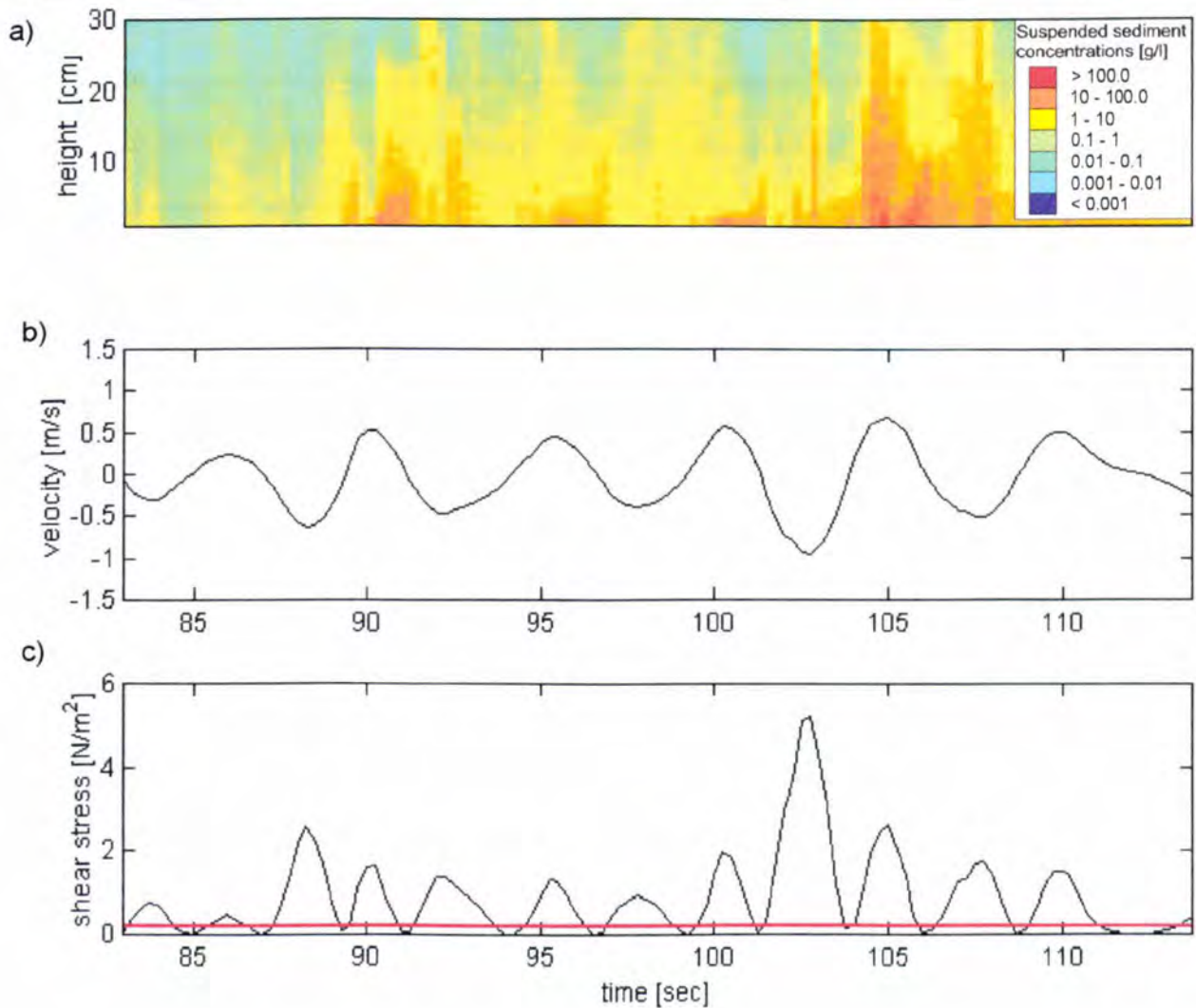


Figure 6.8: a) Calibrated 1.0 MHz ABS record for burst a12a (irregular waves, $H_s = 1.26$ m, red and dark blue indicate high and low suspended sediment concentration, respectively); b) corresponding near-bed horizontal fluid particle velocity exhibiting some large waves (ABS data from Dr P.D. Thorne, POL); c) corresponding bed shear stress. The red line indicates the critical shear stress determined from the significant wave height for the burst.

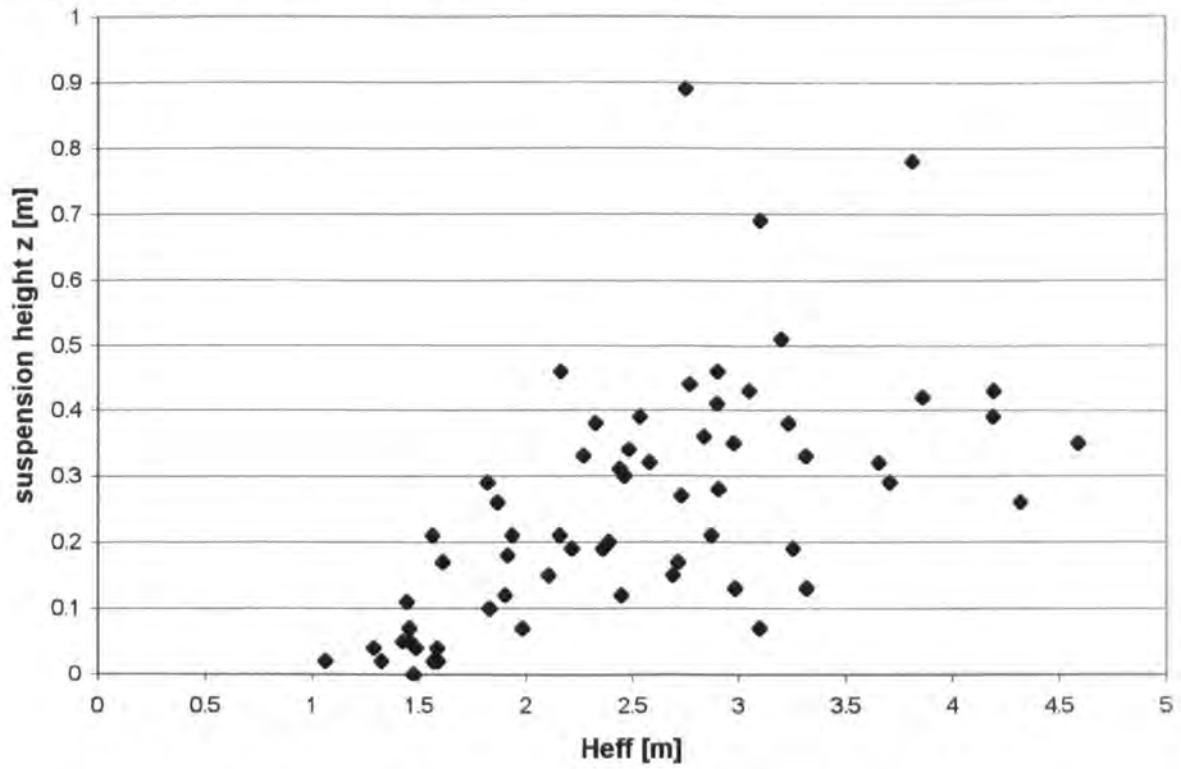


Figure 6.9: Suspension height as a function of an effective wave height calculated by equation 6.1.

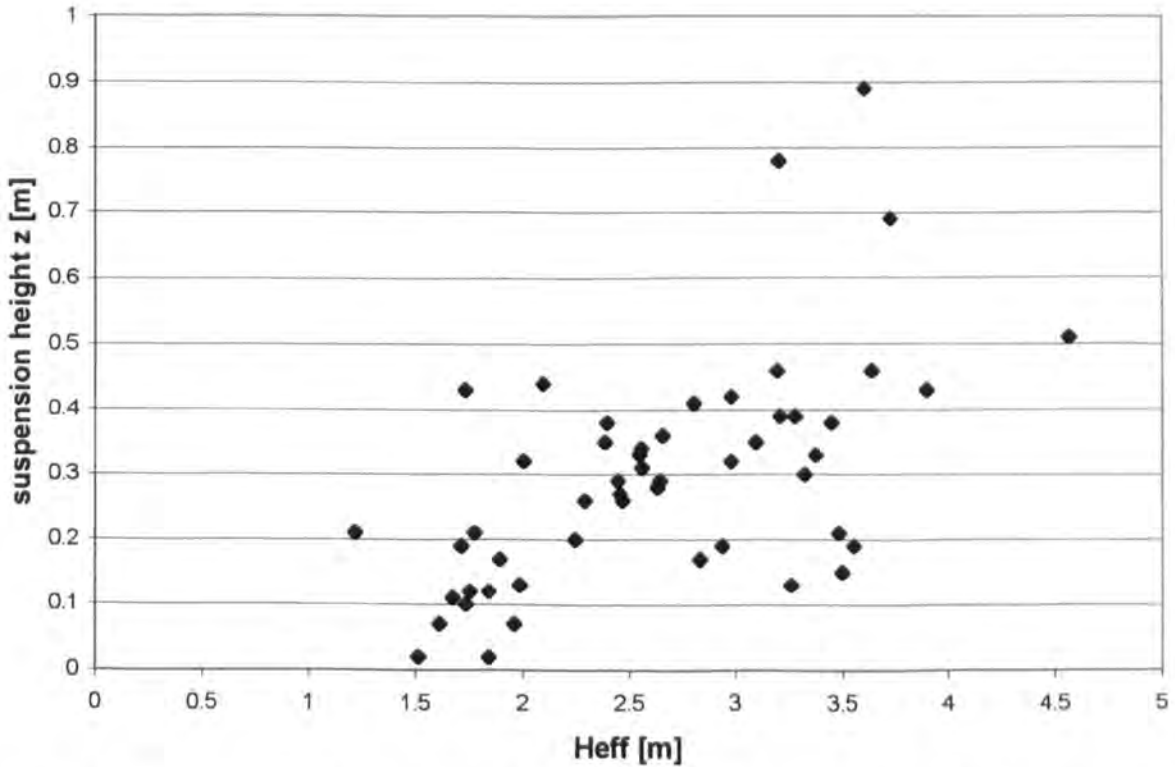


Figure 6.10: Suspension height as a function of an effective wave height calculated by equation 6.2.

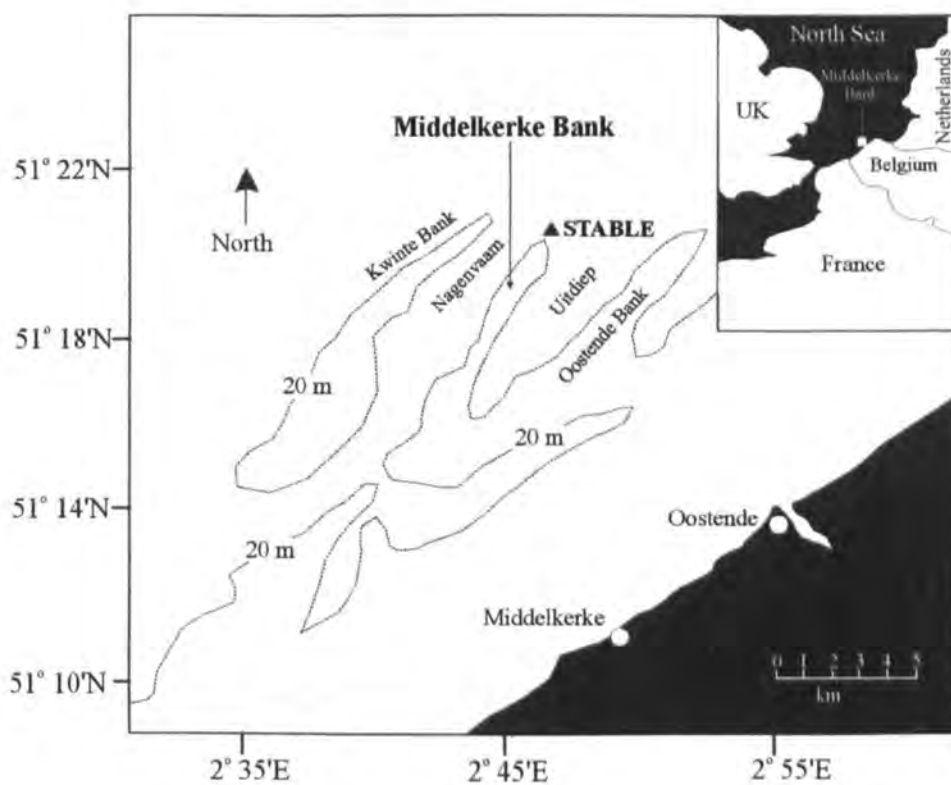


Figure 6.11: Location of the field site at Middelkerke Bank, Belgium (courtesy of Jon Williams, POL).

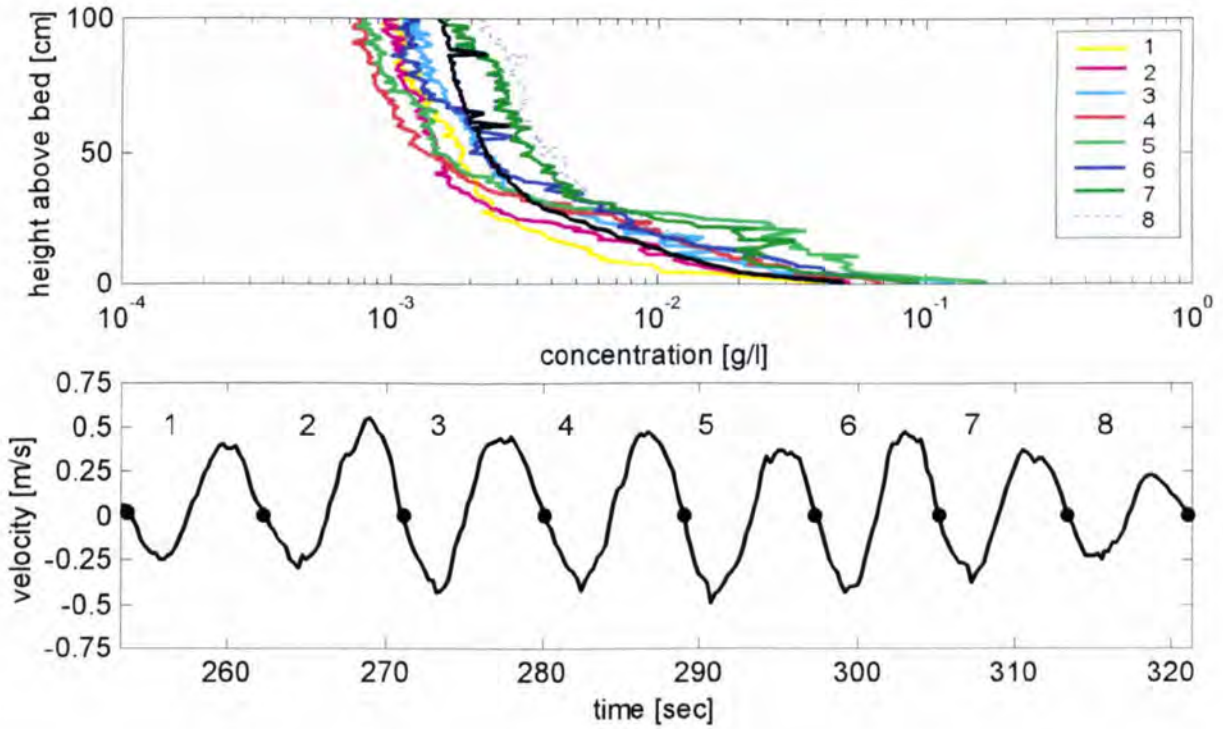


Figure 6.12: Wave cycle mean concentration profiles for a wave group in burst 38 (Middelkerke Bank, $H_s = 2.88$ m).

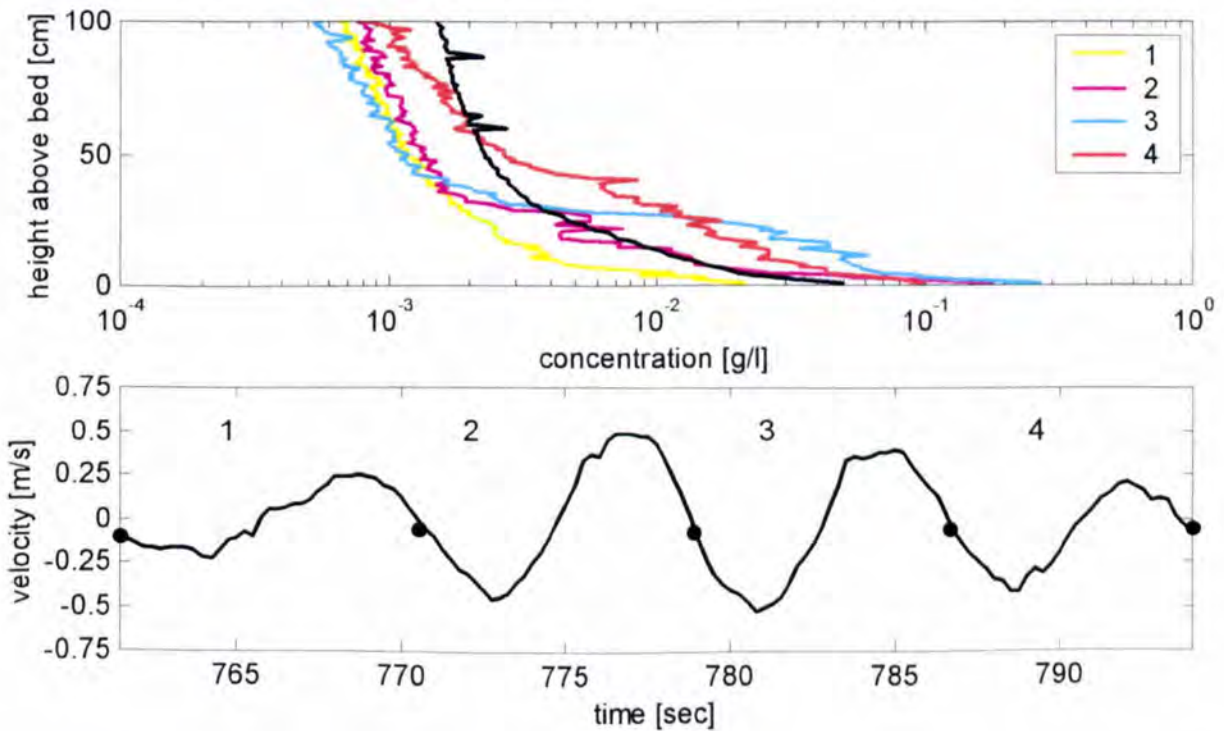


Figure 6.13: Wave cycle mean concentration profiles for a wave group in burst 38 (Middelkerke Bank, $H_s = 2.88$ m).

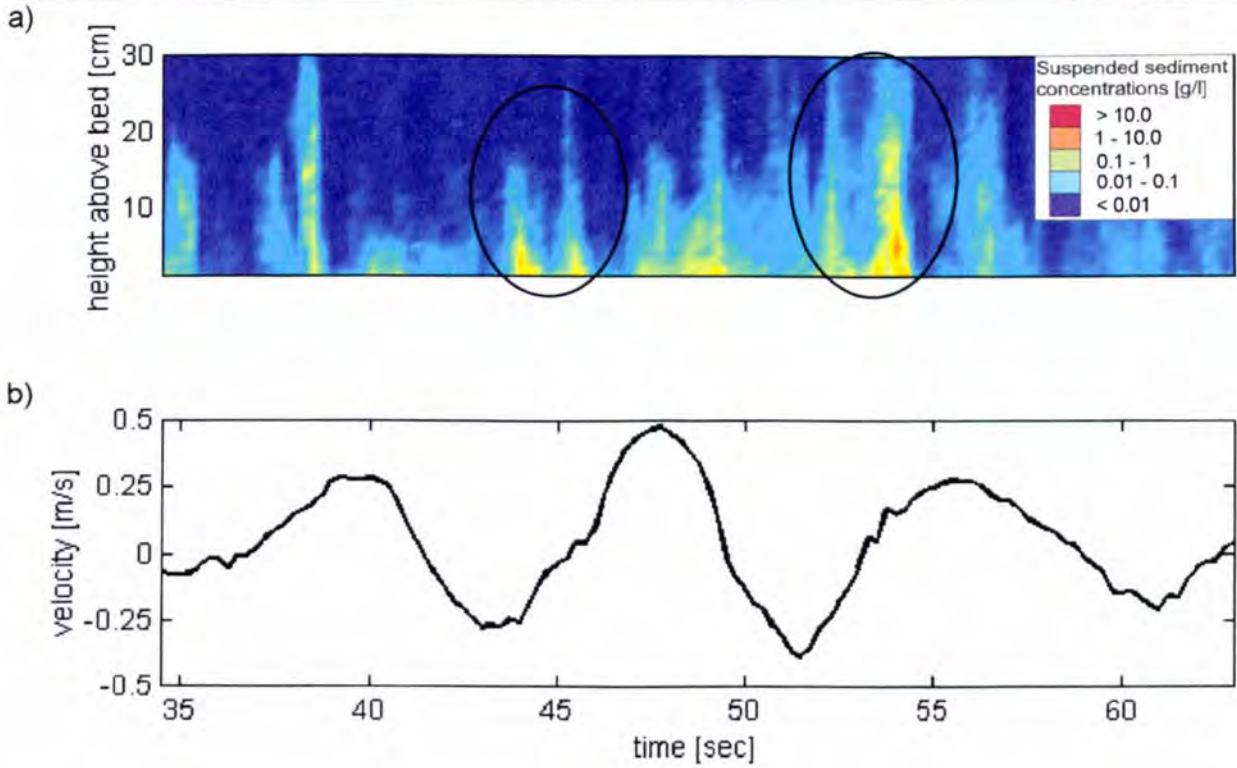


Figure 6.14: a) ABS record for MK Bank data ($H_s = 2.88$ m, red and dark blue indicate high and low suspended sediment concentration, respectively); b) corresponding near bed (40 cm above the bed) horizontal fluid particle velocity exhibiting some large waves.

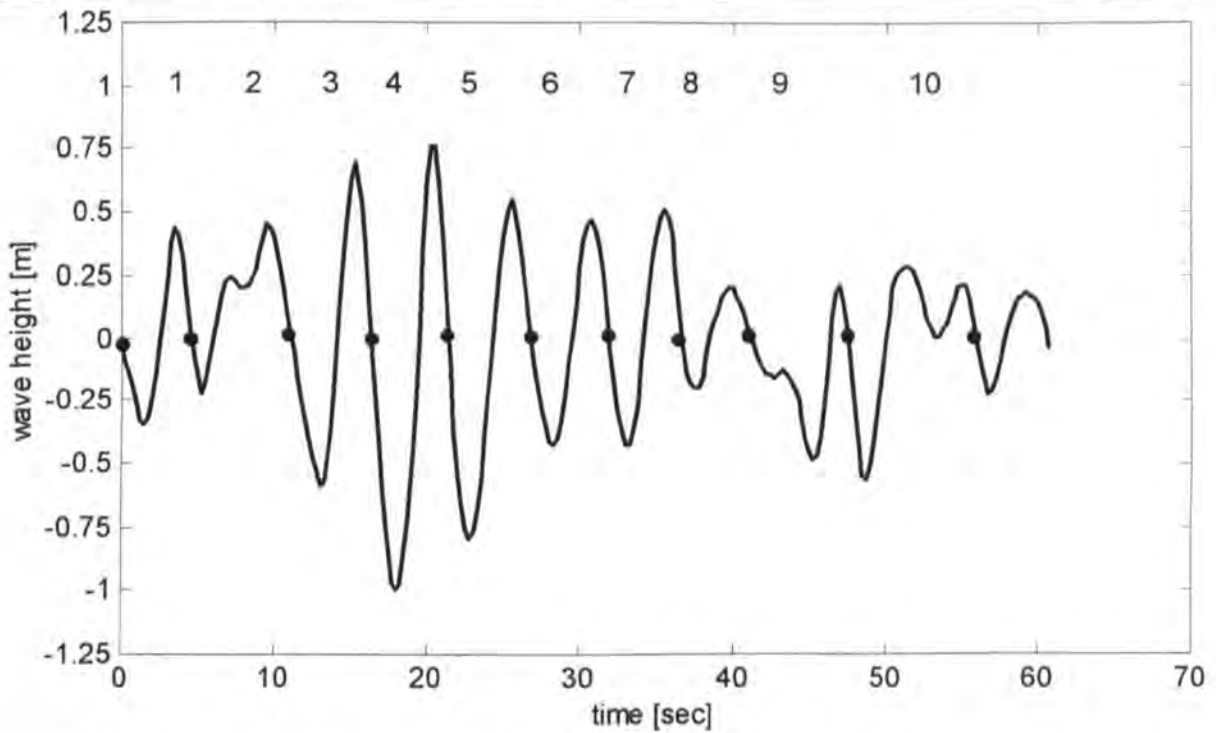


Figure 6.15: Wave elevation for a wave group from burst a12a (irregular waves $H_s = 1.26$ m). Ten individual waves can be identified. Their wave heights and periods are listed in table 6.1.

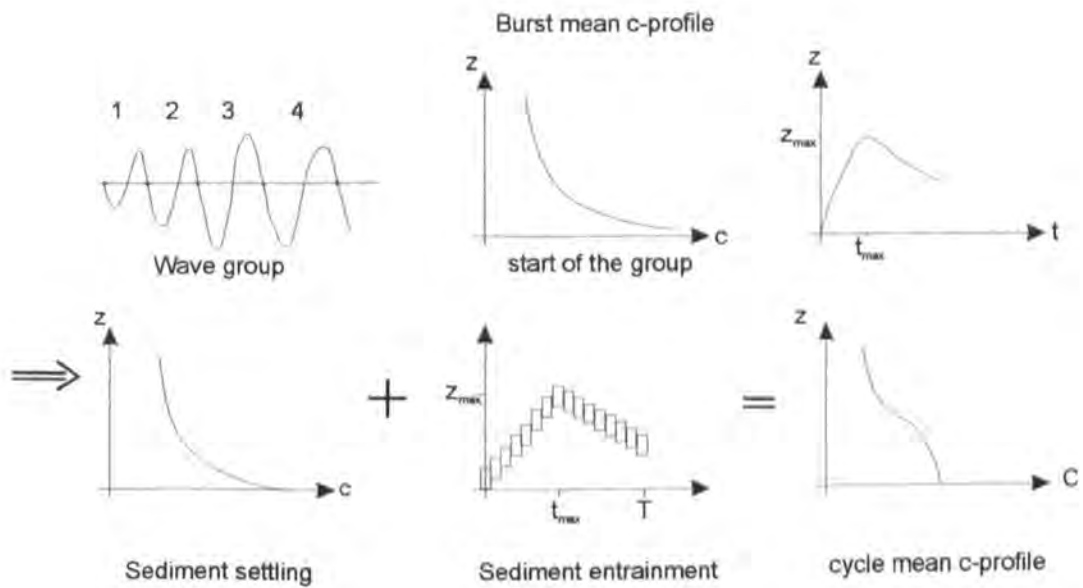


Figure 6.16: Schematic of the steps involved in the sediment entrainment model.

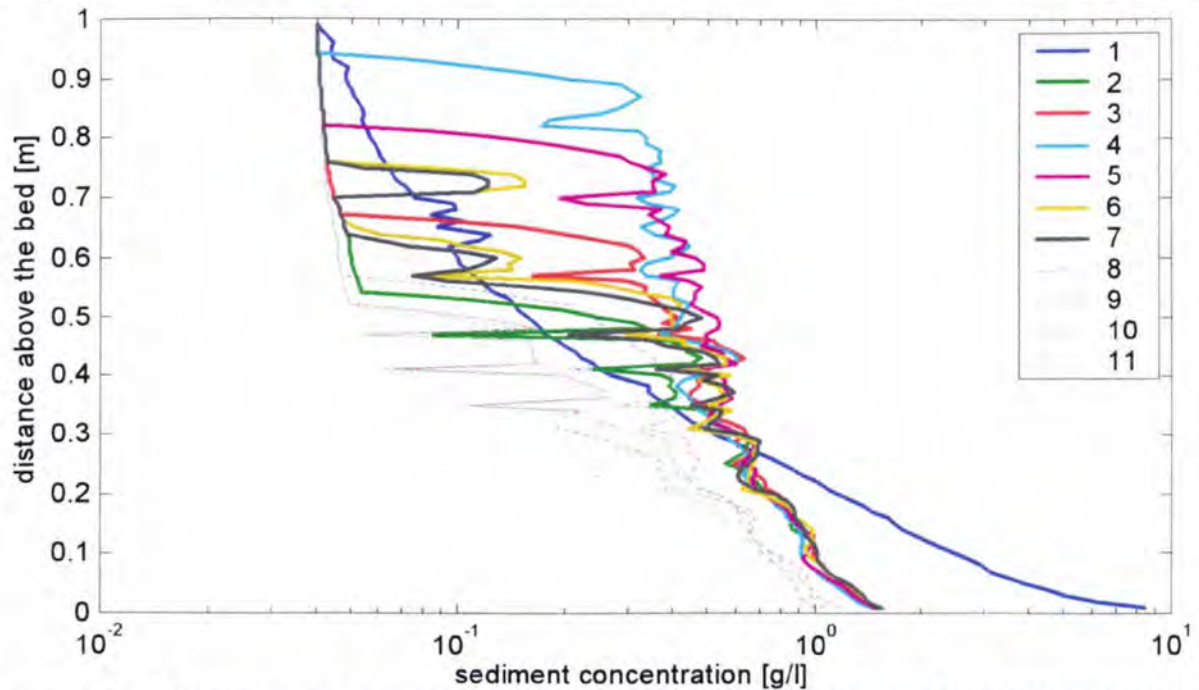


Figure 6.17: Cycle mean c-profiles for the wave group in figure 6.15 determined by the model. The sediment concentration entrained by the “cloud of sediments” was constant. The solid blue line represents the burst mean concentration profile.

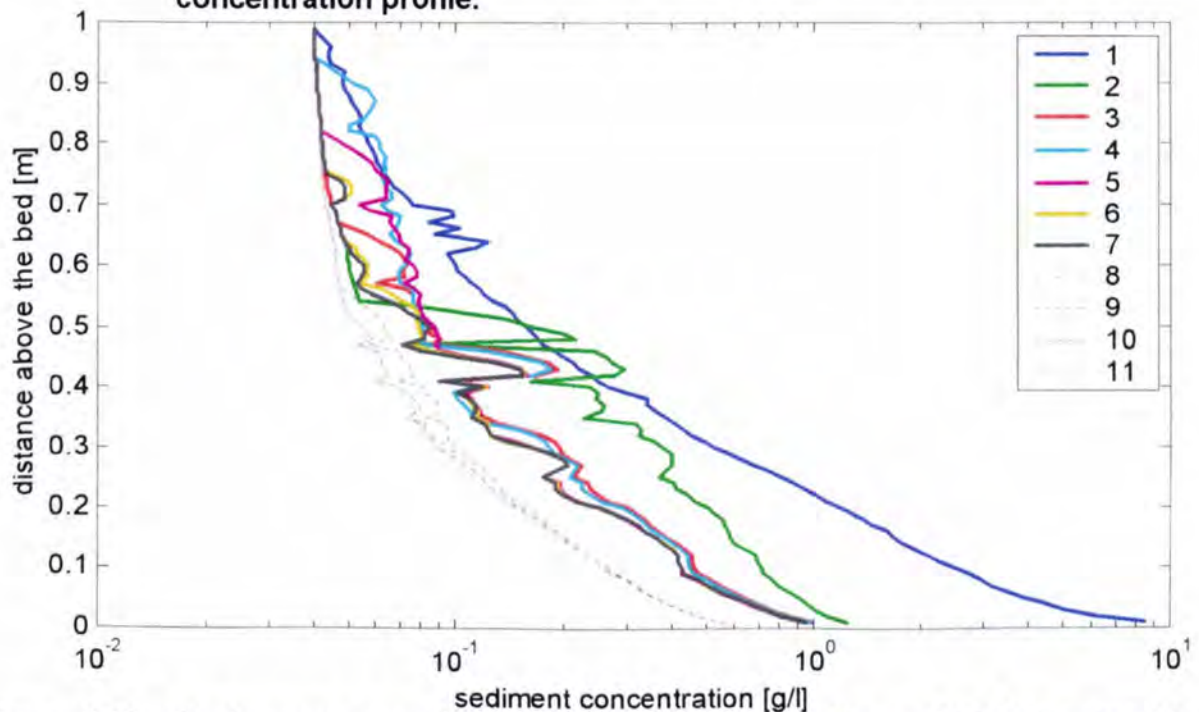


Figure 6.18: Cycle mean c-profiles for the wave group in figure 6.15 determined by the model. The sediment concentration entrained by the “cloud of sediments” was determined from the previous cycle mean concentration value 1 cm above the bed. The solid blue line represents the burst mean concentration profile.

Chapter 7 Vortex Ejections from a rippled bed

7.1 Introduction

The suspension of sediment in oscillatory flow over a rippled bed is driven by diffusive and convective processes. The diffusion mechanism depends on a concentration gradient, while for the convective mechanism larger flow structures are of importance. In chapter 5 the different suspension mechanisms of convection and diffusion were described. One cause of convective entrainment of sediment particles is the development of a vortex pair, which acts to lift the sediment further above the bed than a diffusion process alone is capable of doing. The existence of a vortex pair and the modelling of convective entrainment is the subject of this chapter.

Under oscillatory flow, vortices form in the lee of the ripples. The ejection of vortices behind ripples was reported by AYRTON (1910), using a simple experimental set up consisting of a small water basin and sand. He analysed the formation of ripples under different flow conditions and described the requirements for vortices to develop in the lee of a ripple. Later BAGNOLD (1946), found that once the orbital velocity exceeded twice the critical speed for initiation of sediment motion, vortex ripples developed. These were characterised by vortices forming in the lee of the ripple in each half wave cycle. The vortex picked up sediment from the ripple trough until the flow reversed when it was then lifted over the ripple crest into the flow. This process is schematically shown in figure 7.1 and has been described by many researchers (e.g. NIELSEN, 1979 and 1992, SLEATH, 1984, DYER, 1986).

The generation of vortices behind cylinders has been studied for many years. There might be an analogy between the generation of vortices behind cylinders and those in the lee of ripples. In oscillatory flow, the type of flow regime around a smooth, circular cylinder is dependent on the Reynolds number and the Keulegan-Carpenter number, where the latter describes the ratio of the orbital amplitude to the diameter of the cylinder. If the Keulegan-Carpenter number is small, the water particles do not travel far enough for flow separation to occur. However, large Keulegan-Carpenter numbers are likely to result in vortex shedding behind the cylinder. SUMER AND FREDSSØE (1999), suggested a classification of the type of

flow separation behind a cylinder for oscillatory flow depending on the Reynolds and Keulegan-Carpenter numbers. These findings might be transferable to oscillatory flow over rippled beds, where the ripple height is the length scale equivalent to the diameter of the cylinder.

7.2 Evidence of vortices in the literature

TUNSTALL AND INMAN (1975), reported laboratory experiments conducted by DARWIN (1883), of flow above ripples for which he noted the existence of vortices created by the flow over the rippled bed. AYRTON (1910), then tried to visualise the formation of vortices over the ripples using a dye injection technique. BAGNOLD (1946), used oscillatory beds to study the motion of vortices above the rippled bed. Figure 7.2 shows a photograph taken by BAGNOLD (1946), of sediment suspension and vortex formation using aluminium powder for the flow visualisation. The ripple wavelength and height were 10 cm and 1.5 cm, respectively. The amplitude and half period were 20 cm and 3.4 seconds, respectively. The formation of vortices is clearly visible. Furthermore, a jet of sand particles between the vortex pair can be seen.

After the early experiments had shown evidence of the existence of vortices under oscillatory flow over a rippled bed, a number of tests were carried out to identify some characteristics of the vortices. Apart from visualisation of vortices, TUNSTALL AND INMAN (1975), were interested in determining experimentally the energy dissipation in the vortex field created by oscillatory flow over symmetrical ripples. They performed experiments in a wave channel of 45 m length, 2.5 m width and 2.5 m depth. The nominal still water depth used in the tests was 1.7 m. The experiments have shown that the vortices generated under oscillatory flow over ripples dissipate about 7 % of the total energy due to bottom effects, of which the rest can be attributed to bottom shear and sediment transport. They have also shown that the vertical velocity component, induced by the vortices, is of the same order as the horizontal orbital wave velocity just outside the boundary layer. Further tests by SLEATH (1987), were concerned with identifying turbulence in oscillatory flow over a rough, flat bed. He carried out detailed measurements of turbulence in an oscillating flow water tunnel on a flat bed consisting of a single layer of sand, gravel or pebbles of median diameters 0.20 mm, 1.63 mm, 8.12 mm and 30.0 mm. He measured the variation of turbulence intensities during the course of the cycle and with distance from the bed. From the data analysis, Sleath concluded that jets of fluid associated with vortex ejection on flow reversal were produced in his experiments, which lead to the formulation of an expression for the upward propagation velocity of 'turbulent packets'.

GRASS (1981), stated that vortices form in the lee of ripples during each half-cycle and subsequently form into pairs, which can migrate into the flow immediately above the bed when the flow reverses. These bed vortices were entrained up to ten ripple heights into the flow, before they broke down due to turbulence and associated diffusivity. The effect of vortex pairing on sediment suspension was briefly discussed by ROSE (1997). He used a very simple approach considering a vortex pair, each individual vortex rotating initially at the orbital velocity, which yielded a first estimation of the upward convection velocity.

Apart from the experimental measurement of vortices in the literature, a number of papers deal with the modelling of vortices. LONGUET-HIGGINS (1981), simulated vortex behaviour over rippled beds using an irrotational point vortex model. The predictions of the model indicate that the pattern of point vortices above the bed form into a larger vortex pair. This can be seen in figure 7.3, which shows successive stages of the computation of the point vortices for sinusoidal oscillation. Each small semicircle represents a vortex. The strength of each vortex is proportional to the area of the corresponding small circle of the semicircle. Thus, the smaller the semicircle, the less the strength of the vortex. Negative and positive vorticity is represented by semicircles \cap and \cup , respectively. When $t = 6.3$, the clouds of vorticity have separated from the ripple crest. The two clouds of vorticity have a positive and negative vorticity respectively, and thus form a vortex pair. According to LONGUET-HIGGINS (1981) it is the fact that a vortex pair has formed that allows the cloud to rise to its actual height and escape from the neighbourhood of the ripple boundary. Similar findings were reported by BLONDEAUX AND VITTORI (1991), who treated a laminar flow situation by solving the vorticity transport equation. They also showed the formation of a vortex pair in the lee of a ripple due to flow separation.

HANSEN ET AL. (1994), looked at the distribution of suspended sediment over wave generated ripples using a discrete vortex model. The outer part of the flow was described by a discrete vortex model, while the boundary layers formed along the ripple surface, were described by an integrated momentum equation. The vorticity in the boundary layer was represented by discrete vortices. A value of $1.2 \cdot 10^{-5} \text{ m}^2/\text{s}$ was chosen for the eddy viscosity, which was as large as possible to reduce the computational effort without reducing the number of vortices substantially. In the model, the ripples were represented by parabolas. The sediment concentration field over the ripples was simulated by tracking individual sediment particles through the flow and satisfactory agreement with data from experiments by RIBBERINK AND AL-SALEM (1989), was found. Figure 7.4 shows an example of a) calculated flow and b) calculated suspended sediment distribution over the rippled bed at

three different phases in the wave cycle determined by the numerical model proposed by HANSEN ET AL. (1994).

Recently, FREDSE ET AL. (1999) have looked at wave plus current flow over a rippled bed. They developed a numerical model, where they concentrated on the flow over one ripple. The turbulence was simulated using a $k-\omega$ model. The result of the model for purely oscillatory flow is shown in figure 7.5. Vortex pairing can be observed at $\omega \cdot t = 110^\circ$. The sequence of vorticity plots was very similar to the one measured in a small laboratory wave flume. Further findings were that the lee wake vortex development, under wave only conditions, was very similar to the one in the combined wave and current case (following current). Also, they determined from the measurements that the near bed turbulence level increases at times when the vortex is washed over the ripple crest.

7.3 Visualising vortices ejected from a rippled bed in a laboratory wave flume

7.3.1 Laboratory Experiment

Experiments were carried out in a wave flume, 0.3 m in width, 0.6 m in depth and 9.2 m in length. The bed of the flume sloped at 1:15 starting about 3 m from the wave paddle. A 1 m section of the bed was covered with fixed ripples (figure 7.6 and 7.7). The ripples were manufactured out of a solid piece of plastic in two sections (0.5 m in length and 0.298 m in width). Whilst the manufacturing process caused the surface of the ripples to be slightly uneven, it was considered that this was representative of grain roughness. The ripples had a wavelength of 100 mm and a height of 20 mm (figure 7.6b). The bed was made up of a number of parabolas, with the ripple height and length as their constraints. The ripples were chosen such that they were sharp crested to produce vortex shedding and further limitation was due to the manufacturing process.

The water depth on the horizontal section of the flume was 45 cm. The wavelength and wave height during the tests were approximately 8 cm and 75 cm, respectively with a period of approximately 2.0 s. Cylindrical shaped plastic particles (type Polystyrol 495 F, donated by BASF, Germany) were used to aid flow visualisation. The particles were $O(3 \text{ mm})$ long, $O(3 \text{ mm})$ wide, $O(2 \text{ mm})$ thick and had a density of about 1.05 g/cm^3 . The plastic particles were chosen to have a density of close to one so that they were almost neutrally buoyant and thus, behaved like the water particles. In contrast, the sand particles in the *Deltaflume* had a relative density of about 2.65. The settling velocity was determined in a measuring

cylinder to be approximately 0.027 m/s. This resulted in the particles settling down to the bed without wave action (figure 7.8), but at the same time they did not disturb the flow considerably and were observed to follow the water particles. There is a difference between the behaviour of the sand and the water particles. This has to be kept in mind when analysing the movement of the plastic particles in the laboratory wave flume.

A video was used to film the particle movement in the flume. It showed that the particles were lifted up into the water column. There was also evidence of the particles moving across two to three ripples in a horizontal direction. This is slightly surprising, considering that the water particles should move along elliptical paths, as the conditions in the laboratory flume were in the intermediate flow range. Though, the plastic particles were supposed to track the flow of the water particles, it cannot be excluded that they behaved slightly differently.

Individual video frames were then captured using a computer software package (Zipshot). The aim was to trace individual particles and record their trajectories. Figure 7.9 shows an example of suspended particles under the influence of wave motion and shows how the particles were placed in suspension by wave action.

Figure 7.10 shows a trace of a plastic particle (red) over eighteen frames. The position of the particle for each individual frame was determined and this position was then marked on the first frame by the ellipse representing the particle. Figure 7.11a-r shows the individual frames that were captured. The particle of interest was marked again with a red ellipse. The total time for the particle to reach the highest recorded position in the water column was 0.72 seconds. The movement of the particle was divided into two sections, the first one being where there was a large horizontal as well as vertical movement and the second one where there was predominantly vertical movement. In the first section the particle moved a total horizontal and vertical distance of about 10 cm and 5 cm, respectively, which is equivalent to a horizontal and vertical velocity of 4.6 cm/s and 2.25 cm/s, respectively. In the second section the particle moved a total horizontal and vertical distance of 1.2 cm and 2.2 cm, respectively, which is equivalent to a horizontal and vertical velocity of 0.34 cm/s and 0.63 cm/s, respectively. With waves in the intermediate flow regime, the equations for linear wave theory yielded a horizontal, orbital velocity of approximately 4.8 cm/s at the bed, which was close to the initial, horizontal velocity of the particle.

Turning the attention now to figure 7.11, there are some particles which indicate rotational movement. As these are two-dimensional pictures, it is impossible to identify the plane across the flume, in which the particles were positioned. Thus, suggesting that the rotational structures in the figures are vortices may be pre-emptive. However, if they were vortices,

figure 7.11a-f shows a type of vortex pair, which transformed into a single vortex. The assumption of a vortex pair seems to be disproved by the fact that the pair did not move up into the water column, which would be expected from a vortex pair. Further difficulties associated with the individual frames captured in figures 7.11a-f are the determination of the direction of movement of the particles. The particles might be moving in different directions when captured and only appear to move together on a circular path in the captured frames. The video evidence has to be used in support for any conclusions, which indicated that the particles were indeed moving along a rotational path.

A program developed by Dr P. Atkins (Acoustics & Sonar Group, The University of Birmingham) allowed the automatic trace of a particle over a number of frames. This was determined by firstly recording the positions of all the particles from the video. Then analysing each individual frame, the positions of the particles from frame to frame were compared, assuming that the particles only moved a small distance. In this way, the trajectories of the particles were determined. Further, short video clips highlighting one individual particle were produced allowing the visualisation of a particle trajectory. These video clips were also used to check the identification of individual particles by the computer program, in order to ensure that the same particle was traced over time. In general, the video clips revealed that the vertical acceleration of a particle was larger than its horizontal acceleration, which seemed driven by the orbital movement of the water particles. Figures 7.12a-e show examples of particle trajectories. Figure 7.12a shows the entrainment of a particle to approximately eight times the ripple height. The entrainment of the particle in figure 7.12a is along a straight path, and the video evidence suggested large acceleration in this region, which could indicate a jet-like ejection of the particle from the bed. Figure 7.12b shows the particle movement over 6.12 s, covering a horizontal distance of about two ripple wavelengths (movement is from left to right). It reached up to about six ripple heights before settling back to the bed. An accelerated upward movement was observed in the video clip. A large vertical acceleration can also be seen in figure 7.12c. Once the particle has reached its maximum height, there is pure horizontal movement for some time before the particle settles back to the bed. So far, the figures have exhibited particle entrainment further into the water column, but did not concentrate on the movement close to the bed, which is highlighted in figures 7.12d and e. The traces were recorded over 1.4 s and 1.7 s, respectively, which was less than the wave period of 2 s. There, the trajectories follow circular paths close to the bed suggesting that they were trapped in vortices. The video evidence was used to back up the still images of the trajectory and revealed a large rotational speed of the particles.

Figure 7.13a shows the trajectory of a particle tracked over 7.6 seconds, which is about four times the wave period. Figure 7.13b indicates the positions of the particle for each frame marked by a cross. This allows the identification of areas of large and small acceleration. Firstly, the plastic particle stayed close to the bed moving along the bed over a distance of approximately two ripple wavelengths. It then accelerated straight into the water column after being swept a short distance passed a ripple crest. It was lifted a few ripple heights up into the water column before settling back to the bed under the influence of gravity. During this time, there was no indication of oscillatory movement and the particle followed a straight path. This is the same phenomenon as seen in figure 7.10. When the particle was settling, it moved on an elliptical path marking the orbital paths of the water particles. OSBORNE AND VINCENT (1996), suggested that under the laboratory wave and ripple conditions (multidirectional wave basin at the NRC Hydraulics laboratory with wave heights in the range of 0.2 m to 0.4 m, a period of 3.9 s and ripple heights of 1.7 cm), 5 cm is the approximate height of the vortex roll-up behind the ripples. Above 5 cm the ejection process is still convective, but suspended sand is now advected horizontally by the wave oscillatory flow and therefore loses its phase couplings to the bedforms.

The video evidence was found useful to aid the visualisation of the particle trajectories. It helped identifying tracks, where the program traced two different particles over a number of frames, which were then meaningless.

7.4 A simple model to determine the influence of a vortex pair on a single particle of sand

The intra-wave concentration profiles have shown a very interesting pattern (see chapter 6). Under a wave group, pumping of sediment was observed. Over the first two to three waves the sediment concentration measured at 1 cm above the bed, increased (figure 6.4 burst a12a). For the next waves this concentration dropped and at the same time the concentration further away from the bed increased, indicating that sediment was entrained further into the water column. The governing mechanism behind this process can no longer be explained by means of diffusion, which only happens on a small length scale with a large sediment concentration gradient.

It has long been known that vortices form in the lee of ripples under oscillatory flow, if the orbital amplitude is large enough. This has been observed by many researchers, e.g. BAGNOLD (1946), SLEATH (1984), NIELSEN (1979), DYER (1986), VILLARD ET AL. (2000), amongst others. The vortex forms in the lee of the ripple during the forward stroke of the

wave. At the end of the stroke, the vortex mounts up the slope past the crest and gets separated from the ripple. On the way up the slope, the vortex scoops up grains from the trough. AYRTON (1910) observed that some of the sand scooped up from the trough is pushed up the ridge with the vortex while it carried the remaining sediment whirling around with it. On the return stroke, a new vortex develops in the lee of the ripple. Due to the influence of the previous vortex, which has now moved past the ripple crest, and the images of the two vortices, the new vortex gets separated before flow reversal and the two vortices travel as a pair until they dissipate. It has long been suspected that this vortex pair is the driving mechanism for entraining sediment a considerable distance into the water column. However, the question as to how the sediment is entrapped in the vortex pair remains. At first, the most obvious mechanism seems to be that the sand is caught in the vortices until they dissipate. Thus, the particles are carried up inside the vortices to the peak elevation of the vortices, before they break up into the flow. This releases the sediment which is then subject to gravity. This seems to be in line with the observations made by AYRTON (1910), who reported sand whirling around with the vortices at the bed. Experiments conducted in the small laboratory wave flume, reported in section 7.4, extended the above observations. A simplistic consideration of the motion of sediment grains within vortices suggests that the mass of the particles, within what is effectively a centrifuge, should lead to sediment being thrown out of the vortex. NIELSEN (1992) however, reported on experimental results from TOOBY ET AL. (1977) in developing a kinematic explanation for how sediment can in fact be trapped within a single vortex under the combined action of the fluid velocity and the settling velocity. He suggested that the sediment is trapped by the vortices and is carried up the water column in circles similar to the paths followed by a water particle under waves (figure 7.14).

It is perhaps possible that this analysis could be extended to the case of a vortex pair, but it is not clear whether the entrapment would still occur. Another concern is that a single vortex cannot in itself move through an otherwise still fluid and so cannot explain how sediment is transported into the water column.

In the description above, the lee vortex, developed during the forward stroke of the flow, convects backwards due to the proximity of the ripple boundary. In classical analysis of vortices near plane boundaries the resulting motion can be simulated by the assumption of an image vortex. In the case of the more complicated ripple geometry, the formation of a single image may not be accurate, but the effect of the boundary is likely to be similar. As the return stroke of the flow develops and if a vortex pair is then ejected again, classical analysis will give an indication of the speed of propagation.

The experimental evidence of sediment particles suggests that some particles do indeed get trapped in either of the vortices in a pair, but that such particles do not get more than a few ripple heights above the bed before the tendency of the vortices to break up into three-dimensional turbulence limits their motion.

Present visualisation studies showed evidence that there is also a possibility of some particles being lifted significantly higher if they escape from the vortices and are carried by the jet of water in between them. During half of a wave cycle, a vortex developed in the lee of a ripple with the plastic particles moving along a rotational path. On flow reversal, some of the particles were flung over the ripple crest and into the water column on a straight, non-rotational path. This is in contrast to the description given by NIELSEN (1992), who suggested that the sediment particle follows an elliptical path up the water column. It has to be emphasised again that the relative density of the plastic particles was close to unity and therefore they followed the water particles closely. The sand particles have a relative density of about 2.65 and thus behave differently, depending on their size. However, due to the small settling velocity of the sand particle used in the *Deltaflume* compared to the orbital velocity of the waves, the centre of the sediment path is very close (an offset of about 20 mm) to the centre of the water particle path as described by NIELSEN (1992). Hence, the paths of the plastic particle observed, might show some resemblance of the paths followed by a sediment particle. Though, the vortex pair itself would have also separated from the ripple crest and moved into the flow, there was no evidence that the plastic particles were trapped in the vortices and carried by them. Thus, the assumption of the sand being trapped inside the vortices and being deposited in the water column when the vortices dissipate seems invalid. It is considered here that a more likely explanation is that the sediment particles are caught between the vortex pair causing the particles to accelerate. Their velocity will be greater than the speed of propagation of the vortex pair and related to the angular velocity of the vortices, and thus they escape from the direct influence of the vortices. Therefore, sediment is jetted away from the bed under the action of the vortex pairs until they dissipate. Once clear of the vortices, sediment moving through the water column is slowed down by the particle drag forces and by gravity, and then settles back to the bed. If the next wave approaches before the sediment has settled to the bed, then the sediment may be jetted back into the water column and may reach even further distances away from the bed. This process has been termed wave pumping and is especially effective under wave groups. A model to simulate the jet like ejection of a sediment particle between a vortex pair will be presented in the next section.

7.4.1 Simplifications for the modelling of vortex ejection

In order to examine the possibility of a particle being lifted up into the water column along a jet of fluid generated between the vortex pair a simple model was developed. A number of assumptions and simplifications have been made during the development of the model. The initial vortex is assumed to be governed by the orbital velocity of the waves and the ripple height. Once the vortex pair has developed, the distance between the centres of the two vortices has been taken to be equal to the ripple height. In the model the spherical sediment particle sits initially on the centre line between the vortex pair, with an initial velocity of zero. Further, only movement of the vortex pair in the vertical direction has been considered. An additional simplification has been made by assuming that only one vortex pair develops during a wave period. These assumptions and simplifications are discussed further below.

In the case where a vortex develops in the lee of a ripple with height h_r and wavelength λ_r , the vortex strength can be estimated from $\Gamma_0 = U_{\max} \cdot \pi \cdot h_r$ (figure 7.15). Visual observations by RIBBERINK AND AL-SALEM (1994), of vortex development on a rippled bed in oscillatory flow showed that the ripple dimensions of the vortices are approximately the same as the ripple heights. Further, it is assumed that once the vortex pair has established, it is separated by approximately the ripple height (figure 7.16). The decay of the speed of propagation of the individual vortex in the vortex pair can be described by (DUNCAN ET AL., 1978):

$$U_p = \frac{\Gamma_0}{2 \cdot \pi \cdot h_r} \cdot \left[1 - \exp\left(\frac{-h_r^2}{4 \cdot \varepsilon_s^* \cdot t}\right) \right] \quad (7.1)$$

Whilst strictly speaking, this is valid for an isolated viscous vortex decaying with time, equation 7.1 is used here to describe each vortex in the vortex pair. The parameter ε_s^* is related to the kinematic viscosity and influences the rate of dissipation of the vortex pair. It is a fluid property rather than a sediment property. This parameter can be modified to change the relative influence of the vortex pair on the sediment particle. It can be varied to suit different hydrodynamic conditions for the model requirements. From observations it is known that the vortex pair loses its two-dimensional structure before it finally dissipates into the flow. This is not part of the model and thus the modified kinematic viscosity, ε_s^* has to take this behaviour into account.

The initial speed of propagation of the vortex is given by

$$U_{p,initial} = \frac{U_{max} \cdot \pi \cdot h_r}{2 \cdot \pi \cdot h_r} = \frac{U_{max}}{2} \quad (7.2),$$

where U_{max} is the maximum orbital velocity during half a wave period. The two vortices only move due to the influence of each other and to their images in the bed, which have been neglected in this model. The initial speed of propagation at the centre line between the two vortices (figure 7.16) level with the centre of the vortices is given by two times the initial strength divided by half the ripple height (both vortex fields contribute to the velocity). Thus the initial velocity at the centre line between the vortex pair is

$$U_{initial} = 2 \cdot U_{max} \quad (7.3)$$

This is the initial flow velocity of the fluid generated by the vortex pair around a particle sitting between the two vortices. The initial velocity of the particle itself is assumed to be zero.

Assuming the sediment particle is exposed to the flow of fluid with the initial velocity exerted by the vortex pair, it is then subject to a drag force, which is a function of the relative flow. As an initial simplification, it is assumed that the sediment and the vortex pair move along a vertical path up the water column. In reality the vortex pair separates from the ripple crest at an angle and the sediment particle moves initially at that angle. Assuming the sediment particle is a sphere and applying Newton's second law for the particle in the vertical direction yields

$$C_d \cdot \frac{1}{2} \cdot \rho_w \cdot (U - V) \cdot |U - V| \cdot Area - m^* \cdot g = m \cdot \frac{dV}{dt} \quad (7.4)$$

where C_d is the drag coefficient, U is the velocity of the flow at the position of the particle and V is the velocity of the sand particle. The dry mass of the particle is m and the mass of the submerged particle is m^* .

$$\text{With } \frac{Area}{m} = \frac{\pi \cdot d_{50}^2 / 4}{\rho_s \cdot \pi \cdot d_{50}^3 / 6} = \frac{3}{2 \cdot \rho_s \cdot d_{50}} \text{ and } \frac{m^*}{m} = \frac{s-1}{s} \quad (7.5a, b),$$

equation 7.4 can be rearranged to

$$\frac{dV}{dt} = \frac{3}{4} \cdot C_d \cdot \frac{1}{s} \cdot \frac{1}{d_{50}} \cdot (U - V) \cdot |U - V| - \frac{(s-1)}{s} \cdot g \quad (7.6)$$

where s is the relative density, ρ_w is the density of water and ρ_s is the density of the sediment. Using the modified Euler method for numerical integration, equation 7.6 yields the variation of the velocity of the sediment particle with time.

Given the change of velocity with time, this now enables the calculation of the vertical position of the particle at any time. The particle has settled to the bed if the total distance travelled is equal to zero. If this happens within a wave period, sediment is suspended from the bed by the next wave and none is picked up from within the water column, thus no pumping takes place. Furthermore, the maximum height above the bed reached by the sediment particle before settling back to the bed can be determined. This also gives some indication of the length scale involved in this convective suspension mechanism. For simplification it is currently assumed that only one vortex pair develops during a wave period.

7.4.2 Sensitivity Analysis of the Model

In section 7.4.1 a convective mechanism to entrain sediment further away from the bed has been suggested. In order to analyse the influence of various parameters in the model, a sensitivity analysis was performed. The results of this analysis are presented in this section.

A number of parameters were chosen to represent the conditions found in the *Deltaflume* in a number of tests. The initial model parameters chosen are listed in table 7.1. The enhanced kinematic viscosity, ε_s^* is larger than the kinematic viscosity, due to turbulence of the fluid and the vortex flow. The variation of the particle and vortex pair velocities and the vertical distance travelled by the vortex pair and the particle are determined for a period of 8 seconds, keeping in mind that the period of the waves during the experiments in the *Deltaflume* was about 5 seconds.

The drag coefficient is considered to be constant throughout a model run. This is a simplification, as the drag coefficient changes as a function of the particle velocity. Figure 7.17 (lecture notes from Prof. D.W. Knight, The University of Birmingham) shows the drag coefficient as a function of the Reynolds number for a sphere. At low velocities (thus small Re), the drag coefficient is larger than ten. With increasing velocity the drag coefficient reduces and is reasonably constant at a value of 0.4 for Reynolds numbers in the range of 10^3 to $2 \cdot 10^5$. At the beginning the sediment particle has a velocity of zero. Due to the influence of the vortex pair it accelerates quickly, exceeding the range of viscous flow, where the drag coefficient can be determined by $24/Re$. For the orbital velocity values measured in the *Deltaflume*, the Reynolds number does not exceed 600. As mentioned above, the model does not take the variation of the drag coefficient as a function of the velocity of the particle into account, but treats it as a constant value for simplification. A compromise value of $C_d = 1$ has been chosen for an initial value before the sensitivity analysis.

The strength of the vortex pair decays with time. Observations have shown that the two-dimensional vortex pair breaks up into the flow and eventually dissipates. Thus, no more fluid acceleration being exerted from the vortex pair onto the sediment particle. The time, at which the vortex pair dissipates into the flow is not known and cannot be simulated with this simple model. In order to include the complete disappearance of the vortex pair, it is assumed that it disappears at the time at which its strength is equal to half the initial strength of the vortex pair. The choice of the condition when the vortex pair disappears is open for discussion. The chosen method includes the complete decay of the vortex structure into the flow in this two-dimensional model. In order to judge the influence of the minimum strength of a vortex pair before it dissipates into the flow (i.e. time at which the vortex pair disappears), an analysis, where the vortex pair does not disappear into the flow, but just reduces in strength was carried out.

Figure 7.18 shows the path of the sediment particle and the vortex pair with time for the initial conditions. Datum refers to the initial position of the vortex pair and the sediment particle before the model starts (see figure 7.16). The vortex pair disappears when the strength is equal to half its initial strength. The sediment particle reaches a height of up to 22 cm above datum, which is about 4 times the ripple height. While the particle is lifted into the water column, it is always moving ahead of the vortex pair. The vortex disappears after about one second. The particle travels up the water column for a further tenth of a second, before it falls back to the bed. It hits the bed after approximately 3.3 seconds (when z is equal to zero). Figure 7.19 shows the velocities of the sediment particle and the vortex pair, respectively. The particle has an initial velocity of zero, while the initial velocity of the vortex pair is twice the orbital velocity, i.e. 1 m/s. The maximum velocity of the particle is about 0.9 m/s. After the vortex pair has disappeared, the velocity of the sediment particle drops abruptly before it reaches its terminal settling velocity. The terminal settling velocity, determined by this model, is about twice the settling velocity calculated by empirical equations. An increase in the drag coefficient reduces the terminal settling velocity of the model and thus, it can be used to calibrate the model. Later it was discovered that a smaller enhanced kinematic viscosity of $5 \cdot 10^{-4}$ is a more appropriate value. This then resulted in a peak elevation of the particle of 37 cm, which is about 8 times the ripple height. In order to test the influence of the ripple height, the orbital velocity, the drag coefficient and the enhanced kinematic viscosity a sensitivity analysis of the model to these parameters was carried out.

For the sensitivity analysis, the maximum height the particle reaches before it settles back to the bed, the time when it hits the bed and the velocity profile are of interest. For a number of

different model parameters, these values are listed in tables 7.2 to 7.5. Figures 7.20 to 7.23 show the results of the sensitivity analysis.

With increasing ripple height the peak elevation of the sediment particle increases (figure 7.20). The ripple height influences the initial strength of the vortex, because it was assumed that the diameter of the vortex is equivalent to the ripple height when it develops in the lee of the ripple. At the same time the ripple steepness has to be large enough for vortices to be generated in the lee of the ripple. The ripple height also influences the dissipation of the vortex pair, because the assumption was made that the centres of the vortices are separated by a distance equal to about the ripple height. Furthermore, this then has an effect on the geometry between sediment particle and vortex pair and therefore, the velocity induced by the vortex pair on the sediment particle. For a ripple height of 6 cm, the particle travels up to 25 cm into the water column before settling back to the bed. This is about four times the ripple height. It hits the bed after approximately 4.7 seconds. The time at which the vortex disappears also increases with increasing ripple height.

There is a linear increase of peak elevation of the sediment particle with increasing orbital velocity (figure 7.21). This is due to an increase in vortex strength with increasing orbital velocity. Also the time at which the particle hits the bed extends with increasing orbital velocity up to about 5.5 seconds for an orbital velocity of 1 m/s. The time at which the vortex disappears is unaffected by the change in orbital velocity.

Figure 7.22 shows the effects of a variation of the drag coefficient. For a drag coefficient greater than one, the peak elevation of the sand particle is almost independent of the drag coefficient. However, it prolongs the settling dramatically, such that for a drag coefficient of five the particle hits the bed after approximately 6.5 seconds, while for a drag coefficient of ten it does not hit the bed within the time period of 8 seconds of the model run. As expected a change in drag coefficient does not influence the time at which the vortex pair disappears, as this is independent of the drag coefficient.

The effect of changes of the enhanced kinematic viscosity is shown in figure 7.23. The enhanced kinematic viscosity has an effect on the dissipation of the vortex pair. The smaller the viscosity, the slower the vortex pair decays. Reducing the enhanced kinematic viscosity by a factor of ten from 0.001 m²/s to 0.0001 m²/s increases the maximum height the particle reaches by a factor of 10 from 0.17 m to 1.7 m. The time at which the particle hits the bed is above 10 seconds and about 3 seconds for an enhanced kinematic viscosity of 0.0001 m²/s and 0.001 m²/s, respectively. For a value of 0.0001 m²/s, the vortex pair decays so slowly that there is no noticeable difference between including the disappearance of the vortex pair

at half its strength or not. The time it takes for the vortex pair to decay to half its strength is about 9 seconds, which is close to the 10 seconds of the model run for this case.

Without the vortex disappearance at the time it reaches half its original strength, all the relationships between the maximum height the particle travels into the water column and the various parameters (ripple height, orbital velocity, drag coefficient and enhanced kinematic viscosity) were the same as without the complete dissipation of the vortex pair into the flow. However, due to the continuous force exerted by the vortex pair onto the sediment particle the absolute values of the peak elevation of the particle were significantly larger.

It was discovered that the various parameters concentrated on in the sensitivity analysis can be grouped in two dimensionless groups and then the peak elevation can be expressed as a function of a type of Reynolds number. This is shown in figure 7.24. The effect of all the parameters, except the drag coefficient, can be expressed in terms of the one graph. This graph is valid for the one sediment diameter chosen in the analysis ($d_{50} = 0.329$ mm). It allows the prediction of the peak elevation for the dimensionless group $A \cdot \omega \cdot h_r / \varepsilon_S^*$. At the moment the physical significance of the two dimensionless groups [h/h_r and $A \cdot \omega \cdot h_r / \varepsilon_S^*$] is not clear. The graph suggests a linear relationship between the dimensionless groups. The proportionality between the parameters grouped in the dimensionless group $A \cdot \omega \cdot h_r / \varepsilon_S^*$ can be expressed as $h \propto A \cdot \omega$, $h \propto 1/\varepsilon_S^*$ and $h \propto h_r^p$, which can be seen in figures 7.21-22 and 7.24. A linear trendline through the data presented in figure 7.24 was determined, which yielded the following equation for the relationship between the two dimensionless groups:

$$\frac{h}{h_r} = 0.1395 \cdot \left(\frac{A \cdot \omega \cdot h_r}{\varepsilon_S^*} \right) \quad (7.7)$$

The linear trendline has a R^2 value of 0.9983 and hence, is statistically significant. The graph has been plotted on a linear/log scale for clarity.

The sediment diameter is not included in this graph. A number of different sediment diameters were analysed and their effects on the peak elevation of the particle and the time it hits the bed were recorded. Figure 7.25 and table 7.6 show the results of this analysis. The effects of a variation of the sediment diameter on the peak elevation is small in the range of 10^{-4} to 10^{-3} m, but the time it takes to settle to the bed decreases rapidly with increasing sediment diameter. This suggests that equation 7.7 is valid for the range of diameters encountered in the present experiment. The above analysis was also performed for a $d_{50} = 0.2$ mm, which yielded a slope of 0.135 for the trendline, which is within 3 % of the slope in equation 7.7. Therefore, it is likely that a number of different constants have to be

determined if the sediment diameter diverges considerably from the present one (see figure 7.25).

7.5 Summary and Conclusions

Evidence of the existence of vortex pairs as being the driving mechanism of the entrainment of sediment into the water column is documented in the literature. The intra-wave concentration data discussed in chapter 6 and video images of plastic particles, subject to oscillatory flow over a fixed, plastic rippled bed in the laboratory flume, suggested that the particles get more than a few ripple heights above the bed before the tendency of the vortices to break up into three-dimensional turbulence limits their motion.

Experiments to visualise vortices under oscillatory flow over a fixed, rippled bed were carried out in a small laboratory flume. Plastic (approximately neutrally buoyant, $s = 1.05$), cylindrical particles of length 3 mm were used to track the flow. A video taken of the movement of the particles presented evidence of vortices. The video footage showed particles moving with the vortex close to the bed and were on occasions ejected into the flow along a linear path. This was consistent throughout the experiments. The peak elevation of the particle cannot be explained by pure diffusion. It was considered that particles were ejected from the bed by the jet like flow occurring between a given vortex pair.

It has been shown that the existence of a vortex pair can lead to a sediment particle being carried up the water column up to a height of 100 cm. This distance is significantly greater than the length scale involved in sediment diffusion. Video evidence suggested that sediment particles were not trapped inside the vortices of a vortex pair, but scooped up from the ripple trough before they were ejected into the water column by the jet between the vortex pair. There was no evidence of the particles being carried up the water column, while rotating with the vortex. However, this is not to say that it could not happen.

A simple model was developed that assumed the existence of a vortex pair, which exerts a force onto a sand particle, causing it to travel up the water column. For simplification, it was assumed that there is no acceleration in the horizontal direction and thus the motion can be taken as purely vertical. This model is a crude approach to the problem of vortex shedding on a rippled bed under oscillatory flow and presents an advance on the analysis performed by ROSE (1997). However, it did not address the following problems:

- The model only includes the movement of a single particle in the centre of the vortex pair with an initial velocity of zero. In practice a number of sand particles are distributed just

above the ripple crest and are thus subject to the effects of the vortex fields. Due to their different positions relative to the centre of the vortices, the velocities induced by the vortices on the sediment particles vary. For further studies a statistical approach is suggested, which assumes a random distribution of the particles close to the bed. This would then lead to a variation of concentration above the bed, because the sediment particles are escaping the influence of the vortex pair at different heights.

- It is also unlikely for the sediment particle to have an initial velocity of zero, as it has been scooped up by the vortex forming in the lee of the ripple, which has induced an initial velocity on the particle. This analysis is the subject of future work.
- As a further simplification embedded in the model, it is assumed that initially there was no sediment in suspension when the vortex pair and the particle are released into the water column. In reality this is not the case, as there will always be some sediment in suspension in the water column. Thus, particles settling through the water column interact with the vortex pair and the sediment moving up through the water column. Including this in the model will be the subject of further studies.

Though, the above shortcomings of the present model need to be subject of further studies, the model in its present state is satisfactory. It models a convective entrainment mechanism, which allows a sediment particle to be lifted more than ten ripple heights into the water column. Incorporating the present model in the re-suspension of sediment model, presented in chapter 6, allowed the simulation of the so called pumping effect under a wave group.

TABLES

	model parameters
ripple height [m]	0.05
orbital velocity [m/s]	0.5
initial velocity of particle [m/s]	0
drag coefficient [-]	1.0
enhanced kinematic viscosity [m ² /s]	1.0*10 ⁻³
vortex disappearance included	no

Table 7.1: Initial parameters of the convective entrainment model.

ripple height	max height vortex pair [m]	max height particle [m]	time of max height [s]	time particle hits bed [s]	time vortex dissipates [s]
0.03	0.06	0.08	0.337	1.311	0.325
0.035	0.08	0.11	0.454	1.727	0.442
0.04	0.11	0.14	0.59	2.205	0.578
0.045	0.14	0.17	0.744	2.74	0.731
0.05	0.17	0.2	0.915	3.333	0.902
0.055	0.21	0.24	1.105	3.987	1.092
0.06	0.25	0.28	1.312	4.698	1.299

Table 7.2: Change in maximum height of the vortex pair, the sediment particle and the time the particle hits the bed with variation of the ripple height. The numbers in bold indicate the initial parameters chosen for the model.

orbital velocity	max height vortex pair [m]	max height particle [m]	time of max height [s]	time particle hits bed [s]	time vortex dissipates [s]
0.3	0.1031	0.13	0.911	2.445	0.902
0.35	0.1203	0.15	0.912	2.673	0.902
0.4	0.1375	0.17	0.913	2.895	0.902
0.45	0.1547	0.18	0.914	3.115	0.902
0.5	0.17	0.2	0.915	3.333	0.902
0.55	0.189	0.22	0.9155	3.549	0.902
0.6	0.2062	0.24	0.916	3.763	0.902
0.65	0.2234	0.26	0.916	3.976	0.902
0.7	0.24	0.27	0.917	4.188	0.902
0.75	0.26	0.29	0.917	4.4	0.902
0.8	0.28	0.31	0.918	4.61	0.902
1	0.34	0.38	0.919	5.447	0.902

Table 7.3: Change in maximum height of the vortex pair, the sediment particle and the time the particle hits the bed with variation of the orbital velocity. The numbers in bold indicate the initial parameters chosen for the model.

C_d	max height vortex pair [m]	max height particle [m]	time of max height [s]	time particle hits bed [s]	time vortex dissipates [s]
10	0.17	0.21	0.9076	does not	0.9017
5	0.17	0.21	0.9095	6.4588	0.9017
1	0.17	0.2	0.915	3.333	0.902
0.5	0.17	0.2	0.917	2.602	0.902
0.1	0.17	0.19	0.919	1.651	0.902
0.05	0.17	0.18	0.917	1.434	0.902
0.01	0.17	0.003	0.082	0.126	0.902

Table 7.4: Change in maximum height of the vortex pair, the sediment particle and the time the particle hits the bed with variation of the drag coefficient. The numbers in bold indicate the initial parameters chosen for the model.

ε_s	max height vortex pair [m]	max height particle [m]	time of max height [s]	time particle hits bed [s]	time vortex dissipates [s]
0.01	0.017	0.05	0.106	0.679	0.091
0.005	0.034	0.07	0.193	0.996	0.181
0.001	0.17	0.2	0.915	3.333	0.902
0.0005	0.34	0.37	1.817	6.27	1.804
0.0001	1.72	1.75	9.03		9.017

Table 7.5: Change in maximum height of the vortex pair, the sediment particle and the time the particle hits the bed with variation of the modified kinematic viscosity. The numbers in bold indicate the initial parameters chosen for the model.

sediment diameter [mm]	max height vortex pair [m]	max height particle [m]	time of max height [s]	time particle hits bed [s]	time vortex dissipates [s]
0.10	0.1719	0.2077	0.9108	5.3834	0.9017
0.20	0.1719	0.2052	0.913	4.04	0.902
0.329	0.1719	0.2	0.915	3.333	0.902
1.0	0.1719	0.1967	0.917	2.271	0.902
5.0	0.1719	0.1827	0.918	1.511	0.902
10.0	0.1719	0.1664	0.908	1.318	0.902
15.0	0.1719	0.1351	0.711	1.073	0.902
20.0	0.1719	0.0832	0.441	0.679	0.902
30.0	0.1719	0.005	0.1	0.155	0.902

Table 7.6: Change in maximum height of the vortex pair, the sediment particle and the time the particle hits the bed with variation of the sediment diameter. The numbers in bold indicate the initial parameters chosen for the model.

FIGURES

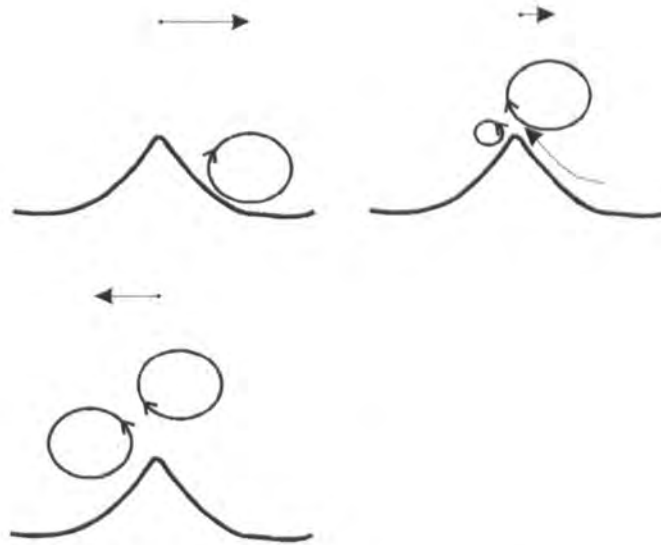


Figure 7.1: Diagrammatic sequence of vortex pair generation, separation and advection under waves. The phase of the wave is shown by rotation of the vector on the left.

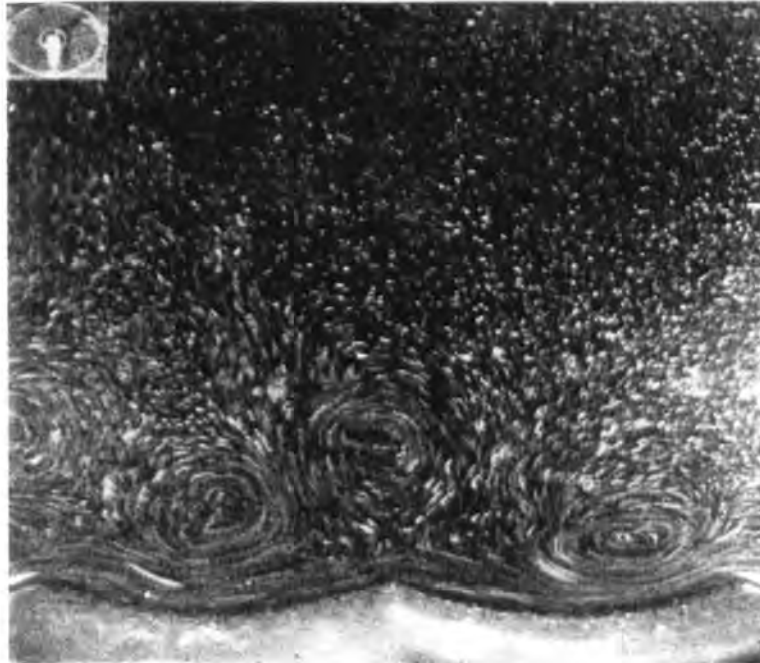


Figure 7.2: Photograph of vortices on a rippled bed under oscillatory flow from BAGNOLD (1946). The ripple wavelength and height were 10 cm and 1.5 cm, respectively. The amplitude and half period were 20 cm and 3.4 seconds, respectively. Aluminium powder was used for flow visualisation.

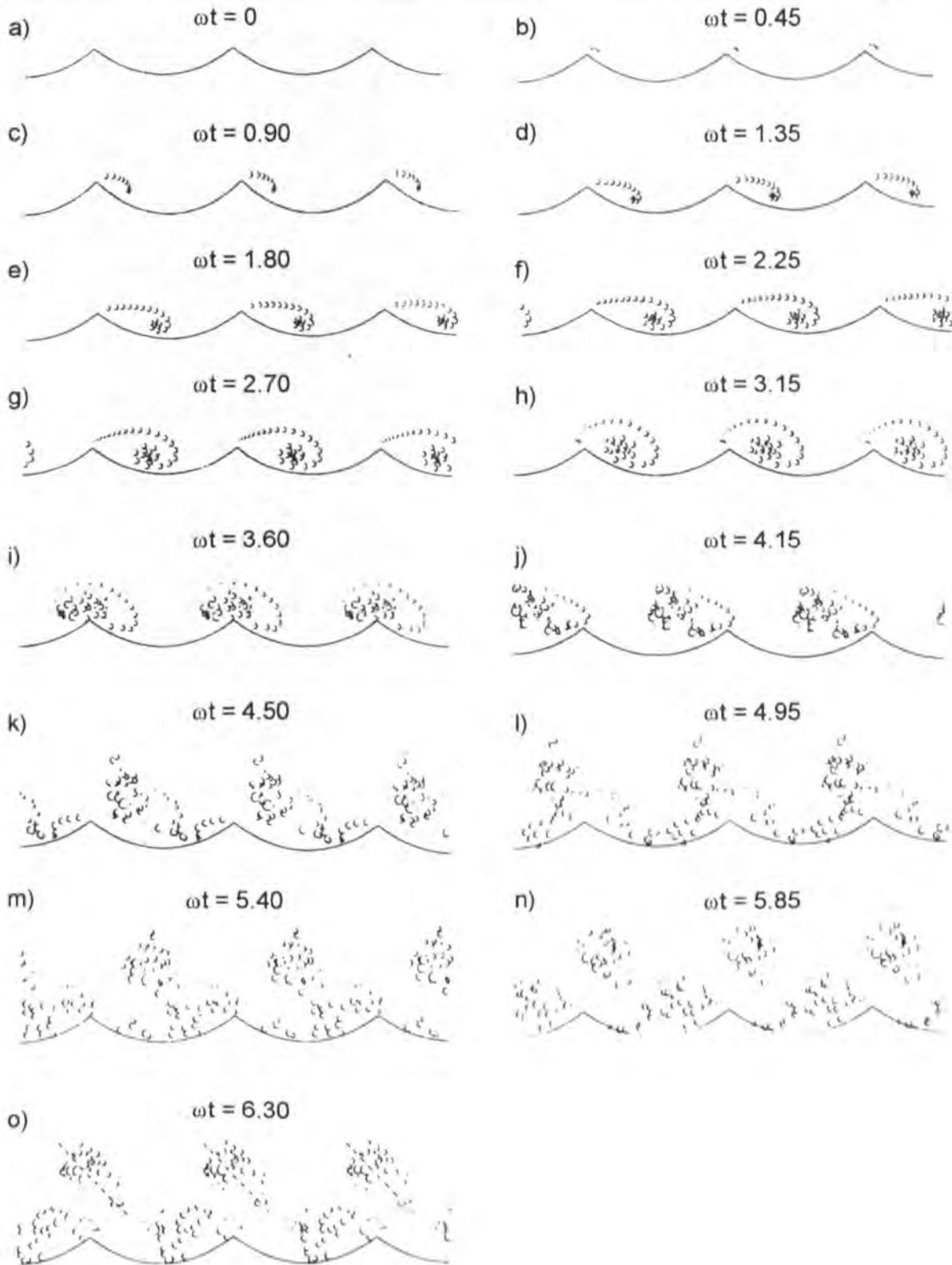


Figure 7.3: Successive positions of point vortices in a sinusoidal flow with $U = 0.75 \sin(\omega t)$ starting from rest at time $t = 0$ (from LONGUET-HIGGINS, 1981).

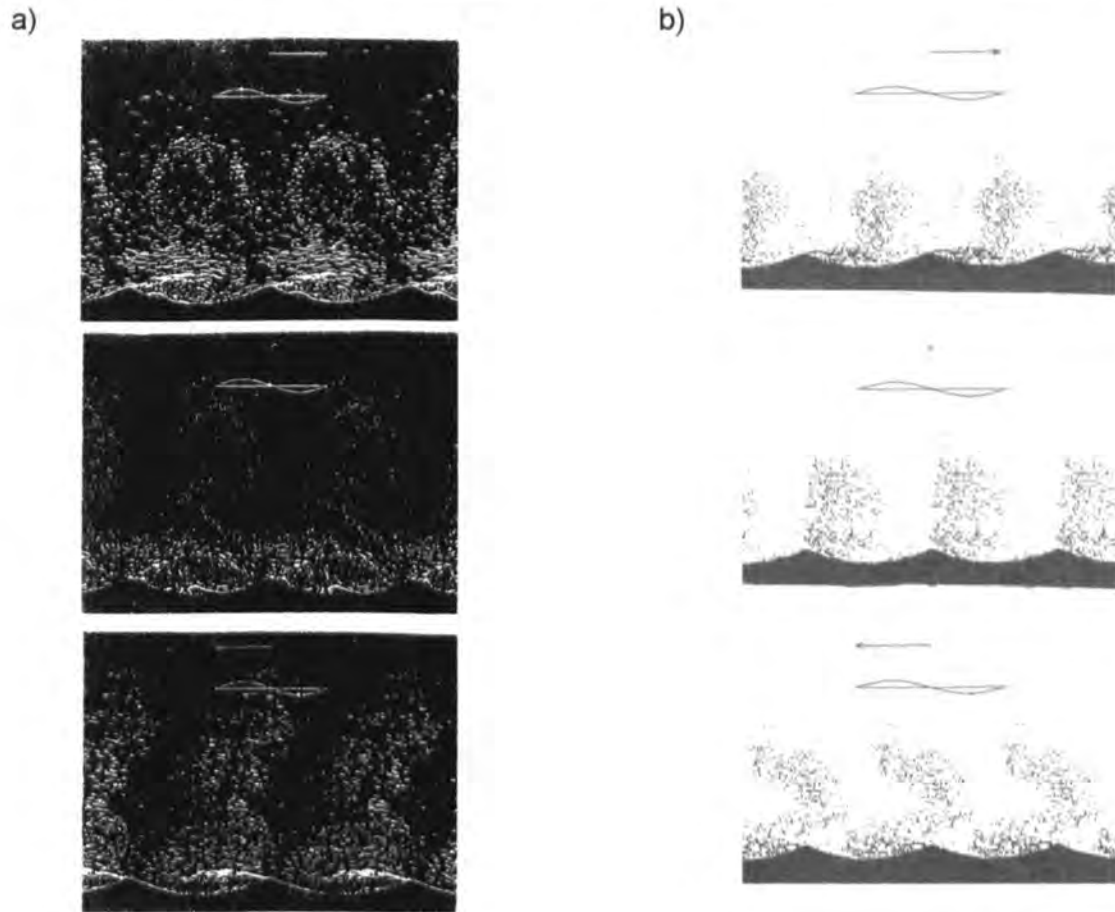


Figure 7.4: a) Calculated flow and b) calculated suspended sediment distribution presented by HANSEN ET AL. (1994), based on a discrete vortex model.

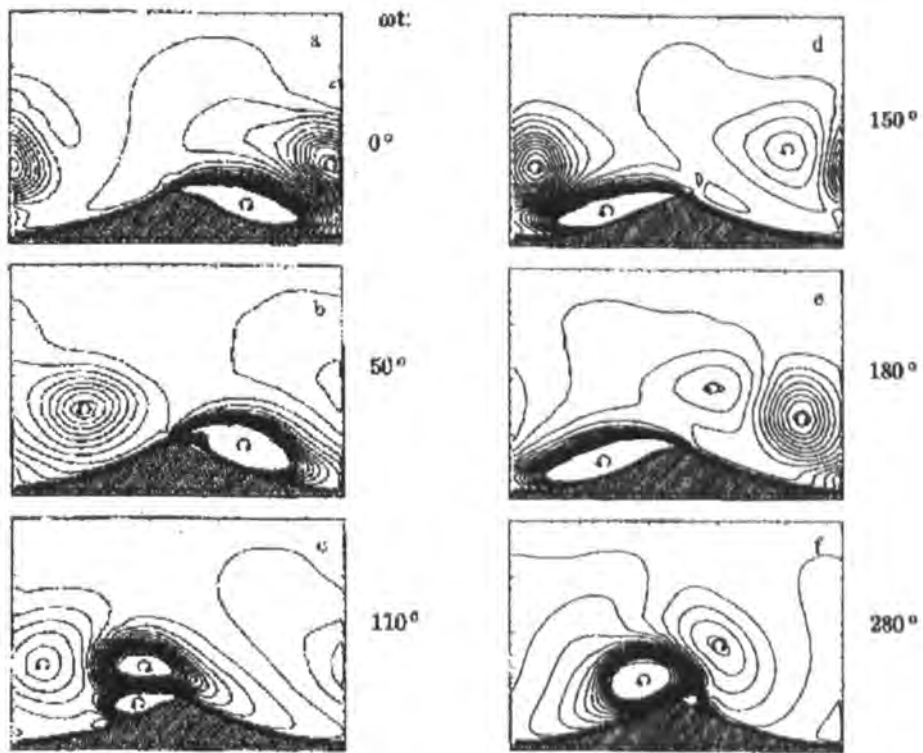
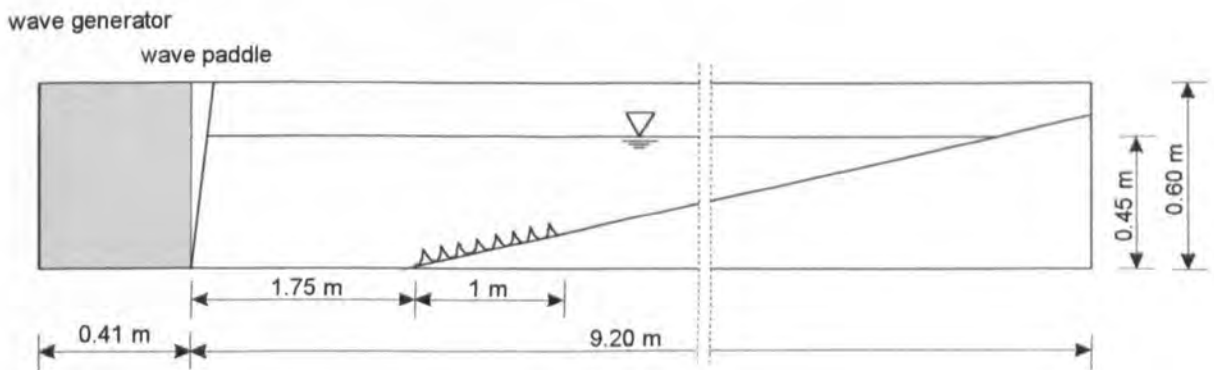


Figure 7.5: Flow visualisation over a ripple in wave only conditions simulated by a numerical model by FREDSE ET AL. (1999). The vortex pairing at a phase of 110° can be clearly identified.

a)



b)

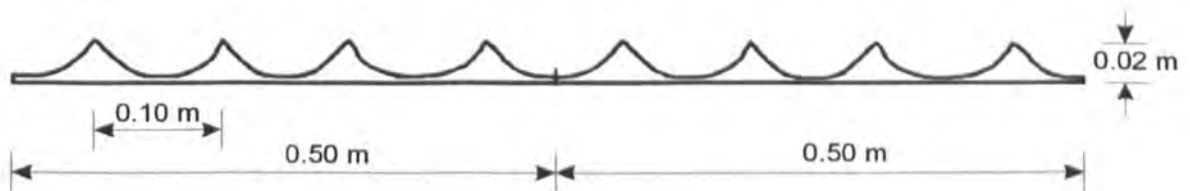


Figure 7.6: a) Schematic of the laboratory wave flume with the 1 m rippled bed section on the bottom of the flume. b) Schematic detail of the rippled bed with its dimensions.



Figure 7.7: Plastic rippled bed in the laboratory wave flume. The ripple height is 2 cm and the wavelength is 10 cm.



Figure 7.8: Plastic particles, with a relative density of 1.05 kg/m^3 , laying on the rippled bed. No waves were generated at this time.



Figure 7.9: Suspension of plastic particles under wave motion. The wave height, wavelength and water depth were about 8 cm, 75 cm and 45 cm, respectively.



Figure 7.10: Composed picture of the movement of a single particle under waves. The wave height, wavelength and water depth were about 8 cm, 75 cm and 45 cm, respectively. Two stages of movement can be identified. The first one with horizontal and vertical movement and the second one with predominately vertical movement.

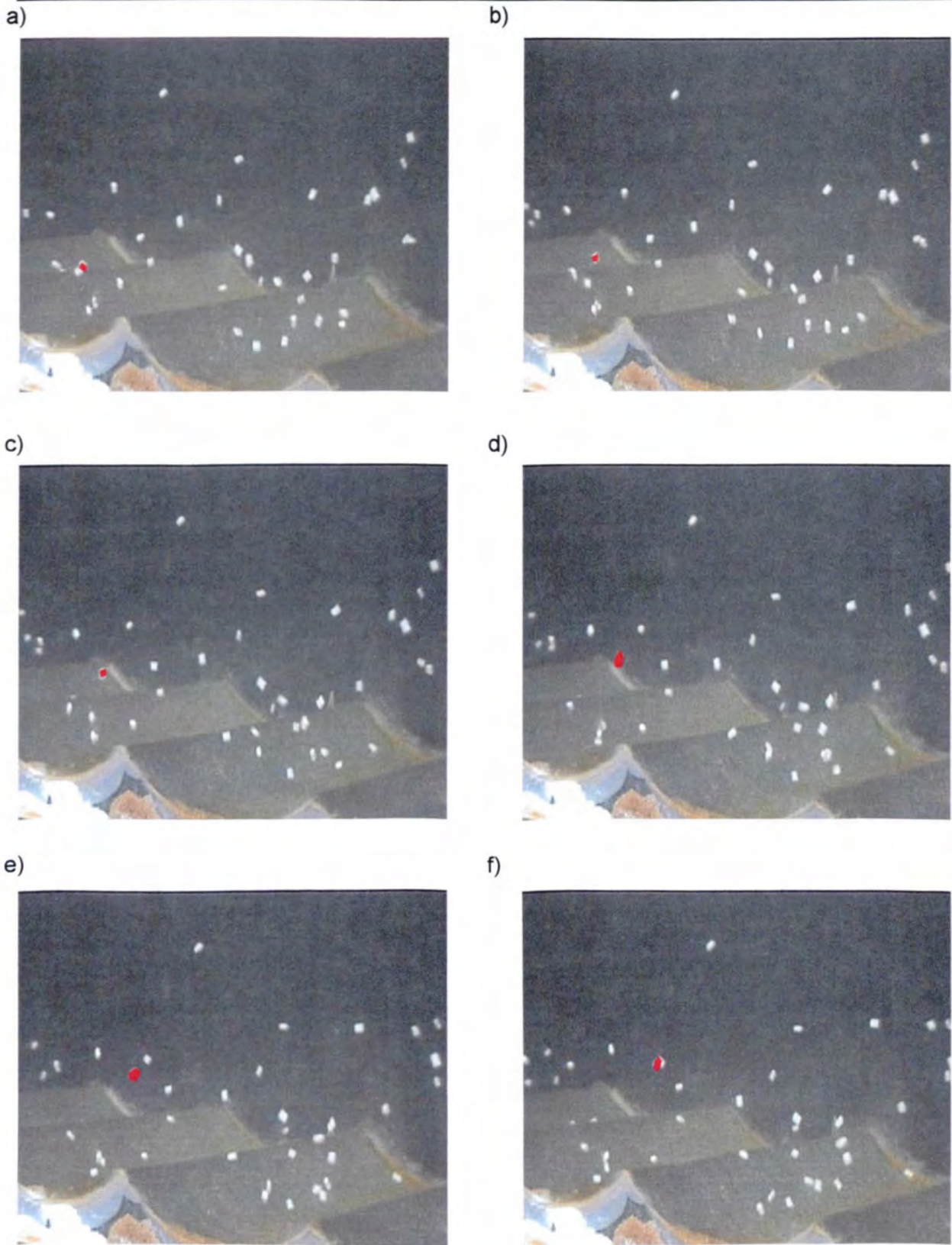


Figure 7.11: Individual frames of particle motion in the laboratory wave flume recorded by a video camera. The wave height, wavelength and water depth were about 8 cm, 75 cm and 45 cm, respectively.

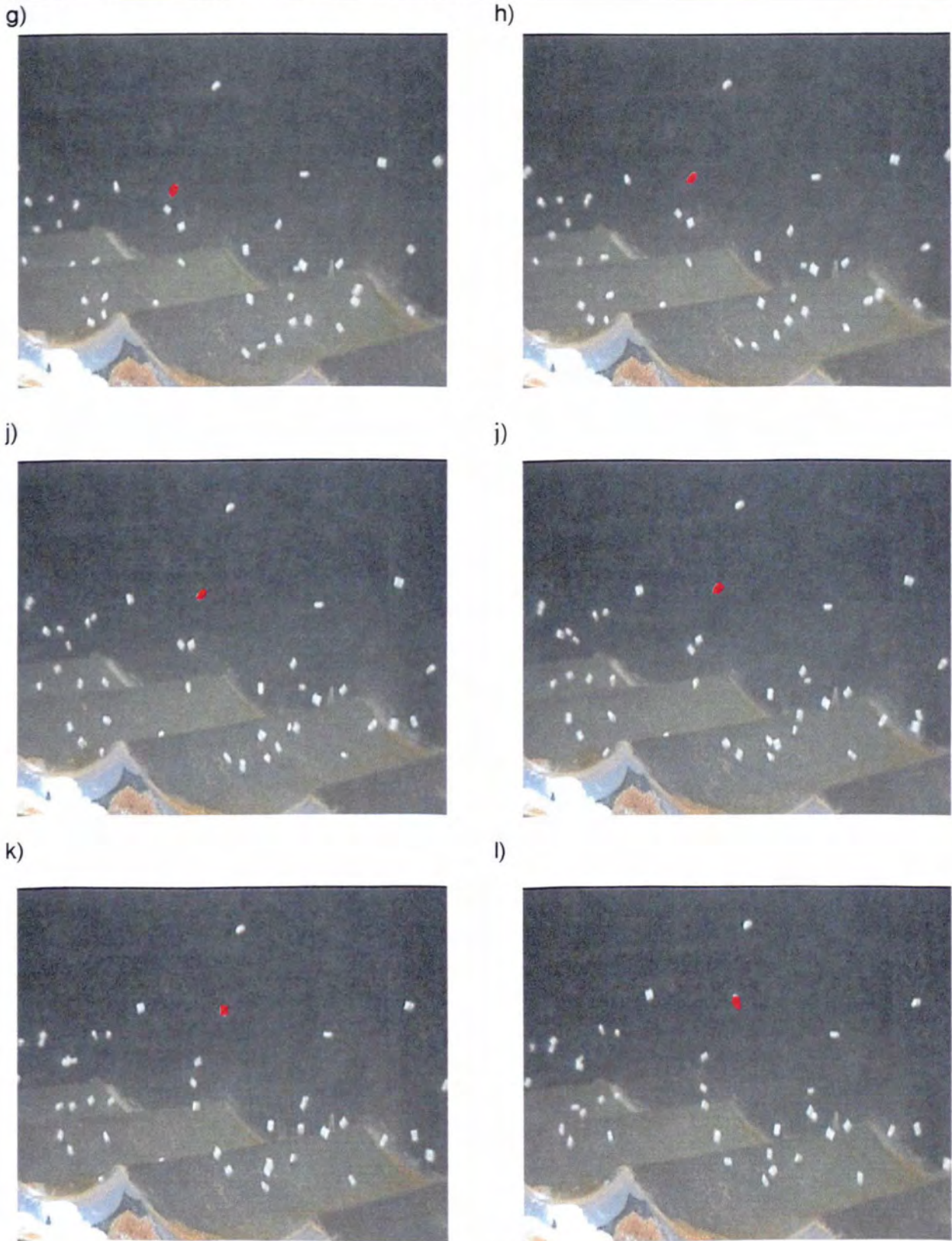


Figure 7.11: Individual frames of particle motion in the laboratory wave flume recorded by a video camera. The wave height, wavelength and water depth were about 8 cm, 75 cm and 45 cm, respectively (continue).

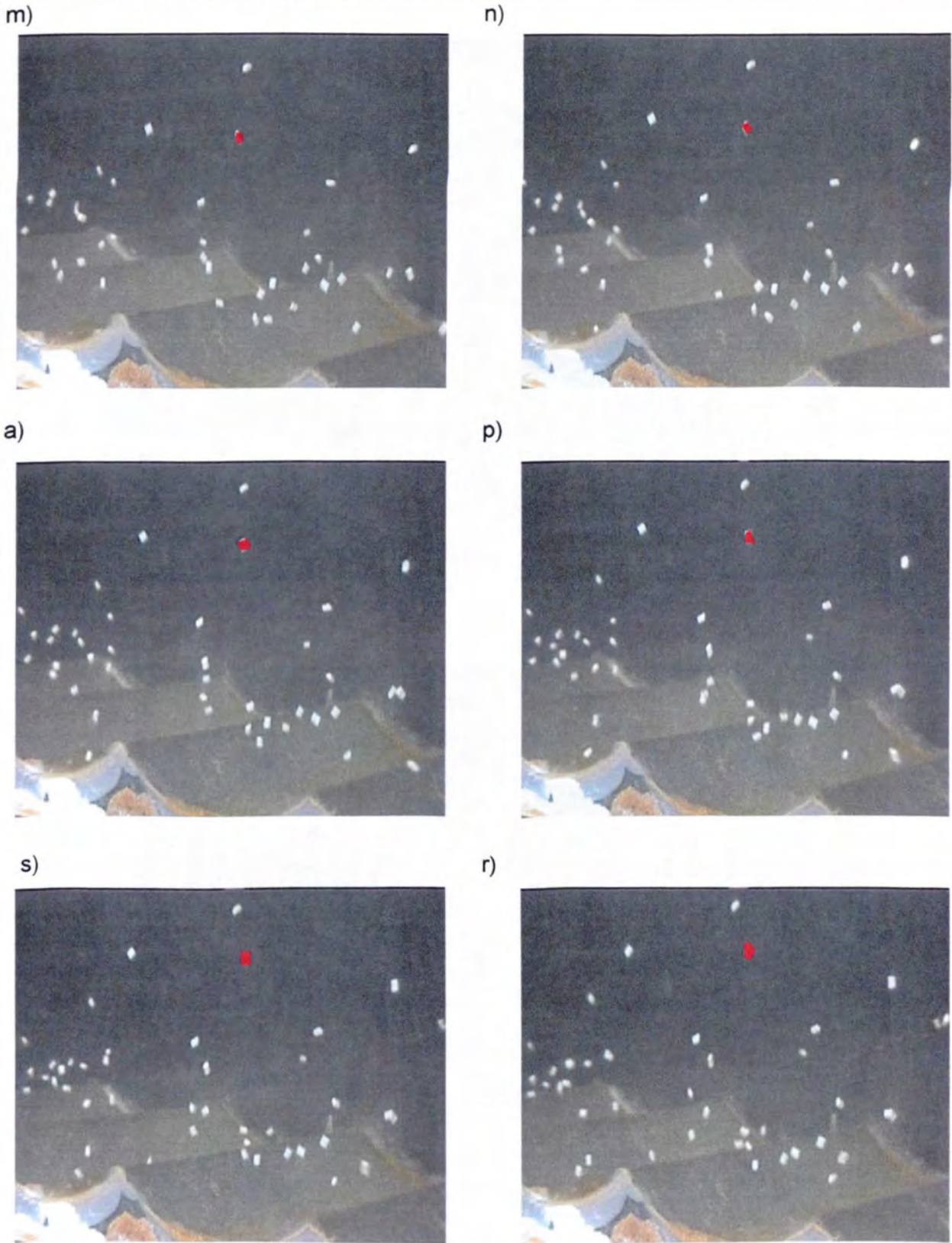


Figure 7.11: Individual frames of particle motion in the laboratory wave flume recorded by a video camera. The wave height, wavelength and water depth were about 8 cm, 75 cm and 45 cm, respectively (continue).

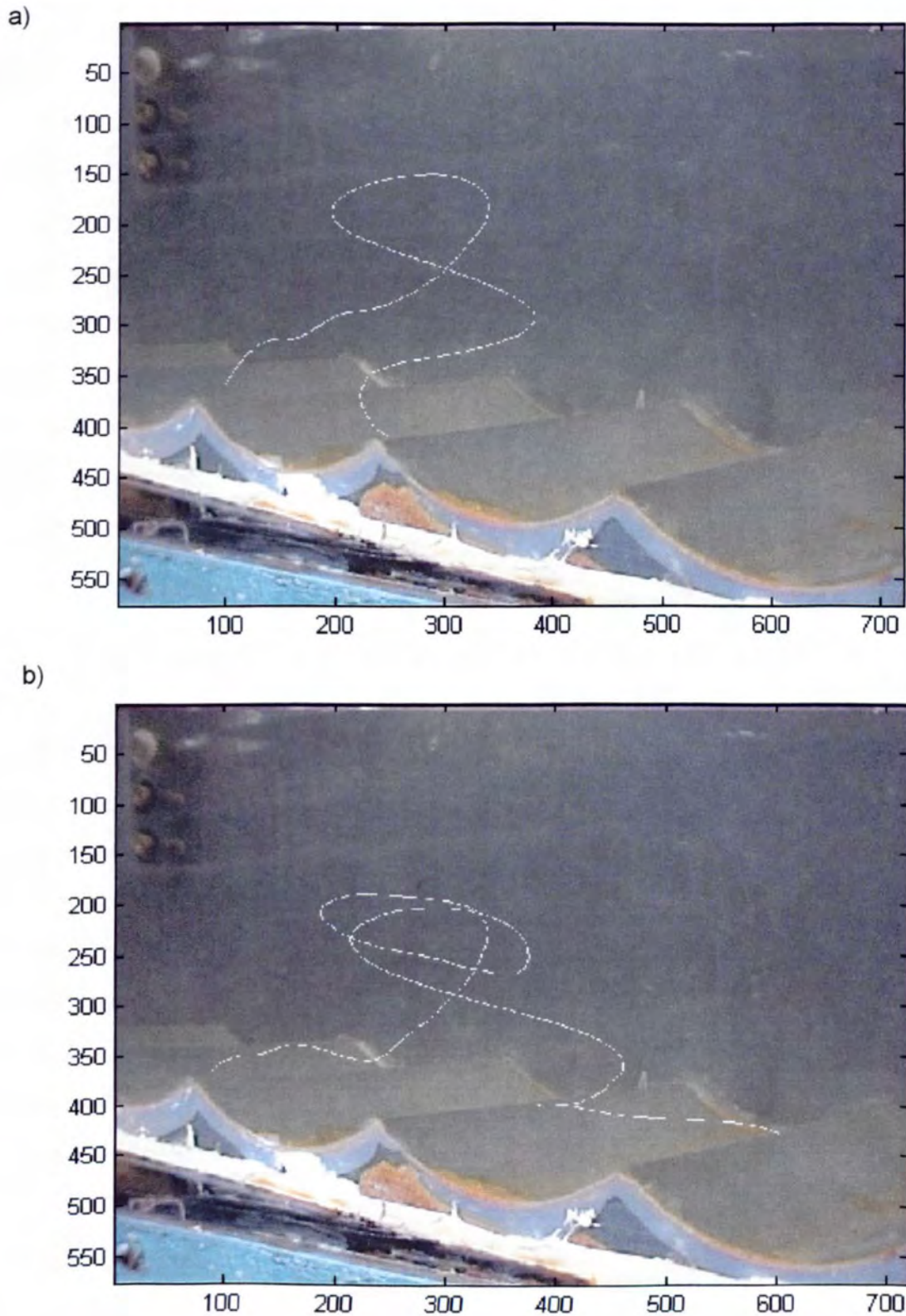


Figure 7.12: Particle trajectories extracted from the video taken of the particle movement in the laboratory wave flume recorded for a) 3.8 s, b) 6.12 s, c) 3.56 s, d) 1.4 s and e) 1.7 s.

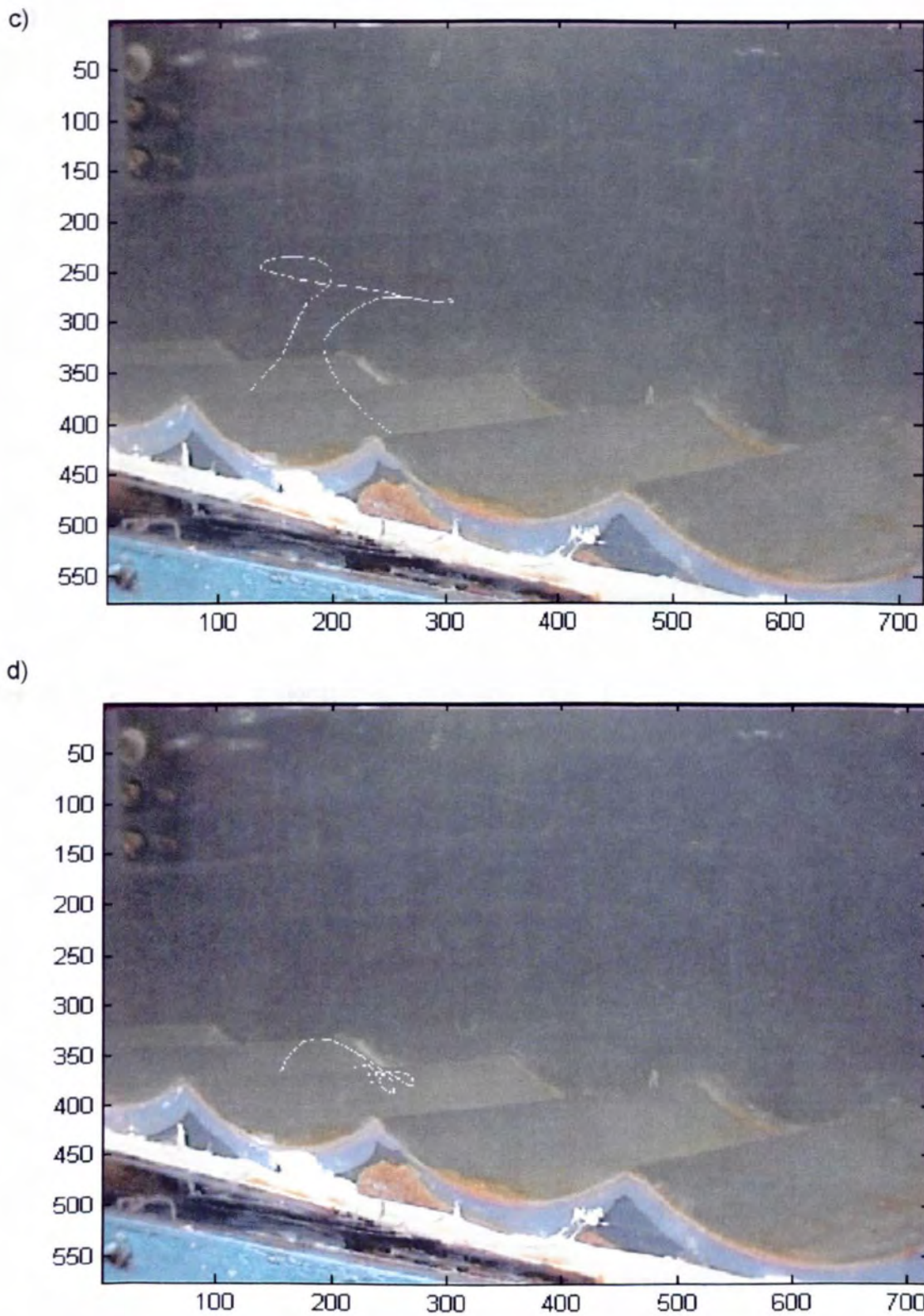


Figure 7.12: Particle trajectories extracted from the video taken of the particle movement in the laboratory wave flume recorded for a) 3.8 s, b) 6.12 s, c) 3.56 s, d) 1.4 s and e) 1.7 s (continue).

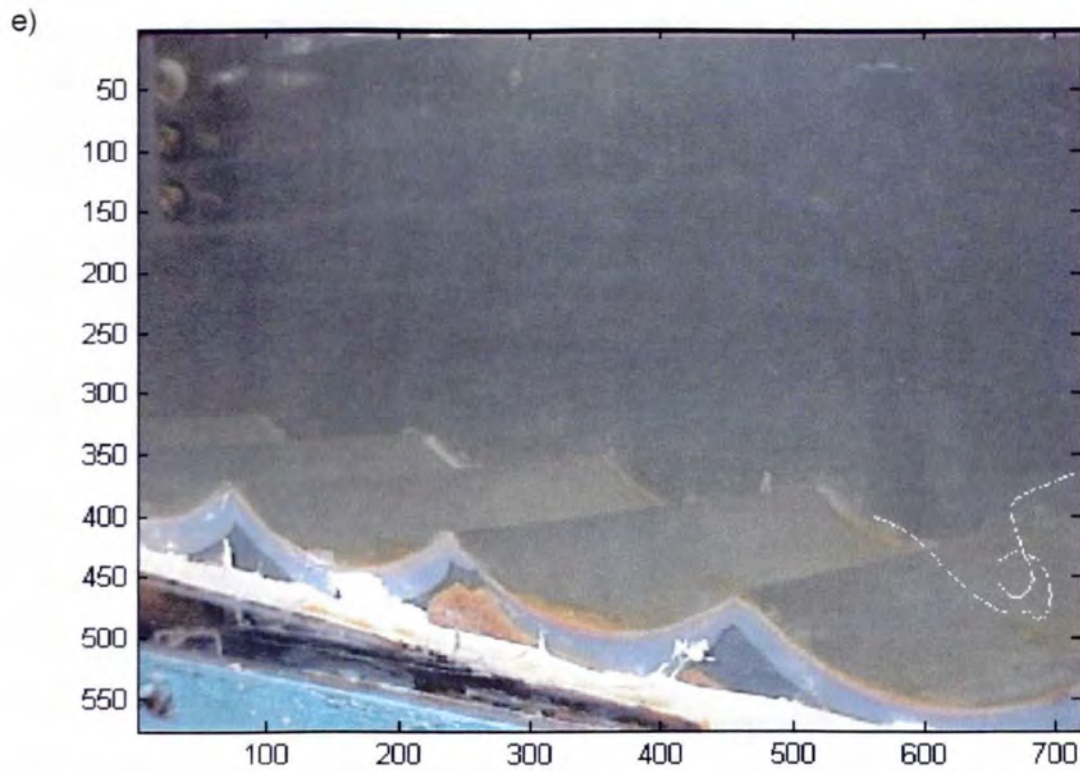


Figure 7.12: Particle trajectories extracted from the video taken of the particle movement in the laboratory wave flume recorded for a) 3.8 s, b) 6.12 s, c) 3.56 s, d) 1.4 s and e) 1.7 s (continue).

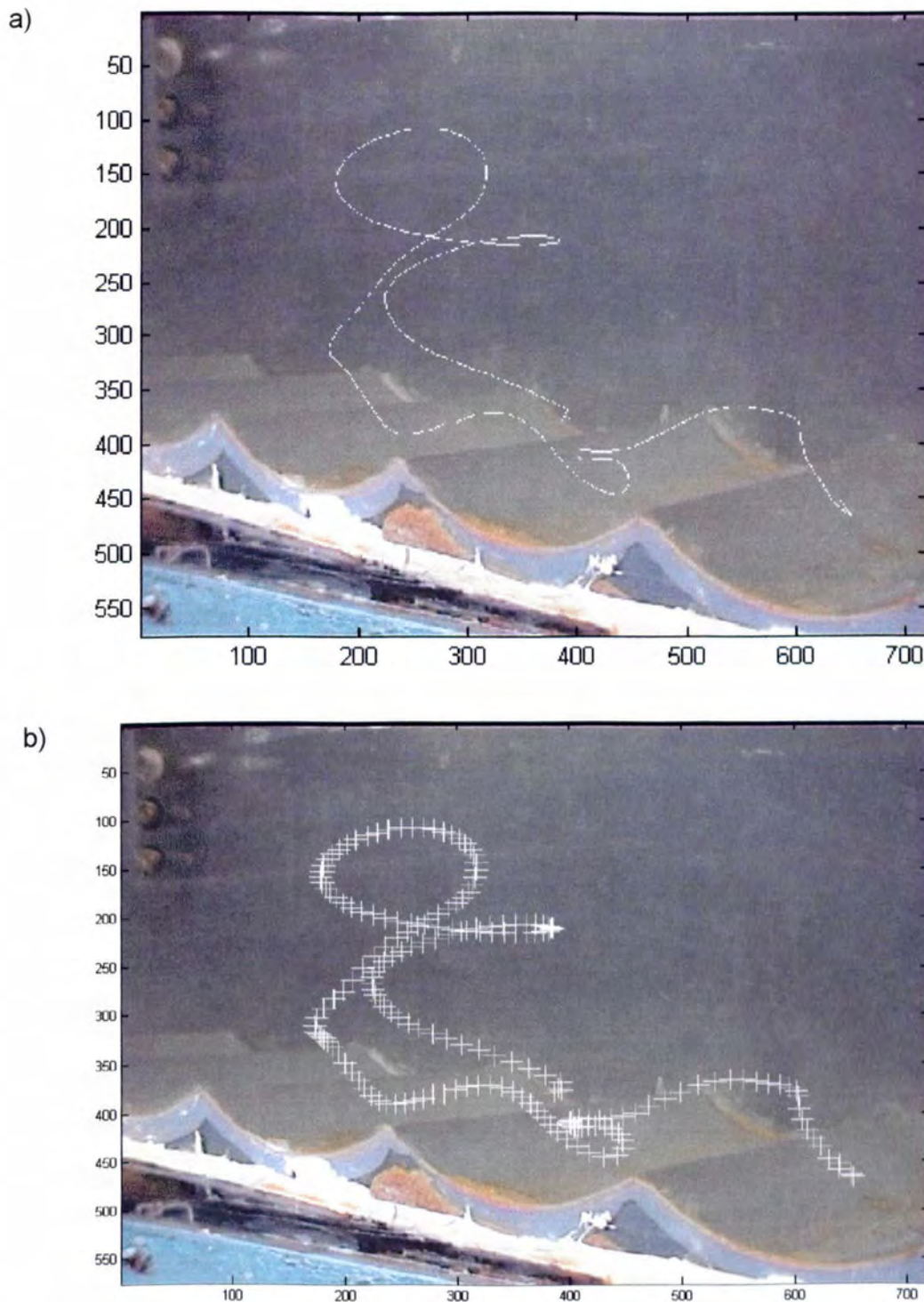


Figure 7.13: a) Trajectory of a plastic particle extracted from the video taken of the particle movements in the laboratory wave flume and tracked over 7.6 seconds. b) cross hairs indicating the position of the particle in every frame (25ths of a second) and highlighting times of acceleration due to the spacing of the crosses.

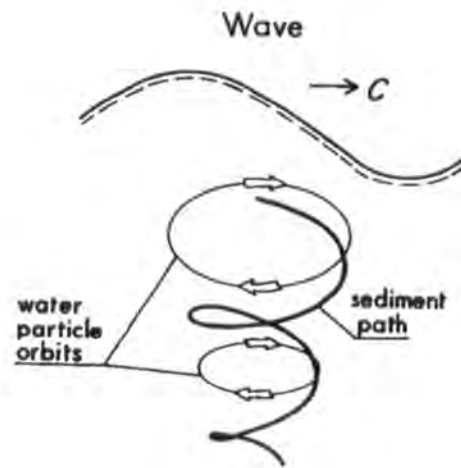


Figure 7.14: Path of a sediment particle trapped in a vortex under waves (from NIELSEN (1992), figure 4.11).

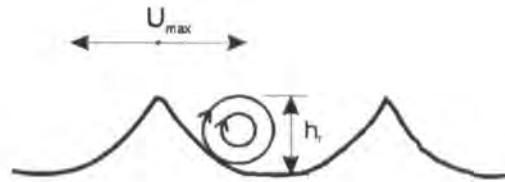


Figure 7.15: Vortex development in the lee of a ripple. Its strength is assumed to be equal to $\Gamma_0 = U_{max} \cdot \pi \cdot h_r$.

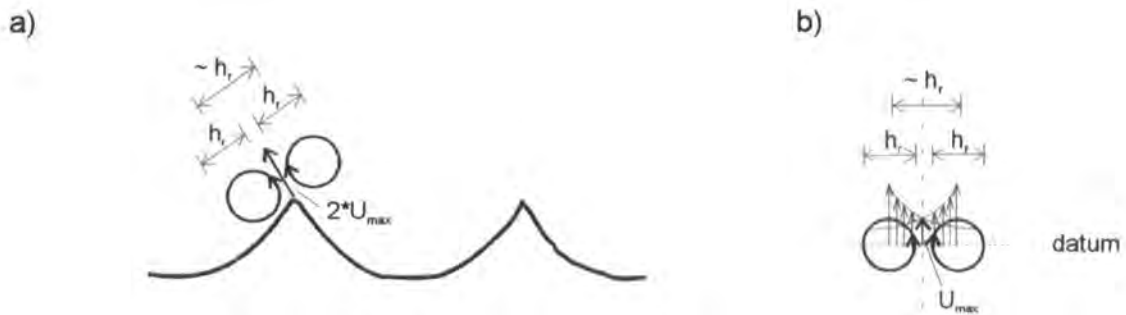


Figure 7.16: Vortex pair ejection from a ripple crest. a) Actual direction of propagation of the vortex pair. b) Simplified vortex movement in the vertical direction.

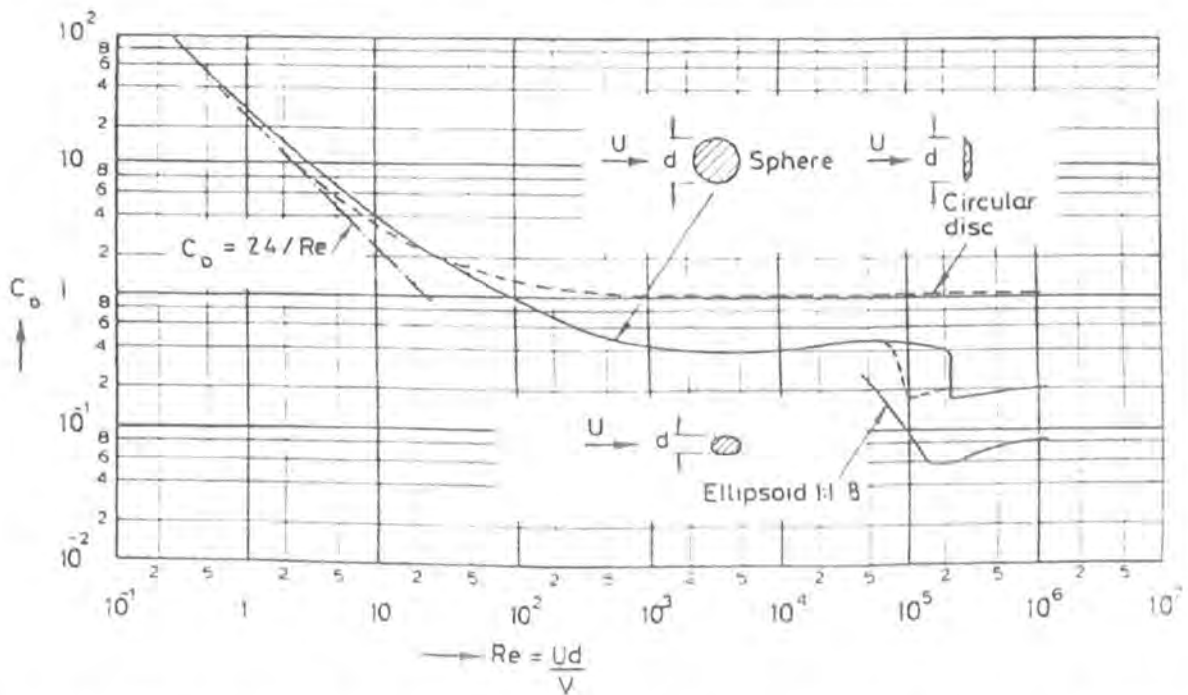


Figure 7.17: Drag coefficient as a function of the Reynolds Number for a sphere (lecture notes from Prof. D.W. Knight, The University of Birmingham).

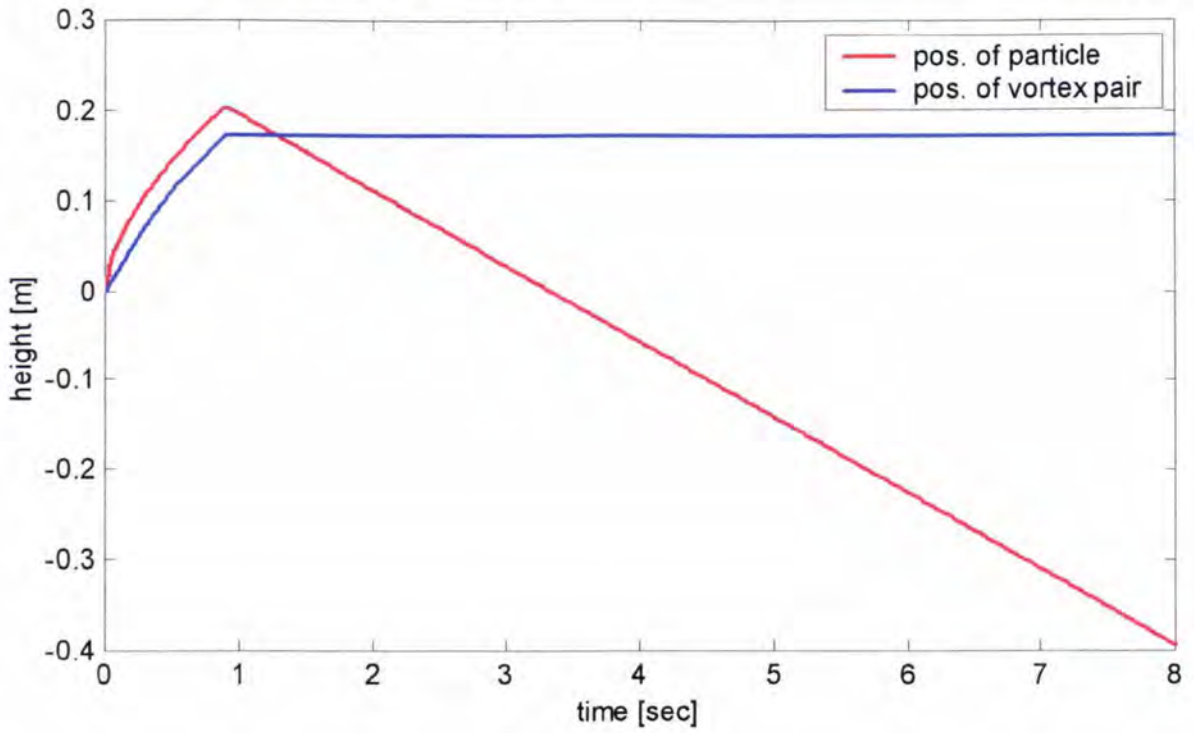


Figure 7.18: Trajectory of the sediment particle and the vortex pair as a function of time.

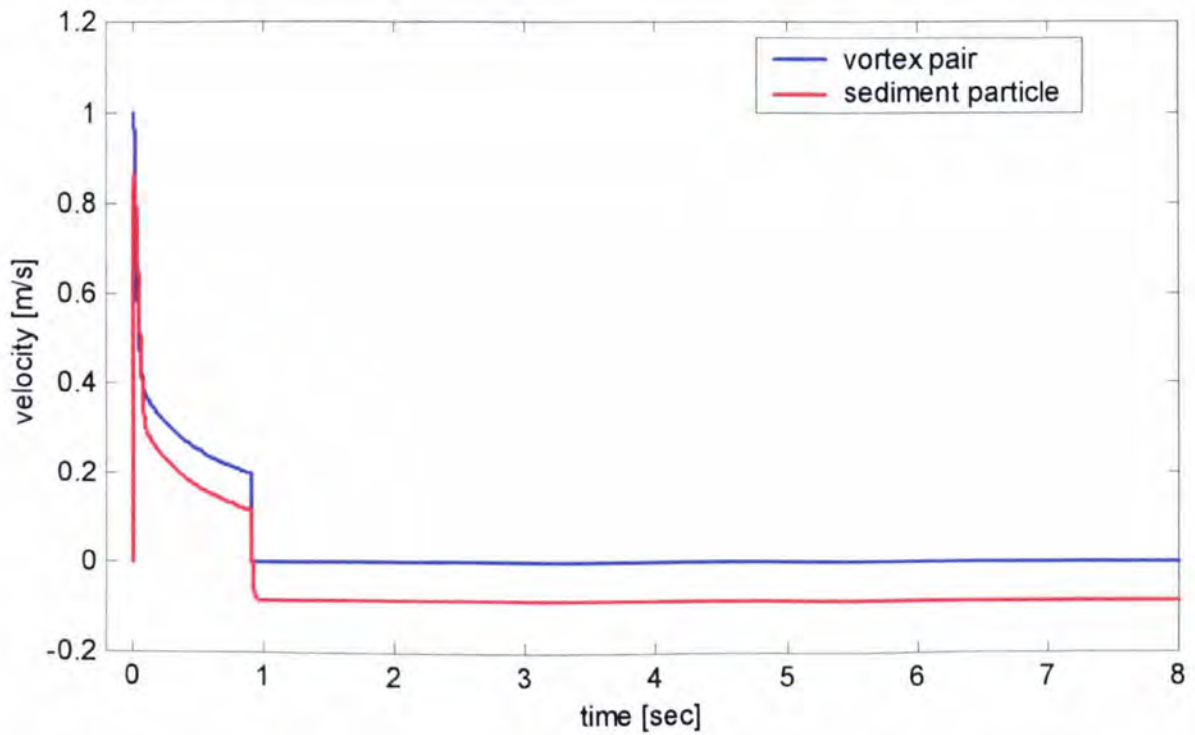


Figure 7.19: Velocity of the vortex pair and the sediment particle as a function of time. At the time the vortex pair dissipates into the flow the velocity, its velocity is set to zero.

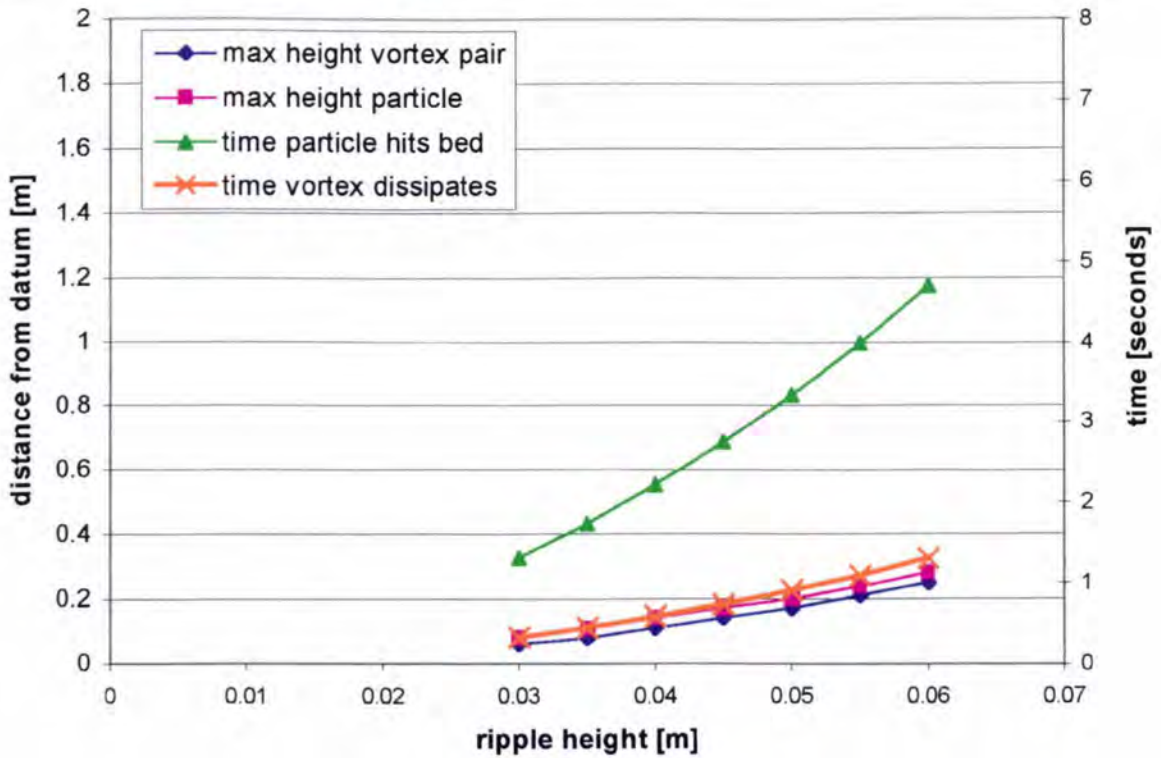


Figure 7.20: Effects of changes of the ripple height and thus the spacing between the two vortices on the peak elevation of the particle and the vortex pair and the time it hits the bed.

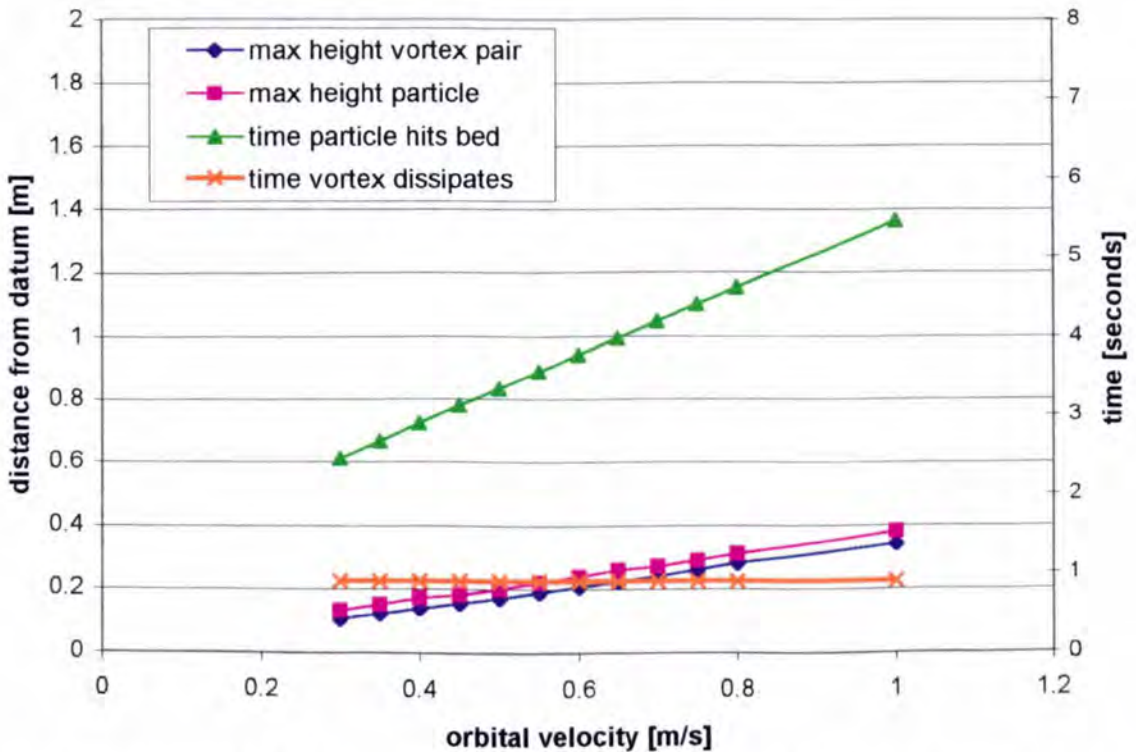


Figure 7.21: Effects of changes of the orbital velocity on the peak elevation of the particle and the vortex pair and the time it hits the bed.

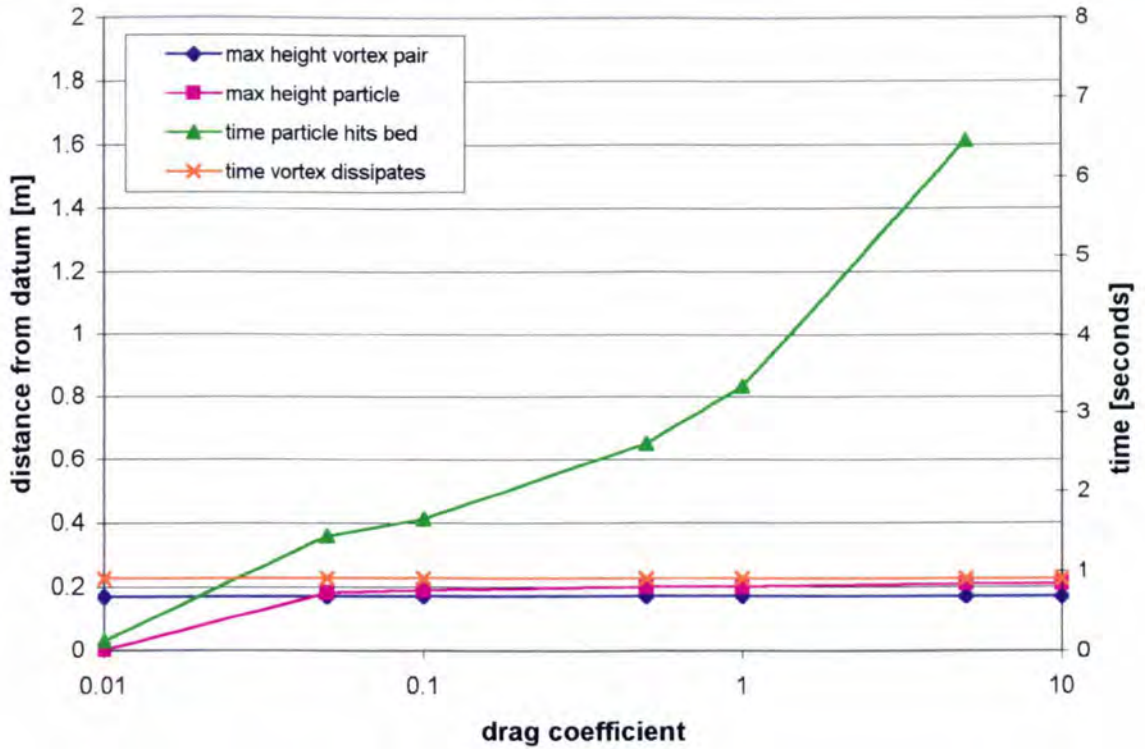


Figure 7.22: Effects of changes of the drag coefficient on the peak elevation of the particle and the vortex pair and the time it hits the bed.

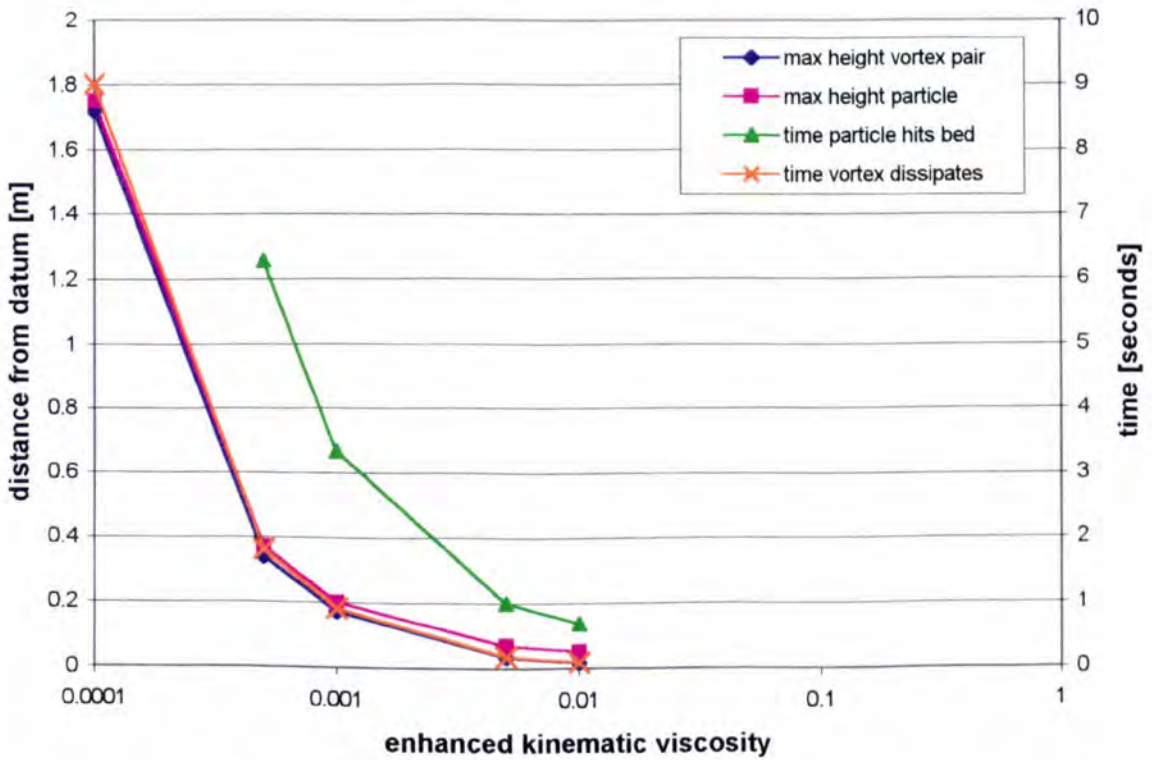


Figure 7.23: Effects of changes of the enhanced kinematic viscosity on the peak elevation of the particle and the vortex pair and the time it hits the bed.

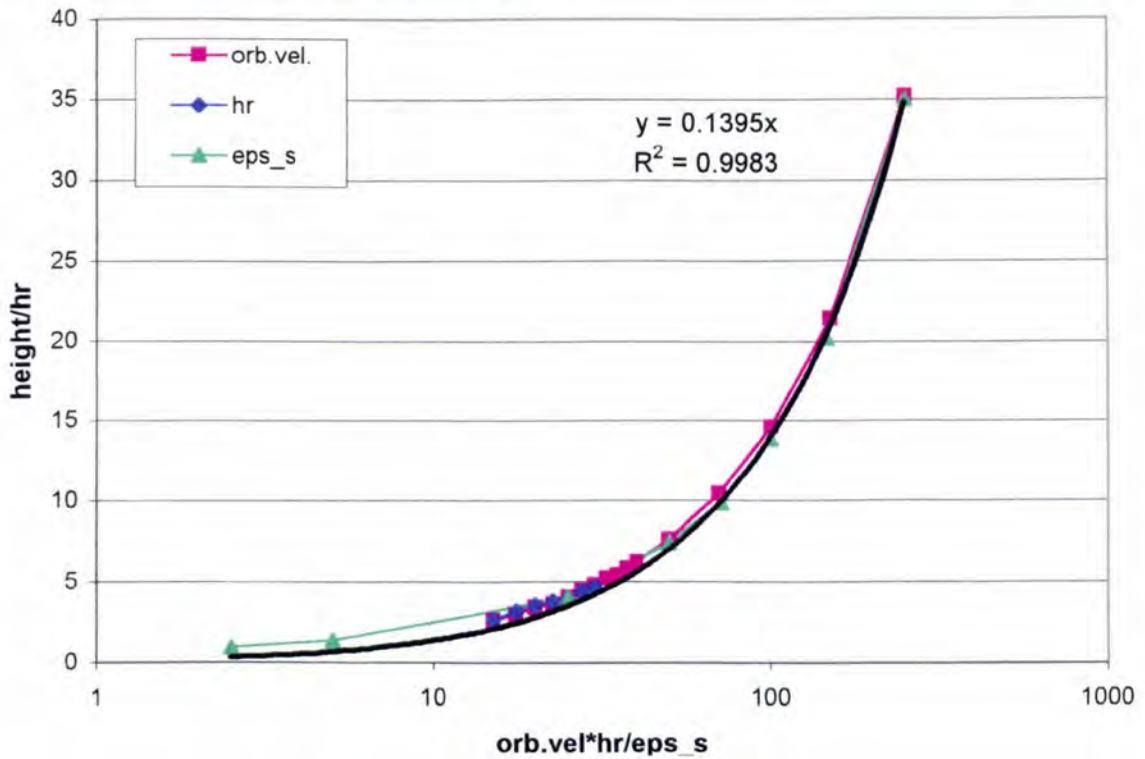


Figure 7.24: Dimensionless graph to relate the peak elevation of a sediment particle ($d_{50} = 0.329$ mm), the orbital velocity of the waves, the ripple height of the bed and the modified kinematic viscosity.

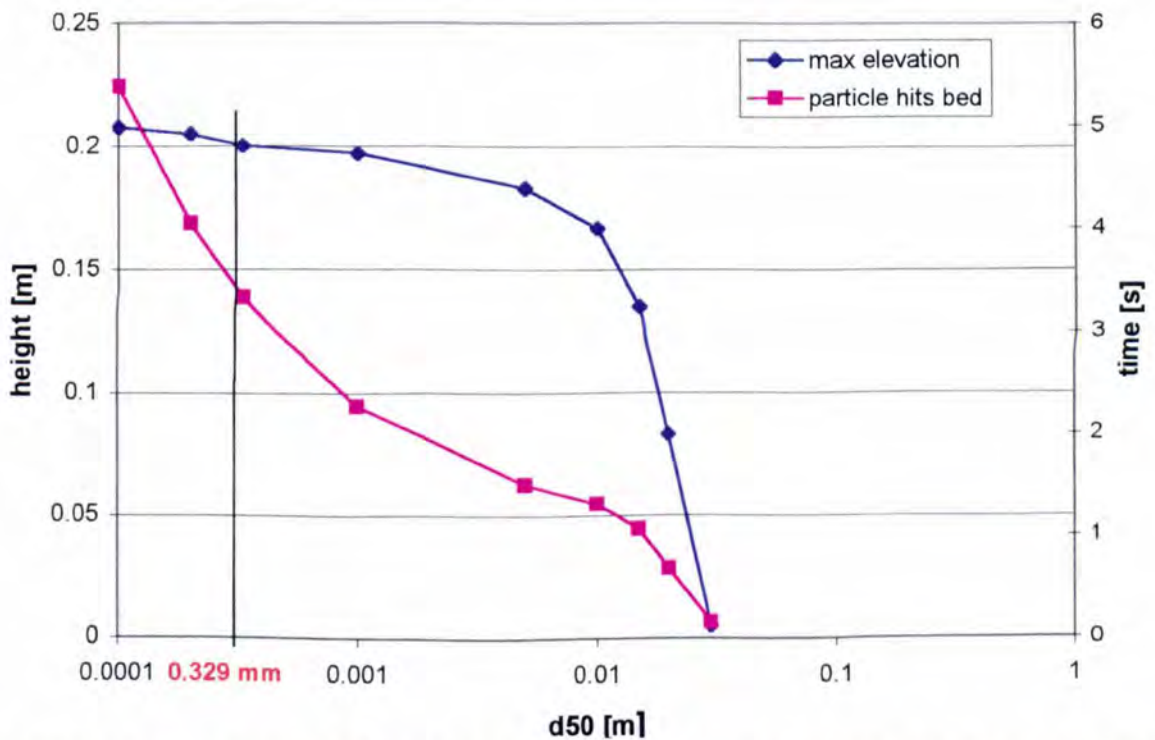


Figure 7.25: Effects of the sediment diameter on the peak elevation of the particle and the time it hits the bed.

Chapter 8 Conclusions and Recommendations for Future Work

8.1 Conclusions

The present work has addressed fundamental questions concerned with understanding and quantifying the influence of STABLE on its measuring environment and on the local sediment and hydrodynamic processes. This is essential before conclusions can be reached pertaining to data collected in the field. Using the controlled environment of the *Deltaflume* local bedform morphology and sediment re-suspension by waves on time-averaged and intra-wave time-scales has been investigated. The experiments also provided an opportunity to examine the influence of wave groups on sediment re-suspension processes and the ensuing enhancement of the mean concentration profile. Analyses performed here have enabled quantification of the small modifications to local processes that result from the presence of STABLE. These results add greatly to the confidence that may be placed in the accuracy of field data obtained using this and similar benthic frames. During the course of the investigations, a simple model simulating entrainment processes on an intra-wave scale was developed to investigate suspension processes. The importance of the convective entrainment mechanism for the re-suspension of sediments was discussed and a model developed based on the existence of a vortex pair as the driving mechanism for sediment entrainment.

The present data set was unique as it provided comprehensive measurements of hydro- and morphodynamics in controlled conditions. The deployment of sensors measuring identical parameters at two different locations allowed the assessment of the repeatability of measurements and hydro- and morphodynamic conditions. Conclusions that may be drawn from data analysis presented here are summarised below.

- Differences between the suspended sediment data measured at the side of the flume and those measured on STABLE illustrate the difficulties related to multiple data recording of the same parameter. Although the data collected at the side of the flume was thought not to be influenced by STABLE, other boundary conditions restricted a direct comparison. In

the case of irregular waves the most likely cause for the observed differences was an imbalance in wave energy between the first and second half of a burst data set resulting in a difference of about 14 % in the reference concentration determined by an empirical equation (equation 2.70). As the pump-sampling equipment had to be swapped between the sampling array on STABLE and the one at the side of the flume half way through the burst this is considered to influence the measured pump-sampling values for the two locations.

- STABLE has been shown not to affect the development of vortex ripples on the medium sand ($d_{50} = 0.329$ mm). On the fine sand ($d_{50} = 0.162$ mm) there was evidence of localised scour behind the feet. Since the bed morphology is linked closely with the near bed hydrodynamic conditions, this result demonstrates clearly that STABLE exerts little influence on local processes. The novel use of the Wavelet Transform to analyse bedforms proved a very useful tool to identify the local influence of the feet on the bedforms and to quantify bed morphology along different sections of the test beds. The Morlet wavelet was found to be a good representative of vortex ripples developed in the present experiments. The use of wavelets in future analyses of bedform characteristics is advocated.
- The 'blockage effect' due to the placement of STABLE in the flume was small and no influence of the frame on the velocity data was detected by the present sensors. It is considered that the bulk of turbulence generated by the STABLE frame in oscillatory flow dissipated into the flow and did not influence data recorded by STABLE sensors.
- Under similar wave conditions, the burst-averaged suspended sediment concentration profiles for irregular waves decayed quicker with height than ones for regular waves. Above the re-suspension threshold under regular waves, sediment re-suspension occurs every half wave cycle whilst under irregular waves, re-suspension events are more closely correlated with groups of large waves and are characterised by the re-suspension of large quantities of sediments into the water column.
- The bed ripples under irregular waves were dominated by relics of ripples formed during the previous burst under regular waves, even though the waves were running for approximately 1 hour before any measuring commenced. The long time taken for bedforms to adjust to new hydrodynamic conditions has implications for some sediment modelling applications in the field where predicted bedforms may not correlate with the antecedent conditions and lead to inaccurate estimation of bed roughness and associated parameters.

- The ABS data provided time-dependent sediment concentration values with a good temporal and spatial resolution. The burst mean c-profiles for irregular waves exhibited two different gradients. The first three centimetres were dominated by a rapid decay in sediment concentrations, while the decay over the next 50 cm was smaller. It was suggested that the two regions represent two different layers, a bedload and a suspension layer. Empirical equations proposed by NIELSEN (1992) and WILLIAMS ET AL. (1999b) showed good agreement with measurements after modifying the equations to suit the present data. The influence of the ratio of sediment diffusivity to turbulent viscosity was investigated. A value of around 0.5 for the ratio was found to give good agreement between measured and predicted c-profiles.
- Analysis of the vertical and horizontal coherence of the sediment suspension showed that the vertical coherence of the suspension under regular waves was linked to the wave period, while under irregular waves the suspension was driven by event like structures linked to wave pumping under wave groups even on a burst mean scale. Horizontal coherence was larger at 50 cm than at 5 cm above the bed suggesting that any coherent structures developed close to the bed were too small to be picked up by the two ABS sensors, laterally separated by about 11 cm.
- The wave cycle ensemble averaged concentration for regular waves was investigated. However, owing to different relative positions of the ABS transducers to a ripple crests caused by migration of the ripples (up to 0.05 cm/s), no conclusive phase relationship between the near bed horizontal velocity and the ensemble averaged concentration could be established. The limited amount of available data further restricted this analysis.
- The intra-wave suspension events for irregular waves were analysed. It was shown that a group of waves can lift sediment further away from the bed than a single wave alone. Analysis of the influence of the position of a wave in a group revealed that the sediment concentration peaks under the third or fourth wave in a group of waves consisting of more than three waves. Sediment concentrations of up to 1 g/l above 70 cm into the water column at the end of some groups were of the same order as the concentrations within the first 10 cm above the bed at the beginning of the group (figure 6.4). A simple model taking the history of sediment re-suspension during the passing of a wave group into account was developed. The model was capable of simulating the entrainment of sediment further into the water column, whilst at the same time reducing the near bed sediment concentrations. The model is considered to describe well the well-known wave pumping effect observed in the field under a group of large waves.

- The re-suspension of sandy sediments by waves above a rippled bed is dominated by the vortex ejection or convective process. The role played by vortex pairing was investigated and a model of vortex-sediment interaction was developed. In the model a particle is ejected through the jet like structure between adjacent counter-rotating vortices and then lifted up into the water column through the influence of the vortex pair. Once the vortex pair dissipated the particle was allowed to settle to the bed. A sensitivity analysis on the model parameters showed that given certain assumptions, sediment particles can be lifted between 10 and 30 ripple heights above the bed. This result is in accord with present observational data. A non-dimensional graph was presented allowing the prediction of the peak elevation of a sand particle as a function of the orbital velocity, the ripple height and the enhanced kinematic viscosity.
- Approximately neutrally buoyant plastic particles were used to visualise the oscillatory flow over a fixed, rippled bed in a laboratory flume. Some particles moved along the bed over up to three ripple wavelengths before being ejected into the flow with a large vertical acceleration. Video footage was used to track individual particles and show their trajectories and to identify the observed movement of the particles. The rapid ejection of these particles up to 8 ripple heights above the boundary supports the concept of vortex pairing as a primary mechanism driving re-suspension. The particles were found to be ejected rapidly into the water column along a linear path, before settling to the bed under the influence of the orbital wave motion. During the entrainment process particles did not appear to be caught in a vortex. This fundamentally alters present views of processes operating to distribute sediments vertically under wave conditions.

8.2 Recommendation for Future Work

Knowledge gaps in the field of sediment transport under waves were identified at the end of the literature review (chapter 2). The need for a rigorous investigation into the performance of the measuring frame was pointed out in view of future deployments of similar benthic frames. The effects of wave pumping on sediment suspension and transport were addressed and the need for parameterising this mechanism to model enhanced sediment suspension was discussed. Further work is needed in order to fulfil the needs of the knowledge gaps and to address issues raised in this study.

- Originally the sand bed was designed to be horizontal at the position of STABLE. It turned out that, on the medium sand, the bed was disturbed to such an extent that no section of it remained horizontal. If a similar experiment was conducted in the future a

set-up stopping the wash out of sand at the ends of the bed should be designed.

- Given the relatively long time taken for bedforms to develop in response to new hydrodynamic conditions the possibility of flattening the bed between successive experiments should be investigated. Further, whether or not equilibrium bedforms were produced during the present tests remains uncertain. Studies relating time histories of bed morphology to changing wave conditions would provide further insight into this.
- During the present experiments in the *Deltaflume*, STABLE was also positioned at approximately 45° and 90° in the flume, resulting in a longitudinal set-up arrangement for the ABS transducers. In future studies these data have to be analysed to investigate the coherence of sediment clouds along the flume and their advection passed the sensors. Further, the vertical entrainment velocity of a sediment cloud might be estimated if the same cloud could be identified in two sensors with some time delay. For the present study, data for those deployments were not available.
- To study phase relationships between the near bed horizontal velocity and the ensemble averaged concentration it is necessary to develop a method of deploying instrumentation at a known location above a ripple. Such a system should allow instrumentation to follow ripple migration.
- Regular and irregular waves were generated in the *Deltaflume*. Though the irregular waves show some elements of groupiness, they were not generated as groupy waves. The need for a series of experiments beginning with regular waves and gradually changing into groupier and groupier waves, but with the same H_s , thus allowing the quantification of effects of groupiness as an additional parameter is recommended. Ideally these tests would be associated with the deployment of an ABS sensor. A parameterisation, that takes the groupiness factor and the significant wave height for irregular waves into account, needs to be determined and could aid the prediction of sediment transport on larger scales. This might result in the determination of an effective wave height taking the antecedent wave conditions in a wave group or the groupiness factor for the whole burst into account.
- Future work should not only concentrate on sediment suspension into the water column, but should include sediment transport. The vertical sediment distribution has to be coupled with the hydrodynamics to provide a measure of transport. This is a vital information for a civil engineer investigating deposition and erosion processes in rivers and along the coast. The lowest ECM sensor mounted on STABLE was about 30 cm

above the bed and thus, did not provide measurements in the region of large sediment transport. The coherent Doppler velocimeters mounted on STABLE did not provide reliable data for the present experiments.

- The simple empirical model simulating the suspension of sediments during the passing of a wave group was based on a number of assumptions. Here, it assumed a vertical concentration distribution equal to the burst mean *c*-profile. The influence of this assumption should be investigated. Further, the entrainment is based on a purely convective mechanism, namely a vortex pair. Although this is the dominant mechanism in the present oscillatory flow, inclusion of diffusion in the model must be investigated in future studies.
- The background flow in the model, simulating the entrainment of a sediment particle under the influence of a vortex pair, is zero. In order to make it more applicable for oscillatory flow, orbital motion could be included as the background flow. However, it is thought that this flow could be treated independently and superimposed on the existing results. First attempts including the oscillatory flow in the model were made, but to this point no conclusive results were obtained. Further, the drag coefficient as a function of the Reynolds Number and not a constant value could be included in any future versions of the model.
- The visualisation experiments in the laboratory flume could be extended by the use of two video cameras. This would help to create a three-dimensional picture of the flow in the flume and aid the identification of the plane across the flume a plastic particle is moving in.

References

- ADDISON, P.S.: Wavelet analysis of the breakdown of a pulsed vortex flow. *Proceedings of the Institution of Mechanical Engineers*, Vol. 213, Part C, pp. 217-229, 1999.
- ADDISON, P.S.; WATSON, J.N.: The Wavelet Transform as a Tool for the Analysis of Surface Roughness. *SiF News*, Paint Research Association, Issue No. 9, 1997.
- ADDISON, P.S.; WATSON, J.N.: Wavelet Analysis: A Brief Description. Unpublished notes, 1999.
- ALLEN, J.R.L.: Asymmetrical ripple marks and the origin of water-laid closets of cross-strata. *Liverpool and Manchester Geol. Journal* 3, 1963.
- AYRTON, H.: The origin and growth of ripple-mark. *Proceedings of the Royal Society of London*, Series A, Vol. 84, pp. 285-311, 1910.
- BAGNOLD, R.A.: Motion of Waves in Shallow Water. *Proceedings of the Royal Society*, A 187, 1946.
- BELL, P.S.; THORNE, P.D.: Measurement of sea bed profile evolution in an estuarine environment using a high resolution acoustic sand ripple profiling system. *Oceans '97 MTS/IEEE Conference*, Halifax, Nova Scotia, 1997.
- BELL, P.S.; THORNE, P.D.; WILLIAMS, J.J.: Acoustic measurements of sand ripple profile evolution under controlled wave conditions. *Proceedings of the 4th European Conference on Underwater Acoustics*, September 21st-25th, Rome, Italy, pp. 353-358, 1998.
- BLONDEAUX, P.; VITTORI, G.: Vorticity dynamics in an oscillatory flow over a rippled bed. *Journal of Fluid Mechanics*, Vol. 226, pp. 257-289, 1991.
- BOSMAN, J.J.; VAN DER VELDEN, E.T.J.M.; HULSBERGEN, C.H.: Sediment concentration measurement by transverse suction. *Coastal Engineering*, 11, pp. 353-370, 1987.
- BOURKE, P.: Cross Correlation. Published notes on the world wide web: <http://www.swin.edu.au/astronomy/pbourke/analysis/correlate>, 1996.

- BOUSSINESQ, J.: Essai sur la Theorie des Eaux Courantes. *Mem. Divers Savants a L'Academie des Science*, No. 32, 1877.
- BOYD, R.; FORBES, D.L.; HEFFLER, D.E.: Time sequence observations of wave-formed sand ripples on an ocean surface, *Sedimentology*, 35, pp. 449-464, 1988.
- CARSTENS, M.R.: Similarity laws for localised scour. *Proc. A.S.C.E. Journal of the Hydraulic Division* 92 (HY5), 1966.
- CARTWRIGHT, D.E.: On estimating the mean energy of sea waves from the highest waves in a record. *Proceedings of the Royal Society*, A247, 1958.
- CARTWRIGHT, D.E.; LONGUET-HIGGINS, M.S.: The statistical distribution of the maxima of a random function. *Proceedings of the Royal Society*, A237, 1956.
- COLEMAN, N.L.: Flume studies of the sediment transfer coefficient. *Water Resource*, 6 (3), pp. 801-809, 1970.
- DARWIN, G.H.: On the formation of ripple-mark in sand *Proceedings of the Royal Society of London, Series A*, 36, pp. 18-43, 1883.
- DEAN, R.G.; DALRYMPLE R.A.: Water Wave Mechanics For Engineers and Scientists. *Advanced Series in Ocean Mechanics*, Vol. 2, World Scientific, 1984.
- DINGLER, J.R.; INMAN, B.L.: Wave-formed ripples in nearshore sands. *Proc. 15th Coastal Engineering Conference*, Honolulu, Hawaii, 1976.
- DUNCAN, W.J.; THOM, A.S.; YOUNG, A.D.: Mechanics of fluids. Second Edition, Edward Arnold, 1978.
- DYER, K.R.: Coastal and Estuarine Sediment Dynamics. Wiley-Interscience, John Wiley and Sons, 1986.
- DYER, K.R.; SOULSBY, R.L.: Sand transport on the continental shelf. *Annual Review of Fluid Mechanics*, 20, pp. 295-324, 1988.
- ENGELUND, F.; FREDSE, J.: Sediment ripples and dunes. *Annual Review of Fluid Mechanics*, 14, pp.13-37, 1982.
- FARGE, M.: Wavelet transforms and their application to turbulence. *Annual Review Fluid Mechanics*, 24, 395-457, 1992.

- FREDSØE, J.; DEIGAARD, R.: Mechanics of Coastal Sediment Transport. *World Scientific Publication, Advanced series in Ocean Engineering*, Vol. 3, 1992.
- FREDSØE, J.; ANDERSEN, K.H.; SUMER, B.M.: Wave plus current over a ripple-covered bed. *Coastal Engineering* 38, pp. 177-221, 1999.
- FUNKE, E.R.; MANSARD, E.P.D.: On the synthesis of realistic sea states in the laboratory flume. Laboratory technical report, No. LTR-HY-66, Division of Mechanical Engineering, Canada, 1979.
- GIBBS, R.J.; MATHEWS, M.D.; LINK, D.A.: The relationship between sphere size and settling velocity. *Journal of Sedimentary Petrology*, Vol. 41, pp. 7-18, 1971.
- GODA, Y.: Random sea and design of maritime structures. *University of Tokyo press*, 1985.
- GODA, Y.; SUZUKI, Y.: Estimation of incident and reflected waves in random wave experiments. Proceeding of the 15th *Conference of Coastal Engineering*, ASCE, New York, pp. 828-865, 1976.
- GRASMEIJER, B.T.; CHUNG, D.H.; VAN RIJN, L.C.: Depth-integrated sand transport in the surf zone. *Proceedings of Coastal Sediments 1999*. pp. 325-340, ASCE, New York, 1999.
- GRASS, A.J.: Sediment Transport by waves and currents. *London Centre for Marine Technology*, Report No: FL29, University College London, 1981.
- GREEN, M.O.; BLACK, K.P.: Suspended-sediment reference concentration under waves: field observations and critical analysis of two predictive models. *Coastal Engineering* 38, pp. 115-141, 1999.
- GREEN, M.O.; VINCENT, CH.E.: Wave Entrainment of Sand from a Rippled Bed. *Proceedings of the 22nd Coastal Engineering Conference* in Delft, The Netherlands, 1990.
- GURLEY, K.; KAREEM, A.: Applications of wavelet transforms in earthquake, wind and ocean engineering. *Engineering Structures* 21, 1999.
- HALLERMEIER, R.: Sand Motion Initiation by Water Waves: Two Asymptotes. *Journal of Waterway, Port, Coastal and Ocean Engineering*, Vol. 106, No. WW3, Proceeding Paper 15603, 1980.
- HANNAY, A.; WILLIAMS, J.J.; WEST, J.R.; COATES, L.E.: A field study of wave:current interactions over rippled sandy bed. *EUROMECH 310: Sediment Transport*

Mechanisms in Coastal Environments and Rivers, M. Belorgey, R.D. Rajaona, J.A.F. Sleath (editors), World Scientific, pp. 345-359, 1994.

HANES, D.M.: Suspension of Sand Due to Wave Groups. *Journal of Geophysical Research*, Vol. 96, No. C5, pp. 8911-8915, 1991.

HANES, D.M.; HUNTLEY, D.A.: Continuous measurements of suspended sand concentration in a wave dominated nearshore environment. *Continental Shelf Research*, Vol. 6, No. 4, pp. 585-595, 1986.

HANSEN, E.A.; FREDSE, J.; DEIGAARD, R.: Distribution of Suspended Sediment over Wave-generated ripples. *Journal of Waterway, Port, Coastal and Ocean Engineering*, Vol. 120, No. 1, 1994.

HAY, A.E.; BOWEN, A.J.: Space-time variability of sediment suspension in the nearshore zone. In: Arcilla, A.S., Stive, M.J.F., Kraus, N.C. (Eds.), *Coastal Dynamics '94*, Proceeding of An International Conference on the Role of the Large Scale Experiments in Coastal Research. American Society of Civil Engineers, New York, pp. 962-975, 1994a.

HAY, A.E.; BOWEN, A.J.: Coherence scales of wave-induced suspended sand concentration fluctuations. *Journal of Geophysical Research*, Vol. 99, No. C6, pp. 12749-12765, 1994b.

HAY, A.E.; SHENG, J.: Vertical Profiles of Suspended Sand Concentration and Size From Multifrequency Acoustic Backscatter. *Journal of Geophysical Research*, Vol. 97, No. C10, pp. 15661-15677, 1992.

HINO, M.: Equilibrium-range spectra of sand waves formed by flowing water. *Journal of Fluid Mechanics* 34, 1968.

HUMPHREY, J.D.: STABLE – an instrument for studying current structure and sediment transport in the benthic boundary layer. *Proceedings of the Electronics of Ocean Tech. Conference*, Heriot-Watt university, Edinburgh, IERE London, 27, pp. 57-62, 1987.

HUMPHREY, J.D.; MOORES, S.P.: STABLE II – An improved benthic lander for the study of turbulent wave-current-bed interactions and associated sediment transport. *Electronic Engineering in Oceanography*, IEEE Conf. Pub. No. 394, pp. 170-174, 1994.

- JANSEN, R.H.J.: Het meten van sedimenttransport in de natuur door middel van ultrageluidsverstrooiing. *Nederlands Akoestisch Genootschap*, publication no. 44, pp. 78-92, 1978.
- JONSSON, I.G.: Wave boundary layers and friction factors. *Proceedings of the 10th International Conference on Coastal Engineering*, Tokyo, pp. 127-148, 1966.
- JONSSON, I.G.; CARLSEN, N.A.: Experimental and theoretical investigations in an oscillatory turbulent boundary layer. *Journal of Hydraulic Research*, 14, pp. 45-60, 1976.
- KACZMAREK, L.M.: Movable sea bed boundary layer and mechanics of SEDIMENT TRANSPORT. *Institute of Hydroengineering of the Polish Academy of Sciences (IBW PAN)*, 1999.
- KAMPHUIS, J.W.: Friction factors under oscillatory waves. *Journal of Waterway Harbours Coastal Engineering Division*, ASCE, 101 (WW2), pp. 135-144, 1975.
- KETABDARI, M.J.: The effect of waves and wave groups on the movement of bed sediment. *Ph.D. thesis*, The University of Birmingham, 1999.
- KORTWEG, D.J.; DE VRIES, G.: On the Change of Form of Long Waves Advancing in a Rectangular Canal, and on a New Type of Long Stationary Waves. *Philosophical Magazine*, 5th Series, 1895.
- LAMB, Sir H.: *Hydrodynamics*. Cambridge University Press, 1932.
- LEE, T.H.; HANES, D.M.: Direct inversion method to measure the concentration profile of suspended particles using backscattered sound. *Journal of Geophysical Research*, Vol. 100, No. C2, pp. 2649-2657, 1995.
- LEE, T.H.; HANES, D.M.: Comparison of field observations of the vertical distribution of suspended sand and its prediction by models. *Journal of Geophysical Research*, Vol. 101, No. C2, pp. 3561-3572, 1996.
- LEES, B.J.: Relationship between eddy viscosity and eddy diffusivity of suspended particles. *Geo-Marine Letters*, Vol. 1, pp. 249-254, 1981.
- LE MEHAUTE, B.: An Introduction to Hydrodynamics and Water Waves. *Water Wave Theories*, Vol. II, TR ERL 118-POL-3-2, U.S. Department of Commerce, ESSA, Washington D.C., 1969.

- LIGHTHILL, M.J.: Waves and Hydrodynamic Loading. *Conference on the Behaviour of Offshore Structures*, Imperial College, London, August, 1979.
- LIST, J.H.: Wave groupiness variations in the near-shore. *Coastal Engineering*, Vol. 15, pp. 475-496, 1991.
- LOFQUIST, K.E.B.: Drag on naturally rippled beds under oscillatory flows. *Miscellaneous Paper CERC-86-13*, 1986.
- LONGUET-HIGGINS, M.S.: Mass Transport in Water Waves. *Philosophical Transactions of the Royal Society of London, Series A*, Vol. 245, No. 903, 1953.
- LONGUET-HIGGINS, M.S.: Mass Transport in the Boundary Layer at a Free Oscillatory Surface. Vol. 8., *National Institute of Oceanography*, Wormley, Surrey, England, 1960.
- LONGUET-HIGGINS, M.S.: Oscillating flow over steep sand ripples. *Journal of Fluid Mechanics* 107, pp. 1-37, 1981.
- MACDONALD, N.J.; O'CONNOR, B.A.: Changes in wave impact on the Flemish coast due to increased mean sea level. *Journal of Marine Systems*, 7, pp. 133-144, 1996.
- MADSEN, O.S.; GRANT, W.D.: Sediment transport in the coastal environment. Report No. 209, Palph M Parson Lab, MIT, 1976.
- MANOHAR, M.: Mechanics of bottom sediment movement due to wave action. *U.S. Army Corps Engineers*, Beach Erosion Board Tech. Memo No. 75, 1955.
- McFETRIDGE, W.F.; NIELSEN, P.: Sediment suspension by non-breaking waves over rippled beds. *Tech. Rep.UFL/COEL-85/005*, Coastal & Oceanographical Engineering Dept., University of Florida, Gainesville, 1985.
- MICHE, R.: Mouvements Ondulatoires de la Mer en Profendeur Constante ou Decroissante. *Annales des Ponts et Chaussees*, 1944.
- MICHELL, J.H.: On the highest Waves in Water. *Philosophical Magazine*, 5th Series, Vol. 36, 1893.
- MILLER, M.C.; MCCAIVE, I.N., KOMAR, P.D.: Threshold of Sediment Motion under Unidirectional Current. *Sedimentology*, Vol. 24, pp. 507-527, 1977.
- MITCHIM, C.F.: Oscillatory Waves in Deep Water. *The Military Engineer*, 1940.

- MURRAY, K.B.; ADDISON, P.S.: Thresholding Coherent Flow Structures from a Turbulent Wake using Wavelet Transform Analysis. *ASCE Engineering Mechanics Conference*, 1999.
- NELSON, M.E.; BENEDICT, P.C.: Measurement and analysis of suspended sediment loads in streams. *Proceedings of the ASCE*, 76, pp. 1-28, 1950.
- NIELSEN, P.: Some basic concepts of wave sediment transport. *Series paper 20*, Institute of Hydraulic Engineering, Technical University of Denmark, 1979.
- NIELSEN, P.: Dynamics and geometry of wave-generated ripples. *Journal of Geophysical Research*, Vol. 86, No. C7, 1981.
- NIELSEN, P.: Entrainment and distribution of different sand sizes under water waves. *Journal of Sedimentary Petrology*, Vol. 53, No. 2, pp. 423-428, 1983.
- NIELSEN, P.: Field measurements of time-averaged suspended sediment concentrations under waves. *Coastal Engineering*, Vol. 8, pp. 51-72, 1984.
- NIELSEN, P.: Suspended sediment concentrations under waves. *Coastal Engineering*, 10, pp. 23-31, 1986.
- NIELSEN, P.: Towards modelling coastal sediment transport. *Proceeding of the 21st International Conference of Coastal Engineering*, Torremolinos, pp. 1952-1958, 1988.
- NIELSEN, P.: Coastal bottom boundary layers and sediment transport. In P Bruun ed. *Port Engineering* (4th edition), Vol. 2, pp. 550-585, 1990.
- NIELSEN, P.: Coastal bottom boundary layers and sediment transport. *World Scientific Publication, Advanced series in Ocean Engineering* , Vol.4, 1992.
- O'CONNOR, B.A., KIM, H.S., WILLIAMS, J.J.: Hydrodynamics of random wave boundary layers. *Coastal Dynamics '94*, February 21-25, 1994, Universitat Politècnica de Catalunya, Barcelone, Spain, 1994.
- OSBORNE, P.D.; GREENWOOD, B.: Sediment suspension under waves and currents: time scales and vertical structures. *Sedimentology*, 40, pp. 599-622, 1993.
- OSBORNE, P.D.; VINCENT, CH.,E.: Vertical and horizontal structure in suspended sand concentrations and wave induced fluxes over bedforms. *Marine Geology*, 131, pp. 195-208, 1996.

- OSBORNE, P.D.; VINCENT, CH.,E.; GREENWOOD, B.: Measurement of suspended sand concentrations in the nearshore: field intercomparison of optical and acoustic backscatter sensors. *Continental Shelf Research*, Vol. 14, No. 2/3, pp. 159-174, 1994.
- PERRIER, V.; PHILIPOVITCH, T.; BASDEVANT, C.: Wavelet spectra compared to Fourier spectra. *Journal Math. Physics*, 36(3), pp. 1506-1519, 1995.
- QUI, L.J.; ER, M.H.: Wavelet spectrogram of noisy signals. *International Journal of Elec.*, 79, pp. 665-677, 1995.
- RIBBERINK, J.S.: Bedload transport for steady flows and unsteady oscillatory flows. *Journal of Coastal Research*, Vol. 34, pp. 59-82, 1998.
- RIBBERINK, J.S.; AL-SALEM, A.A.: Bedforms, near-bed sediment concentrations and sediment transport in simulated regular wave conditions. *Rep. H840*, Part 3, Delft Hydraulics, Delft, The Netherlands, 1989.
- RIBBERINK, J.S.; AL-SALEM, A.A.: Sediment transport in oscillatory boundary layers in cases of rippled beds and sheet flow. *Journal of Geophysical Research*, Vol. 99, No. C6, pp. 12707-12727, 1994.
- RIBBERINK, J.S.; AL-SALEM, A.A.: Sheet flow and suspension of sand in oscillatory boundary layer. *Coastal Engineering* 25, pp. 205-225, 1995.
- ROSE, C. Suspended sediment transport in storm conditions. *Ph.D. thesis*, The University of Birmingham, 1997.
- RUSSELL, R.C.H.; OSORIO, J.D.C.: An Experimental Investigation of Drift Profiles in a Closed Channel. *Proceedings of the Sixth Conference on Coastal Engineering*, American Society of Civil Engineers, 1958.
- SEYMOUR R.J.: Threshold Effects of Sediment Transport by waves. *Journal of Waterway, Port, Coastal and Ocean Engineering*, Vol. 111, No. 2, 1985.
- SHENG, J.; HAY, A.E.: An examination of spherical scatter approximation in aqueous suspensions of sand. *Journal of the Acoustical Society of America*, Vol. 83, No. 2, 1998.
- SHI, N.C.: Reverse Sediment Transport induced by Amplitude-modulated Waves. *University of Washington*, Washington, USA, 1983.

- SHIELDS, A.: Anwendung der Ähnlichkeitsmechanik und der Turbulenzforschung auf die Geschiebebewegung. *Mitteilungen der Preußischen Versuchsanstalt für Wasserbau und Schiffbau*, Heft 26, 1936.
- SLEATH, J.F.A.: Transition in oscillatory flow over rippled beds. *Proceeding of the Institute of Civil Engineers*, 59, 1975.
- SLEATH, J.F.A.: Measurements of bed load in oscillatory flow. *Proceedings ASCE, Journal of Waterway, Port, Coastal and Ocean Engineering*, Div. 104 (WW3), pp. 291-307, 1978.
- SLEATH, J.F.A.: *Sea Bed Mechanics*. John Wiley and Sons, New York, p. 39, 1984.
- SLEATH, J.F.A.: Turbulent oscillatory flow over rough beds. *Journal of Fluid Mechanics*, 182, pp. 369-409, 1987.
- SOULSBY, R.: Calculating bottom orbital velocity beneath waves. *Coastal Engineering*, 11, pp. 371-380, 1987.
- SOULSBY, R.: *Dynamics of marine sand*. Thomas Telford Publications, London, 1997.
- SPM: *Shore Protection Manual, Vol. 1*. Coastal Engineering Research Center. *Department of the Army, Waterways Experiment Station, Corps of Engineers, Washington D.C.*, 1984.
- STOKES, G.G.: *On the Theory of Oscillatory Waves*. *Mathematical and Physical Papers*, Vol. 1, Cambridge University Press, London, England, 1880.
- SUMER, B.M.; BAKIOGLU M.: On the formation of ripples on an erodible bed. *Journal of Fluid Mechanics*, Vol. 144, 1984.
- SUMER, B.M.; FREDSE, J.: *Hydrodynamics around cylindrical structures World Scientific Publication, Advanced series in Ocean Engineering*, Vol. 12, 1999.
- SYLVESTER, R.: *Coastal Engineering 1: Generation, propagation and influence of waves. Developments in Geotechnical Engineering 4A*, 1974.
- TANN, H.M.: The estimation of wave parameters for the design of offshore structures. *Institute of Oceanographic Sciences, Rep. No. 23*, 1976.
- THORNE, P.D.; CAMPBELL, S.C.: Backscattering by a suspension of spheres. *Journal of the Acoustic Society of America*, 92(2), pp. 978-986, 1992.

- THORNE, P.D.; HARDCASTLE, P.J.: Acoustic measurements of suspended sediments in turbulent currents and comparison with in-situ samples. *Journal of the Acoustic Society of America*, 101(5), pp. 2603-2614, 1997.
- THORNE, P.D.; HARDCASTLE P.J.; HOGG, A.: Observations of Near-bed Suspended Sediment Turbulence Structures using Multifrequency Acoustic Backscattering. *Coherent Flow Structures in Open Channels*, John Wiley and Sons Ltd., pp. 343-358, 1996.
- THORNE, P.D.; HARDCASTLE P.J.; SOULSBY, R.L.: Analysis of Acoustic Measurements of Suspended Sediments. *Journal of Geophysical Research*, Vol. 98, No. C1, pp. 899-910, 1993.
- THORNE, P.D.; WILLIAMS, J.J., DAVIES, A.G.: Suspended sediments under waves measured in a large scale flume facility. *Journal of Geophysical Research* (submitted) 2001.
- TOOBY, P.F.; WICK, G.L.; ISAACS, J.D.: The Motion of a Small Sphere in a Rotating Velocity Field: A Possible Mechanism for Suspending Particles in Turbulence. *Journal of Geophysical Research*, Vol. 82, No. 15, 1977.
- TORRENCE, CH.: Wavelet Analysis, Published notes on the world wide web: <http://paos.colorado.edu/research/wavelets/>, 1999.
- TORRENCE, CH.; COMPO G.P.: A practical guide to Wavelet Analysis. *Bulletin of the American Meteorological Society*, Vol. 79, No.1, 1998.
- TUCKER, M.J.: Analysis of Records of Sea Waves. *Proceedings of the Institution of Civil Engineers*, Vol. 26, 1963.
- TUNSTALL, E.B.; INMAN, D.L.: Vortex Generation by Oscillatory Flow over Rippled Surfaces. *Journal of Geophysical Research*, Vol. 80, No. 24, pp. 3475-3484, 1975.
- URSELL, F.: Mass Transport in Gravity Waves. *Proceedings of the Cambridge Philosophical Society*, Vol. 49, 1953.
- VAN RIJN, L.C.: Handbook of sediment transport by currents and waves. *Delft Hydraulics*, Delft, The Netherlands, 1989.
- VILLARD, P.V.; OSBORNE, P.D.; VINCENT, CH.E.: Influence of wave groups on sand re-suspension over bedforms in a large wave flume. *Coastal Sediments '99*, 1999a.
- VILLARD, P.V.; OSBORNE, P.D.; VINCENT, CH.E.: Description of SSC events under wave groups. *Canadian Coastal Conference*, 1999b.

- VILLARD, P.V.; OSBORNE, P.D.; VINCENT, CH.E.: Influence of wave groups on SSC patterns over vortex ripples. *Continental Shelf Research* 20, pp. 2391-2410, 2000.
- VINCENT, CH.E.; DOWNING, A.: Variability of suspended sand concentrations, transport and eddy diffusivity under non-breaking waves on the shoreface. *Continental Shelf Research*, Vol. 14, No. 2/3. pp. 223-250, 1994.
- VINCENT, CH.E.; GREEN, M.O.: Field Measurements of the Suspended Sand Concentration Profiles and Fluxes and of the Resuspension Coefficient γ_0 Over a Rippled Bed. *Journal of Geophysical Research*, Vol. 95, No. C7, pp. 11591-11601, 1990.
- VINCENT, CH.E.; OSBORNE, P.D.: Bedform dimensions and migration rates under shoaling and breaking waves. *Continental Shelf Research*, Vol. 13, No. 11, pp. 1267-1280, 1993.
- VINCENT, CH.E.; HANES, D.M.; BOWEN, A.J.: Acoustic measurements of suspended sand on the shoreface and the control concentration by bed roughness. *Marine Geology*, 96, pp. 1-18, 1991.
- WILLIAMS, J.J.: CSTAB – Circulation and sediment transport around banks. *Cruise report No. 16, Proudman Oceanographic Laboratory internal report*, 53 pp, 1993.
- WILLIAMS, J.J.; ROSE, C.P.; THORNE, P.D.; COATES, L.E.; WEST, J.R.; HARDCASTLE, P.J.; HUMPHREY, J.D.; MOORES, S.P.; WILSON, D.J.: Observed Suspended Sediments in Storm Conditions. *International Conference Coastal Engineering Research Council/ASCE*, Orlando, Florida, 1996.
- WILLIAMS, J.J.; BELL, P.S.; COATES, L.E.; HARDCASTLE, P.J.; HUMPHREY, J.D.; MOORES, S.P.; THORNE P.D.; TROUW, K.: Evaluation of Field Equipment used in Studies of Sediment Dynamics. *Proudman Oceanographic Laboratory, Report No. 53*, 45pp., 1998.
- WILLIAMS, J.J.; ROSE, C.P.; THORNE, P.D.; O'CONNOR, B.A.; HUMPHREY, J.D.; HARDCASTLE, P.J.; MOORES, S.P.; COOKE, J.A.; WILSON, D.J.: Field observations and predictions of bed shear stress and vertical suspended sediment profiles in wave-current conditions. *Continental Shelf Research*, 19 (4), pp. 507-536, 1999a.
- WILLIAMS, J.J.; ROSE, C.P.; VAN RIJN, L.C.: Suspended Sediment Concentration Profiles in Wave-Current Flows. *Journal of Hydraulic Engineering*, Vol. 125, No.9, pp. 906-911, 1999b.

- WILLIAMS J.J.; BELL P.S.; THORNE P.D.; TROUW K., HARDCASTLE P.J.; HUMPHERY J.D.:
Observed and Predicted Vertical Suspended Sediment Concentration Profiles and
Bedforms in Oscillatory-Only Flow. *Journal of Coastal Research*, 16(3), 698-708, 2000.
- WILLIAMS J. J., ROSE C. P. & THORNE P. D.: Role of wave groups in resuspension of sandy
sediments. *Marine Geology* (in press), 2001.
- YALIN, M.S.: Geometrical properties of sand waves. *Proceeding of the A.S.C.E. Journal of
Hydraulic Division* 90 (HY5), 1964.
- YALIN, M.S.: On the Determination of Ripple Geometry. *Journal of Hydraulic Engineering*,
Vol. 111, No.8, 1985.
- ZYSERMAN J.A.; FREDSE, J.: Data analysis of bed concentration of sediment. *Journal of
Hydraulic Engineering*, 120 (9), pp. 1021-1042, 1994.

Appendix A

A.1 Reflection Analysis

For the reflection analysis the following equations were applied (KETABDARI, 1999):

Consistent with linear order wave theory, a non-breaking regular wave can be expressed as:

$$\eta(x,t) = a_i \cdot \cos(k \cdot x - \omega \cdot t + \Phi_i) + a_R \cdot \cos(k \cdot x + \omega \cdot t + \Phi_R) \quad (A.1)$$

with: a_i = incident wave amplitude
 Φ_i = incident phase shift
 a_R = reflected wave amplitude
 Φ_R = reflected phase shift

The first term indicates an incident wave moving in the positive x-direction and the second term indicates the reflected wave moving in the opposite direction.

The two measured time series of surface waves are given by:

$$\eta_1(t) = \sum_{i=1}^{\infty} [a_{i_i} \cdot \cos(\Phi_{i_i} - \omega_i \cdot t) + a_{R_i} \cdot \cos(\Phi_{R_i} + \omega_i \cdot t)] \quad (A.2)$$

$$\eta_2(t) = \sum_{i=1}^{\infty} [a_{i_i} \cdot \cos(\Phi_{i_i} - \omega_i \cdot t + k_i \cdot \Delta l) + a_{R_i} \cdot \cos(\Phi_{R_i} + \omega_i \cdot t + k_i \cdot \Delta l)] \quad (A.3)$$

with: a_{i_i} = incident wave amplitude for each frequency component
 a_{R_i} = reflected wave amplitude for each frequency component
 Φ_{i_i} = incident wave phase for each frequency component
 Φ_{R_i} = reflected wave phase for each wave component

Applying a FFT to the time series records of wave elevation, the wave profiles can be expressed as:

$$\eta_1(t) = \sum_{i=1}^{\infty} [A_i \cdot \cos(\omega_i \cdot t) + B_i \cdot \sin(\omega_i \cdot t)] \quad (A.4)$$

$$\eta_2(t) = \sum_{i=1}^{\infty} [C_i \cdot \cos(\omega_i \cdot t) + D_i \cdot \sin(\omega_i \cdot t)] \quad (A.5)$$

$$\text{with: } A_i = a_{i_i} \cdot \cos \Phi_{i_i} + a_{R_i} \cdot \cos \Phi_{R_i} \quad (A.6)$$

$$B_i = a_{i_i} \cdot \sin \Phi_{i_i} + a_{R_i} \cdot \sin \Phi_{R_i} \quad (A.7)$$

$$C_i = a_{i_i} \cdot \cos(k_i \cdot \Delta l + \Phi_{i_i}) + a_{R_i} \cdot \cos(k_i \cdot \Delta l + \Phi_{R_i}) \quad (A.8)$$

$$D_i = a_{i_i} \cdot \sin(k_i \cdot \Delta l + \Phi_{i_i}) + a_{R_i} \cdot \sin(k_i \cdot \Delta l + \Phi_{R_i}) \quad (A.9)$$

This is a system of four equations with four unknown parameters a_{i_i} , a_{R_i} , Φ_{i_i} and Φ_{R_i} for each frequency component. Solving these equations the spectral components at each discrete Fourier coefficient are given by:

$$a_{i_i} = \frac{1}{2|\sin(k_i \cdot \Delta l)|} \cdot \left[\begin{aligned} & (C_i - A_i \cdot \cos(k_i \cdot \Delta l) - B_i \cdot \sin(k_i \cdot \Delta l))^2 \\ & + (D_i - B_i \cdot \cos(k_i \cdot \Delta l) + A_i \cdot \sin(k_i \cdot \Delta l))^2 \end{aligned} \right]^{1/2} \quad (\text{A.10})$$

$$a_{R_i} = \frac{1}{2|\sin(k_i \cdot \Delta l)|} \cdot \left[\begin{aligned} & (C_i - A_i \cdot \cos(k_i \cdot \Delta l) + B_i \cdot \sin(k_i \cdot \Delta l))^2 \\ & + (D_i - B_i \cdot \cos(k_i \cdot \Delta l) - A_i \cdot \sin(k_i \cdot \Delta l))^2 \end{aligned} \right]^{1/2} \quad (\text{A.11})$$

$$\Phi_{i_i} = \tan^{-1} \left[\frac{(-C_i + A_i \cdot \cos(k_i \cdot \Delta l) + B_i \cdot \sin(k_i \cdot \Delta l))}{(D_i - B_i \cdot \cos(k_i \cdot \Delta l) + A_i \cdot \sin(k_i \cdot \Delta l))} \right] \quad (\text{A.12})$$

$$\Phi_{R_i} = \tan^{-1} \left[\frac{(C_i - A_i \cdot \cos(k_i \cdot \Delta l) + B_i \cdot \sin(k_i \cdot \Delta l))}{(D_i - B_i \cdot \cos(k_i \cdot \Delta l) - A_i \cdot \sin(k_i \cdot \Delta l))} \right] \quad (\text{A.13})$$

In order to test the FFT in EXCEL a data set consisting of a simple sine wave was generated and this was then subjected to the reflection analysis. While doing the analysis of the simulated data set, it turned out that the sign of the imaginary part of the FFT is vital for the correct separation between incident and reflected waves.

Equations A.13 and A.14 contain singularities that occur when

$$\sin(k_i \Delta l) = 0 \quad \text{or} \quad k_i \Delta l = n \cdot \pi \quad (\text{A.14})$$

To avoid this problem, GODA AND SUZUKI (1976), recommended a guideline for the effective range of resolution:

$$0.05 < \Delta l/L < 0.45 \quad (\text{A.15})$$

Appendix B

B.1 Wavelets

In chapter 4 three different wavelet functions or parent wavelets (Morlet, Mexican Hat, Paul) were presented and their effects on the profile data investigated. These are not the only wavelets that can be found in the literature. However, all available wavelets fall into two general categories: continuous and discrete. FARGE (1992), stated that in general the term wavelet function refers to either orthogonal or nonorthogonal wavelets. The term wavelet basis refers only to orthogonal wavelets and also implies the use of the discrete wavelet transform. In contrast, the nonorthogonal wavelet function can be used with either the discrete or the continuous wavelet transform. According to ADDISON AND WATSON (1999), the choice of wavelet function used for a signal processing application depends on a variety of factors including speed of computation, the shape of signal specific features, the frequency resolution and the statistical analysis to be performed.

The main differences between a discrete and a continuous wavelet transform is that the discrete transform is restricted to a dyadic grid structure. This means that the change in translation and scale is restricted to discrete scales, which are an integer power of 2. The continuous wavelet transform is not restricted to this structure, which leads to a high resolution in wavelet space at lower frequencies, but also to a high redundancy. The continuous wavelet transform is presented here.

B.2 The Continuous Wavelet Transform

The wavelet transform for a continuous time signal $x(t)$ is defined as:

$$C(s,b) = \frac{1}{\sqrt{s}} \int_{-\infty}^{\infty} \Psi\left(\frac{t-b}{s}\right) \cdot x(t) dt \quad (\text{B.1})$$

where $\Psi\left(\frac{t-b}{s}\right)$ is the analysing wavelet transform, s is the scale and b depends on the translation of the wavelet along the signal. The wavelet coefficient C is an index of how closely the analysing wavelet matches the signal at a specific time window and a particular scale. If the fundamental wavelet resembles the analysed signal well, then at some scales and positions, where the form of the wavelet matches the form of the signal closely there will be high correlation and therefore a high coefficient.

As mentioned above there are a number of parent wavelets available in the literature. To be

admissible as a wavelet, the function must have zero mean and be localised in both time and frequency space (FARGE, 1992). Additionally, ADDISON AND WATSON (1997), stated that the wavelet function must have finite energy and for a wavelet function described by a complex function its Fourier transform must be real, and must vanish for a wave number less or equal to zero. To ensure that the wavelet transforms at each scale s are directly comparable to each other and to the transforms of other time series, the wavelet function at each scale s is normalised to have unit energy (TORRENCE AND COMPO, 1998).

The Morlet and Mexican Hat wavelet are presented here as examples of wavelet functions. The Morlet wavelet is a product of a sine curve modulated by a Gaussian envelope. It is defined by TORRENCE (1999), as:

$$\Psi_0(\eta) = \pi^{-1/4} \cdot e^{i \cdot k \cdot \eta} \cdot e^{-\eta^2 / 2} \quad (\text{B.2})$$

where Ψ is the wavelet value at non-dimensional time η and k is the wave number, which gives the number of oscillations within the wavelet itself. The wavelet is only marginally admissible, because it has no zero mean. However, in practice if $|k|=6$, the deviation of the mean from zero is of the same order as typical computer round off errors (FARGE, 1992). Equation B.2 is the basic wavelet function. Introducing a scaling factor s for the dilation and a translation parameter the following equation can be written as:

$$\Psi\left[\frac{(n' - n) \cdot \delta t}{s}\right] = \left(\frac{\delta t}{s}\right)^{1/2} \Psi_0\left[\frac{(n' - n) \cdot \delta t}{s}\right] \quad (\text{B.3})$$

$$\text{or } \Psi\left[\frac{t - b}{s}\right] = \left(\frac{\delta t}{s}\right)^{1/2} \Psi_0\left[\frac{t - b}{s}\right] \quad (\text{B.3a})$$

where s is the scaling parameter and n and b are the translation parameter used to slide in time, respectively. The factor of $s^{-1/2}$ is to normalise the total energy to unity.

The Mexican hat wavelet is given by

$$\Psi(\eta) = (1 - \eta^2) \cdot e^{-\left(\frac{\eta^2}{2}\right)} \quad (\text{B.4})$$

The most noticeable difference between the Morlet and Mexican hat is the fine scale structure. This is because the Mexican hat is real valued and captures both the positive and negative oscillations of the time series as separate peaks in wavelet power. According to TORRENCE AND GOMPO (1998), the Mexican hat wavelet produces narrower spikes along the time direction, but is more elongated along the scale direction.

Most of the data to be analysed is in discrete format with N values at time intervals of δt . Therefore equation B.3 together with equation B.1 yields:

$$C(s,n) = \sum_{n'=0}^{N-1} x_{n'} \cdot \Psi^* \left[\frac{(n'-n) \cdot \delta t}{s} \right] \quad (\text{B.5})$$

$$\text{or } C(s,b) = \sum_{n'=0}^{N-1} x(t) \cdot \Psi^* \left[\frac{t-b}{s} \right] \quad (\text{B.5a})$$

where the $*$ denotes the complex conjugate.

The above sum can be evaluated for various values of scales (usually taken as multiples of the lowest possible frequency), as well as all values of n between the start and end of a signal. A two-dimensional picture of the variability of the signal can then be constructed by plotting the power (absolute values squared) of the wavelet transform. This gives information of the relative power at a certain scale and time.

The smallest resolvable scale is $2 \cdot \delta t$ and the larger scales are chosen as multiples of the smallest scale. The largest scale chosen should be less than a half the length of the entire time series. The first wavelet translation has the wavelet centred and covering the entire signal.

In order to speed up the wavelet transform, it is possible to compute the wavelet transform in the frequency domain using a FFT (TORRENCE, 1999), as the wavelet transform is the cross correlation between two functions x and y . However, the Fourier transform of the signal and the wavelet function has to be known for this. In the frequency domain, the wavelet transform is

$$C(s,n) = \sum_{j=0}^{N-1} x_j^{\text{FFT}} \cdot \Psi_{\text{FFT}}^* (s\omega_j) \cdot e^{i\omega_j \cdot n \cdot \delta t} \quad (\text{B.6})$$

where FFT indicates the Fourier Transform and $*$ is the complex conjugate. The Fourier transform of the wavelet function is given by

$$\Psi_{\text{FFT}}(s\omega_j) = \left(\frac{2 \cdot \pi \cdot s}{\delta t} \right)^{1/2} \cdot \Psi_{0,\text{FFT}}(s\omega_j) \quad (\text{B.7})$$

According to TORRENCE (1999), the FFT allows the computation of all n points simultaneously, which is in contrast to the computation of the cross correlation in the time domain.

B.3 Wavelet Energy Density

After determining the wavelet coefficients the wavelet energy density function can be calculated using

$$E(s,n) = \frac{|C(s,n)|^2}{C_g \cdot s^2} \quad (\text{B.8})$$

where C_g is the admissibility constant, which is determined by the wavelet used in the transform. For the Mexican hat wavelet $C_g = \pi$. Dominant structures are then characterised by large local $E(s,n)$ values (ADDISON, 1999). By integrating the wavelet energy $E(s,n)$ over the translation range n , it is possible to produce one dimensional energy spectra $E(n)$. After converting the scale to frequency and dividing by the total length of the signal, T , the one dimensional wavelet power spectrum can be obtained and compared with the energy spectrum determined by Fourier Transform. Examples of this can be found in ADDISON (1999). He stated that the wavelet power spectrum is smeared over the peak in the Fourier spectrum due to the frequency distribution within each wavelet.

The specific shape of a wavelet spectrum is very dependent upon the choice of wavelet functions used due to the different shapes of the wavelet functions (QUI AND ER, 1995, PERRIER ET AL., 1995). This can be seen as an advantage or disadvantage. As the chosen wavelet ought to represent the features in the signal, good correlation between the wavelet function and the signal results in higher wavelet coefficients. A scalogram then reflects the features in the signal. Using a wavelet function that does not represent the data or important features of the signal well, results in a weaker correlation and smaller wavelet coefficients.

Now when comparing Wavelet and Fourier Transform, it has to be kept in mind that the wavelet spectrum contains information of the energy distribution within the signal that is attributable to a specifically shaped wavelet over the range of scales. Therefore, wavelet coefficients only reflect the correlation between the chosen wavelet and the signal.

The total energy can then be determined by

$$E = \frac{1}{C_g} \iint \frac{1}{s^2} \cdot |C(s,n)|^2 \cdot dsdn \quad (\text{B.9})$$

B.4 Wavelet Thresholding

According to MURRAY AND ADDISON (1999), wavelet thresholding is a relatively new technique typically used to remove noise or compress data.

The decomposition of a time series using discrete wavelets results in wavelet coefficients corresponding to features in the signal at specific scales and times. If these features and hence the wavelet coefficients are small, they may be omitted without substantially affecting the main features of the data set. Thresholding introduces the idea of reducing (sometimes setting to zero) all coefficients that are less than a particular threshold value. An inverse wavelet transform is then performed to recover the reduced signal.

A number of thresholding techniques can be found in the literature. Scale thresholding is simple (MURRAY AND ADDISON, 1999), and just sets all wavelet coefficients below a certain scale to zero. Alternatively, coefficient dependent thresholds are used. In the literature there are two different ways of using a coefficient dependent threshold, a hard and a soft method. For the hard thresholding, the threshold is set at a value λ , which is a proportion of the absolute value at each scale and time. Coefficients above this threshold correspond to main features in the signal and are significant, whereas coefficients below the threshold correspond to noise or weaker feature in the signal.

$$C^{\text{hard}}(s, n) = \begin{cases} 0, & C(s, n) < \lambda \\ C(s, n), & C(s, n) \geq \lambda \end{cases} \quad (\text{B.10})$$

Soft thresholding sets all coefficients below the threshold λ to zero and all other values above λ are shrunk towards zero by an amount λ (MURRAY AND ADDISON, 1999). They defined soft thresholding as:

$$C^{\text{soft}}(s, n) = \begin{cases} 0, & |C(s, n)| < \lambda \\ \text{sign}(C(s, n)) \cdot (|C(s, n)| - \lambda), & |C(s, n)| \geq \lambda \end{cases} \quad (\text{B.11})$$

In general wavelet thresholding is a way of denoising the signal. Care has to be taken when removing noise to ensure that no important low energy information is removed. In contrast to normal filters it allows the denoising at different levels at different positions throughout the signal. According to GURLEY AND KAREEM (1999), this cannot be avoided. Defining the threshold is a topic of current research.

B.5 Significance Tests

To determine the significance of results of a wavelet transform, the spectrum has to be compared with a background noise spectrum. If the energy in the spectrum is above the background level, it is significant and likely to be a true feature in the signal.

Appendix C

C.1 Sediments

The median diameter of grains in suspension, d_{50s} , was calculated using

$$d_{50s} = d_{50} \cdot [1 + 0.001 \cdot (\sigma_s - 1) \cdot (T_* - 25)] \quad \text{for } 0 < T_* < 25 \quad (\text{C.1})$$

$$d_{50s} = d_{50} \quad \text{for } T_* \geq 25, \quad (\text{C.2})$$

VAN RIJN (1989), where the grain sorting parameter, $\sigma_s = 0.5 \cdot [(d_{84}/d_{50}) + (d_{50}/d_{16})]$ is based upon measured sediment properties and the sediment transport parameter T_* , determined by equation 2.35. Methods to calculate the peak skin-friction component of bed shear stress, $\hat{\tau}_{wg}$, and the critical bed shear stress for sediment entrainment, τ_{cr} are described below.

The settling velocity of grains in suspension was calculated using the formula

$$w_0 = \frac{v}{d_{50s}} \cdot \left[\left(10.36^2 + 1.049 \cdot D_{*s}^3 \right)^{1/2} - 10.36 \right] \quad (\text{2.56})$$

SOULSBY (1997), where the dimensionless grain size in suspension, D_{*s} , is given by

$$D_{*s} = \left[\frac{g \cdot \left(\frac{\rho_s}{\rho} - 1 \right)}{v^2} \right] \cdot d_{50s} \quad (\text{2.34}).$$

Here v and ρ are the kinematic viscosity ($\approx 1.11 \cdot 10^{-6}$ at 16°C), and the density ($\approx 999.0 \text{ kg/m}^3$) of water, respectively, and ρ_s is the measured density of the sediment (2653 kg/m^3).

The critical wave shear stress for sediment, τ_{cr} , was calculated using

$$\tau_{cr} = \Theta_{cr} \cdot g \cdot (\rho_s - \rho) \cdot d_{50} \quad (\text{C.3})$$

where the critical Shields parameter, Θ_{cr} , is

$$\Theta_{cr} = \frac{0.3}{1 + 1.2 \cdot D_*} + 0.055 \cdot [1 - \exp(-0.02 \cdot D_*)] \quad (\text{C.4}),$$

SOULSBY (1997). In this case the dimensionless grain size, D_* , was calculated using $d_{50s} = d_{50}$ in equation C.4.

C.2 Hydrodynamics

For monochromatic waves, the peak orbital amplitude at the bed, U_w , was calculated from linear theory using

$$U_w = \frac{\pi \cdot H}{T \cdot \sinh(k \cdot h)} \quad (\text{C.5}),$$

where H is the measured wave height, T is the measured wave period, k is the wave number ($k = 2 \cdot \pi / L$), L is the wavelength and h is the measured water depth. For irregular waves, U_w was approximated from measured values of the significant wave height H_s and the measured zero-crossing wave period, T_z , using the method given in SOULSBY (1987).

Irrespective of bed morphology, the mobilisation, entrainment and re-suspension of sand grains under moderate wave conditions are governed by the skin friction component of the total bed shear stress. For the rough turbulent wave boundary layer, the skin friction factor for grain-scale roughness, f_{wG} can be approximated using

$$f_{wG} = 0.237 \cdot r^{-0.52} \quad (\text{2.55}),$$

SOULSBY (1997). Here, the relative roughness is given by $r = A/k_{sG}$, the semi-orbital excursion is $A = U_w \cdot T / (2 \cdot \pi)$. The Nikuradse equivalent sand grain roughness is given by $k_{sG} = \beta \cdot D_x$, where β is a constant and D_x refers to x percentile grain roughness. Whilst it is normally assumed that $k_{sG} = 2.5 \cdot D_{50}$, values for $\beta \cdot D_x$ given in the literature vary considerably from $1.25 \cdot D_{35}$ to $5.1 \cdot D_{84}$, SLEATH (1984). Estimates of f_{wG} are therefore subject to a degree of uncertainty. Peak bed shear velocity values for grain-scale roughness, \hat{U}_{*wG} , were calculated using

$$\hat{U}_{*wG} = \left(0.5 \cdot f_{wG} \cdot \hat{U}_w^2 \right)^{0.5} \quad (\text{C.6}).$$

The acoustic ripple profiler (ARP) on STABLE provided *in situ* measurements of bed morphology from which estimates of the average ripple height, h_r , and wavelength, λ_r were determined.

C.3 Concentration profiles

For a rippled bed in wave-only conditions, c -profiles can be determined using the exponential convective model

$$c(z) = c_0 \cdot e^{-z/\ell} \quad (\text{2.66}),$$

NIELSEN (1992), where the vertical length scale parameterising the vortex ejection process in oscillatory flow over ripples, ℓ , is defined as

$$\ell = 0.075 \cdot \frac{U_w}{w_s} \cdot h_r \quad \text{for } \frac{U_w}{w_s} < 18 \quad (2.65a)$$

$$\ell = 1.4 \cdot h_r \quad \text{for } \frac{U_w}{w_s} \geq 18 \quad (2.65b)$$

$\bar{c}(z)$ is the time-averaged suspended sediment concentration value at height z and c_0 is the so called reference concentration of suspended sediment at the bed ($z = 0$) defined as

$$c_0 = 0.005 \cdot \rho_s \cdot \Theta_r^3 \quad (2.70),$$

NIELSEN (1992), p228. The modified effective Shields parameter Θ_r is given by

$$\Theta_r = \frac{\Theta_{2.5}}{(1 - \pi \cdot h_r / \lambda_r)^2} \quad (2.71),$$

where the grain roughness Shields parameter $\Theta_{2.5}$ was calculated by

$$\Theta_{2.5} = \frac{0.5 \cdot f_{2.5} \cdot U_w^2}{(s - 1) \cdot g \cdot d_{50}} \quad (2.72).$$

The special grain roughness friction factor, $f_{2.5}$ is based on SWART'S (1974) equation and a roughness of $k_{eG} = 2.5 \cdot D_{50}$ yields

$$f_{2.5} = \exp \left[5.213 \cdot \left(\frac{2.5 \cdot d_{50}}{A} \right)^{0.194} - 5.977 \right] \quad (C.7).$$

For combined wave-current conditions in the field and in the laboratory it has been shown that measured c -profiles can be simulated accurately using a diffusion-base expression in the form

$$\bar{c}(z) = c(a) \cdot \left(\frac{z + \ell \cdot \alpha}{a + \ell \cdot \alpha} \right)^{-\alpha} \quad (2.64),$$

WILLIAMS ET AL. (1996 and 1999). In Equation 2.64, $c(a)$ is the reference concentration at height a . In the present wave-only conditions, the term parameterising average bed shear velocity in combined wave-current conditions is omitted so that the Rouse-type coefficient α parameterising diffusive processes is defined as

$$\alpha = \frac{w_0}{\gamma \cdot \kappa \cdot u_*} \quad (2.63).$$

Here, it is assumed that the ratio of sediment diffusivity to eddy viscosity $\gamma = 1.0$ and the von Kármán constant $\kappa = 0.4$. In common with equation 2.66, ℓ is used to parameterise the vortex ejection mechanism and is defined here using equation 2.65a and 2.65b.

The reference concentration values, $c(a)$ in equation 2.64, were estimated using two existing expressions. In the first case, $c(a)$ values at $z = 2 \cdot d_{50}$ were calculated using an expression proposed by ZYSERMAN AND FREDSE (1994)

$$c(a) = \frac{0.331 \cdot (\Theta_s - 0.045)^{1.75}}{1 + 0.72 \cdot (\Theta_s - 0.045)^{1.75}} \quad (2.73)$$

for steady flow conditions. Here the skin Shields parameter, Θ_s , is defined as

$$\Theta_s = \frac{\hat{\tau}_{wG}}{\rho \cdot (s - 1) \cdot g \cdot d_{50}} \quad (2.74).$$

In the second case, $c(a)$ values at $z(a) = 0.5 \cdot h_r$ were calculated using an expression proposed by VAN RIJN (1989)

$$c(a) = \frac{0.015 \cdot d_{50} \cdot T_*^{1.5}}{z(a) \cdot D_*^{0.3}} \quad (2.75).$$

In this case, the dimensionless grain size, D_* , was calculated using $d_{50s} = d_{50}$ in equation 2.34. In the VAN RIJN formulation, the transport stage parameter, T_* , is defined by equation 2.35.

FIGURES

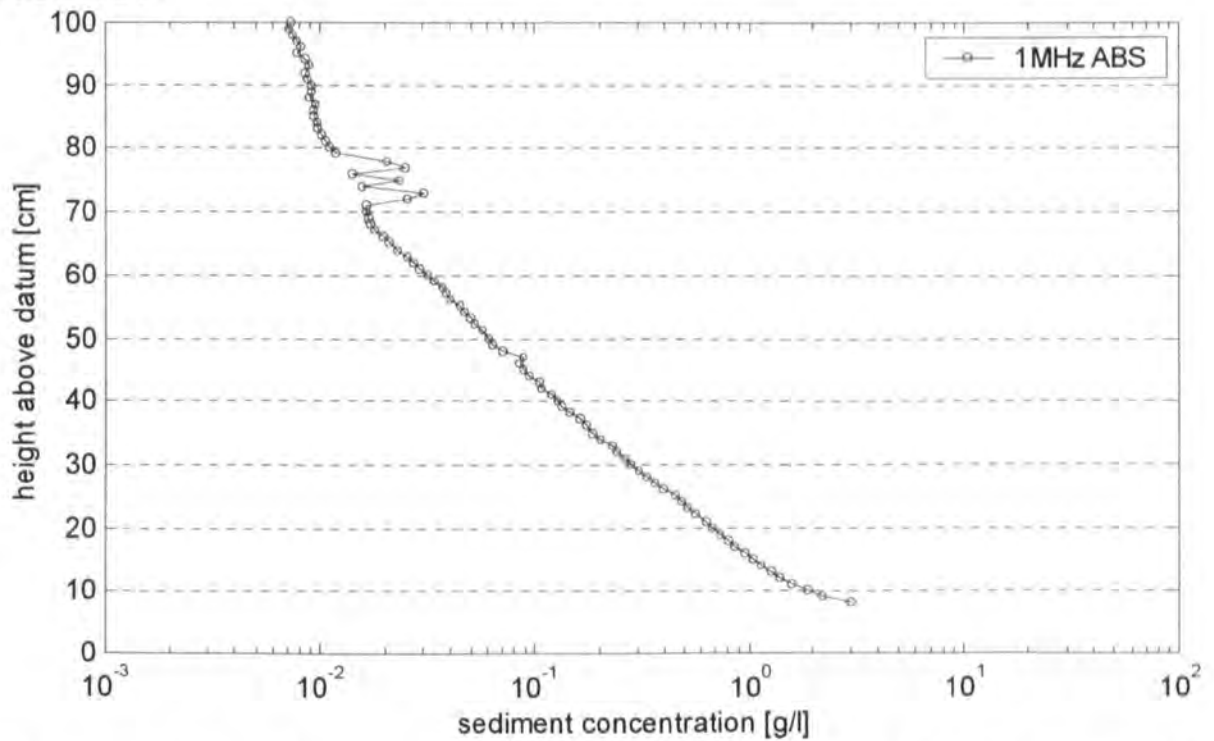


Figure C.1: Burst averaged suspended sediment concentration for burst a10a (irregular waves, $H_s = 1.07$ m).

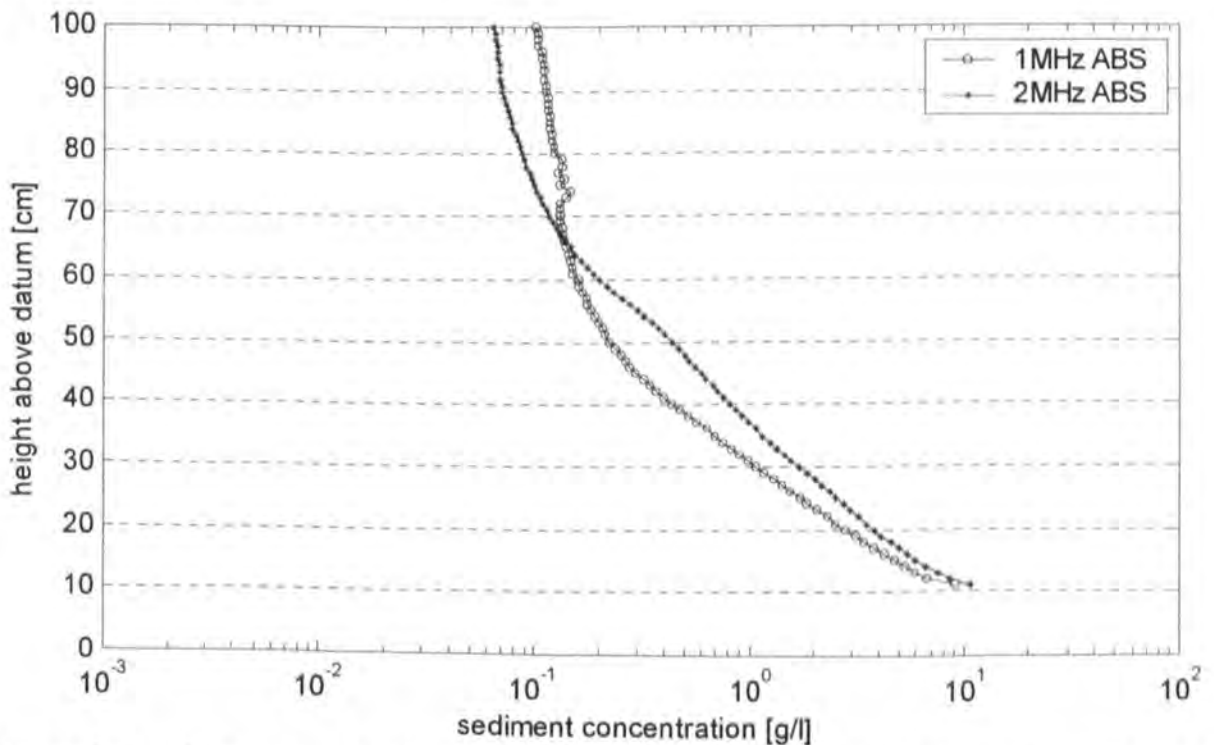


Figure C.2: Burst averaged suspended sediment concentration for burst a11a (regular waves, $H = 1.34$ m).

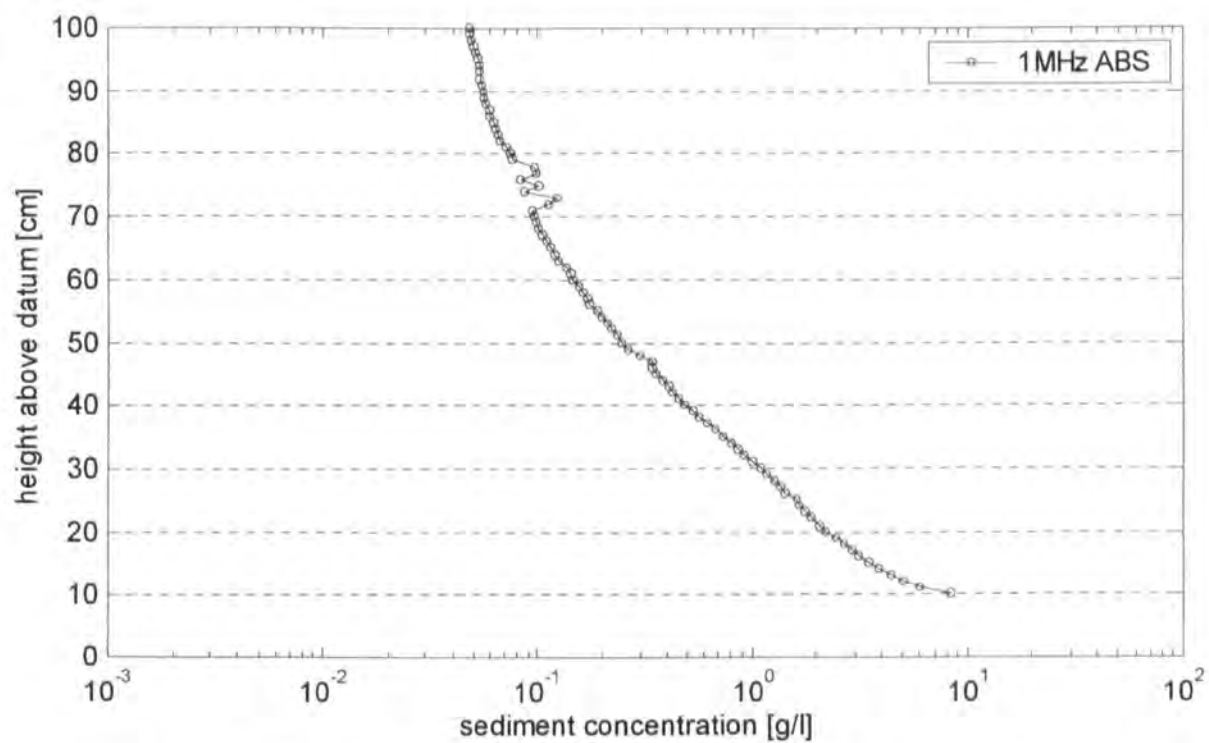


Figure C.3: Burst averaged suspended sediment concentration for burst a12a (irregular waves, $H_s = 1.26$ m).

Publications

- METJE, N.; WILLIAMS, J.J.; COATES, L.E.: Quantification of bed morphology and sediment transport beneath a large field deployment frame. *Poster presentation at the ICCE, 2000.*
- METJE, N.; WILLIAMS, J.J.; COATES, L.E.: Wave-induced sediment transport. *HANSA*, 138, Nr. 3, pp. 66-68, 2001.
- METJE, N.; COATES, L.E., WILLIAMS, J.J., ATKINS, P.R.: Determining the influence of an autonomous measuring rig (STABLE) on its surrounding environment using Fourier and Wavelet Transforms. Submitted to *Coastal Engineering* .
- METJE, N.; WILLIAMS, J.J., COATES, L.E., ATKINS, P.R.: Modelling convective sediment suspension processes. Abstract submitted to ICCE 2002.
- WILLIAMS, J.J.; BELL, P.S.; COATES, L.E.; METJE, N.; SELWYN, R.: Laboratory study of interactions between a large instrument deployment frame and oscillatory flow over a sandy bed. Submitted to *Continental Shelf Research* and under review.